Transport and Spectroscopic Studies of Layered Magnetic and Low-Dimensional Superconducting Materials

A Thesis

Submitted For the Degree of

Doctor of Philosophy (Science)

in

Physics (Experimental)

by

Riju Pal

Department of Physics

University of Calcutta

2025

Dedicated to

Baba & Maa

Acknowledgements

Reaching the end of my doctoral journey has been both a deeply rewarding and humbling experience. As I pause to reflect on the past several years, I am filled with immense gratitude for the people and institutions that have supported and shaped me along the way. This thesis is not just a compilation of years of research, experiments, and results; it is also the story of a personal and professional growth – one marked by perseverance, learning, multiple setbacks, and countless small victories along the way. The journey of a curious student from a small village near Kamarpukur, Hooghly, West Bengal, to becoming an independent research scholar at a renowned research institute like the S. N. Bose National Centre for Basic Sciences (SNBNCBS) in Kolkata has been through a lot of struggles, uncertainties, growth, moments of discovery, and constant inspiration.

My academic path at SNBNCBS began on 1st August 2017, when I joined as an Integrated Ph.D. (IPhD) student. Although I had been passionate about experiments since my early undergraduate days, I had very little understanding of how research in experimental physics actually conducted. The state-of-the-art research facilities and the research-oriented M.Sc. courses at SNBNCBS deeply motivated me and further strengthened my passion for research in experimental physics. Along the way, I shared a lot of experiences with many extraordinary people, and regardless of whether those moments were good or bad, they will remain etched in my memory forever. Though words may fall short in conveying the depth of my gratitude, I sincerely thank everyone who supported and motivated me throughout this long journey.

First and foremost, I would like to express my sincere and profound gratitude to my Ph.D. supervisor, *Dr. Atindra Nath Pal (Atin da)*, for his unwavering support, insightful guidance, continuous encouragement, and boundless enthusiasm throughout my doctoral journey, as well as during the time as a Master's project student under his supervision for more than a year. To me, he was more than just a supervisor. His positive and inspiring attitude played a crucial role in cultivating my strong interest in pursuing doctoral research in experimental condensed matter physics. I still remember the day when I was feeling a bit tense before my candidacy exam to transition from IPhD to Ph.D., and he took me out for tea to cheer me up and encourage me. His mentorship during my Ph.D. enabled me not only to accept the challenge of opening a new research field/direction but also to conceptualize and develop independent research projects. I am deeply thankful for the academic freedom he offered, the trust he consistently placed in me, and the motivating spirit he brought to me, even during moments of frustration and setbacks. Most importantly, his straightforward and approachable nature encouraged me to openly share all the academic problems I faced throughout my Ph.D. journey. His support helped

me navigate challenges with resilience, patience, and continue striving toward meaningful scientific contributions.

I am thankful to SNBNCBS for providing a beautiful green campus inside the urban city, excellent research facilities, and a friendly, intellectually stimulating research environment. I would like to convey my sincere gratitude to Emeritus *Prof. Prabhat Mandal (SNBNCBS, Kolkata)*, whose profound knowledge and deep wisdom greatly inspired me – be it through his guidance during data interpretation, discussions over tea to understand physics concepts, or while drafting final responses to reviewers in the field of magnetism. I sincerely acknowledge *Prof. Prabhat Mandal* and *Dr. Mintu Mondal (IACS, Kolkata)* for providing me with the high-quality single crystals. I would like to extend my gratitude to *Prof. Achintya Singha (Bose Institute, Kolkata)* for his enriching scientific discussions and for granting me the opportunity to conduct Raman spectroscopy in his laboratory. My sincere thanks go to *Prof. Biswajit Karmakar (SINP, Kolkata)* for allowing me to participate in our collaborative experiments using the dilution refrigerator. I respectfully thank *Prof. Tanmoy Das (IISc Bangalore, India), Prof. Tanusri Saha Dasgupta (SNBNCBS, India),* and *Dr. Debjani Karmakar (BARC, India)* for their theoretical calculations, which significantly contribute to the interpretation of our experimental findings. I am extremely grateful to *Prof. Anjan Barman* and *Prof. Priya Mahadevan* from SNBNCBS, who graciously evaluated the progress of my research as members of my thesis committee.

It was quite a unique experience to be a part of setting up the lab from scratch. I would like to express my heartfelt gratitude to my senior labmates – *Shubhadip da, Rafiqul da, Biswajit da, Shubhrasish da*, and the Post Doc. *Buddhadeb da* for providing such lively company on countless occasions in my early Ph.D. days. Special thanks to *Buddhadeb da* for your guidance, positive vibes during tough times, and steady support during lab experiments. You provided me with a very friendly and approachable behaviour, never making me feel the gap of seniority, which allowed me to comfortably share both academic and non-academic matters. Working with you during the first half of my Ph.D. tenure was truly enjoyable and greatly enriched my knowledge and enthusiasm for low-temperature experiments. We had a good understanding, which led to efficient teamwork. I am thankful to *Rafiqul da* for assisting me with LabVIEW, helping with experiment-related challenges, and for the engaging discussions (both scientific and non-scientific) we shared in the Oxford lab. I express my gratitude to all our current and past group members in the "Quantum Transport and Device Lab", including *Taniya di, Soumili di, Tausif, Shatabda da, Shubhankar, Dhriti, Gaurab, Kaustav, Sujoy da, Sayanika di, Safia di, Bikash da, Obai da, Dayal, Premananda, Mohona,* and *Anumita.* A lot of thanks to all of them for fostering a positive lab atmosphere and nurturing a conducive environment for research. I would like to cherish the friendly behaviour created by our initial lab members and other SNB

students during the COVID-19 pandemic. I thank *Shubhankar da (Vidyasagar College, Kolkata)* for his assistance during an analysis related to my research work. My heartfelt gratitude goes to *Dr. Sudipto Chakrabarti (SINP, Kolkata)* and *Suswapna* for assisting with atomic force microscopy characterization during the review process of my manuscript. I gratefully acknowledge *Dr. Vidya Kochat (IIT Kharagpur)* for allowing me to stay on campus and access the EBL facility, and *Vineet* for assisting in device fabrication. I extend my sincere thanks to all of our collaborators - *Prof. Debraj Choudhury, Suchanda di, Arnab da, Satyabrata da, Abhishek da, Aminur da, Chumki di, Swarnamayee di, Bikash, Nur da*, and many others.

I am extremely grateful to my M.Sc. and Ph.D. course teachers from SNBCNBS – *Prof. Amitabha Lahiri, Prof. SS Manna, Dr. M. Sanjay Kumar, Prof. Samir Kumar Pal, Prof. Soumen Mondal, Dr. Ramkrishna Das, Prof. Kalyan Mandal, Prof. Sunandan Gangopadhyay, Prof. Manoranjan Kumar, Prof. Manik Pradhan, Dr. Suman Chakrabarty, Prof. Rajib Kr. Mitra, Prof. Anjan Barman, Prof. Priya Mahadevan, Prof. Ranjan Choudhury, Dr. T. Setti, Prof. Tanusri Saha-Dasgupta*, and many more – for their excellent teaching, help in the clear understanding of concepts, and well-structured courses that laid a strong foundation for my research journey.

I am extremely thankful to *Prof. Tanusri Saha-Dasgupta* and *Prof. Dr. Bernd Büchner* for facilitating the MoU between SNBNCBS, India, and IFW Dresden, Germany. This collaboration provided me with the invaluable opportunity to visit IFW Dresden for approximately ten months over two visits during my Ph.D. tenure, where I was able to carry out Electron Spin Resonance (ESR) spectroscopy experiments on my samples. Thank you, *Atin da*, for believing in me and for enabling this visit. I sincerely appreciate the excellent mentorship, support, and guidance of my project supervisors at IFW Dresden — *Prof. Dr. Bernd Büchner, Dr. Vladislav Kataev, and Dr. Alexey Alfonsov.* I would like to extend my heartfelt gratitude to *Dr. Alexey Alfonsov*, from whom I gained invaluable insights into ESR spectroscopy. His patient and clear explanations, no matter how many questions I asked, significantly enriched my understanding, experience, and interest in this field. I truly appreciate his systematic approach to guidance, meticulous planning, and unwavering focus on achieving research goals. His positive energy and deep engagement with the experiments were truly motivating and left a lasting impression on me. A special acknowledgment to *Dr. Kataev* for his intuitive ideas and valuable input throughout the project. I am thankful to *Joyal* for helping me with ESR experiments. I extend my sincere gratitude to *Prof. Dr. Axel Lubk* and *Dr. Daniel Wolf* for their valuable support and guidance during the Lorentz TEM experiments. It was a privilege to receive such a warm welcome from *Dr. Silvia Seiro* during our first visit to IFW, and I am deeply grateful to her. Her assistance and ever-helpful attitude greatly aided our understanding of various aspects of life and research in Germany, making our experience in IFW and Dresden

truly enriching. I had a wonderful time with my seniors and colleagues — *Susmita di, Shantonu da, Surya Narayan da, Monodip, Aishwaryo, Koushik, Banik*, and *Sourabh* — during my two visits to IFW Dresden. Thanks to them, my stay was never boring — it was both enjoyable and memorable. I also thank *Kranti* for engaging in valuable scientific discussions with me at IFW.

I would like to acknowledge the staff of the technical cell at SNBNCBS – *Debarghya da, Sourav da, Urmi di, Amit da, Dipayan da, Aditya da, Shakti da,* and *Joy da* from the central facility labs, as well as *Amit da* and *Subhabrata da* from the mechanical workshop, for their invaluable technical assistance throughout my research at SNBNCBS. I also extend my heartfelt thanks to all the SNB staff, including those in academic (*Moumita mam, Chandrakana mam, Jaideep da, Rupam da*), accounts, library (*Amit da, Gurudas da*), purchase, engineering (*Supriyo da, Ganesh da, Sani da*), computer (*Bijoy da, Deblina mam*) and electrical sections (*Soumyadip da, Tanmoy da*), as well as the doctors of the medical unit, for their unwavering support. I am grateful to *Ms. Nibedita Konar (DR, Academic)* for always providing timely solutions to all the academic-related issues, to *Mr. Suman Saha (DR, Finance)* for his guidance in navigating the financial aspects in international conferences, and to *Mr. Swarup Dutta* for his constant assistance with bill-related administrative procedures.

Beyond my lab, I sincerely thank all my colleagues at SNBNCBS, especially *Piya di, Didhiti di, Anupam da, Swarnali di, Mahebub da, Koushik da, Aslam da, Shankar da, Sutapa di, Subrata da, Rakesh da, Samiran da, Monalisa di, Sourav da, Ananda da, Surya Narayan da (Panda da), Indranil da, Subhamita di, Tuhin da, Supriyo da, Sudip da, Sayan da, Snehamoyee di, Dhiraj da, Sumanti di, Anirban, Susanta da* and many others, from whom I have learned a lot and who have supported me in numerous ways. I cherish a lot of colorful memories shared with my batchmates during my M.Sc. days — *Samir* (my first roommate), *Shubham, Nivedita, Manjari, Partha,* and *Harmit.* I still fondly remember my first trip to Shillong with *Shubham* and *Samir*, which was filled with fun and unforgettable moments. I will truly miss the enjoyable moments spent with *Tanmoy da, Premashis da, Shobhan da, Prasun da, Susmita di, Debayan da, Krishnendu (1 & 2)*, and *Amit da* at the 2nd-floor students' bay during the early days of my Ph.D. journey. Big thanks to my other batchmates and juniors – *Ardhendu, Subhajit, Shinjini, Anirban, Soumen, Avik, Animesh, Chandan,* and *Sagar* for some wonderful company in several ways.

I feel truly fortunate to have my batchmate and friend, *Sreya*, always by my side during the important part of this journey. From supporting me through life's ups and downs to constantly motivating me, she has always been a source of strength and joy. She stood by me during difficult times, encouraging me to be my true self. I will always be grateful for her patience in tolerating me, for listening and helping me solve my problems, and for the valuable life lessons she has shared with me. Starting as swimming partners, we went

on to explore many corners of Kolkata – visiting countless places, trying out a variety of restaurants, joining a driving school together, and even learning cooking skills from her. Many thanks to you for believing in me, no matter what. Your encouragement to register for my first international conference abroad, INTERMAG 2024, led to my selection as a finalist for both the Best Oral Presentation Award and the Neil Smith Award. Through this journey, I have learned a lot from you, ranging from how to behave professionally with others to how to stay strong during difficult times. I also thank her family members for sharing beautiful moments with me while visiting Kolkata, whether at restaurants or exploring various places.

I am thankful to *Pratap da, Shubham, Sreya, Soma,* and *Suchetana* for making our Goa conference enjoyable and colorful. I would like to thank *Panda da, Ananda da, Sudip da, Shobhan da,* and *Samir* for making the trekking trip to Dzongri in Sikkim such a delightful and unforgettable experience. It was a lot of fun having *Amrit da* as my companion for attending the INTERMAG 2024 conference in Brazil, South America. Those post-research jam sessions with the SNB Khaja Band were truly pleasant times – sharing music and laughter with *Sarowar da, Ejaj da, Jayita di, Sadhu da, Deba da, Lalu da, Paru da, Subrata da, Saniur da,* and *Subhajit* will always remain special memories. I was truly delighted to have the opportunity to represent our institute at the Indian Science Congress (ISC 2020) in Bangalore, India, along with *Subhajit, Ardhendu,* and *Ankur da.* Also, being part of the organizing team for several international conferences hosted by our institute during my early Ph.D. days was a memorable and enriching experience. I would like to extend special thanks to the SNB cricket group members for bringing fun and entertainment to my weekends through cricket. As a sports enthusiast, taking part in marathon, table tennis, badminton, and carrom served as a refreshing break from academic life. Serving as an Editorial Board member for the SNBNCBS magazine 'Sutra' and as a member of the SNB Mess Committee for a year each taught me invaluable life lessons through these responsibilities. I also thank *Dulal da, Bhai da, Utpal da*, along with the institute canteen (Bhagirathi) and the SNB Mess, for consistently providing healthy and delicious snacks and food. *Dulal da's shop* felt like our second home in the afternoons of early Ph.D. days, where we gathered for snacks, and *Dulal da* was always there for us. I am thankful to *Gobinda da* for helping me organize my room at Radhachura and for always being available to assist in any situation, even during the challenging COVID times. I acknowledge *Kamakhha da* for being there at night in the hostel, ready to help in any emergency. I will truly miss the memorable days spent participating in SNB picnic, Diwali rangoli making, Bose fest, photo fest (SNB art fest), fresher's events, and especially those sleepless summer nights filled with the joy of picking buckets of delicious mangoes from the SNB gardens. I deeply appreciate the efforts of the gardeners and security staff for creating and maintaining such a vibrant environment and ensuring our safety throughout.

My special respect and heartfelt gratitude go to an exceptional teacher and remarkable human being, *B. C. da (Bijoy Chongdar)*, who has been an enlightening presence, inspiring me to become not only an avid learner but, more importantly, a better human being. His kindness, positivity, guidance, and teaching have been a constant source of strength and inspiration since my school days. I am deeply indebted to some outstanding physics teachers – *SCD Sir (Prof. Subodh Chandra Dhabal), Manas Sir (Manas Kumar Juin), Santanu Sir (Santanu Kundu)*, and many others – who nurtured my interest in physics and, more importantly, helped me understand and visualize the concepts behind the subject, which further fueled my passion for physics. I am obliged to my college-time friend *Riya* for motivating me on many occasions.

I cannot adequately express my gratitude to my family – *Baba (Chittaranjan Pal)* and *Maa (Kanchan Pal)*, who have stood by me through every challenge and triumph. I owe who I am today to their boundless love, sacrifices, care, guidance, and unwavering support. Their immense sacrifices have been the foundation of all my achievements. Without their encouragement and understanding, this journey would have been unimaginable. I am forever indebted to them for being my greatest pillars of strength, comfort, and inspiration.

Finally, I feel immensely blessed to have been an IPhD and Ph.D. fellow at SNBNCBS, Kolkata. I am grateful to SNBNCBS and the Department of Science and Technology (DST), Government of India, for their financial support throughout my research tenure and to IFW for funding during my visit there. I am also deeply thankful to Calcutta University for my Ph.D. registration, the Council of Scientific and Industrial Research (CSIR), Government of India, and IEEE Magnetics Society for providing the travel grant that enabled me to attend the international conference, INTERMAG 2024, and embrace valuable opportunities.

Last but not least, I owe a deep debt of gratitude to the *Almighty* and *Sri Sri Ramakrishna Paramahansadev* for guiding me throughout my life's journey and for being with me through all the ups and downs, making this achievement possible.

Riju Pal

List of Publications

A. Included in the Thesis

1. **Riju Pal***, Buddhadeb Pal, Suchanda Mondal, Rajesh O Sharma, Tanmoy Das, Prabhat Mandal*, Atindra Nath Pal*, *Spin-reorientation driven emergent phases and unconventional magnetotransport in quasi-2D vdW ferromagnet Fe_4GeTe_2*, npj 2D Materials and Applications 8, 30 (2024), DOI: *10.1038/s41699-024-00463-y*, (* corresponding authors).

2. **Riju Pal***, Joyal John Abraham, Alexander Mistonov, Swarnamayee Mishra, Nina Stilkerich, Suchanda Mondal, Prabhat Mandal, Atindra Nath Pal, Jochen Geck, Bernd Büchner, Vladislav Kataev, Alexey Alfonsov*, *Disentangling the unusual magnetic anisotropy of the near room-temperature ferromagnet Fe_4GeTe_2*, Advanced Functional Materials, 34, 2402551 (2024), DOI: *10.1002/adfm.202402551*, (* corresponding authors).

3. **Riju Pal**, Md. Nur Hasan, Chumki Nayak, Mrinal Deka, Nastaran Salehi, Manuel Pereiro, Suchanda Mondal, Abhishek Misra, Prabhat Mandal, Achintya Singha, Debjani Karmakar, Atindra Nath Pal, *Lattice dynamics and spin-phonon coupling across the spin-reorientation transition in near room-temperature vdW ferromagnet Fe_4GeTe_2*. (Manuscript to be submitted)

4. Arnab Bera, **Riju Pal**, et. al., *Observation of superconductivity and weak ferromagnetism in quasi-1D chain compound, $(TaSe_4)_3I$ at ambient pressure.* (Manuscript submitted)

5. Buddhadeb Pal*, **Riju Pal*** et al., *Signature of phase slip events and quasi-one-dimensional superconductivity in the single crystal of $(TaSe_4)_3I$* (* equal contributions). (Manuscript to be submitted)

B. Not Included in the Thesis

1. **R. Pal** et al., *Anisotropic magnetoresistance and low-frequency noise in van der Waals ferromagnet* Fe_4GeTe_2. (Manuscript under preparation)

2. **R. Pal** et al., *Electron spin resonance spectroscopy of a quasi-two-dimensional van der Waals ferromagnet* Fe_3GeTe_2. (Manuscript under preparation)

3. V. Pandey, P. Ghosh, **R. Pal**, S. Paul, A. M B, K. Watanabe, T. Taniguchi, A. N. Pal, and V. Kochat. *Broken symmetry states and quantum Hall ferromagnetism in decoupled twisted bilayer graphene*, arXiv:2503.20392 (2025). (Manuscript submitted)

4. **R. Pal***, S. Bera, B. Pal, M. Mondal, A. N. Pal, *Intrinsic room temperature ferromagnetism in van der Waals* Fe_5GeTe_2 *crystal*. AIP Conf. Proc. 3067, 020002 (2024). DOI: 10.1063/5.0204358, (* corresponding author).

5. A. Das, **R. Pal**, S. Mehta, KP. Islam, A. Mondal, A. N. Pal, D. Choudhury, *Space-charge driven origin of the reversible pyro-current peaks in* $Cu_{1-x}Cd_xCr_2O_4$, Physical Review B 109 (2), 024104 (2024).

6. S. Bera, S. K. Pradhan, **R. Pal**, B. Pal, A. Bera, S. Kalimuddin, M. Das, D.S. Roy, H. Afzal, A. N. Pal, M. Mondal, *Enhanced coercivity and emergent spin-cluster-glass state in 2D ferromagnetic material,* Fe_3GeTe_2, Journal of Magnetism and Magnetic Materials 583, 171052 (2023).

7. S. Bera, S. K. Pradhan, M. S. Khan, **R. Pal**, B. Pal, S. Kalimuddin, A. Bera, B. Das, A. N. Pal, and M. Mondal, *Unravelling the nature of spin reorientation transition in quasi-2D vdW magnetic material,* Fe_4GeTe_2, Journal of Magnetism and Magnetic Materials 565, 170257 (2023).

8. R. Alam, P. Boyal, S. Roy, R. Singha, B. Pal, **R. Pal**, P. Mandal, P. Mahadevan, A. N. Pal, *Detection of Nontrivial Topology Driven by Charge Density Wave in a Semi-Dirac Metal*, Advanced Functional Materials 33 (44), 2306751 (2023).

9. A. Das, D. Ranaut, P. Pal, **R. Pal**, S. Moulick, M. Das, D. Topwal, P. Mandal, A. N. Pal, K. Mukherjee, and D. Choudhury., *Tuning of magnetic frustration and emergence of a magnetostructural transition in* $Mn_{1-x}Cd_xCr_2O_4$, Physical Review B 108, 064426 (2023).

10. A. Rahaman, T. Paramanik, B. Pal, **R. Pal**, P. Maji, K. Bera, S. Mallik, D. K. Goswami, A. N. Pal, D. Choudhury, *Surface-phase superconductivity in a Mg-deficient V-doped* $MgTi_2O_4$ *spinel*, Physical Review B 107 (24), 245124 (2023).

Abstract

As the demand for faster computation and higher-density memory grows, traditional electronic devices face challenges related to energy efficiency and scalability. To overcome these limitations, researchers are exploring novel low-dimensional quantum materials with unique properties for data storage, sensing, and spintronic applications. Layered van der Waals (vdW) magnetic materials and quasi-1D superconductors lead to ideal platforms to study the interplay of reduced dimensionality, electronic correlations, and emergent quantum phenomena. This thesis presents a comprehensive transport and spectroscopic study of two such systems: the layered ferromagnet Fe_4GeTe_2 and the quasi-1D superconductor $(TaSe_4)_3I$.

Two-dimensional (2D) vdW magnets, despite their potential for next-generation spintronic applications, often exhibit Curie temperatures (T_C) far below room temperature, limiting their practical utility. However, Fe_4GeTe_2, with a near-room-temperature ferromagnetic order ($T_C \approx 270$ K) and enhanced air stability, offers promising avenues for device fabrication. Notably, Fe_4GeTe_2 undergoes a spin-reorientation transition (SRT) at $\sim$ 120 K (T_{SR}), where its magnetization axis shifts with temperature, distinguishing it magnetically special from other 2D magnets. Understanding the electronic transport near this transition and its correlation with the underlying magnetic properties is crucial for both fundamental physics and applications. In this thesis, using detailed electronic transport, electron spin resonance (ESR), and Raman spectroscopic measurements, we tried to understand the origin of this SRT and the anomalous properties of Fe_4GeTe_2. These combined experimental insights, complemented by theoretical interpretations, provide a deeper understanding of the anomalous transport and spin dynamics in this system.

In addition to layered magnets, this thesis explores the interplay between superconductivity and magnetism in $(TaSe_4)_3I$, a non-centrosymmetric, quasi-1D superconductor with strong electronic correlations. Bulk $(TaSe_4)_3I$ exhibits superconductivity below $\sim$ 2.2 K (T_c), accompanied by signatures of weak ferromagnetism near 9 K, demonstrating the coexistence of two competing quantum phases. Through detailed transport measurements, we investigate the nature of superconductivity, anisotropy, and the characteristics of low-dimensional superconductors, highlighting their importance for studying complex ground states driven by disorder, low-dimensionality, and unique electronic structures.

By bridging the fields of low-dimensional magnetism and superconductivity, this thesis contributes to the fundamental understanding of correlated electron systems, highlighting their potential in spintronic applications and quantum computing.

Abbreviations

1D	one-dimensional
2D	two-dimensional
3D	three dimensional
vdW	van der Waals
ESR	electron spin resonance
FMR	ferromagnetic resonance
FM	ferromagnet
AFM	antiferromagnet
PM	paramagnet
ZFC	zero-field cooling
FCC	field-cooled cooling
FCW	field-cooled warming
VSM	vibrating sample magnetometer
SQUID	superconducting quantum interference device
VNA	vector network analyzer
SRT	spin reorientation transition

QPS	quantum phase slips
CQPS	coherent quantum phase slips
TAPS	thermally activated phase slips
SIT	superconductor-insulator transition
IVC	current-voltage characteristics
XRD	X-ray diffraction
FESEM	field emission scanning electron microscopy
EDS	energy dispersive spectrometer
AHE	anomalous Hall effect
MR	magnetoresistance
FFT	fast Fourier transform
ppm	parts per million
FWHM	full width at half maximum
SOC	spin-orbit coupling
MCA	magneto-crystalline anisotropy
MA	magnetic anisotropy
MAE	magnetic anisotropy energy
AF microscopy	atomic force microscopy
SEM	scanning electron microscope

Contents

Chapter 1

Introduction

The rapid advancement of information technology has driven an increasing demand for faster computation, enhanced data storage, processing, and transmission in integrated circuits (ICs). However, as device miniaturization progresses, fundamental constraints related to size and power consumption pose significant challenges, indicating that Moore's Law is approaching its theoretical limits [1, 2]. Spintronics, an emerging field centered on the manipulation of electron spin rather than charge, offers a promising alternative to conventional CMOS-based technologies. Unlike traditional charge-based electronics, spintronic devices leverage spin degrees of freedom for data processing and storage, providing significant advantages such as reduced energy consumption, non-volatility, and resilience to radiation [3].

As electronic dimensions shrink toward atomic scales, thermal fluctuations and quantum effects increasingly compromise the long-range magnetic and superconducting order essential for memory, logic, and quantum functionalities. In two dimensions (2D), the Mermin–Wagner theorem forbids spontaneous magnetic order in an isotropic Heisenberg system at any finite temperature by virtue of gapless spin-wave excitations [4, 5], while in one dimension (1D), thermal and quantum phase slips destroy superconducting phase coherence below the critical temperature [6, 7].

Real materials circumvent these restrictions by introducing anisotropy, which gaps out low-energy fluctuations and breaks continuous symmetry. Among atomically thin vdW magnetic materials, such as $Cr_2Ge_2Te_6$ and CrI_3, strong magnetocrystalline anisotropy stabilizes out-of-plane ferromagnetism at finite temperatures [8–10]. Similarly, ultranarrow superconducting wires sustain dissipationless currents when confinement and anisotropy suppress phase-slip proliferation [11, 12]. These breakthroughs demonstrate

that controlled anisotropy can restore long-range order in truly low-dimensional systems, opening pathways to both novel physics and transformative device concepts.

This thesis is motivated by the fundamental question: *How can anisotropy stabilize and tune the long-range order in 2D magnets and quasi-1D superconductors, and what emergent phenomena arise at the nexus of reduced dimensionality, strong correlations, and broken symmetries*? To address this, we have selected two such new potential systems, 2D ferromagnet Fe_4GeTe_2 and quasi-1D superconductor $(TaSe_4)_3I$.

1. **Fe_4GeTe_2**: A vdW ferromagnet with $T_C \approx 270\,\mathrm{K}$, Fe_4GeTe_2 exhibits a spin-reorientation transition (SRT) near 120 K driven by the competition between magnetocrystalline and shape anisotropy [13–15]. Here, the unusual magnetocrystalline anisotropy opens a gap in the spin-wave spectrum, breaking continuous rotational symmetry and permitting long-range order near room temperature even in few-layer films. By combining detailed low-temperature magneto-transport, electron spin resonance, micro-Raman spectroscopy, and density functional theory, we probe how the charge and magnetotransport properties change near SRT – manifesting as carrier-type switching, giant anomalous Hall conductivity, and negative magnetoresistance, investigating the anisotropy-driven spin dynamics near SRT, and how spin-lattice coupling and anharmonicity feed back into the magnetic ground state.

2. **$(TaSe_4)_3I$ (nTSI)**: A non-centrosymmetric quasi-1D superconductor with ferromagnetism at $T_m \approx 9\,\mathrm{K}$ and superconductivity below $T_c \approx 2.5\,\mathrm{K}$, nTSI manifests an anisotropy in magnetism and superconductivity and phase-slip events in the superconducting regime[16]. Through detailed low-temperature electro-, magneto-transport, SQUID magnetometry, we probe the signature of superconductivity and ferromagnetism, reveal multiple voltage-steps – signature of phase slips, hysteresis from self-heating or underdamped Josephson links, and vacancy-induced magnetism, demonstrating how dimensional confinement and broken inversion symmetry stabilize the superconducting and magnetic orders in the same system.

Systematically, this thesis aims to (i) uncover the microscopic mechanisms by which anisotropy gaps restore long-range order in 2D and 1D systems, and (ii) establish Fe_4GeTe_2 and nTSI as model platforms for emergent low-dimensional quantum phenomena. More broadly, uncovering the interplay of dimensionality, anisotropy, and electronic correlations

in Fe_4GeTe_2 and nTSI paves the way for discovering exotic ground states—topological, multiferroic, and beyond—in truly low-dimensional materials. These insights will guide the design of next-generation spintronic and quantum-coherent devices.

1.1 2D Magnetism

With the continuous progress in device miniaturization, nano-fabrication techniques have surpassed traditional methods of enhancing integration density through process optimization. But, at the sub-nanometer scale, conventional three-dimensional materials can no longer preserve their intrinsic physical properties. In contrast, 2D materials, with their layered atomic structures, retain exceptional physical characteristics due to vdW interfaces, making them promising candidates for next-generation nanoscale technologies. The family of 2D materials has been rapidly expanding due to their extraordinary electrical, thermal, optical, and mechanical properties, since the discovery of graphene [17] in 2004. Their wide range of physical properties highlights their immense potential as viable alternatives to conventional three-dimensional materials. Individually, these 2D materials are discovered in different forms [18] like superconductors (e.g., $NbSe_2$), metals (e.g., TiS_2, VS_2), semimetals (e.g., graphene), half-metals (e.g. CrO_2, CrS_2), topological insulators (e.g., $MoTe_2$, Bi_2Te_3), semiconductors (e.g., TMDCs like MoS_2, WSe_2), insulators (e.g., hBN), etc. However, there was a missing member in this family till 2016, named 2D magnetic materials (including 2D ferromagnetic and antiferromagnetic materials), which have emerged as an exciting addition to the family of atomically thin materials. By integrating 2D magnets into spintronic architectures, it becomes possible to harness both the unique electronic properties of 2D materials and the advantages of spin-based information processing. This combination enables energy-efficient, high-speed data operations while potentially overcoming the power and scaling limitations that currently hinder IC technology. As a result, 2D spintronic devices present a viable path toward extending the progression of Moore's Law and advancing next-generation computing technologies [19, 20].

In 1966, Mermin and Wagner theoretically demonstrated that spontaneous long-range magnetic order cannot be sustained in a 2D isotropic Heisenberg system [21] at any finite temperature. The thermal fluctuations destroy this long-range ordering. This is known as the Mermin-Wagner theorem [4, 5]. This result led to a long-standing belief that intrinsic 2D magnetic materials could not exist. However, this assumption was challenged in 2017 when C. Gong and colleagues at the University of California, Berkeley, successfully

isolated few-layer $Cr_2Ge_2Te_6$ via mechanical exfoliation and characterized its magnetic properties using the magneto-optical Kerr effect [8]. This marked the first experimental confirmation of intrinsic magnetism in atomically thin materials. $Cr_2Ge_2Te_6$ is a magnetic semiconductor, implying that both its electronic and magnetic characteristics can be modulated by an external electric field, making it a promising candidate for 2D spintronic applications [22]. Following this breakthrough, B. Huang et. al. synthesized CrI_3, another layered magnetic material, and employed magneto-optical Kerr measurements to establish its interlayer antiferromagnetic coupling [9]. These experimental findings provided compelling evidence that magnetic ordering can persist in 2D materials at finite temperatures, despite the constraints imposed by the Mermin-Wagner theorem. Importantly, this does not contradict the theorem itself. Rather, the existence of long-range magnetism in these systems can be attributed to magnetic anisotropy, which introduces a gap in the spin-wave energy spectrum and breaks continuous rotational symmetry in the Hamiltonian, thereby stabilizing magnetic order [10].

Since these pioneering studies, extensive research efforts have led to the discovery of numerous 2D magnetic materials possessing a range of distinct properties (summarized in Table 1.1) [22, 23]. Depending on their magnetic configuration, these materials can be classified as ferromagnetic (FM) or antiferromagnetic (AFM). Examples of FM 2D materials include Fe_3GeTe_2 [24, 25], $CrSe_2$ [26], and $CrGeTe_3$ [8], whereas AFM materials such as CrI_3 [27], $CrBr_3$ [28], $CrCl_3$ [29], $FePS_3$ [30], etc. have also been reported. A key challenge in this field is achieving precise control over the magnetic characteristics of 2D magnets, viz, their Curie temperature (T_C) and magnetic anisotropy, to enable their integration into spintronic devices with high operating temperatures and robust thermal stability. Various strategies have been explored to enhance the T_C of 2D magnets, including carrier doping, interlayer stacking manipulation, and strain engineering. While these approaches have shown promise, each comes with inherent limitations, making it challenging to achieve precise, efficient, and easily tunable magnetic modulation [31].

1.1.1 Fundamental Mechanism of 2D Magnetism

The emergence of the long-range ordering of magnetism in 2D vdW magnetic systems is mainly dictated by exchange interactions among their magnetic atoms. Depending on the relative orientation of neighboring spins, these materials can be categorized into Heisenberg, Ising, and XY models [23]. The spin-exchange interactions within a system

Materials	**Conductivity**	**Magnetic Order**	**Anisotropy Axis**	T_C **or** T_N **(K)**
$CrCl_3$ [29]	Insulator	AFM/FM	Weak	14 (T_N), 17 (T_C)
$CrBr_3$ [28]	Insulator	FM	c	34
CrI_3 [27]	Insulator	AFM/FM	c	45
VI_3 [32]	Semiconductor	FM	c	50 (bulk)
Fe_3GeTe_2 [25, 33–35]	Metal	FM	c	130 (1L), 220 (>4L)
Fe_4GeTe_2 [13–15, 36]	Metal	FM	ab/c	270
Fe_5GeTe_2 [37–39]	Metal	FM	ab	310 (bulk)
$CrSe_2$ [26]	Metal	FM	c	65 (1L), 110 (16L)
$CrTe_2$ [40]	Metal	FM	c	200 (1L), 300 (>7L)
VSe_2 [41]	Metal	FM	ab	330 (1L)
Cr_2S_3 [42]	Semiconductor	AFM	ab	120 (15 nm), 300 (45 nm)
CrSe [43]	Metal	FM	c	280
$MnBi_2Te_4$ [44]	Topological Insulator	AFM/FM	c	18 (few layer), 25 (bulk)
$FePS_3$ [30]	Insulator	AFM	c	104 (1L)
$NiPS_3$ [45]	Insulator	AFM	ab	25 (1L), 130 (2L), 155 (bulk)
$CrGeTe_3$ [8]	Insulator	FM	Weak/c	30 (2L), 61 (bulk)
α-$RuCl_3$ [46]	Insulator	AFM	c	–

TABLE 1.1: Some experimentally verified 2D magnetic materials. Collected from Ref. [23]

can be described by the Hamiltonian for the Heisenberg model [21], given by:

$$H = \sum_{j,k} J_{jk} \mathbf{S}_j \cdot \mathbf{S}_k \tag{1.1}$$

Here J_{jk} represents the strength of exchange interaction between two magnetic atoms located at sites j and k, and $\mathbf{S}_j$ and $\mathbf{S}_k$ denote their spin vectors. The summation accounts for all non-redundant spin interactions in the material's crystal structure. To simplify this model, it is common to consider only nearest-neighbor interactions, assuming a constant exchange interaction J. Under this assumption, the Hamiltonian simplifies to:

$$H = \sum_{j,k} J \mathbf{S}_j \cdot \mathbf{S}_k \tag{1.2}$$

The sign of J determines the nature of magnetic ordering: if $J > 0$, parallel spin alignment occurs, leading to ferromagnetic order, whereas if $J < 0$, spins align antiparallelly, resulting

in antiferromagnetic order. Expressing this Hamiltonian in Cartesian coordinates gives:

$$H = \sum_{j,k} \left(J_a S_j^a S_k^a + J_b S_j^b S_k^b + J_c S_j^c S_k^c \right) \tag{1.3}$$

Here J_a, J_b, J_c are the components of the exchange interaction along the respective axes, x, y, z, and S_j^a, S_j^b, S_j^c are the spin components of a magnetic atom.

For the 3D Heisenberg model [21], all three components of J are nonzero ($J_a \neq 0, J_b \neq 0, J_c \neq 0$), meaning the spins can orient freely in three-dimensional space, resulting in a spin dimensionality of 3. If the exchange interaction is confined to the x-y plane ($J_a \neq 0, J_b \neq 0, J_c = 0$), the system follows the 2D XY model [47], where spins lie within the plane, giving a spin dimensionality of 2 and in-plane magnetic anisotropy. In contrast, when interactions are limited to the z-axis ($J_a = 0, J_b = 0, J_c \neq 0$), the system follows the 1D Ising model [48], where spins can only point up or down along the perpendicular direction, resulting in a spin dimensionality of 1 and out-of-plane magnetic anisotropy.

In 2D magnetic materials, an additional term representing magnetic anisotropy is often incorporated into the Hamiltonian of Equation 1.1:

$$H = \sum_{j,k} J_{jk} \mathbf{S}_j \cdot \mathbf{S}_k + \sum_j A (S_j^c)^2 \tag{1.4}$$

where A denotes the single-ion magnetocrystalline anisotropy energy (SIA) arising from spin-orbit coupling. Notably, in the Heisenberg model, the presence of magnetic anisotropy disrupts the Hamiltonian's continuous rotational symmetry, which permits long-range ordering in 2D magnetic systems. Thus, magnetic anisotropy is vital for stabilizing magnetism in materials with reduced dimensionality.

1.1.2 Fe_nGeTe_2 (n = 3, 4, 5) Family

Recently discovered 2D magnetic materials have garnered significant interest for their role in long-range spin transport and highly efficient spin manipulation. Their intrinsic spin properties integrate the benefits of spintronic technologies, including minimal power consumption and non-volatile operation. This has fueled advancements in the spintronics field, enabling developments such as low-dimensional spin filters [19], spin transistors [20], and magnetoresistive devices [49]. Despite these promising attributes, recent investigations into 2D magnets—including CrI_3 [9, 27], $Cr_2Ge_2Te_6$ [8],

$Cr_2Si_2Te_6$ [50], and VSe_2 [41]—have revealed that their T_C remains well below room temperature, posing challenges for practical applications.

The advent of ternary Fe-Ge-Te (FGT) 2D magnetic materials presents a promising avenue to overcome the challenges associated with conventional 2D magnets. Recent advancements in iron-based vdW magnets, such as Fe_nGeTe_2 (n = 3, 4, 5) (FnGT) [13–15, 24, 33, 34, 36, 51–55], have garnered significant interest, particularly Fe_4GeTe_2 [13–15, 36] and $Fe_{5-x}GeTe_2$ [37, 56, 57], due to their ferromagnetic transition temperature (T_C) approaching room temperature. The FnGT family exhibits a range of unconventional magnetic and electronic properties. From an electronic perspective, density functional theory (DFT) calculations indicate that these materials behave as metals, characterized by multiple band crossings at the Fermi level [58, 59]. Notably, variations in crystal symmetry among different FnGT compounds, combined with the influence of spin-orbit coupling (SOC), suggest a possibility for topologically nontrivial phases. These phases could give rise to intriguing quantum phenomena, such as chiral anomaly-driven effects, including negative magnetoresistance or nonlinear conductivity in the diffusive regime [60]. Moreover, the inherent breaking of time-reversal symmetry (TRS) in these materials may lead to exotic ground states, potentially manifesting in remarkable transport signatures. For instance, Fe_3GeTe_2 has been reported to exhibit a pronounced intrinsic anomalous Hall effect [61], while other members of the family display unconventional magnetotransport behavior at low temperatures [62]. Additionally, these systems frequently show temperature-dependent, non-monotonic transport responses that correlate with variations in magnetization, further highlighting their complex interplay between electronic structure and magnetism [63].

Among the FnGT family of vdW ferromagnets, Fe_3GeTe_2—the first experimentally discovered member—has garnered considerable attention due to its relatively high T_C of approximately 220 K, which exceeds that of other 2D magnets reported at the time [24, 33, 34, 51]. In addition, Fe_3GeTe_2 exhibits excellent electrical conductivity, making it a promising platform for investigating spin-dependent transport phenomena in low dimensions. However, as the thickness of Fe_3GeTe_2 is reduced, dimensional constraints significantly suppress long-range ferromagnetic ordering [4], resulting in a drastic drop in T_C (below 20 K) for films thinner than 10 nm [25]. This low transition temperature poses a major challenge for integrating FGT-based materials into practical spintronic devices. Although several external tuning strategies—such as ionic gating [33], laser irradiation [64], and proximity effects [65]—have been explored to raise T_C, these methods often fail to achieve stable room-temperature ferromagnetism and also introducing potential

drawbacks such as structural damage, impurity incorporation, and incompatibility with large-scale integrated circuit fabrication.

We all know that in the 2D limit, the Mermin–Wagner theorem [4] prohibits the spontaneous breaking of continuous symmetries, such as that required for ferromagnetic order, at finite temperatures. Consequently, thermal fluctuations can destabilize magnetic ordering unless suppressed by magnetic anisotropy. So, in 2D ferromagnets, uniaxial magnetic anisotropy is essential for maintaining stable magnetic ordering at finite temperatures. The magnetic anisotropy energy K, together with the spin-exchange interaction J, simultaneously determines the T_C of the system, scaling approximately as $T_C \sim J/\ln(3\pi J/4K)$ [66]. Since K is typically set by the magnetocrystalline anisotropy, which arises from spin-orbit coupling, it is usually much smaller than J, limiting T_C in conventional 2D magnetic systems, as follows from the above equation. This situation contrasts with 3D ferromagnets like bulk iron, where T_C is primarily determined by the exchange interaction (J) alone (e.g., $T_C \sim 1043$ K in Fe [67]). To overcome this limitation in 2D magnetic materials, one can engineer structures that retain the advantages of vdW stacking while incorporating 3D-like exchange pathways with smaller anisotropy [13]. Specifically, if the magnetic atoms form a multilayer slab—where several layers of Fe atoms are strongly coupled within a unit and separated from adjacent slabs by vdW gaps—then the system can exhibit enhanced J and reduced sensitivity to K, resulting in a higher T_C (see Fig. 1.1(b)). This material design principle is embodied in the Fe_nGeTe_2 family (for $n \geq 3$), where Fe-rich slabs are sandwiched between Te layers, enabling strong intralayer magnetic coupling while preserving vdW interlayer characteristics. As such, this family offers a tunable platform for realizing higher T_C ferromagnets suitable for future spintronic applications.

Recent studies have demonstrated that incorporating additional ferromagnetic elements into the FGT framework enables the formation of novel ternary 2D magnetic phases, Fe_4GeTe_2 [13–15, 36] and Fe_5GeTe_2 [38, 52, 68]. The inclusion of extra Fe atoms strengthens internal spin interactions, thereby reinforcing the material's overall magnetism. As illustrated in Fig. 1.1, different FGT phases vary in the number of Fe atoms per structural unit. Thereafter, Fe_5GeTe_2, the brother compound in this family, was synthesized recently, known for its pronounced magnetic anisotropy [38]. Unlike Fe_3GeTe_2, its structure incorporates an additional honeycomb arrangement of iron atoms, leading to a more complex crystalline phase [52]. This complexity arises from the site splitting of Fe and Ge atoms, coupled with the vacancy-driven disorder. Within a single unit cell, there exist three distinct iron sites—Fe(1), Fe(2), and Fe(3). The Fe(1) atoms

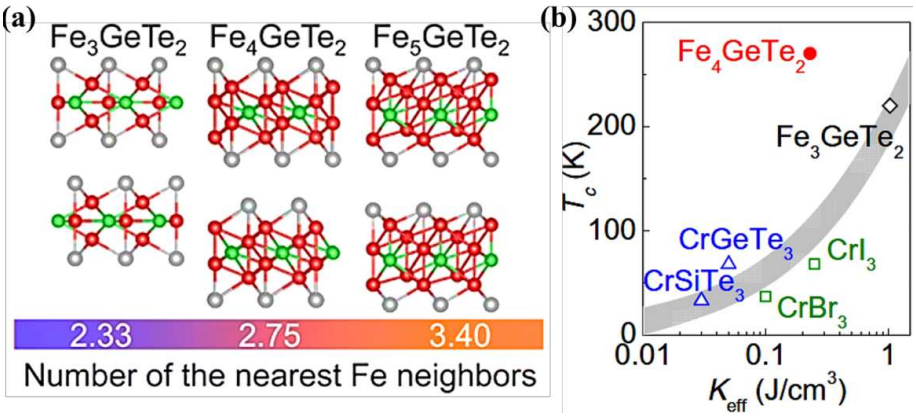

FIGURE 1.1: (a) Schematic representation several 2D ferromagnetic phases of FnGT. (b) Uniaxial magnetic anisotropy energy (K_{eff}) and ferromagnetic transition temperature (T_C) for various vdW ferromagnets. The shaded line indicates a positive correlation between T_C and K_{eff} in vdW magnetic systems. Reproduced from Ref. [13].

can either occupy positions above or below neighboring Ge atoms, with certain sites remaining vacant. In recent years, Fe_5GeTe_2 has been extensively studied due to its intriguing magnetic characteristics and potential applications in spintronic technologies. Research conducted by Stahl et al. in 2018 demonstrated its ferromagnetic behavior below 279 K, with a relatively small coercive field and a saturation moment of about 1.80 μ_B at low temperatures [69]. Subsequently, density functional theory (DFT)-based first-principles calculations were employed to investigate its electronic and magnetic properties, revealing that its 2D counterpart also exhibits ferromagnetism alongside metallic conductivity, aligning with predictions from Stoner's model [70]. Due to its complex crystalline phase, there are a lot of complex properties that are difficult to explain.

1.1.3 vdW Magnet Fe_4GeTe_2

Fe_4GeTe_2 stands out among iron-based vdW magnetic metals due to its distinctive magnetic characteristics, including a high ferromagnetic transition temperature (T_c) reaching up to 270 K even in ultra-thin layers [13, 14, 36]. Unlike conventional methods of modifying magnetic order through external perturbations such as ion gating or laser excitation, Fe_4GeTe_2 offers an intrinsic mechanism to control spin states without compromising structural integrity. A key feature of this material is its tunable magnetic anisotropy, which results from the interplay between magnetocrystalline and shape anisotropies. This interplay leads to a temperature-dependent modification of the easy axis of magnetization, enabling control over spin orientation. Notably, bulk Fe_4GeTe_2

exhibits a spin reorientation transition around 120 K, setting it unique from other members of the FnGT family. SRT phenomena have been observed in several other magnetic materials, including Fe_3Sn_2 [71–74] and $TbMn_6Sn_6$ [75–77] and several others. The underlying mechanism is likely governed by the interplay of magnetic exchange interactions with the effective anisotropy of the system [13, 15, 78].

A monolayer of Fe_4GeTe_2 comprises seven atomic layers, where Fe_1 and Fe_2 atoms are positioned on either side of the central Ge atomic plane, with Te atoms capping the structure symmetrically on both outermost layers, as illustrated in Fig. 1.2. These individual layers are stacked in a rhombohedral arrangement, crystallizing in the $R\bar{3}m$ space group [13]. From an electronic perspective, Fe_4GeTe_2 is theoretically proposed to belong to a distinct class with nontrivial topological characteristics, setting it apart from Fe_3GeTe_2 and Fe_5GeTe_2 [58, 59]. In Fe_4GeTe_2, recent transport studies suggest that this spin reorientation could drive a Lifshitz transition in the electronic structure, potentially giving rise to anomalous transport behaviors, such as unconventional magnetoresistance and anomalous Hall effects [79, 80]. Furthermore, an anomaly in specific heat measurements indicates that SRT in Fe_4GeTe_2 is a true thermodynamic phase transition [81], though its implications for electron transport remain an open question.

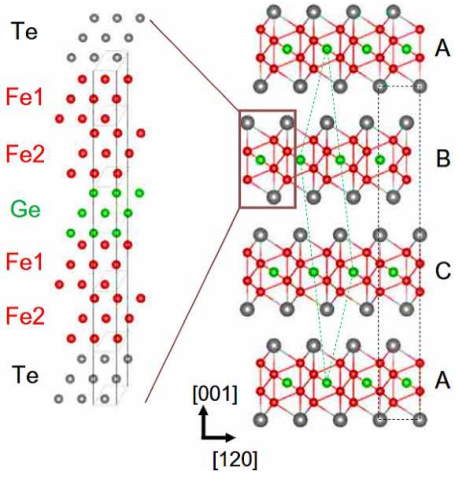

FIGURE 1.2: Stacked plane views along [001] showing the seven-atom-thick Fe_4GeTe_2 monolayer. These monolayers stack in an ABC sequence, forming the rhombohedral ($R\bar{3}m$) structure (green dashed lines), with the corresponding hexagonal cell shown for comparison (black dashed lines). Reproduced from Ref. [13].

The combination of near-room-temperature ferromagnetism, tunable spin reorientation, and small magnetic anisotropy with high coercivity makes Fe_4GeTe_2 an exciting platform for spintronic and high-density magnetic memory applications. These remarkable properties establish Fe_4GeTe_2 as a promising candidate for next-generation spin-based technologies.

1.2 Low-dimensional Superconductivity

The superconducting properties of a material are strongly dictated by its dimensionality. In low-dimensional superconducting systems, where at least one dimension is comparable to or smaller than the superconducting coherence length (ξ) [82, 83], quantum fluctuations and phase coherence effects become dominant, leading to unconventional superconducting phenomena. This stands in contrast to bulk superconductors, where long-range phase coherence is well maintained, ensuring robust superconductivity.

As dimensionality decreases, the superconducting order parameter is more susceptible to thermal and quantum fluctuations, which can influence both the transition temperature and the overall stability of the superconducting phase. In 2D superconductors (when the sample thickness approaches or becomes smaller than ξ), phase coherence is primarily influenced by thermal fluctuations, leading to the Berezinskii-Kosterlitz-Thouless (BKT) [47] transition. This transition, characterized by the binding and unbinding of vortex-antivortex pairs, results in a suppression of the critical temperature and a characteristic superfluid density jump at the BKT transition temperature (T_{BKT}). Unlike conventional superconducting transitions, where T_c is determined primarily by the pairing interaction, the BKT transition emphasizes the critical role of phase coherence in sustaining superconductivity.

A further reduction to quasi-1D geometry (when the width of the sample or wire approaches ξ) introduces even stronger quantum fluctuations, significantly affecting phase coherence. A hallmark of quasi-1D superconductivity is the occurrence of phase slips (PS) [84], where localized disruptions momentarily suppress the superconducting order parameter, inducing resistance even below the transition temperature (T_c). While thermal phase slips dominate at higher temperatures, quantum phase slips (QPS) [6, 7, 11] become prominent at low temperatures due to quantum mechanical tunneling effects. The proliferation of QPS events can ultimately suppress superconductivity, leading to a crossover from a superconducting to a resistive or insulating state. In addition to phase fluctuations, disorder and electron-electron interactions further modify the superconducting behavior in quasi-1D systems. Strong disorder enhances quantum phase slips, potentially driving a superconductor-insulator transition (SIT). This transition is dictated by the competition between Cooper pairing and phase decoherence mechanisms, which are influenced by coherence length, disorder strength, and Coulomb interactions. As a result, quasi-1D superconductors exhibit a complex interplay of superconducting, metallic, and insulating phases, depending on intrinsic material properties and external

tuning parameters. This PS manifests in current-voltage characteristics (IVC), governing multiple voltage steps [12].

Finally, in a 1D superconducting system, the superconducting transition is influenced by distinct mechanisms known as thermally activated phase slips (TAPS) and QPS. A key phenomenon affecting superconductivity in 1D systems is the occurrence of phase slips, which act as localized disruptions in the superconducting order parameter. These phase slips can be thermally activated (TAPS) [85] or arise due to quantum tunneling (QPS) [86]. TAPS occur at finite temperatures ($T \leq T_c$) due to thermal fluctuations, where thermal energy enables the system to overcome energy barriers separating different phase configurations. As a result, resistance persists below the superconducting transition temperature, disrupting the phase coherence of the superconducting state. On the other hand, QPS becomes particularly significant at extremely low temperatures ($k_B T < \Delta_0$, $T \to 0$), where quantum fluctuations allow for the spontaneous formation of phase slips, even in the absence of thermal excitation. The tail in the resistance observed at low temperatures is a characteristic hallmark of QPS. The interplay between these mechanisms governs the stability of superconductivity in 1D structures.

1.2.1 Quasi-1D Superconductor $(TaSe_4)_3I$

Quasi-1D materials, where charge carriers primarily move along linear atomic chains, serve as an ideal platform for investigating low-dimensional quantum phenomena. A notable class within this family includes transition-metal-based chain compounds, such as $(MSe_4)_nI$ (M = Nb, Ta; n = 2, 3, 10/3), which exhibit a wide range of intriguing coexisting phases [87–95]. The structure of these materials consists of MSe_4 chains aligned parallel to the crystallographic c-axis, with iodine atoms acting as spacers between them, forming a quasi-1D structure [87–89].

Earlier theoretical models predicted semiconducting behavior for $(NbSe_4)_2I$ [96, 97] and $(TaSe_4)_2I$ (n = 2) [89, 95], yet recent experimental findings suggest a more intricate electronic structure. In the case of n = 3, $(NbSe_4)_3I$ and $(TaSe_4)_3I$ adopt the same centrosymmetric crystal symmetry having same space group $P4/mnc$ [88], implying that their electronic properties should be closely related. However, while $(NbSe_4)_3I$ remains a band insulator [98], the non-centrosymmetric phase of $(TaSe_4)_3I$ displays metallic characteristics [16, 88].

In quasi-1D materials, the inherent electronic instability often leads to a Peierls transition, which can drive the system into a charge density wave (CDW) phase. This transition

introduces additional complexity, resulting in diverse phase diagrams and the emergence of novel quantum states [99, 100]. Although theoretical models suggest that true long-range order should be suppressed in strictly 1D systems [4], quasi-1D materials frequently exhibit robust superconducting and magnetic correlations [101, 102]. Quantum and thermal fluctuations in these low-dimensional systems contribute to intriguing physical effects, such as phase slips [6, 7, 12], Cooper pair localization [102, 103], and deviations from conventional Fermi liquid behavior [104, 105]. A particularly striking example is $(TaSe_4)_2I$, which has been reported to host an exotic axionic CDW phase, characterized by strong electron-electron interactions [91, 94]. Additionally, both $(TaSe_4)_2I$ [92, 106] and $(NbSe_4)_2I$ undergo superconducting transitions under high pressure [107], with a disorder-driven mechanism proposed in the latter case. In superconducting systems, structural imperfections can serve as pinning centers for vortices, thereby enhancing the stability of the superconducting phase [108]. In magnetic materials, these defects significantly impact spin ordering by influencing spin density wave formation and modifying local exchange interactions [109]. Consequently, the intricate coupling between superconductivity, magnetism, and charge order in the presence of disorder creates an exciting framework for uncovering emergent quantum phenomena and unconventional phase transitions in low-dimensional materials.

Motivated by the intriguing physics of quasi-1D materials, we have synthesized[1] a new quasi-1D compound, $(TaSe_4)_3I$, hereafter referred to as nTSI. We successfully stabilized a non-centrosymmetric structural phase of nTSI (space group: $P\bar{4}2_1c$) across a broad temperature range, which revealed a lot of unconventional properties.

High-quality single crystals of nTSI were grown using the chemical vapor transport method, forming elongated ribbon-like fibers with typical lengths of several millimeters and widths in the micron range. Single-crystal X-ray diffraction analysis performed at 100 K confirms that nTSI crystallizes in a simple tetragonal structure with lattice parameters $a = b = 9.436(5)$ Å, $c = 19.046(11)$ Å, and angles $\alpha = \beta = \gamma = 90°$. Additionally, high-resolution transmission electron microscopy (TEM) imaging (see Chapter 7 for more details) reveals a well-defined $TaSe_4$ chain-like configuration aligned along the c-axis, with an inter-chain separation of $d_{\text{inter}} = 6.677$ Å. Transport measurements indicate that nTSI exhibits robust metallic conduction from room temperature down to sub-Kelvin regimes—an electronic property unprecedented in this class of materials. Upon further cooling, a long-range magnetic transition[2] emerges around

[1] The crystal synthesis and characterization were performed by Dr. Mintu Mondal's group from IACS, Kolkata.

[2] Magnetization measurements were performed by Prof. Prabhat Mandal's group from SINP, Kolkata.

9 K, followed by the onset of superconductivity below 2.5 K in the non-centrosymmetric phase.

To elucidate the possible origin of these emergent phenomena, density functional theory (DFT) calculations[3] suggest that Se_2 dimer vacancies could significantly influence the system's electronic and magnetic properties. These vacancies are proposed to introduce localized magnetic moments while simultaneously acting as charge donors, thereby accounting for the coexistence of ferromagnetism, metallicity, and superconductivity observed in nTSI.

1.3 Objective and Outline of the Thesis

The objective of this thesis is to explore the detailed electronic transport and spectroscopic properties of two distinct quantum materials: the layered vdW ferromagnet Fe_4GeTe_2 and the quasi-1D superconductor $(TaSe_4)_3I$. These materials serve as ideal platforms for investigating the effects of reduced dimensionality, strong electronic correlations, and emergent quantum phenomena.

Chapter 2 presents the theoretical foundation and background of 2D magnetism, along with various magnetic interactions. It covers key concepts such as magnetic anisotropy, scattering mechanisms, the anomalous Hall effect, etc. Additionally, the chapter discusses the principles and methodology of electron spin resonance (ESR), Raman spectroscopy, and provides a brief introduction to superconductivity.

Chapter 3 provides an overview of the experimental methods and techniques utilized in this study. It begins with a discussion on the mechanical exfoliation of 2D magnetic materials and their characterization. The chapter then details the device fabrication process, including electrode patterning and metal deposition, followed by the dry transfer of thin-layer flakes. Additionally, it covers the development and optimization of key experimental setups, such as the low-temperature magneto-transport system, heterostructure setup, and glove box. Finally, various transport and spectroscopic measurement techniques are described in detail.

Chapter 4 explores the detailed electronic transport properties of vdW magnet Fe_4GeTe_2 down to 16 layers, focusing on the origin of its unusual SRT and the associated anomalous behaviors at low temperatures. We examine the resistivity, magnetoresistance (MR),

[3]The theoretical calculations were performed by Prof. Tanusri Saha Dasgupta's group from SNBNCBS, Kolkata.

and finally Hall measurements to investigate the nature of the anomalous Hall effect in this system and its correlation with the underlying magnetic properties. Notably, we observed the direct consequences of the SRT on the charge conduction mechanism, including a change in the majority carrier type, large anomalous Hall conductivity, and negative MR. First principles DFT calculations identified two quasi-degenerate magnetic phases—collinear (cFM) and non-collinear (nFM) ferromagnetic, with Fermi surface reconstruction associated with the SRT.

Chapter 5 contains a detailed ESR spectroscopic study to investigate the nature of magnetic anisotropy (MA) and the origin of the SRT in Fe_4GeTe_2. We examine whether in-plane anisotropy is present and analyze the unusual temperature evolution of the magnetic anisotropy field observed in ESR measurements. We observed, at high temperatures, the total MA is mostly given by the demagnetization effect (due to the plate-like shape of the crystal) with a small contribution of the counteracting intrinsic MA of an easy-axis type, whose growth below a characteristic temperature $T_{shape} \approx 150$ K renders the sample seemingly isotropic at T_{SR}. Additionally, single-crystal X-ray diffraction studies are conducted to determine whether the SRT is driven by a structural transition. Interestingly, all the characteristic temperatures found in the ESR experiment match those observed in transport measurements, indicating an intrinsic interaction between the magnetic and electronic degrees of freedom in Fe_4GeTe_2.

Chapter 6 investigates spin-phonon interactions in Fe_4GeTe_2, where reduced dimensionality amplifies these effects. Through micro-Raman spectroscopy and first-principles analysis, we examine lattice dynamics and spin-phonon coupling in exfoliated Fe_4GeTe_2 nanoflakes to uncover the mechanisms governing their distinctive properties. Polarization-dependent Raman measurements reveal key Raman modes, while temperature-dependent studies indicate strong spin-phonon coupling below T_{SR}, manifested through phonon energy softening and linewidth broadening. The interaction between pronounced spin-phonon coupling and intrinsic anharmonicity becomes evident near T_{SR}.

Chapter 7 explores the interplay between superconductivity and magnetism of a non-centrosymmetric quasi-1D superconductor $(TaSe_4)_3I$. Through detailed electronic transport measurements under varying temperatures and magnetic fields, we investigate the nature of superconductivity, anisotropy, the emergence of phase slip events - a characteristic of low-dimensional superconductors, and the possible influence of charge order and magnetic fluctuations. Our study motivates further investigations into such

systems, which provide an ideal platform for exploring complex ground states that emerge from the interplay of disorder, low dimensionality, and unique electronic structures.

Finally, **Chapter 8** summarizes the thesis findings and discusses future research directions in 2D magnetism and low-dimensional superconductivity in condensed matter physics.

Chapter 2

Theoretical Background

2.1 Magnetism

Magnetism, a fundamental physical phenomenon of solids, arises from the motion of electrons, mainly due to their intrinsic orbital and spin angular momentum. In solids, magnetism mainly arises due to the electron-associated magnetic moments. While atomic nuclei also possess magnetic moments, they are significantly weaker than those of electrons. The microscopic understanding of magnetism is fundamentally rooted in the quantum behavior of electrons' angular momentum. The coupling between an electron's spin and orbital motion arises from spin-orbit interaction. Magnetism varies based on whether electrons are free, as in metals, or localized on ion cores. When subjected to a magnetic field, localized electrons undergo Larmor precession, whereas free electrons follow cyclotron orbits. The free-electron model explains Pauli paramagnetism and Landau diamagnetism in metals, while localized 3d electrons in transition metals and intermetallic compounds show Curie paramagnetism. If magnetic interactions overcome thermal fluctuations, long-range magnetic order can emerge in these systems.

Magnetic ordering in a system arises from the exchange interaction (J) between the neighboring moments. This interaction, initially introduced separately by Werner Heisenberg and Paul Dirac, explains the influence of electrostatic forces while incorporating the Pauli exclusion principle [110–112]. All materials consist of atoms, and their physical properties are fundamentally determined by the atomic arrangement and interatomic interactions. Within an atom, electrons, which carry a negative charge, exhibit motion around the nucleus and possess an orbital angular momentum denoted by $\mathbf{L}$. According

to classical mechanics, this momentum is given by:

$$\mathbf{L} = \mathbf{r} \times m_e \mathbf{v}, \tag{2.1}$$

Here, m_e, $\mathbf{r}$, and $\mathbf{v}$ denote the mass, orbital radius, and velocity of the electron, respectively. The vector $\boldsymbol{\mu}$ is the magnetic dipole moment associated with a microscopic current loop and is expressed as:

$$\boldsymbol{\mu} = IA\hat{\boldsymbol{n}} = I\pi r^2 \hat{\boldsymbol{n}}, \tag{2.2}$$

where I refers to the current, A represents the loop area, and $\hat{\boldsymbol{n}}$ is the unit vector which is normal to the loop area. Mathematically, the current can be defined as

$$I = e\omega = \frac{ev}{2\pi r}, \tag{2.3}$$

Here, e and ω represent the charge and angular frequency of the electron, respectively. Combining the above equations, we obtain

$$\boldsymbol{\mu} = -\frac{e}{2m_e}\mathbf{L}. \tag{2.4}$$

The constant of proportionality $-\frac{e}{2m_e}$ is commonly referred to as the gyromagnetic ratio.

According to Bohr's second postulate, an electron's angular momentum is quantized and given by:

$$L = n\hbar, \tag{2.5}$$

where n is a positive integer, and $\hbar$ is the reduced Planck's constant. Using this along with Equation 2.2, the expression for the magnetic moment of an electron revolving along an orbital path of a hydrogen atom's nucleus can be written as:

$$\mu = -\frac{e\hbar}{2m_e} = -\mu_B, \tag{2.6}$$

where μ_B is the Bohr magneton, representing an electron's intrinsic magnetic moment in its first Bohr orbit. It's value is approximately 9.27×10^{-24} Am^2.

The movement of electrons within atoms naturally gives rise to a magnetic dipole moment, making all materials responsive to magnetic fields. However, this magnetic moment is not solely a result of the orbital angular momentum ($\mathbf{L}$) of electrons. In quantum mechanics, another essential component, known as intrinsic spin angular momentum ($\mathbf{S}$), plays a crucial role. Every elementary particle, including electrons, possesses spin, which can

be considered analogous to intrinsic angular momentum along its axis. Unlike orbital motion, spin is a fundamentally quantum property that lacks a straightforward classical interpretation, yet it significantly contributes to the formation of a magnetic dipole moment. The electron's overall angular momentum ($\mathbf{J}$) results from combining its orbital and spin contributions:

$$\mathbf{J} = \mathbf{L} + \mathbf{S}. \tag{2.7}$$

As highlighted in previous reports, spin ($\mathbf{S}$) has a dominant influence on a material's magnetic properties, often surpassing the contribution of orbital angular momentum ($\mathbf{L}$), which in many cases can be considered negligible [110].

Since all materials exhibit some level of interaction with a magnetic field, it is essential to define magnetic materials considering how their magnetic dipoles are arranged. These materials can be classified according to whether their dipole moments are aligned parallel to each other, anti-parallel, or remain disordered. When the magnetic dipole moments of individual atoms are oriented in random directions, producing a total magnetic moment of zero ($\sum \boldsymbol{\mu} = 0$), then these materials are categorized as either paramagnetic (PM) or diamagnetic. In common terms, these materials are typically described as non-magnetic. Nevertheless, both types can show some degree of dipole alignment when subjected to an externally applied magnetic field. Conversely, if the dipole moments maintain a specific alignment even without an applied field, the material is considered magnetically ordered. This class of materials includes ferromagnets (FM), antiferromagnets (AFM), ferrimagnets, etc., each exhibiting distinct magnetic behaviors based on their dipole interactions (see Figure 2.1).

2.1.1 Magnetic Responses: Diamagnetism & Paramagnetism

In both diamagnetic and PM substances [111, 112], the magnetic dipole moments ($\boldsymbol{\mu}$) of individual atoms act independently without interacting with each other, resulting in a random orientation and an overall magnetic moment equal to zero. However, when external magnetic fields are applied, partial alignment of these dipoles occurs. Upon removal of the field, thermal fluctuations randomize their orientations, preventing any retained magnetization. The primary distinction between these two classes of material systems lies in the response of their induced magnetic field to the external field: PM materials develop a magnetic field aligned with the applied field, whereas diamagnetic materials generate an opposing magnetic field.

Diamagnetism originates from the orbital motion of electrons around the nucleus, as described by Lenz's Law [113], where an external field induces a current, opposing changes in magnetic flux. This effect is universal but often weak, being overshadowed by PM or FM contributions.

Paramagnetism, on the other hand, requires a quantum mechanical framework. In PM materials, atoms possess unpaired electrons with a nonzero spin (S), which tend to align themselves along the applied magnetic field's direction, resulting in the net magnetization along the same direction as of the applied field.

2.1.2 Magnetic Ordering: Ferro-, Antiferro- & Ferrimagnetism

Ordered magnetic materials possess a well-defined arrangement of dipole moments, which align in specific orientations relative to one another [112]. Despite thermal fluctuations, the energy is insufficient to disrupt this alignment, allowing the material to retain its magnetic order. The classification of magnetic materials depends on how the magnetic moments of their atoms are arranged. Unlike PM and diamagnetic materials, which lack spontaneous magnetization, FM, AFM, and ferrimagnetic materials exhibit distinct long-range magnetic orders due to exchange interactions occurring between the neighboring spins (see Figure 2.1 for comparison).

In FM materials, atomic magnetic moments spontaneously align in a parallel configuration even without an applied magnetic field, resulting in a net magnetization. This alignment is driven by exchange interactions that stabilize the parallel spin arrangement. A key characteristic of FMs is hysteresis, enabling the material to maintain its magnetization even after the external field has been withdrawn. In AFM materials, neighboring atomic moments align in a perfectly antiparallel manner, leading to the complete cancellation of net magnetization without any externally applied magnetic field. This arrangement results from exchange interactions favoring alternating spin orientations. When heated above the Néel temperature (T_N), AFMs transition into a PM state as thermal energy disrupts the spin order. Ferrimagnetic materials also exhibit spontaneous magnetization; however, their atomic moments align antiparallel with unequal magnitudes, leading to a nonzero net magnetization. This behavior occurs in materials like magnetite (Fe_3O_4), where different sublattices contribute opposing but unequal spins. AFMs exhibit behavior similar to non-magnetic materials, whereas ferrimagnets resemble ferromagnets due to their net magnetization (see Figure 2.1).

Magnetism	Examples	Magnetic behaviour
Diamagnetism	Bi, Si, Cu, inert gases Susceptibility small and negative (-10^{-6} to -10^{-5})	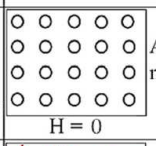 Atoms have no magnetic moments. 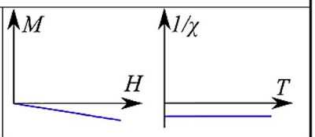
Paramagnetism	Al, O_2, MnBi Susceptibilty small and positive (10^{-5} to 10^{-3})	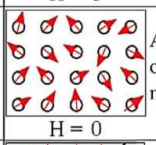 Atoms have randomly oriented magnetic moments. 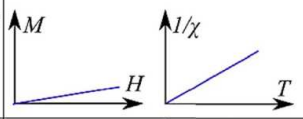
Ferromagnetism	Fe, Ni, Co, Gd Susceptibility large (generally > 100)	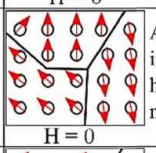 Atoms are organized in domains which have parallel aligned magnetic moments. 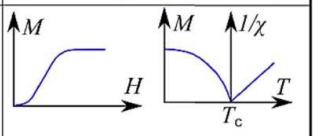
Antiferromagnetism	Cr, MnO, FeO Susceptibilty small and positive (10^{-5} to 10^{-3})	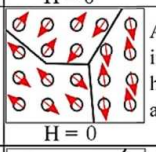 Atoms are organized in domains which have antiparallel aligned moments. 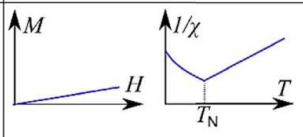
Ferrimagnetism	Fe_3O_4, $MnFe_2O_4$, $NiFe_2O_4$ Susceptibility large (generally > 100)	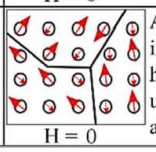 Atoms are organized in domains which have a mixture of unequal antiparallel aligned moments. 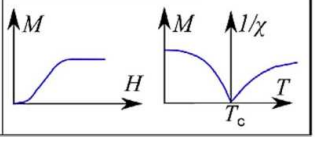

FIGURE 2.1: Summary of the different types of magnetism and their characteristics [117, 118]. This figure is reproduced from Ref. [118].

For FM, ferri-, and AFM materials, long-range magnetic order arises from interactions between the magnetic moments of neighboring atoms, governed by the Heisenberg exchange interaction (J) [114, 115], elucidated through quantum mechanics [111, 112], is discussed later. In 1906, Weiss proposed the concept of magnetic domains [116], attributing their formation to the balance between exchange and dipolar interactions, which play a pivotal role in minimizing the energy of FM materials.

2.2 Zeeman Effect: Magnetic Moment in a Magnetic Field

Any magnetic dipole placed within an external magnetic field ($\mathbf{B}$) experiences a torque, giving rise to potential energy, known as the Zeeman energy. The Hamiltonian for this interaction is expressed classically as:

$$\mathcal{H}_{Zeeman} = -\boldsymbol{\mu} \cdot \mathbf{B} \tag{2.8}$$

However, in quantum mechanics, since magnetic moments have quantized components along specific directions, the Zeeman energy is defined by:

$$E_{Zeeman} = g\mu_B M_J \mathrm{B} \tag{2.9}$$

Here M_J is termed as the magnetic quantum number, taking values from $-J$ to $+J$. Consequently, an external magnetic field splits each J-level into $(2J+1)$ non-degenerate states, with adjacent Zeeman levels split by an energy gap of $g\mu_B \mathrm{B}$. This equates to a few kelvins for a 1 T magnetic field. Such conditions can be easily achieved at low temperatures in laboratory settings. Consequently, very strong fields, around hundreds of Teslas are needed to significantly populate the ground state at room temperature. Figure 2.9 shows a simple diagram of Zeeman splitting for a spin-1/2 system.

In atomic systems, the orbital and spin angular momenta are not individually conserved but interact through spin-orbit coupling (SOC). This coupling produces the total angular momentum, defined as $\mathbf{J} = \mathbf{L}+\mathbf{S}$, where $\mathbf{L}$ and $\mathbf{S}$ are the orbital and spin angular momenta, respectively. The quantum numbers J and M_J are then used to describe the total angular momentum of an electron. The total magnetic moment of a multi-electron system can be described by:

$$\boldsymbol{\mu} = \mu_B(g_L\mathbf{L} + g_S\mathbf{S}) = g_J\mu_B\mathbf{J} \tag{2.10}$$

where g_J is the Landé g-factor, with $g_L = 1$ for orbital and $g_S \approx 2$ for spin contributions. The g-factor, resulting from SOC, is a dimensionless representation of the gyromagnetic ratio (γ). g_J has the mathematical form of:

$$g_J = \frac{3}{2} + \frac{S(S+1) - L(L+1)}{2J(J+1)} \tag{2.11}$$

For multi-electron ions, the Landé g-factor is defined as the ratio between the magnetic moment's z-component (measured in μ_B) and the total angular momentum (expressed in units of $\hbar$).

Combining the expressions for the magnetic moment (Equation 2.10) and the Zeeman energy (Equation 2.8), the Hamiltonian for the system is [117]:

$$\mathcal{H}_{Zeeman} = \mu_B(g_L\mathbf{L} + g_S\mathbf{S}) \cdot \mathbf{B} \tag{2.12}$$

The extent of the Zeeman splitting depends directly on the magnitude of $\mathbf{B}$, reaching its maximum when $\mathbf{B}$ is applied along the magnetic moment direction.

2.3 Magnetic Interactions

Magnetic moments in solids interact with one another, giving rise to various fascinating phenomena, including long-range magnetic ordering. While dipole-dipole interactions are the most intuitive form of coupling, they are relatively weak and cannot fully account for the strong magnetic correlations observed in many materials. In 1928, Heisenberg demonstrated that these strong interactions originate from Coulomb forces and quantum mechanical effects [115], leading to what is now known as the exchange interaction [119, 120]. This fundamental interaction is responsible for magnetic ordering in materials such as FM, where each atomic spin influences its neighbors to align in the same direction, thereby reducing the system's energy.

The subsequent sections provide a detailed discussion of these different types of exchange interactions and their significance in magnetic materials.

2.3.1 Magnetic Dipolar Interaction

The most fundamental interaction between magnetic moments in a system is the dipole-dipole interaction, which occurs between two magnetic dipoles, $\boldsymbol{\mu_1}$ and $\boldsymbol{\mu_2}$, which are separated by a distance $\mathbf{r}$. The energy associated with this interaction is given by:

$$E = \frac{\mu_0}{4\pi r^3}\left(\boldsymbol{\mu_1}\cdot\boldsymbol{\mu_2} - 3\frac{(\boldsymbol{\mu_1}\cdot\mathbf{r})(\boldsymbol{\mu_2}\cdot\mathbf{r})}{r^2}\right). \tag{2.13}$$

To estimate the strength of this interaction, consider two magnetic moments, each approximately $\mu \approx 1\mu_B$, separated by a distance of $r \approx 1$ Å. The magnitude of the dipolar interaction energy can be approximated as $\mu^2/4\pi r^3 \approx 10^{-23}$ J, which corresponds to a thermal energy scale of about 1 K. Given that magnetic ordering in many materials occurs at significantly higher temperatures, often reaching up to 1000 K, dipolar interactions alone are too weak to account for the observed magnetic phenomena.

2.3.2 Exchange Interactions

As discussed above, exchange interactions are fundamental to the emergence of long-range magnetic order. This interaction is expressed mathematically through the exchange energy involving the spins, $\mathbf{S_i}$ and $\mathbf{S_j}$, that is proportional to their scalar product, $\mathbf{S_i}\cdot\mathbf{S_j}$ [119].

First, we consider a simple system consisting of two electrons with spins $\mathbf{S_1}$ and $\mathbf{S_2}$. Since electrons belong to the class of fermions, their total wave function must be antisymmetric. As a result, the symmetry of the spatial component determines the form of the spin part of the wave function. If the spatial wave function is symmetric, the spin state must be an antisymmetric singlet state ($S = 0$) with energy eigenvalue E_S. Conversely, an antisymmetric spatial wave function requires the spin state to be a symmetric triplet ($S = 1$) with energy eigenvalue E_T. The exchange constant (J) is expressed as half the difference between the energies of the singlet and triplet states [119]:

$$J = \frac{E_S - E_T}{2}. \tag{2.14}$$

Therefore, the spin-dependent contribution to the effective Hamiltonian can be written as:

$$\mathcal{H}_{\text{spin}} = -2J\mathbf{S_1} \cdot \mathbf{S_2} \tag{2.15}$$

The nature of the spin alignment depends on the sign of the exchange constant J. When $J > 0$, the system favors parallel spin alignment, corresponding to a triplet state with lower energy (FM interactions, $E_T < E_S$). Conversely, if $J < 0$, the energy minimum corresponds to an antiparallel alignment, forming a singlet state (AFM interactions, $E_S < E_T$).

While the derivation of this equation for a two-electron system is relatively straightforward, extending it to a many-body system is significantly more complex. However, early developments in quantum mechanics suggested that such interactions occur between all neighboring atomic spins. This concept forms the basis of the Heisenberg model, whose Hamiltonian is expressed as [115, 119]:

$$\mathcal{H} = -\sum_{ij} J_{ij}\mathbf{S_i} \cdot \mathbf{S_j} = -2\sum_{i>j} J_{ij}\mathbf{S_i} \cdot \mathbf{S_j} \tag{2.16}$$

Where S_i and S_j are the spin vectors of electrons at neighboring sites i and j, with the summation over all pairs where $i > j$ prevents double-counting. Here, J_{ij} represents the *exchange constant (or exchange integral)* between the spins at sites i and j, determining the strength and nature of the interaction. Hence, $J_{ij} = J$ for neighboring spins and zero otherwise.

Accounting for the interaction energy under an applied external magnetic field ($\mathbf{H}$), the Zeeman term comes into play, and accordingly, the system's overall energy can be

formulated as [120]:

$$E = -2\sum_{i>j} J_{ij}\mathbf{S_i}\cdot\mathbf{S_j} + \sum_i g\mu_B\mathbf{S_i}\cdot\mathbf{H} \tag{2.17}$$

When a pair of electrons occupies the same atomic site, the J_{ij} is generally positive, favoring the triplet state. This results in an antisymmetric spatial wave function, which reduces Coulomb repulsion by increasing spatial separation between electrons, following Hund's principle for electron configuration [119]. However, if electrons occupy neighboring atoms, the relevant states are molecular orbitals rather than atomic orbitals. These molecular orbitals may exhibit spatial symmetry (bonding) or antisymmetry (antibonding), with the latter being energetically unfavorable, having higher energy and thus being less stable.. The higher energy of antibonding orbitals arises from their greater curvature, which leads to increased kinetic energy, as electrons are required to occupy distinct quantum states, as enforced by Pauli's exclusion principle. Consequently, singlet states (which are antisymmetric in spin) become energetically preferred, leading to a negative exchange integral [119].

- **Direct and Indirect Exchange Interactions**

Exchange interactions can be classified based on their underlying mechanism [119, 121]. When electronic wave functions of adjacent magnetic atoms overlap directly, the resulting interaction is called direct exchange. In this case, the magnetic atoms interact through their nearest neighbors' electrons, resulting in strong, short-range interactions. Conversely, if the coupling is mediated by an intermediate entity, such as a nonmagnetic ion or conduction electrons, it is termed indirect exchange.

Although direct exchange is the most intuitive mechanism for magnetic coupling, it is rarely dominant in real materials. In most cases, the overlap between neighboring magnetic orbitals is insufficient to account for the observed magnetic properties. In metallic magnets, conduction electrons play a crucial role, requiring a description that considers both localized and itinerant electron behavior. Consequently, indirect exchange interactions are often essential for accurately understanding magnetism in such materials. Indirect exchange interactions involve itinerant electrons or intermediary ions facilitating magnetic coupling over longer distances [121]. Several key types of indirect exchange interactions are discussed below:

(i) RKKY interactions: The Ruderman-Kittel-Kasuya-Yosida (RKKY) interaction [122, 123] is an indirect exchange mechanism in which conduction electrons in metals mediate the coupling between localized magnetic moments, even in the absence of direct overlap between their wave functions. The strength and sign of this exchange interaction

vary with the separation between moments, leading to a long-range, oscillatory behavior. As a result, the nature of the coupling – whether FM or AFM – depends on the interatomic distance, often resulting in complex and nontrivial spin configurations.

(ii) Superexchange: This mechanism is predominantly observed in ionic solids. In superexchange [124], magnetic cations interact indirectly through a nonmagnetic anion, facilitating exchange coupling. This interaction is characteristic of AFM insulators, such as transition metal oxides, where large oxygen anions spatially separate the transition metal cations. The coupling arises due to electron hopping via the intermediate p-orbitals of the oxygen anions.

(iii) Symmetric anisotropic exchange: The conventional Heisenberg exchange interaction corresponds to isotropic exchange. However, the combined influence of crystal electric field (CEF) effects and SOC can introduce anisotropy, leading to symmetric anisotropic exchange. Despite their distinct physical origins, the effects of symmetric anisotropic exchange and dipolar interactions can exhibit similarities. Notably, symmetric anisotropic exchange is generally much stronger than conventional dipolar interactions.

(iv) Antisymmetric anisotropic exchange:

In materials lacking inversion symmetry, a weak antisymmetric exchange interaction, referred to as the Dzyaloshinskii-Moriya (DM) interaction [125, 126] or anisotropic exchange interaction, can arise. This interaction originates from SOC, which perturbs localized spin states. Here, two neighboring FM atoms are coupled through an indirect exchange mechanism facilitated by a nonmagnetic atom, forming a three-site exchange pathway. The absence of inversion symmetry between two magnetic atoms allows for a nonzero DM vector, $\mathbf{D}$, which introduces a slight canting of spins at a small angle [127], leading to a weak FM component in AFM systems.

For two neighboring spins, $\mathbf{S}_i$ and $\mathbf{S}_j$, the DM interaction (DMI) introduces a bilinear energy term in the Hamiltonian, expressed as:

$$\mathcal{H}_{\mathrm{DM}} = -\mathbf{D_{ij}} \cdot (\mathbf{S}_i \times \mathbf{S}_j). \tag{2.18}$$

The Heisenberg exchange favors collinear spin alignment, while the DMI induces orthogonal spin arrangements, with chirality dictated by the direction of $\mathbf{D}_{ij}$.

2.4 Symmetry Breaking and Ferromagnetism

The interactions described in the previous section (see Section 2.3) drive magnetic ordering in solids. Spins couple to align in specific patterns, leading to a long-range ordered state. Exchange interactions (see Section 2.3.2) generate an effective exchange field ($H_{exchange}$), representing the energy associated with spin-spin interactions. While various forms of magnetic ordering exist, this thesis is limited to FMs.

A key feature of an ordered material is the emergence of a nonzero order parameter and broken symmetry. In FMs, magnetic moments align parallel, with the total magnetization serving as the order parameter. Even without an external magnetic field, spontaneous magnetization emerges in FMs, with moments uniformly aligned within individual domains, while different domains may exhibit varying orientations. For $T > T_C$, the order parameter vanishes, whereas $T < T_C$, there is a non-zero order parameter. Above T_C, a FM exhibits full rotational symmetry, where all directions are equivalent, and magnetic moments are randomly oriented. However, below T_C, the system selects a specific direction for spin alignment, breaking this rotational symmetry. In this low-temperature regime ($T < T_C$), the system retains only a reduced rotational symmetry, allowing rotations solely around the magnetization axis.

The Hamiltonian describing a FM under an external magnetic field ($\mathbf{H}$) is given by:

$$\mathcal{H} = -\sum_{ij} J_{ij}\mathbf{S}_i \cdot \mathbf{S}_j + g\mu_B\mu_0 \sum_i \mathbf{S}_i \cdot \mathbf{H} \tag{2.19}$$

where the first part on the right-hand side denotes the Heisenberg exchange energy term, and the second part corresponds to the Zeeman energy term.

The first modern theory of ferromagnetism, developed by Pierre Weiss, introduces a conceptual field known as the molecular field ($\mathbf{H}_{\mathrm{MF}}$) that is directly proportional to the magnetization, as: $\mathbf{H}_{\mathrm{MF}} = \lambda\mathbf{M}$. Here, λ is a proportionality constant, which quantifies the molecular field's strength. For a FM system, λ is positive ($\lambda > 0$). This field represents the equivalent magnetic field that would produce the same level of ordering in a system of non-interacting spins, as the exchange interaction does in a real system with interacting spins. This approach, known as the mean-field approximation, simplifies the complex spin interactions by considering an averaged interaction ($\mathbf{H}_{\mathrm{MF}}$) experienced by each spin. By incorporating the internal molecular field ($\mathbf{H}_{\mathrm{MF}}$) into the Zeeman term and replacing the

explicit exchange interaction, the Hamiltonian can be rewritten here as [119, 121]:

$$\mathcal{H} = g\mu_B\mu_0 \sum_i \mathbf{S}_i \cdot (\mathbf{H} + \mathbf{H}_{\mathrm{MF}}) \tag{2.20}$$

In this approach, a FM is treated as a non-interacting spin system, similar to a PM, with its Hamiltonian resembling that of a PM in an effective field ($\mathbf{H} + \mathbf{H}_{\mathrm{MF}}$). At low temperatures, $\mathbf{H}_{\mathrm{MF}}$ can spontaneously align the magnetic moments, even without an applied external field. However, thermal fluctuations progressively disrupt this alignment as the temperature rises. At a critical temperature, the FM order is completely lost. This theoretical framework is referred to as the Weiss model of ferromagnetism.

By employing the Brillouin function, the Hamiltonian solution can be determined [119, 121]. Using graphical methods, the Curie temperature (T_C) at zero field ($H = 0$) is derived as [119, 121]:

$$T_C = \frac{g_J\mu_B(J+1)\lambda M_S}{3k_B} \tag{2.21}$$

and,

$$H_{\mathrm{MF}} = \lambda M_S = \frac{3k_B T_C}{g_J\mu_B\mu_0(J+1)} \tag{2.22}$$

Here, g_J is the total angular momentum (Landé) g-factor, which accounts for the contributions from both the electron's spin and its orbital motion to the magnetic moment. For $T \gg T_C$, a small external field ($H \neq 0$) can induce a weak magnetization in the FM system, leading to:

$$M = \frac{\mu_0 T_C}{\lambda(T - T_C)} H \tag{2.23}$$

which gives the susceptibility:

$$\chi = \frac{C}{T - T_C} \tag{2.24}$$

This modified Curie's law is well-known as the Curie-Weiss law.

In many cases, it is useful to introduce a characteristic temperature, known as the Weiss temperature (Θ), and express the magnetic susceptibility (χ) using the Curie-Weiss law (Eq. 2.24):

$$\chi = \frac{C}{T - \Theta} \quad \begin{cases} \Theta < 0 & \text{for AFM interactions,} \\ \Theta = 0 & \text{for ideal PM behavior,} \\ \Theta > 0 & \text{for FM interactions.} \end{cases} \tag{2.25}$$

While the experimentally determined Weiss temperature does not always align precisely with the actual magnetic transition points like the Curie temperature (T_C) or Néel

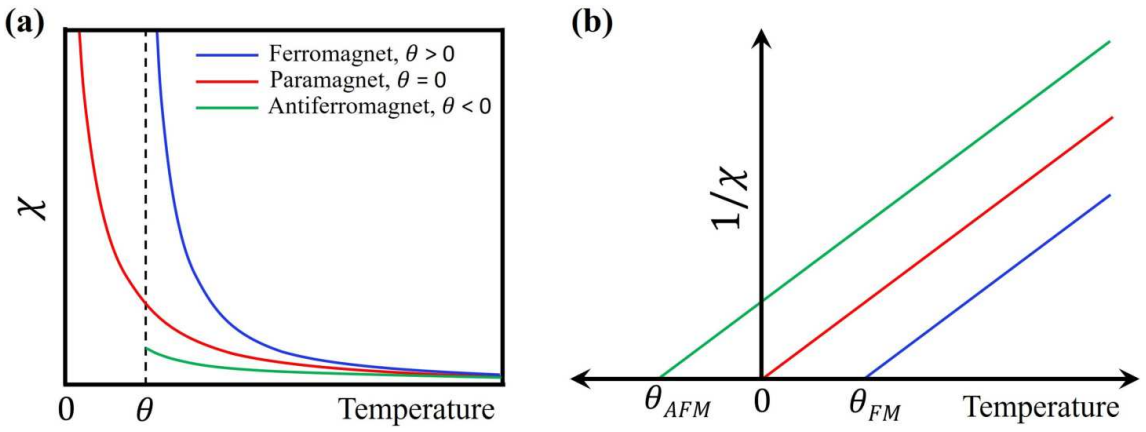

FIGURE 2.2: Graphical illustration of the Curie-Weiss law. (a) Temperature-dependent magnetic susceptibility (χ) for FM, PM, and AFM materials, highlighting that the Curie-Weiss law can predict their behaviors only in the PM regime. (b) Plot of inverse susceptibility ($1/\chi$) versus temperature. The linear extrapolation to the point where $1/\chi = 0$ yields the x-intercept, corresponding to the Weiss temperature (Θ).

temperature (T_N), it serves as a meaningful parameter that reflects the strength and nature of magnetic interactions. Discrepancies between Θ and the true transition temperature often arise due to factors such as reduced dimensionality, magnetic frustration, or thermal/quantum fluctuations. Nevertheless, the Curie-Weiss law remains a valuable approximation for interpreting magnetic susceptibility in the PM phase and offers insight into both the exchange interaction strength and the tendency of a system toward magnetic ordering (see Fig. 2.2).

2.5 Spin Waves in Ferromagnets

At T = 0, a FM exhibits perfect magnetic order, with all spins aligned uniformly. However, at any finite temperature, thermal fluctuations induce spin misalignment, leading to a reduction in spontaneous magnetization as the temperature rises. Now, the simplest form of magnetic excitation involves a minimal disruption in the spin alignment by the misalignment of a single spin. If this misalignment were restricted to a single lattice site, it would represent a single-particle excitation and necessitate a significant energy input. Instead, it is energetically more favorable for the disturbance to be distributed collectively across all atoms or ions within the FM crystal, forming a coherent wave-like collective excitation, known as *spin waves* (see Fig. 2.3). The quantized form of these collective excitations is referred to as a *magnon*. Creating a magnon requires minimal energy if its wavelength is sufficiently long.

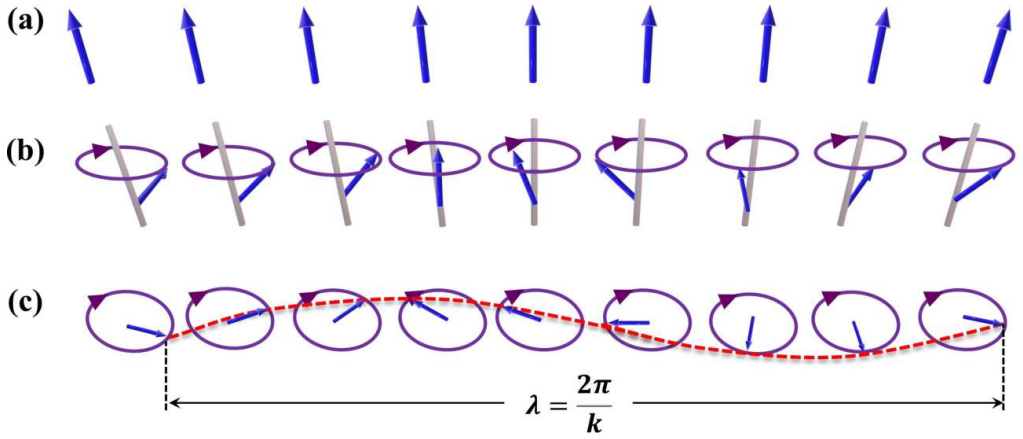

FIGURE 2.3: Semiclassical representation of spin-waves in a FM material. (a) The ground state of magnetic moments. (b) Precession of the magnetic moments with different phases. (c) The top view of the spin waves, showing a complete wavelength (λ). Reproduced from Ref. [23].

Consider a one-dimensional chain consisting of N uniformly spaced spins, each with magnitude S, separated by a distance a. These spins interact via a nearest-neighbor exchange coupling characterized by the exchange parameter J. In this system, the energy of a single magnon is given by the dispersion relation [119, 121]:

$$\hbar\omega_k = g\mu_B\mu_0 H + 4JS(1 - \cos ka) \tag{2.26}$$

This equation expresses the dependence of spin-wave frequency on the corresponding wavenumber k. When $k = 0$, the magnon energy is solely determined by the applied magnetic field, simplifying to $\hbar\omega_0 = \hbar\gamma\mu_0 H$. See Table 2.1 for the dispersion relations and specific heat for different excitations [117].

Excitation		**Dispersion**	**Specific heat**
Electrons	Fermions	$\mathcal{E}_k \approx \frac{\hbar}{2m}k^2$	γT
Phonons	Bosons	$\mathcal{E}_q \approx c_0 q$	T^3
Magnons (FM)	Bosons	$\mathcal{E}_q \approx D_{sw}q^2$	$T^{3/2}$
Magnons (AFM)	Bosons	$\mathcal{E}_q \approx D_{af}q$	T^3

TABLE 2.1: Dispersion relations and specific heat for different excitations [117]. $D_{sw} = 2JSa^2$ is the spin wave stiffness parameter, reduced from Equation 2.26

2.6 Mermin-Wagner Theorem

The spin-wave dispersion relation (refer to Section 2.5) is derived under the assumption of a FM ground state, either in an isotropic 1D chain or within a 3D lattice. The population (numbers) of magnons, thermally excited at temperature T, is expressed as:

$$n_m = \int_0^\infty \frac{N(\omega_q)d\omega_q}{e^{\hbar\omega_q/k_BT} - 1} \tag{2.27}$$

Here, $N(\omega_q)$ denotes the density of states of magnons. As magnons are Bosons, they follow Bose statistics. So, $N(\omega_q) = \omega_q^{-1/2}$ in 1D, constant in 2D and $\omega_q^{1/2}$ in 3D systems. By introducing the substitution $x = \hbar\omega_q/k_BT$, the integral in 3D leads to Bloch's $T^{3/2}$ law [117], which explains the decrease in magnetization within a FM at reduced temperatures due to magnon excitations. However, in 1D and 2D, the integral diverges at finite temperatures, implying that the spontaneous magnetization M vanishes for all $T > 0$ in the isotropic 1D and 2D Heisenberg models. This divergence arises from the excessive number of thermally excited spin waves, which destabilize long-range FM order. Consequently, a FM ordered state is inherently unstable in dimensions lower than three.

This result was first rigorously proven by Mermin and Wagner in 1966 and independently by Berezinskii, forming the basis of what is now known as the *Mermin-Wagner-Berezinskii theorem* [4, 5, 119]. It establishes that, in 1D and 2D isotropic Heisenberg systems, long-range magnetic ordering cannot occur at any nonzero finite temperature, while it remains possible in 3D. Hence, in a 1D spin chain or a 2D system, magnetic ordering can only exist at absolute zero temperature ($T = 0$ K).

The implications of the Mermin-Wagner-Berezinskii theorem are not as severe as they may initially appear. The divergence can be circumvented if the system exhibits some degrees of anisotropy in 1D or 2D, which introduces an energy gap at $q = 0$ in the spectrum of spin-wave excitations. This gap shifts the lower integration limit above zero, preventing the divergence and allowing magnetic order to persist even in lower-dimensional systems.

In another way, this theorem was exclusively for systems with continuous symmetry, such as Heisenberg systems, where the order parameter can revert to its original state through continuous rotation or translation. However, mechanisms like magnetic anisotropy (MA) break this continuous symmetry, allowing for long-range magnetic order even in lower-dimensional systems. In real materials, some degree of anisotropy is always present due to crystal field effects or dipole-dipole interactions. So, in 1D or 2D FM layered systems, this inherent anisotropy (or sometimes, induced anisotropy by applying a small external

magnetic field) stabilizes magnetic ordering at any finite temperature ($T > 0$ K), as observed in experimental systems, that bypasses the Mermin-Wagner-Berezinskii theorem.

2.7 Magnetic Anisotropy

Although the Heisenberg exchange energy is isotropic, most FM materials display direction-dependent magnetic properties, with spins preferentially aligning along specific crystallographic directions. This tendency is known as *magnetic anisotropy* (MA). And, these preferred crystallographic directions, where magnetization is energetically favored, are called 'easy axes', whereas the directions requiring higher energy for magnetization saturation are termed as 'hard axes' (see Figure 2.5). Deviating from preferred magnetization directions incurs an additional energy cost to the system, known as *magnetic anisotropy energy* (MAE). Anisotropy energies typically range from 10^2 to 10^7 J/m^3, corresponding to an energy per atom between 10^{-8} and 10^{-3} eV. Lower-symmetry magnetic ion lattices exhibit higher anisotropy energy, whereas higher-symmetry lattices tend to have lower anisotropy energy [117, 119]. Key contributors to MA include SOC, crystallographic symmetry axes, long-range dipolar interactions, etc.

The simplest form of MA is uniaxial anisotropy. The spatial energy distribution here depends on the angle θ defined by the magnetization direction relative to a specific axis. The related energy density can be expressed as:

$$E_{\text{uni}} = K_{\text{uni}} \sin^2 \theta \tag{2.28}$$

Here, K_{uni} represents the uniaxial anisotropy constant. Based on this equation, ordered materials can be classified into two categories: (i) **Easy-axis type ($K_{\text{uni}} < 0$):** The material prefers magnetization along a specific axis, with a perpendicular hard plane. (ii) **Easy-plane type ($K_{\text{uni}} > 0$):** The material favors magnetization within a plane, with a perpendicular hard-axis.

The anisotropy field (H_A) represents the field strength needed to fully align the magnetic moments along the hard direction (see Figure 2.4). To determine H_A, let us consider a uniformly magnetized system, where all spins align in a particular direction. The total energy density in the presence of uniaxial anisotropy and the external magnetic field ($\mathbf{H}$) (applied $\phi = 90°$ w.r.t. easy axis, see Figure 2.4(b)) can be written from the

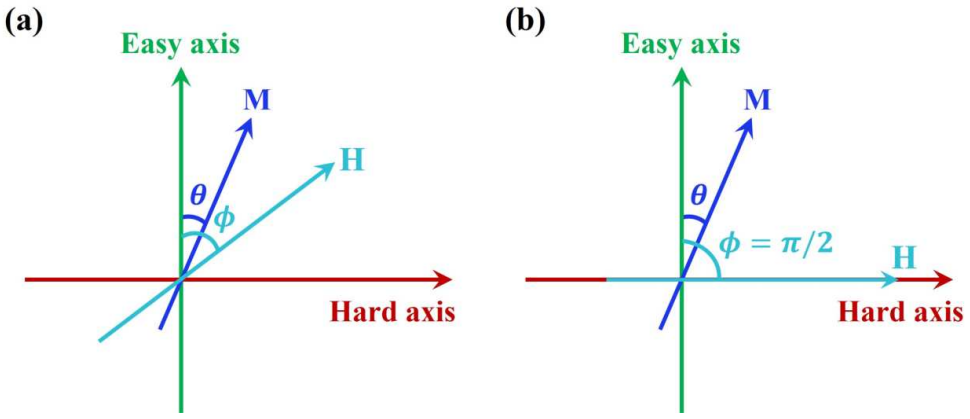

FIGURE 2.4: Representation of Stoner–Wohlfarth model to determine the anisotropy field.

Stoner–Wohlfarth model [117, 128] as:

$$E = K_u \sin^2\theta - \mu_0 M_s H \cos\left(\frac{\pi}{2} - \theta\right) \tag{2.29}$$

Here, the first term represents the uniaxial anisotropy energy, which favors spin alignment along the easy axis, minimizing the system's energy. The second term is the Zeeman energy, which causes the magnetic moments to orient themselves along the applied field (**H**) direction. The competition between these terms determines the equilibrium magnetization direction in the presence of **H**. This competing behavior leads to hysteresis in these magnetic systems. In the uniaxial system, the energy E is minimized by solving $\frac{\partial E}{\partial \theta} = 0$. By setting $\theta = \frac{\pi}{2}$, the Equation 2.29 is expressed as [117]:

$$H_A^{\text{uni}} = -\frac{1}{\mu_0 M_S}\frac{dE_A^{\text{uni}}}{d\theta} \approx \frac{2K_{\text{uni}}}{\mu_0 M_S} \tag{2.30}$$

The main sources of MA arise from intrinsic and extrinsic factors, such as crystal structure (intrinsic), sample shape (extrinsic), and atomic or micro-scale texture.

2.7.1 Magneto-crystalline Anisotropy

The most prevalent intrinsic type of MA is magneto-crystalline anisotropy (MCA), which results from the coupling between electronic spins and the crystal lattice structure [117, 119]. This coupling is primarily governed by single-ion, two-ion anisotropy, or the combination of both. Thus, MCA has primary origins such as crystal-field interactions, SOC, and interatomic dipole-dipole interactions. Although MCA is generally weaker than the exchange interaction, it plays a vital role to determine the easy axis of magnetization,

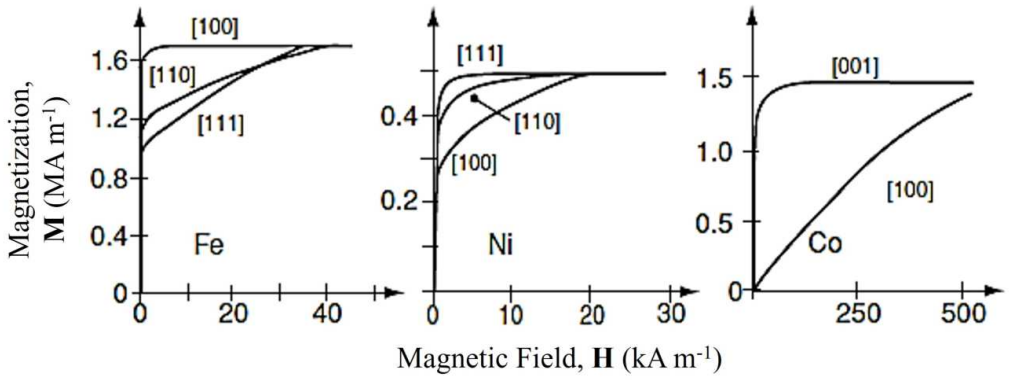

FIGURE 2.5: Magnetization of single crystals of Fe, Co, and Ni, along their different crystallographic axes, showing the easy and hard axes. This figure is reproduced from Ref. [117].

as the exchange interaction only enforces the spins' parallel or antiparallel alignment without influencing their spatial orientation.

The orientation of electronic orbits is influenced by crystallographic axes, and SOC compels electronic spins to align along specific directions dictated by the crystal symmetry. The complexity of MA is directly linked to lattice symmetry. In cubic crystals, the MAE depends on the direction of magnetization relative to the cubic edges and can be expressed as a function of the direction cosines $\alpha_x, \alpha_y, \alpha_z$:

$$E_{\text{MCA}} = K_0 + K_1(\alpha_x^2\alpha_y^2 + \alpha_y^2\alpha_z^2 + \alpha_x^2\alpha_z^2) + K_2\alpha_x^2\alpha_y^2\alpha_z^2 \tag{2.31}$$

Here, K_i's refer to MCA constants, viz., K_0, K_1, and K_2 are MCA constants, representing zero-, first-, and second-order contributions to the anisotropy energy. For uniaxial systems, the anisotropy energy density simplifies to:

$$E_{\text{MCA}} = K_{uni}\alpha_x^2 \tag{2.32}$$

where K_{uni} is the uniaxial anisotropy constant. The primary origins [117] of MCA are discussed in the following points:

(i) Single-ion anisotropy:

In crystals, certain orbitals become more stable due to orbital overlap with the surroundings. When spins couple to these orbitals via SOC ($\mathcal{H}_{\text{SOC}} = \lambda\langle\hat{L}\cdot\hat{S}\rangle$), magnetic moments align along preferred crystallographic directions for $S > 1/2$. However, for $S = 1/2$, Kramer's theorem ensures spin degeneracy remains intact without an external field. This interplay of crystal field and SOC leads to single-ion anisotropy (SIA), a key

source of anisotropy in magnetic materials. For a uniaxial system, the Hamiltonian is given by:

$$\mathcal{H}_{\text{SIA}} = -DS_z^2 \tag{2.33}$$

where D is the SIA constant, determining the preferred spin alignment axis.

(i) Two-ion anisotropy:

This anisotropy primarily arises from dipole-dipole interactions (see Section 2.3.1) or symmetric anisotropic exchange (see Section 2.3.2). The dipole-dipole interaction favors head-to-tail spin alignment, reducing anisotropic energy by $\frac{3\mu_0\mu_1\mu_2}{4\pi r^3}$. However, this contribution is typically small (a few kelvins). In contrast, the anisotropic exchange interaction is significantly stronger and also enforces preferred spin orientations in exchange-coupled systems.

2.7.2 Shape Anisotropy and Demagnetizing Energy

In addition to intrinsic effects, extrinsic factors such as the sample's shape, size, or dimensions contribute to the anisotropic energy. This effect, known as shape anisotropy, arises from demagnetizing energy (E_{demag}) [117, 129]. It originates from the anisotropic dipolar interaction of unsaturated magnetic dipoles (stray and demagnetization fields), emerging due to the asymmetry in the geometry of magnetic elements.

In a magnetic system having finite boundaries, surface poles generate the magnetic stray field (lines of force) extending outside the sample, resulting in a demagnetizing field ($\mathbf{H}_{\text{demag}}$) inside the sample. So, the internal magnetic field within a sample is the combined effect of the externally applied field ($\mathbf{H}_{\text{ext}}$) and the demagnetizing field ($\mathbf{H}_{\text{demag}}$) originates from the sample's own magnetization distribution. Mathematically, this can be expressed as [117]:

$$\mathbf{H}_{\text{int}} = \mathbf{H}_{\text{ext}} + \mathbf{H}_{\text{demag}} \approx \mathbf{H}_{\text{ext}} - N\mathbf{M} \tag{2.34}$$

Here, N is the demagnetizing factor of the sample, which quantifies the strength of the demagnetizing field (degree of self-demagnetization due to its shape) that opposes magnetization within a material. N varies depending on the geometry of the sample. In a sample with uniform magnetization, the sum of the demagnetization factors along the three principal axes is always equal to one (i.e, $N = N_x + N_y + N_z = 1$).

(i) For a sphere, N is isotropic with a value of $1/3$ in all directions.

(ii) An infinitely thin film has $N \approx 1$ perpendicular to the plane (i.e., stray field, $\mathbf{H}_{\text{demag}}$, and shape anisotropy is maximum in out-of-plane direction) and $N \approx 0$ within the plane.

(iii) For a long cylindrical rod, $N \approx 0$ along its length but significantly larger in the transverse directions.

Now, for very thin film samples, the stray field is maximum. The energy associated with this stray field is as follows:

$$E_{\text{demag}} = -\frac{1}{2}\int_0^V \mu_0 \mathbf{M} \cdot \mathbf{H}_{\text{demag}}\, dV \tag{2.35}$$

For an arbitrary shape, $\mathbf{H}_{\text{demag}}$ depends strongly on the sample's geometry and varies spatially in a complex manner. It becomes significant in non-spherical samples, like thin films or elongated structures, where magnetic moments align along specific geometric directions of the sample to minimize energy E_{demag}. For thin films, spins preferentially lie within a plane. The anisotropy field due to shape can be expressed as

$$H_A^{\text{shape}} = 4\pi N M_S \tag{2.36}$$

So, the total anisotropy field for a thin plate-shaped sample is given by:

$$H_A = H_A^{\text{uni}} + H_A^{\text{shape}} = \frac{2K_{\text{uni}}}{\mu_0 M_S} + 4\pi N M_S \tag{2.37}$$

From Equation 2.35, one can derive the shape anisotropy constant [129] as

$$K_{\text{sh}} = \frac{\mu_0}{4}(1 - 3N)M^2 \tag{2.38}$$

So, for the spherical shape, $N = 1/3$, provides shape anisotropy constant is zero.

2.8 Anisotropy Measurements

The characterization of MA is crucial for understanding the directional dependence of a material's magnetic properties. Various experimental techniques [129] are employed to quantify anisotropy, including torque magnetometry, ferromagnetic resonance, magneto-optical methods, X-ray magnetic circular dichroism, etc. These techniques allow for the determination of anisotropy constants, preferred magnetization directions, and energy barriers associated with magnetization reversal.

Torque magnetometry measures the mechanical torque exerted by a magnetized sample when subjected to an applied magnetic field, providing insight into the anisotropic energy landscape. *Ferromagnetic resonance* (FMR), on the other hand, examines the resonance condition of precessing spins in a magnetic field, yielding information about anisotropy fields and relaxation mechanisms. Magneto-optical methods, such as *Kerr effect measurements* (MOKE), offer additional insight into anisotropy by analyzing the polarization changes in reflected light due to magnetization. Additionally, *X-ray magnetic circular dichroism* (XMCD) serves as an effective technique for probing and investigating spin and orbital magnetic moments at the atomic scale. Since single-ion anisotropy is closely linked to the orbital moment, XMCD enables direct investigation of anisotropy by analyzing differential absorption of circularly polarized X-rays, offering a deeper understanding of anisotropic interactions in transition metal magnets.

By combining these techniques, a comprehensive understanding of anisotropy contributions from magnetocrystalline effects, shape-dependent factors, dipolar interactions, etc can be obtained.

2.9 Scattering Mechanisms and Resistivity in Magnetic Metals

The electrical resistivity of magnetic metals arises due to various scattering processes that disrupt the motion of conduction electrons. These scattering mechanisms include interactions with lattice vibrations (phonons), other conduction electrons, magnetic excitations (magnons), and impurities. Each of these processes exhibits a distinct dependence on temperature, leading to complex resistivity behavior in different temperature regimes.

The total resistivity $\rho_{total}(T)$ of a FM metal can be described as the cumulative effect of various scattering sources, with each contribution adding independently within a given conduction band, a principle formulated in Matthiessen's rule [36, 130, 131]:

$$\rho_{total}(T) = \rho_{\text{imp}} + \rho_{\text{e-e}}(T) + \rho_{\text{e-ph}}(T) + \rho_{\text{e-mag}}(T, B) \tag{2.39}$$

where ρ_{imp} represents the temperature-independent resistivity due to static impurities, while the other terms correspond to temperature-dependent contributions from electron-electron, electron-phonon, and electron-magnon scattering.

(i) Electron-Impurity Scattering: The presence of impurities and structural defects introduces static scattering centers, affecting the motion of conduction electrons. This elastic impurity scattering is independent of temperature and contributes a constant resistivity term ρ_{imp}. In a disordered system, such as alloys, impurity scattering can be dominant, leading to an overall resistivity that remains significant even at very low temperatures.

(ii) Electron-Electron Scattering: Interactions between conduction electrons contribute to resistivity through momentum exchange processes. At low temperatures, where phonon-mediated scattering is weak, inelastic electron-electron scattering becomes the primary resistivity mechanism. The temperature dependence follows:

$$\rho_{\text{e-e}}(T) \propto T^2 \tag{2.40}$$

for a Fermi liquid [132], due to the phase-space restrictions imposed by the Pauli exclusion principle. This quadratic dependence is observed in simple metals at sufficiently low temperatures, where phonons do not contribute significantly to scattering.

(iii) Electron-Phonon Scattering: The interaction of conduction electrons with thermal vibrations of the crystal lattice results in inelastic electron-phonon scattering, which dominates resistivity at intermediate and high temperatures. As temperature increases, the number of thermally excited phonons grows, leading to an increase in scattering events.

At low temperatures, the resistivity arising from electron-phonon interactions follows the Bloch-Grüneisen equation [133, 134]:

$$\rho_{\text{e-ph}}(T) = A \left(\frac{T}{\Theta_D} \right)^5 \int_0^{\Theta_D/T} \frac{x^5 e^x}{(e^x - 1)^2} dx \tag{2.41}$$

where A is a material-dependent constant, Θ_D represents the Debye temperature, and the integral accounts for the distribution of phonon states.

The resistivity contribution from electron-phonon scattering at low temperatures ($T \ll \Theta_D$, Bloch-Grüneisen regime) typically follows a power-law dependence:

$$\rho_{\text{e-ph}}(T) \propto T^5 \tag{2.42}$$

While at higher temperatures ($T > \Theta_D$), the resistivity saturates, approaching a linear dependence:

$$\rho_{\text{e-ph}}(T) \propto T \tag{2.43}$$

This occurs because, at temperatures above Θ_D, the phonon population saturates, leading to a resistivity behavior that follows the classical equipartition theorem.

(iv) Electron-Magnon Scattering: In magnetic metals, the spin of conduction electrons interacts with collective excitations of the localized magnetic moments, known as magnons. This inelastic electron-magnon scattering affects resistivity in a temperature-dependent manner. The external magnetic field also modifies the magnon spectrum, thereby influencing electron-magnon scattering rates. For sufficiently large magnetic fields, the magnon gap increases, leading to strong suppression of electron-magnon scattering.

At low temperatures, the resistivity contribution for a FM follows the following relation due to the quadratic magnon dispersion relation in long-wavelength approximations:

$$\rho_{\text{e-mag}}(T) \propto T^2 \tag{2.44}$$

As the temperature increases closer to the Curie temperature (T_C), magnon population increases, leading to:

$$\rho_{\text{em}}(T) \propto T^{3/2} \tag{2.45}$$

for a Bloch-type scattering mechanism in simple FMs. Near T_C, the spin disorder becomes dominant, and the resistivity follows a more complex form, often showing a linear or non-monotonic behavior depending on the material.

While in an AFM, the dependence is generally stronger. As the temperature increases, the thermal disorder in the magnetic system intensifies electron-magnon scattering, often leading to a more complex temperature dependence, which can deviate from the simple quadratic behavior, often scaling as T^4 at low temperatures.

(v) Kondo Effect: In materials with magnetic impurities, an extra source of scattering emerges from the interaction between the delocalized conduction electrons and the localized magnetic impurities. This phenomenon, referred to as the Kondo effect [135], leads to a resistivity that initially decreases with decreasing temperature but then increases as temperature is lowered further.

When a non-magnetic metal contains a small concentration of magnetic impurity atoms (such as Fe or Mn in Cu or Au), the localized spins of these impurities interact with the spin of conduction electrons via an antiferromagnetic exchange interaction. At high temperatures, this interaction causes a weak spin-flip scattering, contributing a small, nearly temperature-independent term to the resistivity. However, as the temperature decreases, the probability of spin-flip scattering increases, due to enhanced quantum interference effects. This leads to an increase in resistivity at low temperatures – a behavior that contradicts the usual trend where resistivity decreases with decreasing temperature. At the low-temperature regime, the characteristic temperature dependence follows:

$$\rho_{\text{Kondo}}(T) \propto -\ln T \tag{2.46}$$

This logarithmic behavior signifies an enhancement of scattering as the system approaches the Kondo temperature T_K, below which a correlated many-body state forms, suppressing the impurity spin fluctuations.

These scattering processes collectively define the transport properties of magnetic metals, with their relative significance varying depending on material composition, temperature, and magnetic ordering.

2.10 Ordinary and Anomalous Hall Effect

In 1879, Edwin H. Hall first discovered the classical Hall effect [67, 136], describing the motion of charged particles of a conducting material when subjected to an external magnetic field. Imagine a situation where electrons are restricted to move only within the x-y plane. When a steady current (I) flows along the x-axis, and a magnetic field (B) is applied in the direction of the z-axis, perpendicular to the direction of the current, then the charge carriers feel a Lorentz force. This force causes the electrons to deviate from their initial trajectory, leading to the buildup of opposite charges at the material's opposite edges. The resulting charge imbalance generates an internal electric field. When this electric force balances the Lorentz force generated by the external magnetic field, electrons are able to travel from one edge to the opposite edge of the material. This movement creates a transverse potential difference between the two edges of the sample, known as Hall voltage (V_H) (see Fig. 2.6(a)). This phenomenon is known as the ordinary Hall effect (OHE) [48, 117, 136].

In the equilibrium condition, the Lorentz force can be represented as:

$$\mathbf{F} = q(\mathbf{E} + \mathbf{v} \times \mathbf{B}) = 0 \tag{2.47}$$

where $\mathbf{v}$ is the velocity of the charge carrier, and q is its charge.

Considering t as the thickness of the sample, the Hall voltage (V_H) is expressed as:

$$V_H = \frac{IB}{nte} = R_H \cdot I \tag{2.48}$$

In this equation, R_H denotes the Hall resistance, n refers to the carrier density, and e is the elementary charge. This relationship indicates that the Hall voltage (or resistance or resistivity) varies linearly with B_z. So, the Hall resistivity [136]:

$$\rho_{xy} = R_0 B_z. \tag{2.49}$$

Here, R_0 represents the ordinary Hall coefficient, a material-specific constant that is temperature-independent. Its magnitude enables the calculation of the effective carrier concentration in a single-band model, with its sign indicating the majority carrier type: positive for holes (p-type) and negative for electrons (n-type) (see Fig. 2.7(a)). When a single type of charge carrier dominates the conduction process, say n-type, the Hall coefficient (R_0) can be expressed as [67, 136]:

$$R_0 = \frac{E_y}{j_x B_z} = \frac{V_H t}{IB} = -\frac{1}{ne} \tag{2.50}$$

where j_x represents the carrier electrons' current density, E_y denotes the induced electric field, and B_z is the z-component of the magnetic field ($\mathbf{B}$).

Subsequently, in 1881, Hall observed that this effect in FM iron was significantly more pronounced, being approximately ten times stronger than the non-magnetic conductors [137]. This enhanced phenomenon in FM materials, even at $B = 0$, was termed the anomalous Hall effect (or, extraordinary Hall effect). So, in FM materials, an additional contribution arises to the measured Hall resistivity, even without any external field, due to the material's magnetization (M), known as the anomalous Hall effect (AHE) [138]. AHE arises from SOC, which induces transverse charge accumulation by deflecting spin-up and -down electrons along the opposite directions (see Fig. 2.6(b)). The empirical relationship between ρ_{xy} (transverse Hall resistivity), B_z (applied magnetic field), and M_z

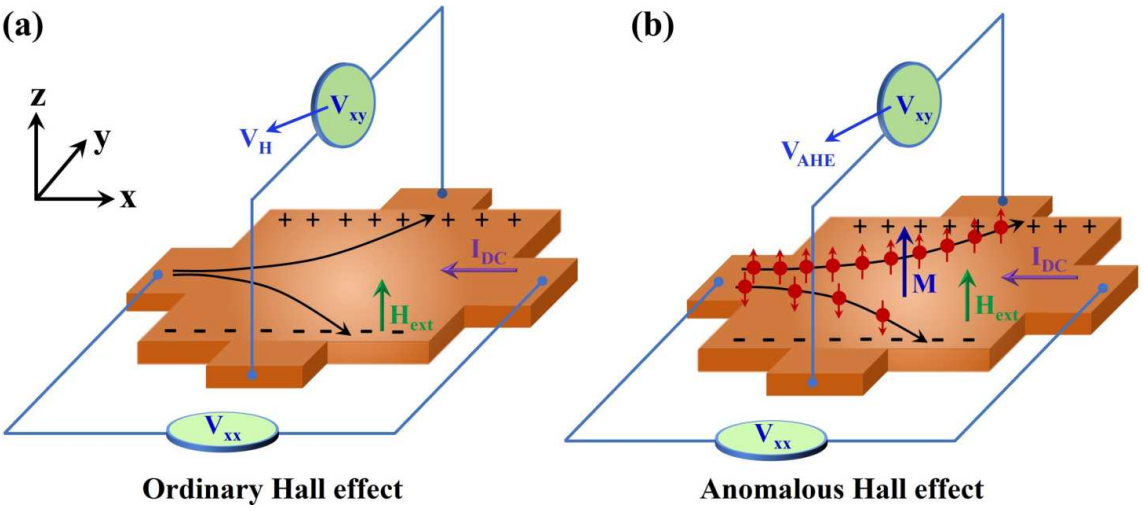

FIGURE 2.6: Schematic representation of (a) ordinary and (b) anomalous Hall effect.

(magnetization) was established by Pugh et al [139, 140], is expressed as:

$$\rho_{xy} = \rho_{xy}^{OHE} + \rho_{xy}^{AHE} = R_0 B_z + R_S M_z \tag{2.51}$$

The first term, ρ_{xy}^{OHE}, represents the ordinary Hall resistivity and arises from the Lorentz force generated by the applied magnetic field. The second term, ρ_{xy}^{AHE}, denotes the anomalous Hall resistivity and is unique to magnetic materials. Notably, ρ_{xy}^{AHE} can have a non-zero value even without applying any external magnetic field, as it is proportional to the material's spontaneous magnetization. R_S is the anomalous Hall coefficient, which is a temperature-dependent parameter. However, it was suggested that the R_S may not scale properly with M when resistivity varies with B or T. Therefore, S_H, a material-specific scaling factor, was introduced to measure the sensitivity of ρ_{xy}^{AHE} to M [141], where,

$$R_S = S_H \rho_{xx}^2 \tag{2.52}$$

The Hall conductivity, σ_{xy}, can be derived from ρ_{xy} and the longitudinal resistivity, ρ_{xx}, using the following relation [138]:

$$\sigma_{xy} = \frac{\rho_{xy}}{\rho_{xx}^2 + \rho_{xy}^2} \tag{2.53}$$

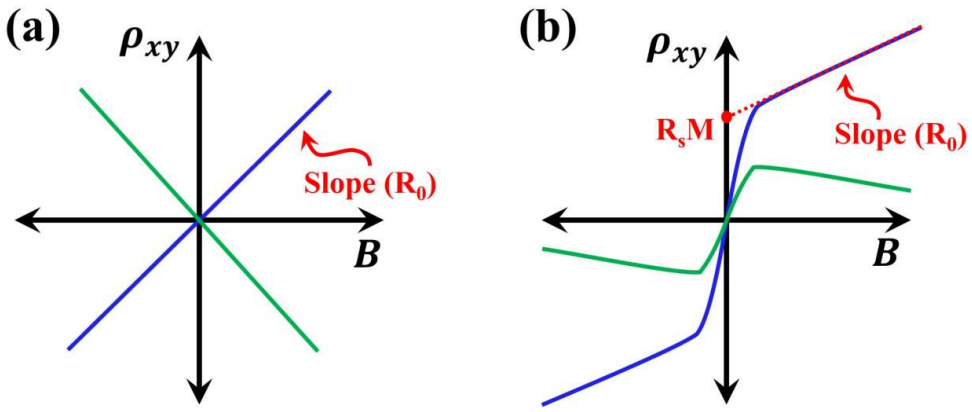

FIGURE 2.7: Schematic illustration of Hall resistivity, ρ_{xy} as a function of perpendicular magnetic fields (B), representing (a) ordinary Hall effect, (b) anomalous Hall effect. The green and blue curves correspond to materials with electron and hole majority charge carriers, respectively, highlighting the carrier-type-dependent behavior in Hall response.

The anomalous Hall conductivity (AHC), σ_{xy}^{AHE}, can be estimated from the σ_{xy} vs. B curve and can be expressed as [138]:

$$\sigma_{xy}^{AHE} \approx \frac{\rho_{xy}^{AHE}}{\rho_{xx}^2} \approx \frac{\mu_0 R_S M_S}{\rho_{xx}^2} \tag{2.54}$$

The anomalous Hall angle (θ_{AHE}) quantifies the magnitude of the transverse current produced relative to the applied longitudinal current, as follows [138];

$$\theta_{AHE} = \frac{\sigma_{xy}^{AHE}}{\sigma_{xx}} \tag{2.55}$$

- **Mechanisms of AHE:**

AHE arises from both intrinsic and extrinsic contributions stemming from various mechanisms. Mainly, three mechanisms [138] have been recognized to explain the AHE in FMs or materials exhibiting strong SOC, such as: (a) the intrinsic Karplus–Luttinger (K–L) mechanism, (b) the extrinsic side-jump mechanism, and (c) the extrinsic skew-scattering mechanism. Figure 2.8 illustrates these three mechanisms for the contributions to the AHC. The intrinsic K–L mechanism [142] arises from the anomalous carrier drift caused by the nonzero Berry curvature in momentum space, which originates from the SOC. This effect largely does not depend on scattering and is dependent exclusively on the crystal's band structure [138, 143, 144]. The extrinsic contributions, however, arise from the interactions between the electrons and impurities. The extrinsic side-jump mechanism [145] involves electrons being scattered in opposite directions as a result of interactions/scatterings with impurities coupled through spin–orbit effects. Here, the electron's velocity is redirected in opposing directions due to the opposing electric fields it feels when approaching and then departing from an impurity. The extrinsic skew-scattering mechanism [146, 147] originates from the asymmetric scattering of electrons by impurities influenced by SOC. All three mechanisms follow the power law as [138]:

$$\rho_{xy}^{AHE} \approx a\rho_{xx}^{\alpha} \tag{2.56}$$

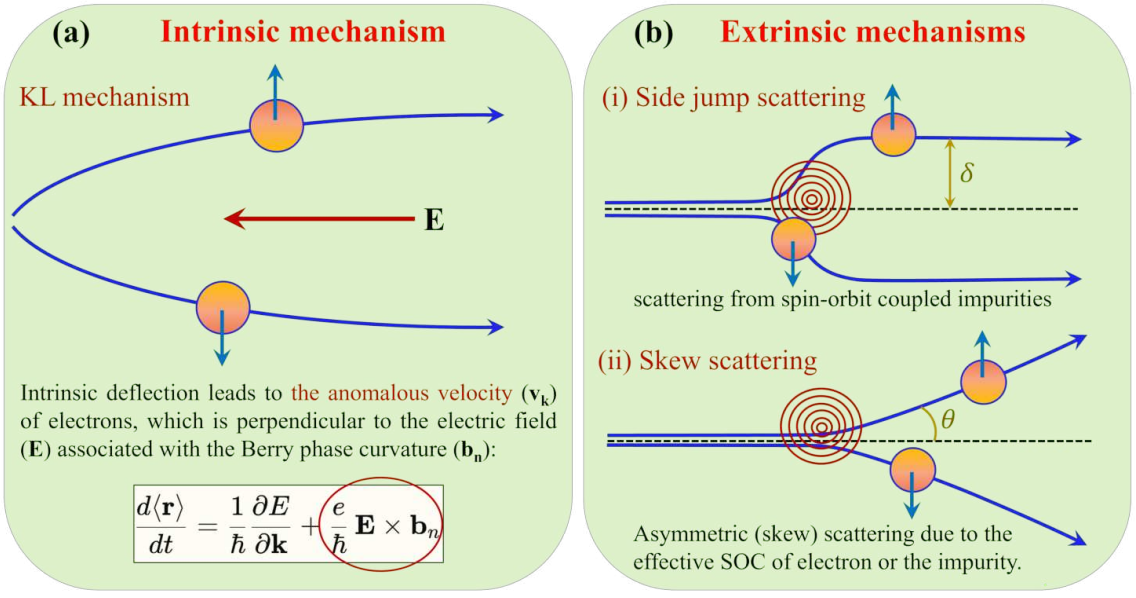

FIGURE 2.8: Schematic representation of different mechanisms involved in AHE. (a) Intrinsic K-L mechanism, (b) Extrinsic mechanisms: (i) Side jump and (ii) Skew scattering mechanisms. The figure is reconstructed from Ref. [138].

For both the intrinsic K-L and extrinsic side-jump mechanisms, the exponent α equals 2, whereas for the extrinsic skew-scattering mechanism, α is equal to 1 [138]. In FM materials, the AHE dominates over the OHE, and its magnitude depends on the interplay of these mechanisms, which occur simultaneously. To empirically define all three contributions, the temperature-dependent ρ_{yx}^{AHE} can be written as [138]:

$$\rho_{xy}^{AHE}(T) = \alpha\rho_{xx0} + \beta\rho_{xx0}^2 + \gamma\rho_{xx}^2(T) \tag{2.57}$$

In this equation, ρ_{xx0} represents the temperature-independent residual longitudinal resistivity. The first and second terms correspond to the extrinsic contributions from skew scattering and the side-jump mechanism, respectively, while the third term accounts for the intrinsic contribution. To isolate the intrinsic contribution, a linear fit is performed on the plot of ρ_{yx}^{AHE} versus ρ_{xx}^2 at various temperatures. The slope (γ) of this linear fit directly gives the intrinsic value of the anomalous Hall conductivity (σ_{xy}^{int}).

2.11 Electron Spin Resonance Spectroscopy

Electron Spin Resonance (ESR), first observed in paramagnetic transition metal salts by Evgeniy K. Zavoisky in 1944 [148], is an indispensable spectroscopic technique used to explore the electronic and magnetic properties of materials [149–151]. Any system containing unpaired electrons is fundamentally suitable for investigation using ESR. In the realm of 2D vdW magnetic systems, ESR is a powerful tool for investigating MA, characterizing magnetic easy axes, estimating magnon excitation gaps, and understanding spin-spin correlations and spin dynamics, thereby offering critical insights into their fundamental physics and potential applications in spintronics [152].

2.11.1 Principles of ESR

ESR primarily focuses on the spin of electrons. Let us consider a simple case involving a paramagnetic center with an unpaired electron characterized by a spin $S = 1/2$. When subjected to an externally applied magnetic field (H_{ext}), the spin states $|+1/2\rangle$ and $|-1/2\rangle$ will be splitted due to the Zeeman effect [153] (see Figure 2.9). This splitting will create an energy gap ΔE between the states, given by:

$$\Delta E = g\mu_B\mu_0 H_{\text{ext}} \tag{2.58}$$

where, g represents the g-factor and μ_B denotes the Bohr magneton. Now, If the spin system is exposed to microwave radiation with a frequency ν, such that the microwave energy ($h\nu$) matches the energy gap (ΔE) between these states, a resonant transition occurs and the electron's spin from the lower-energy state ($|-1/2\rangle$) absorbs the microwave radiation quantum and moves to the higher-energy state ($|+1/2\rangle$) such as: $|-1/2\rangle \rightarrow |+1/2\rangle$. The condition for paramagnetic resonance is expressed as [149, 151]:

$$h\nu_0 = g\mu_B\mu_0 H_{\text{res}} \tag{2.59}$$

Here, the resonance field can be estimated as $H_{\text{res}} = \frac{h\nu_0}{g\mu_B\mu_0}$ for a fixed frequency ν_0, and similarly, the resonance frequency ν_{res} can be calculated when keeping the field H_0 constant, from the relation: $\nu_{\text{res}} = \frac{g\mu_B\mu_0 H_0}{h}$. For instance, in the case of microwave radiation with a frequency in the X-band range (ν between 8 and 12 GHz), the resonance field is approximately in the range of 0.29 - 0.43 T if $g = 2$. It is important to note that, in that simple case for resonance to occur, the microwave radiation with its oscillating

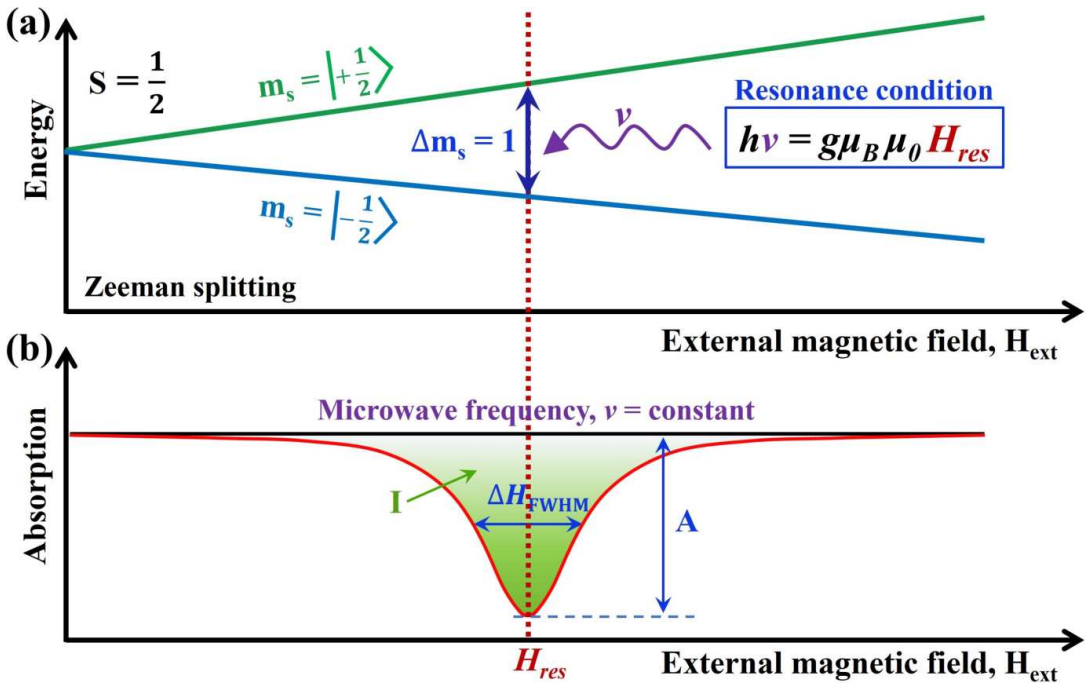

FIGURE 2.9: Zeeman effect and Resonance phenomenon for a spin-1/2 system. (a) Electron spin states split due to the Zeeman interaction when an external magnetic field is applied (H_{ext}). At resonance, microwave radiation having energy $h\nu$ is absorbed, satisfying Equation 2.59, and inducing transitions between these levels. (b) The corresponding ESR absorption spectrum (red curve) at a fixed frequency ν, centered at H_{res}, with amplitude A, full width at half maximum ΔH, and intensity I. This figure is reconstructed from Ref. [154].

magnetic field H_1 (as part of the electromagnetic radiation), need not be perpendicular to the externally applied magnetic field H_{ext} [150].

In this spin-1/2 system, microwave photons are absorbed exclusively during transitions from $|-1/2\rangle$ to $|+1/2\rangle$. Conversely, the reverse transition involves the emission of a photon with the same energy. However, the Maxwell-Boltzmann distribution between the two levels ($N_+/N_- = e^{\Delta E/k_B T}$, k_B denotes the Boltzmann constant and T refers the sample's temperature) dictates that the lower-energy state has a higher thermal population than the upper state [149]. This imbalance leads to a greater number of transitions to the upper level, resulting in net microwave energy absorption by the sample. This absorption phenomenon forms the basis of continuous wave (CW) ESR experiments.

Here, the sample is exposed to microwaves of a fixed frequency, while the external magnetic field is varied to satisfy the resonance condition for microwave absorption, thereby generating an ESR spectrum, as illustrated in Figure 2.9. All experiments described in this thesis were conducted in field-sweep mode, with the microwave frequency kept constant.

2.11.2 Spectral Parameters

The analysis of the resonance spectrum yields parameters such as linewidth, resonance field, line shape, intensity, etc. These parameters (see Figure 2.9(b)) enable the determination of properties like relaxation time, g-factor, energy gap, and many more.

(i) Resonance field: From the value of the resonance field (H_{res}), we can estimate the parameters like total anisotropy field, MCA field, demagnetization field, g-factor, etc.

(ii) Linewidth and line shape: The linewidth is mainly influenced by the relaxation time of the spin in the excited state, as well as by the inhomogeneities present in the system. It is followed from the Heisenberg uncertainty principle $\Delta E \cdot \Delta\tau \geq \hbar$, where τ represents the relaxation time. Dipole-dipole interactions typically produce a broad Gaussian lineshape, while isotropic exchange interactions result in a narrower Lorentzian lineshape. In some cases, a combination of both effects occurs, leading to a mixed lineshape best described by a Voigt profile [154].

(iii) Amplitude and intensity: The amplitude (A) of the ESR line is directly related to the local spin susceptibility of a material, which quantifies the number of spins that respond to an external magnetic field. For the simple PM systems, the intensity (I) of the ESR signal (area under the curve) can be determined from the product of its amplitude and the full width at half maximum (FWHM). In general, spin susceptibility follows the Curie-Weiss law [48], meaning it is inversely proportional to temperature. Consequently, the intensity of ESR lines also decreases as temperature increases.

2.11.3 Resonance Field

Even in the PM phase, some materials exhibit local internal magnetic fields arising from various factors such as low dimensionality, magnetic frustration, or interactions between distinct magnetic centers, which contribute to the development of short-range correlations. These internal fields cause the resonance position to shift from the conventional PM condition. The resonance condition is then modified [150] to:

$$h\nu = g\mu_B\mu_0(H \pm H_{\text{int}}) \tag{2.60}$$

The shift, whether positive or negative, is dependent on how the external magnetic field is oriented with respect to the internal magnetic field (H_{int}). As a magnetic material transitions to a ferromagnetically ordered state, individual spins become strongly coupled

through exchange, dipolar interactions, and anisotropy, resulting in H_{int}. In this regime, the resonance no longer corresponds to the excitation of isolated or weakly interacting spins, as in paramagnetic resonance. Instead, it reflects the collective excitation of spin waves within the ordered system, termed ferromagnetic resonance (FMR).

2.11.4 Ferromagnetic Resonance

2.11.4.1 Classical Approach

If the system is in an ordered state (for magnetic systems), the net magnetization ($\mathbf{M}$) of the system will be excited in this resonance process. When an external magnetic field ($\mathbf{H}_{\text{ext}}$) is applied, $\mathbf{M}$ will precess about the effective magnetic field ($\mathbf{H}_{\text{eff}} = \mathbf{H}_{\text{ext}} + \mathbf{H}_{\text{int}}$) in absence of damping, as formulated in the Landau–Lifshitz equation [155]:

$$\frac{d\mathbf{M}}{dt} = -|\gamma|(\mathbf{M} \times \mathbf{H}_{\text{eff}}), \tag{2.61}$$

where $\gamma = g\mu_B/\hbar$ is the gyromagnetic ratio and $\mathbf{H}_{\text{int}}$ is the internal magnetic field of the system.

For an isotropic FM, the applied magnetic field is the total effective magnetic field, $\mathbf{H}_{\text{eff}} = \mathbf{H}_{\text{ext}}$, and for these systems, the net magnetization will rotate around $\mathbf{H}_{\text{ext}}$ with a frequency known as the Larmor frequency [48, 129], given by $\omega = 2\pi\nu = -|\gamma|\mathbf{H}_{\text{ext}}$, as shown in Figure 2.10.

If the system is anisotropic, the effective magnetic field becomes $\mathbf{H}_{\text{eff}} = \mathbf{H}_{\text{ext}} + \mathbf{H}_a$, where $\mathbf{H}_a$ represents the total anisotropy field. This anisotropy causes a shift of the resonance line from the position determined by the g-factor. So, using this effective magnetic field, one can calculate the analytical expressions for the spin-wave energies of a uniaxial FM as solutions to the Landau-Lifshitz equation.

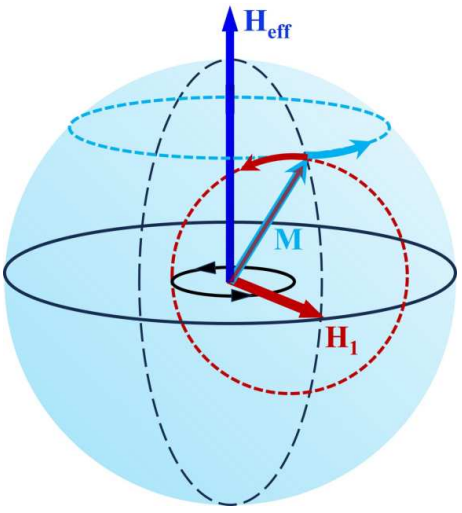

FIGURE 2.10: Schematic representation of the coordinate system rotating with Larmor frequency.

2.11.4.2 Linear Spin Wave Theory

For ordered materials such as FMs, the frequency dependence of the resonance field ($\nu - H$ relationship, see below, Equation 2.64-2.69 and Figure 2.11) can be effectively analyzed using linear spin-wave theory with the second quantization formalism, to provide a precise quantum mechanical description of spin dynamics at $T = 0$ [149, 150]. To achieve this, it is crucial to formulate the phenomenological Hamiltonian that characterizes the ground state of a magnetic single-sublattice spin system. The Hamiltonian is expressed as [120, 156]:

$$\mathcal{H} = K_{\text{uni}} \frac{M_z^2}{M_0^2} + 2\pi N M_z^2 - (\mathbf{H} \cdot \mathbf{M}) + (\text{other anisotropy terms...}) \tag{2.62}$$

The first term in the above Hamiltonian represents the uniaxial part of magnetocrystalline anisotropy, characterized by the constant K_{uni}. M_z represents the z-component of magnetization and $M_0 = M_s$, where M_s is the saturation magnetization. The second term accounts for the shape anisotropy, which arises from the plate-like shape of the crystal. N describes the demagnetization factor. The third term corresponds to the Zeeman interaction, which results from the coupling between the external magnetic field and the material's magnetization. The Hamiltonian might also include other anisotropy terms like cubic anisotropy, anisotropic exchange or Dzyaloshinskii-Moriya interaction, exchange anisotropy or exchange stiffness, etc., depending on the material systems. This formulation provides a comprehensive description of the various contributions to the energy of a magnetic system, capturing the interactions, anisotropies, and external field effects.

A FM with simple uniaxial anisotropy, characterized by an anisotropy field $\mathbf{H}_a$, can be analyzed. The uniaxial anisotropy constant K_{uni} and the anisotropy field H_a are connected by the relation:

$$H_a = \frac{2K_{\text{uni}}}{\mu_0 M_0} \tag{2.63}$$

where μ_0 represents the permeability of free space. This equation defines the internal effective field generated by uniaxial anisotropy, which influences the magnetization to align along the preferred axis. Acting as an equivalent external field, the anisotropy field together with other fundamental forces, including the Zeeman effect and exchange interactions establishes the system's stable magnetization state.

2.11.4.3 Linear Spin Wave Theory Solutions

The spin-wave energy expressions for a uniaxial FM can be represented analytically as follows [150, 157]:

1. Easy-axis Ferromagnet:

For an easy-axis FM (with the c-axis as the easy-axis), where $K_{\text{uni}} < 0$:

(i) For $\mathbf{H} \parallel c$

$$h\nu = g\mu_B\mu_0(H + |\mathbf{H}_a|) \tag{2.64}$$

(ii) For $\mathbf{H} \parallel ab$

$$h\nu = g\mu_B\mu_0\sqrt{H(H - |\mathbf{H}_a|)} \quad \text{for } H \geq |\mathbf{H}_a|, \tag{2.65}$$

$$h\nu = g\mu_B\mu_0\sqrt{|\mathbf{H}_a|^2 - H^2} \quad \text{for } H \leq |\mathbf{H}_a| \tag{2.66}$$

2. Easy-plane Ferromagnet:

For an easy-plane FM, where $K_{\text{uni}} > 0$:

(i) For $\mathbf{H} \parallel c$

$$h\nu = g\mu_B\mu_0(H - |\mathbf{H}_a|) \quad \text{for } H \geq |\mathbf{H}_a|, \tag{2.67}$$

$$\nu = 0 \quad \text{for } H \leq |\mathbf{H}_a| \tag{2.68}$$

(ii) For $\mathbf{H} \parallel ab$

$$h\nu = g\mu_B\mu_0\sqrt{H(H + |\mathbf{H}_a|)} \tag{2.69}$$

Here, the sign of the total magnetic anisotropy field $\mathbf{H}_a$ determines the type of anisotropy in the system. A positive $\mathbf{H}_a$ corresponds to easy-plane anisotropy, while a negative $\mathbf{H}_a$ indicates easy-axis anisotropy. Figure 2.11 schematically illustrates how the resonance frequency varies in response to the magnetic field, as described by the above expressions. These relations highlight the qualitative characteristics of ferromagnetic spin-wave modes, demonstrating the sensitivity of FMR studies to MA. Consequently, FMR serves as an effective tool for probing the magnetic properties of materials.

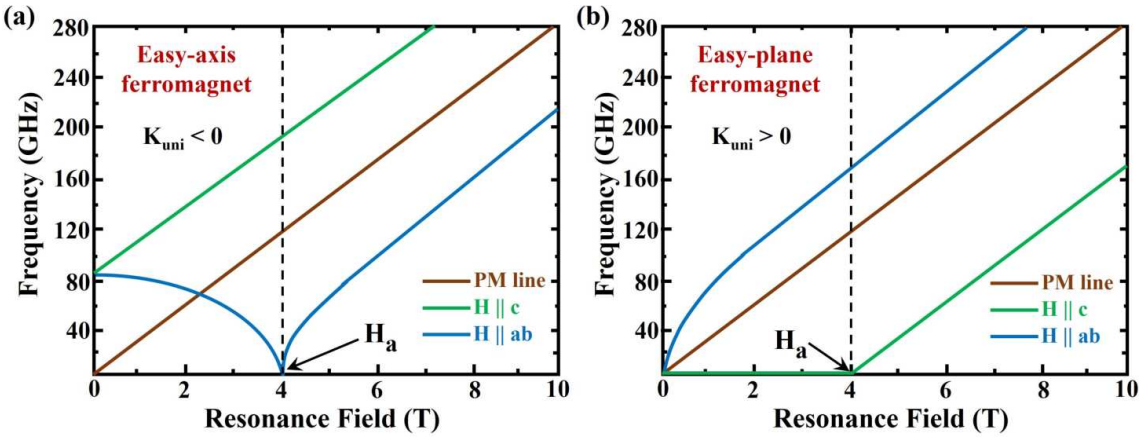

FIGURE 2.11: Illustrative variations of $\nu - H_{res}$ for a FM with (a) an easy-axis anisotropy and (b) an easy-plane anisotropy, obtained using Equations 2.64 - 2.69 with an anisotropy field of $\mathbf{H}_a = 4$ T. The green and blue curves correspond to the applied magnetic field along out-of-plane ($\mathbf{H} \parallel c$) and in-plane ($\mathbf{H} \parallel ab$) relative to the material's symmetry axes, respectively. The brown curve represents the PM line with a g-factor, described by Equation 2.59.

2.12 Superconductivity

2.12.1 Fundamentals of Superconductivity

Superconductivity represents a distinct phase of matter, fundamentally different from conventional electrical conduction in metals. When a material is cooled below a specific temperature, called as critical temperature (T_c), it experiences a thermodynamic phase transition, leading to a dramatic alteration in its electronic properties. The most striking feature of this state is the complete disappearance of electrical resistance. In conventional metals, electrical resistance arises from the scattering of electrons due to interactions with lattice vibrations (phonons), impurities, and other charge carriers. However, in the superconducting state, an effective attractive interaction mechanism between two electrons, known as the pairing mechanism, results in the creation of bound pairs of electrons. These bound pairs, known as 'Cooper pairs', possess an energy gap in their spectrum, preventing their dissociation by small energy perturbations. Once the temperature falls below T_c, the magnitude of this energy gap exceeds the thermal energy, rendering scattering ineffective. As a result, the resistance drops precisely to zero, and the paired electrons condense into a macroscopic quantum state characterized by a single phase.

Superconductivity was first discovered in 1911 by Heike Kamerlingh Onnes, who observed that mercury's electrical resistance dropped abruptly to zero when cooled to a sufficiently

low temperature. The phenomenon was also characterized by the Meissner effect, which ensures the exclusion of magnetic fields from the superconducting interior. The superconducting state can be disrupted by external factors such as magnetic fields or excessive current density. In most cases, when such perturbations exceed critical thresholds, the material reverts to its normal metallic state. The three fundamental characteristics that define the superconducting state in a material are the critical magnetic field (H_c), critical temperature (T_c), and critical current (I_c). A material remains in the superconducting state as long as it operates within these defined limits.

- **Meissner Effect:**

A defining characteristic of superconducting materials is known as the 'Meissner effect', which describes the ability of a superconductor to completely expel an externally applied magnetic field when cooled below T_c. Even if a superconductor is placed in an external magnetic field before cooling, it will actively expel the field upon entering the superconducting state. This distinguishes superconductors from perfect conductors. While a conventional metal with zero resistance can generate persistent eddy currents that counteract an applied field, it does not inherently expel a pre-existing magnetic field. In contrast, a superconductor spontaneously eliminates any applied field from its interior, even when cooled in the presence of a magnetic field. This occurs because superconducting electrons generate screening currents that oppose external flux penetration. However, the magnetic field does not vanish instantaneously; rather, it decays over the penetration depth λ. Within a distance λ from the surface, shielding currents circulate, ensuring that the internal magnetic field remains zero in the bulk of the material.

- **Flux Quantization:**

Another fundamental property of superconductors is the quantization of magnetic flux, a direct consequence of the macroscopic quantum nature of the wavefunction of a superconductor. Since all Cooper pairs form a single macroscopic quantum state, their wavefunction must remain single-valued throughout the material. It imposes a fundamental restriction on the magnetic flux penetrating the material. If a superconducting region encloses a magnetic flux, the quantum phase must return to its original value after a complete loop around the flux. This is only possible if the enclosed magnetic flux is quantized, given by:

$$\Phi_n = n\frac{h}{2e} = n\Phi_0 \tag{2.70}$$

where h is Planck's constant, e denotes the elementary charge, and n refers to an integer. This phenomenon ensures that magnetic flux through a superconducting loop is always quantized in integer multiples of Φ_0 ($= \frac{h}{2e} \approx 2.07 \times 10^{-15}$ Wb). This quantization of flux leads to the formation of quantized magnetic flux bundles known as vortices, which are characteristic of type-II superconductors. The flux quantization phenomenon was initially noted by Fritz London, who misestimated the flux quantum by assuming single electrons carried the supercurrent – a misconception later corrected by BCS theory, which established that superconducting currents arise from electron pairs.

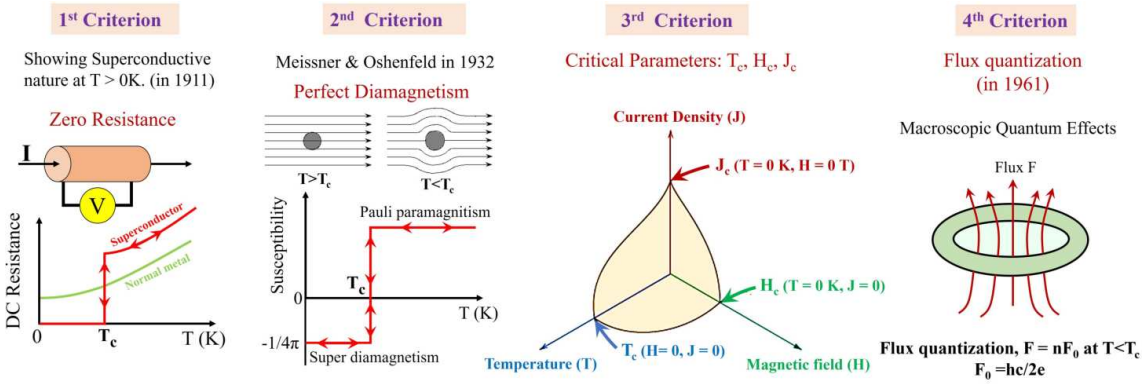

FIGURE 2.12: Four main criteria of superconductivity. 1. The electrical resistance drops to zero as the temperature becomes lower than the critical temperature, T_c, marking the transition into the superconducting state. 2. Illustration of the Meissner effect, where the superconductor exhibits perfect diamagnetism for $T < T_c$, completely expelling the magnetic field from its interior. 3. Schematic illustration of key superconducting parameters: critical temperature T_c, critical current density j_c, and upper critical magnetic field H_{c2}. 4.

- **BCS Theory:**

A key theoretical explanation for this phenomenon is provided by the Bardeen-Cooper-Schrieffer (BCS) theory [158, 159], formulated in 1957, which describes superconductivity as a fundamental rearrangement of the electronic states close to the Fermi level. The transition to the superconducting state occurs due to the formation of Cooper pairs (bosons), where two electrons having opposite momenta ($\mathbf{p}$ and $-\mathbf{p}$) and spins experience a weak attractive interaction mediated by lattice vibrations (phonons), leading to the emergence of a correlated macroscopic quantum state. This transition is characterized by the opening of an energy gap (2Δ), which represents the energy required to break a Cooper pair into individual electrons, known as the superconducting energy gap. The BCS gap equation is given by:

$$\Delta(T) = V \sum_{\mathbf{k}} \frac{\Delta(T)}{2E_{\mathbf{k}}} \tanh\left(\frac{E_{\mathbf{k}}}{2k_B T}\right) \tag{2.71}$$

where, V is the effective interaction potential, $E_{\mathbf{k}} = \sqrt{\xi_{\mathbf{k}}^2 + \Delta^2}$ is the quasi-particle energy, $\xi_{\mathbf{k}}$ is the single-particle energy relative to the Fermi level, depends on its momentum k.

At the Fermi surface ($\epsilon_k = 0$), the minimum excitation energy is simply $|\Delta|$, which characterizes the robustness of the superconducting phase. The energy required to break a Cooper pair is thus $2\Delta \approx 3.5\ k_B T_c$.

As temperature increases, $\Delta(T)$ diminishes, vanishing at T_c, above which the excitation spectrum becomes that of a conventional metal, $E_k \to |\epsilon_k|$. At low temperatures, the gap remains nearly constant, but it declines rapidly near T_c (see Fig. 2.13), approximately following:

$$\frac{\Delta(T)}{\Delta_0} \approx 1.76\sqrt{1 - \frac{T}{T_c}} \tag{2.72}$$

Here, Δ_0 is the zero-temperature gap. The spatial extent of a Cooper pair is characterized by the BCS coherence length (ξ_0):

$$\xi_0 = \frac{\hbar v_F}{\pi \Delta_0} \tag{2.73}$$

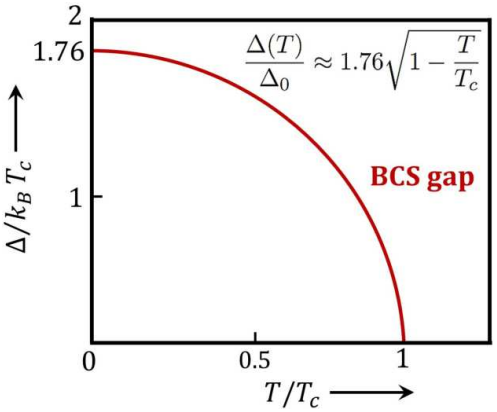

FIGURE 2.13: Temperature dependence of the BCS energy gap Δ, showing the gradual closing of the gap as $T \to T_c$.

Here, v_F is the Fermi velocity. These results are valid within the weak-coupling regime, where $\lambda_{e\text{-}ph} \ll 1$.

The critical temperature T_c is approximated by:

$$T_c \approx 1.14\Theta_D e^{-1/N(0)V} \tag{2.74}$$

where $\Theta_D = \frac{\hbar\omega_D}{k_B}$ is the Debye temperature, ω_D is the Debye frequency, and $N(0)$ denotes the density of available electronic states (DOS) close to the Fermi level for a single spin. Now, the T_c can be roughly estimated from the Eq. 2.74 as:

$$T_c \propto \omega_D \exp(-1/\lambda_{e\text{-}ph}) \tag{2.75}$$

Where $\lambda_{e\text{-}ph}$ $(= N(0)V)$ quantifies the electron-phonon coupling strength.

Within the BCS framework, at temperatures above T_c, Cooper pairs exist only transiently due to superconducting fluctuations. However, below T_c, a macroscopic equilibrium concentration of these pairs establishes long-range phase coherence, defining the

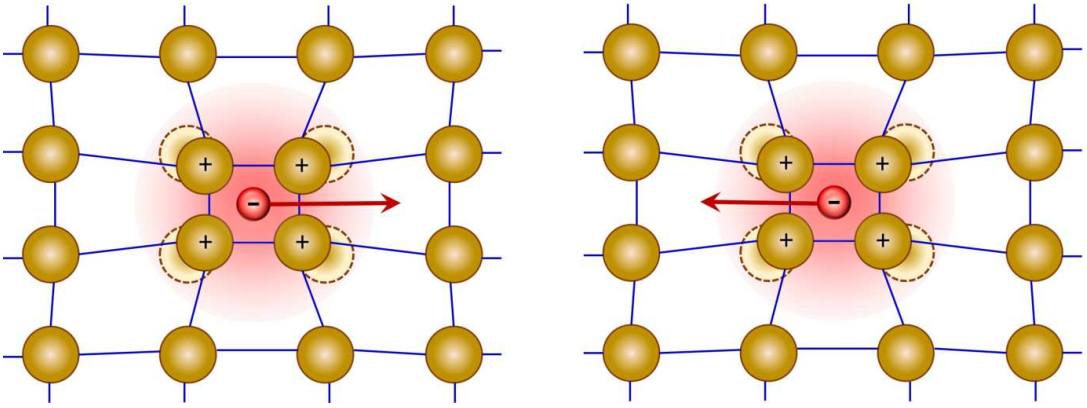

FIGURE 2.14: Schematic illustration of the effective attraction between two electrons mediated by lattice polarization, leading to Cooper pair formation. The first electron polarizes and distorts the lattice, creating a region of positive charge between the ions (left), which subsequently attracts the second electron (right).

superconducting state. The BCS theory provides a comprehensive explanation for key superconducting properties, including the Meissner effect, zero electrical resistance, and flux quantization.

Cooper-pair Formation Mechanism:

At absolute zero, electrons in a superconductor near the Fermi energy can form bound pairs known as Cooper pairs [159]. This pairing arises due to interactions mediated by the lattice ions. Electrons move at the Fermi velocity $v_F = \hbar k_F/m_e$, while the heavier ions in the lattice respond much more slowly, moving at $v_i = v_F m_e/m_i$, where m_e and m_i are the electron and ion masses, respectively.

As a high-speed electron passes through the lattice, it distorts the local ion positions, creating a temporary polarization. Because the ions respond slowly ($\tau \sim 2\pi/\omega_D \sim 10^{-13}$ s), this distortion persists briefly, attracting a second electron. This delayed ionic response effectively generates an attractive interaction between the two electrons over a distance $v_F\tau \sim 100$ nm – provided this attraction exceeds the intrinsic Coulomb repulsion (see Fig. 2.14). Thus, the Cooper pair forms the lowest-energy, most stable state.

The resulting interaction is mediated by lattice vibrations, or phonons, and is restricted by energy conservation: the exchanged phonon must have a frequency less than ω_D. Hence, the upper energy bound for this attraction is defined by $\hbar\omega_D$. When the energy separation between two electrons exceeds this limit, the interaction turns repulsive [160].

Since the Debye frequency scales inversely with the square root of the ionic mass ($\omega_D \propto M^{-1/2}$), the pairing strength, and consequently, the critical temperature, are sensitive to

the atomic mass of the lattice. This dependence underlies the observed isotope effect in superconductors.

- **Ginzburg-Landau (GL) Theory:**

The superconducting state is also mathematically described (phenomenologically) using the Ginzburg-Landau (GL) order parameter, $\psi(\mathbf{r})$, which determines the density of Cooper pairs via $|\psi(\mathbf{r})|^2 = n_s(\mathbf{r})$, where n_s is the Cooper pair density. The GL theory [161] offers a macroscopic framework to analyze spatial variations in the superconducting order and the effects of external magnetic fields. This theory defines two crucial characteristic length scales: the coherence length (ξ), which defines the characteristic length scale where the superconducting order parameter spatially varies without significant energy cost, and the magnetic penetration depth (λ), which quantifies how deeply an external magnetic field can penetrate a superconductor before being fully attenuated.

In the weak coupling limit, the macroscopic condensate wavefunction (from BCS theory) is analogous to the GL order parameter, which describes the quantum coherence of the superconducting state and can be represented as:

$$\psi(\mathbf{r}) = \Delta e^{i\phi(\mathbf{r})} \tag{2.76}$$

where Δ is the magnitude or the absolute value of the BCS order parameter, and $\phi(\mathbf{r})$ denotes the phase coherence of the Cooper pairs. The non-zero spatial variation of the phase ($\nabla\phi(\mathbf{r}) \neq 0$) corresponds to the flow of superconducting currents.

- **Ginzburg–Curzon–Taylor–Fisher (GCTF) Model:**

The GCTF model extends the GL framework to include additional quantum fluctuations and finite-size effects, particularly in low-dimensional superconductors [159]. The model modifies the GL equations to incorporate corrections for strong phase fluctuations and enhanced critical fluctuations near the superconducting transition. Although the GCTF model does not have a single defining equation like GL or BCS theory, it modifies the coherence length and penetration depth by incorporating fluctuation-induced corrections:

$$\xi(T) \sim \xi_0 \left(1 - \frac{T}{T_c}\right)^{-\nu} \tag{2.77}$$

$$\lambda(T) \sim \lambda_0 \left(1 - \frac{T}{T_c}\right)^{-\gamma} \tag{2.78}$$

where, ν and γ describe fluctuation-induced scaling behaviors, ξ_0 and λ_0 are zero-temperature coherence length and penetration depth, respectively.

- **Types of Superconductivity:**

Superconductors are classified into two distinct types based on their response to external magnetic fields, and the relationship between the coherence length ξ and the penetration depth λ. The ratio of these two lengths, known as the Ginzburg-Landau parameter ($\kappa = \lambda/\xi$), serves as a criterion for distinguishing different superconducting behaviors [162]. In type-I superconductors, where $\kappa < 1/\sqrt{2}$, i.e., $\xi > \lambda$, the magnetic fields are completely expelled below the critical field. In contrast, type-II superconductors, for which $\kappa > 1/\sqrt{2}$, i.e., $\xi < \lambda$, allow for the partial penetration of magnetic flux in the form of vortices. These vortices create regions of normal-state material surrounded by circulating superconducting currents. Each vortex carries a single quantum of magnetic flux. If a closed path is taken around a vortex, the superconducting phase winds by 2π, signifying the presence of a quantized vortex. A type II superconductor is said to be in the vortex state when the applied magnetic field falls within the range $H_{c1} < H < H_{c2}$, where H_{c1} and H_{c2} denote the lower and upper critical magnetic fields, respectively. In this state, the external magnetic field partially penetrates the superconductor, forming quantized vortices within the material. As the applied magnetic field increases, the vortices density grows, eventually leading to the complete destruction of superconductivity at H_{c2}. The vortex lattice structure and interactions play a significant role in determining the material's response to external fields and currents.

The interplay of zero electrical resistance, the Meissner effect, flux quantization, and the emergence of Cooper pairs defines the complex yet highly coherent nature of superconductivity. These phenomena, which arise due to fundamental electronic interactions, enable the development of various applications, including superconducting magnets, quantum computing, and lossless power transmission. The interplay of quantum mechanics and electromagnetic interactions in superconductors continues to be an active field of research, particularly in unconventional and high-temperature superconductors.

2.12.2 Coherence length (ξ):

The coherence length (ξ) serves as a fundamental length scale in superconductivity, defining the spatial extent over which the superconducting order parameter remains correlated [159]. Within the framework of the BCS theory, superconductivity arises from the formation of Cooper pairs — pairs of electrons bound together via an attractive

interaction mediated by lattice vibrations. The coherence length represents the average spatial separation between two electrons forming a Cooper pair, i.e., the size of a Cooper pair. Unlike tightly bound electron pairs, Cooper pairs are dynamic, continuously exchanging partners over a characteristic time scale determined by $h/2\Delta$, where Δ is the superconducting energy gap, and h is Planck's constant.

The coherence length is linked to the upper critical field (H_{c2}), which marks the transition between the superconducting and normal states when an external magnetic field is applied. According to the GL theory, H_{c2} near absolute zero is given by:

$$H_{c2}(0) = \frac{\Phi_0}{2\pi\mu_0\xi^2} \tag{2.79}$$

where $\Phi_0 = 2.067 \times 10^{-15}$ Wb is the magnetic flux quantum, and $\mu_0 = 4\pi \times 10^{-7}$ H/m is the vacuum permeability. The coherence length at zero temperature, $\xi_{GL}(0)$, can also be estimated using the BCS-Gorkov equation near the critical temperature T_c:

$$\xi_{GL}(0) = \sqrt{\frac{\Phi_0}{2\pi T_c (dH_{c2}/dT)_{T_c}}} \tag{2.80}$$

This coherence length is a material-specific parameter and is typically much larger than the interatomic spacing. It plays a crucial role in defining the dimensionality of a superconducting system. If all sample dimensions exceed ξ, the system is considered three-dimensional (3D). In contrast, if at least one of the dimensions, such as thickness or width, is comparable to or smaller than ξ, the system is classified as two-dimensional (2D). A system is regarded as 1D if the square root of its cross-sectional area is smaller than ξ.

Chapter 3

Experimental Details

A comprehensive overview of the various experimental techniques and methods employed throughout this thesis work is presented in this chapter. It begins with detailed procedures for preparing 2D flakes using multiple exfoliation techniques and describes characterization methods such as XRD, SEM, EDAX, optical microscopy, atomic force microscopy, and profilometry. The detailed optimization of the device fabrication process of 2D magnetic materials is discussed, including lithography, metallization, liftoff, and bonding techniques, as well as procedures to prevent flake oxidation. Special attention is given to the development and optimization of a glovebox-integrated dry transfer setup for assembling vdW magnets and their heterostructures. The chapter further outlines the setup's development, optimization, and operation of cryogenic systems with high magnetic fields, including the liquid helium plant, low-temperature Hall measurement setup, PPMS, and millikelvin setups like Oxford Teslatron and Heliox-VT systems. Subsequently, various electrical transport measurement techniques, including current-voltage, AC resistance, Van der Pauw, and low-frequency noise measurements, are elaborated. Magneto-transport methods such as magnetoresistance and anisotropic magnetoresistance, anomalous Hall, as well as magnetization measurements using VSM and SQUID, are discussed. The chapter concludes with descriptions of micro-Raman spectroscopy and electron spin resonance (ESR) measurements (both X-band and high-frequency), which are crucial for probing the physical properties and spin dynamics of the materials studied.

3.1 Device Fabrication and Characterization Techniques

3.1.1 Techniques for Preparing 2D Flakes

3.1.1.1 Mechanical Exfoliation (Scotch Tape Method)

Mechanical exfoliation is among the most widely adopted and effective techniques for producing high-quality 2D crystals due to its simplicity and precision [163, 164]. While chemical vapor deposition (CVD) can produce large-area samples of 2D materials such as MoS_2, WSe_2, graphene, hBN, etc., these samples often have lower carrier mobility and are prone to defects and grain boundaries, limiting their suitability for field-effect transistor (FET) applications. Mechanical exfoliation is a straightforward technique that involves peeling thin layers from bulk crystals using adhesive tapes, such as Scotch or Nitto tape. In 2004, graphene became the first 2D material to be discovered when researchers isolated a single atomic layer from bulk highly ordered pyrolytic graphite (HOPG) using this technique [17, 165]. Due to the weak vdW forces between layers in these materials, thin sheets can be separated from bulk crystals with minimal force. After cleaving, small flakes are transferred from the bulk material to a substrate like Si^{++}/SiO_2, where vdW forces bind some of the material to the SiO_2 surface as flakes. These flakes typically range from a few micrometers to hundreds of micrometers, with their size and quality influenced by substrate roughness and composition. For instance, polished SiO_2 may yield fewer layers due to reduced surface roughness compared to rougher SiO_2. Surface treatments like RCA cleaning (DI water : 30% NH_4OH : 30% cold H_2O_2 = 5:1:1), Piranha cleaning (98% conc. H_2SO_4 : 30% cold H_2O_2 = 2:1) or O_2 plasma can roughen polished SiO_2, enhancing flake size and quality. Yields vary by material [166]; for example, graphene exfoliates more effectively on SiO_2 substrates than MoS_2, likely due to weaker vdW interactions between MoS_2 and SiO_2 or stronger interlayer between MoS_2 layers [167, 168]. Some materials have stronger vdW interactions between layers, making exfoliation more challenging. Additionally, isolating atomically thin crystals from certain 2D magnetic materials is difficult due to weak intralayer bonding, which often results in small, fragile flakes that don't withstand standard mechanical exfoliation. As a result, only a small fraction of known layered crystals can be cleaved down to stable monolayers. To optimize yields, vdW magnets like Fe_nGeTe_2 (n=3,4,5), Cr_2GeTe_6, CrI_3, etc. can be exfoliated on alternative substrates and techniques [166, 169], such as on polydimethylsiloxane (PDMS) substrates [36, 170, 171] and by gold exfoliation [166, 172–174], hot exfoliation [175–179], or Al_2O_3 assisted exfoliation [33] techniques, etc., before being transferred to SiO_2. After

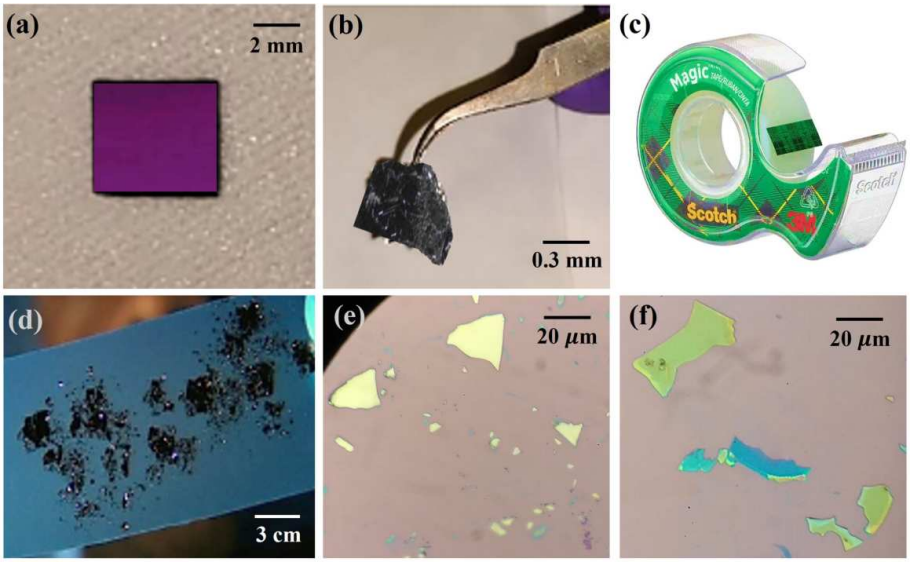

FIGURE 3.1: Illustration of the exfoliation process for vdW crystals. (a) Optical image of the Si/SiO_2 substrate, (b) 2D magnetic bulk crystal, (c) adhesive scotch tape, (d) scotch tape with exfoliated crystal, (e)(f) optical microscopic image of exfoliated multilayer and thin flakes of vdW magnetic crystals on top of cleaned Si/SiO_2 substrate.

the exfoliation process, these small flakes are examined through a high-resolution optical microscope, typically using magnifications of 500x to 1000x. The step-by-step process of the mechanical exfoliation technique is illustrated in Figure 3.1. The alternative methods we used to exfoliate vdW magnets are briefly summarized as follows.

3.1.1.2 Hot Exfoliation

Heat-assisted exfoliation offers several advantages for obtaining few-layer flakes of 2D materials. By heating the substrate and adhesive tape containing vdW materials, the adhesion between the tape and material increases, promoting the transfer of thin, uniform few layers of crystal. As reported by Huang *et al.* [175], this method improves the flake quality and size, often yielding larger and more consistent monolayers or few-layer regions compared to standard room-temperature exfoliation. Additionally, heat helps to reduce the presence of contaminants and improve surface cleanliness, further enhancing the structural integrity and electronic properties of the exfoliated 2D materials. In hot exfoliation techniques for preparing few-layer 2D flakes, a Si/SiO_2 substrate is used along with standard adhesive tape to transfer thick flakes from a highly oriented bulk crystal. To prepare the substrate, it first undergoes ultrasonic cleaning with acetone, IPA, and DI water, followed by oxygen-plasma treatment to remove any surface contaminants. After plasma cleaning, the bulk crystal-loaded tape is applied to the substrate. Unlike

conventional methods, the substrate with the attached tape is then annealed using a hot plate at 80 - 100 °C for 2 to 5 minutes. After reaching ambient temperature, the tape is then gently peeled off, finalizing the exfoliation step. Optical microscopic observation confirms the successful transfer of a few layers of flakes onto the Si/SiO_2 substrate, with uniform thin regions typically spanning from 20 µm to several hundred micrometers [175–177] (see Fig. 3.2). Here, this exfoliation process is primarily influenced by the competing attractive forces: the interlayer vdW forces within the thick crystal flakes adhered to the tape and the forces between the outermost layer and the underlying substrate. Several studies reported that this hot exfoliation greatly improves the exfoliation process for materials with strong vdW interactions and those that are difficult to exfoliate [178, 179]. Additionally, this technique allows for efficient exfoliation and analysis of air-sensitive 2D magnetic materials in an inert atmosphere [169].

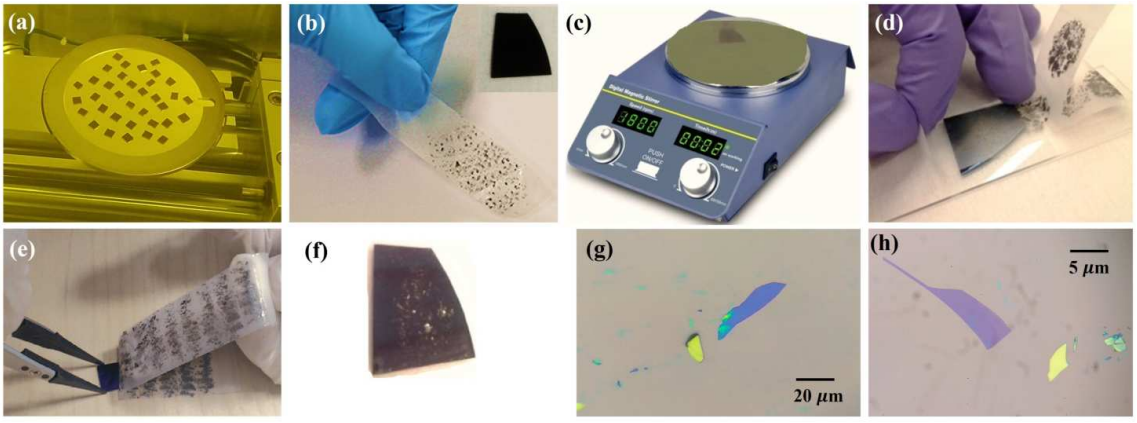

FIGURE 3.2: Illustration depicting the exfoliation procedure used to isolate two-dimensional magnetic layers. (a) Oxygen plasma cleaning of the Si/SiO_2 substrate. (b) Optical image showing the cleaned substrate and adhesive tape containing exfoliated flakes. (c) The tape carrying exfoliated flakes is brought into contact with the substrate surface, then heated on a hot plate in ambient conditions at around 100 °C for approximately 2 minutes. (d, e) After heating, the substrate is removed from the hot plate, and the tape is carefully peeled off to complete the transfer process. (f) Optical view of the substrate following the thermal-assisted exfoliation procedure. (g, h) Optical microscopic images highlighting thinner exfoliated flakes on the substrate.

3.1.1.3 PDMS Assisted Exfoliation

The PDMS-assisted exfoliation technique [180–183] is a well-regarded method for producing high-quality flakes of 2D materials, utilizing the unique properties of a viscoelastic material, polydimethylsiloxane (PDMS), to facilitate both exfoliation and dry transfer. PDMS films are prepared by using the Sylgard 184 monomer and curing agent kit [180], mixed in weight ratios of 10:1 and 20:1 to adjust their elastic modulus

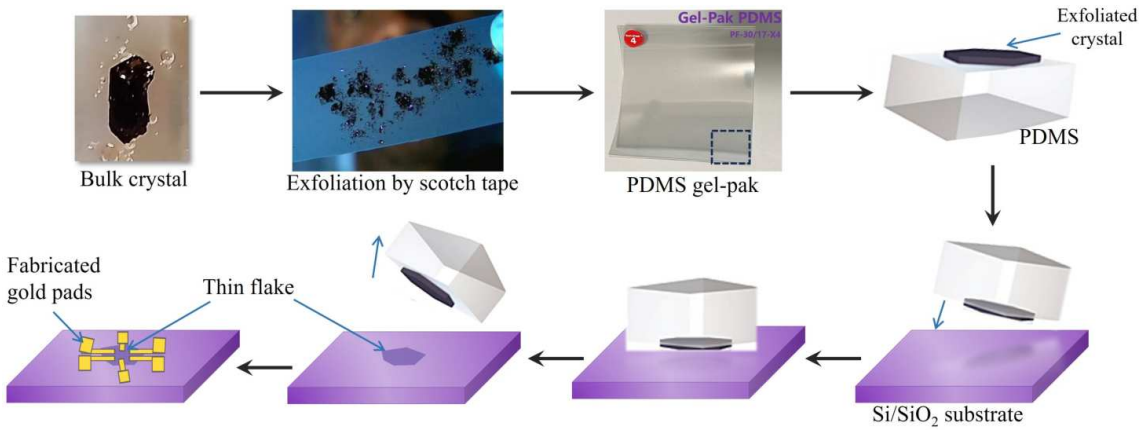

FIGURE 3.3: Schematic representation of the PDMS-assisted exfoliation technique

and adhesive properties. The mixtures are stirred for 3 or 5 minutes accordingly, followed by degassing in a vacuum desiccator at -0.8 KPa for 20 minutes. After degassing, the mixtures are poured into a 50 x 50 x 6.25 mm^3 glass pot and then cured in an oven at 70° C for 20 to 80 minutes. Following the curing process, the samples are stored in a freezer for one hour to mitigate rapid thermal softening. This curing step not only solidifies the film but also allows for fine-tuning of its adhesive properties and flexibility, making PDMS a versatile substrate that can be optimized for different materials and exfoliation requirements. Also, commercially available PDMS gel-pak (GEL-FILM, PF-30x30-0170-X4) was used for this study.

To begin the exfoliation, a bulk crystal of the target 2D material, such as MoS_2, WSe_2, graphite, or any bulk vdW magnetic material, is placed in contact with the PDMS surface. Gentle pressure is applied to encourage adhesion between the bulk material and the PDMS. By carefully peeling back and forth by the PDMS multiple times, thin layers of the 2D material are successfully transferred onto its surface. PDMS's smooth, elastic nature makes it particularly advantageous for this step, as it minimizes the likelihood of damage to the delicate 2D layers and tends to produce larger, more uniform flakes compared to traditional adhesive tapes. Following exfoliation, the PDMS film with the attached thin flakes is aligned with the desired target substrate, typically a Si/SiO_2 wafer, by a standard dry transfer setup to enable further processing. The PDMS is then gently pressed against the substrate, transferring the 2D material flakes to the designated areas (see Fig. 3.3). Once the flakes are properly adhered to, the PDMS can be peeled away carefully, leaving the exfoliated flakes well-adhered to the target surface. Later, optical lithography is performed directly on top of the flake to prepare gold contacts for further investigation.

PDMS-assisted exfoliation enables the controlled and repeatable production of large and

uniform 2D flakes with minimal contamination, making it particularly useful for air-sensitive materials like black phosphorus [184] and 2D magnetic materials, as the process can be conducted in inert atmospheres to prevent their degradation. While PDMS is highly effective, its adhesive strength may sometimes be inadequate for materials with weak interlayer bonding, necessitating modified PDMS formulations for optimal yield. Nonetheless, PDMS-assisted exfoliation remains a popular and widely used technique in 2D materials research due to its adaptability and ability to produce high-quality flakes that are crucial for applications in electronics, optoelectronics, and spintronics.

3.1.2 Structural Characterization Techniques of Crystals

3.1.2.1 X-ray Diffraction (XRD)

X-ray diffraction (XRD) is a powerful, non-invasive technique [185] used to analyze the crystalline structure of materials, revealing details about atomic arrangement, crystal symmetry, crystallite dimensions, phase composition, and structural imperfections. In XRD, an X-ray beam of a particular wavelength λ (generally of wavelength 1.5418 Å, for Cu K_α radiation) is directed onto the sample. This beam interacts with the electron clouds surrounding the atoms in the crystal lattice, resulting in diffraction that generates secondary spherical waves. When an X-ray of wavelength λ is aimed at the lattice planes of a crystal at an angle θ, the atoms' electrons scatter the X-ray beam elastically, maintaining the same angle (see Fig. 3.4 (a)). As the X-rays interact with different lattice planes, variations in path length lead to either constructive or destructive interference. If d represents the distance between two adjacent lattice planes, the path difference between X-rays diffracted by these planes is $2d\ \sin\theta$. Constructive interference occurs when this path difference equals $n\lambda$, where n is an integer, thus satisfying Bragg's law [186]:

$$2d \sin\theta = n\lambda \tag{3.1}$$

By measuring the intensity of X-rays diffracted at varying angles θ, intensity peaks at specific angles indicate constructive interference. Using Bragg's law to calculate the spacing between lattice planes (d), one can determine the crystal's lattice constant and symmetry. Analysis of the angles and intensities of these diffracted beams provides detailed insights into the atomic structure, crystallinity, and film thickness, along with information on strain, orientations, and structural defects. The Scherrer equation provides a straightforward method for estimating crystallite size, expressed as k, expressed as:

$$D = \frac{k\lambda}{\beta \cos\theta} \tag{3.2}$$

During XRD measurements, the angle of incidence of the X-ray is systematically adjusted, and the reflected intensities are recorded based on the angle (2θ) between the reflected and incident beams.

A typical XRD setup is illustrated in Fig. 3.4 (b). X-rays are generated inside a vacuum X-ray tube by thermionically emitting electrons from a heated W-cathode, which are then directed onto a Cu anode to produce characteristic X-rays. These X-rays pass through slits to focus the beam onto the sample surface. The diffracted X-ray beam is then further

focused using slits such as the parallel slit analyzer, Soller slit, and receiving slit to enhance the peak intensity of the XRD data [187]. XRD measurements are performed on a Rigaku SmartLab X-ray diffractometer (9 kW) using Cu-K_α radiation ($\lambda = 1.54$ Å) as in Fig. 3.4 (c). In this system, electrons emitted from the W-cathode are accelerated by a voltage difference of 20-45 kV between the cathode and anode, producing an electron beam with a maximum power of 9 kW. This beam strikes the Cu anode, generating Cu-K_α X-rays. The diffracted X-ray beam is detected by a hybrid photon counting (HPC) detector [188]. This diffractometer uses a θ-θ goniometer, where the sample stage remains stationary while the X-ray tube and detector rotate to get the XRD pattern. The angular positions of both the tube and detector are noted as -θ and θ, respectively. Additionally, other XRD setups, such as the Rigaku MiniFlex II with a θ-2θ goniometer, involve rotating the sample stage by θ and the detector by 2θ, rather than rotating the X-ray tube.

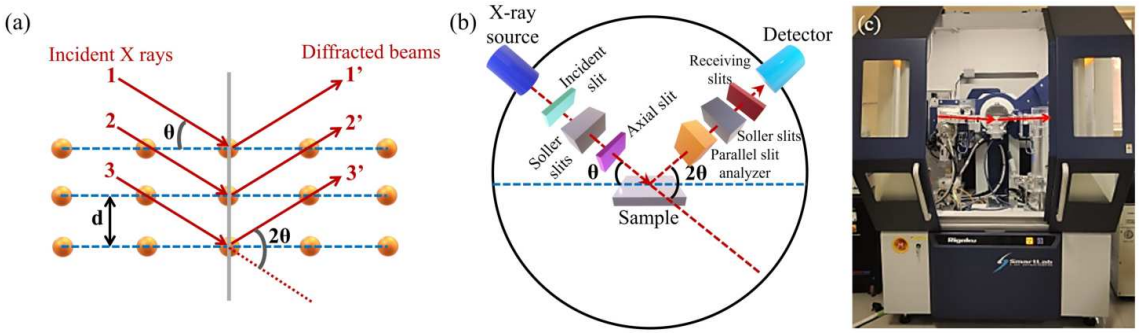

FIGURE 3.4: (a) Schematic of X-ray diffraction from lattice planes. (b) Schematic diagram of an X-ray diffractometer. (c) Rigaku SmartLab X-ray diffractometer used for our measurements at SNBNCBS.

3.1.2.2 Scanning Electron Microscopy (SEM)

In Scanning Electron Microscopy (SEM), an electron beam is generated through either thermionic emission or cold field emission [189]. In thermionic emission, a material such as a tungsten filament, ZrO/W (Schottky emitter), or LaB6 crystal, is heated electrically to emit electrons. These electrons, initially with low energy, are then accelerated by applying a high voltage between the anode and cathode, creating an electrostatic field to guide the electrons. In cold field emission (termed as FESEM, Field Emission Scanning Electron Microscopy), electrons are emitted from a tungsten tip at room temperature. This method provides higher electron yield and lower chromatic aberration, making it ideal for high-resolution imaging at the atomic scale. To prevent damage to the filament from burning or oxidation, the SEM operates under high vacuum conditions (10^{-7} to 10^{-10} mbar).

Once the electrons are emitted and accelerated, an electromagnetic lens system is used to focus and direct the beam. The schematic diagram of a SEM setup is presented in Fig. 3.5 (a). This system consists of insulated copper wire windings, a soft iron core, and a pole piece. By passing a current through the copper winding, a magnetic field is generated, guiding the electron beam along a circular path through the lenses. These lenses adjust the focal point of the electron beam and allow for precise control of the scanning process. The electron beam's horizontal and vertical deflections are controlled using a search coil and magnetic lenses, which together enable the beam to scan the surface of the specimen systematically. The magnetic field strength is also adjustable, which alters the beam's focal width for varying levels of precision. SEM typically operates within a voltage range of 2 kV to 50 kV, with beam diameters ranging from 5 nm to several micrometers. When the electron beam interacts with the sample, various phenomena occur, including the emission of secondary electrons, backscattering, transmission, absorption (leading to heat generation), and the production of characteristic X-rays, along with both elastic and inelastic scattering. A discrepancy between incoming and outgoing electrons can lead to sample charging, which can affect image quality. To prevent this, insulating samples are often coated with a thin metallic layer, typically gold. In most cases, secondary electrons are detected in the detector and processed to produce detailed and high-resolution SEM images of the sample surface. At SNBNCBS, the FEI Quanta 200 SEM (as in Fig. 3.5(b)) was employed to capture images of the nTSI and other 2D flakes.

SEM micrographs provide a three-dimensional view of the surface at various magnifications, offering insights into the sample's morphology, surface structure, and topography. It enables the investigation of crystal grain boundaries, structural dislocations, and material defects. It also allows for the analysis of various low-dimensional structures, including the quantity, size, and shape of quantum dots, nanosheets, and nanowires, making SEM a powerful tool for materials analysis and characterization.

3.1.2.3 Energy Dispersive X-ray Spectroscopy (EDS or EDAX)

Energy Dispersive X-ray Spectroscopy (EDS or EDAX) is a non-destructive analytical tool to determine the elemental composition of materials. This technique involves directing an electron beam onto the sample, which induces the emission of characteristic X-rays [189]. These emitted X-rays provide information about the elements present and their respective weight percentages.

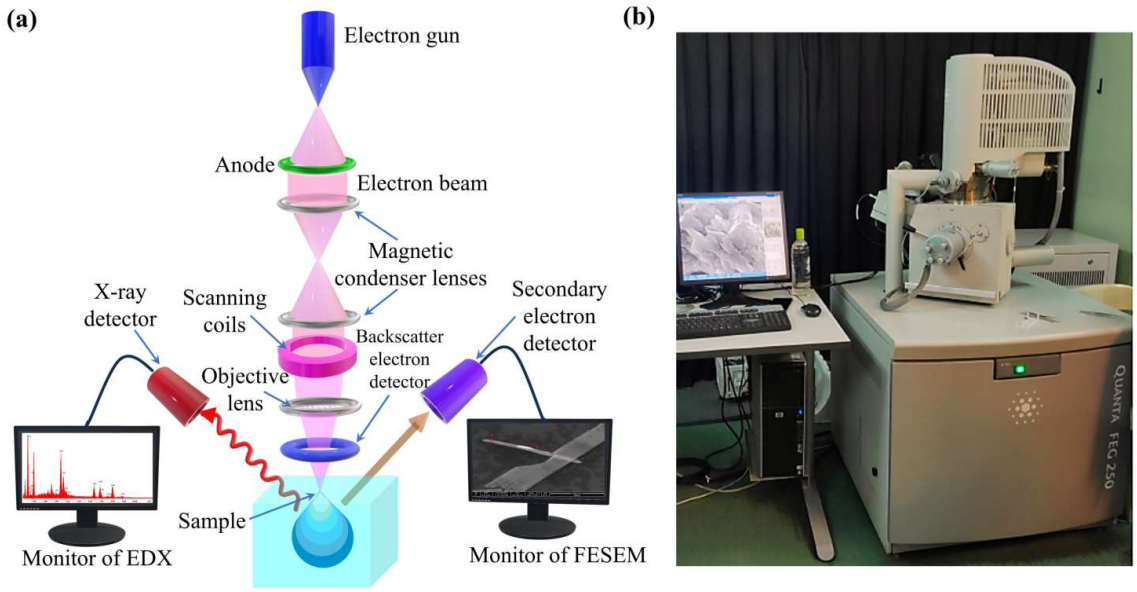

FIGURE 3.5: (a) Schematic diagram showing the different components of a scanning electron microscope (SEM). (b) Energy-dispersive X-ray spectroscopy (EDS) attachment on the FESEM, used for sample characterization at SNBNCBS.

When a sample is struck by a high-energy electron beam, it causes the removal of bound electrons from the inner atomic shells. This creates a vacancy in the inner shell, prompting outer shell electrons to transition to the lower energy inner shells. During this transition, an X-ray is emitted, with energy corresponding to the difference between the two energy levels. These energy levels are identified by the principal quantum number n, where n = 1, 2, 3, 4,..., which correspond to the K, L, M, N,... shells, respectively. Figure 3.6(a) illustrates the process of generating various characteristic X-rays. When an electron transitions from the L shell to the K shell, the resulting characteristic X-ray is referred to as K_α. If an electron transitions from the M shell to the K shell, the emitted X-ray is designated as K_β. In a similar manner, L_α and L_β X-rays are produced when electrons transition from the M and N shells to the L shells, respectively. These X-rays are subsequently detected by the EDX detector (as illustrated in Fig. 3.6(a)), which produces EDX spectra. These spectra enable the identification and quantification of the elemental components present in the sample.

Each element in the periodic table possesses a unique atomic structure, allowing for the identification of elements within a sample by analyzing the emitted characteristic X-rays. Figure 3.6(b) displays the EDS image, showcasing the characteristic X-ray peaks K_α, K_β, L_α, and L_β from various elements present in the $(TaSe_4)_3I$ sample, specifically Ta and Se (see Fig. 3.6(b) inset). The intensity of each X-ray peak corresponds to the likelihood of specific electron transitions, with the transition from the L shell to the K shell being

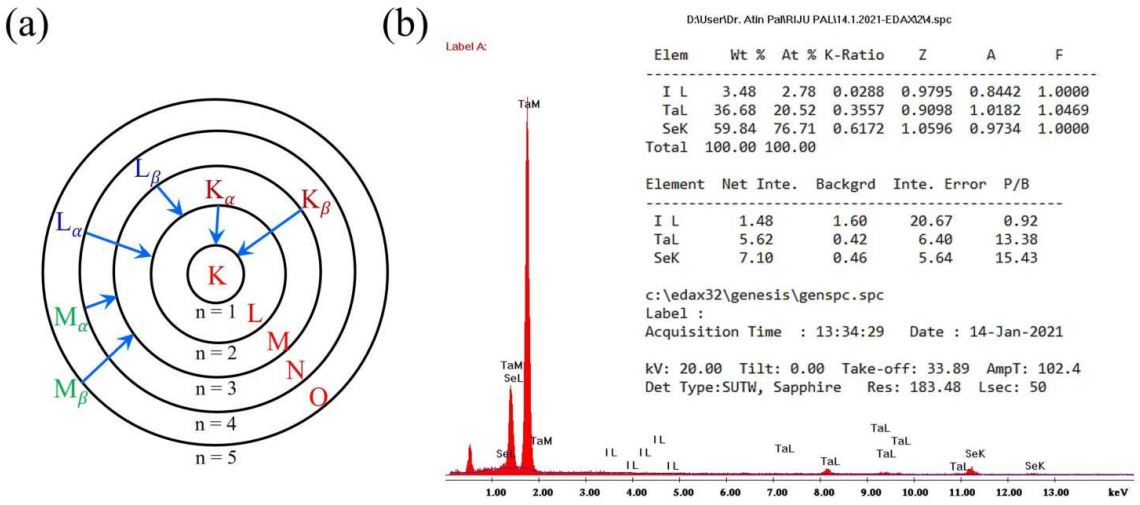

FIGURE 3.6: (a) Schematic diagram of electron transitions to lower atomic levels, resulting in the generation of characteristic K, L, and M lines. (b) The EDS spectrum shows the characteristic X-ray peaks corresponding to different elements present (details are in the inset) in the $(TaSe_4)_3I$ sample.

more probable than that from the M shell to the K shell. Consequently, K_α peaks exhibit greater intensity than K_β peaks. For quantitative analysis, the background intensity is generally subtracted from the measured spectrum. The relative intensities of the peaks from different elements are then used to determine the weight percentages, while atomic percentages can be calculated by taking into account the atomic weight of each element.

3.1.3 Characterization Techniques of 2D Flakes

3.1.3.1 Optical Microscopy

In 2D material characterization on a Si/SiO_2 substrate, an optical microscope serves as a powerful tool for quick identification of layer thickness and uniformity. This method is a cost-effective and efficient method to determine the number of layers in atomically thin vdW material flakes on a 285 nm Si/SiO_2 substrate by examining the intensity contrast between the flake and the substrate [190–192]. The 285 nm thickness of the SiO_2 layer is specifically chosen because it maximizes the contrast of few-layer and monolayer 2D flakes, leveraging interference effects that enhance visibility at certain wavelengths. This method enables differentiation between monolayer, bilayer, and multilayer regions based on their distinct optical colors and contrast levels. With a consistent SiO_2 layer thickness and steady illumination, each layer count exhibits unique optical colors and contrasts. This effect arises primarily from the interference between the reflected light from the SiO_2 substrate and the optical absorption characteristics of the 2D material [193–195]. For example, Fig. 3.7 illustrates the optical micrograph displaying various layers of graphene flakes. We used high-resolution commercial optical microscopes by Leica and Olympus (model BX53) with a typical magnification factor of 500x and 1000x for these purposes. This optical contrast method provides a preliminary, yet reliable assessment of flake uniformity, thickness, and morphology before conducting more advanced analyses such as AF microscopy characterization or Raman spectroscopy.

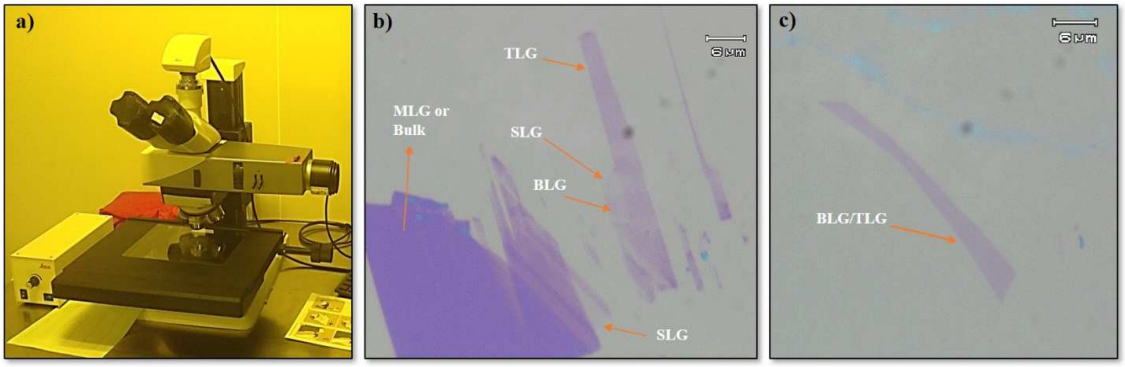

FIGURE 3.7: (a) Leica optical microscope in the cleanroom of SNBNCBS, (b),(c) Optical micrographs of the single layer (SLG), bi-layer (BLG), tri-layer (TLG), and multi-layer (MLG) graphene flakes

3.1.3.2 Atomic Force Microscopy

Atomic Force Microscopy (AF microscopy) [196–198] is a powerful technique within the scanning probe microscopy family [199], specifically crafted for the high-resolution examination of surface characteristics such as morphology, roughness, and magnetic properties, and is even applicable to biological samples. It operates by measuring interaction forces between a sharp probe tip and the sample's surface. The probe typically comprises a cantilever, often coated with conductive or magnetic materials like Co-Cr or Pt-Ir, and a highly sharp tip, sometimes coated with similar materials or doped diamond to improve functionality.

This high resolution is achieved by measuring the interaction forces between the probe tip and the sample, which include vdW, chemical bonding, capillary, electrostatic, and magnetic forces. When the tip is brought close to the sample, it experiences minute deflections in both vertical and lateral directions. These deflections are tracked by a laser beam directed at the cantilever's top surface, which then reflects onto a four-segment photo-detector. Changes in the signals from the photo-detector segments enable precise monitoring of the cantilever's angular deflections, which in turn allow for the construction of a detailed 2D profile of the sample's surface properties. This information is essential for capturing fine details about the sample surface.

The AF microscopy's impressive resolution, exceeding that of traditional optical methods, is made possible by piezoelectric actuators, enabling nanoscale scanning accuracy that precisely controls nanoscale movements of the sample and probe, achieving a resolution that surpasses the optical diffraction limit by a factor of 1000. By raster scanning across a small area, typically a few tens of μm^2, AF microscopy produces a 2D map of surface properties. The sample is positioned on a piezoelectric controller that fine-tunes the raster scan, thus enhancing image precision. This mapping technique, illustrated in Fig. 3.9(a), makes AF microscopy indispensable for an in-depth view of surface properties, aiding in a broad range of studies from morphological analysis, and can even accommodate external influences like magnetic fields or electric currents, enhancing its versatility for a wide range of scientific applications.

AF microscopy can be operated in three distinct modes [200, 201], depending on the sample surface and the interaction forces between the probe and the sample, as briefly described below.

- **Contact Mode**

In contact mode [202], also known as static mode AF microscopy, the tip remains in direct contact with the sample surface under a constant repulsive force. A feedback amplifier adjusts the piezoelectric actuator's voltage to keep this force steady, allowing for accurate height measurement of surface features. Low-stiffness cantilevers are typically used in this mode to achieve significant deflection signals (ranging from a few tens to hundreds of nanometers) while maintaining a manageable interaction force ($\leq$ 1 N/m), minimizing potential damage to both the cantilever and the sample.

- **Non Contact Mode**

In non-contact mode [203, 204], the AF microscopy tip is positioned a few tens of nanometers above the sample surface to avoid degradation caused by direct contact. This technique measures weak attractive forces, such as vdW interactions, to map the surface topography. A small oscillation is applied to the cantilever (typically with an amplitude of less than 1 nm), and changes in the oscillation's amplitude, phase, or frequency are used to detect the weak forces between the tip and sample, providing detailed surface information without causing damage.

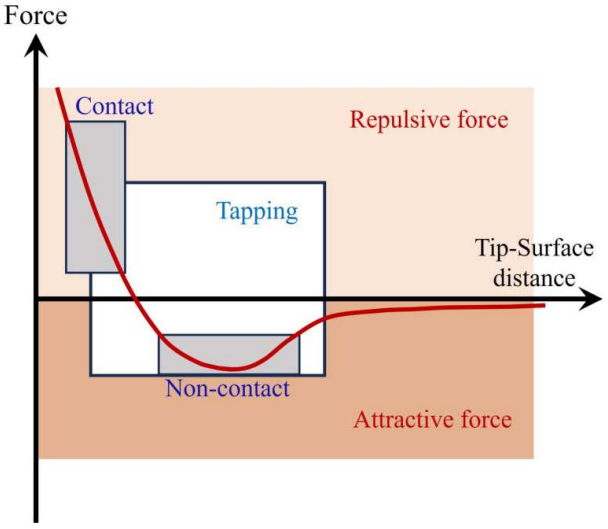

FIGURE 3.8: Graphical representation of the operation regions for Contact, Tapping, and Non-contact modes.

Non-contact mode provides the benefit of minimal interaction between the AF microscopy tip and the sample surface, which helps maintain the sharpness of the tip and allows for high-resolution imaging. However, a key challenge is maintaining the AF microscopy tip within the attractive force regime. To ensure stability at minimal tip-surface separations, advanced feedback control systems are essential. AF microscopy cantilevers featuring high force constants and elevated resonance frequencies are most suitable for Non-Contact Mode operation.

- **Tapping Mode**

Tapping mode [205] is a widely used AF microscopy technique, particularly effective in ambient conditions. In this mode, the cantilever is oscillated at or near the resonant frequency (10 - 100 kHz) using a piezoelectric crystal. The tip is positioned in the

close proximity to the sample, making intermittent contact with the surface, causing the cantilever's oscillation to dampen. The energy loss due to this contact results in changes to the oscillation amplitude, which is used to map and analyze surface features. The feedback loop in the tapping Mode ensures a constant oscillation amplitude of the AF microscopy cantilever, thereby maintaining a consistent interaction force. The dominant forces in this mode are repulsive. For typical Tapping Mode measurements, rigid AF microscopy cantilevers with force constants between 10 and 100 N/m and resonance frequencies exceeding 190 kHz are commonly used. These cantilevers are designed to avoid sticking to the surface when scanning in air. Figure 3.8 is the graphical representation of the operation regions for Contact, Non-contact, and Tapping modes.

Tapping mode can measure a variety of forces beyond atomic interactions. A notable variant is Magnetic Force Microscopy (MFM) [206–208], which detects magnetic interactions between the tip and magnetic materials, allowing the mapping of magnetic surface topology. For MFM, the cantilever tip is coated with a high coercivity magnetic material, such as Co or Co-Cr, ensuring the tip's magnetization remains stable during imaging. As the tip approaches the sample, it detects not only the magnetic forces but also the atomic and electrostatic forces acting between the tip and the sample surface. Initially, the AF microscopy image is captured to enhance magnetic contrast, after which the tip is lifted and scanned again to capture the magnetic signal. MFM can operate in both static and dynamic modes, depending on the strength of the stray magnetic field from the sample.

In this study, the Veeco diInnova AF microscopy system [209] was employed to characterize the surface morphology and height profile of 2D flakes, with the relative height data offering valuable information about the approximate number of layers in the 2D material.

3.1.3.3 Profilometer

A profilometer is a precise measuring instrument used to assess surface profile characteristics, particularly to quantify roughness and other critical dimensions such as step height, curvature, and flatness. By analyzing surface topography, profilometers can detect small vertical features with heights ranging from 10 nm to 1 mm. They operate by moving a diamond stylus vertically along the surface in contact with the sample, followed by lateral movement across the sample over a defined distance. This vertical displacement of the stylus generates an analog signal, which is then converted into a digital format for storage, analysis, and display (see Fig. 3.10). The stylus, typically with a radius

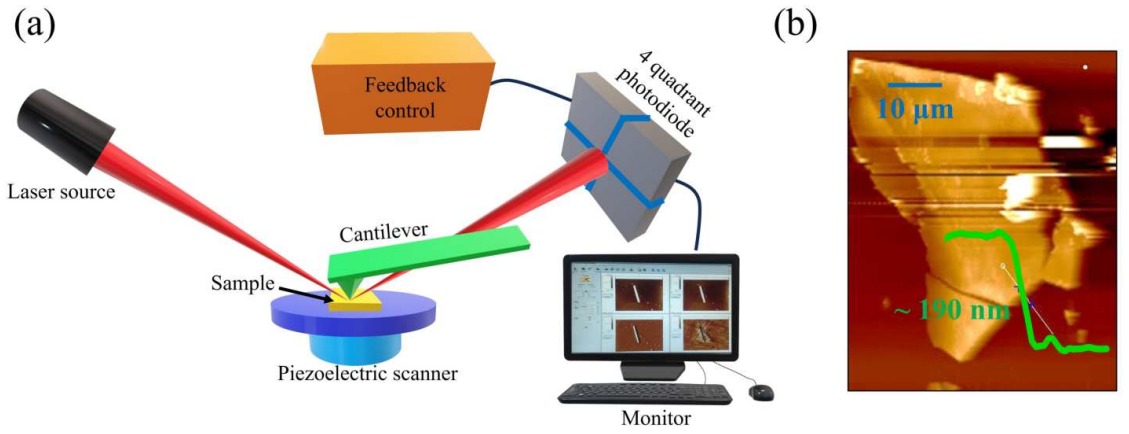

FIGURE 3.9: (a) Schematic diagram of the working principle of AF microscopy. (b) AF microscopy image and corresponding height profile of a thicker flake of Fe_4GeTe_2.

between 20 nm and 50 μm, measures minute variations in height across the sample's surface. The horizontal resolution is influenced by scan speed and data sampling rate, while the tracking force is adjustable from less than 1 mg to 50 mg, allowing accurate measurements across a range of materials and surface types.

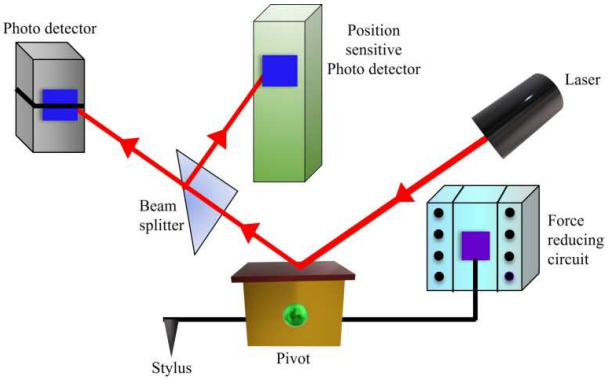

FIGURE 3.10: The schematic diagram of the optical lever design, adopted from AF microscopy principle, enables a faster response to the topographical changes.

The Alpha-Step D-600 profilometer model is particularly noted for its innovative optical-lever sensor technology (inspired by the standard AF microscopy technology), which offers an exceptional vertical measurement range of up to 1200 µm, with sub-Angstrom vertical resolution (0.38 Å) and a low tracking force adjustable between 0.03 and 15 milligrams, along with a sampling rate of ranges between 60 - 2000 Hz. This capability supports applications requiring nanometer-to-millimeter-scale accuracy, such as high-resolution roughness assessments, soft material profiling, and thin-film stress measurements. The system integrates a motorized 200 mm stage with an X-Y motion range of 150 x 178 mm, enabling it to accommodate larger samples with high precision. The D-600's advanced optics include a 5 MP camera with 4x digital zoom and sophisticated video controls, enhancing sample visualization during measurement. Figure 3.11(a) shows the image of the Alpha-Step D-600 profilometer in the clean room, which we used for quick surface characterization of the thick bulk

crystals. The approximated height profile of a transferred thick flake of Fe_4GeTe_2 on top of a pre-patterned gold electrode is shown in Fig. 3.11(b).

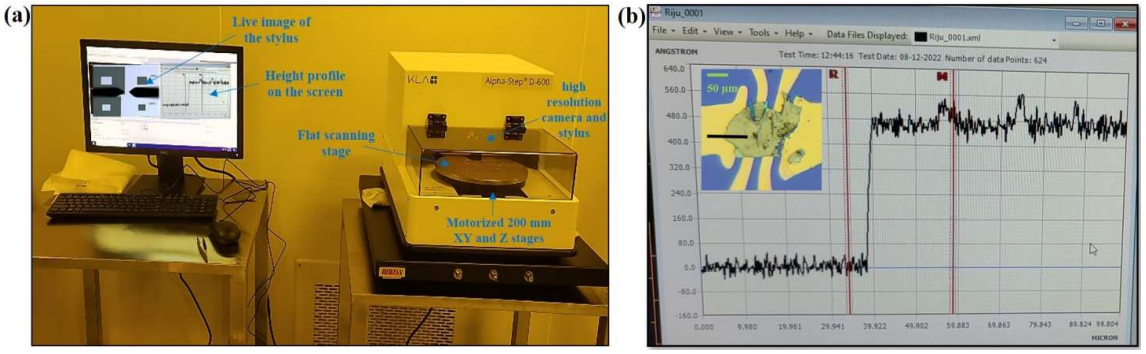

FIGURE 3.11: (a) Profilometer Alpha-Step D-600 in the clean room of SNBNCBS, (b) An estimation of the height profile of a transferred thick flake of Fe_4GeTe_2 on top of the pre-patterned gold electrodes (inset).

One major advantage of stylus-based profilometers is their direct measurement approach, which does not depend on material properties, making them suitable for a variety of structural and material types. With adjustable force and various stylus options, profilometers can measure complex topographies, quantify material additions or subtractions, and assess surface roughness or stress induced by structural changes. This combination of high precision and adaptability makes profilometers essential for quick surface characterization and roughness analysis.

3.1.4 Preparation of the vdW 2D Magnetic Flakes

2D vdW magnetic materials can be exfoliated down to a monolayer using standard mechanical exfoliation techniques, first established in 2017, with clear experimental evidence of magnetism in atomically thin CrI_3 (by B. Huang et. al. [27]) and $CrGeTe_3$ (by C. Gong et. al. [8]) respectively. In both cases, magnetocrystalline anisotropy played a key role in the stabilization of magnetic order down to the monolayer limit, bypassing the Mermin–Wagner–Hohenberg theorem [4, 5, 21]. This groundbreaking discovery opened a new era in research for the advancement in modern technology, with potential applications in magnetic sensors, storage, and future spintronic devices [31].

One of the most interesting high-temperature 2D ferromagnetic families is Fe_nGeTe_2 (n = 3, 4, 5), with a lot of unique properties, synthesized with its first family member Fe_3GeTe_2 [25] in 2017. The Fe_3GeTe_2 [25, 33, 34, 55] or Fe_4GeTe_2 [14, 36, 210] single crystals are synthesized in a controlled furnace lab with the standard chemical vapor transport (CVT) technique. The few-layered flakes are prepared by the mechanical exfoliation technique using a scotch tape, originally developed by Novoselov et al. in 2004 for isolating graphene layers [17]. This method is ideal for device fabrication as it yields high-purity, clean single-crystal flakes. By leveraging the layered structure of Fe_nGeTe_2, few-layer flakes were efficiently separated from the bulk crystal and transferred onto a clean 300 nm Si/SiO_2 (n^{++}) substrate. Initially, we started exfoliating Fe_3GeTe_2 single crystals. The following steps outline the procedure used to obtain the few-layer Fe_3GeTe_2, or Fe_4GeTe_2 flakes from their bulk form.

- **Cleaning of Wafers**

Our experiments revealed that a thoroughly cleaned wafer surface is crucial for obtaining high-quality Fe_3GeTe_2 or Fe_4GeTe_2 flakes. To achieve this, Si/SiO_2 wafers were first cut into 5 mm × 5 mm pieces and then subjected to a rigorous cleaning process. The wafers were placed in an ultrasonic bath with acetone for 5–6 minutes, followed by a rinse in isopropyl alcohol (IPA) for the same duration. This cleaning protocol effectively removes micron-sized dust particles, organic impurities, and oily or greasy contaminants from the wafer surface, ensuring optimal conditions for flake deposition.

Next, the wafers were immersed in a cold 98 % H_2SO_4 : 30 % H_2O_2 solution (Piranha solution) in a 2:1 ratio and heated on a hot plate at 75° C for 10 minutes. This treatment effectively removes any remaining organic residues from the substrate. Additionally,

the process hydroxylates most surfaces by adding -OH groups, rendering them highly hydrophilic and thus more compatible with subsequent processing steps.

Afterward, the wafers were immersed in an RCA cleaning solution consisting of deionized (DI) water, 30% ammonia solution, and 30% H_2O_2 in a 5:1:1 ratio for 15 minutes at 80° C. To prepare this solution, liquid ammonia (30%) and ultra-pure DI water (Millipore) were first heated to 80° C. Then, H_2O_2 (30%) was added drop-wise, causing bubbling due to the chemical reaction. The wafers were then placed into this solution. After 15–20 minutes, once the reaction was complete, the wafers were thoroughly rinsed with DI water, dipped in IPA, and dried with nitrogen gas blowing. Finally, they were placed on a hot plate at 100° C to ensure that the Si/SiO_2 surface was completely free of moisture before preparing the Fe_3GeTe_2 flakes. This base-peroxide mixture effectively removes organic residues, while particles are efficiently cleared, as explained in Sec. 3.1.7.3 and Fig. 3.16.

Additionally, the surface treatments make the wafer hydrophilic, facilitating the spin coating of photoresist. Following this, we performed inductively coupled plasma reactive ion etching (ICP-RIE) with oxygen plasma on the wafers to enhance the roughness of the SiO_2 surface. This process enhances the adhesion of mechanically exfoliated Fe_3GeTe_2 flakes, allowing for the successful isolation of few-layer Fe_3GeTe_2 flakes. It also improves the quality of the photoresist coating in subsequent spin coating steps.

- **Exfoliation of Fe_nGeTe_2 Crystals**

We prepared our samples (Fe_4GeTe_2 or Fe_3GeTe_2 on cleaned Si/SiO_2) using mechanical exfoliation from bulk single crystals through the scotch-tape method introduced by Novoselov et al. [17] for graphene. In this process, a piece of bulk crystal is placed on a piece of scotch tape, and the crystal is made thinner by peeling it off with another tape. The thin flakes on the tape are peeled off repetitively 5-6 times with new and fresh tape until the crystal on the tape appears significantly thinner. Immediately, the tape with thinner crystal is gently pressed onto a cleaned Si/SiO_2 surface using a Teflon-wrapped toothpick to ensure the flakes make contact with the substrate. The tape is then softly taken out from the surface, and the wafer is inspected under an optical microscope to locate faint Fe_3GeTe_2 or Fe_4GeTe_2 flakes, identifiable by their purple/violet hue.

Due to the weak interlayer vdW forces in Fe_3GeTe_2 and Fe_4GeTe_2, the flakes can be easily exfoliated using adhesive tape (scotch tape). The number of layers is subsequently confirmed through various characterization techniques as discussed earlier. Additionally, we explored the hot exfoliation technique at 90° C to obtain thinner flakes with a larger

area, as previously discussed. The step-by-step procedures of the mechanical exfoliation technique are shown in Fig. 3.1.

3.1.5 Characterization of the 2D Magnetic Flakes

- **Optical Micrograph of the Experimentally Prepared Fe_3GeTe_2 Flakes**

The identification of the layer numbers of Fe_3GeTe_2 or Fe_4GeTe_2 flakes can be carried out by using an optical microscope and AF microscopy measurements. In our study, for initial identification, we used an Olympus optical microscope to detect Fe_3GeTe_2 layer thickness based on color contrast against a 300 nm SiO_2 background, which provides optimal visibility and best color contrast for atomically thin layers. On this substrate, thicker Fe_3GeTe_2 flakes (or bulk) appear in shades from yellow to purple as thickness decreases, while few-layer flakes appear as darker to lighter purple tones, as depicted in Fig. 3.12

- **Atomic Force Microscopy on Fe_3GeTe_2 Flakes**

To determine layer numbers with greater precision, we performed AF microscopy on our few-layer Fe_3GeTe_2 samples using the contact mode as discussed earlier. In this mode, the tip-to-sample distance was maintained at less than 0.5 nm, generating a repulsive vdW force. By keeping a constant cantilever deflection via the feedback system, a stable force between the tip and sample surface was achieved, enabling accurate surface topography measurements. We measured the height difference between the Fe_3GeTe_2 surface and the SiO_2 substrate, yielding the total thickness of the Fe_3GeTe_2 flakes. Given that a monolayer Fe_3GeTe_2 thickness is approximately 0.8 nm [33], we calculated the layer number by dividing the measured thickness by the monolayer thickness. The layer numbers and corresponding height profiles are shown in Fig. 3.13, revealing that mechanical exfoliation yielded a minimum of 10 layers. Experimentally, isolating the atomically thin (monolayer) Fe_3GeTe_2 layers from the bulk poses a challenge. Because the intralayer bonding of the Fe_3GeTe_2 flakes is insufficiently strong for thinner flakes of practical size (approximately 5 µm) to withstand traditional mechanical exfoliation methods. To overcome this limitation, an Al_2O_3-assisted exfoliation technique [33] will be explored in future experiments to isolate monolayer Fe_3GeTe_2.

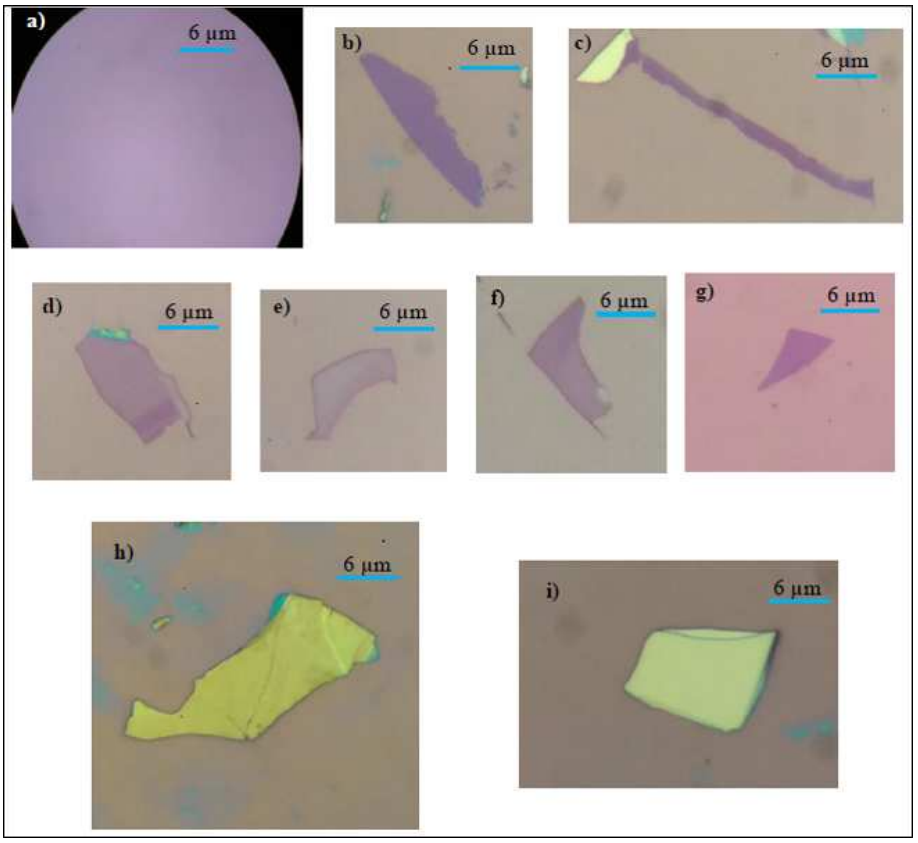

FIGURE 3.12: (a) Optical microscopic image of almost cleaned SiO_2 surface, viewed in 100x. (b), (c), (d), (e), (f), (g) Optical microscopic view of the few-layer flakes of Fe_3GeTe_2 2D FM material of different length scales and sizes, mechanically exfoliated after performing all the cleaning procedures (including oxygen plasma cleaning) mentioned above. (h), (i) The bulk of Fe_3GeTe_2 materials were exfoliated by the mechanical exfoliation technique using scotch tape.

3.1.6 Observation of the Oxidation of the Flakes and Possible Solutions

We have observed that an oxide layer naturally forms on the surface of exfoliated Fe_3GeTe_2 flakes, indicating that Fe_3GeTe_2 is unstable in air [211]. To prevent oxidation, Fe_3GeTe_2 flakes require protective measures, such as exfoliation inside a glove box [212], encapsulation with h-BN [213], or covering with a poly-dimethyl-siloxane (PDMS) or PMMA film stored in an evacuated glass tube at approximately 10^{-6} mbar [34]. For example, Fig. 3.14 shows newly prepared Fe_3GeTe_2 flakes alongside the same flakes after visible oxidation seen under a microscope, after 18 days of exposure in the bare atmosphere. Therefore, it is crucial to follow the procedures outlined above to protect the Fe_3GeTe_2 flakes from oxidation, or alternatively, adhere to the steps described below for device fabrication using the lithography technique.

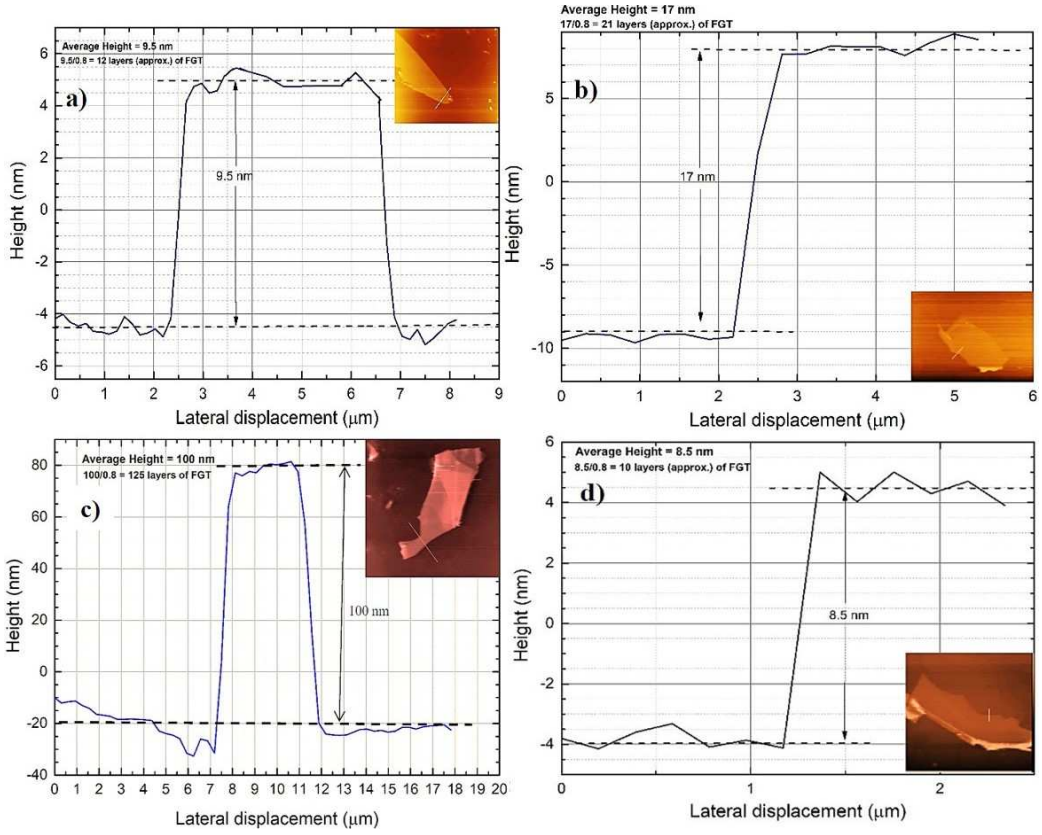

FIGURE 3.13: Height profiles of the Fe_3GeTe_2 flakes (Inset: Corresponding AF microscopy images). (a) 12 layers of Fe_3GeTe_2 flakes (Optical microscope image is in Fig. 3.12 (b)), (b) 21 layers of Fe_3GeTe_2 (see the Fig. 3.12 (d)), (c) 125 layers of bulk Fe_3GeTe_2 (Optical microscope image is in Fig. 3.12 (h)), (d) 10 layers of Fe_3GeTe_2 flakes.

• In this study, to protect the air-sensitive 2D FM flakes from chemical exposure and oxidation, optical lithography was used to pattern electrical contacts on bare Si/SiO_2 substrates, rather than directly on the flakes. This was followed by the deposition of Ti/Au or Cr/Au layers using either thermal evaporation or electron beam evaporation techniques. Afterward, the 2D magnetic materials (Fe_4GeTe_2, Fe_3GeTe_2, etc.) were exfoliated and quickly transferred onto the pre-patterned electrodes using a homemade heterostructure/transfer setup. To protect the flakes from oxidation, they were immediately coated with PMMA resist and then bonded for transport measurements. The detailed step-by-step device fabrication process is presented in the following section.

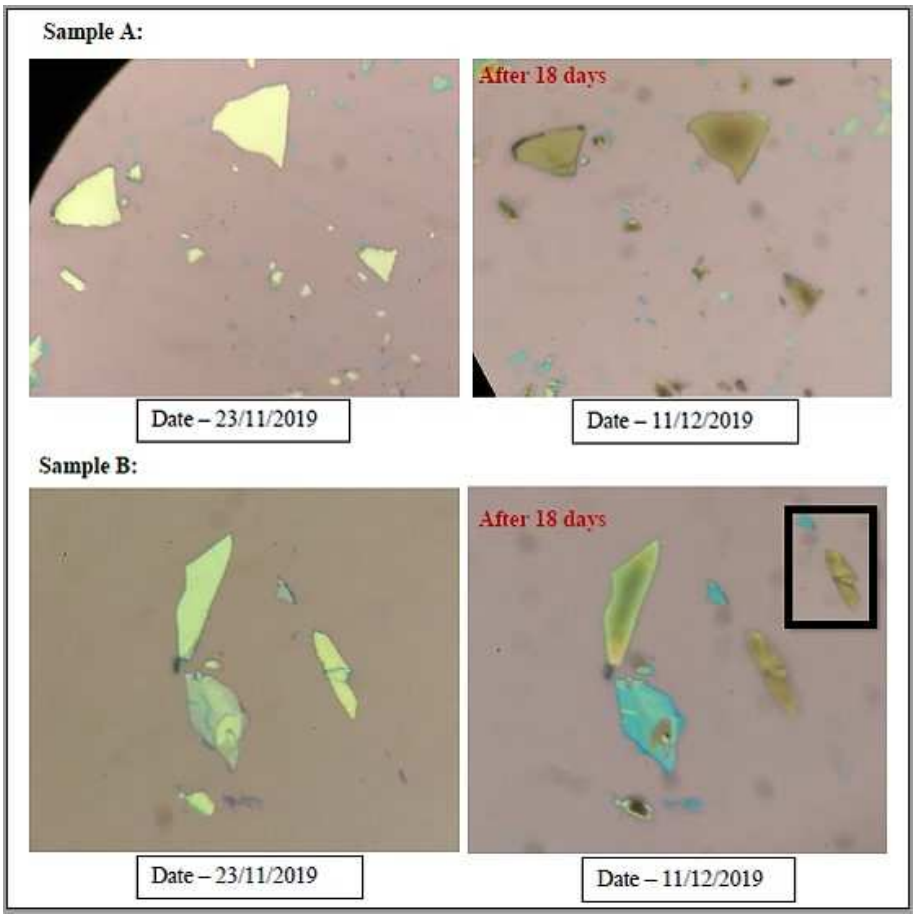

FIGURE 3.14: Fe_3GeTe_2 flakes are getting oxidized with time. Images after 18 days (Right side images) from the date of sample preparation (Left side images). A visible oxide layer is formed on the top of Fe_3GeTe_2 flakes.

3.1.7 Device Fabrication by Optical (Photo-) Lithography

To investigate the magneto- and electro-transport properties of thin flakes of 2D magnetic materials, it is crucial to fabricate electrical contacts at the micron or nano-scale due to the diminishing flake sizes with decreasing thickness. Numerous methods have been developed to achieve reliable and precise electrical contacts on micron-scale flakes, but meeting the growing demand for cost-effective fabrication of nano-scale patterns with fine precision remains a significant challenge. Lithography techniques [214–216], despite their complexity, time consumption, and expense, are indispensable for creating finely patterned structures. These techniques are essential for fabricating devices and heterostructures of thin 2D magnetic flakes, which require careful examination of their physical properties before potential industrial applications.

3.1.7.1 Lithography Technique

- **Lithography**

Lithography, rooted from the Greek terms "lithos" meaning stone, and "graphein" meaning to write, originated as a printing method in 1796, developed by a German playwright, Alois Senefelder. Initially, it involved creating images on smooth limestone surfaces using oil-based ink or wax, which were then transferred onto paper. This technique quickly gained popularity for its ability to produce high-quality prints and later evolved into offset lithography, enabling the mass production of books, maps, and posters. In the mid-20th century, lithography transformed into a cornerstone of the semiconductor industry with the advent of photolithography, allowing intricate patterns to be etched onto silicon wafers. Further advancements led to methods like electron beam and extreme ultraviolet lithography, enabling the fabrication of accurate nanoscale structures essential for modern electronics. Today, lithography continues to evolve, driving innovations in nanotechnology, semiconductor manufacturing, and materials science. Its journey from artistic printing to cutting-edge technology highlights its enduring impact across various fields.

- **Optical lithography, Photo-lithography or UV lithography**

Photolithography, also known as optical or UV lithography [215–217], is a key micro-fabrication process for patterning specific regions of thin films or substrates. Widely used in the microelectronics industry for producing integrated circuits, it enables the creation of microstructures with micron- and sub-micron-scale features. The process involves coating a photosensitive resist on substrates like silicon wafers and projecting an intensity pattern onto the resist. Depending on the type of resists, either the exposed or unexposed regions are removed during development to reveal the desired pattern.

The technique relies on four essential components: (i) an energy source for illumination, (ii) a photomask containing the defined pattern, (iii) an exposure system to project the virtual image of the mask pattern, and (iv) the photoresist to record the pattern, as produced by the exposure system.

Photolithography enables the parallel fabrication of multiple nanostructures using a photo mask, significantly reducing the fabrication time. However, its resolution is limited by light diffraction, making it challenging to produce patterns smaller than 1 micrometer.

- **Principle of Photo-lithography**

The principle of photolithography [215–217] involves transferring a pattern onto a substrate using light. A photosensitive material, known as photoresist, is coated on the surface of the clean substrate. The substrate is then exposed to light, typically ultraviolet (UV) light, through a mask that contains the desired pattern. Depending on the type of resist (positive or negative), the photoresist undergoes a chemical change when exposed to light, making it either soluble or insoluble in another chemical, called photoresist developer. After exposure, the substrate is developed to remove either the exposed or unexposed areas of the resist, creating a patterned layer. This pattern can then serve as a template for subsequent processes such as etching and deposition of the desired metal, followed by the lift-off process, enabling the creation of precise microstructures. Photolithography is widely used in device fabrication, allowing for the production of microstructures with fine features, typically on the micrometer scale. We can easily understand the process of photolithography by the following Fig. 3.15.

3.1.7.2 Photo-resist

A photoresist [215–221] is a light-sensitive material (a liquid chemical) used in processes of photolithography to create patterned coatings on surfaces, essential in electronics fabrication. The process begins by coating a substrate with this chemical, followed by applying a mask to block light and exposing the unmasked regions to light. After exposure, a developer solvent is applied. There are two types of photoresists:

(i) Positive Photoresist: Exposed areas become soluble to the developer, leaving the unexposed areas intact.
(ii) Negative Photoresist: Exposed areas become insoluble, with the unexposed portions being dissolved by the developer.

We used positive photoresist AZ 1512-HS with its developer AZ 326 MIF or AZ 315 (for the laser writer system), another positive photoresist AR-P 3110 with its developer AR 300-35, negative photoresist SU-8 2010 (consists of a Novolac epoxy dissolved in an organic solvent such as gamma-butyrolactone (GBL) or cyclopentanone; which depends on the formulation, contains up to 10 wt% of a mixed triaryl sulfonium/hexafluoroantimonate salt that serves as the photoacid generator) and negative resist developer SU-8 [217, 218] (for the UV exposure and the Mask Aligner system) for our device fabrication. We also used LOR-1A and ma-N 2405 (solution of 1-Methyl-2pyrrolidone, n-Butyl acetate & cyclohexanone) [219] as an undercutting resist. Using the recipe described later, it is possible to achieve a resist coating with a thickness ranging from approximately 0.5 µm

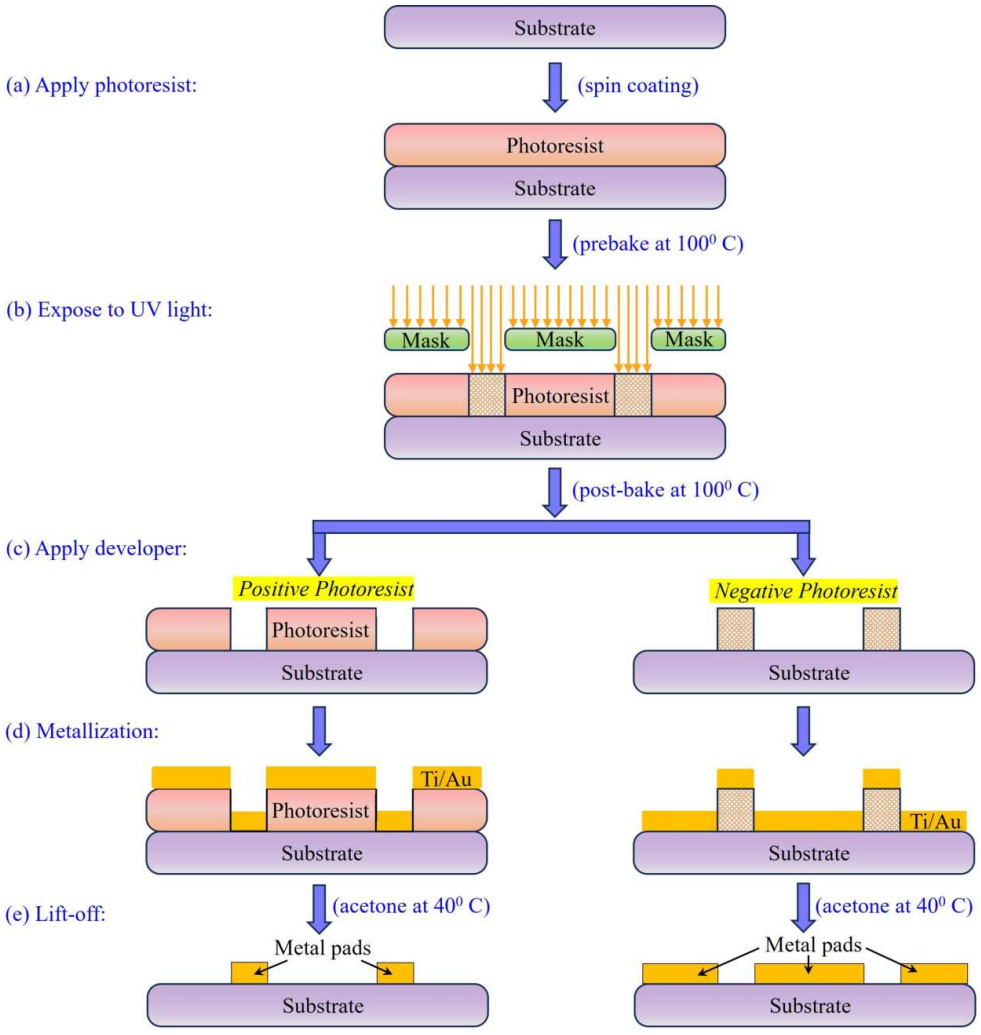

FIGURE 3.15: Schematic diagram of the full photolithography process with positive and negative photoresist.

to 2 µm. The thicknesses of the resist layers depend significantly on their densities and viscosities, as well as on the speed and duration of the spin-coating process.

3.1.7.3 Optimization Procedures of Photo-lithography on Si/SiO_2

In this thesis, metal contacts with micron-sized patterns on Si/SiO_2 substrates or on 2D materials are defined using photolithography. Two photolithography techniques were employed: (I) Hard mask photolithography (UV exposure or Mask Aligner (MJB4) by SUSS MicroTec) and (II) laser writer-based photolithography (Mask-less Pattern Generator, LaserWriter LW405D by MICROTECH). For the hard mask method, a photomask was designed using CAD software such as AutoCAD and CleWin. In contrast,

the laser writer method does not require a hard mask; instead, patterns are drawn directly according to specific requirements.

The device fabrication and photo-lithography process involves several crucial steps to achieve optimal results. These steps are substrate cleaning, resist coating, baking, patterning, light exposure, and development, followed by the metal deposition and crucial lift-off process. Each stage plays a key role in determining the final quality and functionality of the device. A schematic representation of the entire process flowchart is shown in Fig. 3.15, followed by a detailed description of each step.

- **Substrate Cleaning**

For photo-lithography, we generally use 600 µm thick Si/SiO_2 wafers, where an insulating SiO_2 layer (of thickness $\sim$ 300 nm) is present on top of the Si substrate (001 orientation, lightly p-doped, ρ in between 1 - 10 Ω cm). First, the Si/SiO_2 substrate was cut into 5 mm $\times$ 5 mm wafer pieces by a standard diamond scriber (Micro Diamond Scriber MR200) or a diamond scriber pen. Then the pieces were subjected to rigorous cleaning processes to remove the surface contaminants and residues. Importantly, careful cutting and handling of the wafer is crucial throughout the process to prevent scratches on its top surface, as this could result in a leaky device.

(a) Acetone-IPA cleaning:

To clean a wafer, an acetone and IPA cleaning process is typically used [222]. First, an individual wafer is placed in a glass beaker containing acetone, which is then transferred to a larger beaker containing a small amount of water. This setup is placed in an ultrasonic bath at 45° C for 5 - 6 minutes. Afterward, the wafer is removed from the acetone and immediately immersed in IPA for 2 minutes. Then, the wafer is dried using a nitrogen (N_2) gas blower at a grazing angle. Finally, the wafer is placed on a hot plate at 120° C to ensure that no moisture remains on the wafer surface.

Acetone effectively removes organic impurities from the wafer substrate, particularly dissolving oily or greasy contaminants. However, since acetone evaporates quickly and can redeposit some contaminants, the wafer is immediately placed in IPA. IPA dissolves acetone and its contaminants, acting as an excellent rinse agent. This cleaning protocol effectively removes micron-sized dust particles, organic impurities, and oily or greasy contaminants from the wafer surface, ensuring optimal conditions for optical lithography.

(b) Piranha cleaning (acid cleaning):

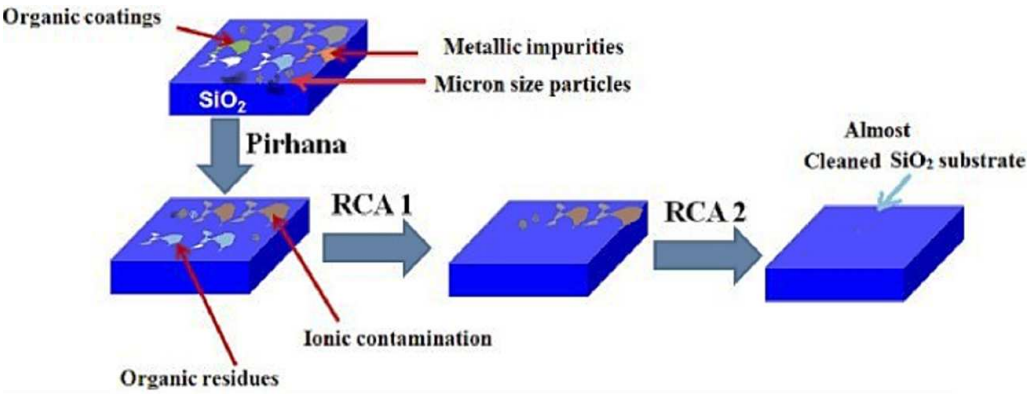

FIGURE 3.16: Cleaning procedures of Si/SiO_2 substrate. Adopeted from Ref. [225].

Piranha solution, or piranha etch [223, 224], is a powerful mixture of sulfuric acid (H_2SO_4) and hydrogen peroxide (H_2O_2) used for cleaning organic residues from substrates. As a strong oxidizing agent, it effectively removes most organic material and hydroxylates surfaces (adds -OH groups), making them highly hydrophilic and more compatible with water.

The piranha solution is prepared by mixing 98 % conc. H_2SO_4 and 30 % cold H_2O_2 solution in a 2:1 ratio. This mixture must be handled with great care, as it is highly corrosive and an extremely powerful oxidizer. Piranha solution works by dissolving organic contaminants, and if too much contamination is present, it can lead to violent bubbling and gas release, posing a risk of explosion. Therefore, extreme caution is necessary when using this solution. The step-by-step process is as follows:

Piranha solution:- 98 % conc. H_2SO_4 : 30 % cold H_2O_2 = 2:1 (ratio)

i) Teflon tweezers should always be used for handling the wafers.
ii) For preparation, 4 mL of 98 % conc. H_2SO_4 is carefully taken in a beaker, and 2 mL of cold H_2O_2 is slowly added. (An exothermic reaction occurs, generating temperatures up to approximately 1000° C).
iii) The wafers are then immersed in the solution and heated on a hot plate at 75° C for 10 minutes.
iv) After 10 minutes, the wafers are removed from the solution and immediately placed in de-ionized (DI) water.
v) The DI water is changed, and the wafers are rinsed 4-5 times to ensure thorough cleaning.
vi) Finally, the wafers are dried using nitrogen (N_2) gas. (A fresh solution should be prepared for each wafer-cleaning process).

(c) RCA cleaning:

The RCA cleaning [222, 226, 227] is a standard cleaning procedure for silicon wafers, performed prior to high-temperature processing in semiconductor manufacturing. First developed by Werner Kern [226] in 1965 while working at RCA (Radio Corporation of America), the process involves a sequence of chemical treatments to ensure the wafer is thoroughly cleaned. The steps include:

(i) Removal of organic contaminants (particle and organic clean): A mixture is prepared with 5 parts DI water, 1 part ammonia water (29 % NH_3), and 1 part aqueous hydrogen peroxide (H_2O_2, 30 %). The solution is typically heated to 75 or 80° C and the wafer is immersed for 10 minutes. This base-peroxide mixture effectively removes organic residues and small particles while also rendering the surface hydrophilic, which aids in the spin coating of photoresist.

(ii) Rinsing and drying: When performing the cleaning with high-purity chemicals and glassware, this procedure results in a very clean wafer surface while still submerged in water. Proper rinsing and drying are crucial to avoid re-contamination from organic and particulate matter floating on the water's surface. Various procedures can be employed to rinse and dry the wafer effectively (see Fig. 3.16).

Step-by-step process:

RCA solution:- DI water : 30% ammonia solution : 30% H_2O_2 = 5:1:1 (ratio)

(i) Teflon tweezers are used to handle the wafers.
(ii) For preparation, 20 ml of DI water is poured into a clean beaker, and 4 ml of ammonia solution is added.
(iii) The solution is heated for 2-3 minutes at approximately 75° C.
(iv) 4 ml of cold H_2O_2 is slowly poured into the heated solution, causing bubbles to form.
(v) The wafers are completely submerged in the solution and heated for 20 minutes, or until bubbling ceases, indicating the reaction has stopped.
(vi) The wafers are removed from the solution, gently shaken to remove excess liquid, and immediately placed into DI water.
(vii) The DI water is replaced, and the wafers are rinsed thoroughly 4-5 times.
(viii) The wafers are then transferred to IPA and dried using N_2 gas.

(d) Oxygen Plasma cleaning:

Oxygen plasma etching [220, 224, 228, 229] of Si/SiO_2 substrates is a process where a high-energy plasma, generated by ionizing oxygen gas, is used to etch or remove a thin layer of SiO_2. This technique is widely employed in micro-fabrication and device preparation for modifying substrate surfaces with high precision. In this process, reactive oxygen species (ions, radicals, and neutral particles) in the plasma chemically react with the SiO_2 surface. The etching primarily occurs through the formation of volatile byproducts, such as silicon monoxide (SiO) and carbon dioxide (CO_2), which are removed from the reaction chamber. The process is also employed to create hydrophilic surfaces on silicon wafers by removing a native oxide layer and generating hydroxyl (-OH) groups, which enhance water molecule attraction. Oxygen plasma etching serves as a precautionary step to remove residual impurities that may be invisible under an optical microscope. The power and duration of the etching process are tailored based on the oxide layer's thickness and the desired surface roughness.

In this study, an inductively coupled plasma reactive ion etcher (ICP-RIE) system (SI 500 by SENTECH Instruments) was used, operating at 150 W ICP power, 50 W RF generator power, and 0.6 Pa reactor pressure. The flow of O_2 was 20 sccm for 20 sec, and the etch rate of SiO_2 was estimated to be $\sim$ 50 nm/min. This mild etching enhanced the surface properties of Si/SiO_2 substrates by removing the surface contaminants and improving the compatibility for adhesion of photo-resists in lithography, subsequent material deposition, or the mechanical exfoliation process.

(e) HF buffer etching:

Buffered Hydrofluoric Acid (buffered HF) [223, 230, 231] is a widely utilized etchant in semiconductor processing and micro-fabrication for removing silicon dioxide (SiO_2) layers from Si/SiO_2 substrates. It is made by combining hydrofluoric acid (HF) with a buffering compound, usually ammonium fluoride (NH_4F), which helps regulate the etching rate and stabilize the process. The buffer also reduces the etchant's aggressiveness, making it safer to handle compared to pure HF.

A 6:1 buffered HF solution was prepared to etch a few layers of the oxide surface to enhance its adhesive nature, and hydrophobic behavior and to remove the contaminants from its top surface. First, a 40 % NH_4F solution was made by dissolving 40 grams of ammonium fluoride in DI water to make a total volume of 100 ml. Then, 6 parts of the 40 % NH_4F solution were mixed with 1 part of commercially available 40 % HF (40 % NH_4F : 40 % HF = 6:1 ratio). HF and NH_4F react with silicon dioxide (SiO_2) to form soluble silicon hexafluoride ($SiF_6{}^{2-}$) and ammonium hexafluorosilicate ($(NH_4)_2SiF_6$) respectively, which

are then removed. The reactions are as follows:

$$SiO_2 + 6HF \rightarrow H_2SiF_6 + 2H_2O$$

$$SiO_2 + 4HF + 2NH_4F \rightarrow (NH_4)_2SiF_6 + 2H_2O$$

The etching rate of SiO_2 we estimated is $\sim$ 75 nm/min. Hydrofluoric acid is an extremely hazardous substance. Direct contact with HF can cause severe chemical burns and systemic toxicity. It is particularly dangerous because it can penetrate the skin, potentially reaching deeper tissues and causing damage to bones. So, all preparation steps were conducted using plastic beakers, plastic/Teflon tweezers, and plastic gloves, maintaining all the safety protocols.

- **Resist Coating**

Spin coating is a technique used to apply thin, uniform films to flat surfaces. In this process, a small amount of coating material is placed at the center of the cleaned substrate, which may either remain stationary or rotate at a low speed initially, as connected to a vacuum chuck. The substrate is then spun rapidly to distribute the material across the surface through centrifugal force. This procedure is carried out using a device called a spin coater or spinner. As the substrate continues to rotate, excess material is spun off the edges, and the film reaches the desired uniform thickness, although there can be some non-uniformity at the edges. The solvent used in the process typically evaporates quickly due to its volatility. The film's thickness can be controlled by adjusting the spinning speed: higher rotational speeds result in thinner films. The final thickness also depends on factors such as the solution's viscosity, concentration, and solvent. Spin coating is commonly used in photolithography to apply photoresist layers, typically $\sim$ 0.5 - 2.5 µm thick [217, 220], and the speed ranges from 2000 to 8000 rpm for durations of a few seconds to several minutes.

$\Rightarrow$ **For the UV exposure or Mask Aligner system**, we used positive photoresist AR-P 3110 with its developer AR 300-35. The optimized procedures are as follows:

(i) The cleaned SiO_2 wafer is placed on top of the spindle of a spin coater using a vacuum pump.

(ii) A drop of ma-N (which offers excellent resistance to both wet and dry etching, strong thermal stability, superior pattern resolution down to 3 nm, improved undercut control, and straightforward removal) is added onto the SiO_2 wafer, followed by spinning at 3000 rpm for 60 seconds.

(iii) The wafer is then baked in a prebake chamber at 120° C for 2 minutes. Baking primarily serves to remove the solvent from the photoresist and enhance its adhesion to the substrate.

(iv) The wafer is placed back into the spin coater, and a drop of positive photoresist, AR-P 3110, is applied. The wafer is spun again at 3000 rpm for 30 seconds, achieving approximately uniform 1.9 µm thickness.

(v) The wafer was again baked on a hot plate at 90 - 100° C for 15 minutes (prebake).

⇒ **For the mask-less laser writer system**, we used a positive photoresist (AZ 1512 HS) with its developer AZ 315. The optimized procedures are as follows:

(i) The cleaned SiO_2 wafer is placed on a vacuum chuck of the spin coater.

(ii) A drop of AZ1512-HS (positive photoresist) was spin-coated onto the wafer at 4000 rpm for 60 seconds, achieving approximately uniform 1.4 µm thickness except at the edges (edge bead).

(iii) To ensure complete solvent evaporation and achieve a uniform coating, the wafer underwent baking using a hot plate at 100° C for 1 minute (prebake).

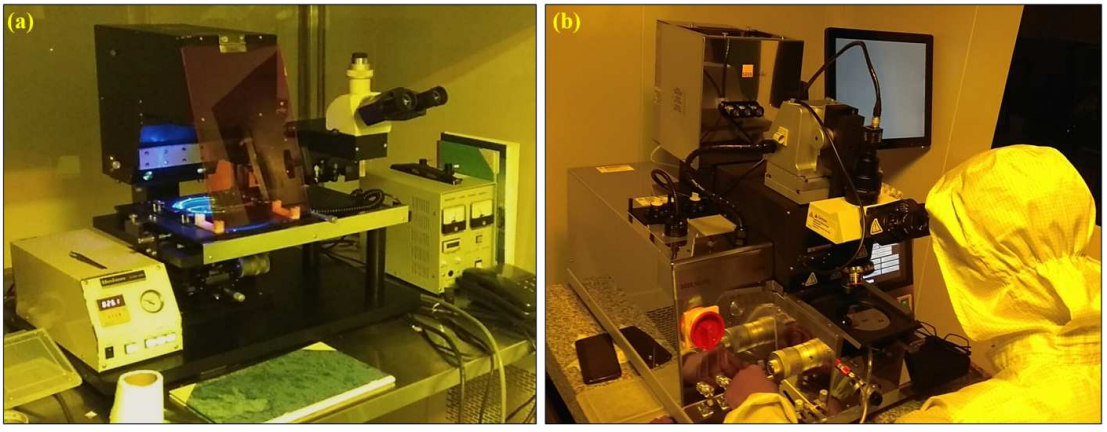

FIGURE 3.17: Image of the (a) UV exposure system, and (b) Mask Aligner (MJB4, SUSS MicroTec) system in the clean room of SNBNCBS

- **UV light based lithography and photoresist removal**

In UV light-based lithography, we used a UV exposure system (Hg lamp with emission at 435.8 nm) and a Mask Aligner (MJB4) by SUSS MicroTec (UV source: Hg 350 W (405 nm) & HgXe 500 W (250 nm) and with resolution ∼ 1.5 µm) (see Fig. 3.17). In

this hard mask-based technique, a photomask was designed using computer-aided design (CAD) software such as AutoCAD [232, 233] and CleWin [234, 235]. Here, the contact method was employed, wherein the designed mask was placed directly in contact with the substrate on a vacuum-connected chuck. This method offers the advantage of minimizing proximity effects caused by diffraction, thereby enhancing the accuracy of the pattern. Using this technique, resolutions as fine as 1.5 µm were achieved.

To obtain the finger pattern (for example, pad width $\sim$ 2 µm, separation between the pads $\sim$ 1.5 µm), the designed mask was properly aligned to allow UV radiation to pass through and fall onto the exact uniform position of the prebaked and spin-coated wafer. The wafer was then exposed to UV light with typical energy (70 - 90 mJ/mm^2) through the mask containing the pattern for 120 seconds. Thereby, the resist reacts at the exposed part, which becomes soluble/insoluble in the developer depending upon the positive/negative resist. The UV-exposed sample is then placed in a post-bake oven set to a temperature of 60 – 70°C for 10 minutes. The wafer is then immersed in a developer solution (AR 300-35 developer for positive AR-P 3110 [236], SU8 developer for negative SU8 resist [217–219]) for a few seconds (10 - 70 sec) depending on the optimized parameters, patterns, and the resists. For positive photoresist, the UV-exposed wafer is placed in the AR 300-35 developer for 15 seconds to obtain the finger pattern. During this time, the portion of the photoresist exposed to UV light becomes soluble in the developer, while the unexposed areas remain intact. As a result, the patterned regions are revealed with SiO_2 exposed, while the unexposed areas remain covered with photoresist. After development, the wafer is rinsed with DI water (for AR 300-35) or IPA (for SU8) for about 1–2 minutes, followed by drying with a flow of nitrogen (N_2). This process reveals the resist pattern, with the exposed or unexposed areas becoming visible depending on whether a positive or negative resist is used, and then can be checked with an optical microscope (with a proper light filter).

The step-by-step optimized process is as follows:

(i) The resist-coated wafer is exposed to the UV light for 120 seconds for the finger pattern.

(ii) The wafer is then kept in a post-bake oven at 60 - 70°C for 10 minutes.

(iii) After exposure, the pattern is developed using AR 300-35 positive photoresist developer for 15 seconds to get the finger pattern.

(iv) Once development is complete, the sample is rinsed thoroughly with DI water and dried using N_2 gas.

- **Laser writer based lithography and photoresist removal**

In this mask-less, laser writer-based lithography process, direct patterning is achieved using a laser writer (LaserWriter LW405D by MICROTECH) (see Fig. 3.18), eliminating the need for a hard mask. Instead, desired designs are created by the 'CleWin' software, and these patterns are precisely drawn according to specific design requirements by using a GaN laser with a wavelength of 405 nm.

During the patterning stage, photo-resist-coated samples are exposed to a laser dose of 160 - 180 mJ/cm^2 to form the intended shapes. After exposure, the patterned areas are developed using a positive resist developer (AZ 326 MIF or AZ 315). Precise control of the developing time, typically between 40–50 seconds, is crucial to preserve the integrity of fine patterns and to avoid overdevelopment. In this process, the exposed regions of the resist dissolve in the developer, while the unexposed areas remain intact. Once development is complete, the sample is rinsed thoroughly with DI water and dried using N_2 gas. The resulting pattern is then inspected under an optical microscope to verify the accuracy of the pattern.

The step-by-step optimized process is as follows:

(i) The cleaned wafer is spin-coated with the positive photoresist AZ1512-HS at a speed of 4000 rpm for 60 seconds, achieving approximately uniform 1.4 µm thickness except at the edges of the wafer (edge bead).

(ii) The wafer is then baked at 100° C for 1 minute (prebake).

(iii) The sample is then exposed in the laser writer system, with the laser power 161 mJ/cm^2, following a pre-designed pattern (here, the pad widths are 3 µm and the separation between the pads is 2 µm).

(iv) After exposure, the pattern is developed using AZ 315 developer for 40-45 seconds.

(v) Once development is complete, the sample is rinsed thoroughly with DI water and dried using N_2 gas.

After the developing process, a common observation is that the material beneath the photoresist etches at a faster rate than the resist itself. This phenomenon, known as

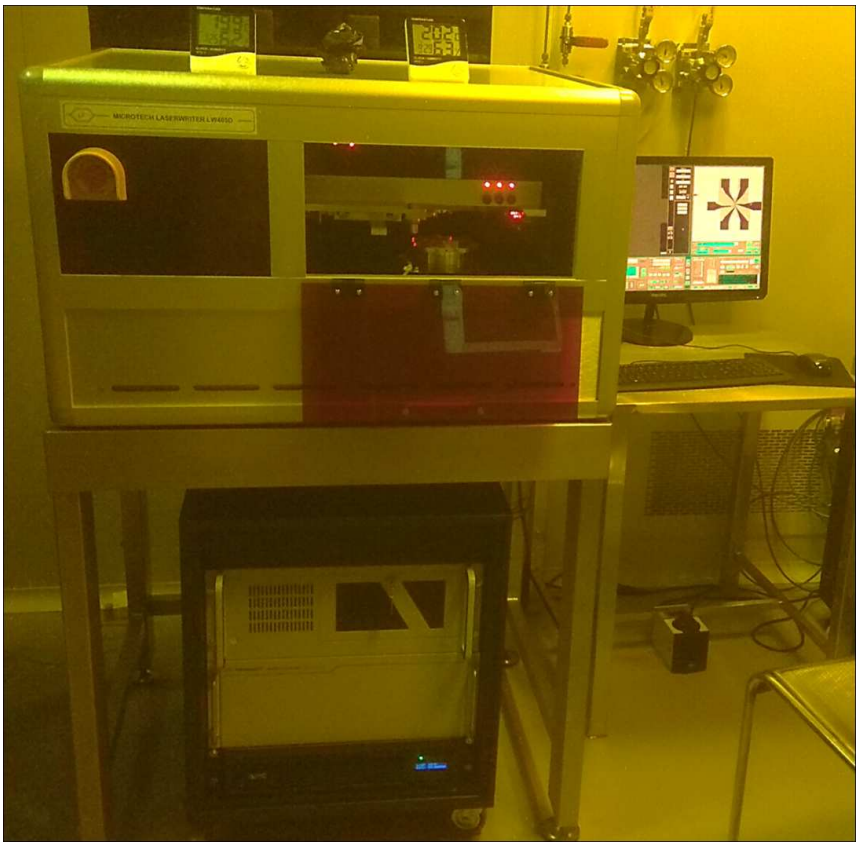

FIGURE 3.18: Image of the laser writer system (LW405D, MICROTECH) in the clean room of SNBNCBS

'undercut' in lithography [217, 231, 237], causes the photoresist layer to slightly overhang the underlying material. A good undercut profile results in a sharp and precise pattern after metal deposition and liftoff (see Fig. 3.19). However, poor undercutting (or overcut profile) can lead to feature deformation after metal deposition, making it difficult to remove excess material during the liftoff process, often leaving unwanted metal residues. Poor undercut can also cause uneven or distorted metal patterns, compromising the precision and resolution of the final structure. Additionally, improper undercutting may reduce the mechanical stability of the metal layer, resulting in poor adhesion or peeling from the substrate.

- To achieve high-quality, precise, and reproducible lithographic patterns with a proper undercut profile, a bilayer-resist coating method [221, 238] is often utilized. The process begins by applying a resist with a high solubility in the developer solution to the surface of the sample. Following this, a second layer of photoresist, which is less soluble in the developer, is carefully applied over the first layer. During the development phase, the bottom layer dissolves at a faster rate than the top layer, causing the top layer

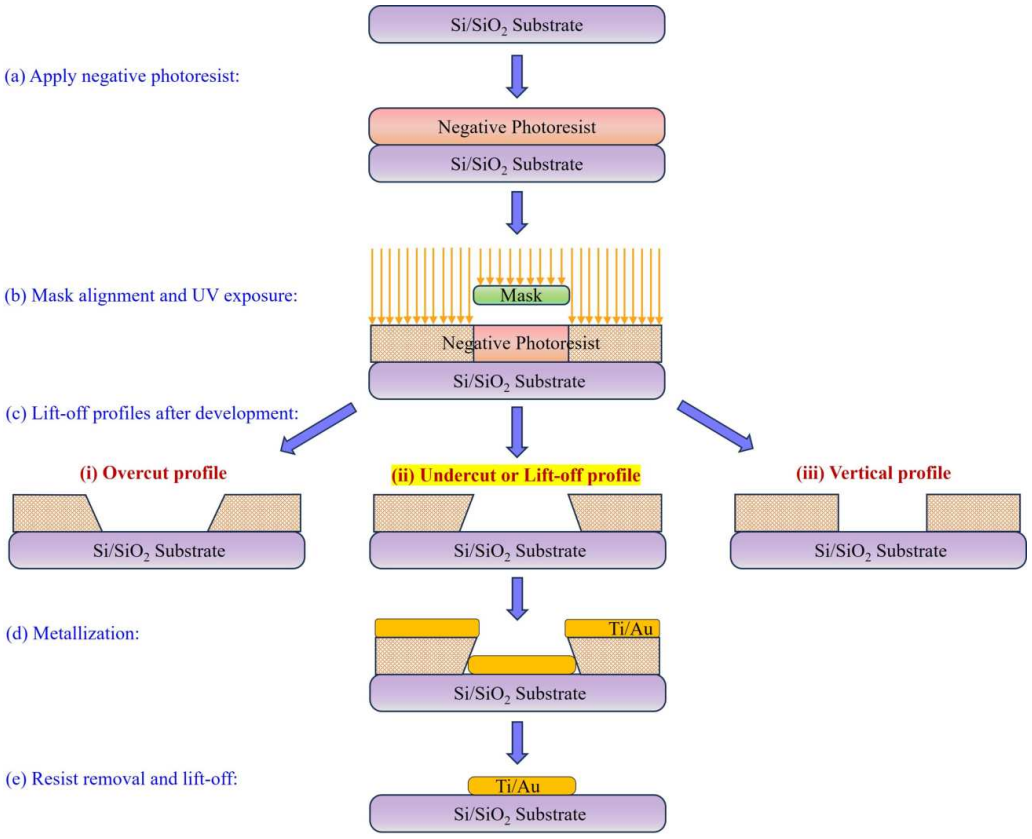

FIGURE 3.19: Schematic illustration of three different photoresist profiles. The undercut (lift-off) profile is commonly used for metal patterning in the lift-off process, allowing clean removal of unwanted material.

to overhang the bottom slightly, creating a good undercut profile. This bilayer resist technique enhances the precision and reliability of the lithographic pattern, leading to clear and consistent features.

The process for this bilayer resist coating method is as follows:

(i) The cleaned wafer is spin-coated with LOR-1A, an undercutting resist, at a speed of 4000 rpm for 60 seconds.

(ii) The wafer is then baked at 180° C for 1 minute (prebake).

(iii) Next, the second resist, AZ1512-HS, is spin-coated at 4000 rpm for 60 seconds.

(iv) The resist-coated wafer is baked again at 100° C for 60 seconds.

(v) The sample is then placed in the laser writer system, exposed with a laser power of 161 mJ/cm^2 along with a predefined pattern.

(vi) After exposure, the pattern is developed in AZ 315 developer for 40 seconds.

(vii) The sample is again baked at 100° C for 1 minute (post-bake), followed by an additional 45 seconds of development. This second development step ensures the proper formation of the undercut in the pattern.

Although an optimal development time is typically determined, remnants of resist may still remain in the patterned regions, which might not be visible under an optical microscope. Additionally, the polymer residues from lithography processes often contaminate the SiO_2 surface, leaving unwanted remnants. When polymer residues are present, the contact metal deposited on SiO_2 does not stick/attach effectively, leading to failure in the wire bonding process (see Fig. 3.20). This also leads to increased contact resistance and can deteriorate the overall performance of the device.

As a precautionary measure, buffered HF or ICP-RIE etching (refer to Section 3.1.7.3, Substrate Cleaning) is typically used to remove any residual resists from the SiO_2 surface. In this case, just before the deposition, lithographically patterned wafers are etched by immersing them in buffered HF solution for 10 seconds (see Fig. 3.20). This process etches a thin layer (approximately 10 - 12 nm) of SiO_2 along with the contaminants and residual resists, ensuring clean surfaces for optimal metal deposition. The deposited metal is now directly attached to the SiO_2 surface, free of residues, and adheres securely. The strong adhesion of Ti/Au facilitates the bonding of metal pads, ensuring a reliable bond even at room temperature.

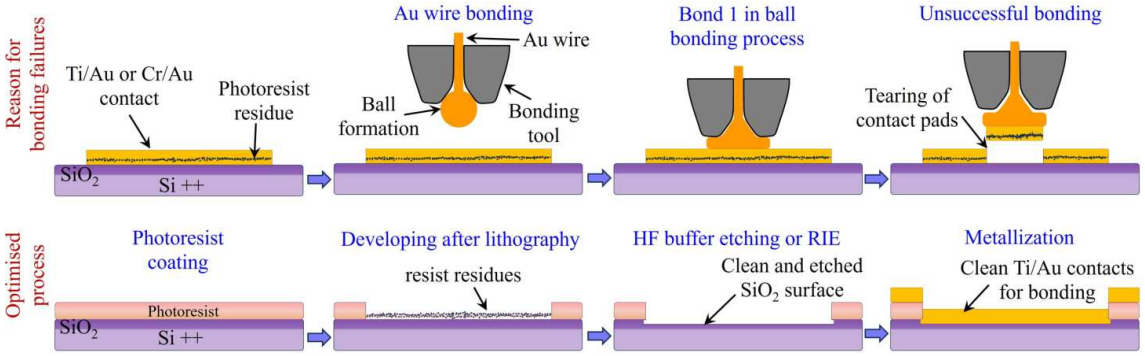

FIGURE 3.20: Common cause of bonding issues and the corresponding optimization strategies to achieve improved and reliable bonding performance.

3.1.7.4 Metallization Techniques

Metal deposition is a crucial step following lithography, as it establishes the necessary metal contacts on the sample. Various metals, such as Titanium (Ti), Chromium (Cr), and Gold (Au), are commonly used in device fabrication to ensure reliable electrical connections and functionality. In this thesis, thermal deposition and the e-beam evaporation methods are primarily utilized to fabricate contacts for most of the devices, discussed as follows:

(a) Thermal Evaporator:

Thermal evaporation [239–241] is a widely employed physical vapor deposition (PVD) technique used to create uniform thin films by vaporizing solid materials in a high-vacuum environment. As the name suggests, the target materials are evaporated by a resistive/Joule heating method, typically employing Tungsten, Molybdenum, or Tantalum boats (see Fig. 3.21 (b)). Thermal evaporation systems (TES) are versatile and capable of depositing a wide range of metals and nonmetals, such as Aluminum (Al), Indium (In), Silver (Ag), Titanium (Ti), Chromium (Cr), Gold (Au), etc.

In thermal evaporation, the source material is placed in a boat and heated to achieve the vapor pressure required for evaporation [239]. Joule heating can provide temperatures as high as 2800 K, enabling sufficient vapor pressures for the evaporation of most metals. Once the material evaporates, the vapor travels through the vacuum chamber following a specific solid angle with adequate thermal energy and condenses on the substrate. Generally, the substrate is mounted perpendicularly to the vapor source to ensure its uniform deposition. The quality of the deposited film depends significantly on maintaining a high vacuum environment within the chamber, typically below $\approx$ 1 x 10^{-6} mbar. To achieve and maintain the necessary vacuum levels, thermal evaporation systems are equipped with a high-vacuum pump system, typically combining a rotary pump with a turbo-molecular pump (Edwards). This low-pressure environment ensures a long mean free path for vaporized particles, preventing interference from gas molecules, avoiding oxidation of the source material, and minimizing contamination from the deposition chamber, which ensures the formation of high-purity films [240]. For instance, achieving a mean free path of $\sim$ 30 cm for a particle size of $\sim$ 0.3 nm necessitates maintaining a vacuum level of around 10^{-3} mbar. The deposited film's thickness is accurately regulated by a quartz crystal thickness monitor, which ensures accurate measurement and consistency throughout the deposition process. The system operates with a power source capable of delivering up to 300 A current, providing sufficient energy to heat the resistive sources and vaporize the material effectively. This high-power capability ensures the efficient evaporation of

materials, including those requiring higher temperatures [241]. These high-power sources and the turbo pump are cooled by a chiller controller unit.

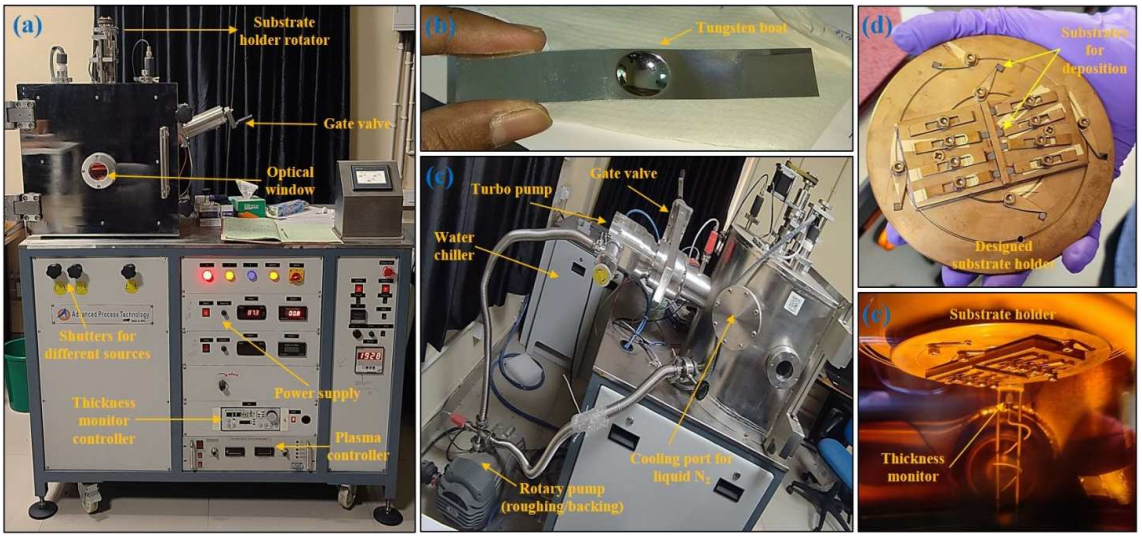

FIGURE 3.21: (a) Image of the thermal evaporator system. (b) Image of the Tungsten boat used to evaporate the target materials. (c) Backside image of the thermal evaporator system. (d) Substrate holder designed for deposition. (e) Image showing the substrate holder inside the thermal evaporator chamber during the deposition process.

We used a thermal evaporator system by Advanced Process Technology Pvt. Ltd. as shown in Fig. 3.21 (a), (c). Here, substrate heating is feasible during the deposition process, with external control enabling temperatures to range from 77 K to 650 K. This feature provides precise thermal regulation, ensuring optimal conditions for uniform and high-quality thin-film deposition. A rotator is connected to our customized homemade substrate holder (see Fig. 3.21 (d),(e)), allowing it to rotate the substrates during deposition. This rotation enhances film uniformity by ensuring even distribution of the deposited material across the substrate surface. A plasma system, integrated within the thermal evaporator, is employed to etch or clean the substrate's top surface prior to deposition. This process removes the surface contaminants and improves the adhesion of the deposited material, ensuring a high-quality thin film (see Fig. 3.21 (a)).

We used the thermal evaporator system for fabricating electrical contacts after doing lithography, with commonly used metals such as Au, Ti, or Cr. Our common deposition procedure involves first applying an adhesion layer of Ti ($\sim$ 5 nm), followed by a thicker Au layer ($\sim$ 20 - 70 nm, as required) on patterned substrates.

(b) E-beam Evaporator:

Electron Beam Evaporation (EBE) [242–244] is a precise PVD technique widely used for depositing high-quality thin films, especially in micro-fabrication or nano-fabrication. It offers versatility in material selection and ensures uniform deposition, making it essential for creating patterned microstructures as well as for modern thin-film applications.

The process begins with placing the target material in a water-cooled graphite crucible housed within an evacuated chamber. Achieving a high vacuum ($\sim 10^{-6}$ mbar) is essential for minimizing contamination during deposition. This vacuum is typically attained using a turbo-molecular pump supported by a rotary pump. Samples are mounted onto a circular metal plate using Kapton tape and loaded into the chamber, ensuring stable positioning throughout the process.

The deposition process [244] is driven by a beam of electrons generated via thermionic emission from a hot tungsten filament. This electron beam is directed and focused onto the target material with the help of deflecting and focusing magnets. The focused beam heats the material to its melting point, causing it to evaporate. The vaporized material then travels through the vacuum chamber and condenses uniformly onto the substrate surface. To ensure uniform deposition, the substrate is mounted on a rotating holder that continuously rotates during the process. The relatively long distance ($\sim$ 15 – 20 cm) between the crucible and the substrate allows the evaporated material to deposit perpendicularly. This feature is particularly advantageous when depositing films on arrays of patterned micro- or nanostructures, as it reduces unwanted sidewall coatings. By minimizing such side deposits, the lift-off process becomes more efficient, as the solvent can easily penetrate the resist layer without obstruction.

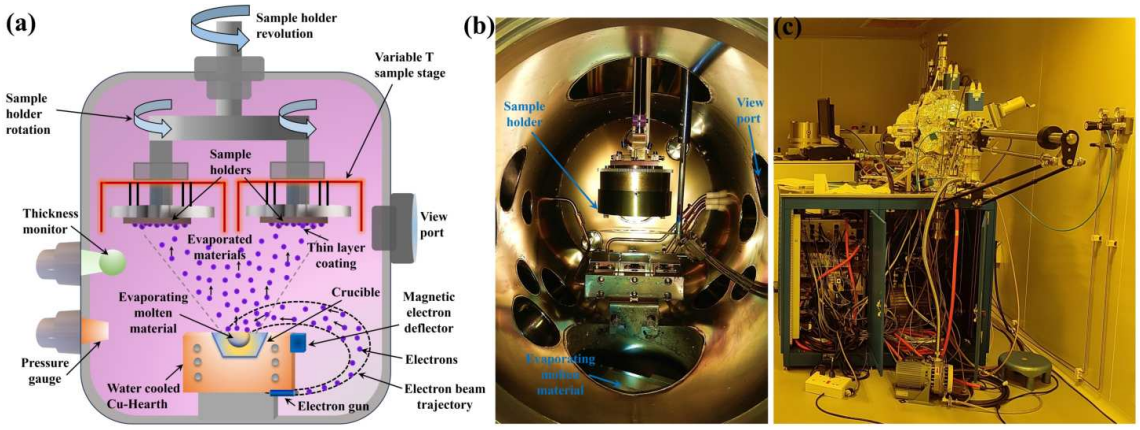

FIGURE 3.22: (a) Schematic diagram of the e-beam evaporator system. (b) Image of the internal chamber of the EBE. (c) EBE system inside the clean room of SNBNCBS.

EBE systems are versatile and capable of handling a wide range of materials [244]. Nonmagnetic materials such as Au, Ti, Cr, aluminum oxide, and silicon dioxide can be deposited with precision, as can FM elements like Ni, Fe, Co, and their alloys. To accommodate multiple materials, the system is equipped with separate crucibles arranged on a linear or circular train. The position of these crucibles can be adjusted externally without breaking the vacuum, allowing for seamless transitions between materials during deposition. The deposition process is carefully monitored to ensure consistency and precision. A piezoelectric thickness monitor is employed to track the deposition rate and film thickness in real time. For our case of Cr/Au or Ti/Au deposition of $\approx$ 5 nm/40 nm, the rate is optimized to around 0.3 - 0.5 Å/s. This meticulous control of deposition parameters ensures high-quality films with uniform thickness. The schematic diagram of EBE is represented in Fig. 3.22(a). The image of the internal chamber of the EBE system inside the clean room of SNBNCBS is shown in Fig. 3.22(b), (c).

3.1.7.5 Liftoff

Metal lift-off is a micro-fabrication technique used to define patterns after depositing a thin metal film over a pre-patterned photoresist. The process involves dissolving the photoresist with a suitable solvent, such as acetone or a specialized photoresist remover, which removes the metal from the resist regions while leaving it on the substrate in the desired pattern. A key feature of this process is the undercut profile of the photoresist (see Fig. 3.19), which ensures that the deposited metal does not form a continuous layer between the resist and the substrate. This method is widely used for precise metal patterning in semiconductor and microelectronic devices.

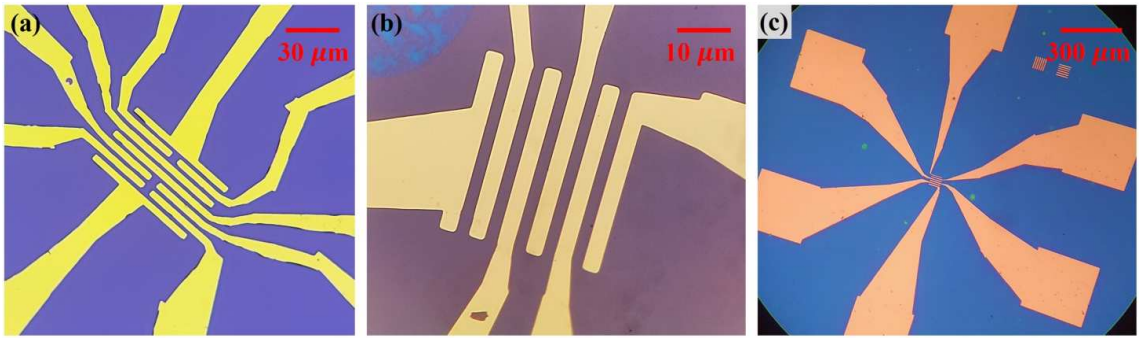

FIGURE 3.23: Optical microscopic images of some of the fabricated patterns after the successful lift-off process.

In our case, after the deposition of metals, the samples were taken out for liftoff. They are submerged in acetone for 3 - 4 hours, during which the acetone dissolves the photoresist, leaving the deposited metal on the substrate behind. acetone is also injected into the sample using a syringe to assist in removing any unwanted metal, such as Au, from the substrate. The sample is then rinsed in IPA and blow-dried with a nitrogen gun to complete the process. Some of the optimized and successful fabricated patterns are shown in Fig. 3.23.

3.1.8 Development of Dry Transfer Setup for Making vdW Heterostructures inside Glovebox

The fabrication of air-sensitive vdW FM samples as well as vdW heterostructures possesses unique challenges, particularly in identifying and attaching atomically thin flakes, typically a few nanometers thick, with lateral dimensions of only a few micrometers. These small flake sizes are a natural outcome of the mechanical cleaving process used to isolate them from bulk crystals [17, 245]. The heterostructures are composed of different layered materials with intriguing electronic, optical, magnetic, thermal, and spintronic properties. The fundamental objective is to arrange these layers, ranging from a single atomic layer to a few layers thick, in a specific sequence. Also, it has been observed in Fig. 3.14 that an oxide layer naturally forms on the surface of exfoliated flakes of vdW magnetic materials. To prevent oxidation, these flakes require protective measures, such as encapsulating them with hBN inside a glove box or coating them with PMMA immediately after transferring them onto patterned electrodes, etc., without direct contact with the chemicals used in the photolithography processes. The 'pick-up and transfer technique', an improved nanoflake transfer method [225], enables precise positioning of selected flakes, facilitating the fabrication of custom-designed devices. Consequently, the development of a dry-transfer setup, controlling it by computer, and refinement of various techniques [169], such as the pick-orient-attach (or pick-and-attach) method [225] have become essential for precise manipulation and attachment of the flakes on top of lithographically prepared patterned electrodes or for vdW heterostructure fabrication inside a glovebox.

3.1.8.1 Development of Dry Transfer Setup

A dedicated heterostructure (dry transfer) setup was designed and developed to facilitate the precise transfer and stacking of these small flakes with high translational and rotational accuracy, ensuring the integrity and functionality of the fabricated heterostructures inside a glovebox. Figure 3.24 (a) depicts the dry transfer setup along with all of its components. High-precision micro-manipulators equipped with piezo controllers and joysticks enable automated control of the XYZ stages via computer, ensuring accurate control over the positioning and orientation of layers during stacking, even from outside the glovebox. The system also integrates a commercially available optical microscope objective (Mitutoyo) with a zoom lens (Navitar) and a microscope camera (Moticam S6). Additionally, it incorporates a customized sample holder on top of an XYZ with a rotation stage (Stage 1) (ThorLabs), an XY stage (Stage 2) (ThorLabs), and a Z-axis movement

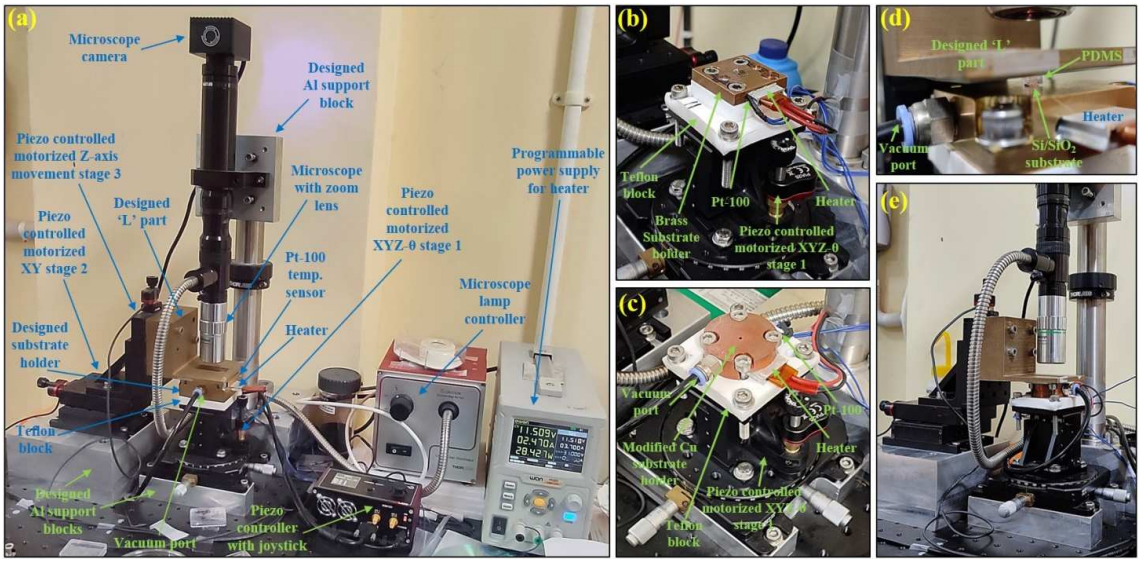

FIGURE 3.24: (a) Image of the microscope-based dry transfer setup designed for use inside a glovebox, constructed with a combination of ThorLabs components and custom-designed parts manufactured in the workshop. (b) Initially designed substrate holder made of Brass. (c) Modified small-sized substrate holder made of Copper with a vacuum port. (d) Image showing the moment during the transfer of flakes using PDMS onto a Si/SiO_2 substrate. (e) The stages of the final optimized dry transfer setup for transferring flakes and heterostructure fabrication, designed for use inside a glovebox.

stage (Stage 3) (ThorLabs) with a custom-designed 'L' part. A programmable power supply is used for controlling the heater under the sample holder, along with a Pt-100 temperature sensor and various custom-built support structures, providing a cost-effective and efficient solution (see Fig. 3.24 (a)). Height adjustments for the stages are achieved using custom-designed aluminum blocks[1]. The entire setup is mounted on an optical honeycomb breadboard (Holmarc Opto-Mechatronics Ltd.), providing a stable and vibration-free base. The selection of optical and mechanical components plays a pivotal role in optimizing the performance and accessibility of the transfer setup inside the glove box.

The schematic of the transfer setup is illustrated in Fig. 3.26 (a). The setup comprises three piezo-controlled micro-manipulation stages designed for precise alignment of flakes. These stages form the core of the transfer module, which includes a rotation-enabled sample holder stage (X1, Y1, Z1, θ) (Stage 1) and a mask holder stage (X2, Y2, Z2). The mask holder stage is detachable and consists of an XY stage (Stage 2) and a Z stage (Stage 3), with the mask mounted using the L-shaped block. Using the joystick of the piezo-controlled XYZ micro-controllers, the system enables precise vertical alignment of

[1]The design of these block structures and the 'L' part (see Fig. 3.25) were carried out with the assistance of Mr. Shubhadip Moulick from SNBNCBS, India

two desired samples, S1 and S2, with a precision of 1 µm. The Z stages play a critical role in transferring flakes for device and heterostructure fabrication.

Stage 1 (X1, Y1, Z1, θ_1) is equipped with a custom-designed Copper sample holder (see Fig. 3.24 (c)) featuring heating arrangements for sample S1. The sample can be heated using a resistive chip heater (resistance = 9.4 Ω at 300 K, 12V, 220° C, Model - SKU: JYA01660-03), which is precisely controlled via a programmable power supply (Owon), while its temperature is monitored using a resistance temperature sensor (Pt-100). A diaphragm pump attached to the vacuum outlet of the sample holder ensures easy vacuum-based mounting of the lower substrate/sample (S1). Initially designed Brass substrate holder (see Fig. 3.24 (b)), due to its larger volume, required extended heating times, posing challenges for optimizing the transfer process. To overcome this, a redesigned Copper substrate holder with a reduced volume and surface area, along with a vacuum port, was introduced (see Fig. 3.24 (c)). This improved design enables rapid heating and cooling of samples, achieving 120° C in just 5 minutes, providing ideal conditions for flake transfer and heterostructure fabrication. Teflon heat isolation is applied to Stage 1 to minimize heat conduction, leveraging Teflon's significant thermal expansion and contraction properties for gradual and precise cooling, which prevents flake tearing or folding during the transfer.

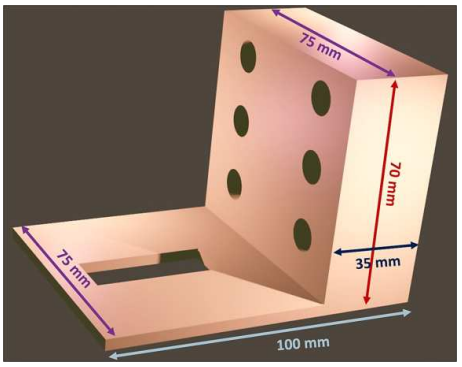

FIGURE 3.25: Custom-designed 'L' part for the transfer setup.

The mask holder, the second major component of the setup, is an L-shaped structure (made of Brass) mounted on the detachable Stage 3 for Z movement (Z2) and Stage 2 for XY movement (X2, Y2). The mask holder features a window and a stepped height to accommodate the mask, with sample S2 attached to the bottom side via a glass slide (see Fig. 3.24 (e)). Custom-designed Aluminium metal blocks serve as the stable base of these stages, as shown in Fig. 3.24 (a).

For visual alignment, the setup includes an optical microscope equipped with a long-working-distance objective lens (20x) and a zoom lens (magnification 70x) with 3 mm fine focus. This allows precise observation of flake placement during the transfer process, viewed by a microscope camera from the top of the stages without disturbing them. The microscope fiber-coupled illuminator (ThorLabs - OSL2) enables adjustments to brightness and contrast, ensuring clear visualization of the live images during the operation.

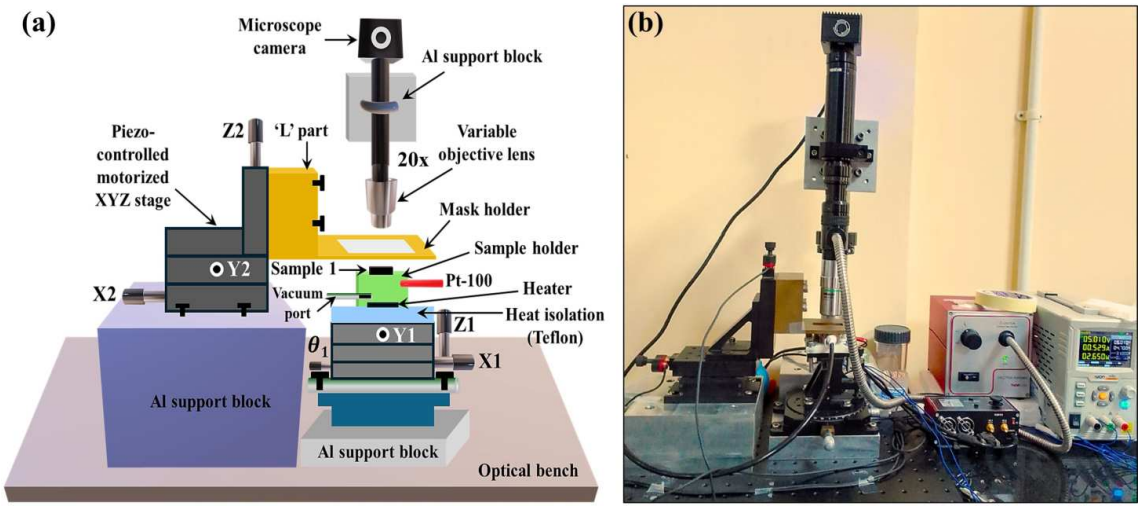

FIGURE 3.26: (a) Schematic diagram of the dry transfer/heterostructure setup. (b) Final optimized dry transfer setup with all of its components for transferring flakes and heterostructures fabrication, designed in our lab, for use inside a glovebox.

The final optimized dry transfer setup with all of its components is shown in Fig. 3.26 (b). The setup is now ready to be incorporated inside the glovebox. However, before proceeding, it is essential to optimize the flake transfer procedures and refine the process of fabricating heterostructures to ensure consistent and reliable outcomes.

3.1.8.2 Preparation of Transparent and Flexible Masks

While layers adhere to substrates through vdW forces, they are fragile and susceptible to mechanical damage, such as tearing or folding, due to stress or thermodynamic instability. Flexible substrates address this challenge by enabling the safe transfer of flakes without damage. The stacking process leverages the strong interlayer vdW forces to ensure stable adhesion. To facilitate this, a customized substrate coated with a sacrificial layer is used, allowing the sequential attachment of mono- or multilayer materials in any desired order.

A flexible mask is a specialized substrate designed with a sacrificial layer to facilitate the stacking of flakes during transfer. It comprises a spherical cap formed on a transparent 0.5 mm-thick cover glass. The spherical design minimizes the contact area during pickup, enabling precise collection of desired flakes while avoiding undesired regions. Transparency of the substrate is essential for real-time monitoring of the process using an optical microscope, ensuring precise control when working with micrometer-sized flakes.

The flexible mask incorporates an adhesive sacrificial layer, whose viscosity can be adjusted via temperature. Residual adhesive can be removed after the final transfer using a solvent. To fabricate the spherical cap (for making the flexible mask), a tiny drop of Polydimethylsiloxane (PDMS) prepared by mixing Sylgard 184 silicone elastomer and curing agent in a 10:1 ratio (Dow Corning), is placed on the center of a clean glass coverslip and then baked on a hot plate at 150 – 200° C for 20 – 30 minutes. The inherent surface tension and viscosity of the drop allow it to form a spherical shape, with its size controlled by the volume of the drop, typically ensuring a diameter of 1 – 2 mm.

To enhance adhesion between the mask and flakes, a sacrificial layer is applied to the PDMS cap. This layer must exhibit stronger adhesion than the vdW forces holding the flakes on the substrate, while being easily dissolvable post-transfer. Polymers like Polymethyl methacrylate (PMMA), Polypropylene carbonate (PPC), or Polycarbonate (PC) can serve as sacrificial layers, but Lakmé Color Crush (LCC) has shown excellent adhesion and dissolves easily in acetone, effectively removing any residual material and leaving the assembled heterostructure clean and intact. To prepare the mask, LCC is spin-coated at 8000 rpm onto the PDMS cap and baked at 90 – 120° C for 2 hours.

For the dry transfer process, the flexible mask is mounted onto a metallic holder and aligned with the optical axis of a microscope for precise positioning. When inverted, the height of the spherical cap serves as a global minimum, ensuring that the mask makes contact with the flakes at a specific and controlled point, which is aided by the optical

transparency of both the PDMS and the cover glass for real-time observation under a high-resolution microscope. Although PPC is explored for minimizing residue, we generally use LCC due to its performance in achieving clean and stable adhesion during transfer.

3.1.8.3 Pick-up and Dry Transfer Process

The dry transfer process for fabricating two-layered hybrid heterostructures involves the precise manipulation of the flexible mask and a flake-containing wafer. As illustrated in Fig. 3.27, the flexible mask is affixed onto a cover glass and then onto the metal support structure ('L' part) and positioned downward on the top stage (Stage 3). Securing the proper attachment of a flake onto the mask involves a precise process of alignment, contact, and subsequent detachment between the lower substrate and the mask.

First, the convex surface of the mask (LCC-coated PDMS stamp) is carefully aligned with the optical axis of the microscope to ensure accuracy. Using X, Y, and Z stage controls of Stage 1, the bottom wafer containing the desired flake is brought closer to the stamp, aligning the target flake at the convex curvature part along the center of this spherical stamp.

Before the contact process, the temperature of the substrate holder on the bottom stage (Stage 1) is increased to 65° C, employing the integrated heating setup mounted on the stage. During the contacting procedure, the relative alignment between the substrate 2 and the stamp is fine-tuned using the XYZ movement of the stages. Stage 1 is then gradually moved upward (in the Z direction) until the flake on the wafer makes contact with the convex part of the LCC-coated stamp. When the stamp contacts the SiO_2 surface, it exhibits a distinct color accompanied by circular interference fringes around the contact region. The elastic nature of PDMS ensures that the LCC conforms to all contact areas, covering even the flake boundaries. In the case of thicker flakes ($\geq$ 100 nm), a dark outline typically forms along the edges at first. Nevertheless, allowing the system to rest for 10 – 15 minutes enables the LCC to conform to the stepped regions, resulting in a uniform color. This conformation is a critical step in the attachment process. It has been observed that attachment failures are more likely if proper conformation is not achieved, particularly for thicker flakes. The strong adhesive force of the LCC, which surpasses the vdW forces binding the flake to the substrate, causes the flake to adhere to the LCC layer.

The detachment of the mask from the lower substrate is a crucial step in the process (see Fig. 3.27), as uncontrolled detachment speed can result in flake tearing and stacking failures. To reduce the risk of distortion in the LCC structure, the temperature of the

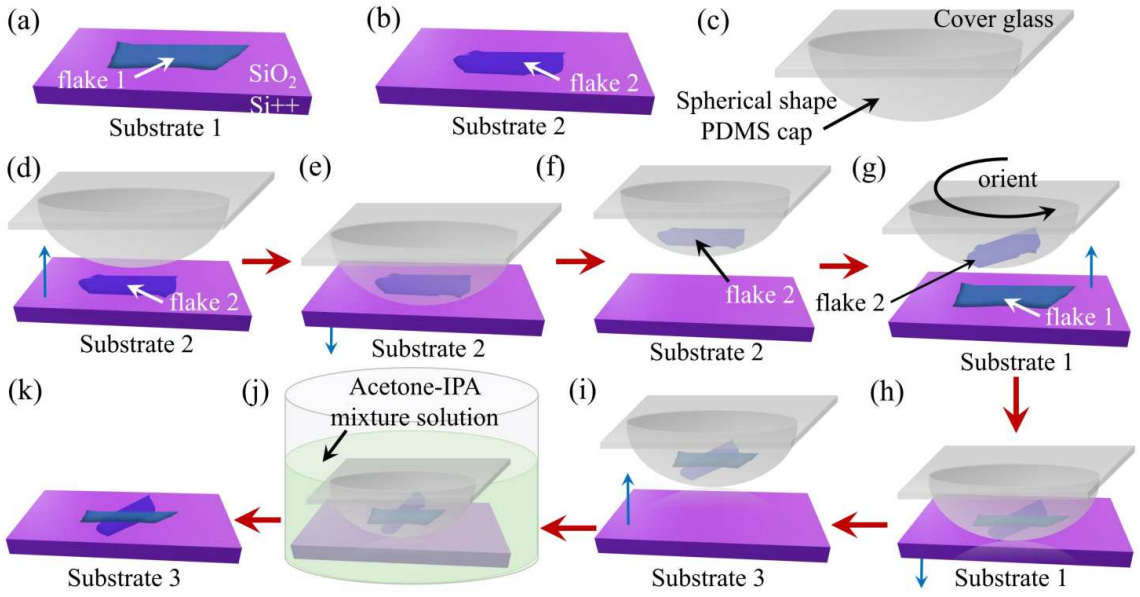

FIGURE 3.27: Schematic diagram of the process flow of pickup and dry-transfer technique to make a heterostructure. (a–b) Two individual flakes prepared for assembly into a bilayer heterostructure. (c) Diagram of the stacking mask used for transferring individual flakes. The setup includes a thin cover glass (thickness $\sim$ 0.2–0.4 mm) supporting a flexible dome made from PDMS. A sacrificial polymer film (e.g., PMMA, LCC) is spin-coated on top of the mask. The adhesion between the sacrificial film and the flake exceeds the vdW interaction holding the flake to the $SiSiO_2$ substrate. (d–k) Sequential flake assembly steps, with bold red arrows representing the progression direction of the stacking process. (g) Steps followed for attaching the second flake, with proper orientation ensured through rotational alignment. (i) After completing the stacking sequence, the mask is aligned with a new, pre-cleaned substrate and brought into contact at a higher temperature (80–120° C), followed by cooling without lifting the mask. (j) Step showing sacrificial layer removal. The entire assembled structure is immersed in a suitable solvent to dissolve the sacrificial film. (k) Final stack schematic. Once the sacrificial layer is eliminated, the mask detaches cleanly, leaving the stacked layers intact on the target substrate.

substrate is carefully lowered to 60° C before initiating the detachment. This process is carried out with the precisely controlled Z-axis movement of Stage 3. The strong adhesive force of the LCC ensures that the flake remains securely attached to the stamp (picked up) after separation. Additionally, as the interference with the SiO_2 ceases during the detachment process, optical contrast and the flake's color disappear. Similarly, this process is repeated for picking up multiple desired flakes one after another, by the same stamp.

Once all the required flakes are collected (similar to the previous steps) in the desired sequence for preparing a heterostructure (detailed step-by-step processes are presented schematically in Fig. 3.27), the stack is brought into contact with a pre-patterned/cleaned Si/SiO_2 wafer for final transfer. This step is carried out at an elevated temperature to improve adhesion. During this contact process, the pre-patterned/cleaned substrate's

temperature is initially kept steady at 85° C and then gradually increased to 125° C. The entire heating and contact process lasts approximately 15-20 minutes. Once the heating is completed, the vacuum suction is released, and the substrate is allowed to cool to room temperature while remaining attached to the stamp. For residue removal and cleaning, the stamp and substrate are immersed in a 1:3 acetone-IPA mixture very carefully and kept for 3 hours. This low acetone concentration dissolves the sacrificial LCC layer, allowing the successful release of the hybrid structure onto the pre-patterned/cleaned substrate (see Fig. 3.27). To ensure further cleanliness, the pre-patterned/cleaned substrate along with the assembled stack is subsequently rinsed in pure acetone, followed by IPA, and dried using N_2 gas.

3.1.8.4 Dry Transfer Using PDMS

The commercially available PDMS films (Gel-Film® PF-40-X4 sold by Gel-Pak) with a thickness of 1 mm are suitable for a quick transfer process of exfoliated flakes onto pre-patterned gold electrodes on a Si/SiO_2 substrate [169].

This PDMS (Polydimethylsiloxane) acts as a clean and transparent substrate, which is placed on top of a glass slide after removing the protective polymeric layers. VdW materials are transferred to the PDMS substrate by gently pressing the exfoliated flakes onto its surface using the standard scotch tape method. Due to the inherent adhesive properties of PDMS, the flakes are easily transferred onto it. The next step involves locating isolated flakes on PDMS using a high-resolution optical microscope. Once the desired flake is identified, the PDMS substrate, along with the glass slide, is affixed upside down to the 'L' shaped holder on Stage 3, following the procedure as used in the previous pickup method (Section 3.1.8.3). A pre-patterned Si/SiO_2 substrate is placed onto the substrate holder on Stage 1.

Subsequently, the PDMS substrate containing the flake is aligned with the pre-patterned Si/SiO_2 substrate using XYZ and rotational stages. In this upside-down configuration, the flakes on the transparent PDMS can be clearly seen under the microscope by adjusting its focus. Careful alignment is crucial: the XYZ stages (1, 2, and 3) must be fine-tuned such that the flake and the corresponding gold pads align properly along the same vertical axis. The goal is to ensure that, by merely changing the focus of the microscope, both the flake and the gold pads can be observed simultaneously, confirming proper alignment. Once the alignment is confirmed, Stage 3 is gradually lowered, bringing the PDMS containing flake into contact with the patterned gold pads region on the Si/SiO_2 substrate. After the

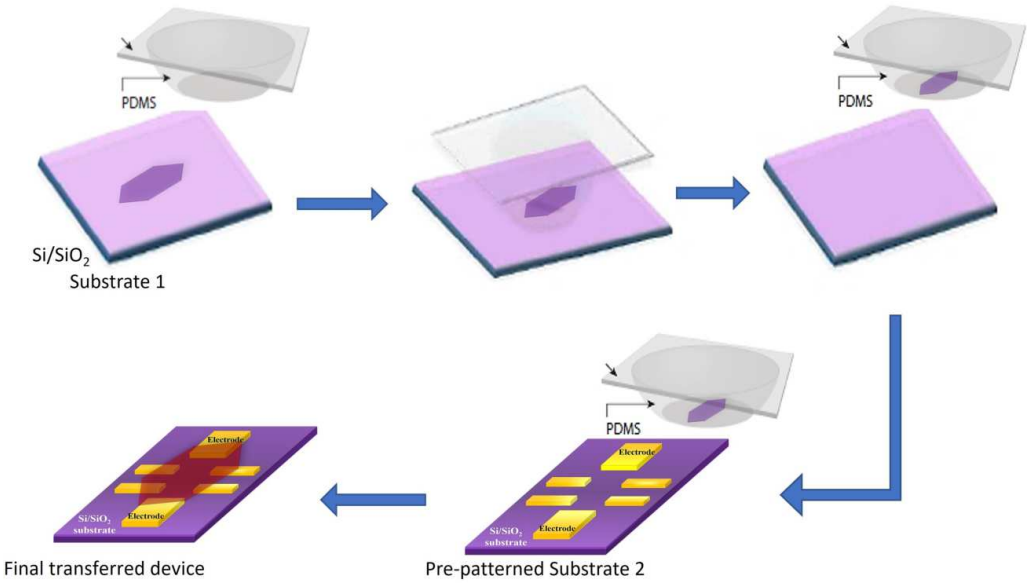

FIGURE 3.28: Schematic diagram of the dry transfer process using PDMS.

proper touchdown, the temperature of the substrate is raised to 110° C and maintained for 10 minutes. This heating reduces the adhesion of the PDMS relative to the Si/SiO_2 substrate and gold pads, facilitating the detachment of the flake from PDMS.

After 10 minutes, the detachment process is initiated at that temperature. The Z-axis movement of Stage 3 is controlled precisely and incrementally reversed to separate the PDMS substrate from the flake. As the PDMS is withdrawn, the flake will detach from the PDMS surface and remain transferred onto the pre-patterned gold electrodes on the Si/SiO_2 substrate (see Fig. 3.28).

In this thesis, we employed this PDMS-assisted exfoliation and dry transfer technique for the rapid transfer of freshly exfoliated, air-sensitive 2D FM flakes onto the pre-patterned gold electrodes. This was immediately followed by the application of PMMA drops as a protective coating to prevent environmental oxidation of the flakes, as discussed in the following section 3.1.9.

3.1.9 Protecting Transferred Flakes Using PMMA Drops

PMMA is a positive e-beam resist, specifically 950 PMMA C4, where 950 denotes the molecular weight of the resist, PMMA refers to polymethyl methacrylate, and C4 indicates a 4 % solution of the resist in Chlorobenzene. Renowned for its ability to achieve sub-10 nm

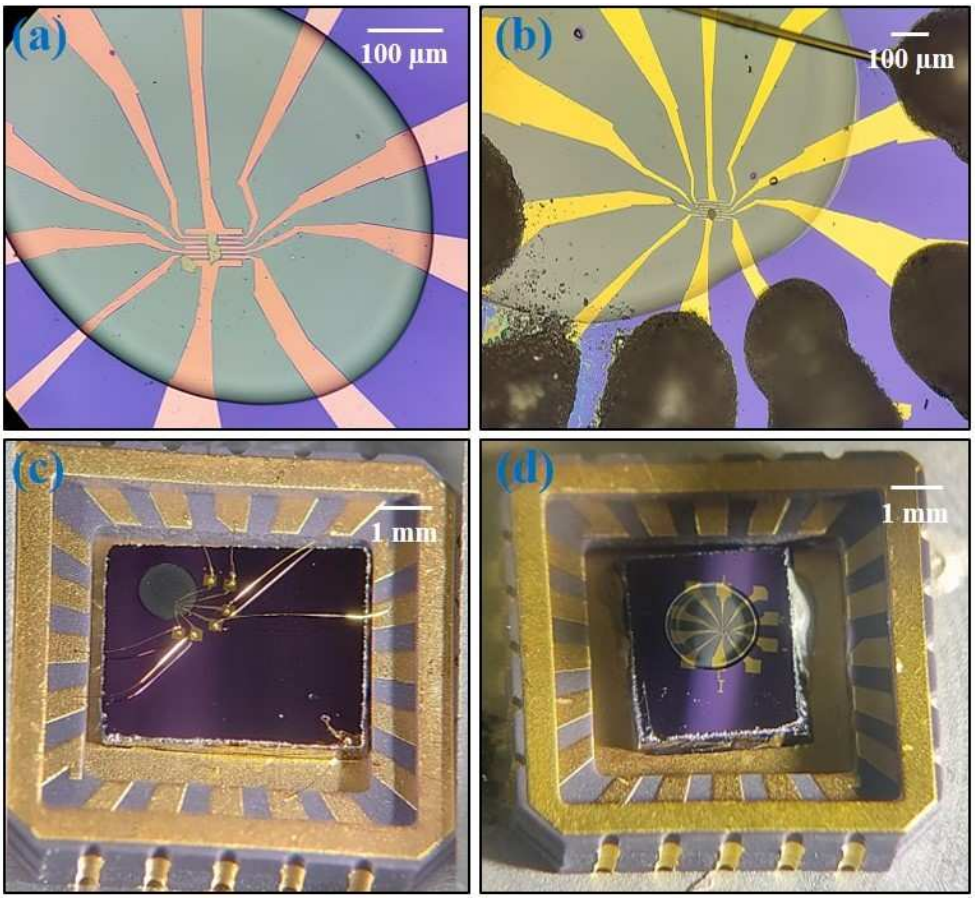

FIGURE 3.29: (a), (b) PMMA-coated flakes transferred on top of pre-patterned gold electrodes. (c), (d) PMMA-coated devices bonded and mounted in 20-pin LCC chip carriers.

resolution, PMMA is widely used for nanoscale patterning in electron beam lithography due to its versatility and precision.

In this study, however, we employed PMMA not for lithography but as a protective layer for air-sensitive 2D FM thin flakes. As a lightweight, transparent resist, PMMA acts as a non-reactive barrier that safeguards the flakes from environmental oxidation, ensuring they remain stable and uncontaminated. Its excellent thermal stability, enabling it to maintain structural integrity at moderate temperatures, further makes it suitable for sensitive experiments involving wide ranges of temperature variations.

Here, PMMA was applied in the form of small drops using a narrow syringe, immediately after transferring the flakes onto pre-patterned gold electrodes. Then the wafer was heated at 70 - 80° C on a hot plate for 5 minutes. Some images of PMMA-coated transferred devices are shown in Fig. 3.29. This approach effectively shields the flakes from

environmental oxidation, preserving their structural and electronic integrity for subsequent analysis and experimentation.

3.1.10 Bonding of the Devices

The final stage of the fabrication process involves device packaging. After transferring the flakes and applying the PMMA coating, the sample wafer is mounted onto either a ceramic chip carrier or inside the groove (5 mm x 5 mm) of a leadless 20-pin LCC chip carrier (Kyocera, Japan). The 20-pin LCC chip carrier contains 20 gold-plated pads, which provide contact points for connecting the device's contact pads by wire bonding. The gold-coated base of the chip carrier can also serve as a global back-gate for the device. Electrical connections between the sample's contact pads and the chip carrier's pads are made using gold wire (of diameter 25 µm) bonding. Two types of gold wire bonding techniques were used: (i) Ball bonding with a wire bonder and (ii) Direct bonding with conducting silver paint or epoxy. The bonding process details are described below:

3.1.10.1 Ball bonding by Wire Bonder

- **Wire Bonder**

Wire bonding [246–249] is an electrical interconnection technique that uses thin micro-scale wires, typically made of gold (Au), aluminum (Al), or occasionally copper (Cu) [250]. This process combines heat, pressure, and ultrasonic energy to create solid-phase welding between the metallic wire and the bonding pad surface. When these metallic surfaces come into close contact, bonding occurs due to electron sharing or an atomic interdiffusion process. The bonding force deforms the material, breaking any contamination layer and smoothing surface irregularities, while ultrasonic energy enhances this effect. Heat further accelerates interatomic diffusion, strengthening their bond.

The process begins by attaching the wafer's backside to a chip carrier using adhesives (e.g., GE-varnish, Apiezon N grease, or Silver paste/epoxy). A bonding tool, such as a capillary or wedge, then welds the wires. Based on the parameters used (mainly heat and ultrasonic energy), wire bonding can be classified into three main types: Thermosonic Bonding, Thermo-compression Bonding, and Ultrasonic Bonding, each with subcategories tailored for specific applications, wire types, and materials. Two types of bonding techniques are briefly discussed below.

(a) Wedge Bonding:

In wedge bonding [251], the wire (Au or Al) is clamped and brought into contact with the bonding pad. Ultrasonic energy is applied while holding the wire under controlled force,

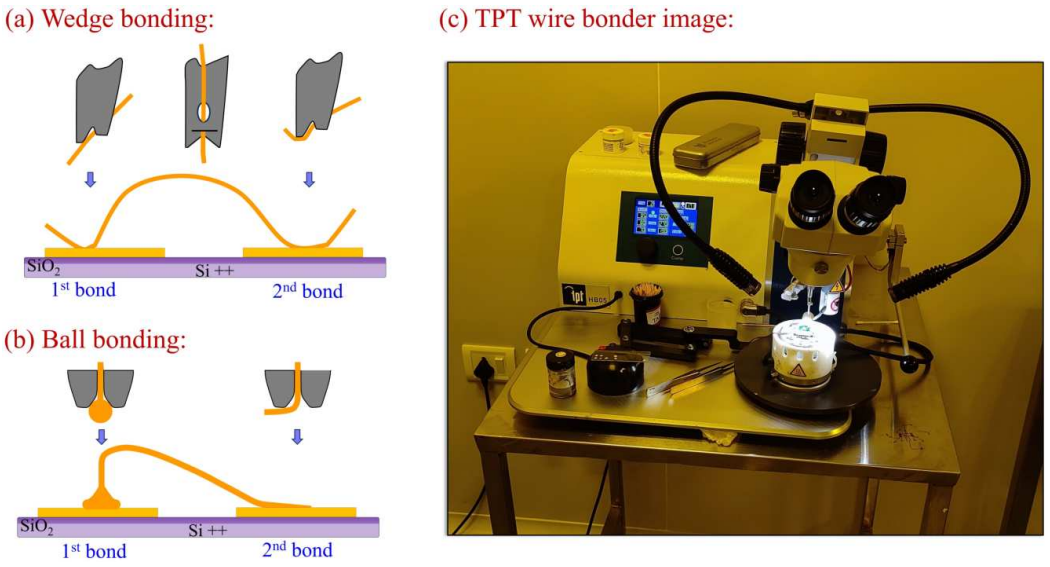

FIGURE 3.30: (a) Wedge bonding process. (b) Ball bonding process. (c) Image of the TPT wire bonder inside the cleanroom of SNBNCBS.

forming the first bond. The wire is then extended to a second location, where the process is repeated to create the second bond. The wire is finally broken off by clamping and wire movement, completing the bond (see Fig. 3.30 (a)).

(b) Ball Bonding:

Thermosonic ball bonding [252, 253] is a widely preferred technique for creating reliable electrical connections between the gold pads of the wafer and the contact pads of a chip carrier. This method is favored due to its speed and efficiency compared to ultrasonic wedge bonding. It allows the gold (Au) wire to move flexibly without stress along the x- or y-axis.

The process begins with threading a gold (Au) wire through a ceramic capillary tip. A high-voltage spark, generated through an electronic flame-off (EFO), melts the end of the wire, forming a spherical gold ball due to surface tension. This ball, typically 1.5 to 2.5 times the diameter of the wire, is held by the capillary and brought into contact with the sample's gold pads. To create a secure bond, suitable amounts of heat, pressure, and ultrasonic forces are applied to the gold ball for a specific duration. This process forms a strong metallurgical weld between the ball and the bond pad while also shaping the ball into its final form. The wire is then guided to the desired position of the contact pads of the chip carrier, creating an arc or loop of gold wire. Consequently, at the second bonding point, ultrasonic energy and pressure are applied to secure the wire without forming another ball. Finally, the wire bonding machine clamps the wire and lifts the capillary, breaking

the wire to prepare for the next bonding cycle (see Fig. 3.30 (b)). This technique ensures precise and reliable connections essential for microelectronic applications.

In this thesis, a TPT HB05 wire bonder was employed for ball bonding by using Au wires of diameter 25 µm, as shown in Fig. 3.30 (c). This system includes a stereo microscope with adjustable focus and magnification, as well as an optical illuminator for precise visibility. The system includes a heating stage capable of reaching temperatures up to 250° C, allowing for rapid thermal stabilization and precise temperature control. Some images in Fig. 3.31 showcase PMMA-coated devices mounted in 20-pin LCC chip carriers, with electrical connections established through the ball bonding technique using gold wires.

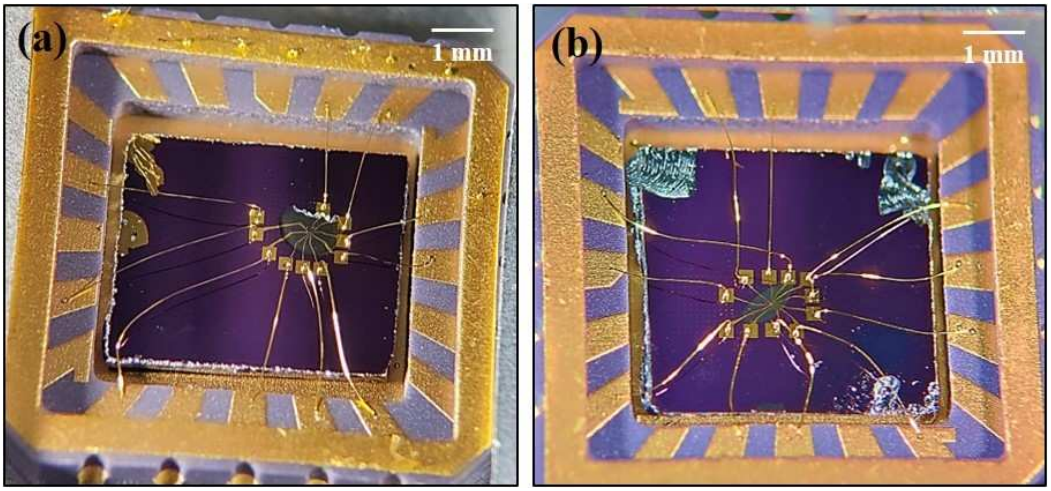

FIGURE 3.31: (a), (b) PMMA-coated devices, mounted in 20-pin LCC chip carriers, are bonded by the ball bonding technique using gold wires.

3.1.10.2 Bonding by Silver Epoxy/Paint

As an alternative method, the device and chip carrier contact pads were directly bonded using Au wires and conducting silver epoxy/paints.

For silver epoxy bonding, a small amount of conducting silver epoxy (RS components, UK) blob was applied to the gold pads, connecting them with gold wires. The device was then cured by heating at 120° C to ensure a secure bond (see Fig. 3.32 (a)).

Similarly, for silver paint bonding, a small amount of conducting silver paint (SPI supplies, USA, having sheet resistance $\sim$ 0.02 Ω/sq/mil) drop was applied to the gold pads and connected with the gold wires, as shown in Fig. 3.32 (b). The device was then cured in the air for at least 12-14 hours at room temperature.

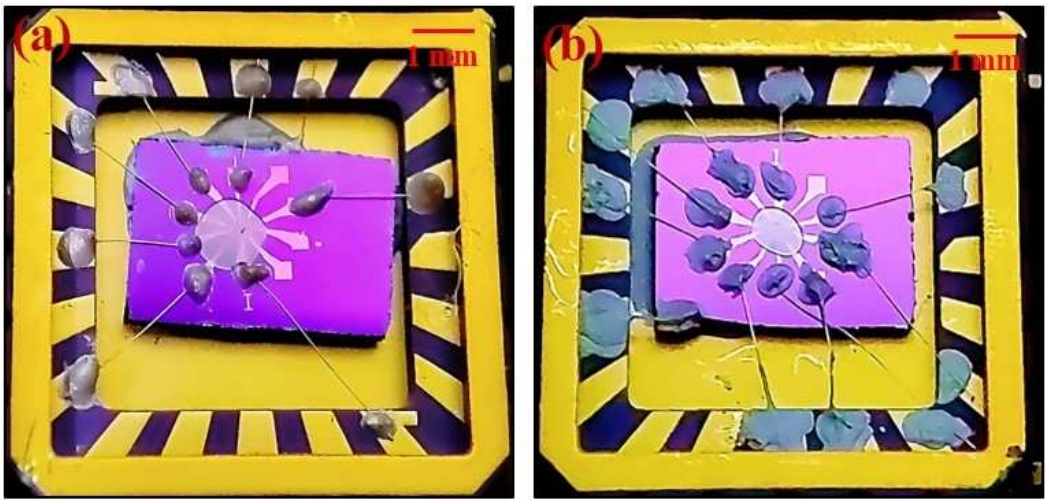

FIGURE 3.32: PMMA-coated devices, mounted in 20-pin LCC chip carriers, are bonded by (a) silver epoxy and (b) silver paint, using gold wires.

• When handling and connecting a few-layer fabricated and bonded device to the cryostat, we always used an antistatic wristband. This device helps safely ground the user, preventing the buildup of static electricity on the body, which can cause electrostatic discharge (ESD) [254–256]. Such discharges are strong enough to damage such delicate devices [257].

3.1.11 Vacuum Annealing

Vacuum annealing [258–261] is a crucial step following device fabrication and transfer of flakes, used to improve the robust interface between the layers, enhancing the mechanical, thermal, and electrical transport properties as well as the overall performance of the devices. This technique involves heating the devices in a vacuum or inert environment to eliminate residual solvents, lithographic residues, impurities, trapped moisture, and gas molecules that may remain after the device fabrication and transfer process, causing additional negative impact on their properties.

During vacuum annealing, the devices are placed in a high vacuum chamber (with pressure $\leq 10^{-6}$ mbar) to prevent oxidation or contamination during the heating process. The temperature (typically ranging from 100° C to 250° C) and duration (typically 3 - 4 hours) are optimized based on the materials used in the device. Annealing the sample in a vacuum facilitates the coalescence of smaller bubbles into larger ones, reducing the overall surface energy. This mechanism traps contaminants within discrete bubbles, balancing

the elastic energy required to create the bubbles with the vdW surface energy that drives the formation of a clean interface.

An alternative method involves annealing the sample in an Ar+H_2 atmosphere [262–265] at 200 - 400° C. It also promotes the merging of smaller bubbles into larger ones, reducing surface energy and resulting in a smoother, cleaner interface in the heterostructures and lithographic devices. The procedure involves placing the sample inside a quartz tube in a furnace at room temperature. Moisture is removed from the tube using a vacuum gradient by introducing a 5% H_2+Ar gas mixture at a flow rate of 200 sccm. The sample is then heated there at $\sim$ 300° C and annealed for 3–4 hours.

In our cases, most of the devices were annealed in a cryostat under ultra-high vacuum conditions ($\sim 10^{-6}$ mbar) at $\sim$ 100 - 130° C for $\sim$ 1 hour prior to the measurements. Some of the devices are also tried to annealed at 200° C with Ar+H_2 gas within a separate chamber for 2 hours to improve contacts.

3.1.12 Current Annealing

Traditional methods [266], such as annealing at elevated temperatures in an ultrahigh vacuum (UHV) or an inert gas environment (e.g., Ar/H_2) are often used to eliminate interfacial contamination in fabricated or heterostructure devices (as discussed in Section 3.1.11). However, implementing such processes within a low-temperature measurement cryostat presents significant challenges. Also, transferring samples from a dedicated annealing chamber to a cryostat often reintroduces contamination due to air exposure, making the methods less practical. To address these limitations, current annealing [267] offers a practical, reproducible, and effective technique for in-situ cleaning by removing surface contamination and improving the performance of electrical contacts in devices.

Current annealing [267–275] involves applying a high-bias current directly through the device's contacts under UHV conditions and at low temperatures. This electrical current generates localized heat via Joule heating, where power dissipation (proportional to the product of the current squared and the material's resistance, I^2R) causes a temperature rise in the small conductive regions of the device. This localized heating initiates various micro-structural and thermodynamic processes at the atomic scale, which improve contact quality and effectively remove contamination from the interfaces. At the atomic level, this localized heat induces thermal diffusion, facilitating the reorganization of surface and subsurface atoms, which reduces defects from dislocations and grain boundaries. The high current density (because several milliamperes of current are passed through micron-scale

devices) minimizes unwanted electromigration effects (where metal atoms are displaced by the momentum of conduction electrons) by relieving stress within the material, promoting atomic stability. The intense current density also generates sufficient energy to desorb contaminants and residual fabrication byproducts from the interface. When performed under UHV conditions, this process avoids the counterproductive re-adsorption of ambient molecules such as oxygen, which could otherwise degrade the device's performance. The combination of these effects results in improved electrical conductivity and enhanced stability of the contacts.

This method offers several advantages over traditional annealing approaches [267–272]. By performing the process entirely within the cryostat, current annealing eliminates the risk of introducing additional contaminants during cleaning. It also significantly reduces the chances of air exposure and re-contamination that often occur during sample transfers between the chambers. Furthermore, the technique demonstrates high reproducibility, consistently yielding clean and operational devices. The key benefit of this process is that the heating is highly localized, confining thermal effects to specific regions of the device while maintaining the overall device at low temperatures, thus protecting sensitive components from damage.

Despite its advantages, the application of current annealing requires careful control of the current to prevent overheating or damage caused by the large current densities involved. Excessive current or uneven current distribution can lead to structural degradation, deformation, increased defects, higher contact resistance, and even device failure [273–275]. Nonetheless, when implemented correctly, current annealing is a reliable, efficient, and practical method for getting good electrical contacts in mesoscopic and nanoscale devices. Its compatibility with low-temperature operations and ability to achieve contamination-free interfaces make it particularly valuable for sensitive experimental applications.

In this thesis, the current annealing process was carefully executed in a stepwise manner to ensure optimal device performance and prevent damage[2]. The current was incrementally increased only after securely mounting the device inside a cryostat operating under high vacuum conditions ($\sim 10^{-6}$ mbar) and at temperatures below 5 K. Throughout the process, the current was strictly limited to a maximum of 100 mA. Additionally, each annealing cycle involved a full sweep (positive and negative bias) with precise step sizes to maintain control and reproducibility.

[2]This was performed with the help of Mr. Rafiqul Alam from SNBNCBS, India

3.2 Development and Optimization of Experimental Setups

Before proceeding with measurements on the fabricated devices, we focused on the development and optimization of several experimental setups. This included restarting the liquid helium plant, customizing a low-temperature (6 K) setup to integrate with a magnet and power supply, designing a dipstick, optimizing the Physical Property Measurement System (PPMS by Quantum Design) and the Oxford Teslatron mK system for low-temperature transport measurements, and as well as the glovebox system. The following sections provide a concise overview of the optimization and development efforts for these setups. We also discuss the challenges faced during these processes and outline the solutions implemented to overcome them.

3.2.1 Restart of Liquid Helium Plant

A helium plant is a helium liquefaction facility that produces liquid helium (LHe) by compressing and cooling high-purity helium gas (99.999 %). LHe, with a boiling temperature of 4.2 K, is essential for performing low-temperature transport measurements in solid-state physics. Additionally, most metals exhibit superconductivity at such low temperatures, making LHe a crucial resource for studying these phenomena. Modern research increasingly focuses on observing the behavior of materials at extremely low temperatures, further emphasizing the importance of helium plants.

At our institute, the LHe plant (CRYOMECH, USA) had been non-operational for approximately 4 to 5 years, and it required significant efforts to restore it to its operational condition. We worked extensively to revive the plant, successfully overcoming numerous challenges during the process. Due to the absence of a recovery system, the produced LHe was directly transferred into an empty Dewar for measurement purposes. However, this method resulted in the loss of nearly 50% of the LHe during the transfer. Once a recovery system is installed, the full amount of LHe produced will be utilized efficiently, enabling low-temperature transport measurements by immersing a dipstick in the helium within a vibration-free and clean environment.

3.2.1.1 Liquid Helium Plant

The LHe plant [276] comprises two primary components: (i) a special helium Dewar equipped with a cold head, (ii) a compressor. The front view of the LHe plant is illustrated

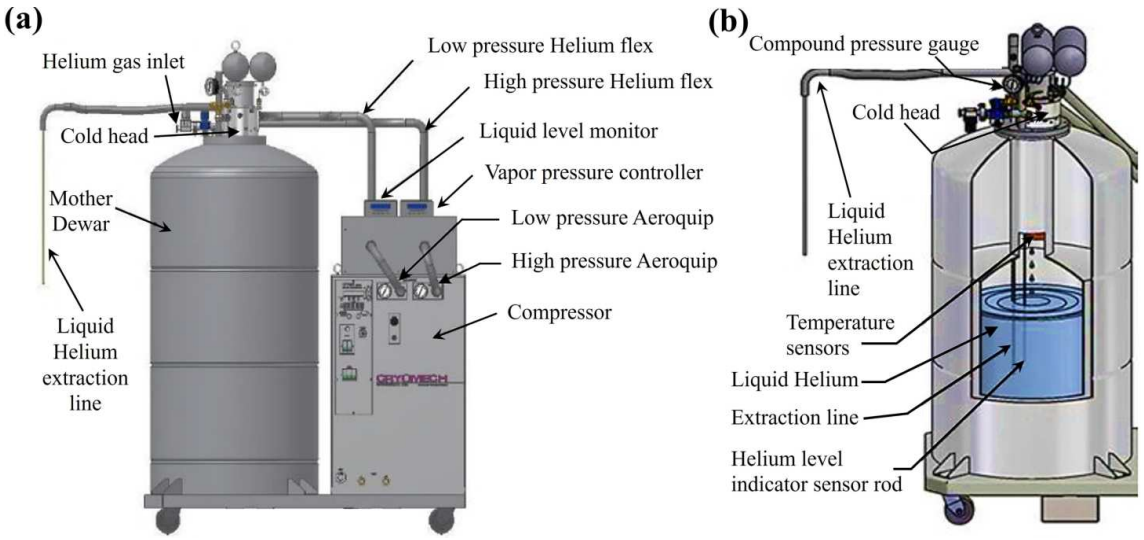

FIGURE 3.33: (a) Schematic diagram of the front side of the LHe plant. (b) Schematic diagram of the helium Dewar. Pic. collected from Ref. [276]

in Fig. 3.33(a).

(i) Helium Dewar with Cold-head:

This special LHe Dewar (mother Dewar) [276] is a stainless steel, vacuum-insulated container specifically designed to store LHe with minimal evaporation losses. It is hermetically sealed to prevent atmospheric air from entering, ensuring that only helium gas, supplied by the gas system, can flow into it. Positioned at the Dewar's top, the cold head serves as an expansion device that reaches extremely low temperatures. It is bolted securely to the Dewar's flange with an O-ring positioned between them to create an airtight seal for the helium gas inside. A lifting eye is provided for safely lifting the cold head and the Dewar flange assembly. The pressure inside the helium gas system is tracked using a compound gauge with a range spanning 30" Hg to 15 PSIG. The inlet regulator for helium is set at the factory to sustain an internal pressure of roughly 1 PSIG (0.07 bar) within the Dewar. A liquid level monitor receptacle, connected to a probe inside the Dewar, tracks the LHe level.

Pressure safety mechanisms include a primary relief valve that activates above 10 PSIG and a secondary relief valve set at 15 PSIG, which serves as a backup in case the primary valve fails. LHe is extracted via a vacuum-insulated extraction line and valve, which minimize boil-off losses during the transfer of LHe. The liquid level detector, calibrated beforehand, measures the quantity of LHe produced in the Dewar.

Temperature monitoring is facilitated by a silicon diode sensor mounted on the helium condenser of the cold head inside the Dewar, which is connected to a temperature sensor diode receptacle and linked to the helium compressor package via a diode cable. Additionally, a Cernox sensor is employed to verify temperature readings for accuracy. The internal structure of the Dewar is illustrated in Fig. 3.33(b).

(ii) Compressor:

The helium compressor (CP1000 Series, manufactured by CRYOMECH, USA) [276] functions by taking helium gas from the cold head that has low pressure, compressing it, and delivering purified, high-pressure helium back to the cold head. In this system, a low-pressure helium line is connected via an Aeroquip fitting (low-pressure), enabling helium gas to move from the cold head toward the compressor unit. Likewise, the compressor unit sends compressed high-pressure helium gas to the cold head via the helium line connected by an Aeroquip fitting designed for high pressure.

To monitor system performance, pressure gauges are installed on both the low-pressure and high-pressure lines, providing real-time pressure readings for each line. Additionally, the compressor package includes a cooling system with water inlet and outlet connections to regulate its temperature during operation.

3.2.1.2 LHe Plant Startup Procedure

To begin, we have to ensure that the helium gas cylinder is securely attached to the designated gas line and verify the pressure in the Dewar, which should read approximately 3 PSI. Once this is confirmed, the helium plant can be started by following these steps [276]:

(i) Activation of the Chiller Unit and Main Compressor Power: The chiller unit should first be turned on to ensure proper cooling. Following this, the compressor power must be turned on using the MAIN circuit breaker.

(ii) Powering On the Compressor Controls: The POWER circuit breaker should be switched on to supply power to the compressor controls. Once activated, the green ON indicator located above the circuit breaker, along with the yellow OFF light for the compressor, will both light up. A sequence of beeps will sound, and the front display panel will briefly present the model number, current date, and time of the compressor. Within several seconds, the screen will automatically update to indicate “COMPRESSOR OFF”

FIGURE 3.34: Compressor display panel [276] after powering on

on the upper row and "RMT START INTERLOCK" on the lower row, as depicted in Fig. 3.34.

FIGURE 3.35: Liquid level monitor display panel [276] after power is turned on.

(iii) Liquid Level Monitor Avtivation: The power switch of the LHe level monitor should be turned on. Once powered on, the upper row of the screen will display "Liquid helium Level," while the lower row will remain blank, as shown in Fig. 3.35.

(iv) System Initiation: The system is initiated by pressing the ENTER button on the monitor. An asterisk briefly appears on the bottom line, which is then replaced by a negative value in cm and the code "FA", signaling the start of the system. This is depicted in Fig. 3.36.

FIGURE 3.36: Typical view of the liquid level monitor's display panel [276].

(v) Compressor Activation Confirmation: The activation of the compressor is confirmed when the ON indicator (in green color) above the ON button of the compressor lights up. The upper line of the display will show "COMPRESSOR ON", while the lower line presents the temperature reading from the silicon diode connected to the helium condenser on the cold head. It should be noted that Diode 2 is not used in this setup.

Additionally, the Cernox temperature sensor provides temperature readings for the cold head, as illustrated in Fig. 3.37.

FIGURE 3.37: Display panel of the compressor package [276] at startup.

(vi) Cold Head Condenser and Pressure Monitoring: During the first 4 to 6 hours of operation, the temperature value of the condenser on the cold head will gradually decrease. As the temperature approaches approximately 100 K, the rate of cooling will slow down. The typical pressure difference between the high and low helium gas line gauges will range from 220 to 250 PSI, with a fluctuation of 5 to 10 PSI on the pressure gauge readings.

(vii) Formation of LHe and Cooling of Dewar: When the condenser of the cold head attains helium's liquefaction temperature point ($\sim$ 4.2 K), LHe will condense and accumulate at the Dewar's bottom. When the LHe comes into contact with the Dewar, it will evaporate, causing the Dewar to gradually cool down to LHe temperature. Cooling the Dewar down to 4.2 K typically requires around 20 hours. Once this temperature is reached in the Dewar, LHe will begin to accumulate at its bottom. Figure 3.38 illustrates the display panel showing the accumulation status of LHe inside the Dewar.

FIGURE 3.38: Display panel of the compressor package after starting LHe production.

(vii) Temperature and Pressure Correlation: When the Dewar pressure is maintained at 1 PSIG, the temperature sensor shows roughly 4.17 K. If the pressure inside the Dewar increases to the upper threshold of 10 PSIG, the corresponding temperature will be around 4.76 K. During steady LHe production, if the Dewar pressure stays constant, the condenser temperature varies by less than ± 0.1 K.

3.2.1.3 Typical Parameters

The optimized parameters for the LHe plant, when it was functioning normally, are summarized in the following Table 3.1.

Temp. of Cold -head (K)	Dewar pressure (PSI)	Low pressure gauge (PSI)	High pressure gauge (PSI)	Water -line temp. (^{0}C)	He-gas line pressure (PSI)	Rate of produced liq. He (Litre/day)	The amount of liq. per He gas cylinder (Litre)
4.23	01	85	290	29	05	12	08

TABLE 3.1: Typical parameters obtained when the LHe plant worked normally at SNBNCBS.

3.2.1.4 Routine Daily Monitoring

The LHe plant is built for stable, consistent, reliable, and uninterrupted operations; however, daily inspections are essential to detect potential issues and prevent system failures [276]. The following steps were and should be performed regularly:

(i) **Dewar Pressure Monitoring:** The Dewar pressure should be checked and recorded regularly. Under typical conditions, when the system is running and the Dewar has reached LHe temperature, the pressure reading should be close to 1 PSIG. While the system is not operational, the system's pressure gauge should display a maximum pressure of 10 – 12 PSIG. If the Dewar pressure exceeds 15 PSIG, the helium regulator shutoff valve must be closed, and the pressure should be released via the vent valve.

(ii) **Low and High Pressure Tracking:** The low and high-pressure readings must be monitored periodically, with observations recorded regarding any changes in their relative values over time.

(iii) **Temperature Change Recording:** Temperature fluctuations, which serve as critical diagnostic indicators, should be tracked using the sensor mounted to the helium condenser of the cold head regularly. The temperature readings must be recorded at appropriate intervals based on system usage.

(iv) **Cooling Water Parameter Monitoring:** The temperatures at the inlet and outlet of the cooling water system, along with the cooling water flow rate, should be consistently documented to ensure proper system function.

(v) **Discrepancy Management:** In case of any abnormal readings, the compressor system must be shut down by pressing the "Compressor OFF" (black color) found on the compressor package's front panel. Furthermore, the front-panel circuit breakers should be turned off to power down the entire system.

3.2.1.5 Transfer of Liquid Helium

- **Safety Measures and Procedures for Handling LHe:**

Handling and transferring liquid helium [276] can be dangerous if the proper safety protocols are not observed. These risks include exposure to extremely low temperatures, the potential for over-pressurization in containers lacking proper venting, because minor amounts of liquid expand into extensive gas volumes, creating a hazard of oxygen being displaced and causing asphyxiation in enclosed areas. LHe appears colorless and without any scent/smell, existing as an ultra-cold liquid (with a temperature of - 452° F or - 269° C), and able to cause immediate cryogenic skin burns and rapid freezing of underlying tissue almost instantly upon contact. Therefore, appropriate safety measures [276] should always be implemented when transferring LHe, as outlined below.

(i) **Personal Protective Equipment (PPE):** When handling LHe, it is essential to wear appropriate PPE. This consists of a full face shield worn on top of safety glasses, loose leather or insulated gloves, shirts with long sleeves, boots, and trousers without cuffs. Trousers should not be tucked into boots. Gloves should fit loosely to allow for quick removal in case LHe spills onto them. Note that insulated gloves are not designed for direct immersion into LHe; they provide only short-term protection from accidental contact.

(ii) **Handling and Ventilation:** LHe rapidly vaporizes, expands into much larger gas volumes. At room temperature (300 K, 68° F or 20° C), one liter of LHe converts

to approximately 754 liters of helium gas. To prevent over-pressurization, ensure that any vessel being filled with LHe is properly vented. Closed containers must be equipped with multiple pressure relief devices to mitigate the risk of rupture due to excessive internal pressure.

(iii) **Oxygen Displacement Hazards:** As LHe transitions to gas and it lacks color, odor, taste, and irritation, it can quietly replace oxygen in the enclosed atmosphere, potentially lowering oxygen levels below the threshold required for safe breathing. Exposure to high concentrations of helium can lead to dizziness, vomiting, nausea, unconsciousness, and in extreme cases, death. Oxygen depletion can occur rapidly, with unconsciousness and fatality in seconds at low oxygen levels. Therefore, LHe must only be stored and handled in well-ventilated spaces. The use of oxygen monitors is strongly advised in enclosed environments to ensure safe oxygen levels.

- **Extraction and Transfer Process of Liquid Helium:**

At any time, LHe can be safely drawn from the Dewar by applying its internal pressure to force the liquid to come outward [276]. A flexible, stainless steel extraction line is employed for this purpose. Both the transfer line and associated valves have vacuum jackets, significantly reducing the losses due to boil-off during the transfer process and safeguarding operators from contact with extremely cold surfaces. The detailed steps for transferring LHe from the primary (mother) Dewar to the recovery Dewar are outlined below:

(i) **Inserting the Extraction Line:**

To initiate the transfer, the extraction line needs to be correctly placed into the mother Dewar's designated extraction port.

1. The system should first be turned off by pressing the Compressor Off button on the front panel of the compressor unit. The shutoff valve on the helium regulator must then be closed to stop helium flow into the Dewar.

2. The 0.5 PSI atmospheric relief valve should be opened to release the internal pressure of the Dewar, and the isolation valve connected to the vapor pressure controller should be closed.

3. The vent valve should be closed after the compound pressure gauge indicates zero PSIG.

4. The extraction port plug should be removed by loosening the port sleeve anticlockwise while pulling the port plug upward.

5. The extraction line's transfer tube must be inserted carefully into the extraction port on the Dewar, and the port sleeve should be tightened clockwise.

6. Now, the 0.5 PSI atmospheric relief valve should be closed, and the helium regulator shutoff valve slowly reopened to pressurize the Dewar. The isolation valve connected to the vapor pressure controller should also be opened.

7. When the compound pressure gauge indicates 1 PSIG or above, the system is ready for liquid helium withdrawal.

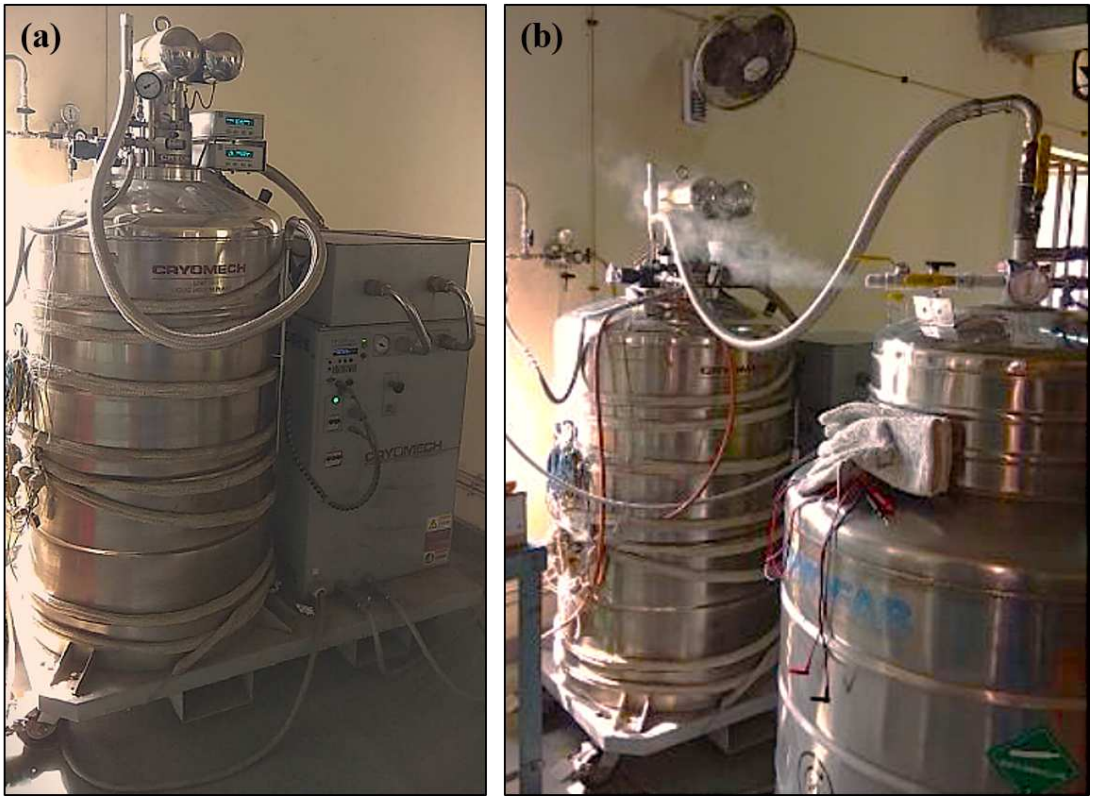

FIGURE 3.39: (a) Mother Dewar and compressor in our liquid He plant (LHe Plant laboratory) and (b) Transfer of the liquid He from the mother Dewar to the recovery Dewar in our lab.

(ii) **Withdrawal of Liquid Helium:**

1. LHe can be taken out from the mother Dewar by opening the extraction line's valve [276]. Upon initially opening the valve, the release of helium gas will produce an audible sound, accompanied by the appearance of white vapor exiting the end of the extraction line. This indicates that the extraction hose's internal line is cooling

down to LHe temperature levels. LHe will only begin to flow once the hose reaches the appropriate cryogenic temperature.

2. When closing the valve, care must be taken to avoid over-tightening. Gentle finger pressure is sufficient to secure the valve once the valve stem comes into contact with the valve seat. Over-tightening may lead to the valve stem malfunction. After closing the valve, any residual LHe within the extraction hose will keep flowing naturally.

3. To complete the process, the helium regulator shutoff valve should be closed to halt the flow of helium into the recovery Dewar. Figure 3.39 illustrates the experimental setup used for transferring LHe from the mother Dewar to the recovery Dewar in our laboratory.

3.2.1.6 Results and Conclusion

Approximately 38.5 cm (about 100 liters) of LHe was produced in the mother Dewar by the expenditure of 14 helium gas cylinders. After production, we closely monitored the condition of the helium plant on a daily basis with awareness. Several issues arose, such as the unexpected shutdown of the plant, problems with the chiller, a sudden increase in pressure (above 10 PSI) in the main Dewar, elevated water and oil temperatures due to chiller pump failure, and some problems related to voltage fluctuations. Immediate actions were taken to address and resolve these problems. Additionally, a helium leak was detected at the junction of the transfer tube in the mother Dewar. Using a helium leak detector, the issue was resolved by applying cryogenic grease.

As a result, we successfully preserved the LHe in the mother Dewar for approximately one month without significant loss. Subsequently, the transfer of LHe from the mother Dewar to the recovery Dewar was initiated. To begin the process, the recovery Dewar was primarily filled with liquid nitrogen (77 K) to cool the inner environment from room temperature (300 K) to 77 K. Then, all the liquid nitrogen was extracted from the recovery Dewar. To prepare the recovery Dewar, it was purged with cool helium gas to eliminate contaminants from the liquid nitrogen and other gases, and to cool the environment inside the Dewar to around 50 K. Once the nitrogen and all the contamination were fully removed, the LHe was transferred from the mother Dewar to the recovery Dewar, ensuring the successful transfer of the LHe.

The transfer process took approximately 5 to 6 hours. Due to the absence of a recovery system, significant amounts of LHe were lost (transformed into gas) to the outer environment as it vaporized. However, we were able to successfully transfer about 50

liters (as indicated by the LHe detector) of LHe into the recovery Dewar from the mother Dewar. The entire process was carried out with Dr. Budhhadeb Pal, SNBNCBS. This setup enables vibration-free low-temperature measurements down to 4.2 K by immersing a dipstick into the LHe within the recovery Dewar. This process was used and became helpful while using LHe in a wet Oxford system, as explained in ESR techniques (see Section 3.7).

3.2.2 Development of Low Temperature Hall Measurement Setup

The 6 K cryostat is a specialized device used to conduct experimental measurements at low temperatures down to 6 K. It is designed to sustain these low temperatures for extended periods, ensuring stable conditions for the mounted sample. In general, cryostats are extensively used in condensed matter physics to achieve ultra-low temperatures, enabling investigations of electronic transport, magnetic susceptibility, specific heat, superconductivity, quantum phase transitions, and the optical and spectroscopic properties of materials in these low-temperature regimes. In this case, a 2-Tesla electromagnet (Polytronic, Model: HEM 150) has been integrated with this 6 K cryostat to facilitate low-temperature magneto-transport and spin-transport measurements in our laboratory. Consequently, certain modifications to the 6 K cryostat and the electromagnet power supply (Polytronic, Model: CCP-150Y) have been made to couple these two systems, which are detailed below.

3.2.2.1 6 K Cryostat

- **Principle of Operation:**

The 6 K cryostat is a closed-cycle cryostat, which consists of four primary components: the expander, compressor, vacuum shroud, and radiation shield. The expander, often called the cold head or cold finger, is the site where the Gifford-McMahon refrigeration cycle [277] principle works. It is connected to the compressor through two gas lines and an electrical power cable. Helium gas of high pressure is sent to the expander via one gas line (typically narrower in diameter compared to the other), while a separate line returns the low-pressure helium back to the compressor from the expander.

The expander requires helium gas at specific flow rates and pressures, which are provided by the compressor to achieve the targeted cooling performance. The cold section of the expander is surrounded by a vacuum shroud, which significantly reduces thermal load from the environment through conduction and convection. Thermal isolation for the second stage is achieved using a radiation shield, which is actively cooled by the expander's first stage, protecting it from room-temperature thermal radiation emitted by the vacuum shroud [278]. The valve motor operates the rotating valve disc, which regulates the flow of helium gas. High-pressure helium gas powers the reciprocating displacer assembly within the cylinder assembly. The valve disc is designed with ports that enable the displacer to complete two full cycles for every rotation of the valve disc. High-pressure helium,

directed by the rotating valve disc, passes through channels in the slack cap and enters the regenerator. This regenerator, pre-cooled during the prior exhaust stroke, reduces the temperature of the incoming gas as it flows through. Helium gas flowing through the passages in the slack cap lifts the cap, raising the displacer and creating an expansion space at the heat stations for gas that has passed through the regenerator. While the displacer moves upward, part of the gas situated above the slack cap undergoes compression and is forced through an orifice into the surge chamber. The valve closes just before the displacer contacts the valve stem, and the increased pressure above the slack cap decelerates and eventually stops the displacer, avoiding impact with the stem.

During the exhaust phase, when the valve opens, the high-pressure gas present at the heat stations is permitted to expand, resulting in cooling of those regions. The regenerator is additionally cooled during the exhaust phase. With the drop in pressure, the semi-compressed gas stored in the surge chamber is released, propelling the displacer and the slack cap toward the thermal stations, aiding in exhaust and resetting the displacer for a new cycle. The valve shuts once more, and the remaining gas provides a cushioning effect that slows and halts the displacer, preventing it from striking the heat stations. The temperature at the heat stations is incrementally lowered, enabling refrigeration at cryogenic temperatures [279].

3.2.2.2 Modifications of the 6 K Set-up

To carry out low-temperature magneto-transport measurements, some significant modifications were required for both the 6 K setup and the electromagnet system. The changes made to the 6 K setup are discussed here.

(i) Sample holder modification:

The small sample holder of the cryostat was replaced with a custom-designed, elongated copper sample holder to facilitate the placement of the sample head in the gap between the two magnetic poles of the electromagnet for magnetic field-dependent low-temperature transport measurements. Additionally, new electrical wiring was implemented with proper thermalization using GE varnish (which is thermally conductive but electrically insulating) to ensure uniform temperature distribution within the sample space. A silicon diode (DT-670) (see Fig. 3.40(b)), a Pt-100 temperature sensor (Hayashi Denko Japan, CRZ series, Model: 2005, $\alpha = 0.003851$ /°C) (Fig. 3.40(c)) were incorporated into the sample head location (Fig. 3.40(g)), another Pt-100 sensor (Fig. 3.40(e)) and a thermocouple (K-type) sensor (Fig. 3.40(f)) was incorporated in the cold head portion (Fig. 3.40(h)),

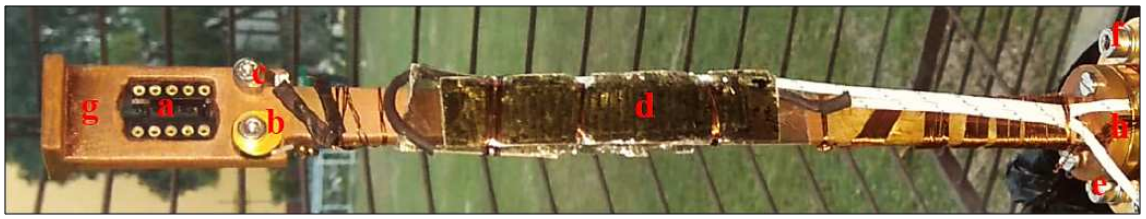

FIGURE 3.40: Modified homemade copper (Cu) sample holder with full electrical connections. (a) Chip carrier holder, (b) Silicon diode (DT 670) sensor, (c) Pt-100 sensor in sample head, (d) Heater wires, (e) Pt-100 in the cold head, (f) Thermocouple sensors in the cold head, (g) Sample head, (h) Cold head.

and a Cernox sensor (CX-1050) was kept to the sample space, to monitor temperatures at various points of the cryostat. A Manganin heater wire (of resistance $\sim$ 28 Ω) (Fig. 3.40(d)) was wrapped around the middle of the sample holder for controllable resistive heating, which was managed using appropriate PID values in the temperature controller (Lakeshore 336). A 10-pin chip carrier holder (Fig. 3.40(a)) was employed for sample mounting in the sample head. Details of the modifications are shown in Fig. 3.40.

(ii) Radiation shielding:

One of the most substantial thermal loads in any cryogenic system arises from radiation. Every material or body emits thermal radiation at a rate determined by its temperature and emissivity, as described by the Stefan-Boltzmann law: $E = \epsilon\sigma T^4$, where ϵ is the emissivity, σ is the Stephan-Boltzmann constant, and T is the material temperature of the material. The emissivity (ϵ) is a property of the material's surface, determining the fraction of incident light it absorbs and emits. This parameter plays a crucial role in managing radiative thermal loads in cryogenic systems.

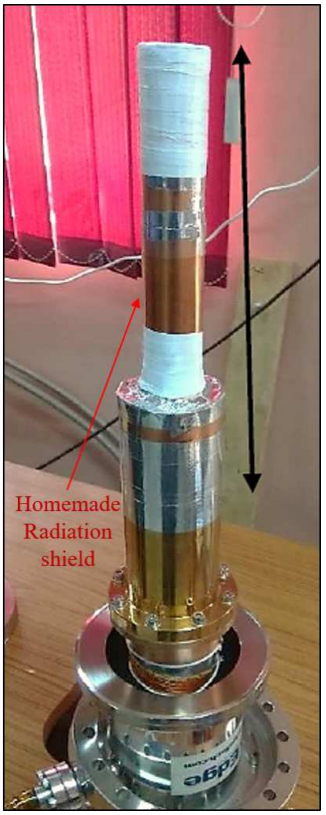

FIGURE 3.41: Homemade thermal radiation shielding (indicated by black arrow sign).

For a perfectly black body, the emissivity $\epsilon = 1$. To minimize thermal radiation in a cryogenic system, two key factors must be addressed: reducing the emissivity and lowering the temperature of the surrounding environment. These objectives can be achieved by employing materials with low emissivity that are cooled via thermal contact while shielding the experimental region. Polished copper, with emissivity values in the range of ϵ = 0.02 - 0.04, is an excellent choice for radiation shielding due to its exceptionally low emissivity

and resistance to oxidation. This radiation shield not only minimizes thermal radiation but also offers the added benefit of significantly increasing the surface area available for cryo-pumping, which effectively reduces the background pressure at low temperatures.

To achieve a base temperature close to 6 K, a thermal radiation shield was designed using a 0.5 mm thick copper sheet, which can minimize heat radiation effectively. It was installed around the sample holder in such a way that it did not come into direct contact with the outer metallic cover of the sample head. This arrangement ensured a vacuum-insulating medium between the shield and the outer metallic cover, preventing thermal radiation or heat exchange between the inner and outer environments. At the junctions, Teflon and aluminum tape were used to enhance insulation and maintain structural stability. The final design of the thermal radiation shielding used to enclose the sample holder is illustrated in Fig. 3.41.

3.2.2.3 Modifications in Magnet & Power Supply:

A 30A unipolar magnet power supply by Polytronic (Polytronic, Model: CCP-150Y) was available in our lab. However, for magneto-transport measurements of samples, a continuous and computer-controlled sweep of the magnetic field from the negative to the positive field is required. Hence, the magnet power supply was converted from a unipolar to a bipolar configuration, facilitating continuous measurements, and subsequently integrated with the low-temperature 6 K setup. The detailed steps of these modifications are outlined below.

(i) The electromagnet was initially calibrated to ensure a stable magnetic field by adjusting the current in smaller increments. It was then observed that the system could generate a maximum field of 1.6 Tesla, as indicated by the Gaussmeter, at a peak current of 29.2 A supplied by the magnet power supply.

(ii) To enable computer control of the unipolar magnet power supply (+30 A), modifications were made using its back interface. Here, in the back panel, there are connections such that we can get 0 to 30 A as output, in association with the applied 0 to 5 V in the back panel. So, an additional DC power supply (Owon) was used to provide the required 0 to 5 V input to the back panel, enabling the magnet power supply to provide an output of 0 to 30 A precisely (see Fig. 3.42). The input to the DC power

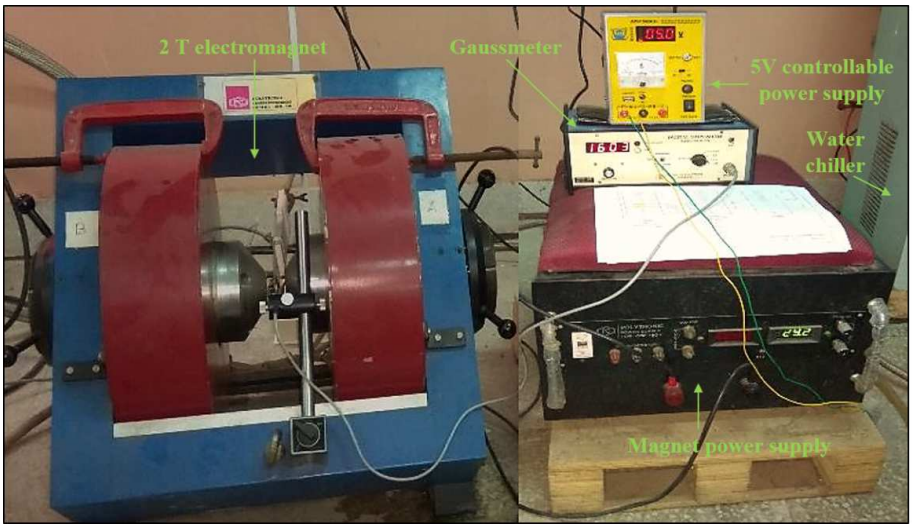

FIGURE 3.42: Picture of the Magnet power supply in our lab. Inserting a 0 to 5 V DC power supply, we can control the output of the magnet power supply.

supply was made controllable via a computer using a USB interface, thus facilitating computer-based control of the magnet power supply output.

(iii) Now, the next task was to enable polarity switching of the magnet power supply, from 0 to 30 A to the opposite direction, i.e., from - 30 A to 0, without disconnecting any cables or turning off the system. This was achieved by introducing a relay circuit[3] controlled by an Arduino microcontroller. The entire circuit operation can be fully automated and controlled via a computer through an Arduino program.

To implement this, we used two relay switches (SONGLE, Model No. SLA-12VDC-SL-C), connected in a configuration that allowed the polarity of the magnet power supply's output to be reversed, as shown in Fig. 3.43 (a). A typical relay board consists of three output terminals: COM (C, common), NC (normally closed), and NO (normally open). The operation of the relay switch is such that, in the absence of an applied voltage, the COM terminal remains connected to the NC terminal. However, when a trigger voltage (typically 5 V) is applied to the relay, it switches the connection from COM to the NO terminal. By utilizing two such relay switches and applying a digitized trigger signal (in the form of 0 or 1) within a controlled time frame, it is possible to precisely control the switching mechanism and manipulate the polarity across a resistor. This approach allows precise control of the direction of current flow, making it highly effective for tasks requiring polarity switching as illustrated in Fig. 3.43 (a).

[3]The idea of introducing the relay circuit came from a discussion held with Dr. Sayak Ghoshal, Seagate Technology, UK

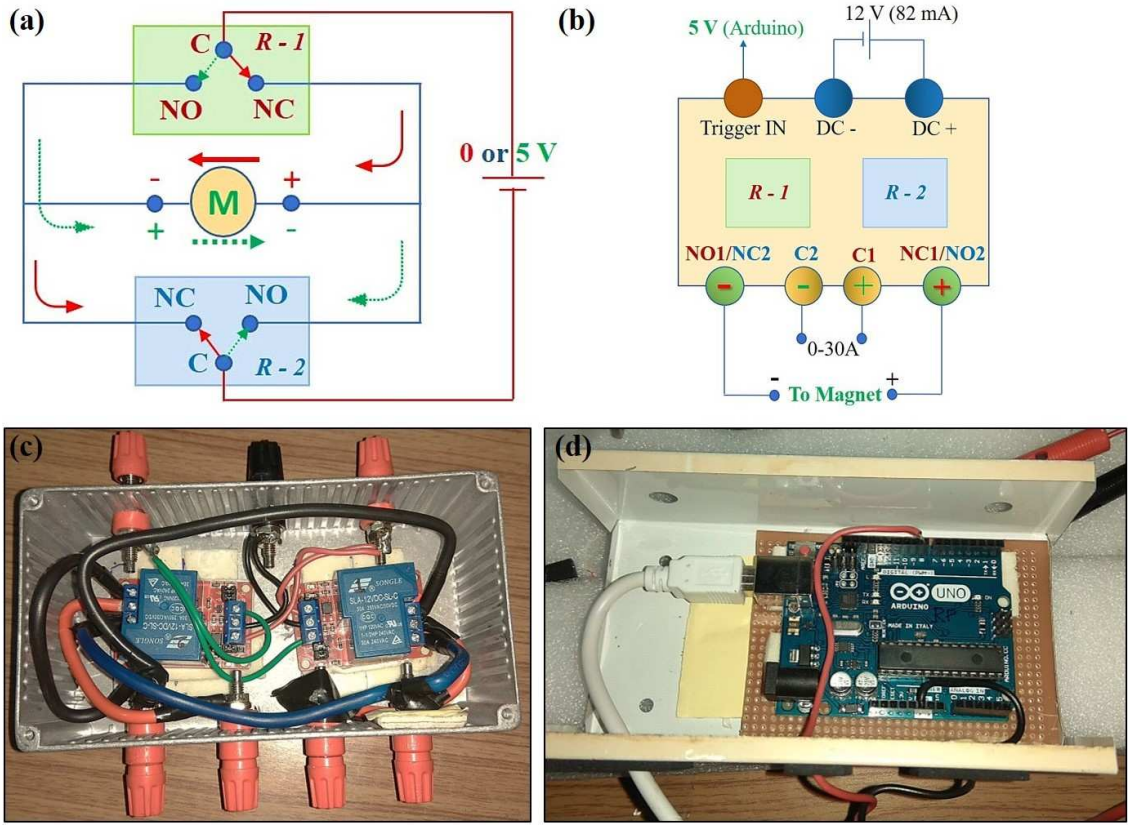

FIGURE 3.43: (a) Circuit diagram for the modification in magnet power supply, (b) Homemade relay circuit board, (c) Arduino board in our lab.

Before integrating the circuit into the magnet power supply, we first tested it on a breadboard. In this test setup, the current was passed through a sample resistor (1 kΩ), a DC power supply (Owon) was used to provide the 12 V DC startup voltage required for the relay switches, and an Arduino (Arduino UNO R3) (see Fig. 3.43 (d)) as a trigger input (0/5V) required for the relay switches, was implemented to control the circuit via a computer. The constructed Arduino program is added here:

The program is made for activating the relay module SLA-12VDC-SL-C. The input DC voltage of the relay module, 12 V (current 82 mA), is supplied from a power supply, at the relay port DC+ & DC-(ground). The triggering IN of the relay module is connected to the Arduino digital pin 7, to supply (controllable) 5 V (current 82 mA) to activate the triggering input. The GND port of Arduino is connected to the common ground with the power supply DC-(ground). The Arduino code is as follows:

```
const int triggerpin = 7;
```

```
void setup() {
pinMode(triggerpin, OUTPUT);
}
void loop() {
digitalWrite(triggerpin, HIGH);
delay(10000);
digitalWrite(triggerpin, LOW);
delay(10000);
}
```

Here, turn the relay ON (HIGH is the trigger voltage level) & (RED & GREEN LED will glow in the relay module). After the HIGH state, make a delay(0) to keep the relay in the LOW state forever. Turn the relay OFF (LOW is the trigger voltage level) & (Only the RED LED will glow in the Relay module). Here, after the LOW state, make a delay(0) to keep the relay in the HIGH state forever. The loop function runs over and over again forever.

With the above circuit, we can now successfully toggle the voltage polarity between +V and -V, and vice versa. Once the circuit was successfully tested, we replaced the wires with appropriate thick wires capable of handling 30 A of current. The relay circuit was then inserted in connection with the magnet and the magnet power supply for testing. Using the Arduino program, we successfully switched the polarity of the magnet current, achieving ± 30 A. This allowed us to start from 0 A, ramp up to 30 A, return to 0 A, switch polarity, ramp to -30 A, and return to 0 A again. The final relay circuit board setup is depicted in Fig. 3.43 (b) and (c).

(iv) Now, in the OFF state of the relay, applying a controlled and tunable voltage (0 – 5 V) to the back panel of the magnet power supply, using a programmable voltage source, enables us to precisely (0.01 V step) regulate the corresponding output current of 0 to 30 A for the electromagnets. This will allow us to access positive field ranges from 0 to 2 T. Again, in the ON state of the relay (polarity flipped), by applying a controlled and tunable voltage (0 – 5 V) to the back panel of the magnet power supply, we can get the corresponding output current of 0 to -30 A for the electromagnets, allowing us to access negative field ranges from 0 to -2 T.

With this system in place, we can now sweep the magnetic field from -2 T to +2 T (corresponding to -30 A to +30 A) with precise step control. This setup was further

integrated with a LabVIEW program, enabling magneto-transport and spin-transport measurements in the future.

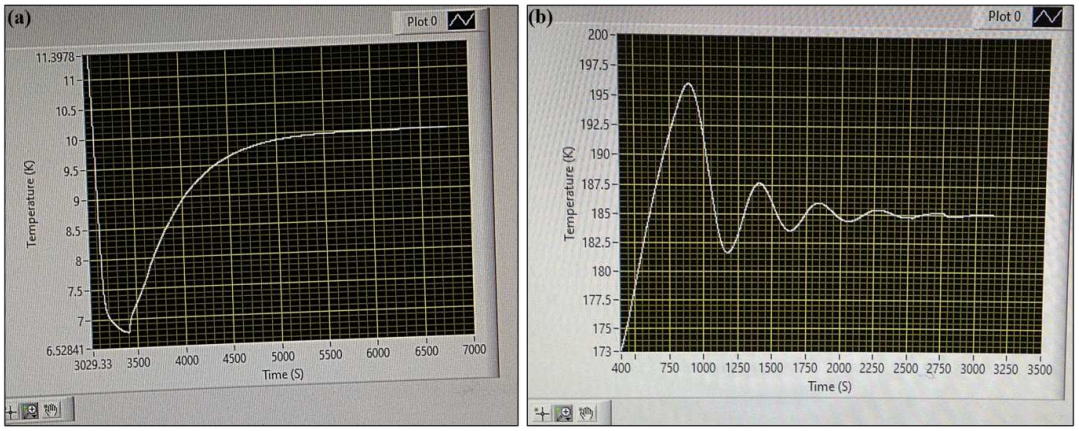

FIGURE 3.44: PID optimization. (a) For low-temperature regimes (below 100 K), PID values are 20, 7, 10, shown for the set temperature of 10 K, and (b) above 100 K, the non-optimized PID values (18, 8, 12) show the oscillatory behavior for the set temperature of 185 K.

3.2.2.4 Coupling of 6 K Setup with the Electromagnet

We successfully integrated the 6 K setup with the magnet power supply and incorporated the entire system into a single LabVIEW program to perform R vs B measurements across various temperature (T) regimes. The optimization of the complete setup required numerous iterative runs. Through these efforts, we determined that the minimum achievable temperature in the 6 K setup is approximately 6.3 K. Additionally, we optimized the PID control parameters to achieve stable and controlled heating once the system reached low temperatures (see Fig. 3.44). The partially optimized PID values were identified as P = 20, I = 7, and D = 10 for the low-temperature regime (below 100 K), however the PID values P = 30, I = 5, and D = 12 (above 100 K) created oscillatory behavior and took a long time to stabilize the temperatures. Further refinements are done later (P = 24, I = 10, D = 10) to achieve fully optimized PID values for high temperatures.

We also calibrated the Cernox temperature sensor (CX-1050) by recording its resistance values at various temperatures, such as when dipped into LHe (4.2 K), liquid nitrogen (77 K), ice temperature (273 K), and room temperature (300 K). This was done using another calibrated Cernox sensor placed in the same environment for comparison. After obtaining the resistance-temperature data, we generated the calibration curve and input

the corresponding resistance values and temperatures into the temperature controller using Curve-Handler software.

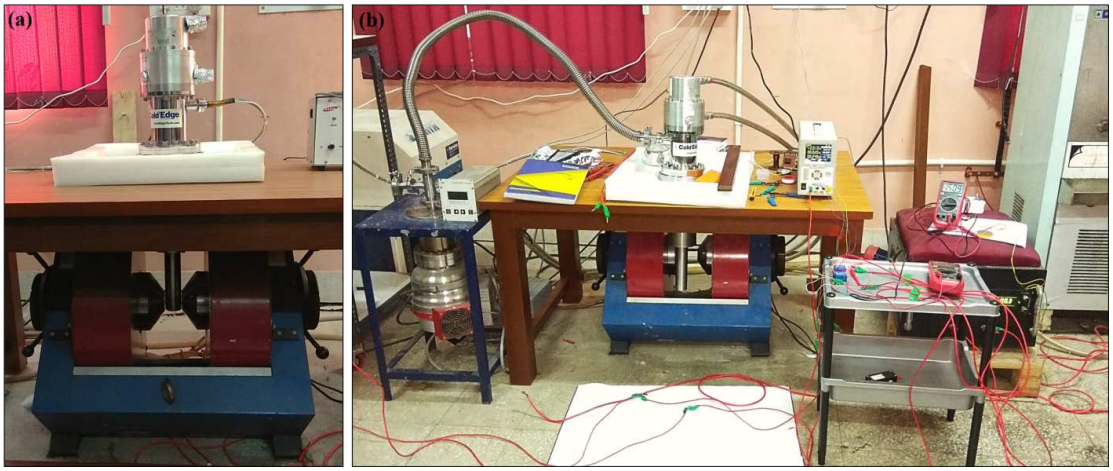

FIGURE 3.45: (a) The modified 6 K setup with the sample holder positioned between the poles of the electromagnet. (b) The complete 6 K-Hall setup, including the electromagnet and magnet power supply, is in our laboratory.

With the calibration complete, the 6 K setup was ready for performing temperature-dependent resistivity, Hall, I-V, and other transport measurements at varying magnetic fields. To verify the accuracy of the temperature at the sample space, we measured the predefined critical temperature (T_C) of an NbN superconductive thin film in the 6 K setup. The results of these measurements are presented in the experimental data section. Our complete 6 K setup, including the electromagnet and power supply, is shown in Fig. 3.45.

3.2.2.5 Characterization of the 6 K Setup Using Superconducting Thin-film

After the successful completion of the low-temperature system with magnetic field control, we characterized the system by measuring the resistance (R) as a function of temperature (T) for a Niobium Nitride (NbN) superconducting thin film. From these measurements, we determined the superconducting critical temperature (T_C) and matched it with the already known T_C of this sample. Below T_C, we performed I-V measurements at different magnetic field strengths and determined the critical current value I_c.

The NbN film was grown on a Si/SiO_2 substrate using the sputtering technique. The typical thickness of the film is around 100 nm. We carried out temperature-dependent four-terminal resistance measurements, using the van der Pauw method, and observed the superconducting transition in our 6 K setup. The four-probe resistance at room temperature was measured as 69.825 Ω (Fig. 3.46). We found the critical temperature

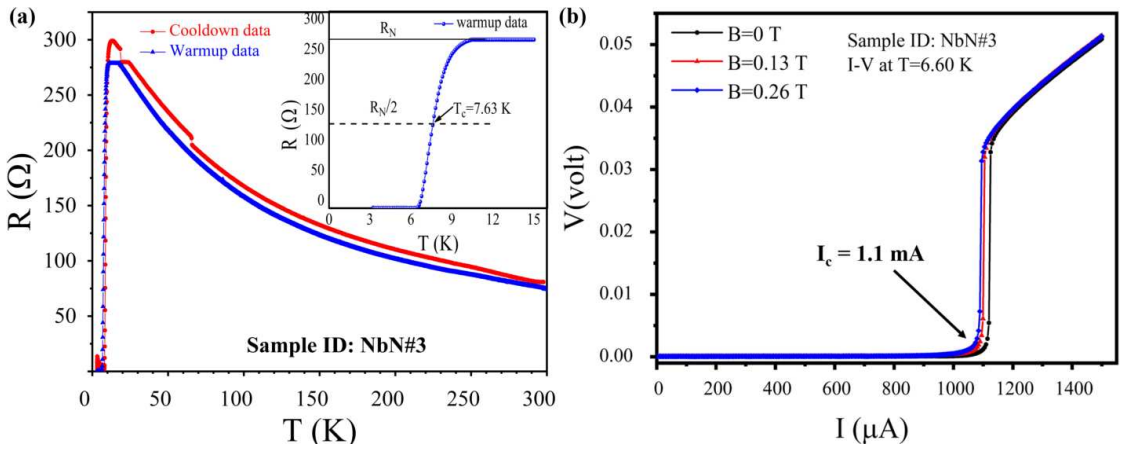

FIGURE 3.46: (a) Temperature-dependent four-terminal resistance of a NbN thin film and (inset) superconducting transition and the critical temperature $T_C = 7.63$ K (b) I-V measurements below T_C to determine I_c value and with different magnetic fields.

T_C of the NbN film to be $\sim$ 7.63 K. T_C refers to the temperature where the electrical resistance drops to half (50 %) of its normal state resistance value, as shown in the inset of Fig. 3.46. In Fig. 3.46(a), the derivative of resistance with respect to temperature (dR/dT) is negative before the superconducting transition, indicating a transition from the insulating state to the superconducting state.

Below T_c, we conducted I-V measurements to determine the critical current (I_c) of the NbN thin film. From the data shown in Fig.3.46(b), the critical current was estimated to be 1.1 mA. Additionally, we performed I-V measurements under varying magnetic fields in the superconducting state. The corresponding I-V curves for different magnetic field strengths are presented in Fig. 3.46 (b). We observed minor variations in the critical current (I_c) across different magnetic fields. These variations were relatively small due to the higher critical field of the NbN film, which provides robustness against external magnetic influences.

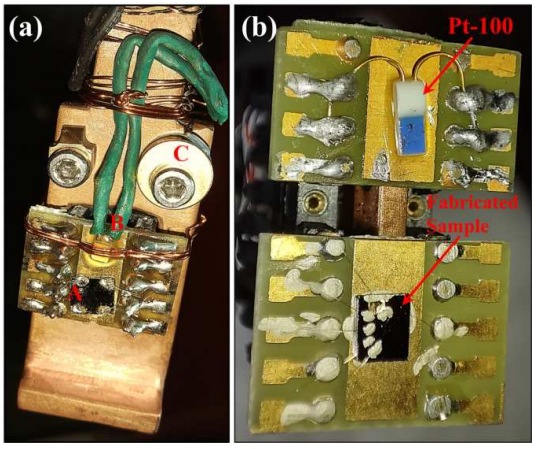

FIGURE 3.47: (a) Sample head of 6 K setup with NbN sample and Cernox sensor. (b) Modified process for measuring the actual temperature of the sample. Image of the chip carriers with a sample and a Pt-100 mounted on the same sample space.

We also determined the sheet resistance of the NbN thin film using the Van der Pauw method

(as discussed in Section 3.3.3), calculating it to be 260.94 Ω. Additionally, we strategically placed the Cernox (CX-1050) temperature sensor within the sample space to ensure accurate measurement of the temperature directly at the sample location. This setup allowed us to reliably monitor the actual temperature achieved during the experiments. To ensure proper thermalization and accurate temperature detection, we applied Apiezon N grease (cryogenic grease) beneath the Cernox sensor, as shown in Fig. 3.47. This grease acted as an efficient thermal transfer medium, enabling the sensor to measure the actual temperature of the sample reliably. The recorded temperature values (T) were subsequently used in the temperature-dependent four-probe resistance (R vs T) measurements, as presented in Fig. 3.46.

Figure 3.47 (a) illustrates the sample head of the 6 K setup, where the sample is mounted and electrically connected via a chip carrier. In the Fig., 'A' represents the NbN thin film sample, labeled as NbN3, which is connected to the chip carrier pins using very thin Cu wires at its four corners. This specific arrangement facilitates four-probe resistance measurements following the van der Pauw method. 'B' denotes the Cernox sensor (CX-1050), which measures the sample's temperature as described earlier. 'C' is the Diode sensor (DT-670), used to determine the temperature of the metallic sample head. Thick Cu wires, coated with enamel, were employed to secure the Cernox sensor and other wires in place, as depicted in Fig. 3.47. A revised strategy was later implemented to accurately determine the actual sample temperature, without needing to remove the sensor every time. As shown in Fig. 3.47 (b), one chip carrier holds the sample, while another chip carrier with a Pt-100 sensor is mounted in close proximity on the same stage, enabling continuous and precise monitoring of the sample temperature.

3.2.3 Design of a Dipstick for Low Temperature Transport Measurements

A variable temperature cryostat is an indispensable tool for performing electrical transport measurements at low temperatures. To facilitate these experiments, we have carefully designed a custom dipstick specifically tailored for characterizing fabricated devices, mounted on a 20-pin LCC chip carrier (Kyocera, Japan) for measurements down to liquid N_2 temperature (77 K). This preliminary characterization is essential before conducting rigorous and sensitive measurements in the Oxford Teslatron system, which operates under ultra-low temperatures and high magnetic fields. The schematic representation of the dipstick is shown in Fig. 3.49 (a).

This dipstick consists of several critical components designed to facilitate precise and controlled measurements. These include two chip carrier holders mounted on a copper plate for efficient thermal conduction and a primary stainless-steel (SS) rod for wire connection. The dipstick incorporates a seamless SS tube serving as a vacuum jacket, which effectively insulates the main sample space from the surrounding liquid nitrogen, thereby achieving a gradual and controlled cooling process for the sample. The system is capable of maintaining vacuum levels on the order of 10^{-6} mbar, ensuring optimal thermal isolation and stability during experiments.

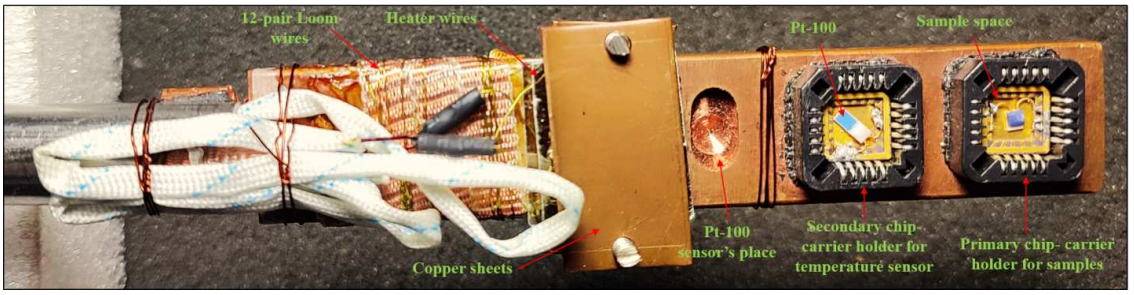

FIGURE 3.48: Sample space portion of the designed dipstick.

For the electrical connections of the 20-pin chip carrier holder, a 12-pair Copper Loom (Cryoloom by CMR Direct) is employed. Each pair of wires is twisted together to minimize induction effects and effectively cancel electromagnetic interference from external equipment. This configuration ensures a less noisy and interference-free signal transmission, which is crucial for reliable measurements. At the sample holder portion, a $\sim$ 25 Ω Manganin heater wire is employed around mica sheets to provide precise control over the temperature of the sample stage, ensuring stable and accurate thermal conditions during experiments. Importantly, two thin copper sheets are added here to increase the heater's thermal mass, ensuring better temperature stability. A Pt-100 temperature sensor

(as its operation remains above 77 K) is strategically placed on the identical secondary chip carrier holder, placed next to the primary chip carrier holder, designed to accurately monitor the sample's temperature (see Fig. 3.48). To enhance thermal conductivity, wires from the room-temperature source are carefully wound around the copper stage and thermalized by GE varnish. This design ensures effective heat dissipation from the sample, which primarily occurs through these wires during the cooling process. The wires extending from the dipstick are routed to multiple control units housed within a breakout box, which is securely attached to the head of the dipstick. This arrangement facilitates seamless connections between the sample, heater, and temperature sensors with control instruments, ensuring efficient and organized operation during measurements.

The temperature regulation and heater power are finely tuned by a Lakeshore temperature controller (Model: 336, 340) to maintain the desired conditions for accurate measurements. The optimized PID parameters of the controller ensure temperature stability at the sample stage within an accuracy of 10^{-3} K. For interfacing the sample wires with the instruments, we use BNC cables connected to the breakout box. To prevent the sample from ever being

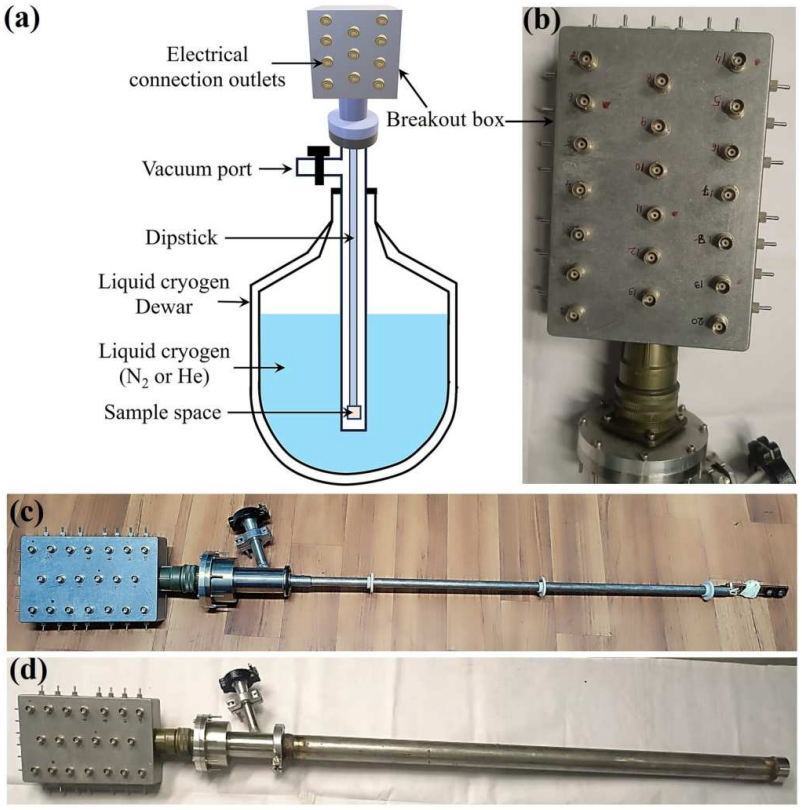

FIGURE 3.49: (a) Schematic of a dipstick for low temperature transport measurements. (b) Breakout box of the dipstick. Full image of the dipstick (c) without and (d) with the outer vacuum jacket.

in a floating state, a three-way switch is incorporated, allowing the sample to be either grounded or set to the desired voltage level required for the experiment. This setup provides precise control and reliable operation during measurements. The final dipstick image is shown in Fig. 3.49(b).

3.2.4 Optimization of Low Temperature & High Magnetic Field Transport Measurement Setups

Before the measurement of the 2D vdW FM devices and superconducting samples, we focused on optimizing two newly installed low-temperature transport and magnetic measurement setups. The first is a Physical Property Measurement System (PPMS) by Quantum Design, USA (DynaCool) equipped with Electrical Transport Option (ETO) (1.8 - 400 K, ± 9 T) and Vibrating Sample Magnetometer (VSM) capabilities (1.8 - 400 K, 300 - 1000 K, ± 9 T), enabling temperature-dependent electro-transport, magneto-transport, and magnetic measurements. The second setup is the Oxford Teslatron with Heliox VT (300 mK - 300 K, ± 12 T) (Oxford Instruments, UK), designed for ultra-low-temperature magneto-transport measurements down to 300 mK and magnetic fields up to ± 12 T. Now, we will delve into the working principles and the optimization procedures of these setups.

3.2.4.1 Physical Property Measurement System (PPMS)

The PPMS (Physical Property Measurement System) is an advanced automated system designed for studying a material's physical properties under well-controlled temperature and magnetic field conditions. It facilitates various measurements, including electrical transport (AC/DC resistivity, Hall effect, I-V characteristics), magneto-transport, VSM-based magnetic studies (AC/DC susceptibility, magnetization), and thermal transport properties (thermoelectric figure of merit, heat capacity, thermal conductivity, Seebeck effect).

The PPMS DynaCool (designed by Quantum Design, USA) is an upgraded PPMS system capable of performing these measurements on small samples at cryogenic temperatures (as low as 1.6 K) and strong magnetic fields (± 9 T) without requiring liquid cryogens. Rather, it utilizes a dual-stage pulse tube cryocooler to lower the temperature of the superconducting magnet as well as the temperature control unit, maintaining minimal vibration for high-precision measurements [280].

The PPMS DynaCool features an advanced cryocooler system comprising a Cryomech cold head and compressor. It uses minimal liquid He^4 to cool the sample chamber and superconducting magnet, relying instead on a limited volume of compressed helium gas for automatic initialization and functioning. An integrated cryopump achieves a vacuum of $< 10^{-4}$ Torr in the sample chamber, ensuring compatibility with Quantum Design

FIGURE 3.50: PPMS setup image with VSM option at SNBNCBS

hardware and custom experiments [280]. DynaCool regulates temperature through a controlled helium gas flow system, offering enhanced thermal stability and improved cooling efficiency over previous PPMS designs. This setup enables seamless transitions across the temperature range (400 K to < 1.8 K), with rapid cooling from 300 K down to 1.9 K in under 40 minutes. Enhanced design of the sample chamber ensures superior thermal uniformity, while integrated thermometers and heaters manage gradients effectively. The robust 12-pin sample puck serves to hold the sample along with the sample holder.

Inside the DynaCool, a 9 T superconducting magnet cooled by conduction process is paired with a combined digital-analog controller to provide accurate and silent magnetic field regulation. Its bipolar design enables continuous ramping through zero fields, with software monitoring at multiple points to prevent quenches and ensure optimal operation [280]. A built-in magnetic shield keeps the 5-gauss line within 30 cm of the cryostat cabinet, allowing closer placement to sensitive instruments and optimizing lab space usage. The setup image is shown in Fig. 3.50.

• Principle of Operation

The Cryostat Control System ensures the proper temperature regulation of the cryostat components for optimal functionality of the following subsystems:

(i) Pulse Tube (PT) Cryocooler: The PT cryocooler, which eliminates the need for liquid cryogens, provides the necessary cooling for the PPMS DynaCool system. It has two cooling stages: (I) the first stage operates around 45 K, cooling the main radiation shield, first stage cryopump, and heat load containing electrical wiring; (II) The second stage runs around 4.2 K, mainly cooling the 4 K plate along with the superconducting magnet, second stage cryopump, and sample chamber (see Fig. 3.51). The cryocooler operates in a helium gas-filled tank, with the radiation shield cooled via conduction to the first stage and the 4 K plate by LHe. The 4 K plate then cools the second-stage components with its direct contact. Evaporated helium from the heat load is condensed on the second stage and returns to the 4 K plate, forming a thermosiphon [280].

(ii) Thermal Isolation: The PPMS DynaCool features thermal isolation between

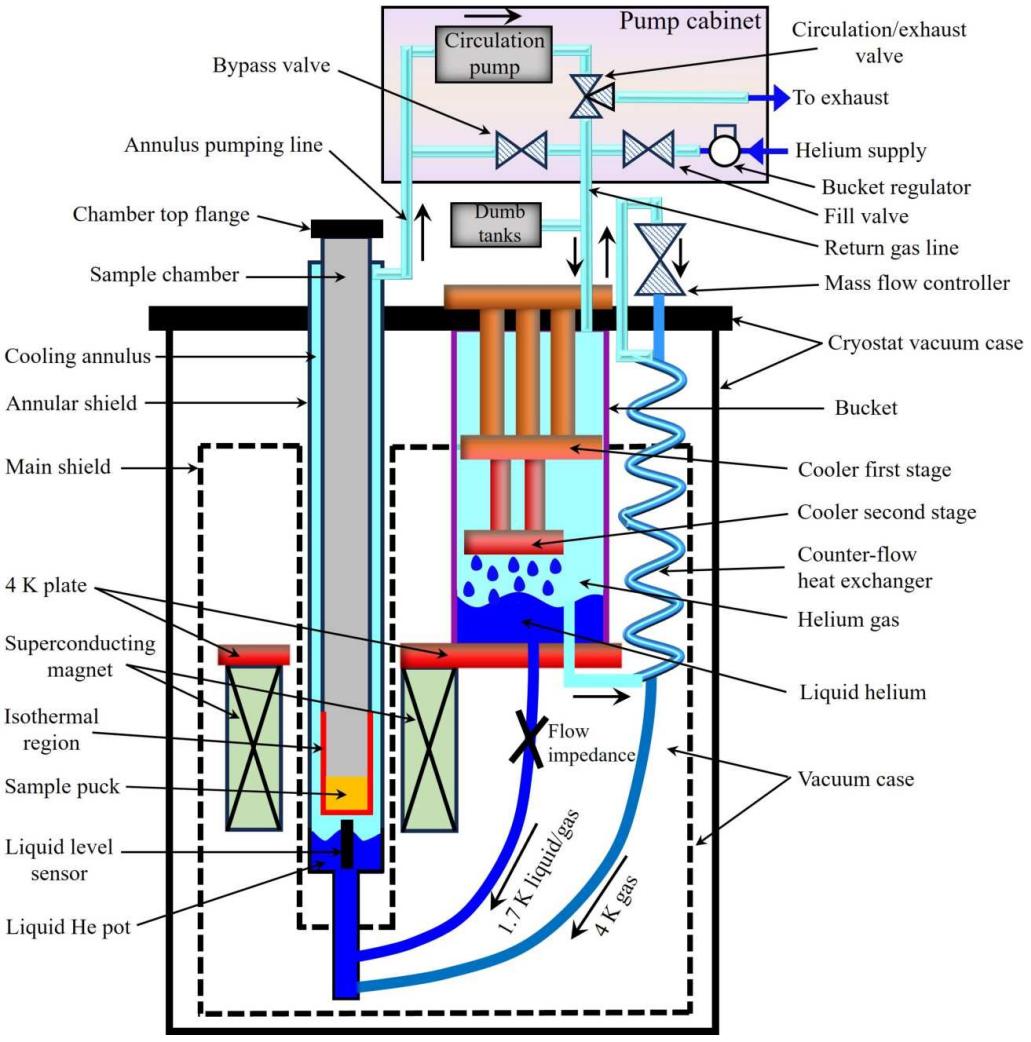

FIGURE 3.51: Schematic diagram of the internal structure and working principle of low-temperature operation in PPMS setup. Reconstructed from Ref. [280]

components operating at various temperatures. Mechanical supports minimize heat leakage, while low-conductivity materials reduce thermal transfer. The sample chamber is insulated from thermal radiation by the main radiation shield, which absorbs and conducts heat away to the first cryocooler stage. The radiation shield, shaped as an annulus encircles the cooling ring, prevents radiation heat load on the superconducting magnet by conducting thermal radiation to the main shield [280].

The DynaCool's temperature regulation system keeps the isothermal region inside the sample chamber stable, employing a high-conductivity copper construction to ensure uniform temperature distribution. The chamber's bottom puck interface is closely coupled with the block thermometer, which is controlled by a feedback loop to regulate temperature using a block heater. The cooling supplied through helium gas is counterbalanced by heating power. The circulation loop, which includes components such as the cooling annulus, pump, valves, and mass flow controller, circulates helium to cool the sample chamber. The loop can supply up to 5000 sccm of 4.2 K helium gas, with flow rates adjusted depending on the temperature ramping speed. Approximately 1000 sccm of helium gas at 1.7 K is circulated by the low-temperature system below 10 K, with helium expansion controlling the cooling. Stable temperature control is achieved by adjusting liquid levels and gas flow while avoiding excessive heat load on the sample chamber. By maintaining stringent control over the cooling process and system components, DynaCool optimizes sample temperature and minimizes thermal gradients during experiments.

• Electrical Transport Option (ETO)

The Quantum Design Electrical Transport Option (ETO) enables a variety of transport measurements across a broad resistance range and diverse sample types [281]. It features two independent channels, each equipped with a precise current source and voltage preamplifiers connected to a Digital Signal Processor (DSP), allowing simultaneous resistance measurements on two samples. Measurements are typically conducted using a sinusoidal AC drive current and detecting the corresponding AC voltage. For high-resistance samples, a special 2-wire mode applies an AC voltage and measures the resulting AC current with a current amplifier.

A DSP filters the AC response, isolating the frequency and phase of the drive signal, eliminating noise, DC offsets, and instrument drift. The DSP also calculates harmonic components. The current source operates from 1 nA to 100 mA, offering both DC and AC currents at frequency ranges of 0.1 – 200 Hz. The preamplifiers, including high-gain,

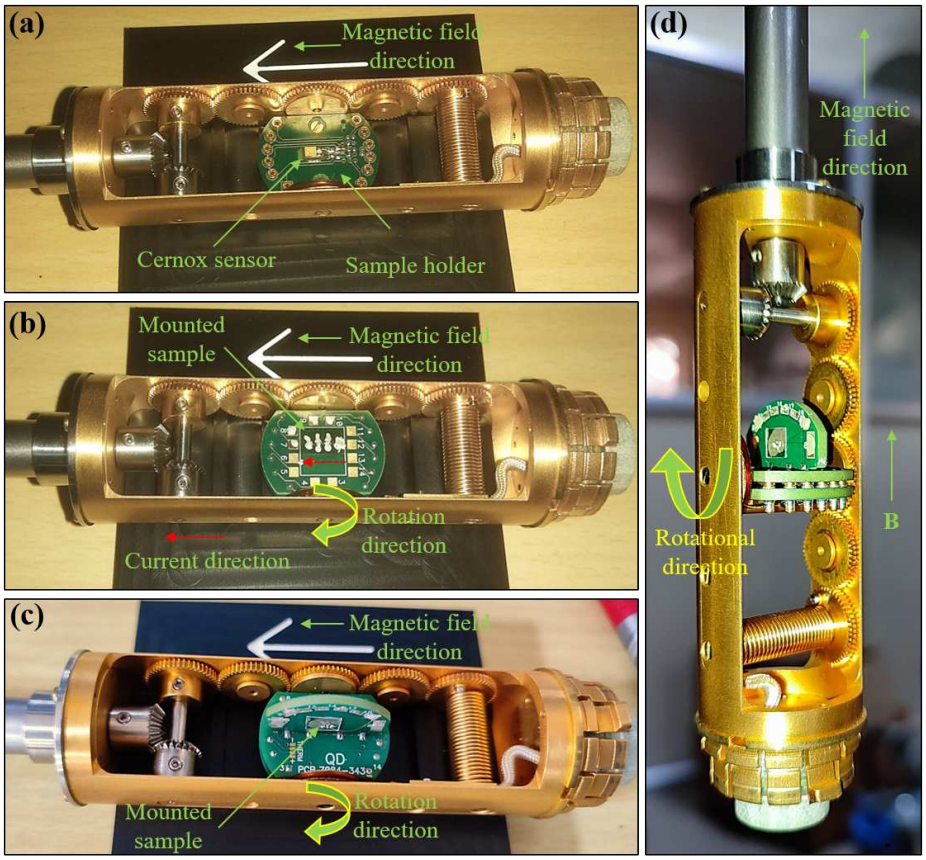

FIGURE 3.52: ETO rotator probe's sample holder images. (a) A bare sample holder with a Cernox temperature sensor. (b) A sample (connected with a four-probe geometry) is mounted on a chip carrier on top of the sample holder. The red dashed line indicates the current flow direction in the sample. (c) A sample is mounted on a perpendicular chip carrier for magnetic field with in-plane measurement. (d) The perpendicular chip carrier with the sample is rotated by 90°.

programmable-gain, and current amplifiers, ensure a noise floor of 10 nΩ and resistance measurement capability up to 5 GΩ.

ETO integrates seamlessly with MultiVu software [282], enabling automated control and data acquisition on the PPMS system. We can perform automated measurements such as Resistance, IV Curves, and Differential Resistance, using MultiVu sequences for unattended operation [281].

The Electrical Transport Option (ETO) is compatible with various probes in the PPMS setup, including the standard resistivity probe, 360° rotator probe (minimum resolution of angle is 2°), and a multifunctional probe. In our study, the ETO was employed alongside the rotator option to conduct low-temperature electrical transport measurements on the quasi-1D superconductor $(TaSe_4)_3I$, as detailed in subsequent sections. Figure 3.52

displays the ETO rotator probe's sample holders configured for out-of-plane and in-plane measurement orientations.

• **Vibrating Sample Magnetometer (VSM) Option**

The VSM option for the PPMS is a high-speed, highly sensitive DC magnetometer [283]. It measures magnetization by oscillating the sample near a detection coil (pickup coil) and synchronously detecting the induced voltage. Utilizing a compact gradiometer pickup coil configuration, an oscillation amplitude of 1–3 mm, and a frequency of 40 Hz, the VSM resolves magnetic moment changes down to 10^{-6} emu at a 1 Hz sampling rate.

The VSM system includes a linear actuator to oscillate the sample, a detection coilset puck, electronics for motor control and signal detection, and MultiVu software for control and automation. Its linear motor operates at 40 Hz, with a 6.5 cm travel range, enabling rapid, automated sample centering without manual adjustments. The detection coil integrates seamlessly with the PPMS sample chamber using a standard interface, facilitating easy reconfiguration with alternative coil designs, similar to changing a puck. Activation and deactivation of the VSM option are user-friendly and follow the same process as other system options [283]. This VSM maintains sensitivity even in high magnetic fields, allowing measurements up to the maximum field of the magnet. The theory of VSM will be discussed later.

⇒ VSM Measurements Procedures [283]:

VSM measurements involve precise sample positioning, oscillation of the sample, and synchronous detection of the induced voltage in the pickup coil. The procedure is automated through the VSM software, which manages sample centering, measurement parameter setup, and advanced operations.

(i) Sample Centering: Accurate VSM results require the sample to oscillate precisely at the center of the pickup coil pair. The system maintains this position within 0.1 mm using periodic "touchdown" operations to adjust for positional changes.

(ii) Touchdown Operation: Sample centering is achieved via the touchdown operation, where the sample holder is lowered until it contacts the puck surface. The system calculates the precise position using:

$$\text{Measurement Location} = (\text{Touchdown Location}) + (\text{Coilset Height}) - (\text{Sample Offset}),$$

where the calibrated coilset height is approximately 40 mm.

(iii) Measurement Process (Synchronous Detection): The VSM motor module (Model CM-A) oscillates the sample at a fixed frequency and amplitude, while the detection module (Model CM-B) synchronously measures the induced voltage. Real-time position data ensures precise magnetization measurements for each oscillation cycle. At 40 Hz, the system can produce up to 40 measurements per second, averaged based on user-specified intervals. Calibration files correct for preamp gain, phase shifts, and coilset geometry for accurate magnetic moment determination.

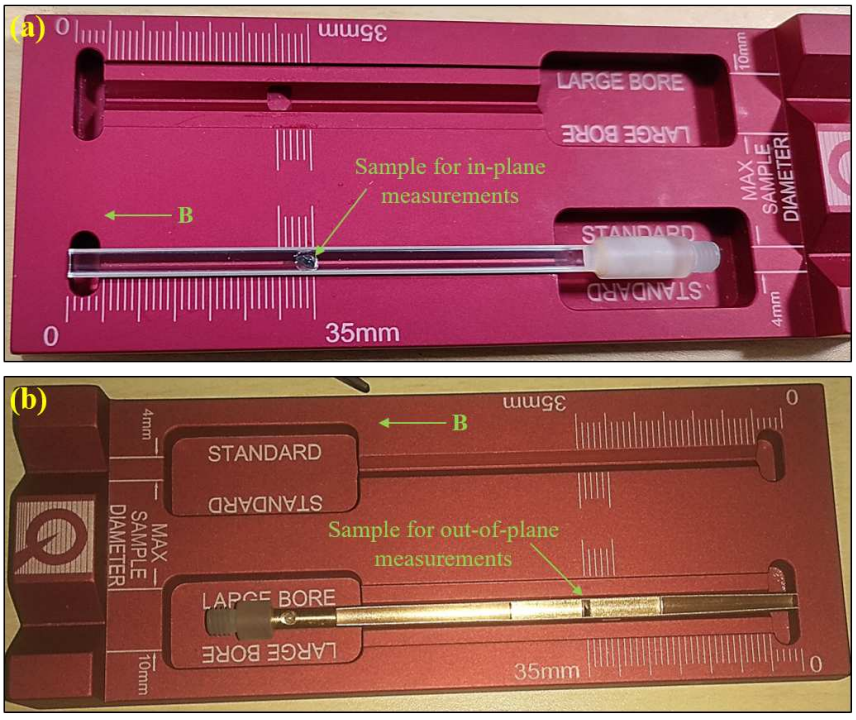

FIGURE 3.53: Images of the VSM sample holders. (a) A quartz sample holder for mounting the sample along the in-plane direction. (b) The sample holder for mounting the sample along the out-of-plane direction. The magnetic field (B) direction is indicated by the arrow sign.

(iv) Sample Mounting and Offset Measurement: The sample offset—the distance from the sample's center to the holder's bottom—is measured using a mounting station, accurate to 0.5 mm. Offsets between 0 and 35 mm are permissible, but offsets below 30 mm may introduce magnetic end-effect noise, while offsets above 35 mm risk mechanical interference (see Fig. 3.53). Once measured, the sample holder is secured to the sample rod, ensuring straight alignment to avoid rubbing, noise, or heating effects during measurement. This automated and precise procedure ensures high-quality, reproducible magnetization data across a range of sample configurations.

3.2.4.2 Oxford Teslatron with Heliox-VT (mili-Kelvin) System

The Teslatron-PT is a cryogen-free superconducting magnet system (Oxford Instruments, UK) with a Variable Temperature Insert (VTI), providing precise control of sample temperature and a stable magnetic field for cryogenic measurements. The system is newly installed and it includes a universal mechanical rotator (MR) probe insert, enabling temperature control from 300 K down to 1.6 K and featuring a rotator system for 360° sample rotation. Additionally, the setup includes another Heliox-VT insert (Oxford Instruments, UK), which supports ultra-low-temperature magneto-transport measurements down to 300 mK to 300 K. The Heliox-VT insert allows for in-plane or out-of-plane measurement configurations under the system's magnetic fields up to ± 12 T. We optimized and maintained the measurement system by designing a new breakout box, developing custom LabVIEW programs, and implementing other necessary enhancements after a lot of effort. The system components and their fundamental operational principles are outlined below.

The magnet and the VTI of the Teslatron-PT are cooled by a pulse tube refrigerator (PTR), powered by a helium compressor. The VTI features a sealed helium circuit circulated by an external pump. This helium gas is pre-cooled, liquefied in the cryostat, and passed through a needle valve and into a heat exchanger thermally linked to the sample tube. Static helium exchange gas in the sample tube facilitates sample cooling. The VTI enables temperature control from 300 K to base temperature (1.5 K), with easy sample access via a top-loading probe. System control is managed using Oxford Instruments' MercuryiPS (magnet control) and MercuryiTC (temperature regulation) units [284].

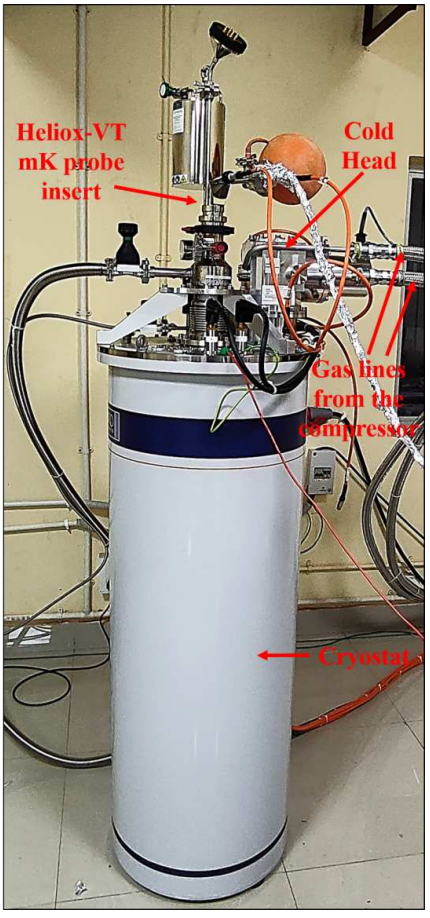

FIGURE 3.54: Image of the Teslatron-PT cryostat with Heliox-VT mK probe insert.

The Teslatron-PT [284] consists of the following principal components:

(i) Cryostat: Includes the PTR cold head (Sumitomo, Japan, Model: RP-082T2), VTI, and superconducting magnet.
(ii) PTR Compressor: Provides cooling power (by

Sumitomo, Japan, Model: F-70H).
(iii) VTI Gas Handling System: Features a circulation pump and helium (He^4) storage vessel.
(iv) Top-loading Sample Probe: Basic dummy probe, Basic MR probe with rotator system, Heliox-VT mK insert.
(v) Electronics Rack: Contains the MercuryiPS for magnet control and PTR temperature monitoring, and the MercuryiTCs for VTI and sample probe temperature management.

(a) The Cryostat:

The cryostat (see Fig. 3.54) serves as an evacuated enclosure that thermally and mechanically insulates the cold components of the system, including (i) the PTR cold head, (ii) VTI, and (iii) the superconducting magnet. The cryostat's top plate acts as the interface between the room-temperature components (above the plate) and the cryogenically cooled components (below the plate). This plate facilitates room-temperature access to essential system features such as diagnostic wiring, magnet current terminals, cryostat vacuum pump-out ports, VTI needle valve control, VTI pumping ports, and top-loading access to the VTI sample space.

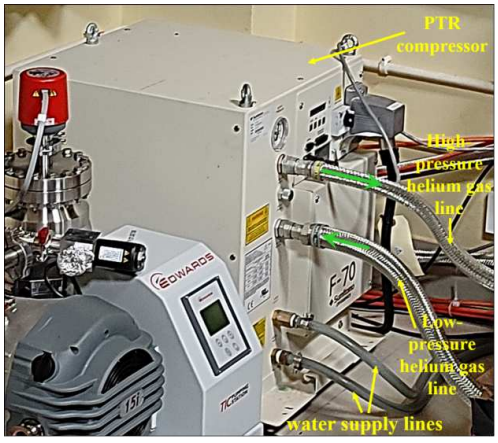

FIGURE 3.55: Image of the Sumitomo F-70 compressor.

(i) The Pulse Tube Refrigerator:

The Teslatron system's cooling engine operates on a closed-loop helium expansion cycle, utilizing highly pure (99.999 %) He^4 as the refrigerant. The cooling mechanism comprises three main components [284]: a compressor package that compresses helium and dissipates the system's heat (see Fig. 3.55), a rotary valve integrated into the cold head to alternate the helium flow between high and low pressure, and the cold head where additional helium expansion cycles achieve cryogenic temperatures (see Fig. 3.54).

Semi-flexible stainless steel gas lines connect the compressor to the cold head via the rotary valve. Low-pressure helium returning from the cold head is recompressed, with the compression heat removed through a heat exchanger, before being delivered to the cold head. Adiabatic expansion of the helium gas within the cold head facilitates the cooling, with heat loads extracted at two key locations: the pulse

tube 1st stage (PT1) with temperature typically below 50 K, and the pulse tube 2nd stage (PT2) with temperature generally below 4 K (see Fig. 3.56). This system, equipped with a 12 T magnet, uses Sumitomo RP-082T2 cold heads (see Fig. 3.54) and Sumitomo F-70H compressors (see Fig. 3.55).

(ii) The Variable Temperature Insert:

The Variable Temperature Insert (VTI) enables precise sample temperature control over a wide range, typically from 1.5 K to 300 K, within a vacuum-insulated environment shared with the cryostat vacuum [284]. Samples are mounted on a top-loading probe (MR probe or Heliox-VT mK probe) and inserted into the central tube of the VTI (referred to as the sample space) via an NW50 flange on the cryostat's top plate. To ensure effective thermal contact between the sample and the VTI heat exchanger, the sample space is filled with He^4 exchange gas, which remains entirely separate from the fixed helium charge circulating within the sealed VTI gas circuit. The top-loading probe and sample can be safely removed at any temperature, although precautions should be taken to prevent thermal shock and condensation if removed at low temperatures.

FIGURE 3.56: Internal structure of the Oxford cryostat during installation.

The VTI gas handling system employs a sealed circuit with a storage vessel and an external mechanical pump to circulate helium. The helium is pre-cooled and liquefied within the cryostat before passing through a needle valve and into the VTI heat exchanger. After exiting the heat exchanger, the helium is recovered via the VTI pumping port and compressed by the pump before being returned to the circuit through filters and a zeolite trap to ensure purity.

Narrow capillary tubes in the VTI circuit are cooled to cryogenic temperatures, making contamination of the helium gas problematic. Therefore, only ultra-high-purity ^{4}He (99.999 %) should be used, and the circuit must remain leak-tight. Adhering strictly to the prescribed gas handling and maintenance procedures, especially during installation and warm-up, is crucial for the VTI's optimal operation [284]. The image

depicting the internal structure of the Oxford cryostat, captured during its installation at SNBNCBS, is presented in Fig. 3.56.

(iii) The Superconducting Magnet:

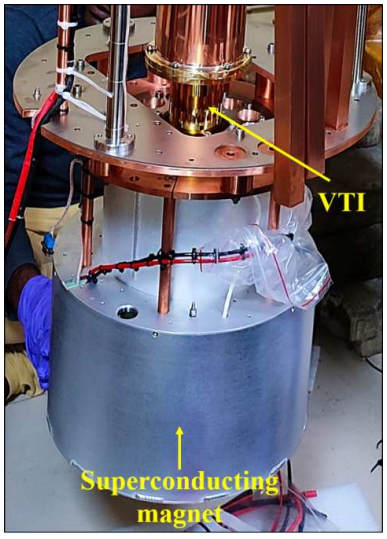

FIGURE 3.57: Image of the superconducting solenoidal magnet during installation.

Superconducting magnets enable the generation of extremely high magnetic fields in compact laboratory-scale cryostats while avoiding the substantial power consumption of equivalent resistive electromagnets. A key feature of these magnets [284] is their ability to operate in a persistent mode, where the superconducting circuit connection forms a continuous loop, allowing the power supply to be ramped to zero while maintaining the magnetic field. This functionality is facilitated by a superconducting switch, installed parallel to the main windings, which transitions between open and superconducting states using a heater. The magnetic field decays minimally in this mode, determined by factors such as inductance, joint design, and conductor material. To energize the magnet, the switch is heated to open the circuit (Hold), enabling control via the magnet power supply. Once the desired field is reached, the switch heater is turned off, returning it to a superconducting state, and the power supply current is reduced to zero over time.

Due to the substantial stored energy in superconducting magnets, rapid de-energization can induce high voltages. For safety [284], the cryostat must be properly grounded through a low-impedance link capable of handling peak de-energization currents. This system includes an appropriately rated earthing cable to connect the cryostat to the functional ground terminal on the MercuryiPS magnet power supply, which itself is grounded via its main supply cable. These grounding connections are essential for safe operation and must remain secure whenever the magnet is energized.

The Oxford Teslatron-PT system at SNBNCBS features a ± 12 Tesla vertical field superconducting solenoid magnet (Model: VS12TMAG) with the superconducting element NbTi ($T_C = 9.8$ K) as shown in Fig. 3.57. This magnet operates with a maximum current of 120 A (for 12 T). The operating principle of this superconducting magnet is outlined below:

• **Operational Principle:**

A superconducting magnet typically consists of a solenoid or coil set paired with a protection circuit that includes high-power, low-value resistors and high-power diodes [284, 285]. Additionally, a superconducting link equipped with a separate wired heater acts as a superconducting "Persistence SWITCH". When the switch is in its superconducting state, its impedance is significantly lower than the magnet, but in its resistive state, the impedance becomes much higher. The switch also has its own protection circuit for safety [285].

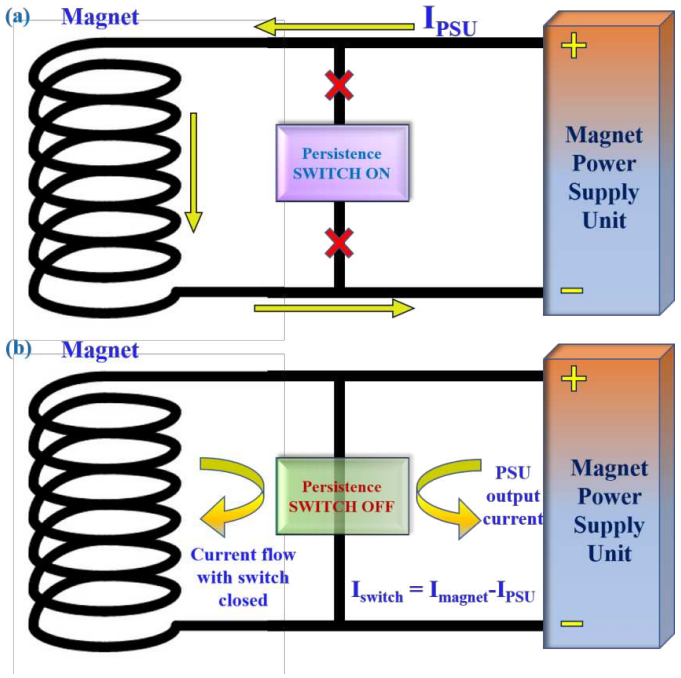

FIGURE 3.58: Diagram illustrating a simple solenoid magnet equipped with a persistent switch: (a) With the persistence switch heater ON, the switch is in an open state, allowing current from the power supply to flow through the magnet; (b) With the persistence switch heater OFF, the switch is in a closed state (analogous to closed relay circuit), creating two distinct current loops as the current flows through the switch.

When the switch heater is made ON, the superconducting link enters its resistive state, allowing current from the power supply to flow through the magnet due to its lower impedance (see Fig. 3.58 (a)). The stability of this ramped current depends on the solenoid's inductance, lead resistance, power supply output filter, and control loop parameters.

When the switch heater is made OFF (like a relay switch), the link becomes superconducting, directing current through the link (superconducting switch with lowest impedance) rather than the magnet's path. This configuration is used to energize

the magnet to a target current (switch heater ON) and to ramp down the power supply (Switch heater OFF) so that the magnet remains energized at that target current (see Fig. 3.58 (b)).

The current through the switch in this state is the difference between the magnet current and the power supply current, $I_{\text{switch}} = I_{\text{magnet}} - I_{\text{PSU}}$. So, during the power supply ramp-down, the switch current approaches its maximum as the power supply current approaches zero. To avoid overheating and potential quenching of the switch, the ramp rate (always less than a rate of 0.3 T/min) must be carefully controlled. Any abrupt opening or closing of the switch introduces a transient perturbation in the power supply output due to the large inductance of the magnet being connected or disconnected, affecting the control loop's time constant.

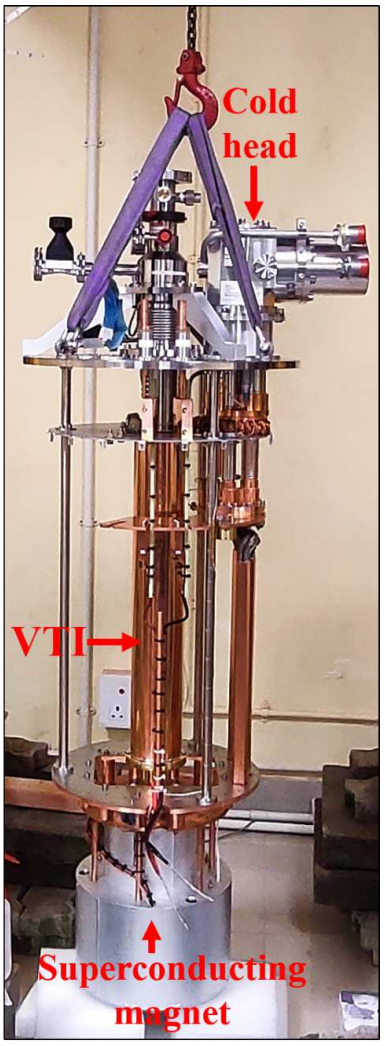

FIGURE 3.59: Image of the internal structure of the Oxford cryostat with the 12 T superconducting magnet, during installation at SNBNCBS.

• **Magnet Quenching:**

During normal magnet operation, a quench [284, 285] is a rare event when the superconducting coils of the magnet come back to a normal resistive state. In low-temperature superconductors like NbTi and Nb3Sn, this transition happens rapidly, causing a significant rise in electrical resistance and generating high-voltage transients across the coil terminals. This creates rapid current fluctuations, leading to substantial resistive heating in the coils, resulting in significant power dissipation ($R_{\text{coil}}(t) \cdot I^2_{\text{coil}}(t)$), an increase in coil temperatures, and rapid stress transients ($I_{\text{coil}}(t) \times B(t)$). This heating rapidly evaporates the LHe and immediately raises the magnet's temperature significantly above 4.2 K.

To protect the magnet coils and prevent dangerous voltage surges at the cryostat terminals, 'protection circuits' comprising power resistors and high-power diodes are employed [285]. These diodes block current leakage during

normal operation and allow the protection circuit to activate only when the voltage exceeds a defined threshold.

When a quench occurs, the power supply detects the voltage transient exceeding the configured threshold and enters quench mode. It attempts to manage the voltage by switching on rundown resistors to dissipate excess current. However, if the magnet has fully quenched, the terminal voltage continues to rise. In some cases, small windings or cancellation coils may quench without the entire magnet doing so, leading to localized overheating and potential damage to wires or the persistent switch, especially if LHe cooling is no longer available.

For this, to safeguard the system, the power supply reduces the current to zero within approximately 20 seconds of detecting a quench and puts the circuit in 'Clamped' mode [284]. Then, immediately, it clamps the output and turns off the switch heater to stabilize the system. The current at the time of the quench is logged as the "Magnet Trip Current" and displayed in red on the system interface, with an entry in the alarms log. The QUENCH state can be cleared, and control can be regained by pressing the HOLD button at any time.

Figure 3.59 shows the internal structure of the Oxford cryostat with the 12 T superconducting magnet at SNBNCBS, during installation.

(b) Gas Handling System:

The gas handling system [284] is mounted on a mobile trolley and includes the circulation pump, zeolite trap, and connections to the VTI of the cryostat. The circulation pump used is an Edwards nXDS10iR scroll pump. The helium circulation circuit is responsible for cooling the VTI and sample probe. Its external components consist of a sealed Edwards scroll pump, a 5-liter helium storage tank, a pump and flush manifold with a pressure relief valve and fine filter for pump exhaust, a zeolite trap with a coarse outlet filter and associated isolation valves, and two flexible low-pressure stainless steel lines connecting to the VTI pumping port (NW25) and VTI inlet port (NW16). These components are pre-assembled and mounted on a metal plinth for ease of installation, as shown in Fig. 3.60.

The helium storage tank contains high-purity (99.99 % pure He^4) gas at approximately 0.6 bar gauge pressure. After collecting all the gases in the tank during the warming up of the system or before starting the circulation process, the tank's isolation valve is

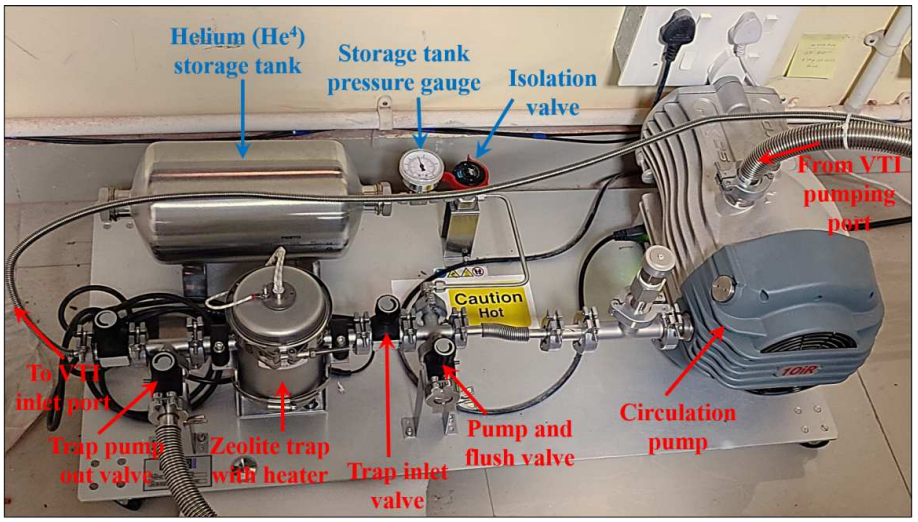

FIGURE 3.60: Image of the pump trolley of Gas handling system at SNBNCBS.

kept closed and secured with a red plastic anti-tamper safety lock to prevent accidental opening. Before use, the pressure gauge on the storage tank should be verified, ensuring it reads 0.6 bar (± 0.1 bar) gauge.

(c) Basic Mechanical Rotator (MR) Probe Insert:

The sample mechanical rotator (MR) probe with a rotator motor (Model: FCPR50-SVP01) is an integral component provided with the Teslatron VTI platform (see Fig. 3.65 (a)). This probe is optimized for conducting electrical transport and Hall effect measurements at temperatures as low as 1.6 K, with full 360° sample rotation capability, and supports a frequency range from DC to low-frequency AC. Its modular design allows for the sample to be configured in either gas or vacuum environments and supports both fixed and rotator measurement options. The probe features demountable sample holders that accommodate in-plane and out-of-plane measurement setups, with integrated ESD protection and electrical isolation for enhanced experimental precision and safety. Additionally, this top-loading sample probe is electrically isolated from the cryostat, enabling the separation of the measurement ground and cryostat protective earth ground.

The probe includes a robust sample rod chassis (stainless steel) with baffle plates to minimize radiative heat loads (see Fig. 3.61) and an earthing tag for connecting the probe to the instrument ground if required. These baffles plates/shafts are essential for maintaining low temperatures in cryogenic sample probes by minimizing heat transfer from higher-temperature components to the cryogenic environment around the sample. Constructed from highly reflective materials like polished aluminum or stainless steel,

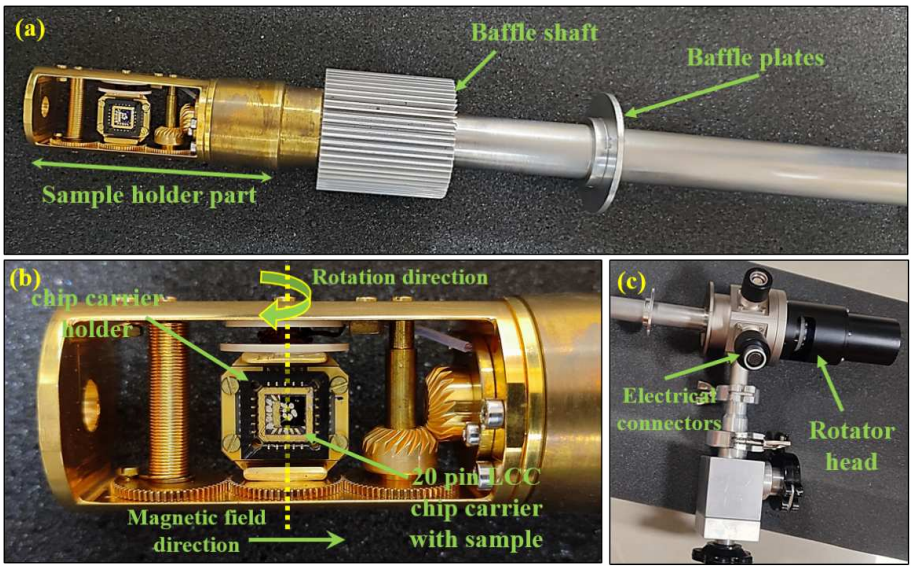

FIGURE 3.61: Image of the basic MR probe with all of its components at SNBNCBS. (a) MR probe's bottom part, (b) MR probe's sample holder part, and (c) MR probe's top portion.

they reduce emissivity and enhance thermal reflection. These baffles act as thermal barriers, significantly slowing heat transfer from external sources through radiative and convective pathways. Additionally, they help maintain the structural integrity and alignment of the probe shaft within the cryostat. Temperature control is facilitated by a Cernox temperature sensor and a heater (power rating of 20 W) integrated into the sample mounting block, both of which are compatible with the Teslatron control system for seamless operation. The wiring loom (constantan wire) is equipped with two 24-pin Fischer connectors at the top part of the probe. The connector is pre-wired with 12 twisted pairs of wires, providing insulation greater than 10 GΩ. The mechanical rotator provides precise rotation for sample positioning. It offers a rotation range of 360° with the rest position parallel to the probe axis. The rotation speed is 1°/s with a resolution of 1°, ensuring controlled and accurate adjustments during experiments.

(d) Heliox-VT mK Insert:

The Heliox-VT system [286] is a helium-3 (He^3) refrigerator designed for use within the VTI of the Oxford Teslatron systems (see Fig. 3.65 (a)). The VTI enables cooling down to 1 K (< 2 K), facilitating the condensation of the He^3, with sample space temperatures reaching as low as 300 mK.

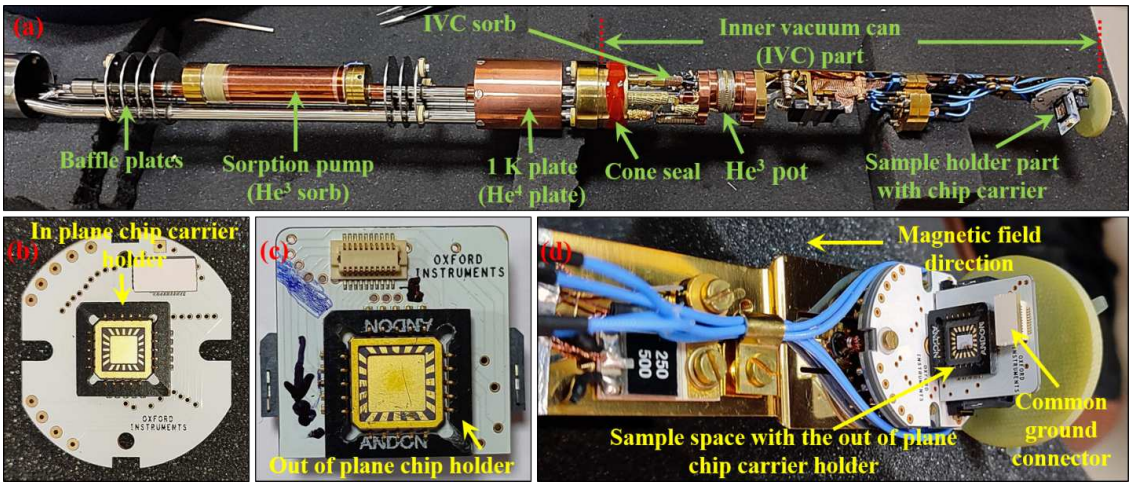

FIGURE 3.62: Image of Heliox-VT mK probe's (a) bottom part with all the components, (b) In-plane chip carrier holder, (c) Out-of-plane chip carrier holder, and (d) The sample space portion containing out-of-plane chip carrier holder, at SNBNCBS.

The insert is equipped with a vacuum seal that ensures contamination-free loading into the VTI, preventing the neck of the VTI from accumulating ice. The Inner Vacuum Can (IVC) is sealed using a silicon-based paste (CAF 1, Elkem Silicones) applied to a cone seal, providing a reliable barrier. Normal vacuum grease is avoided due to its potential to leak in the superfluid He^4 environment at the VTI's base temperature.

He^3 is securely stored in a self-contained vessel (He^3 storage tank), eliminating the need to remove this valuable gas when warming the insert to room temperature. This simplifies system operation. The He^3 with a nominal volume of 2.7 liters (measured at NTP) is stored at approximately 2 bar absolute pressure. For safety, the storage vessel includes a pressure relief device.

Samples are changed by warming the Heliox-VT insert to room temperature and removing the IVC. The sample is mounted in the vacuum on the He^3 pot's base. After mounting, the IVC seal must be secured, and the IVC evacuated. Before loading the insert into the VTI, a small amount ($\sim$ 1 cc) of He^4 exchange gas is introduced by a gas balloon.

The Heliox-VT insert is equipped with several temperature sensors at key locations to monitor system behavior and enable automated operation via the MercuryiTC temperature controller [286]. Typically, the configuration includes a generically calibrated 100 Ω Allen-Bradley sensor and a 100 Ω wire-wound heater on the He^3 sorb (MB1), a ruthenium oxide (RuO_2) sensor on both the He^4 plate (or, He^4 pot) (DB5) and He^3 pot (low temp.) (DB8), and a fully calibrated Cernox sensor on He^3 pot (high temp.) (DB7). A Fire-rod heater (2 x 100 Ω) is also attached to the He^3 pot. The calibration

data for individually calibrated sensors is preloaded into the MercuryiTC. RuO_2 sensors are suitable for temperatures between 0.02 K and 20 K (for the He^3 pot and He^4 plate), while Cernox works optimally between 1.5 K and 300 K (for the He^3 sorb and He^3 pot). One RuO_2 sensor and a Cernox sensor are incorporated at the sample space to monitor the sample's real-time temperature. An IVC sorb, composed of copper mesh and charcoal cloth, is used to adsorb the exchange gas (99.99 % pure He^4 gas) from the IVC below 10 K. Several components of the Heliox-VT probe are as shown in Fig. 3.62. The operational principle is outlined below.

• **Principles of Base temperature Operation:**

The Heliox-VT cryostat employed sorption pump technology to achieve and maintain ultra-low temperatures of 250 mK. At sufficiently low temperatures, gases generally adsorb onto cold surfaces. When cooled to these temperatures, materials with large surface areas (like charcoal) can adsorb the gases, so they can function as a 'pump'. In the Heliox-VT system [286], this principle is used, and these sorption pumps (made of charcoal) are employed

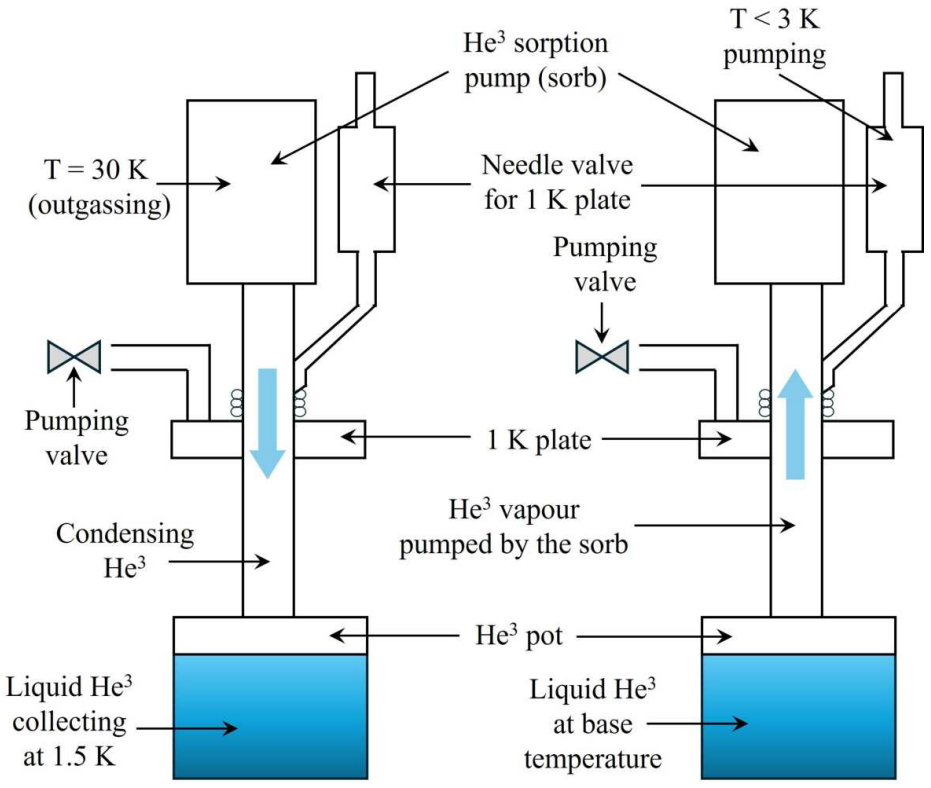

FIGURE 3.63: Schematic of the principle of base temperature operation. Reconstructed from Ref. [285].

to reduce the vapor pressure above the surface of liquid He^3, enabling the attainment of extremely low temperatures (below 300 mK).

The sorption pump (or sorb) absorbs He^3 gas when cooled below 40 K, with its gas absorption capacity dependent on temperature. A heater integrated with the sorb allows precise temperature control. The VTI provides a sub-2 K environment, facilitating the condensation of He^3 and minimizing heat conduction to the sample space.

During the condensation process, the sorb is heated to approximately 35 K to release the absorbed He^3 gas. Now the released He^3 gas is condensed on the 1 K surface assembly (1 K plate), cooling the sample and filling the He^3 pot with liquid He^3 at around 1.3 K. Once the pot is filled, the heater on the sorb is turned off, allowing it to function as a cold cryopump. The sorb is subsequently cooled to reduce the vapor pressure above the liquid He^3 surface. As a result, the average kinetic energy of the liquid particles decreases, causing the liquid to cool further, thus further lowering the sample temperature. As the vapor pressure approaches its limit, the liquid He^3 temperature drops below 0.3 K.

The sample temperature is regulated by adjusting the sorb's temperature. By maintaining the sorb temperature between 10 K and 40 K, the vapor pressure of He^3 can be controlled, thereby setting the liquid He^3 temperature (see schematic in Fig. 3.63). For optimal stability, a temperature controller (MercuryiTC) monitors the sample temperature and adjusts the power supplied to the sorb heater. This indirect heating method avoids excessive evaporation of the liquid He^3. Continuous adjustments by the controller ensure stable sample temperatures throughout the system's hold time [286].

(e) Design of Breakout Box:

A breakout box with 20 BNC connectors was designed to separate the 20 sample wires and facilitate their connection to instruments via BNC cables for voltage or current measurements across the sample (see Fig. 3.64 (a)). Each BNC connector is equipped with a two-way switch to prevent the sample from entering a floating state, allowing it to be either grounded or set to the desired voltage level for the experiment. In the grounded state, all wires are maintained at the same potential as the instrument chassis and the breakout box, which are securely connected to the proper earthing of the measurement line. A single breakout box with properly shielded cables was designed and utilized for connections with both the Heliox VT mK probe and the basic MR probe. To facilitate this, the PINs of the 20-pin LCC chip carriers were clearly marked and separated, ensuring that the sample could be mounted once and measured using both probes with identical

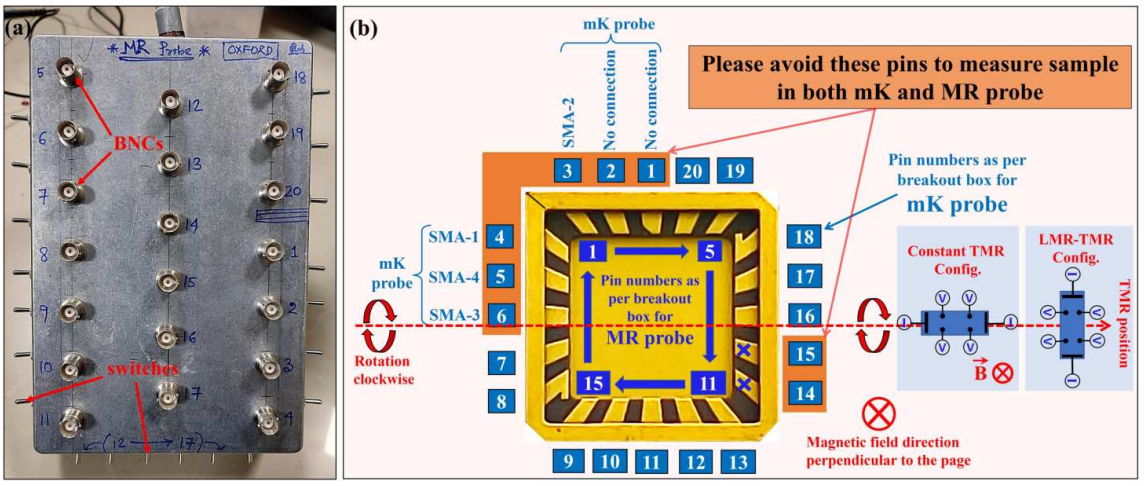

FIGURE 3.64: (a) The breakout box with 20 BNC connectors and switches, (b) Guide for different pin assignments of LCC chip carriers for mounting the devices in both mK and MR probes in our lab at SNBNCBS.

configurations, but with different pin assignments as shown in Fig. 3.64 (b)[4]. Additionally, the measurement UPS is isolated from the chiller UPS to eliminate power fluctuations caused by the sudden activation of the compressor or other high-load systems.

[4]This guide figure is drawn with the help of Dr. Bikash Gajar, SNBNCBS, Kolkata

(f) Heliox-VT mK Probe Cool-down Procedures:

After mounting the device onto the sample holder of the Heliox-VT probe, the IVC sorb is activated by heating it with a heat gun or hairdryer for approximately 3–4 minutes until a noticeable odor is emitted. Once cooled to room temperature, the IVC sorb is returned to its original position. The IVC tail is inserted and sealed tightly using vacuum-sealing CAF paste, and then the IVC is evacuated with a high-vacuum turbo pump until a pressure of 10^{-6} mbar is achieved. A small amount of exchange gas (approximately 1 cc of 99.99% pure He^4 gas) is then introduced into the IVC, typically using a bladder balloon, to accelerate cooling down to 10 K.

Subsequently, the Heliox-VT probe is inserted into the cryostat (using a crane or chain block) following the same procedure used for the MR probe. Now the cool-down process can be started. The Variable Temperature Insert (VTI) or He^4 pot is set to a temperature of 10 K, and the He^4 pressure is adjusted to 15 mB. All other heaters should remain turned off. Once the sample space temperature reaches 10 K, the activated IVC sorb adsorbs the He^4 exchange gas from the IVC, ensuring effective thermal isolation from the outer IVC. At this point, all heaters are switched off, and the He^4 pressure is reduced to 7 mB. The system is then allowed to stabilize as the VTI (or He^4 pot) and 1 K pot temperatures drop below 1.8 K. Additionally, the He^3 pot temperature should decrease to below 10 K (with lower temperatures being preferable).

For helium-3 regeneration, the temperature setpoint is set to 0 K to allow automatic regeneration. If the automatic process fails, manual regeneration can be performed as follows:
(i) It must be ensured that the He^4 pot temperature (or VTI temperature) is below 1.8 K.
(ii) The He^4 pressure (VTI pressure) is then set to 7 mB, and the He^3 sorb temperature is raised to 15 K. A waiting period of approximately 30 minutes is required.
(iii) If the He^3 pot and He^4 pot temperatures remain below 1.8 K, the He^3 sorb temperature is increased to 35 K, followed by an additional waiting period of 45 minutes.
(iv) If the He^3 pot and He^4 pot temperatures exceed 1.8 K, the He^4 pressure must be adjusted to bring the temperatures below 1.8 K. The He^3 sorb temperature is then set to 32 K, and another 45 minutes is allowed for stabilization.
(v) Once the He^3 pot reaches the desired conditions, the He^3 sorb heater is turned off, the He^4 pressure is reduced to 5 mB, and the system is left to stabilize until the He^3 pot temperature reaches approximately 250 mK.

Now the system is ready for measurements at approximately 250 mK. In our case, the sample space temperature stabilizes at a base temperature of ≈ 266 mK within 50 – 60 minutes. This base temperature remains stable for about 36 hours after condensation, provided there is no heat load on the sample and the 1 K pot is maintained at around 1.6 K. Figure 3.65 (b) shows the image of the Oxford laboratory at SNBNCBS.

FIGURE 3.65: (a) Three probes/inserts for transport measurements using Oxford Teslatron system, (b) Image of the Oxford laboratory at SNBNCBS.

3.2.5 Optimization of Glovebox

The LABPRO (Model: 1250 and 1800) glove boxes (Vacuum Techniques Pvt. Ltd., India) are engineered to create and maintain an ultra-pure inert gas environment, essential for handling materials sensitive to moisture and oxygen. Its operation relies on the continuous circulation of high-purity gases, such as nitrogen or argon, to sustain an atmosphere with oxygen and moisture levels below 1 part per million (ppm). The core components of the glovebox include a gas purifier with a regeneration unit, a filter column, an inert gas enclosure, and a main antechamber. Optional features such as a mini-antechamber and a solvent adsorption system were integrated to enhance functionality.

The glovebox operates using an inert gas (nitrogen or argon) with a purity of 99.997% or higher to build and maintain the internal ultra-pure atmosphere. Regeneration of the purifier/filter columns, which removes moisture and oxygen, requires a gas mixture containing 90–95% of the working gas (nitrogen, argon, or helium) and 5–10% hydrogen, with a similar purity level. Before initiating operations, the glovebox is leak-checked and purged with inert gas to eliminate air and ensure optimal performance. Figure 3.67 shows the image of the different components of two glove boxes in our lab at SNBNCBS.

• **Operation Principles and Procedures:**

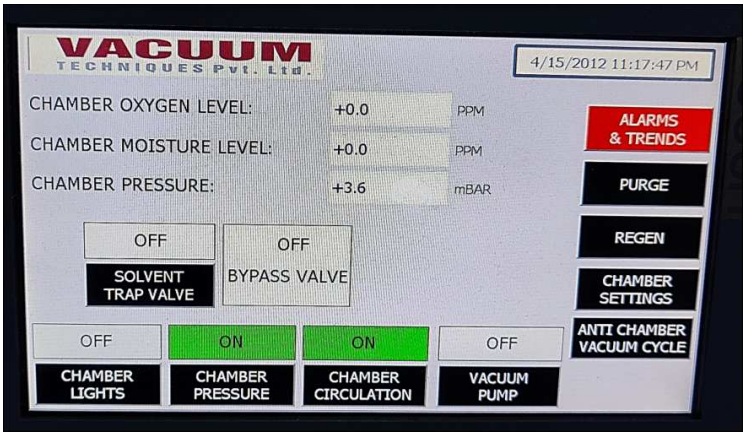

FIGURE 3.66: Final status of the glovebox in our lab at SNBNCBS after regeneration, indicating zero oxygen and moisture levels.

The glovebox employs automated pressure regulation to control the internal atmosphere, with pre-set pressure limits ranging between 0.5 mbar and 2.5 mbar. Foot pedals are provided to assist in maintaining pressure during glove insertion or removal. Purging is conducted with inert gas at 20–30 PSI and a flow rate of 15 liters per minute, effectively

FIGURE 3.67: Image of the glove-boxes in our lab at SNBNCBS (a), (d) Image indicating the different components of the (b) main glovebox and (c) glovebox for transfer setup.

displacing air. Following purging, the circulation system is activated to pass the internal atmosphere through the filter column, removing residual contaminants.

For long-term use, the system includes a 'Regeneration Mode', which reactivates the gas purifier and filter materials to restore effectiveness. Regeneration is initiated when the glovebox circulation is turned off, and pressure control is active. The process uses regeneration gas with precise pressure and flow conditions (15 PSI and 15 liters per minute) and involves four phases: heating, purging, evacuation, and cooling. The entire cycle takes approximately 13 hours, with durations of 3, 3, 3, and 4 hours for each respective phase.

After regeneration, circulation is re-enabled to restore the glove box's functionality. Proper adherence to these steps ensures the glovebox maintains an ultra-clean atmosphere, essential for applications requiring minimal oxygen and moisture levels (see Fig. 3.66).

In our setup, the glovebox was made operational through a regeneration process and by establishing proper gas circulation within the chamber. It was maintained and optimized to achieve zero oxygen and moisture levels, ensuring a pristine inert atmosphere with argon gas (see Fig. 3.66). This controlled environment was essential for preserving air-sensitive materials (see Fig. 3.67 (b)). Moreover, it provided ideal conditions for integrating the transfer setup inside the glovebox, facilitating the exfoliation and fabrication of air-sensitive vdW magnetic materials and their heterostructures (see Fig. 3.66(c)). Although the transfer setup has not yet been incorporated into the glovebox, the system is now fully prepared for its integration.

3.3 Electrical Transport Measurement Techniques

This section presents a concise summary of the electrical measurement techniques employed in this thesis, including current-voltage (I-V) characterization, two-terminal and four-terminal AC resistance measurements, and low-frequency noise analysis.

3.3.1 Current-Voltage (I-V) Measurement

The DC current-voltage (I-V) characteristics of a four-contact device are essential for evaluating the sample's behavior and distinguishing between the ohmic and non-ohmic responses of the contacts. A Source Measuring Unit (SMU, Model: 2450, Keithley) is used to apply current across two contacts, with the corresponding voltage drop precisely measured (see Fig. 3.68 (a)). Additionally, the SMU supports 4-terminal DC I-V measurements by applying a current across the two outer contact terminals and accurately determining the voltage drop between the two inner contacts (see Fig. 3.68 (b)). The SMU thus determines the I-V characteristics of the sample.

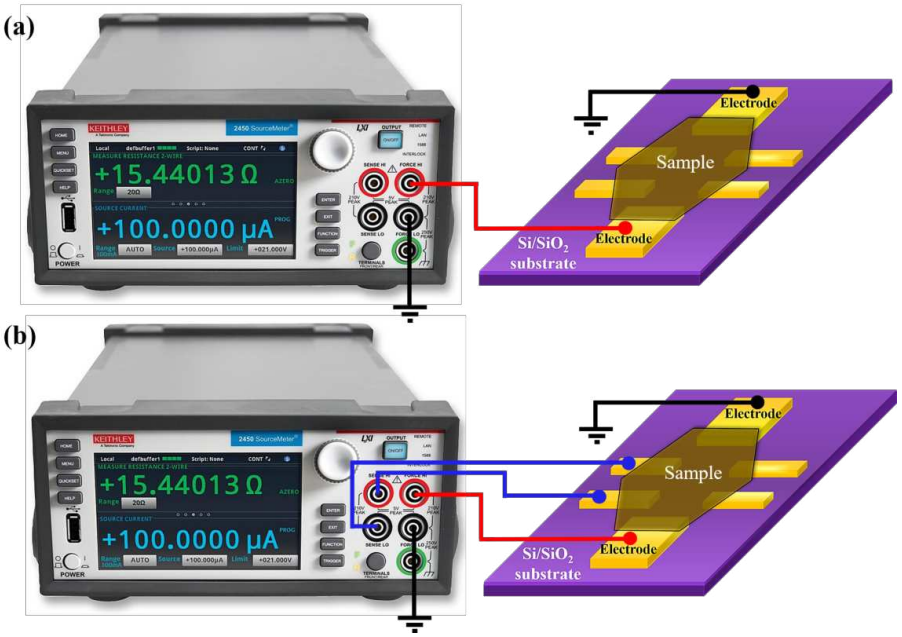

FIGURE 3.68: Schematic representation of electrical measurement techniques. (a) 2-terminal DC IV, (b) 4-terminal DC IV measurements using Keithley 2450 source-meter.

Linear I-V characteristics indicate an ohmic response, whereas non-linear characteristics suggest non-ohmic behavior. Non-ohmic contacts are identified when the voltage drop between the contacts is not linearly proportional to the current, typically due to oxide

films or other non-linear components in low-voltage circuits [287]. If the source contacts are non-ohmic, reversing polarity may cause notable compliance voltage differences. Non-ohmic voltmeter contacts can rectify AC signals, leading to DC offset errors. In such cases, offset correction is performed using the offset-compensated ohms method, rather than the current-reversal method. To minimize non-ohmic behavior, suitable contact materials like indium or gold are chosen, and the compliance voltage is set high enough to eliminate non-linear behavior at the source contact. Using shielding and proper grounding helps reduce the AC pickup, minimizing voltmeter non-ohmic contact-related errors. The I-V measurement configuration, as shown in Fig. 3.68, provides a detailed understanding of the sample's electrical properties, facilitating the identification of both ohmic and non-ohmic contacts.

3.3.2 Two and Four Terminal AC Resistance Measurement

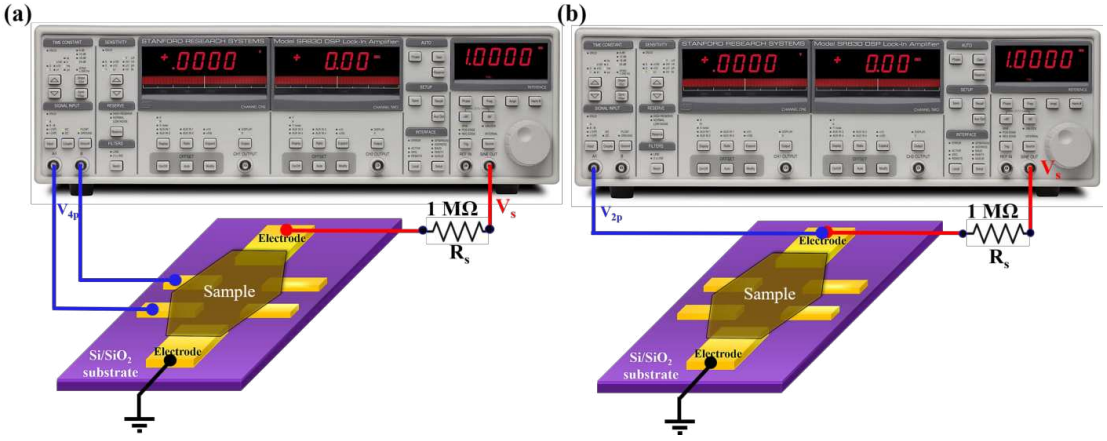

FIGURE 3.69: Schematic representation of electrical measurement techniques. (a) 4-terminal AC resistance, (b) 2-terminal AC resistance measurements in voltage mode using SR830 lock-in amplifiers.

Accurately determining the resistance of a device requires minimizing the influence of contact resistance, which can obscure the true measurement. This is achieved by employing the four-probe measurement technique, where voltage is measured independently of the current-carrying contacts. Alternating current (AC) resistance measurements, both two-terminal and four-terminal, were conducted using lock-in amplifiers (MFLI from Zurich Instruments and SR830 from Stanford Research Systems). For these measurements, a low-frequency (7-240 Hz) AC voltage bias (V_s) was applied by the lock-in amplifier, with a high-value current-limiting resistor (R_s), typically in the megaohm (MΩ) range, connected in series, such that a small current ($I_s = V_s/R_s$) can flow through the sample. The

voltage drop across two voltage probes of the sample (V_{4p}) was measured using the lock-in amplifier, allowing the four-probe resistance (R_{4p}) to be calculated using the relationship $R_{4p} = \frac{V_{4p}}{I_s} = \frac{V_{4p} \times R_s}{V_s}$.

Now, the longitudinal (ρ_{xx}) and transverse (ρ_{xy}) resistivity of the three-dimensional sample can be calculated from the following expressions: $\rho_{xx} = \frac{R_{4p}^{xx} \times A}{L} = \frac{R_{4p}^{xx} \times W \times t}{L}$ and $\rho_{xy} = R_{4p}^{xy} \times t$, with A representing the cross-sectional area normal to the direction of current flow, W the flake's width, t its thickness, and L the spacing between two voltage probes along the length. The longitudinal resistivity can be derived from Ohm's law in its local form for a homogeneous and isotropic conductor [288], $\mathbf{J} = \sigma\mathbf{E}$, where $\mathbf{J}$ represents current density, σ denotes electrical conductivity, and $\mathbf{E}$ stands for the electric field. For isotropic and homogeneous conductors, $\sigma = \sigma_{xx}$ and it is treated as a scalar quantity rather than a 3×3 tensor. If the conductor is simply a cuboid with length L, thickness t and width W, the current will be $I = JWt$, and the electric field will be $E = V/L = IR/L$. Using these relationships, the conductivity is expressed as $\sigma = L/RWt$. Consequently, the longitudinal resistivity becomes $\rho = R(Wt/L)$, where $\sigma = 1/\rho$.

To avoid device heating, the source current was kept low by ensuring that V_{4p} did not exceed the thermal energy scale (k_BT/e, where k_B represents the Boltzmann constant, T refers the temperature, and e denotes the elementary charge). The maximum measurable resistance was determined by the input impedance of the lock-in amplifier, which imposes an intrinsic limitation based on the characteristics of the experimental setup.

To enhance the detection of weak signals and improve the signal-to-noise ratio, external voltage amplifiers (e.g., SR554 (transformer) and SR560 low-noise voltage preamplifiers from Stanford Research Systems, Basel SP1004 preamplifier from Basel Precision Instruments) were often used. The amplified voltage (V_m) was then measured in either the A-mode or A-B mode of the lock-in amplifier. Schematic representations of two-terminal and four-terminal resistance measurements, without and with amplification, are illustrated in Figs. 3.69 and 3.70, respectively.

3.3.2.1 Measurements by Offset and Expand Mode

The Lock-in SR830 offers features such as offset and expand functionality for its output voltages, which can be adjusted independently. The offset and expand functionalities are particularly advantageous for making relative measurements and for analyzing small variations within a measurement.

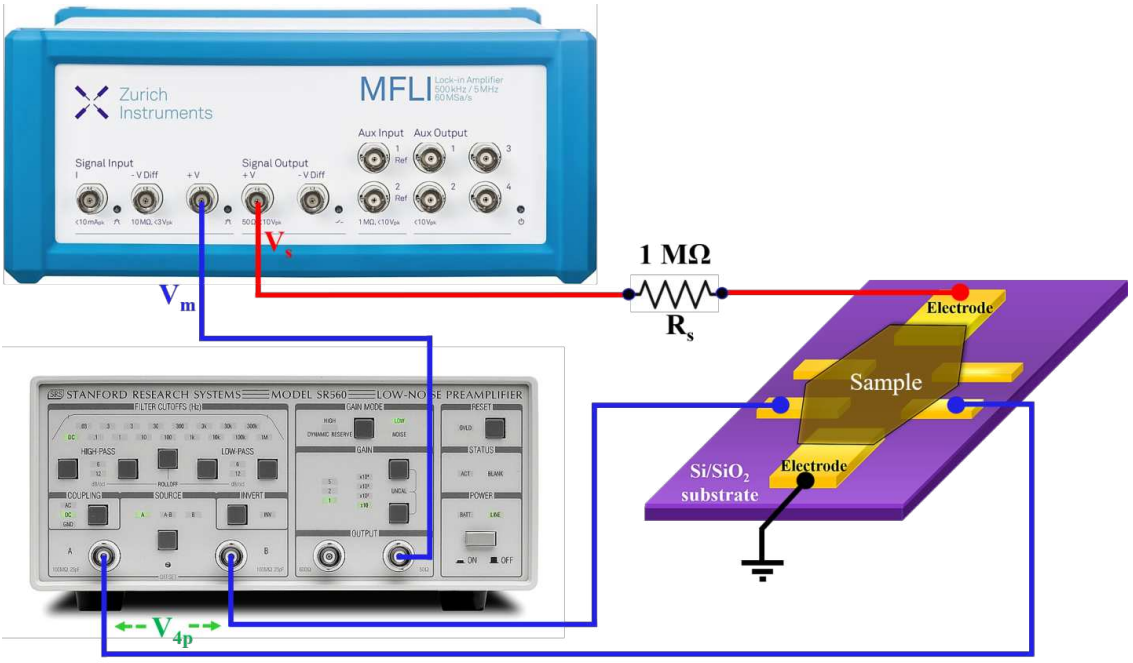

FIGURE 3.70: Schematic representation of 4-terminal AC resistance measurement technique in voltage mode, using MFLI lock-in amplifier and SR560 preamplifier.

The offset functionality enables the addition or subtraction of values from the displayed measurements, allowing for fine-tuning around a nominal signal value. This capability is particularly beneficial for detecting deviations in a signal relative to a predefined baseline, as the offset can be set to zero the output. The percentage of offset is referenced to the full-scale value and remains constant even when the sensitivity setting is adjusted.

The expand function enhances measurement resolution by amplifying the output signal (after offset adjustment) by a specified factor, either 10 or 100. This is useful for signals that occupy a small fraction of the full-scale range, as it increases their resolution without exceeding the full-scale limit. For instance, a signal representing 10% of the full-scale range can be expanded to produce a 10 V output instead of the default 1 V.

The relationship governing the X and R analog outputs is expressed as:

$$\text{Output} = \left(\frac{\text{Signal}}{\text{Sensitivity}} - \text{Offset} \right) \times \text{Expand} \times 10\,\text{V}$$

Under normal conditions, a full-scale signal corresponds to a 10 V output. The combined use of offset and expand allows precise control and enhanced resolution in various measurement scenarios. To get back the exact value of the signal coming from the sample,

we have used the following formula:

$$\text{Sample's actual signal} = \text{Output voltage in lock-in} + \left(\frac{\text{Offset in \%}}{100} \times \text{Sensitivity}\right)$$

3.3.3 Van der Pauw Method for Resistance Measurements

The Van der Pauw (VdP) method [289] is a widely used technique for determining the sheet resistance and Hall coefficient of materials in thin films or flakes with arbitrary shapes, even when a well-defined Hall bar geometry is not available.

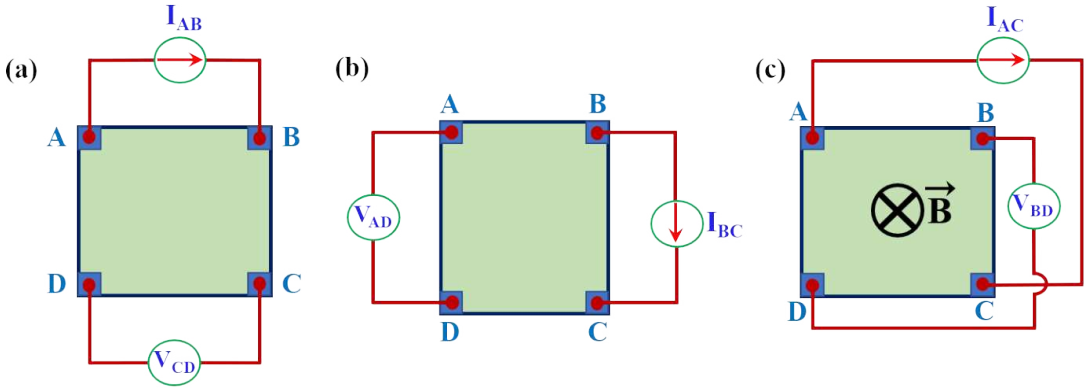

FIGURE 3.71: Schematic of the configurations (a) Config. 1 (b) Config. 2 for van der Pauw sheet resistance measurement, (c) for Hall measurements.

3.3.3.1 Sheet Resistance Measurement

Using the principles of conformal mapping, van der Pauw demonstrated that the method for measuring sheet resistance remains applicable to finite samples of arbitrary shape, provided that the four contacts are positioned on the four edges of the sample [288, 289]. The sheet resistance of a thin film sample is described by the following equation:

$$R_s = \frac{\pi}{\ln 2} \cdot \frac{(R_1 + R_2)}{2} \cdot f\left(\frac{R_1}{R_2}\right) \tag{3.3}$$

Where $R_1 = \frac{V_{CD}}{I_{AB}}$ and $R_2 = \frac{V_{AD}}{I_{BC}}$ are the measured resistances in the vdP configurations, Config. 1 and Config. 2 respectively (see Fig. 3.71 (a) and (b)). $f\left(\frac{R_1}{R_2}\right)$ is a correction factor, called vdP's function of the ratio $\frac{R_1}{R_2}$ ($R_1 > R_2$). The vdP's function (f) can be expressed as:

$$\frac{R_1 - R_2}{R_1 + R_2} = \frac{f}{\ln 2} \cosh^{-1}\left[\frac{\exp(\ln 2/f)}{2}\right] \tag{3.4}$$

By simplifying, it can be rewritten as (where $Q = \frac{R_1}{R_2}$):

$$\frac{Q-1}{Q+1} = \frac{f}{\ln 2}\cosh^{-1}\left[\frac{\exp(\ln 2/f)}{2}\right] \tag{3.5}$$

If Q is nearly equal to 1, the approximation for f is given by a series expansion as follows:

$$f \simeq 1 - \left[\frac{Q-1}{Q+1}\right]^2 \frac{\ln 2}{2} - \left[\frac{Q-1}{Q+1}\right]^4 \left[\frac{(\ln 2)^2}{4} - \frac{(\ln 2)^3}{12}\right] \tag{3.6}$$

If the sample has a perfectly square shape, the ratio $R_1/R_2 = 1$, which results in the correction factor $f = 1$. Otherwise, the table in [290] can be referenced, where various f values corresponding to different R_1/R_2 ratios are provided. After determining the sheet resistance, it can be multiplied by the thickness of the film or flake to obtain the 3D (bulk) resistance of the sample.

3.3.3.2 Hall Resistance Measurement

For Hall resistance measurement, the current is applied across one pair of diagonal edges, while the voltage is measured across the other pair of diagonal edges, as illustrated in 3.71(c), to determine $R_1(B)$. Subsequently, the terminals are shifted by one position to determine $R_2(B)$ using that different configuration. In both cases, the magnetic field, current, and measured voltage directions are all kept mutually perpendicular to each other. Subsequently, by measuring $R_1(B)$ and $R_2(B)$, the Hall resistivity can be determined by the following expression [288]:

$$\rho_{xy}(B) = \frac{R_1(B) - R_1(0) + R_2(B) - R_2(0)}{2} \tag{3.7}$$

3.4 Magneto-transport Measurement Techniques

3.4.1 Magneto-resistance

The change in a material's resistance, R, when subjected to an applied magnetic field, B, is referred to as magnetoresistance (MR) [119]. The effect was first observed in 1856 by Lord Kelvin (formerly William Thomson) during his investigation of the resistance of an iron sample [291]. MR is mathematically defined as the normalized change in resistance (or resistivity) caused by an applied magnetic field, relative to its zero-field resistance (resistivity) [48, 117]:

$$\mathrm{MR} = \frac{R(B) - R(0)}{R(0)};\ or,\ \mathrm{MR} = \frac{\rho(B) - \rho(0)}{\rho(0)} \tag{3.8}$$

The phenomenon of MR originates from the deflection of electrons by the Lorentz force, causing a deviation from their path along the electric field and resulting in an increase in resistivity as the magnetic field increases. This effect is typically minimal in low magnetic fields but becomes significantly pronounced at higher field strengths. According to classical ordinary MR (OMR) theory [119], OMR is inherently positive and arises from the restricted orbital motion of charge carriers under the Lorentz force. It follows a quadratic relationship with the magnetic field when the product of the cyclotron frequency (ω_c) and the relaxation time (τ) is very small ($\omega_c\tau \ll 1$), that is, for low-field conditions. Conversely, when $\omega_c\tau \gg 1$, that is for high-field, OMR reaches a constant value. For stoichiometric semiconductors, where the electron and hole concentrations are equal, the behavior of MR deviates from this norm. The relationships are expressed as: MR $\propto \mathrm{B}^2$ (for $\omega_c\tau \ll 1$, low-field condition); MR $\propto$ constant (for $\omega_c\tau \gg 1$, when n $\neq$ p, high-field condition) [48, 117, 119].

In the classical Hall effect, the presence of a perpendicular magnetic field (B) and a longitudinal current generates a Hall voltage (V_{xy}) orthogonal to the current direction. In systems dominated by a single type of charge carrier, such as electrons or holes, the Hall voltage induces an electric field that neutralizes the Lorentz force, allowing carriers to move linearly. However, in semi-metals, both electrons and holes are deflected laterally in the same direction, effectively canceling out V_{xy} and rendering it negligible or zero. This consistent sideways deflection under a small magnetic field (B), combined with open electronic orbits, gives rise to giant magnetoresistance (GMR), which exhibits a quadratic dependence on the magnetic field [119].

Positive MR is commonly found in metals, semiconductors, and semi-metals, whereas negative MR typically occurs in magnetic materials [119]. In most nonmagnetic substances, MR is relatively weak, showing a quadratic dependence at low fields and saturating at magnitudes of only a few percent in metals. Non-saturating negative MR in FMs primarily results from the suppression of electron-magnon scattering in the presence of an external magnetic field [292]. In FM materials, unlike nonmagnetic ones, MR is strongly influenced by the material's intrinsic magnetic properties, especially the alignment of electron spins and the interactions between conduction electrons and localized magnetic moments [48, 117, 119].

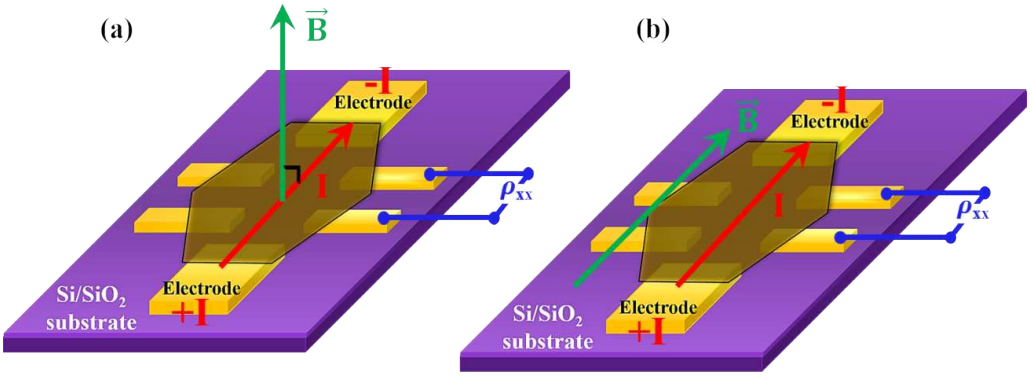

FIGURE 3.72: Schematic representation of (a) TMR and (b) LMR measurement technique

If the change in resistance is measured when a magnetic field is applied perpendicular to the direction of current flow, it is referred to as transverse magnetoresistance (TMR). On the other hand, when the resistance change is measured with a magnetic field applied along the direction of current flow, it is called longitudinal magnetoresistance (LMR). Figure 3.72 shows the schematic representation of TMR and LMR measurement techniques. In the low-field region, TMR shows a quadratic dependence on the magnetic field (B^2), transitioning to an almost linear behavior at the high-field regime. LMR and TMR have different temperature dependencies, causing them to compete as temperature increases [293–295]. If the misalignment angle between the electric and magnetic fields is slightly larger, and TMR varies more slowly with temperature than LMR, the negative LMR becomes too weak to detect above a certain temperature.

Minor misalignments of the electrical contacts can introduce magnetoresistive components into the measured Hall signal and vice versa. To correct for these misalignment effects, asymmetric contributions to the longitudinal resistivity (ρ_{xx}) and Hall resistivity (ρ_{xy})

were determined using the following equations:

$$\rho_{xy}^{\text{asy}}(B,T) = \frac{\rho_{xy}(+B,T) + \rho_{xy}(-B,T)}{2} \tag{3.9}$$

$$\rho_{xx}^{\text{asy}}(B,T) = \frac{\rho_{xx}(+B,T) - \rho_{xx}(-B,T)}{2}. \tag{3.10}$$

To obtain the true values of $\rho_{xy}(B,T)$, the asymmetric component $\rho_{xy}^{\text{asy}}(B,T)$ was subtracted from the measured $\rho_{xy}(B,T)$ for each field direction. A similar correction was applied to $\rho_{xx}(B,T)$ to derive its actual value. This process was consistently implemented for both magnetic field-sweep and temperature-sweep measurements.

For instance, in temperature-dependent Hall effect and MR measurements, data were collected for two magnetic field orientations—positive and negative. These datasets were symmetrized to eliminate misalignment effects and ensure reliable results. The symmetrization of the Hall and longitudinal resistivity data was performed using the following expressions:

$$\rho_{xy}(B) = \frac{\rho_{xy}(+B) - \rho_{xy}(-B)}{2}. \tag{3.11}$$

$$\rho_{xx}(B) = \frac{\rho_{xx}(+B) + \rho_{xx}(-B)}{2}. \tag{3.12}$$

3.4.2 Anisotropic Magneto-resistance

When an external magnetic field is introduced, the electrical resistivity of a magnetic material can vary depending on its magnetization, which is influenced by the field. This MR phenomenon encompasses several notable effects, including giant magnetoresistance (GMR) [296, 297], colossal magnetoresistance (CMR) [298], tunneling magnetoresistance effect (TMR) [299, 300], and anisotropic magnetoresistance (AMR) [301]. We will briefly discuss the AMR here.

In FM materials, magnetoresistance is influenced by the orientation of magnetization relative to the direction of electric current. This phenomenon, referred to as anisotropic magnetoresistance (AMR) [119, 301], involves a change in electrical resistivity driven by the combined effects of magnetization and spin-orbit interaction. The resistivity variation depends on the alignment of the material's

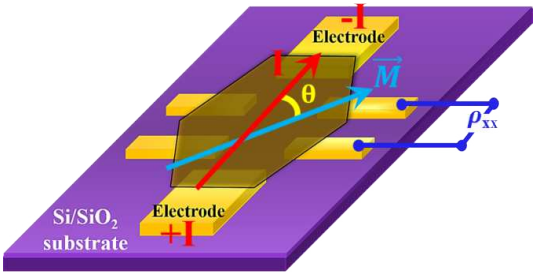

FIGURE 3.73: Schematic representation of AMR

magnetization. This may be due to the enhanced probability of the scattering of s-d electrons along the magnetization's direction, which is modulated by an applied magnetic field. Generally, resistivity is higher when the magnetization vector (**M**) is aligned parallel to the charge current and lower when **M** is transverse to it. This effect originates from spin-orbit coupling, which alters the scattering cross-section of conduction electrons based on M's orientation. The shape of atomic orbitals, influenced by total angular momentum (comprising spin angular momentum), adjusts as the magnetization rotates. When the magnetization is transverse, the orbitals lie in-plane, minimizing the scattering cross-section for conduction electrons. Conversely, when the magnetization aligns in-plane, the orbitals reorient perpendicular to the charge current, increasing the scattering cross-section. As a result, resistance is lower for transverse magnetization and higher for in-plane magnetization [119].

The resistivity values for in-plane and transverse magnetization are expressed as:

$$\rho_{\text{in-plane}} = \rho_{\perp} + (\rho_{\parallel} - \rho_{\perp}) \cos^2(\theta) \tag{3.13}$$

$$\rho_{\text{transverse}} = \rho_{\perp} + \frac{(\rho_{\parallel} - \rho_{\perp})}{2} \sin^2(\theta) \tag{3.14}$$

Here, $\rho_{\parallel}$ represents resistivity when M is parallel to the current, $\rho_{\perp}$ refers to resistivity when M is transverse to the current, and θ is the angle between M and the current. The AMR ratio [302] is defined as:

$$\text{AMR ratio} = \frac{\Delta\rho}{\rho_0} = \frac{\rho_{\parallel} - \rho_{\perp}}{\rho_0} \tag{3.15}$$

where $\rho_0 = (\rho_{\parallel} + \rho_{\perp})/2$. For FMs, the AMR ratio typically ranges between 1-2%, with larger values observed at lower temperatures. This effect only occurs in materials exhibiting FM ordering.

To analyze AMR's influence on conduction electron scattering, the two-current model [303], incorporating spin-orbit coupling, is applied. In 3d transition metals [119], spin-up electrons have a higher density of states at the Fermi level compared to spin-down electrons. Most spin-down states are occupied, leaving spin-up states available for conduction. Electric conduction is primarily carried by 4s electrons, with their resistivity determined by scattering into 3d states. Spin flips are inhibited due to the 4s-3d exchange interaction. Given the larger number of empty 3d spin-up states, most 4s electrons scatter into this band, creating two conduction channels for spin-up and spin-down

electrons. Spin-orbit coupling intermixes 3d spin-up and spin-down states, further affecting resistivity [119].

3.5 Magnetization Measurement Techniques

Magnetic characterization and measurements mentioned in this thesis were carried out using both a SQUID magnetometer and a commercially available VSM [304].

3.5.1 Vibrating Sample Magnetometer (VSM)

Magnetization of a material can be quantified through direct measurement or indirectly by observing associated physical quantities. Various methods, including inductive, force, magneto-optical, and electrical techniques, are available for static magnetization measurement of a magnetic material with high sensitivity [304]. Among these, the inductive method is widely used, where voltage generated by electromagnetic induction is monitored to determine changes in magnetic flux through pickup coils (see schematic in Fig. 3.74). This flux change correlates with magnetization and determines its value in different materials. Instruments like VSM, flux-gate magnetometers, and extraction magnetometers utilize this principle [304].

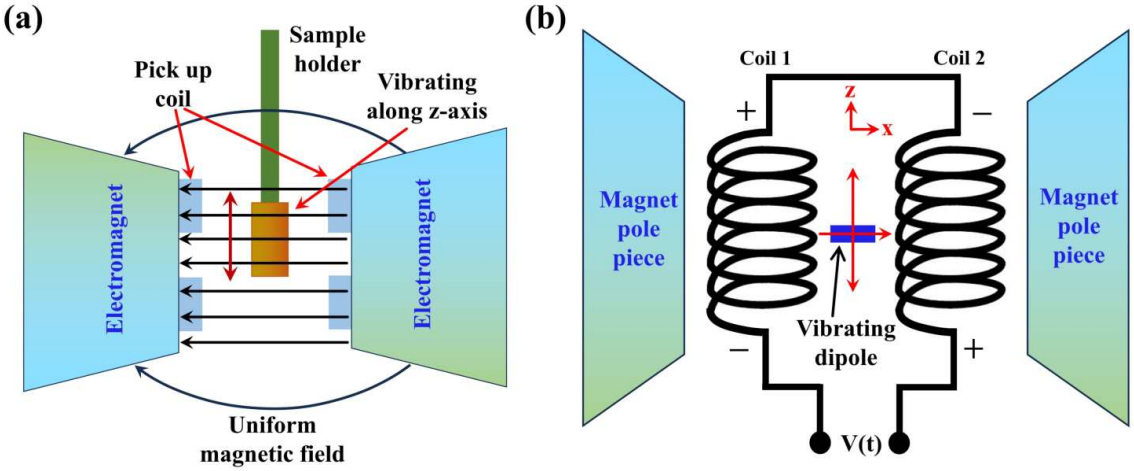

FIGURE 3.74: (a) Schematic illustration of VSM, (b) Details near the pickup coil.

VSM is particularly popular for studying the magnetic properties of thin layers and small single crystals under varying magnetic fields and temperatures, with a sensitivity of 10^{-5} emu. Following Faraday's law of electromagnetic induction – a time-varying magnetic flux induces an electric field – VSM measures magnetic moment by detecting voltage changes in pickup coils. A sample placed in a uniform magnetic field is oscillated sinusoidally at a fixed frequency near detection coils. If magnetic, the sample's dipole moment creates a time-varying magnetic flux, inducing a voltage (V_{coil}) in the coils proportional to the

magnetic moment of the sample. The relationship follows [304]:

$$V_{coil} = -NA\frac{dB}{dt}$$

where V_{coil} is the induced emf, N is the number of coil turns, A is the coil area, and B is the magnetic induction. Substituting $B = \mu_0(H + M)$, the emf is related to magnetization M as:

$$V_{coil} = -NA\frac{dM}{dt}$$

The sample, mounted on a nonmagnetic plastic or quartz rod connected to a piezoelectric transducer, vibrates sinusoidally, creating magnetic flux perturbations detected by the pickup coils. The emf generated [283] depends on the sample's oscillation frequency (f), oscillation amplitude (A), external magnetic field, and sample geometry:

$$V_{coil} = -m\omega CA\sin(\omega t)$$

Here $\omega = 2\pi f$, m is the sample's DC magnetic moment, and C is the coupling constant. By analyzing the induced emf, magnetization can be deduced. Proper calibration allows the precise estimation of magnetization [283].

By varying the magnetic field, hysteresis loops can be recorded, revealing the sample's magnetic properties. Additionally, temperature-dependent magnetization measurements enable the determination of Curie, Néel, and compensation temperatures for different magnetic materials [304].

3.5.2 SQUID Magnetometer

SQUID (Superconducting Quantum Interference Device) magnetometers [304] are highly sensitive devices, achieving a resolution of magnetic moment of 10^{-8} emu compared to 10^{-6} emu for VSMs, making them more suitable for samples with low magnetic moments. The operating principle of a SQUID is based on the quantum interference of Cooper pairs' wave functions. A SQUID consists of an interferometer loop containing two Josephson junctions, which are the weak links created by a thin insulating barrier interrupting a superconducting path.

The SQUID magnetometer consists of several components [304]. A detection coil detects the variations in the magnetic field and converts them into an electrical response. This current is transformed into a magnetic flux by an input coil connected to the SQUID

sensor. The detection coil is positioned within the LHe bath outside the sample chamber; the coil arrangement minimizes noise and background drift caused by the superconducting magnet. The electronics convert this flux into a voltage signal, which is further processed using specialized hardware and software for data acquisition, storage, and analysis. Both the detection coils and the SQUID amplifier are superconducting components (see Fig. 3.75).

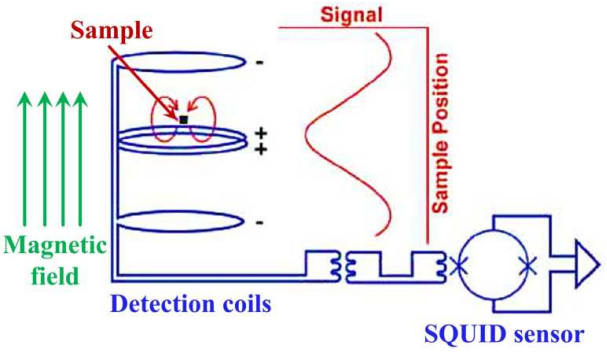

FIGURE 3.75: Schematic of SQUID VSM detection technique.

In a SQUID magnetometer, feedback mechanisms nullify the current in the detection coils, ensuring no current flows through them. Instead, the feedback current produces the SQUID voltage, which directly corresponds to the sample's magnetization. In contrast, a VSM vibrates the sample around the center of the detection coils at a fixed frequency, generating a signal that depends on the sample's position. For small vibration amplitudes, the sample position can be described as $z(t) = B\sin(\omega t)$, where B is the vibration amplitude and ω is the frequency. The SQUID output voltage, $V(t)$, then follows the relationship $V(t) = AB^2\sin^2(\omega t) = \frac{1}{2}[1 - \cos(2\omega t)]$, where A represents a scaling constant associated with the magnetic moment of the sample. So, a lock-in amplifier isolates the signal at 2ω, which is generated exclusively by the sample. This isolation is accomplished by multiplying the measured signal by a phase-corrected reference signal at frequency 2ω, followed by retrieval of the resulting DC output, which is proportional to the measured signal's 2ω component. This method effectively separates the sample's signal from noise sources, including mechanical vibrations and drift in the SQUID signal. The lock-in amplification is performed digitally within the control module, ensuring precise and noise-free measurements of the sample's magnetization.

3.6 Micro-Raman Spectroscopy

Micro-Raman spectroscopy [305, 306] is a powerful, non-invasive, and non-destructive analytical tool, used to investigate the vibrational modes of molecules in materials, providing insights into chemical composition, crystallography, stress, phase transitions and lattice dynamics at microscopic scales. This method is particularly effective for

studying low-dimensional and nanostructured materials [306–309], such as graphene [310], TMDCs, layered vdW magnetic materials, etc., due to its high spatial resolution and sensitivity to vibrational characteristics. The addition of a microscope in micro-Raman spectroscopy enables focusing the laser onto a very small area typically down to a few micrometers (laser spot diameter of ~ 0.7 µm). This feature allows for spatially resolved Raman measurements, making it possible to analyze specific regions of heterogeneous samples, such as defects, grain boundaries, or phase inclusions within a material, including detailed analysis of phonon modes, structural phases, spin- charge-lattice coupling, and lattice dynamics of micron size flakes of 2D vdW materials [308, 309].

The Raman effect [311, 312], on which this technique is based, was discovered by the Indian physicist C. V. Raman in 1928, who later received the Nobel Prize in Physics in 1930 for his groundbreaking work. Micro-Raman spectroscopy is based on inelastic light scattering, where incident photons interact and carry the energy of the characteristic molecular vibrations in a sample, causing a small fraction of scattered photons to shift in frequency, which is the main principle of the Raman effect. In a typical Raman experiment, a monochromatic laser source illuminates a sample, and the scattered light is collected and analyzed. Most of the scattered photons retain the same energy (or frequency) as the incident photons, a process referred to as Rayleigh scattering (elastic scattering). However, a small fraction of photons undergo a shift in energy (or frequency) due to interactions with molecular vibrations, known as Raman scattering (inelastic scattering). This energy shift, called the Raman shift, corresponding to the vibrational energy levels of the molecules, provides a unique "fingerprint" for each material. This shift is observed as peaks in a Raman spectrum, where the positions of the peaks correlate to the vibrational energies of the material.

Raman spectra [305, 311] are characterized by two distinct types of scattering: Stokes and anti-Stokes lines. These lines arise from different interactions between the incident light and the vibrational modes of the material.

(i) Stokes Line: The Stokes shift occurs when the scattered photon loses energy to the material, causing an increase in the vibrational energy of the system. As a result, the scattered light has a lower frequency (longer wavelength) than the incident light. This corresponds to a peak in the Raman spectrum at a frequency lower than that of the exciting laser.

(ii) Anti-Stokes Line: In contrast, anti-Stokes scattering occurs when the scattered photon gains energy from the material, resulting in a decrease in the vibrational energy

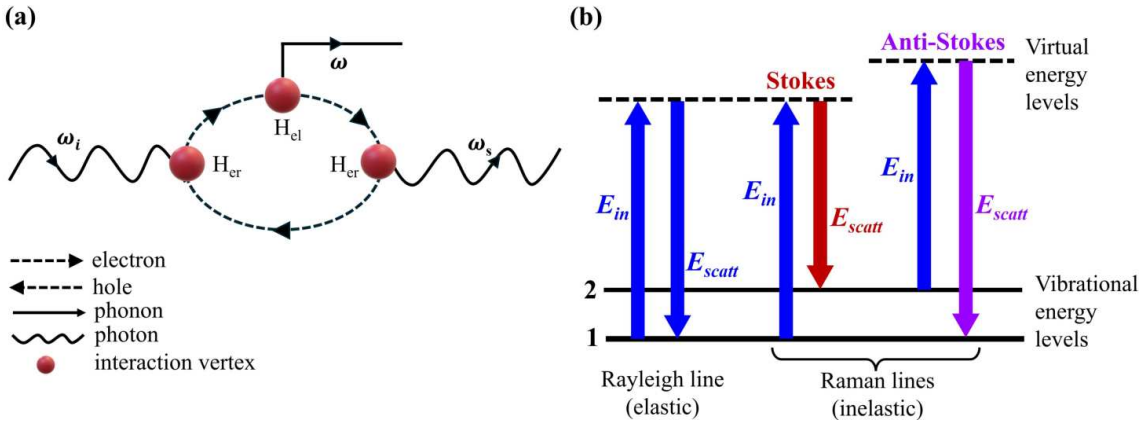

FIGURE 3.76: Schematic representation of the mechanism of the Raman effect.

of the system. This leads to a scattered light that has a higher frequency (shorter wavelength) than the incident light. The anti-Stokes peaks in the Raman spectrum appear at frequencies higher than the excitation wavelength.

Valuable insights into the material's thermal characteristics can be gained from the relative intensities of the Stokes and anti-Stokes lines. At higher temperatures, the population of higher vibrational states increases, leading to stronger anti-Stokes scattering. At lower temperatures, the population of the lower vibrational states is more significant, making the Stokes lines more intense.

• The Microscopic Theory of Raman Effect:

The microscopic theory of the Raman effect [313] can be understood as follows: an incoming photon with angular frequency ω_i interacts with a material, either creating or annihilating lattice vibration quanta (phonons). During this interaction, the lattice gains or loses energy $\hbar\omega$, which is reflected in the scattered photon's frequency ω_s, resulting in either a frequency reduction (Stokes scattering, $\omega_s = \omega_i - \omega$) or an increase (anti-Stokes scattering, $\omega_s = \omega_i + \omega$) (see Fig. 3.76 (a)).

Focusing on the first-order Raman effect, where a single phonon is involved, the Stokes scattering process consists of three steps: absorption of an incident photon (ω_i), creation of an optical phonon (ω), and emission of a scattered photon (ω_s). Initially, the material occupies the electronic ground state, where valence bands are full and conduction bands are empty, and it reverts to this state after the scattering process. During the intermediate stage, virtual electronic states are formed through electron-hole pair excitations. The energy shift in the scattered photons depends on the initial vibrational state of the molecule. If the molecule starts in its vibrational ground state, Stokes scattering occurs,

producing a lower-energy scattered photon. In contrast, anti-Stokes scattering occurs when the molecule starts in an excited vibrational state, producing a scattered photon with higher energy. As shown schematically in Fig. 3.76 (b), Stokes scattering elevates the scatterer to a higher energy state, while anti-Stokes emission corresponds to a transition from an excited to a lower energy state. Both Stokes and anti-Stokes modes are symmetrically positioned around the Rayleigh line because they originate from identical energy transitions. However, generally, the anti-Stokes line's intensity signal tends to be weaker due to the lower population of molecules in excited vibrational states.

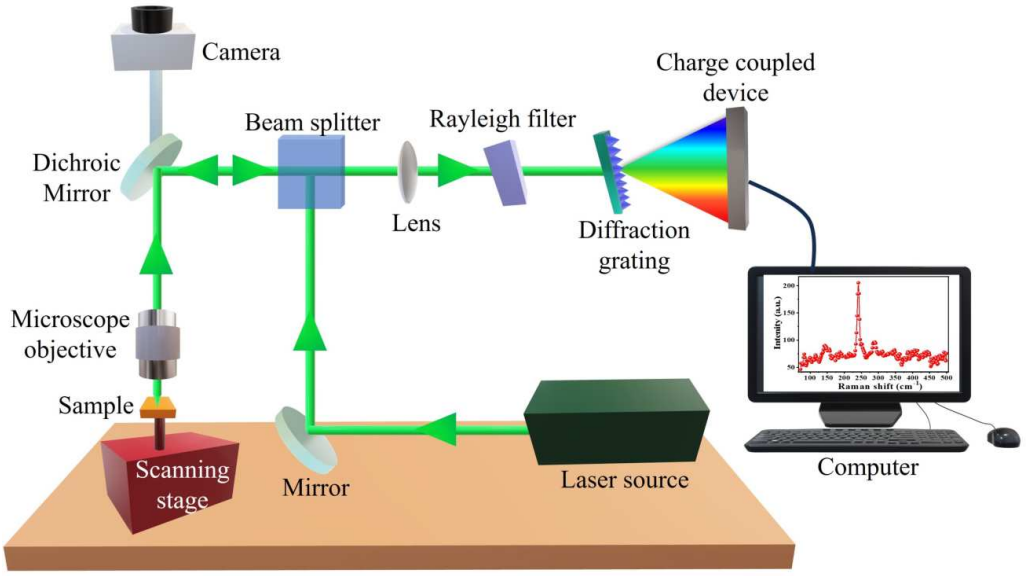

FIGURE 3.77: Schematic diagram of Raman spectrometer.

Micro-Raman spectroscopy [307] instruments generally consist of a laser source, a microscope, a sample stage, a spectrometer, and a sensitive detector. A monochromatic laser, often in the visible or near-infrared range, serves as the excitation source. The sample, positioned on a stage beneath the microscope, is illuminated by the focused laser beam, with scattered light collected through the same optical path. The Raman-scattered photons, which are of the same wavelength as the incident photons, are typically filtered out using a notch filter. Optical fiber cables are employed to collect the transmitted laser beams from the samples, and the sensitive charge-coupled device (CCD) detector displays the resulting Raman spectrum. Different configurations, such as confocal Raman microscopy, are used to enhance spatial resolution, enabling 3D imaging of the sample's chemical composition. Additionally, polarized Raman spectroscopy and temperature-controlled stages can be integrated to obtain further insights into the sample's anisotropic properties or phase transitions. Furthermore, each 2D material has a distinct vibrational

FIGURE 3.78: Image of the Raman setup at SNBNCBS.

spectrum, and these spectra exhibit variations in intensity or position depending on the material's thickness. The experimental setup is depicted schematically in Fig. 3.77.

In SNBNCBS, we used the Horiba LabRAM HR800 micro-Raman spectrometer (see Fig. 3.78), which consists of a 532 nm or 488 nm wavelength argon-ion laser, a thermoelectrically cooled (Peltier-cooled) CCD detector with 1024 × 256-pixel resolution, a 100x objective lens, and a 600 gr/mm or 1800 gr/mm grating with a numerical aperture of 0.9, which produced a laser spot diameter of approximately 0.7 µm. For temperature-dependent measurements down to liquid nitrogen temperature ($\sim$ 80 K), Linkam THMS600 was used.

In this thesis, micro-Raman spectroscopy was employed to conduct an in-depth experimental investigation of phonon modes and spin-phonon coupling in exfoliated Fe_4GeTe_2 nanoflakes.

3.7 ESR Instruments and Techniques

Resonance in ESR or FMR typically occurs in the microwave range, with external magnetic fields generated by water-cooled electromagnets for standard frequencies, or by superconducting magnets for higher frequencies. The standard frequency bands include X (8.20-12.40 GHz), K_u (12.40-18.00 GHz), and K (18.00-26.50 GHz), while higher frequency bands such as K_a (26.50-40.00 GHz), Q (33-50 GHz), V (50-75 GHz), W (75-110 GHz), and mm or G (110-300 GHz) bands require superconducting magnets [129]. Among these, the X-band spectrometer ($\sim$ 10 GHz) is the most widely used due to its suitability, convenience, and cost-effectiveness. Additionally, for higher frequencies, HF-ESR spectrometers are employed, and both systems are discussed briefly in the following sections.

3.7.1 X-band ESR Spectrometer

The X-band spectrometer, operating at a microwave frequency of approximately 9.56 GHz (wavelength $\sim$ 30 mm) within the X-band range of 8–12 GHz, is a widely used tool for detecting electron spin resonance in various materials. In this study, a commercially available Bruker EMX X-band spectrometer with a Bruker rectangular resonator (4104OR-C/0801) was utilized [314]. Figure 3.79 displays the schematic representation of the spectrometer.

The spectrometer includes an electromagnet capable of generating a static magnetic field H_0, which can be swept within a range of 0 to 0.9 T. A microwave source, which also functions as a detector, is connected to the sample chamber via a rectangular waveguide. Samples are placed inside a resonant cavity that is tuned to match the waveguide's impedance, achieving a high quality factor (Q) to enhance measurement sensitivity. Additionally, a gas-flow cryostat integrated into the cavity allows precise temperature control within the range of 5-300 K.

Once the resonator is properly tuned, a magnetic field sweep is performed to achieve resonance. During this process, the sample absorbs microwaves, leading to a change in impedance and detuning of the cavity. This detuning causes a reflected signal, which is detected and produces an ESR signal. The detector operates in reflection mode, recording variations in microwave power as a function of the applied magnetic field.

To enhance detection sensitivity, a small modulation field (H_{mod}) is applied alongside the static magnetic field. This modulation enables lock-in detection of the microwave

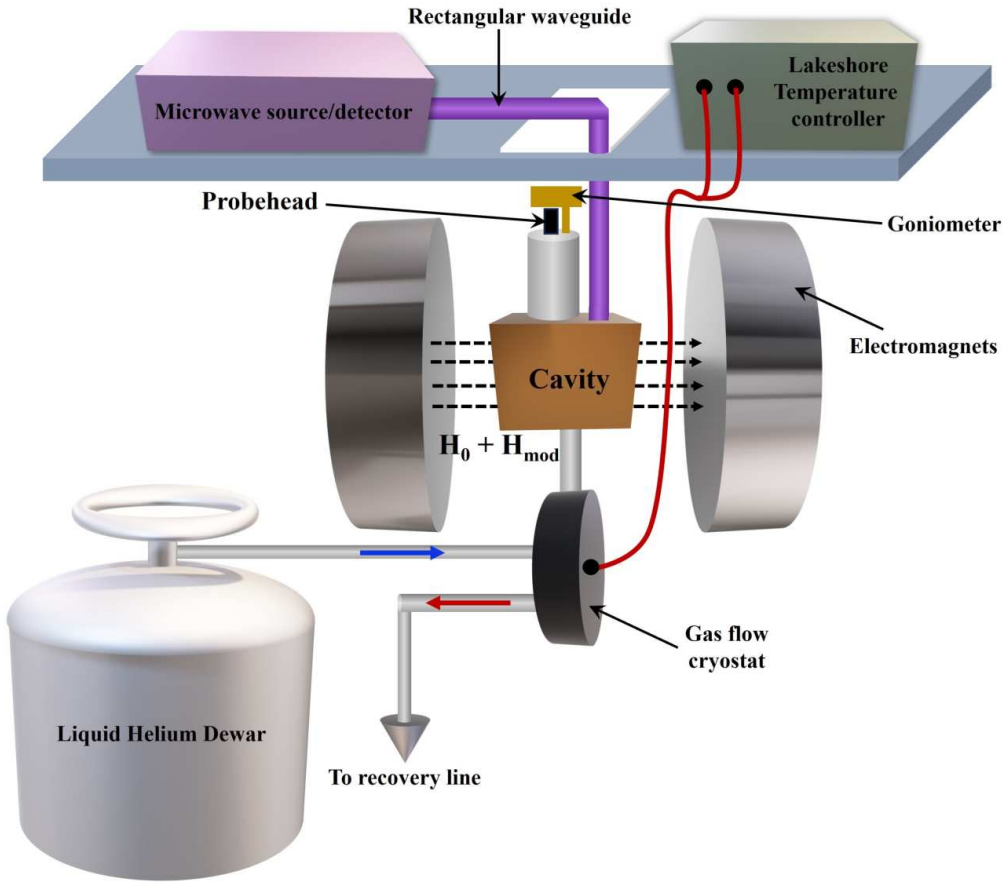

FIGURE 3.79: Illustration of an X-Band spectrometer setup. The sample is affixed to the probehead and positioned within the cavity in a particular orientation with the magnetic field direction. A goniometer enables precise adjustment of the sample's orientation relative to the applied magnetic field. LHe circulates through the heat exchanger for cooling down to 4 K. Temperature stabilization is managed via a Lakeshore temperature controller, which controls the heaters accordingly. The EMX console and magnet controller, responsible for microwave and magnetic field control, are not depicted in the schematic.

intensity at the modulation frequency, significantly improving the signal-to-noise ratio. It also minimizes background interference by removing signal offsets and linear background effects from the spectra. As a result of this field modulation, the recorded ESR spectrum is the first derivative of the original absorption signal.

3.7.2 HF-ESR Spectrometer

High-frequency Electron Spin Resonance (HF-ESR) necessitates a more sophisticated setup compared to conventional X-band spectrometers, as it operates with higher magnetic fields and wider frequency ranges. This advanced technique offers several significant

advantages, such as improved spectral resolution, the ability to detect modes with large zero-field gaps (Δ), the exploration of magnetic phase transitions at higher fields, and the study of fast relaxation phenomena.

The HF-ESR setup [154] (see Fig. 3.80) comprises four key components, briefly described below.

1. Magneto-cryostat and Variable Temperature Insert (VTI):

The cryostat, manufactured by Oxford Instruments, ensures cryogenic temperatures for the sample and cools the superconducting magnet. It consists of three chambers: a liquid nitrogen tank, a LHe bath, and a VTI. The nitrogen tank serves as a thermal shield, reducing helium boil-off and increasing the efficiency of LHe usage, while an outer vacuum chamber (OVC) insulates the cryostat from the surroundings. The helium bath stores LHe (see similar process of LHe transfer in Section 3.2.1.5) and maintains the superconducting magnet at low temperatures, and this is vacuum-insulated from the nitrogen tank to minimize thermal leakage. A needle valve regulates helium flow into the VTI, enabling precise temperature control of the sample from 300 K to 1.6 K. The VTI, insulated by an inner vacuum chamber (IVC), allows rapid temperature adjustments and minimizes helium consumption during high-temperature experiments. Heating coils and a Cernox sensor, controlled by an Oxford iTC temperature controller, maintain stable temperature conditions. For temperatures below 4.2 K, the VTI is pumped to a pressure of a few mBar.

The superconducting magnet, also from Oxford Instruments, consists of coaxial solenoid sections made of multi-filamentary superconducting wires. It generates fields up to $\pm$ 16 T, supports back-and-forth sweeping fields at a maximum of 1 T per minute, and maintains constant fields in persistent mode.

2. Vector Network Analyzer (PNA-X):

The PNA-X millimeterwave vector network analyzer (VNA) from Keysight Technologies (Agilent Technologies) serves as the central instrument for HF-ESR experiments. It generates microwaves across a frequency range of 10 MHz to 67 GHz, extendable to higher frequencies (up to 330 GHz) using external modules with frequency ranges of 75–110 GHz, 140–220 GHz, and 220–330 GHz from Virginia Diodes. The device offers high precision in measuring the relative signal intensity and phase shifts, with a high dynamic range of 129–134 dB, essential for detecting weak signals even in the presence of stronger ones. Phase-locked detection technique distinguishes amplitude and phase changes, corresponding to absorption and dispersion components of the signal.

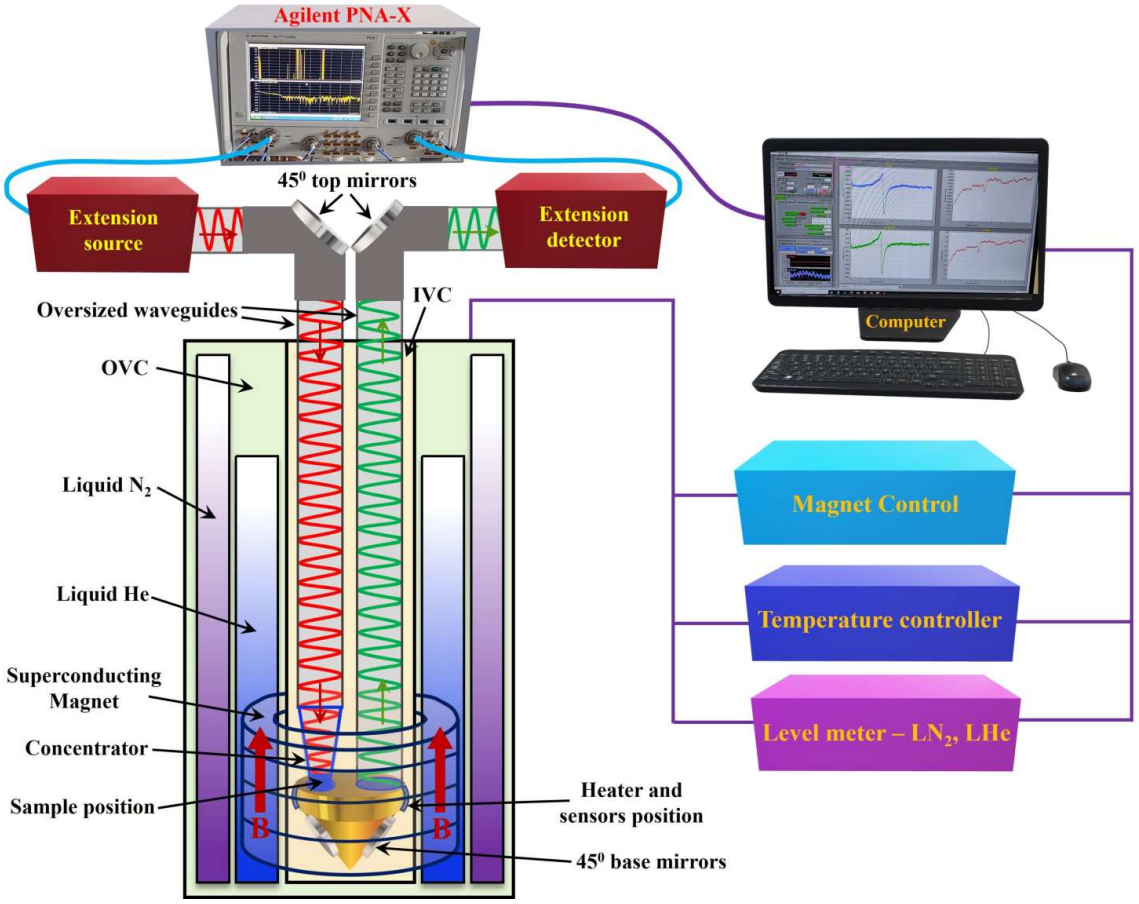

FIGURE 3.80: Illustration of the HF-ESR spectrometer setup. The transmission probehead is housed within a vacuum-sealed variable temperature insert (VTI), which is immersed in a LHe bath and further insulated from the environment by a liquid nitrogen bath. Microwave signals are generated and detected through extensions, with precise control managed by a PNA-X network analyzer. Acting as an oversized waveguide, the probehead efficiently channels microwaves toward the sample and subsequently directs the transmitted signal to the detector.

During a measurement, absorption and dispersion occur simultaneously because of the complex magnetic response of the material to an oscillating field. To correct for signal mixing, a "rotation" of the as-obtained signals to pure absorption is performed using the Kramers-Kronig relation [315, 316], enabling to obtaining of the pure absorption spectra. HF-ESR spectra presented in this work are processed using this method. Also, thermal expansion in the waveguides and signal leaks are accounted for, ensuring accurate signal analysis. To define a general fit function, it is important to consider the slight temperature variations in the waveguides, which lead to continuous thermal expansion and introduce a linear background in the signal. Any signal leakage that does not interact with the sample can also cause a constant offset, which is also accounted for.

3. Waveguides and Sample Space:

A transmission probe head with an oversized 9 mm diameter waveguide transmits microwaves from the microwave source to the sample and detector. Gold-plated mirrors direct the waves through the waveguides. The sample, mounted on a Teflon disc for microwave transparency, is positioned near a concentrator that focuses the microwaves. The sample space is equipped with heating coils and sensors for temperature regulation, enabling measurements over a wide temperature range.

This comprehensive setup (see Fig. 3.80 for schematic) facilitates high-resolution HF-ESR measurements, allowing for advanced exploration of magnetic phenomena. Further details can be found in the PhD dissertations of C. Golze [317], A. Alfonsov [154], and J. J. Abraham [318].

Chapter 4

Transport Measurements in Quasi-2D vdW Ferromagnet Fe_4GeTe_2

Nontrivial spin textures driven by strong exchange interaction, magneto-crystalline anisotropy, and electron correlation in a low-dimensional magnetic material often lead to unusual electronic transitions. Through a combination of transport experiments in exfoliated nanoflakes down to 16 layers and first principle calculations, we unravel emergent electronic phases in quasi-2D van der Waals ferromagnet, Fe_4GeTe_2, possessing ferromagnetic $T_C \sim 270$ K, along with a spin reorientation transition ($T_{SR} \sim 120$ K) with the change of magnetic easy axis. Two electronic transitions are identified. The first transition near T_{SR} exhibits a sharp fall in resistivity, followed by a sign change in the ordinary Hall coefficient (R_0), together with maximum negative magnetoresistance (MR) and anomalous Hall conductivity. Another unusual electronic transition, hitherto unknown, is observed near ~ 40 - 50 K (T_Q), where R_0 again changes sign and below which, the resistivity shows a quadratic temperature dependence and MR becomes positive. An analysis of the experimental data further uncovers the role of competing inelastic scattering processes in anomalous magnetotransport behavior. The DFT-based first-principle calculations unveil two possible magnetic phases, followed by a low-energy model Hamiltonian that captures the essence of these phases as well as explains the observed magnetotransport behavior. Thus, we demonstrate an interplay between magnetism and band topology and its consequence on electron transport in Fe_4GeTe_2, important for spintronic applications.

4.1 Introduction

The discovery of quasi-two-dimensional van der Waals (vdW) magnets [19, 319–323] has opened up a new platform for investigating low-dimensional magnetism and its possible application in two-dimensional (2D) spintronic devices [22, 324–326]. With the recent developments, the family of iron-based vdW magnets, like Fe_nGeTe_2 ($n = 3, 4, 5$) (FnGT) [14, 33, 34, 37, 51–57, 60, 68, 70, 80, 81, 210], especially Fe_4GeTe_2 [14, 70, 80, 81, 210] and $Fe_{5-x}GeTe_2$ [37, 56, 57], have attracted immediate attention due to their ferromagnetic transition temperature (T_C) close to room temperature. The Mermin-Wagner theorem [4] in the 2D limit dictates that there is no spontaneous magnetic order at finite temperature, but the uniaxial magneto-crystalline anisotropy stabilizes the long-range order in these vdW systems against the thermal fluctuations. The enhanced T_C is achieved by increasing the exchange interaction as a result of the metal-rich unit cell [66, 67, 210]. However, the magnetism in these materials is rather complex in nature as compared to a typical ferromagnet, due to the presence of different inequivalent Fe atoms in the unit cell. For example, Fe_3GeTe_2 possesses antiferromagnetic order and noncollinear spin structure below 152 K [35], and also an unusual magnetic behavior was observed in Fe_5GeTe_2 at low temperature due to structural ordering of one of the Fe-atoms in the unit cell at $\sim$ 120 K [37]. More recently, it has been reported that bulk Fe_4GeTe_2 single crystal exhibits a change in easy axis of magnetization when cooled below $\sim$ 120 K, termed as the 'spin reorientation transition' (SRT) [14, 210], making it magnetically quite different from the other two family members. A similar spin reorientation transition was observed in materials like Fe_3Sn_2 [71–74], $Nd_2Fe_{14}B$ [327], $TbMn_6Sn_6$ [75–77], $LiMn_6Sn_6$ [80], $NdCrSb_3$ [328], $La_{0.4}Sm_{0.3}Sr_{0.3}MnO_3$ [329] etc. The interplay between magnetic exchange and effective magnetic anisotropy is possibly the reason for this spin reorientation [78, 81, 210]. The recent transport measurements indicate that the SRT may lead to Lifshitz transition in the electronic structure and, as a result, the system may exhibit unusual magneto-transport and anomalous Hall effect (AHE) [79, 80]. While in the case of Fe_4GeTe_2, an anomaly in the specific heat was seen, indicating that it is indeed a thermodynamic phase transition [81], its consequence on electron transport is still elusive.

Besides the unusual magnetic properties, electronically, these materials possess interesting features. All the members of the Fe_nGeTe_2 family are predicted to be semimetal as the DFT-based calculations show multiple band crossings at the Fermi level [58, 59]. More importantly, the presence of different crystal symmetries and the spin-orbit coupling (SOC) may suggest a topologically nontrivial phase with unusual effects induced by the chiral anomaly, like negative MR or nonlinear conductivity in the diffusive limit [60].

Furthermore, the broken time-reversal symmetry (TRS) in these topological phases hints a more exotic ground state leading to observations like large intrinsic AHE (in Fe_3GeTe_2) [61] or unusual magnetotransport behavior at low temperatures [62]. These systems often exhibit non-monotonic transport features correlated with temperature-dependent magnetization [63]. While the low-temperature transport is relatively easy to address as the effect of inelastic electron-phonon or electron-magnon interactions is negligible compared to the intrinsic effect, the role of these competing interactions on the transport behavior at intermediate or high temperatures is not fully established [330].

In this chapter, we study the temperature-dependent electronic and magnetotransport behavior of Fe_4GeTe_2 single crystal in detail. By fabricating multilayer Hall bar devices on predefined Ti/Au contacts using the dry transfer method, we studied the temperature-dependent resistivity, MR, and Hall effect from room temperature (300 K) down to 1.6 K. In particular, we observe the direct consequences of the SRT on the charge conduction mechanism, leading to a change in the majority carrier types, confirmed by the temperature-dependent ordinary Hall coefficient. Remarkably, a sharp decrease in resistivity, followed by the enhanced negative MR and the maximum anomalous Hall conductivity, was observed near the SRT. While the analysis of resistivity data uncovers the role of different inelastic scattering mechanisms like electron-electron, electron-magnon, and electron-phonon interaction in the different temperature ranges, we find that electron-magnon scattering is also responsible for the temperature-dependent MR and AHE. Finally, we report an electronic transition (T_Q) occurring near $\sim$ 40 - 50 K, below which, the resistivity shows a quadratic temperature dependence, consistent with Fermi-liquid behavior, along with a weak positive MR. All the above experimental results were verified and compared to elucidate the electronic properties in the thin limit using two distinct exfoliated devices with thicknesses of $\sim$ 95 nm (D95) and $\sim$ 16 nm (D16). DFT-based first-principle calculations unravel two quasi-degenerate magnetic phases, collinear FM (cFM) and non-collinear FM (nFM), which are associated with the spin reorientation transition. The electronic structures and fermiologies of the two magnetic phases also reveal Fermi surface reconstruction near this transition. Motivated by the DFT result, a two-channel Heisenberg Hamiltonian is introduced to explain the SRT in Fe_4GeTe_2.

4.2 Experimental Methods

4.2.1 Crystal Structure, Sample Preparation, and Characterization

• **Crystal Structure:** A single layer of Fe_4GeTe_2 consists of seven atoms (Fe_1 and Fe_2 arranged on both sides of the Ge atomic plane and they are connected with Te atoms directly on both sides) as shown in Figure 4.6**a**. The stacking of these Fe_4GeTe_2 monolayers forms a rhombohedral structure with space group $R\bar{3}m$ (Point group No. 166) [210]. Electronically, this has been predicted to be a different class with nontrivial topology, unlike Fe_3GeTe_2 or Fe_5GeTe_2 [58, 59]. The thickness of the monolayer Fe_4GeTe_2 is around 1 nm [210].

• **Fe_4GeTe_2 Single Crystal Growth:** The high-quality single crystal Fe_4GeTe_2 was grown[1] by the standard chemical vapor transport (CVT) method along with I_2 as a transport agent. Here, we have used the mixture of highly pure (99.99%) Fe, Ge, and Te materials powder with a molar ratio of 5:1:2 in a high vacuum quartz tube and this was heated for seven days at 725^0 C. The resultant material was further inserted inside an evacuated quartz tube and placed in a gradient temperature-based horizontal furnace with temperatures 800^0 C and 750^0 C maintained on each end for seven days along with the transport agent I_2 (2 mg cc^{-1}). Tiny pieces of thin single crystals were collected from the cold end of the quartz tube, each one having the typical dimensions of 1.3 × 1.3 × 0.05 mm^3. The details of the crystal preparation are given in the earlier report [14].

• **Crystal Characterizations:** Basic characterizations like X-ray diffraction (XRD) are performed on a freshly cleaved thin and shiny single crystal of Fe_4GeTe_2 [14]. The presence of very sharp (0 0 l) peaks in the diffraction pattern confirms the high crystalline quality of the as-grown crystals. It also proves that the flat plane of the crystal is perpendicular to the crystallographic c-axis. From the Rietveld refinement of the XRD pattern, the calculated value of the lattice parameter c is estimated to be 28.74 Å, consistent with the earlier reports. The extracted lattice parameters from the XRD analysis were found to be, a = 9.97 Å and $\alpha = 23.3°$, which are also consistent with the reported value. The high-resolution transmission electron microscopy (HRTEM) image in our earlier report clearly illustrates the high-quality crystalline nature of the single crystals. The value of the lattice parameter c calculated from interlayer separation is 28.8 Å, which matches well with that determined from XRD and the previous report on Fe_4GeTe_2 for hexagonal crystal structure. The fast Fourier transform pattern obtained from the HRTEM image is also

[1]The single crystals were grown and characterized by Suchanda Mondal from Prof. Prabhat Mandal's lab at Saha Institute of Nuclear Physics, Kolkata, India

shown there. The energy-dispersive X-ray (EDX) spectroscopy data confirm almost perfect stoichiometry [Fe:Ge:Te = 4.2:1:1.9] and the absence of any impurity in the Fe_4GeTe_2 crystals. The maximum relative error in the calculated atomic ratio is $\sim$ 5 %. All of the details of the characterization are provided elaborately in our earlier reports [14].

4.2.2 Magnetization Measurement Techniques

The magnetization measurements of the bulk Fe_4GeTe_2 crystal were performed at ambient pressure in a superconducting quantum interference device vibrating sample magnetometer (SQUID-VSM) (MPMS 3, Quantum Design, USA) with the magnetic field applied along both out-of-plane and in-plane directions. Before starting the measurement, the remanence of the sample and the superconducting coil was removed by applying a magnetic field to 5 T and then by making it zero with oscillating mode. For each magnetization isotherm in M-B curves, the temperature was stabilized for around 25 min, and data were collected at different stable magnetic fields. The temperature-dependent dc magnetization was measured in the zero-field-cooled (ZFC) condition for the applied magnetic field of B = 0.5 kOe and 0.1 kOe with $B\|$ab and $B\|$c crystallographic axis of Fe_4GeTe_2 crystal. For M-T curves, The data were taken with an interval of 0.25 K with a rate of temperature change of 0.5 K min^{-1}.

4.2.3 Device Fabrication and Characterization

4.2.3.1 Device Fabrication

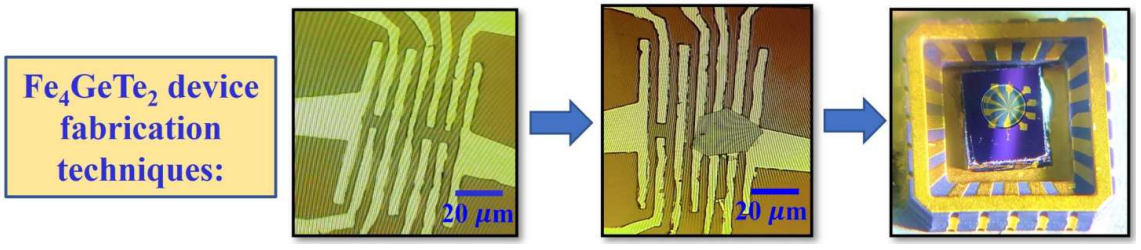

FIGURE 4.1: Thin flakes of Fe_4GeTe_2 are transferred by standard dry transfer technique on pre-patterned gold electrodes on Si/SiO_2 substrate.

As these ferromagnetic materials are sensitive in ambient conditions, we fabricated the Hall bar devices through the dry-transfer method on pre-patterned Ti (10 nm)/Au (45 nm) contacts on a 285 nm SiO_2/Si(p++) substrate. First, we fabricate gold pads using optical lithography (LW405 by MICROTECH) and a lift-off process followed by oxygen

plasma treatment (ICP-RIE unit by SENTECH 500) to clean the organic residues (see Section 3.1.7.3). Then we exfoliate thin layers of Fe_4GeTe_2 crystal by standard mechanical exfoliation on a thin polydimethylsiloxane (PDMS) layer and transferred onto the gold pads at an elevated temperature (90^0 C - 110^0 C) using a home-made dry-transfer set up (see Section 3.1.8.1). The device was then immediately coated with PMMA (microresist technology) e-beam resist to avoid any oxidation of the flake (see Section 3.1.9). The whole transfer process was completed within 30 minutes. The device was then bonded with silver paint (SPI supplies) (see section 3.1.10).

4.2.3.2 Device Characterization

• Determination of the Thickness via AFM:

Atomic force microscopy (AFM) was conducted to determine the thickness of the exfoliated Fe_4GeTe_2 crystal. After completing all measurements, the PMMA layer was removed from the top of the Fe_4GeTe_2 crystal, and AFM was immediately performed at different positions. The mean thickness of the exfoliated crystal for the D95 device is 95 nm ($\sim$ 95 layers), and for the D16 device, it is 16 nm ($\sim$ 16 layers), as determined from the height profile.

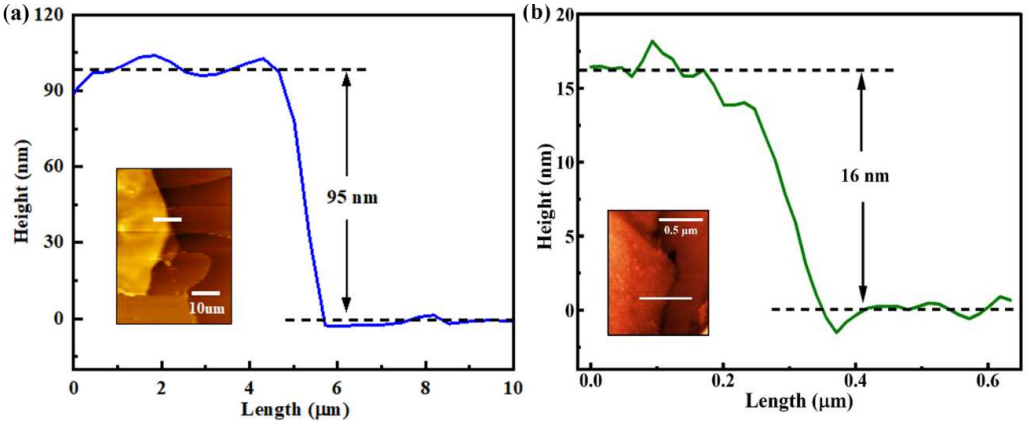

FIGURE 4.2: Height profile of the Fe_4GeTe_2 flakes of the device D95 (a) and D16 (b). The inset shows the corresponding AFM images.

• Raman Spectra of Fe_4GeTe_2 Crystals of Different Thicknesses:

Raman spectroscopy measurements were conducted at room temperature (300 K) for Fe_4GeTe_2 crystals with three different thicknesses: $\sim$ 0.1 mm thick bulk, 95 nm flake (D95), and 16 nm nanoflake (D16), as shown in Figure 4.3. These measurements were

performed using the LabRam HR Evolution (HORIBA, France SAS) setup with a laser wavelength of 532 nm.

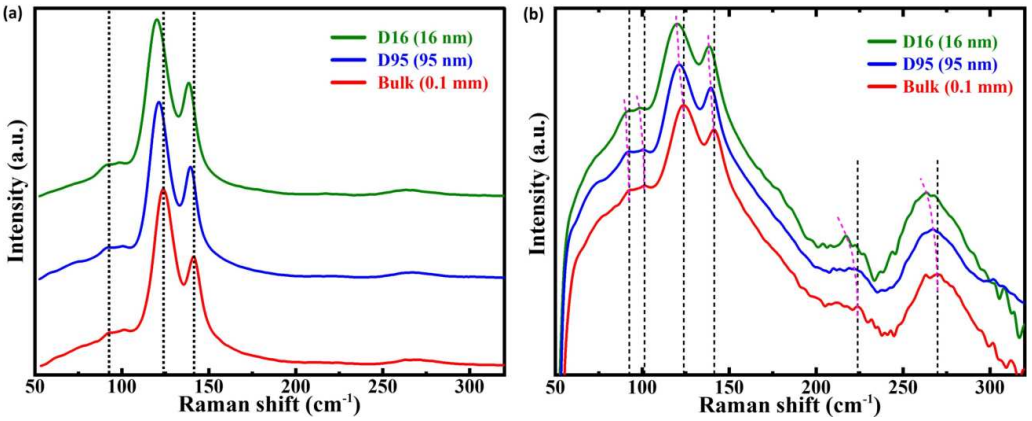

FIGURE 4.3: Room temperature Raman spectra of Fe_4GeTe_2 crystal of three different thicknesses, D16 (16 nm), D95 (95 nm) and bulk ($\sim$ 0.1 mm). (b) The Raman data is plotted in a log scale to observe the low intense peaks. All the peaks are red-shifted with decreasing thickness. The black dotted lines indicate the peak positions of the bulk sample and the redshift for thinner flakes is shown by the pink dotted line.

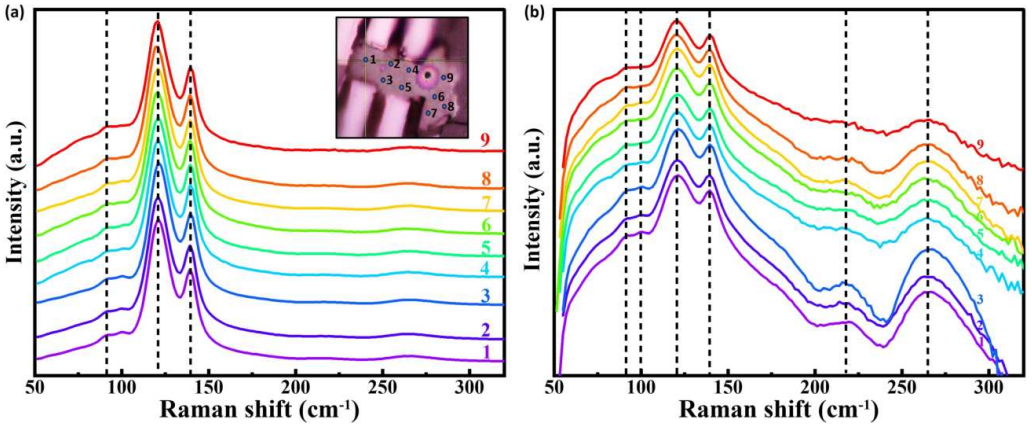

FIGURE 4.4: Raman spectra to determine the uniformity of thickness of the thin flakes. (a) Raman spectra were obtained at room temperature for the 16 nm Fe_4GeTe_2 crystal (D16) across its nine different positions. Inset: The positions of the laser spot where the scanning was performed. (b) The Raman data is presented in a logarithmic scale to facilitate clear observation of all the peaks. Almost uniform peak positions are observed across the crystal, indicating consistent thickness throughout. The black dotted line serves as a visual guide near the position of the peaks.

In the bulk sample, two prominent peaks were observed at $\sim$ 124 cm^{-1} and $\sim$ 141.4 cm^{-1}, along with several smaller, less intense peaks that are better visualized in the semi-logarithmic plot of the same data (see Figure 4.3 (b)). Four additional peaks at $\sim$ 92.5 cm^{-1}, $\sim$ 101.2 cm^{-1}, $\sim$ 224 cm^{-1}, and $\sim$ 269 cm^{-1} were also identified. A continuous red shift was observed in the thinner flakes as the thickness decreased down to 16 nm. Since the thickness-dependent Raman spectra have not been reported previously, the origin of

the peaks remains unclear at this stage. The red shift observed in the thinner layers may be attributed to the phonon confinement effect in the 2D limit [331], although a systematic investigation and theoretical understanding are necessary to elucidate the exact nature of these peaks. Nevertheless, our data clearly indicate that both the D95 and D16 devices exhibit properties distinct from the pure bulk. Furthermore, Raman spectra were collected across various positions of the flake. As depicted in Figure 4.4(a) and (b) (for D16), it is evident that the positions of the peaks remain consistent throughout the flake, signifying its uniform thickness.

4.2.4 Magneto-transport Measurement Techniques

The contacts of the fabricated devices were checked using SR830 lock-in and Keithley 2450 source meter. All the contacts were found to be ohmic. The in-plane resistivity, Hall coefficient, and other transport measurements are performed using standard lock-in techniques at frequency 234.1 Hz in a low-temperature magneto-transport setup (Teslatron, Oxford Instruments) in the temperature range: 1.6 K - 300 K. The four-terminal resistivity (ρ) is calculated from the measured resistance (R) (see Section 3.3.2 and 3.3.3 for measurement techniques) using the formula, $\rho = R \times (W \times t/L)$, where W is the width of the flake, t is the thickness of the flake and L is the distance between two longitudinal electrodes. To eliminate the longitudinal component due to small misalignment of the Hall electrodes, the Hall resistivity (ρ_{xy}) was measured by taking the data for both positive and negative magnetic fields and then taking the anti-symmetric components of the Hall resistivity by using the formula: $\rho_{xy}(B) = (\rho_{xy}(+B) - \rho_{xy}(-B))/2$.

4.2.5 Theoretical Calculation and Computational Details

The density-functional theory (DFT) simulation was performed[2] by using the Vienna Ab initio Simulation Package (VASP) [332, 333]. For the exchange-correlation between electrons, the generalized gradient approximation (GGA) was employed and it was parametrized by Perdew-Burke-Ernzerhof (PBE) [334]. The projector-augmented wave (PAW) approach was employed to characterize the interaction between the core and valence electrons [335, 336]. The plane-wave energy cutoff is set at 400 eV. The Brillouin zone (BZ) is sampled using the Monkhorst−Pack technique [337] with a grid spacing of 0.01 for all calculations, which yields equivalent $29 \times 29 \times 29$ and $30 \times 30 \times 3$ k-point

[2]Theoretical calculations were performed by Dr. Rajesh O. Sharma from Prof. Tanmoy Das's group at IISc Bangalore, India

meshes for rhombohedral and hexagonal unit cells, respectively. The structural relaxation was carried out until the forces acting on each atom were less than 0.0001 eV/Å. The convergence threshold for energy in the electronic self-consistent cycle was set to 10^{-8} eV. The simplified method suggested by Dudarev *et al.* [338] was used to make the GGA+U calculations, which simply considers the difference of U and J ($U_{\text{eff}} = U - J$). The value of U_{eff} for Fe $3d$ was set at 4.0 eV [339], while it is zero for the other atoms. We also performed the spin−orbit coupling (SOC) calculations. The Fe_4GeTe_2 crystal structure belongs to the space group $R\bar{3}m$ (No. 166). The position of the atoms was relaxed while maintaining the lattice constants at the experimental values [14, 210] of $a = b = 4.044$ Å and $c = 29.247$ Å for the hexagonal unit cell. The band structure and Fermi surface (FS) calculations were performed using the rhombohedral primitive cell (see Figure 5.7**a-c**), which was generated using the VASPKIT code [340]. Fe atoms in the primitive cell are shown in different colors. All the crystal structures shown here were created using VESTA software [341].

4.3 Experimental Results and Discussion

4.3.1 Magnetization Measurement

• Temperature Dependence of Magnetization in Bulk Fe_4GeTe_2:

Single crystal of Fe_4GeTe_2 exhibits the ferromagnetic transition where the dM/dT shows the minimum at $T_C \sim 270$ K, followed by the SRT at ~ 120 K below which the magnetization along out-of-plane direction becomes larger than that of its in-plane value (see Figure 4.6**b**).

• Magnetic Field Dependence of Magnetization in Bulk Fe_4GeTe_2:

The magnetic field (B) dependence of the bulk Fe_4GeTe_2 sample's magnetization was evaluated at various temperatures ranging from 5 K to 300 K for both $B \parallel c$-axis and $B \parallel ab$-plane orientations, as shown in Figure 4.5(a) and (b). The saturation magnetization (M_s) was determined as the point where the magnetic moment becomes nearly independent of the applied magnetic field. Notably, at high fields (above 7 T), M saturates ($M = M_s$) at lower temperatures (approximately 5 K to 100 K) for both $B \parallel c$-axis and $B \parallel ab$-plane orientations. However, above 100 K, the magnetization does not saturate, and a weak dependence of magnetization on the applied magnetic field is observed. To achieve a more accurate evaluation of the temperature dependence of the saturation magnetization (M_s),

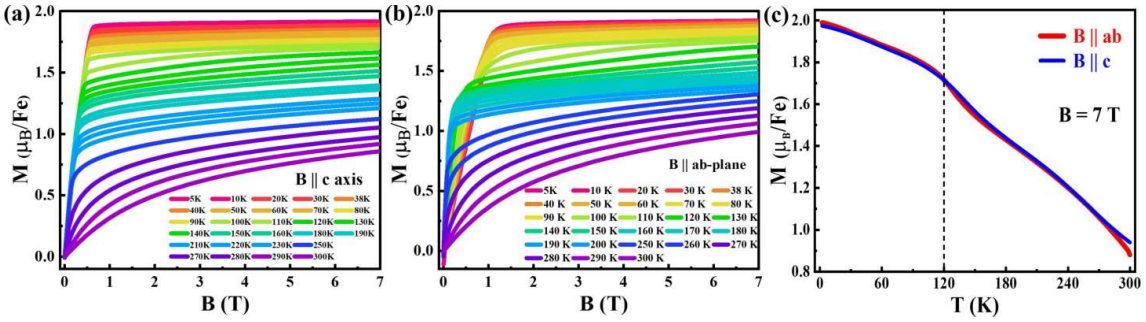

FIGURE 4.5: Magnetic field and temperature dependent magnetization data. Magnetic field dependence of magnetization data at different temperatures, while the magnetic field (B) is applied (a) along the c-axis and (b) along the ab-plane of the Fe_4GeTe_2 crystal. (c) The temperature dependence of magnetization data at constant B = 7 T field gives us the approximate saturation magnetization (M_s) while this magnetic field (B) is applied along the ab-plane and c-axis of the Fe_4GeTe_2 crystal.

M-T measurements were conducted at a constant magnetic field of 7 T for both $B \parallel c$ and $B \parallel ab$-plane orientations, as illustrated in Figure 4.5 (c). At 5 K and a high field of 7 T, the saturation magnetization ($M = M_s$) is approximately 1.9 μ_B/Fe for both $B \parallel c$-axis and $B \parallel ab$-plane, consistent with previously reported values [14, 78, 210]. However, as depicted in Figure 4.5, the magnetization does not saturate above 100 K, even under a 7 T magnetic field for both orientations. Consequently, the M_s values shown in Figure 4.5 (c) are underestimated above 100 K for both cases.

Since the energy difference between the cFM and nFM phases is non-negligible, a significantly higher magnetic field (above 7 T) is required along both the *ab*-plane and *c*-axis to eliminate the kink-like feature observed near 120 K, as seen in Figure 4.5 (c).

4.3.2 Resistivity Measurement

Figure 4.6 **d** shows the temperature-dependent normalized in-plane resistivity (ρ_{xx}) of two Hall bar devices D95 and D16, fabricated on 300 nm Si/SiO_2 substrate (see section 4.2.3 for details), both measurements were done with a constant ac excitation of 50 μA at zero magnetic field. ρ_{xx} exhibits a metallic behavior, with almost negligible change near the FM transition. However, the resistivity falls dramatically near SRT. ρ_{xx} shows a weak anomaly near T_Q ($\sim$ 40 K), indicated by a clear kink in the $d\rho_{xx}/dT$ curves (blue and green dotted line in Figure 4.6**d**), whose consequence on the transport will be discussed. The residual resistivity ratio (RRR = ρ_{xx}(300 K)/ρ_{xx}(1.6 K)) values of both the exfoliated devices are 3.87 (D16) and 3.04 (D95), while the corresponding absolute conductivity (σ) at T_C ($\sim$ 270 K) are $\sim 9.6 \times 10^5$ $\Omega^{-1}m^{-1}$ (D16) and $\sim 8.6 \times 10^5$ $\Omega^{-1}m^{-1}$ (D95), being relatively

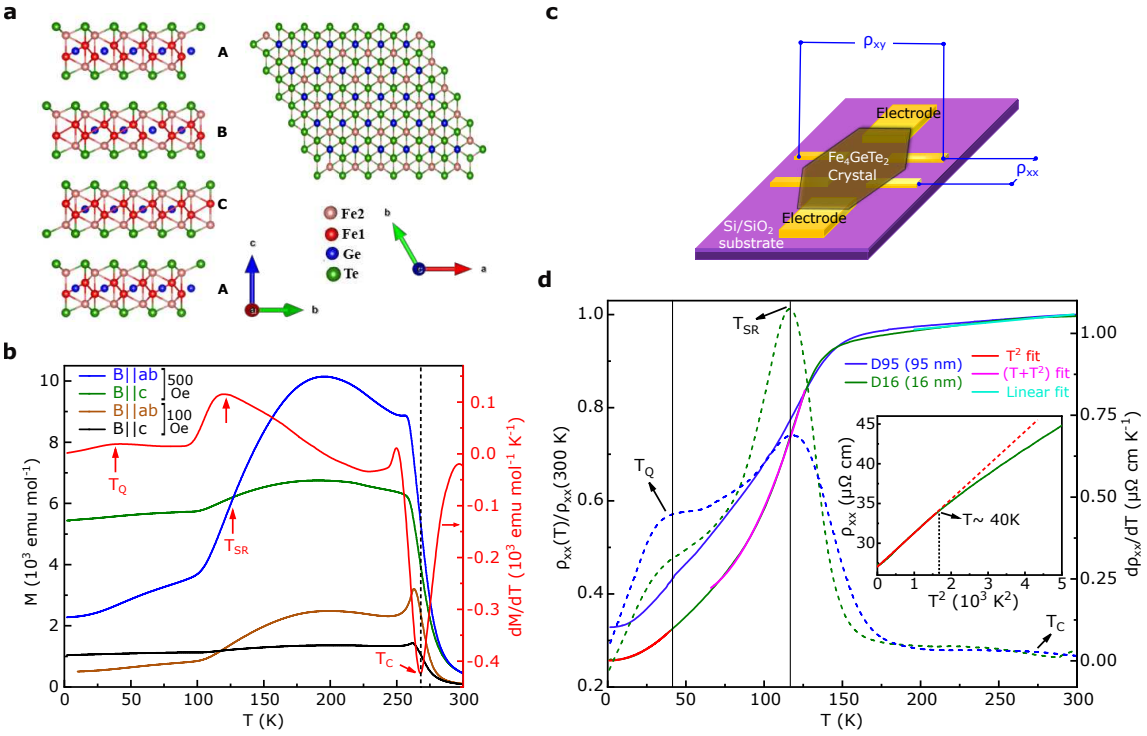

FIGURE 4.6: **Crystal structure, temperature-dependent magnetization, and resistivity. a** Schematic diagram of the structure of Fe_4GeTe_2 crystal: side view (left) and the top view (right). Seven atom-thick Fe_4GeTe_2 monolayers are arranged in the ABC configuration, leading to the formation of the rhombohedral structure with the space group $R\bar{3}m$. **b** The dc magnetization data as a function of temperature are plotted with applied field 500 Oe and 100 Oe along B ∥ ab and B ∥ c of the crystallographic axis of Fe_4GeTe_2 crystal, measured in zero-field-cooled (ZFC) condition. The red curve shows the temperature derivative of the magnetization (dM/dT) data of 500 Oe with B ∥ ab plane, indicates three transitions, Curie temperature (T_C) around 270 K, the spin-reorientation transition (T_{SR}) at around 120 K, and a small kink (T_Q) near ∼ 40 K. **c** Schematic diagram of six-terminal Hall-bar electrodes with transferred Fe_4GeTe_2 multilayer crystal for low-temperature magneto-transport measurements. **d** Temperature dependence of the normalized zero-field electrical resistivity (ρ_{xx}) curves for two different nanoflake devices with thicknesses 95 nm (D95, blue) and 16 nm (D16, green). The corresponding temperature derivatives of resistivity for both devices are shown by the blue and green dotted curves, respectively. Here, the current is applied to the in-plane direction (I ∥ ab plane). Theoretical fits to the temperature dependence of zero-field resistivity data of D16 at different temperature ranges are indicated with red, purple, and cyan colors. Inset: ρ_{xx} vs T^2 curve shows a clear change of slope above ∼ 40 K.

higher compared to several other 2D ferromagnets [24, 60, 323] and consistent with the reported value for this material [210]. Comparatively, a higher conductivity is observed for the thinner device (D16) at the lowest temperature (1.6 K), indicating enhancement of metallicity at reduced thicknesses. This observation also aligns with the findings from earlier reports [210].

According to Matthiessen's rule, the total resistivity of a metallic ferromagnet consists of

all the contributions coming from various scattering mechanisms and they are additive within each conduction band [292, 342]. The temperature dependence of longitudinal resistivity can be written as:

$$\rho_{xx}(T) = \rho_0 + \rho_{e-p}(T) + \rho_{e-e}(T) + \rho_{e-m}(T, B) \tag{4.1}$$

where ρ_0 is the residual resistivity arising due to the temperature-independent elastic scattering from the static defects. ρ_{e-p}, ρ_{e-e}, and ρ_{e-m} are the inelastic electron-phonon, electron-electron, and electron-magnon scattering contributions, respectively. Among these, ρ_{e-p} varies linearly with temperature ($\propto T$) and both ρ_{e-e} and ρ_{e-m} exhibit quadratic behavior with temperature ($\propto T^2$). As the electron-magnon term is strongly dependent on the magnetic field, whereas other terms remain insensitive, the field-dependent resistivity can be used to identify the actual mechanism. It is clear from

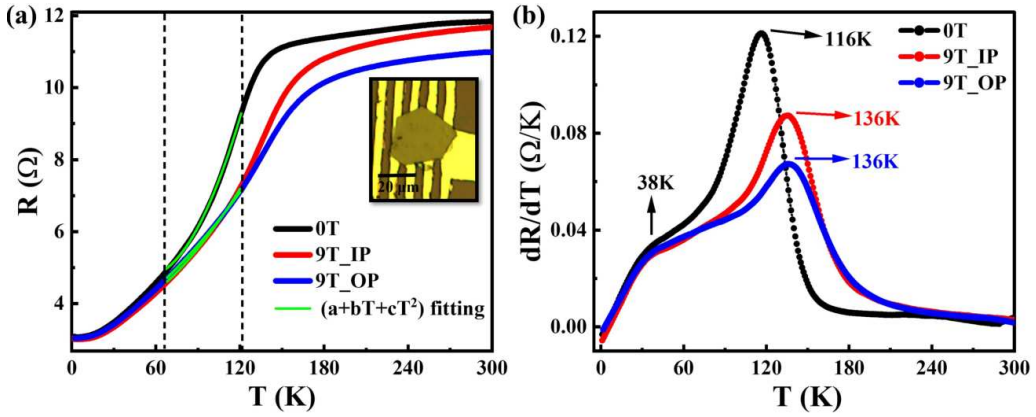

FIGURE 4.7: (a) Temperature dependence of resistance for the Fe_4GeTe_2 nanoflake (D16) measured at 0 T and in a 9 T magnetic field, for both in-plane (IP) (red curve) and out-of-plane (OP) directions (blue curve). The data is fitted using a $(T + T^2)$ dependence in the range 62 K to 122 K, with the coefficient of the T^2 term decreasing in the presence of the magnetic field, indicating a significant electron-magnon contribution in this temperature range. *Inset:* Optical micrograph of the flake on gold electrodes on a Si/SiO_2 substrate, covered with PMMA. (b) Temperature derivatives of the R-T curves show no magnetic field dependence up to approximately 40 K, supporting electron-electron interaction below T_Q. However, strong magnetic field dependence is observed in the range of approximately 40 K to 240 K.

Figure 4.6 (**d**) that the nature of the temperature dependence of resistivity is extremely sensitive to temperature regions. At low temperature regime of 1.6 K to $\sim$ 40 K, ρ follows a perfectly quadratic behavior ($\rho \propto T^2$), corresponding to either electron-electron (e-e) scattering or electron-magnon (e-m) scattering. To identify the actual mechanism, we measured the temperature-dependent resistivity at a high magnetic field (9 T) in both the in-plane and out-of-plane direction of the crystal (See Figure 4.7). It is observed that the resistivity is almost independent of the magnetic field, which suggests that the

dominant scattering mechanism is indeed the electron-electron interaction, rather than electron-magnon scattering, confirming Fermi-liquid behavior [132]. The magnitude of the coefficient of the quadratic term is the measure of the electron-electron scattering rate. Focusing on D16, we found the value of this coefficient to be 4.24 $\times 10^{-9}$ Ω cm K^{-2}, which is nearly two orders of magnitude larger than the elemental ferromagnets like Fe, Co, and Ni, but comparable to the value of the semi-metals like Bi, graphite, etc. [343–348].

In the intermediate range (65 - 125 K), ρ_{xx} can be fitted with the admixture of both linear and quadratic contributions i,e. $\rho = \rho(T, T^2)$. While the linear dependence corresponds to the electron-phonon coupling, the T^2 dependence signifies the electron-magnon scattering. We have fitted the field-dependent resistivity data with $(T + T^2)$ in the intermediate regime between 62 K and 122 K. From the fitting parameters, for zero-field resistance data, the coefficient of T^2 is 9.54 $\times$ $10^{-4}\,\Omega\,K^{-2}$, but for 9 T in-plane and out-of-plane data, this coefficient of T^2 reduces significantly to $2.56 \times 10^{-4}\,\Omega\,K^{-2}$ and $1.44 \times 10^{-4}\,\Omega\,K^{-2}$, respectively. This indicates that the electron-magnon scattering contribution is suppressed due to the application of a higher magnetic field (9 T). This is evident from the fact that the resistivity has a strong dependence on the magnetic field in this regime and the coefficient of the T^2 term is reduced significantly at a high magnetic field. Also, it is important to note that the electron-magnon scattering strength is larger by a factor of four for D16 compared to D95 (see Table 4.2), indicative of an enhanced electron-magnon scattering contribution with reducing thickness.

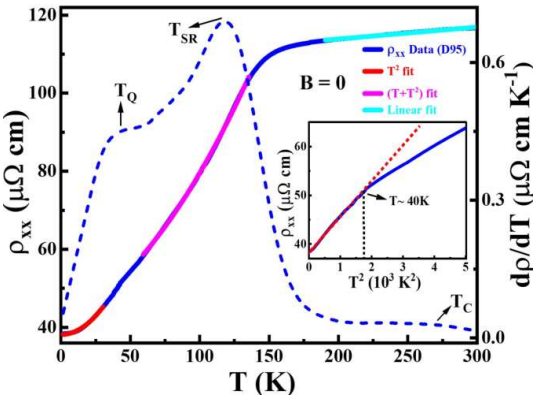

FIGURE 4.8: Temperature dependence of resistivity of the 95 nm thick Fe_4GeTe_2 device (D95). Inset: ρ_{xx} vs. T^2 also shows a clear change in the slope above 40 K.

At high temperatures ($T > 190$ K), well above the T_{SR}, a complete linear dependence of resistivity on temperature is observed ($\rho \propto T$), indicating the dominance of the electron-phonon scattering mechanism. A similar analysis is consistent for device D95 (see Figure 4.8) .

4.3.3 Magnetoresistance Measurement

We next concentrate on the temperature dependence of magnetoresistance (MR). Figure 4.9 (**a**) shows the MR [$= ((\rho_{xx}(B) - \rho_{xx}(0))/\rho_{xx}(0)) \times 100\%$] at different temperatures starting from 300 K down to 1.6 K with the applied magnetic field along the out-of-plane direction (c-axis) of the Fe_4GeTe_2 crystal (D95).

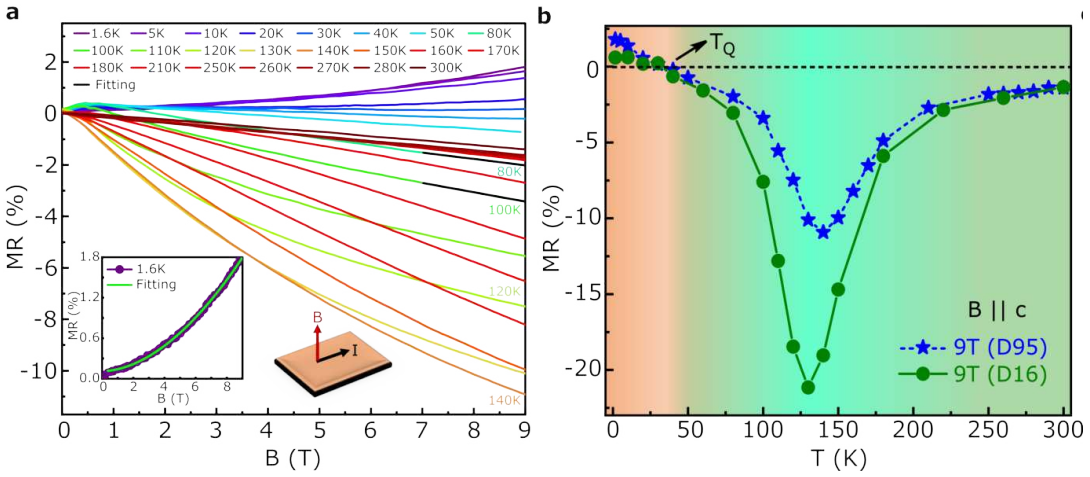

FIGURE 4.9: **MR at different temperatures.** (**a**) Magnetic field dependence of MR measured from temperature 1.6 K up to 300 K. Here, the external magnetic field is applied parallel to the c-axis and the current is in the ab plane of the Fe_4GeTe_2 sample (D95). Black lines are the fitting of Equation 4.4 at 80 K and 100 K. Inset: Low-temperature (3 K) MR is fitted with Equation 4.3. Fitting results provide the value of the parameters, $\mu = 0.147$ m^2 V^{-1} s^{-1} and n = 1.847. (**b**) Temperature dependence of MR is plotted for two devices with applied field 9 T along the c-axis of the crystal, indicating a maximum negative MR at around T_{SR} and a small positive MR below T_Q. Background colors indicate two different regimes, positive and negative MR. Color contrast signifies the magnitude of MR.

In order to eliminate the contribution from the Hall resistance due to a small misalignment of the electrodes, we symmetrize the data using the expression, $\rho_{xx}(B) = (\rho_{xx}(+B) + \rho_{xx}(-B))/2$. The high-field (9 T) MR (Figure 4.9 (**b**)) exhibits several interesting features. MR is predominantly negative in the range between $\sim$ 40 K to 300 K and its value is maximum near the SRT, being $\sim$ 11% for D95 and $\sim$ 21.2% for D16 (see Figure 4.9 (**b**)). As the thinner device is more susceptible to electron-magnon scattering (see Table 4.2), the application of a magnetic field suppresses the resistance more in the case of the thinner device, providing greater negative MR. Below T_Q, MR is small but positive ($\sim$ 1.8% for D95 and 0.6% for D16 at 1.6 K), quite unusual for a metallic ferromagnet. To test whether the electronic properties are isotropic or not, the angle-dependent transverse magnetoresistance (TMR) measurements at 9 T are performed at different temperatures,

as shown in Figure 4.11 (a). While the low-temperature data below 100 K show cosine-like behavior, it shows a phase shift by 90 degrees above the T_{SR}, depicting the easy axis change from the c-axis to the ab-plane with increasing temperature. Figure 4.11 (b) shows the TMR at 9 T within a close temperature interval near the SRT, ranging from 120 K to 150 K. A gradual orientation of spins from the *ab*-plane to the *c*-axis of the crystal is observed as the temperature increases from 120 K to 150 K, with a significant phase change in the MR-θ curve occurring between 140 K and 150 K.

In general, the resistivity of a ferromagnetic material can be expressed as a function of the electronic relaxation time (τ) and its field dependence as [349, 350],

$$\rho_{\text{total}} = k_1(\omega_c\tau)^n + k_2(1/\tau) \tag{4.2}$$

where, ω_c is the cyclotron frequency of the free carriers. Here, the first term is the orbital contribution to the resistivity arising due to the constrained orbital motion of the free carriers under the Lorentz force and is responsible for positive MR. The second term describes the contributions from the various scattering mechanisms as explained in Equation (4.1). The field dependence of the orbital term can be expressed as,

$$\rho_{\text{orb}} \propto (\omega_c\tau)^n = (\mu B)^n \tag{4.3}$$

where μ is the mobility of the free carriers. Ideally, for a nonmagnetic metal, the exponent $n = 2$ [351], but for other systems like doped semiconductors [352], ferromagnetic metallic thin films [292], spin-glass systems [353], etc., its value deviates from 2 and lies in between 1 and 2 ($1 < n < 2$). The orbital MR term in the total resistivity of a ferromagnetic material arises due to the constrained orbital motion of free carriers under the Lorentz force, which increases rapidly with the application of an external magnetic field at low temperatures. We have fitted the low-temperature MR data using Equation 4.3. The obtained parameters are as follows: (i) At 1.6 K, $\mu = 0.147$ $m^2V^{-1}s^{-1}$ and $n = 1.847$ (See Figure 4.9 (**a**) inset); (ii) At 5 K, $\mu = 0.138$ $m^2V^{-1}s^{-1}$ and $n = 1.711$;

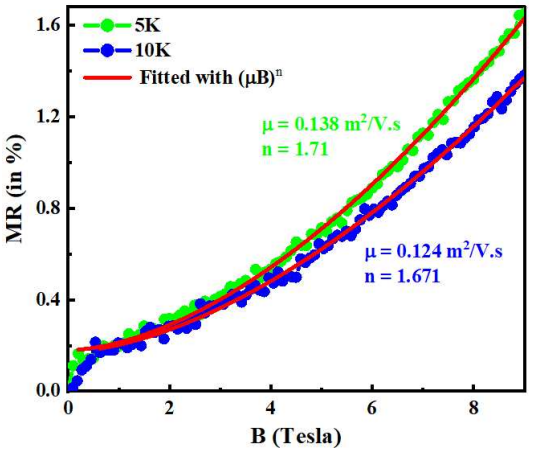

FIGURE 4.10: Magnetic field-dependent MR at 5 K and 10 K with $B \parallel c$-axis, along with the corresponding fitting using the orbital MR term described by the equation MR $\propto (\mu B)^n$.

(iii) At 10 K, $\mu = 0.124$ $m^2V^{-1}s^{-1}$ and $n = 1.671$ (as shown in Figure 4.10). By fitting the positive MR at low temperature, we observe that the exponent n is close to 2, being closer to the behavior of a typical metal having pure orbital contribution. With decreasing temperature, the mobility of free carriers and the exponent n both increase, indicating the dominance of the orbital MR term at much lower temperatures.

At higher temperatures above T_Q, we have observed a crossover in MR from positive to negative (see Figure 4.9**a**), and its value becomes maximum near the SRT. The enhanced MR is associated with the dominance of electron-magnon scattering in this intermediate range, due to the strong coupling between charge and spin degrees of freedom driven by the SRT.

The role of electron-magnon scattering on negative MR in a ferromagnet has been discussed in Ref. [292] and an analytical expression is given, which is valid for magnetic field below 100 T and in the temperature range of $T_C/5$ to $T_C/2$,

$$\Delta\rho_{xx}(T,B) \propto \frac{BT}{D(T)^2} ln(\frac{\mu_B B}{k_B T}) \tag{4.4}$$

where, $D(T)$ is the magnon stiffness or magnon mass renormalization constant, μ_B is the Bohr magneton and k_B is the Boltzmann constant. The high field MR data ($B > 7$ T) above 50 K in the temperature range 80 K and 100 K ($T_C/5 < T < T_C/2$) can be well-fitted with Equation (4.4) (see Figure 4.9**a**), confirming that the non-saturated negative MR is originated primarily due to the suppression of electron-magnon scattering under the external magnetic field.

4.3.4 Hall Measurements

Now, we focus on the Hall effect in Fe_4GeTe_2. Typically, the Hall resistivity (ρ_{xy}) of a ferromagnetic material can be described by an empirical formula [139, 140],

$$\rho_{xy} = \rho_{xy}^{OHE} + \rho_{xy}^{AHE} = R_0 B + \mu_0 R_S M \tag{4.5}$$

Here, the first term is the ordinary Hall resistivity (ρ_{xy}^{OHE}) and the second term represents the anomalous Hall resistivity (ρ_{xy}^{AHE}). From the magnitude of the ordinary Hall coefficient, R_0, one can calculate the effective carrier concentration when a single band picture is valid and its sign determines the type of majority carriers present in the material. On the other hand, the anomalous Hall part is proportional to the spontaneous magnetization (M) and

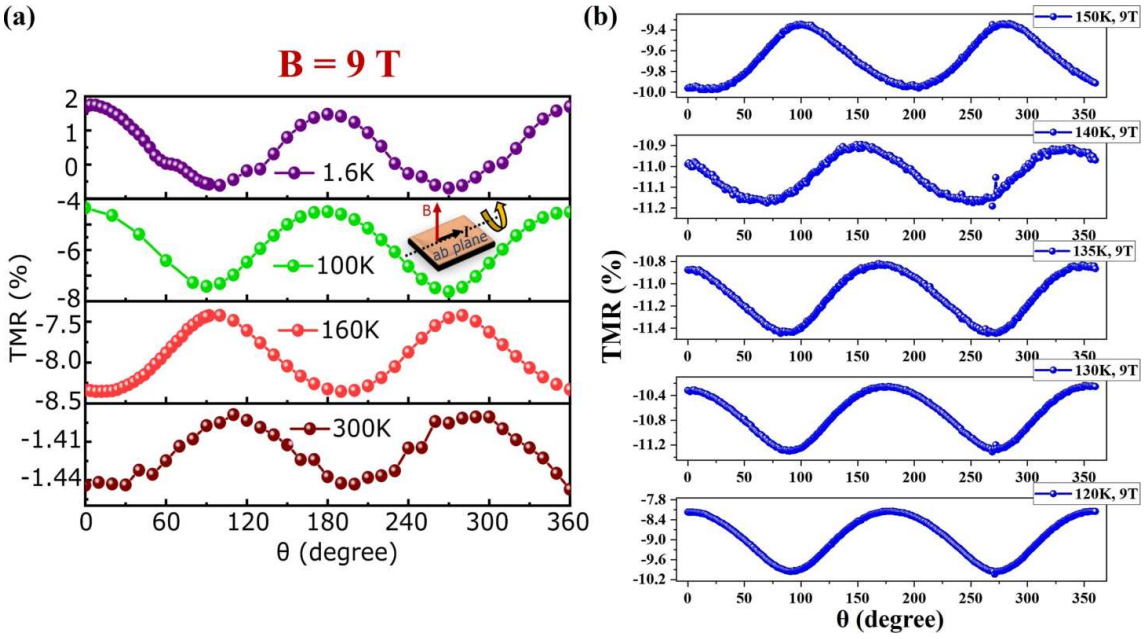

FIGURE 4.11: **a** Angle-dependent TMR at 9 T at different temperatures shows a definite spin reorientation between 100 K and 160 K and it confirms the anisotropic behavior of the crystal. **b** TMR at 9 T with the temperature range from 120 K to 150 K, provides a clear indication of SRT in between this temperature range.

the proportionality constant, R_S, is defined as the anomalous Hall coefficient [138]. In most ferromagnets, as the magnetization saturates well below T_C above some critical field, ρ_{xy} varies linearly with B. From the linear fitting of ρ_{xy} in the high-field regime, one can obtain R_0 from the slope and the anomalous Hall resistivity (ρ_{xy}^{AHE}) from the intercept. Also, the anomalous Hall coefficient, R_S, can be calculated by using the relation, $\rho_{xy}^{AHE} = \mu_0 R_S M_S$, where M_S can be extracted from the $M - B$ curves (see Figure 4.12**a**) above $B \geq 7$ T.

However, the above-mentioned technique is not applicable when the magnetization does not saturate at a high field as can be seen from the $M - B$ plots (see Figure 4.12**a**, Section 4.3.1, and Figure 4.5). We observe that the magnetization does not show complete saturation as T approaches T_{SR} even till $B = 9$ T (see Figure 4.12**a**). To circumvent the problem, we incorporate the field dependence of magnetization in Equation 4.5 and use the modified equation for fitting as,

$$\frac{\rho_{xy}}{B} = R_0 + \mu_0 R_S \frac{M}{B} \tag{4.6}$$

From the fitting of $\frac{\rho_{xy}}{B}$ vs $\frac{M}{B}$ at very high field regime ($B > 7$ T), we can determine the slopes and y-axis intercepts, which provide us the temperature-dependent values of R_S and R_0 respectively. Both methods qualitatively provide equivalent results except for some

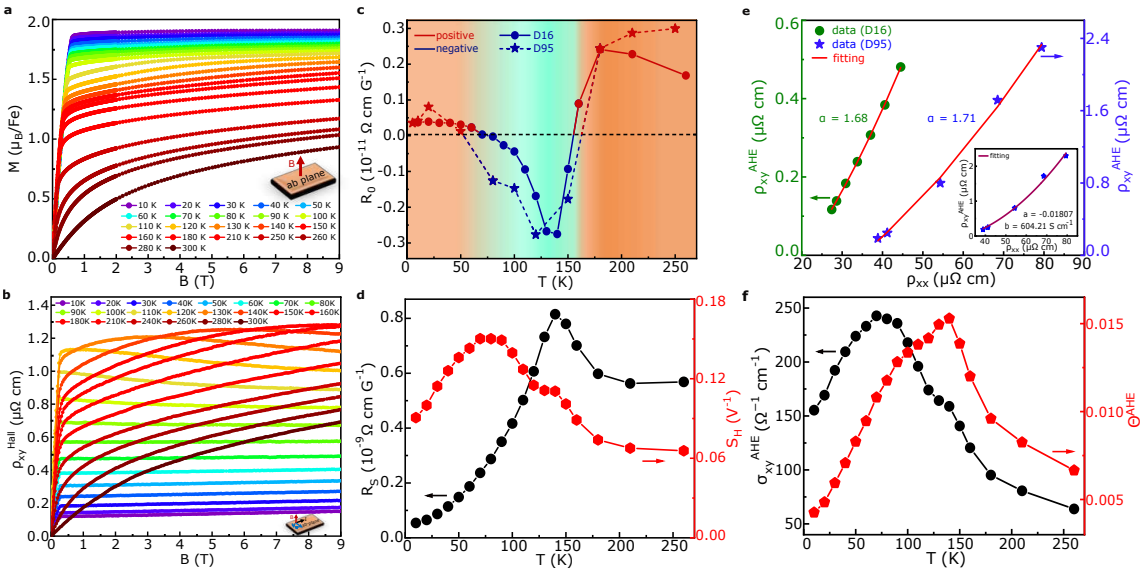

FIGURE 4.12: **Temperature dependent magnetization and Hall effect with analysis. a** Magnetic field dependence of magnetization (M) at different temperatures with B normal to the ab-plane of the crystal. **b** Magnetic field dependence of Hall resistivity (ρ_{xy}) of D16 measured at temperatures from 10 K to 300 K, with current in ab-plane and magnetic field along the c-axis of the Fe_4GeTe_2 crystal. **c** Temperature dependence of the ordinary Hall coefficient (R_0) for the two devices (D16 and D95), indicating both positive and negative regimes through the background colors. **d** Temperature dependence of anomalous Hall coefficient R_S and scaling coefficient $S_H = R_S/\rho_{xx}^2 = -\sigma_{xy}^{AHE}/M$ are plotted for device D16. **e** Scaling behaviour of anomalous Hall resistivity (ρ_{xy}^{AHE}) vs in-plane resistivity (ρ_{xx}) for both devices. The red curve indicates the fitting of the experimental data with the equation $\rho_{xy}^{AHE} \approx a\rho_{xx}^{\alpha}$, which helps to understand the origin of the AHE. Inset: The data (D16) are fitted with the equation $\rho_{xy}^{AHE} = a\rho_{xx} + b\rho_{xx}^2$. **f** Temperature dependence of anomalous Hall conductivity (σ_{xy}^{AHE}) provides a larger value of 243 Ω^{-1}cm^{-1} at 80 K for device D16. Temperature dependence of anomalous Hall angle $\theta^{AHE} = \sigma_{xy}^{AHE}/\sigma_{xx}$ has an anomaly near the spin reorientation transition (T_{SR}).

quantitative differences in the high-temperature range. Details of calculation procedures are explained in Figure 4.13.

Figure 4.12 (**b**) demonstrates the magnetic field-dependent Hall resistivity (ρ_{xy}) for D16 measured at different temperatures down to 10 K (for D95, see [36]). Here, the similarity in the nature of magnetic field dependence curves of Hall resistivity and magnetization in the low-field region suggests the presence of AHE.

We first discuss the behavior of the temperature dependence of the ordinary Hall coefficient, R_0, which shows a rather complex nature. Figure 4.12**c** shows that R_0 changes sign from positive (red) to negative (blue) in the proximity of T_{SR}, reaching its maximum negative value at $\sim T_{SR}$ and becomes positive again in the vicinity of $\sim T_Q$. Almost identical behavior was observed in both of the devices, D95 and D16. This indicates

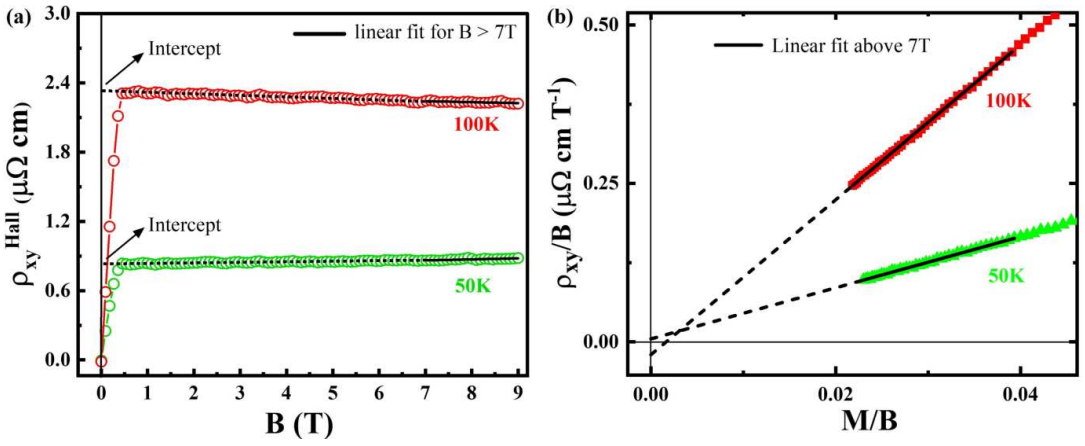

FIGURE 4.13: Calculation procedures of AHE. (a) ρ_{xy}^{Hall} vs B data for two characteristic temperatures, 50 K and 100 K, with a linear fit using Equation 4.5 at high fields ($B > 7$ T). The intercept provides the anomalous Hall contribution. (b) Analysis of the same AHE data using Equation 4.6.

the change in the majority carrier from holes to electrons, possibly due to the Fermi surface reconstruction or Lifshitz-like transition occurring as a result of the SRT [79, 80], however, the actual origin is not yet known. We compare the observed behavior of R_0 for Fe_4GeTe_2 with the reported result [61] on Fe_3GeTe_2. Unlike Fe_4GeTe_2, the slope of the Hall resistivity (R_0) in Fe_3GeTe_2 is positive from 2 K to 300 K, indicating the hole-dominating majority carrier throughout this temperature range [61]. Nevertheless, the Hall resistivity clearly demonstrates a strong correlation between spin structure and the Fermi surface, which leads to the non-monotonic temperature dependence of R_0 in Fe_4GeTe_2 down to 16 layers.

The temperature-dependent anomalous Hall coefficient (R_S) for D16, derived using the Equation 4.6, is shown in Figure 4.12**d**. R_S shows a non-monotonic behavior with its maximum at $\sim$ 140 K and a strong decrease below the SRT. However, it was argued that the R_S may not describe the proper scaling with M when there is a significant variation in resistivity with T or B and a material-specific scaling factor S_H was introduced where $R_S = S_H\rho_{xx}^2$ [141]. Figure 4.12**d** (red curve) shows the variation of S_H with temperature, which shows a weak variation with the temperature well above the SRT transition and changes significantly below SRT, indicating its complex dependence with resistivity and magnetism below the SRT. A nearly identical behavior is noticed for device D95 with the distinction lying in its enhanced values at elevated temperatures (see Section 4.3.5 for the comparisons between D16 and D95).

4.3.4.1 Investigation on the Origin of Anomalous Hall Effect in Fe_4GeTe_2

To investigate the origin of the AHE, typically one looks at the scaling behavior of ρ_{xy}^{AHE}, $\rho_{xy}^{AHE} \approx a\rho_{xx}^{\alpha}$[138]. Primarily, three mechanisms were identified to describe the AHE for ferromagnets or materials with strong spin-orbit coupling (SOC): intrinsic Karplus-Luttinger (K-L) mechanism, extrinsic side-jump mechanism, and extrinsic skew-scattering mechanism [138]. Intrinsic K-L mechanism [142] is associated with the anomalous drift of carriers due to the finite Berry curvature in the momentum space, appearing due to the SOC. It is mostly independent of scattering and solely dependent on the band structure of the crystal [138, 143, 144]. Extrinsic side-jump mechanism [145] is related to the deflection of electrons due to scattering from the spin-orbit coupled impurities, and extrinsic skew-scattering mechanism [146, 147] is caused by the asymmetric scattering of electrons from the impurities due to the spin-orbit interactions. All of these three mechanisms are associated with the power-law, $\rho_{xy}^{AHE} \approx a\rho_{xx}^{\alpha}$. For the intrinsic K-L mechanism and extrinsic side-jump mechanism $\alpha = 2$ and for the extrinsic skew-scattering mechanism $\alpha = 1$ [138].

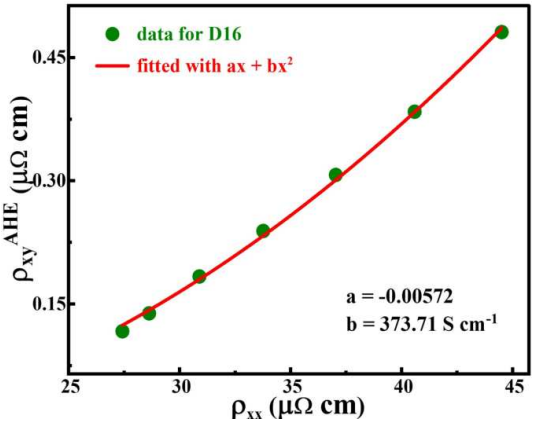

FIGURE 4.14: The scaling curve between ρ_{xy}^{AHE} and ρ_{xx} for D16, fitted using the equation $\rho_{xy}^{AHE} = a\rho_{xx} + b\rho_{xx}^2$.

To get a quantitative estimate, we have calculated the anomalous Hall conductivity ($|\sigma_{xy}^{AHE}| \approx \rho_{xy}^{AHE}/\rho_{xx}^2 \approx \mu_0 R_S M_S/\rho_{xx}^2$) and the anomalous Hall angle ($\theta_{AHE} = \sigma_{xy}^{AHE}/\sigma_{xx}$), which is a measure of the strength of the transverse current generated with respect to the applied normal current [138]. It must be noted that the anomalous Hall conductivity is overestimated at the higher temperatures ($T > T_{SR}$) as M does not show full saturation even with 9 T magnetic field (see Figure 4.12**a**). The temperature dependence of $|\sigma_{xy}^{AHE}|$ and θ_{AHE} exhibit a non-monotonic behavior, as shown in Figure 4.12**f** (for D16). While at low temperature (10 K), $|\sigma_{xy}^{AHE}| \approx 155\ \Omega^{-1}\text{cm}^{-1}$, it increases and attains a maximum value of $\sim 243\ \Omega^{-1}\text{cm}^{-1}$ at ~ 80 K, then decreases with increasing temperature. In case of D95, a similar non-monotonic temperature-dependent behavior is observed, with $|\sigma_{xy}^{AHE}| \approx 121\ \Omega^{-1}\text{cm}^{-1}$ at 10 K and a relatively higher maximum value of $\sim 376\ \Omega^{-1}\text{cm}^{-1}$ at ~ 80 K (see Section 4.3.5 for detail comparison). For thinner nanoflake device, D16, θ_{AHE} and S_H reach the values of ~ 0.015 and $\sim 0.15\ \text{V}^{-1}$ respectively, near T_{SR} (see Figure

4.12**d** and **f**). The corresponding values for D95 are ~ 0.032 and ~ 0.24 V^{-1}, respectively (see Figure 4.17). These results are quite high among these classes of 2D ferromagnetic materials at such higher temperatures, especially in devices with lower thicknesses [60, 354].

The low-temperature value is almost three times smaller than the expected AHE conductivity in the 'resonant' condition, $\sim e^2/ha \approx 390$ $\Omega^{-1}cm^{-1}$ [60, 144] in three dimensions, where e is the electronic charge, h is the Planck constant and $a = 9.97$ $\AA$ [210], being the lattice constant of Fe_4GeTe_2. Also, the recent DFT-based calculations show that Fe_4GeTe_2 belongs to a different magnetic symmetry class compared to the other two members, having a non-trivial Berry curvature leading to the low-temperature AHE conductivity via intrinsic K-L mechanism [58]. However, the strong temperature dependence of the AHE suggests that extrinsic mechanisms might play a role in determining the AHE in Fe_4GeTe_2. The extrinsic side-jump contribution to the AHE conductivity (σ_{xy}^{AHE}) is of the order of $e^2/(ha)(\varepsilon_{SO}/E_F)$ [355], where ε_{SO} is the spin-orbit coupling interaction and E_F is the Fermi energy. While for ferromagnetic metals, the ratio, ε_{SO}/E_F is usually small (~ 0.01) and so the extrinsic side-jump contribution [60, 71], it may enhance due to the complex nature of magnetic interaction in this class of van der Waals ferromagnets.

It is hard to identify the exact mechanism responsible for AHE due to the observed strong temperature dependence of the AHE coefficient below the SRT. The theory of AHE does not include the role of inelastic scattering like electron-electron, electron-magnon, or electron-phonon interaction. As both our resistivity and MR data indicate a dominant electron-magnon scattering in the intermediate temperature range, the AHE might also have a similar origin. First, ρ_{xy}^{AHE} vs ρ_{xx} is plotted to check the scaling behavior of ρ_{xy}^{AHE} of both devices (D16 and D95) in the temperature range from 5 K to 100 K, as shown in Figure 4.12**e**. From the fitting (red curve in Figure 4.12**e**) of the equation $\rho_{xy}^{AHE} \approx a\rho_{xx}^{\alpha}$, we have determined the values of $\alpha = 1.68$ (for D16) and 1.71 (for D95), i. e., almost quadratic dependence of ρ_{xy}^{AHE} on ρ_{xx}, which indicates that the AHE of Fe_4GeTe_2 could be originated dominantly from the intrinsic K-L mechanism or extrinsic side-jump mechanism, rather than the extrinsic skew-scattering mechanism where ρ_{xy}^{AHE} linearly dependent on ρ_{xx}. To understand the dominant contributions, we have plotted ρ_{xy}^{AHE} with ρ_{xx} (inset of 4.12**e** for D95, see Figure 4.14 for D16) and fitted with the equation $\rho_{xy}^{AHE} = a\rho_{xx} + b\rho_{xx}^2$, where a is the strength of the skew scattering contribution and b denotes the strength of the side jump/intrinsic contribution. From the fitting, we estimate a = - 0.0181 and b $\sim$ 604 S cm^{-1} for D95 and a = - 0.00572 and b $\sim$ 373.7 S cm^{-1} for D16 device, which indicates that the intrinsic Berry phase and/or extrinsic side-jump contribution highly dominate

over the skew scattering contribution. Here, the negative sign of a indicates that the skew scattering contribution is acting in the opposite direction as compared to the other two mechanisms [330, 356].

Since the extrinsic side-jump contribution is independent of the strength and density of the scatters similar to intrinsic mechanisms and both of them follow the quadratic dependence to the longitudinal resistivity ($\propto \rho_{xx}^2$), it is difficult to separate the intrinsic K-L and extrinsic side-jump contributions. Usually, the intrinsic part does not change with temperature in most cases unless there is an electronic transition with temperature leading to a non-monotonic Berry phase contribution [138, 357]. Recently, Yang *et al.*, [358] theoretically proposed that the side-jump contribution can be affected by the electron-magnon scattering, which may lead to the temperature dependence of anomalous Hall conductivity (AHC). To investigate further, we decouple different scattering terms of $R_S(T)$ using the procedure mentioned in Ref. [330, 342, 356, 358].

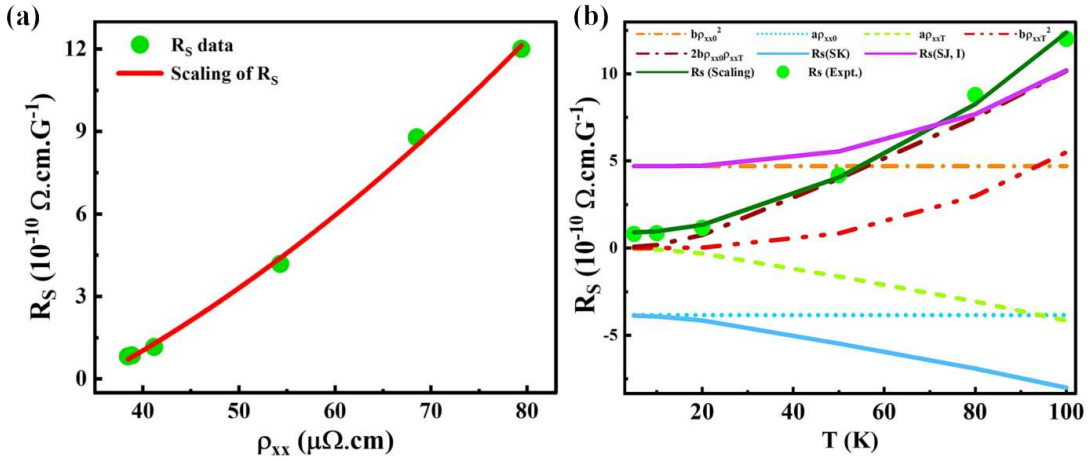

FIGURE 4.15: Decoupling different scattering mechanisms. (a) Scaling between R_S and ρ_{xx} using Equation 4.7. (b) The temperature dependence of the anomalous Hall coefficient (R_S) is plotted. The individual terms contributing to R_S from Equation 4.8 are also shown as a function of temperature. The temperature dependencies of skew-scattering and side-jump/intrinsic contributions to R_S are represented by the cyan and purple solid lines, respectively.

4.3.4.2 Decoupling Different Scattering Mechanisms

Depending on the various scattering mechanisms in ferromagnets, the anomalous Hall resistivity (ρ_{xy}^{AHE}) or anomalous Hall coefficient (R_S) relates to the longitudinal resistivity (ρ_{xx}) by the following scaling relation:

$$R_S = a\rho_{xx} + b\rho_{xx}^2 \tag{4.7}$$

Here, a and b represent the strengths of the skew-scattering and intrinsic/side-jump contributions to the anomalous Hall coefficient, respectively. Both intrinsic and side-jump contributions exhibit a ρ_{xx}^2 dependence. The intrinsic Karplus-Luttinger (K-L) mechanism, being an inherent property of any sample, is nearly temperature-independent even when ρ_{xx} varies with temperature, whereas the side-jump contribution depends on temperature. Separation of these two mechanisms can be achieved by analyzing the temperature dependence of the R_S vs T curves using the following procedures.

The total longitudinal resistivity (ρ_{xx}) can be expressed as the sum of a temperature-independent residual resistivity (ρ_{xx0}) and a temperature-dependent part (ρ_{xxT}). Substituting $(\rho_{xx0} + \rho_{xxT})$ in the place of ρ_{xx} in the above scaling relation, the modified scaling equation becomes:

$$\begin{aligned} R_S(T) &= a(\rho_{xx0} + \rho_{xxT}) + b(\rho_{xx0} + \rho_{xxT})^2 \\ &= (a_1\rho_{xx0} + a_2\rho_{xxT}) + (b_1\rho_{xx0}^2 + b_2\rho_{xxT}^2) + c\rho_{xx0}\rho_{xxT} \end{aligned} \tag{4.8}$$

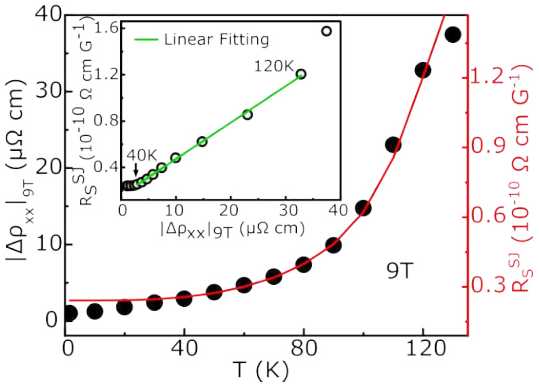

FIGURE 4.16: Confirmation of the magnons' dependency on the side-jump mechanism. Temperature dependence of the change in longitudinal resistivity ($|\Delta\rho_{xx}|_{9T}$) (black solid circles) and the extrinsic side-jump contribution (R_S^{SJ}) (red line). *Inset:* The linear fitting between $|\Delta\rho_{xx}|_{9T}$ and R_S^{SJ} shows a linear behavior in the temperature range between T_Q and T_{SR}.

Here, $(a_1\rho_{xx0} + a_2\rho_{xxT})$ represents the total skew scattering contribution ($R_S^{(\mathrm{SK})}$), $(b_1\rho_{xx0}^2 + b_2\rho_{xxT}^2)$ corresponds to the total side-jump scattering or intrinsic K-L contribution ($R_S^{(\mathrm{SJ,\ I})}$) to the total $R_S(T)$. The term $c\rho_{xx0}\rho_{xxT}$ represents the cross term, which accounts for the competition between the different scattering contributions. Additionally, $a_1 = a_2 = a$, $b_1 = b_2 = b$, and $c = 2b$.

Hence, R_S is fitted with Equation 4.7 to determine the coefficients a and b. Figure 4.15 (a) illustrates the scaling of Equation 4.7 with ρ_{xx}, which shows good agreement with the experimentally determined R_S data. Figure 4.15 (b) presents the temperature dependence of each contribution associated with R_S. Here, $a_1\rho_{xx0}$ and $b_1\rho_{xx0}^2$ terms are temperature independent, while the terms $a_2\rho_{xxT}$, $b_2\rho_{xxT}^2$, and $c\rho_{xx0}\rho_{xxT}$ are temperature dependent. It is evident that $a_2\rho_{xxT}$ and $b_2\rho_{xxT}^2$ act oppositely with increasing temperature.

Among these, $b_2\rho_{xxT}^2$ and $c\rho_{xx0}\rho_{xxT}$ dominate the temperature-dependent part of R_S. Additionally, the total side-jump mechanism or intrinsic K-L contribution dominates over the skew-scattering mechanism in the experimentally determined R_S value. The scaling relation of Equation 4.8 shows excellent agreement with the experimentally determined temperature-dependent R_S value, as indicated by the green solid line in Figure 4.15 (b). Since the intrinsic AHE is weakly temperature dependent [138, 143, 357] compared to the side-jump mechanism, and as previously recognized, electron-magnon scattering can drive the temperature dependence of the side-jump contribution [358]. Therefore, it can be concluded that magnons may be responsible for the side-jump contribution to the AHE in this material.

Figure 4.16 shows the temperature dependence plot of change in resistivity ($\Delta\rho_{xx}$) at 9 T magnetic field and the extrinsic side-jump contribution, R_S^{SJ}. The red line shows the extracted side jump contribution to the resistivity, which scales perfectly in the temperature range $T_Q < T < T_{SR}$, but deviates in the low-temperature regime ($T < T_Q$) as well as for $T > T_{SR}$. Additionally, R_S^{SJ} also shows a linear relation with $|\Delta\rho_{xx}|_{9T}$ (see the inset in Figure 4.16). This linear behavior in the temperature range (40 K - 120 K) supports the role of electron-magnon scattering on the AHE via the side-jump mechanism. The analysis directly indicates that the $R_S^{SJ}(T)$ primarily originates from the spin-flip electron-magnon scattering. The above analysis is also consistent with the observed reduction in the AHE conductivity near T_{SR} for the thinner layer device (see Figure 4.3.5). As the observed electron-magnon scattering coefficient deduced from the resistivity data is higher for thinner flake, it leads to the enhanced side jump contributions [359, 360] which further reduces the AHE conductivity near T_{SR} for thinner layer devices, consistent with the above analysis.

4.3.5 Comparison Between the Transport Data of Two Devices, D95 and D16

We have compared the temperature-dependent behavior of the anomalous Hall parameters in both the 95 nm thick device (D95) and the 16 nm thinner nanoflake device (D16). Several extracted parameters from both devices are plotted and compared on the same scale, as shown in Figure 4.17. Notably, an almost identical pattern is observed in both devices, with the main difference being the parameter values at higher temperatures.

The temperature-dependent anomalous Hall coefficient (R_S) extracted from the D95 and D16 devices, as determined from Equation 4.6, is depicted in the 1st figure of Figure 4.3.5.

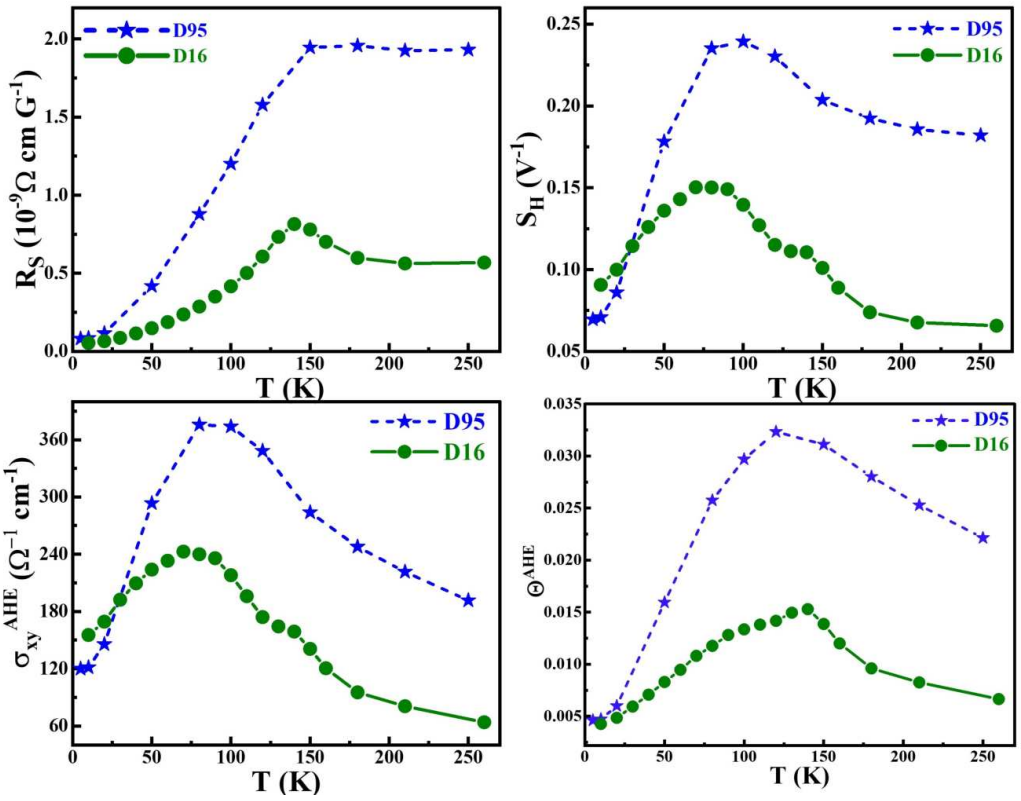

FIGURE 4.17: Comparison of the transport data of two measured devices. Several parameters are extracted from the Hall data of devices D95 and D16 and compared by plotting them as a function of temperature on the same scale. Here, R_S, S_H, $\sigma_{xy}^{\mathrm{AHE}}$, and θ^{AHE} are plotted against temperature. The data for D95 is represented by blue lines and symbols, while the data for D16 is shown in green.

Similar to D16, R_S displays a non-monotonic trend for D95, peaking around 140 K and sharply declining below the SRT. However, the low-temperature value of R_S for both D16 and D95 is similar, but with increasing temperature, the value of R_S for D95 rises faster than that of D16, although the trends remain similar.

It has been argued, however, that R_S may not adequately represent the proper scaling with magnetization (M) when there is significant variability in resistivity with temperature (T) or magnetic field (B). To address this, a material-specific scaling factor, S_H, was introduced, where $S_H = R_S/\rho_{xx}^2$. The 2nd figure in Figure 4.17 shows the variation of S_H with temperature for both devices. This curve exhibits a subtle dependence on temperature well above the SRT transition but undergoes significant changes below the SRT, indicating a complex relationship of S_H with resistivity and magnetism below the SRT.

The behavior of anomalous Hall conductivity ($|\sigma_{xy}^{\mathrm{AHE}}|$) and anomalous Hall angle (θ^{AHE})

with respect to temperature shows a non-monotonic trend, peaking around the T_{SR}, as depicted in Figure 4.17 (3rd and 4th figure). At a temperature of 10 K, $|\sigma_{xy}^{\mathrm{AHE}}|$ for D16 is approximately 155 $\Omega^{-1}\,\mathrm{cm}^{-1}$, increases to a maximum value of $\sim 243\,\Omega^{-1}\,\mathrm{cm}^{-1}$ around 80 K, and subsequently decreases as the temperature rises. Similarly, for D95, a nearly identical non-monotonic temperature-dependent trend is observed, with $|\sigma_{xy}^{\mathrm{AHE}}|$ measuring around 121 $\Omega^{-1}\,\mathrm{cm}^{-1}$ at 10 K and reaching a higher maximum value of $\sim 376\,\Omega^{-1}\,\mathrm{cm}^{-1}$ at $\sim$ 80 K.

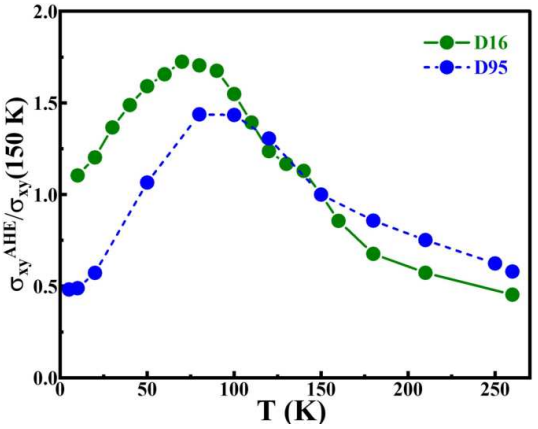

FIGURE 4.18: Comparison in anomalous Hall conductivity. The temperature dependence of $|\sigma_{xy}^{\mathrm{AHE}}|$, normalized by its value at 150 K, shows a similar trend to the previously reported data.

Notably, the maximum anomalous Hall conductivity near T_{SR} decreases as the thickness decreases. Moreover, for the D95 device, the parameters θ^{AHE} and S_H attain values of ~ 0.032 and $\sim 0.24\,\mathrm{V}^{-1}$, respectively, near T_{SR}. In contrast, for the thinner nanoflake device D16, θ^{AHE} and S_H reach values of ~ 0.015 and $\sim 0.15\,\mathrm{V}^{-1}$, respectively, near T_{SR}. Here, θ^{AHE} represents the strength of the transverse current generated relative to the applied normal current, and S_H quantifies the sensitivity of the anomalous Hall conductivity with respect to magnetization (M). These values are significantly large over a wide temperature range, highlighting the distinct characteristics and uniqueness of Fe_4GeTe_2 compared to other known metallic magnets.

Importantly, a nearly identical trend is observed in both devices, with the primary distinction being the parameter values at elevated temperatures. We have plotted (see Figure 4.18 the normalized values of anomalous Hall conductivity with respect to 150 K, which exhibit a trend similar to previously reported data [210].

4.3.6 Comparison in Hysteresis of ρ_{xy} of Two Devices, D95 and D16

The comparison in the hysteresis behavior of anomalous Hall resistivity for both devices explains the distinctness in D95 and D16 and evidence of hard ferromagnetism with decreasing thickness. While the bulk Fe_4GeTe_2 crystal exhibits almost negligible magnetic hysteresis, as reported by Seo et al (2020), both our 95-layer and 16-layer exfoliated

nanoflake devices displayed finite and substantial hysteresis areas (see Figure 4.19). More importantly, the 16-layer nanoflake exhibits a significantly larger and square-shaped magnetic hysteresis area with a higher coercive field compared to the 95-layer flakes, indicating hard-magnet-type behavior in thinner flakes, as expected.

4.4 First Principle Study of Fe_4GeTe_2

We now present the theoretical calculations and analysis[3] of the electronic and magnetic phases of Fe_4GeTe_2. It is one of the outstanding puzzles in this material class that despite strong ferromagnetic transitions (nearly reaching room temperature), the materials' charge degrees of freedom are not frozen and the material behaves as a ferromagnetic metal. Moreover, the above experimental results clearly indicate that within the ferromagnetic phase, there are multiple phase transitions – with lowering the temperature, there exists a spin re-orientation (SR) transition (T_{SR}), while another electronic phase transition occurs at a much lower temperature T_Q giving a Fermi liquid-like behavior. A ferromagnetic metal suggests a Hubbard model as a starting Hamiltonian, while the SR phase suggests an anisotropic Heisenberg coupling term, and the electronic phase transition within a magnet entails a Kondo coupling. After delineating the electronic properties within the DFT calculation, we propose a low-energy model Hamiltonian to capture the essence of these phases.

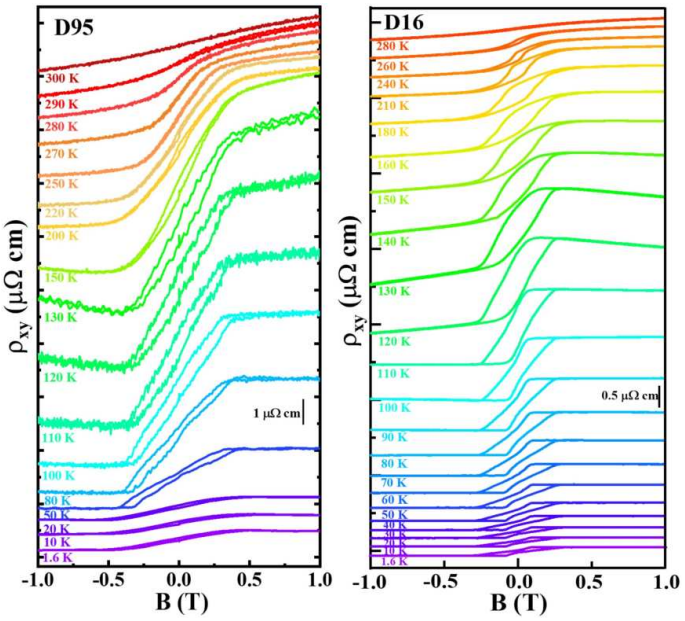

FIGURE 4.19: Temperature-dependent magnetic hysteresis behavior of anomalous Hall resistivity is plotted for both devices D95 and D16.

We first present the results from the DFT calculation in two nearly degenerate magnetic configurations as shown in Figure 5.7. The details of the DFT calculation are given

[3]Theoretical calculations were performed by Dr. Rajesh O. Sharma from Prof. Tanmoy Das's group at IISc Bangalore, India

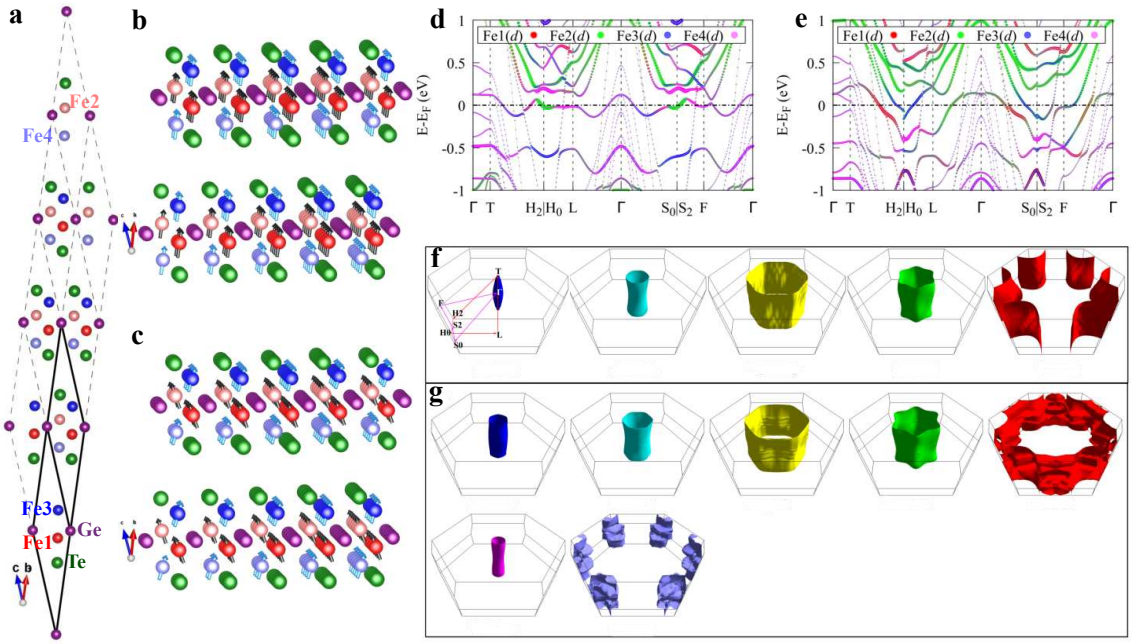

FIGURE 4.20: **Results from theoretical calculations.** **a** A 2x2 supercell is constructed using the Rhombohedral primitive cell (depicted by the solid line) of the Fe_4GeTe_2 compound. Four Fe atoms are labeled as Fe1, Fe2, Fe3, and Fe4 in different colors. **b** The cFM phase with all Fe atoms having magnetic moments along the ab-plane, as indicated by black (Fe1-Fe2) and cyan (Fe3-Fe4) arrows. Only two layers, each composed of Fe, Ge, and Te, from the 4x4 supercell are displayed here for simplicity. **c** In the nFM phase, the magnetic moments of all Fe atoms are shown reoriented and shown by corresponding arrows. **d-e** The projected band structure is shown in the cFM and nFM phases. We also plot the total d orbital weights of all four Fe atoms, with the thickness of the line indicating the orbital weight, while different color reflects different Fe atoms. **f-g** Corresponding Fermi surfaces in the two phases are drawn here. Here, color has no physical meaning except to distinguish different bands.

in the section 4.2.5. The Fe_4GeTe_2 compound has two well-separated quarter-layers of Fe, in which two pairs of equivalent Fe atoms reside as Fe1, Fe2 and Fe3, Fe4. Due to van der Waals interaction between these quarter-layers, and hence having negligible exchange interaction between their spins, we can essentially focus on a given quarter-layer. The energy optimization within the non-collinear DFT+U calculation yields two FM configurations which are nearly 10 meV (see Table 4.1). The lowest energy configuration is a collinear ferromagnet, with an easy axis pointing along the ab-plane for all Fe-atoms. In the other phase, there is a relative tilt ($\sim 60^o$) between the spin easy axes of the two Fe atoms, with the overall spin orientation also nearly 40^o from the c-axis. Experimentally, the spin orientation is nearly 90^o, and this difference between theory and experiment could be related to the global spin rotational symmetry. In both phases, the magnetic moment of Fe1 (and Fe2) is lower than that of Fe3 (Fe4). We refer to the first phase as collinear FM (cFM) and the second one by non-collinear FM (nFM). The quasi-degeneracy in the

two reoriented spin configurations is responsible for the T_{SR} transition in this compound.

The band structure and the Fermi surface topology for the two phases are shown in Figure 5.7**d-g**. We observe significant band structure differences near the Fermi level, with spectral weight redistribution as well as the appearance of new FS pockets in the nFM phase. Remarkably, all FSs are significantly 2D in nature, consistent with the vdW type interaction along the *c*-direction. In the cFM phase (see Figure 5.7**f**), we have five FS pockets, four of which are hole-like while the fifth one is electron-like. On the other hand, in the nFM phase (see Figure 5.7**g**), we find that two new FS pockets develop, with one of them being hole-like but much smaller in area, while the other one is electron-like and much larger in area. In addition, the area of all other FS pockets also increases. This result suggests that owing to the smaller magnetic moment of the Fe1 (and Fe2) compounds, the itinerant characteristics of the Fe-orbitals are enhanced here. This is evident by the fact that the two-electron pockets are dominated by the Fe3 and Fe4 atoms, as shown in Figure 5.7**e**. The appearance of the new electron pockets is consistent with the sign change in the Hall resistivity from positive to negative in the intermediate temperature region. In addition, in the nFM phase, the wider bandwidth of the bands leads to higher velocities for electrons near the Fermi level due to a larger range of available states for them to occupy. This wider range of available energy states reduces the likelihood of electron scattering events, resulting in a sharp drop in resistivity at T_{SR} in the nFM phase.

The DFT results indicate that the low-energy electronic states are dominated by Fe-*d* orbitals (hybridized with *p*-states of the Te atoms. Therefore, the effective low-energy model requires a multi-band tight-binding model. But with an eye to the active spin degrees of freedom, one starts with a multi-band Hubbard model for two Fe-*d* orbitals with Hund's coupling, projects to the highest spin states in the ferromagnetic phase, and obtains a Heisenberg model (where we suppress the charge degrees of freedom for simplicity). The model Hamiltonian is

Ions	cFM phase E = -32.094 eV			nFM phase E = -32.083 eV		
	m_x	m_y	m_z	m_x	m_y	m_z
Fe1, Fe2	0	0	2.8	1.6	1.6	1.7
Fe3, Fe4	0	0	3.2	1.0	1.0	2.7

TABLE 4.1: DFT deduced values of the magnetic moment in both spin orientations are presented in μ_B unit.

$$\begin{aligned} H &= -J_1 \sum_{<i,j>} \mathbf{s}_i \cdot \mathbf{s}_j - J_3 \sum_{<i,j>} \mathbf{S}_i \cdot \mathbf{S}_j \\ &\quad -K_1 \sum_i (\mathbf{s}_i \cdot \hat{\mathbf{n}})^2 - K_3 \sum_i (\mathbf{S}_i \cdot \hat{\mathbf{N}})^2 \\ &\quad -J' \sum_i \mathbf{S}_i \cdot \mathbf{s}_i. \end{aligned} \tag{4.9}$$

Here $\mathbf{s}$, and $\mathbf{S}$ correspond to the spin vectors at the Fe1 and Fe3 atomic sites, with corresponding exchange and anisotropy interactions J_1, J_3, and K_1 and K_3, while J' is the inter-atomic exchange interaction. For $J' = 0$, the model enjoys spin-rotational symmetry for each Fe atom with respect to their easy axes $\hat{\mathbf{n}}$ and $\hat{\mathbf{N}}$, and a Ferromagnetic phase appears for $J_i > 0$ and $K_i \geq 0$. For $J' \neq 0$, the individual spin-rotational symmetry is lost, and a rotational symmetry with respect to the total spin $\mathbf{S} + \mathbf{s}$ with a common quantization axis is present.

Given that both phases are ferromagnetic along each Fe-layer, therefore the in-plane exchange terms $J_1 > 0$ and $J_3 > 0$, do not play any role in the cFM to nFM phase transition. We rotate the spin-quantization axis by the polar angles $n_z = \cos(\theta_1)$ and $N_z = \cos(\theta_3)$ (with respect to the c-axis). Clearly, a trivial classical ferromagnetic solution exists at $\theta_i = 0$ for all values of J', which is the cFM phase.

Is there any other ferromagnetic order ($|\theta_3 - \theta_1| < \pi$) possible in the realistic parameter region in this model? The $\partial H/\partial\theta_i = 0$ condition of the Hamiltonian in Equation 4.9 yields $K_1 s^2 \sin 2\theta_1 = -K_3 S^2 \sin 2\theta_3$, where S and s are the spin magnitudes of Fe3 and Fe1. In the Fm region ($|\theta_3 - \theta_1| < \pi$), the condition is satisfied for $K_1/K_3 < 0$ for any $J' \neq 0$. Furthermore, $\partial^2 H/\partial\theta_i^2 > 0$ condition for the energy minimum imposes $K_1 < 0$ and $K_3 > 0$ for $J' > 0$ and $\theta_i < \pi/4$, which is satisfied in the parameter range of $2|K_2| s \cos 2\theta_1 < |J'| S \cos(\theta_3 - \theta_1) < 2|K_3| \cos 2\theta_3$. This gives the nFM phase. The self-consistent DFT result gives $\theta_1 = 10^o$ and $\theta_3 = 71^o$ and $s = 1.7\mu_B$ and $S = 2.7\mu_B$ in this phase.

Due to the presence of an inter-atomic spin-spin exchange term J', there arises a temperature scale below which the spins in the lower-moment Fe-d states are screened and give rise to a metallic phase. This characteristic temperature is the $T_Q \sim k_B J'$ in this material.

Properties	***D*16** (16 nm)	***D*95** (95 nm)	**Bulk**
RRR	3.87	3.04	1.31 [210] 1.75 [361]
Conductivity (σ) at T_C (Ω^{-1} m^{-1})	9.6×10^5	8.6×10^5	5×10^5 [210] 4.1×10^5 [361]
Conductivity (σ) at 1.6 K (Ω^{-1} m^{-1})	36.8×10^5	26.1×10^5	6.4×10^5 [210] 7.1×10^5 [361]
Coeff. of T^2 below T_Q (Ω cm K^{-2})	4.24×10^{-9}	7.73×10^{-9}	not reported
Coeff. of T^2 within 65 – 125 K (Ω cm K^{-2})	8.12×10^{-9}	2.41×10^{-9}	not reported
Negative MR (max) near T_{SR} (at 9 T)	21.2 %	11 %	not reported
Positive MR (max) below T_Q (at 9 T)	0.6 %	1.8%	not reported
$\lvert\sigma_{xy}^{AHE}\rvert$ at 10 K (Ω^{-1} cm^{-1})	155	121	495 [361]
$\lvert\sigma_{xy}^{AHE}\rvert$ (max) near T_{SR} (Ω^{-1} cm^{-1})	243	376	400 [361]
S_H (max) near T_{SR} (V^{-1})	0.15	0.24	0.0235 [210] 0.22 [361]
θ_H (max) near T_{SR}	0.015	0.032	0.028 [210] 0.106 [361]
Scaling parameter α	1.68	1.71	1.89 [361]
Coercive field near T_{SR} (Oe)	1050	270	negligible [210]

TABLE 4.2: Comparison of several parameters deduced from the transport measurement data of devices D16 and D95, with that reported for bulk Fe_4GeTe_2 [210, 361].

4.5 Summary

In summary, a comprehensive magneto-transport study is presented in a quasi-two-dimensional van der Waals ferromagnet, Fe_4GeTe_2, followed by the understanding of different magnetic and electronic phases through first-principle calculations. By combining various transport properties like resistivity, ordinary Hall effect, AHE, and MR from two exfoliated nanoflake devices, we have identified two electronic transitions specified by T_{SR} and T_Q. While T_{SR} was reported before, the second transition, T_Q, was not identified earlier. We do observe these two transitions in both devices; however, the values of the transport parameters are sensitive to the sample thickness. A comparison (Table 4.2) of various transport parameters can be drawn from our devices with that of the reported data on bulk single crystals.

While at low temperatures, below T_{Q}, resistivity is governed mainly by electron-electron scattering, the other inelastic scattering contributions, electron-magnon and electron-phonon, become significant in the intermediate temperature range ($T_{\mathrm{Q}} < T < T_{\mathrm{SR}}$). Beyond T_{SR}, electron-phonon scattering dominates the resistivity. Notably, both the RRR and the absolute value of the conductivity increase with the reduction of thickness. Our analysis clearly indicates that the electron-magnon interaction is stronger in the thinner device, consistent with the larger negative MR near T_{SR}. For both devices, MR becomes positive below T_{Q}, and the ordinary Hall coefficient exhibits a clear sign change in the vicinity of T_{SR} and T_{Q}. Finally, we observe significant AHE contribution in both devices; however, the AHE conductivity near T_{SR} reduces with decreasing thickness. While the low-temperature AHE possibly arises due to the intrinsic K-L mechanism, our analysis reveals that the extrinsic side-jump mechanism arising from spin-flip electron-magnon scattering is responsible for the strong temperature dependence of AHE in the intermediate temperature range. Theoretical calculations reveal that the difference in the environment of Fe1 and Fe3 atoms and the inter-atomic exchange coupling (J') are responsible for complex phases, which in turn lead to a Fermi surface reconstruction. Our study deciphers an intriguing connection between charge and spin degrees of freedom, important for fundamental understanding as well as for possible futuristic applications.

Chapter 5

Understanding of Magnetic Anisotropy of Fe_4GeTe_2 by Electron Spin Resonance Spectroscopy

In the quest for 2D conducting materials with high ferromagnetic ordering temperature, the new family of the layered Fe_nGeTe_2 compounds, especially the near-room-temperature ferromagnet Fe_4GeTe_2, receives significant attention. Fe_4GeTe_2 features a peculiar spin reorientation transition at $T_{SR} \sim 110\,K$, suggesting a non-trivial temperature evolution of the magnetic anisotropy (MA) – one of the main contributors to the stabilization of the magnetic order in the low-dimensional systems. An electron spin resonance (ESR) spectroscopic study reported here provides quantitative insights into the unusual magnetic anisotropy of Fe_4GeTe_2. At high temperatures, the total MA is mostly given by the demagnetization effect with a small contribution of the counteracting *intrinsic* magnetic anisotropy of an *easy-axis* type, whose growth below a characteristic temperature $T_{shape} \sim 150\,K$ renders the sample seemingly isotropic at T_{SR}. Below one further temperature $T_d \sim 50\,K$, the *intrinsic* MA becomes even more complex. Importantly, all the characteristic temperatures found in the ESR experiment match those observed in transport measurements, suggesting an inherent coupling between magnetic and electronic degrees of freedom in Fe_4GeTe_2. This finding, together with the observed signatures of the intrinsic two-dimensionality, should facilitate optimization routes for the use of Fe_4GeTe_2 in the magneto-electronic devices, potentially even in the monolayer limit.

5.1 Introduction

Magnetic van der Waals (vdW) compounds have become increasingly attractive for fundamental investigations in the past few years since they provide an immense possibility to study quantum magnetic phenomena in low dimensions [27, 29]. Furthermore, they appear as very promising functional materials that enable to employment of their intrinsic two-dimensionality (2D) for continuous scaling of electronic devices towards the quantum limit [362]. As such, these layered materials become advantageous candidates for use in next-generation spintronic devices [363–366]. One of their most important parameters from both fundamental and functional points of view is the magnetic anisotropy (MA). First, MA in the presence of a significant intra-layer exchange interaction between magnetic ions enables higher magnetic ordering temperatures (T_C). This is because MA stabilizes long-range magnetic order in low dimensions, which otherwise would be destroyed at any finite temperature by spin fluctuations according to the Mermin-Wagner theorem [367]. Second, the type and the strength of the MA of the dedicated vdW material define the specific functionalities of the potential spintronic device where this material is used, e.g., it affects the spin-polarization of the generated current.

A particularly interesting subclass of the layered magnetic vdW compounds, which currently are promising candidates to fulfill the requirements of high T_C, significant MA and large magnetization at elevated temperatures, is represented by the Fe-rich ferromagnetic Fe_nGeTe_2 ($n = 3, 4, 5$) family, where the variation of the Fe content strongly impacts their properties [24, 25, 38, 39, 53, 368–373]. One member of this family, Fe_4GeTe_2 [210], attracts special attention because of its high, nearly room-temperature value of $T_C \approx 270\,K$, which likely owes an enhanced interaction between Fe spins arranged according to Figure 5.1(a),(b). Interestingly, the T_C of Fe_4GeTe_2 is reported to be sensitive to the thickness of the sample and to the Fe concentration [80], offering a possibility to further tune the properties of this ferromagnet. Moreover, this compound is capable of generating a very high transport spin polarization [374], shows large anomalous Hall conductivity [36, 375] and is predicted to demonstrate high performance in a magnetic tunnel junction device [376], as well as to generate strong Néel spin currents [377] after doping induced change of the ferromagnetic ground state to an antiferromagnetic one [378]. The MA of Fe_4GeTe_2 is found to be temperature-dependent with a peculiar change of the preferable spin orientation from in-plane to out-of-plane at the spin reorientation transition temperature $T_{SR} \sim 110$ K [36, 80, 210]. Such a change of the spins orientation was explained by the competition between the magnetocrystalline (intrinsic) anisotropy and the shape anisotropy [80, 210], however, the disentanglement and the quantification

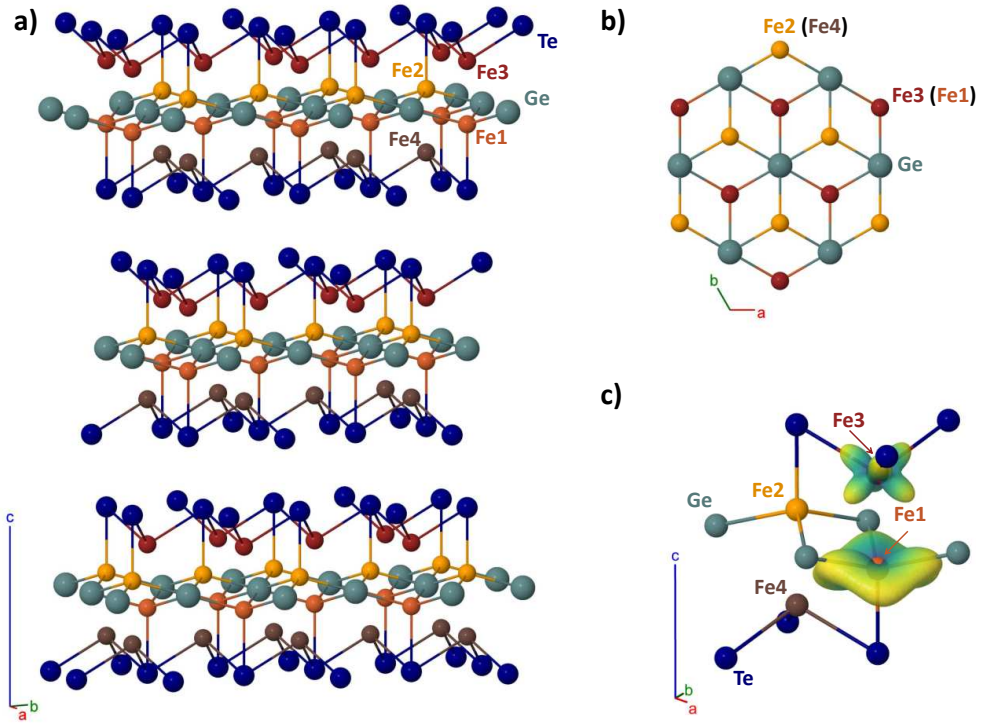

FIGURE 5.1: a) Crystal structure of Fe_4GeTe_2 featuring vdW layers along c direction. b) Top view of the crystal structure of Fe_4GeTe_2. Te atoms are hidden. c) Local crystal structure of four Fe sites. The iso-surface represents the crystal field potential, with the size proportional to the overall potential strength.

of both contributions are essential for the understanding of the nature of the peculiar spin reorientation are lacking so far.

To address this intriguing aspect of magnetism of the quasi-2D vdW ferromagnet Fe_4GeTe_2 we have performed a detailed ESR spectroscopic study of single crystals of this compound in a broad range of excitation frequencies, magnetic fields, and temperatures. In using the ESR spectroscopic technique, we exploited its extreme sensitivity to magnetic anisotropies, which enables a straightforward measurement and accurate quantification of the MA parameters of the studied magnetic material. Moreover, the direct measurement of the magnetic excitations allowed us to address the dynamic aspects of the magnetism in Fe_4GeTe_2. For instance, we observed that at temperatures up to 300 K, which is ~ 30 K above T_C, the anisotropy field measured on the time scale of the ESR experiment does not vanish likely due to the sizable short-range correlations characteristic of a 2D-spin system. Such an intrinsic low-dimensionality should ensure the persistence of the peculiar magnetic properties when reaching the monolayer limit of the Fe_4GeTe_2 sample. As for the ordered state, we found that the evolution of the total MA field H_a features several characteristic

temperatures. Importantly, the main contribution to the *intrinsic* MA disentangled in our ESR study is of the uniaxial *easy-axis* type in the entire experimental temperature range. Its growth with decreasing temperature counteracts the demagnetization effect given by the plate-like shape of the sample, which eventually renders the sample seemingly isotropic by approaching the spin reorientation transition temperature T_{SR}. Moreover, the characteristic temperatures found in the ESR experiment coincide with those observed in the transport measurements [36], suggesting an intimate interplay between the static and dynamic magnetism, on one side, and the electronic properties of Fe_4GeTe_2, on the other side. Such an interplay appears to provide a new attractive functionality of this material for its application in the next generation spintronic devices, where the transport properties of Fe_4GeTe_2 could be tuned by magnetic excitations, and vice versa.

5.2 Experimental Methods

5.2.1 Fe_4GeTe_2 Crystal Details

Single crystals of Fe_4GeTe_2 were grown with the standard chemical vapor transport (CVT) method with iodine as a transport agent. The details of the synthesis and comprehensive analytical and physical characterization of these grown crystals, proving their high quality, were reported in Refs. [14, 36]. In particular, they crystallize in a rhombohedral structure with space group $R\bar{3}m$ and have lattice parameters $a = b = 4.036 \pm 0.003$ Å, $c = 29.2 \pm 0.1$ Å, $\gamma = 120 \pm 0.1\,^\circ$ (hexagonal representation), close to the previously reported values [210]. For the ESR study, a bulk crystal of Fe_4GeTe_2 with the lateral dimensions of ~ 1.2 mm $\times \sim 0.6$ mm $\times \sim 0.15$ mm was chosen. The characteristic temperatures $T_C \approx 270$ K and $T_{SR} \approx 110$ K of this particular sample were reconfirmed by the DC magnetization measurements with a magnetic field (**H**) of 100 Oe applied both parallel to the *ab*-plane and the *c*-axis, respectively (See Figure 5.2). This measurement was performed in a superconducting quantum interference device vibrating sample magnetometer (SQUID-VSM) from Quantum Design. To remove any remanent or residual magnetization present in the sample, an external magnetic field of 5 T was applied at 300 K and then gradually reduced to zero while periodically changing the direction of the field's polarity. All the measurements were done in the zero field cooled (ZFC) condition, where the sample was cooled down to 1.8 K from 300 K without a field, and data was taken during warming up with a constant field.

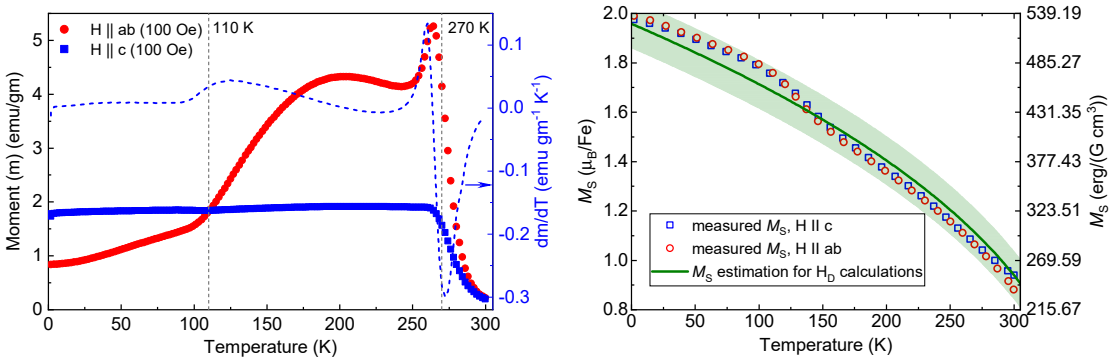

FIGURE 5.2: left) Temperature dependence of the magnetization and its derivative measured at the magnetic field of 100 Oe in $\mathbf{H} \parallel c$ and $\mathbf{H} \parallel ab$ configurations. right) Temperature dependence of the saturation magnetization M_S measured in $\mathbf{H} \parallel c$ (squares) and $\mathbf{H} \parallel ab$ (circles) configurations, the data is taken from [36]. Solid line represents the average M_S used for the shape anisotropy field (H_D) calculation, and the shaded area around this line depicts the uncertainty of the estimated M_S.

5.2.2 Single Crystal X-ray Diffraction Techniques

Single crystal X-ray diffraction (XRD) measurements were performed[1] in 10 – 320 K temperature range at a high-performance laboratory XRD facility "VEGA" (Versatile Extreme conditions Generating diffraction Apparatus), optimized for resolution and sensitivity. This custom-made instrument is equipped with a monochromatized Mo K_α radiation source ($\lambda = 0.70930$ Å) and a CdTe area detector DECTRIS Pilatus with 300,000 pixels and no readout noise for high detection efficiency and minimum background. The cooling of the sample down to 10 K was accomplished by a low-vibration pulse-tube cryostat, which was itself mounted on a specialized four-circle diffractometer. A detailed study of the 100 – 150 K range has been performed due to expected structural changes accompanied by spin-reorientation transition [36].

Data collection and reduction were performed with the CrysAlisPro package program from Oxford Diffraction [379]. Based on the indexation of CrysAlisPro, the lattice parameters a and c of the hexagonal unit cell were analyzed using the python library pyfai [380] and a weighted minimization algorithm over 16 peaks. The structure solution is performed by Superflip [381], which is employed in JANA2020 [382], and subsequent refinements are performed in the JANA2020 software package. The data was plotted using MagicPlot software [383]. The crystal structure shown in Figure 5.1 was created using Jmol software [384].

[1] This single crystal XRD study was performed by Prof. Jochen Geck's group at TU Dresden, Germany

5.2.3 ESR Measurement Details

The ESR measurements were performed[2] using a home-made high-field/high-frequency ESR (HF-ESR) spectrometer. Here, a vector network analyzer (PNA-X) from Keysight Technologies with extensions from Virginia Diodes, Inc. (VDI) was used for the generation and detection of microwaves (MW) in the frequency range from 75 GHz to 330 GHz. Higher frequencies were generated with a set of amplifier multiplier chains (AMC) and detected by a set of zero bias detectors (ZBD), all from VDI. For continuous magnetic field sweeps, a superconducting magnet from Oxford Instruments was used. The homemade probehead with oversized waveguides was inserted into a variable temperature insert (VTI) of a He^4 cryostat (from Oxford Instruments) to obtain stable temperatures of the sample from 300 K down to 3 K. All measurements were performed by continuously varying the magnetic fields from 0 T to 16 T and back at a constant temperature and frequency. The ESR spectra were recorded with the external magnetic field applied along the *c*-axis and along two orthogonal directions within the *ab*-plane, respectively.

5.2.4 Analysis of the HF-ESR Spectra

In the employed HF-ESR setup based on PNA-X, the instrumental mixing of the absorption S_{abs} and dispersion S_{disp} components of the detected signal S_{D} is unavoidable due to the complex impedance of the broadband probehead. Therefore both components of the measured signal at the detector $S_{\text{D}}^{\text{amplitude}}$ and $S_{\text{D}}^{\text{phase}}$ can be presented as:

$$\begin{aligned} S_{\text{D}}^{\text{amplitude}} &\propto S_{\text{abs}} \sin(\alpha) + S_{\text{disp}} \cos(\alpha) \\ S_{\text{D}}^{\text{phase}} &\propto S_{\text{abs}} \sin(\alpha) - S_{\text{disp}} \cos(\alpha) \end{aligned}$$

where α is a parameter which defines the degree of instrumental mixing of the absorption and dispersion components. However, since the vector network analyzer measures both the amplitude $S_{\text{D}}^{\text{amplitude}}$ and the phase $S_{\text{D}}^{\text{phase}}$ of the transmitted MW radiation simultaneously, the absorption component of the signal S_{abs} can be rectified from the as-measured spectra by varying α parameter:

$$S_{\text{abs}} \propto S_{\text{D}}^{\text{amplitude}} \sin(\alpha) + S_{\text{D}}^{\text{phase}} \cos(\alpha) \tag{5.1}$$

[2]We performed these ESR measurements in person at IFW Dresden, Germany, in the framework of the MoU signed between IFW Dresden and SNBNCBS, India

In the case of the noisy phase measurement channel, $S_{\mathrm{D}}^{\mathrm{phase}'}$ can be numerically reconstructed by applying the Kramers-Kronig transformation to the signal detected in the amplitude measurement channel $S_{\mathrm{D}}^{\mathrm{amplitude}}$. The resulting $S_{\mathrm{D}}^{\mathrm{phase}'}$ is then used in Equation 5.1 to obtain the absorption component of the signal S_{abs}. In order to make sure that S_{abs} is reliably rectified both procedures - direct utilization of the measured $S_{\mathrm{D}}^{\mathrm{phase}}$, or calculation of $S_{\mathrm{D}}^{\mathrm{phase}'}$ - were used in this work.

5.3 Experimental Results

For all magnetic field orientations, the ESR spectra of Fe_4GeTe_2 consist of a single resonance line, having shoulders at certain temperatures. Representative spectra (the absorption part of the signal S_{abs}, see Section 5.2.4) recorded at different temperatures, frequencies and field geometries are shown in Figure 5.3 (also in Figures 5.4, 5.5). ESR measurements are performed in the single domain regime since the lowest measured resonance field of about 2 T exceeds the saturation fields (see e.g. [210]), especially at lower temperatures. The resonance field H_{res} was defined as the position of the minimum of the absorption signal $S_{\mathrm{abs}}(H)$.

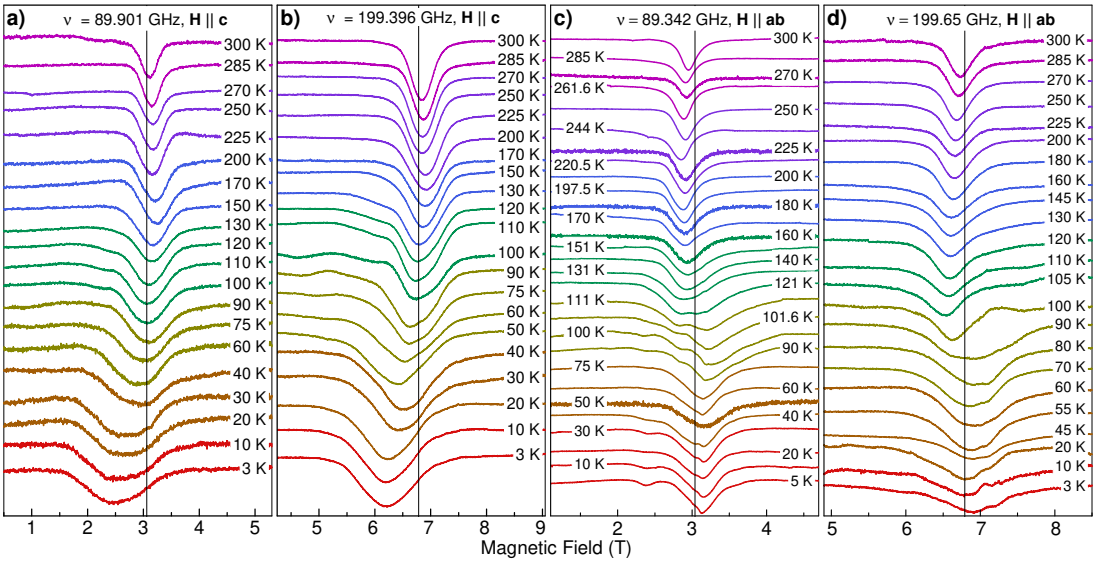

FIGURE 5.3: Temperature dependence of the HF-ESR spectra in the $\mathbf{H} \parallel c$ configuration (a, b) and $\mathbf{H} \parallel ab$ configuration (c, d) at fixed excitation frequencies $\nu \sim 89\,\mathrm{GHz}$ (a, c) and $\nu \sim 199\,\mathrm{GHz}$ (b, d). The spectra are normalized to unity and shifted vertically for clarity. Vertical solid lines represent the expected resonance position of the paramagnetic response according to Equation (5.2).

Vertical solid lines in the panels of Figure 5.3 and horizontal dashed lines in the panels of Figure 5.6 represent the position of the expected isotropic paramagnetic response at the resonance field H_{res}^{para} which is calculated using the conventional paramagnetic resonance relation [385]:

$$h\nu = g\mu_{\mathrm{B}}\mu_0 H_{\mathrm{res}}^{para} \ . \tag{5.2}$$

Here ν is the microwave frequency, g is the g-factor, h is the Plank constant, μ_{B} is the Bohr magneton, μ_0 is the free space permeability. The g-factor of ~ 2.1 is determined from the frequency dependence of the resonance field $\nu(H_{\mathrm{res}})$ measured at $T = 300\,\mathrm{K} > T_{\mathrm{C}} \approx 270\,\mathrm{K}$ as discussed below in Section 5.3.2.

5.3.1 Temperature Dependent ESR Measurements

For $\mathbf{H} \parallel c$ configuration, the HF-ESR spectra were measured at four frequencies $\nu =$ 89.901 GHz, 199.396 GHz, 301.801 GHz and 348 GHz (Figure 5.3(a),(b), and Figure 5.4). As can be seen in these figures, at $T = 3\,\mathrm{K}$ the ESR lines are at a magnetic field lower than the paramagnetic resonance field H_{res}^{para} estimated using Equation 5.2. Temperature increase causes the shift of the line towards higher magnetic fields, continuing up to ~ 200 K, and above this temperature, the line shifts towards lower magnetic fields. At around

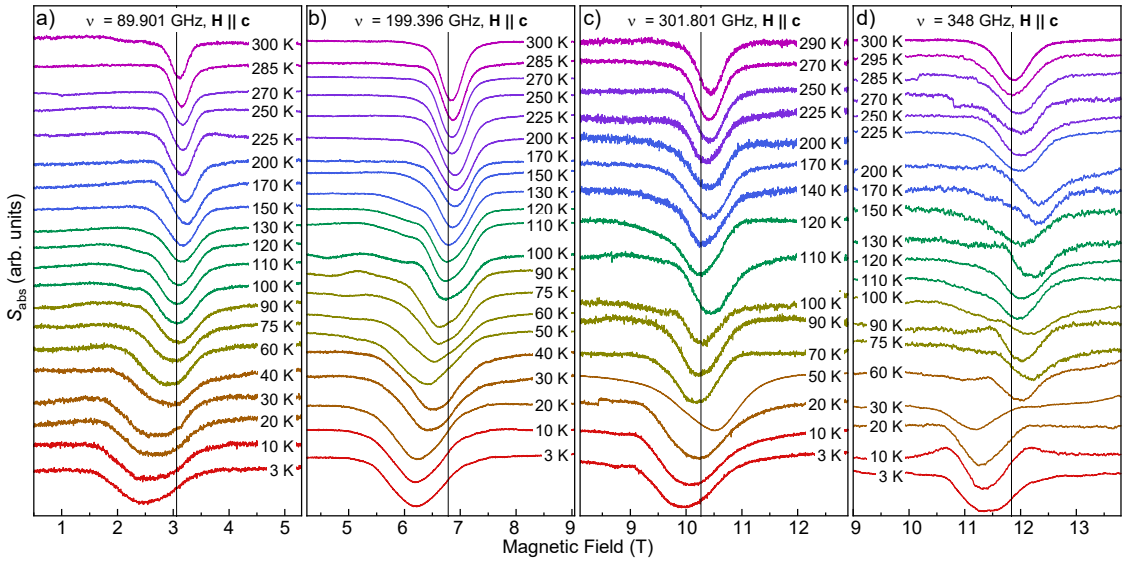

FIGURE 5.4: Temperature dependence of the HF-ESR spectra in the $\mathbf{H} \parallel c$ configuration at fixed excitation frequencies $\nu = 89.901\,\mathrm{GHz}$ (a), $199.396\,\mathrm{GHz}$ (b), $301.801\,\mathrm{GHz}$ (c), and $348\,\mathrm{GHz}$ (d). The spectra are normalized to unity and shifted vertically for clarity. Vertical solid lines represent the expected resonance position of the paramagnetic response.

$T_{\text{cross}} \sim 110\,\text{K}$, the resonance position of the measured ESR signal matches that of the expected paramagnetic line at H_{res}^{para}. These observations are practically independent of the excitation frequency, as shown in the panels of Figure 5.3. For $\mathbf{H} \parallel ab$ configuration, the ESR response was measured at five frequencies $\nu = 75.0405$ GHz, 89.342 GHz, 199.65 GHz, 299.88 GHz, and 348 GHz (Figure 5.3(c),(d), and Figure 5.5). In contrast to the $\mathbf{H} \parallel c$ configuration, here at all measurement frequencies, the low-T ESR lines have higher resonance fields than the estimated position of the paramagnetic line H_{res}^{para}. With increasing temperatures from 3 K to $\sim$ 200 K, the ESR lines are shifting progressively towards lower magnetic fields, crossing the corresponding paramagnetic line position around 110 K. Above $T \sim 200\,\text{K}$ the shift of the line changes direction. Interestingly, in both magnetic field configurations, the ESR lines develop shoulders and generally change shape with decreasing temperature below $\sim$ 130 K. This is especially well seen in the low-frequency data of the $\mathbf{H} \parallel ab$ configuration (Figure 5.3(c)).

The quantitative description of the shift of the ESR lines discussed above is presented in Figure 5.6, where the resonance field H_{res} is plotted as a function of temperature at different microwave frequencies and for both $\mathbf{H} \parallel ab$ and $\mathbf{H} \parallel c$ configurations. There for all frequencies, resonance fields measured in different configurations of the magnetic field are crossing around the temperature $T_{\text{cross}} \sim 110\,\text{K}$. The maximum shift of the resonance field

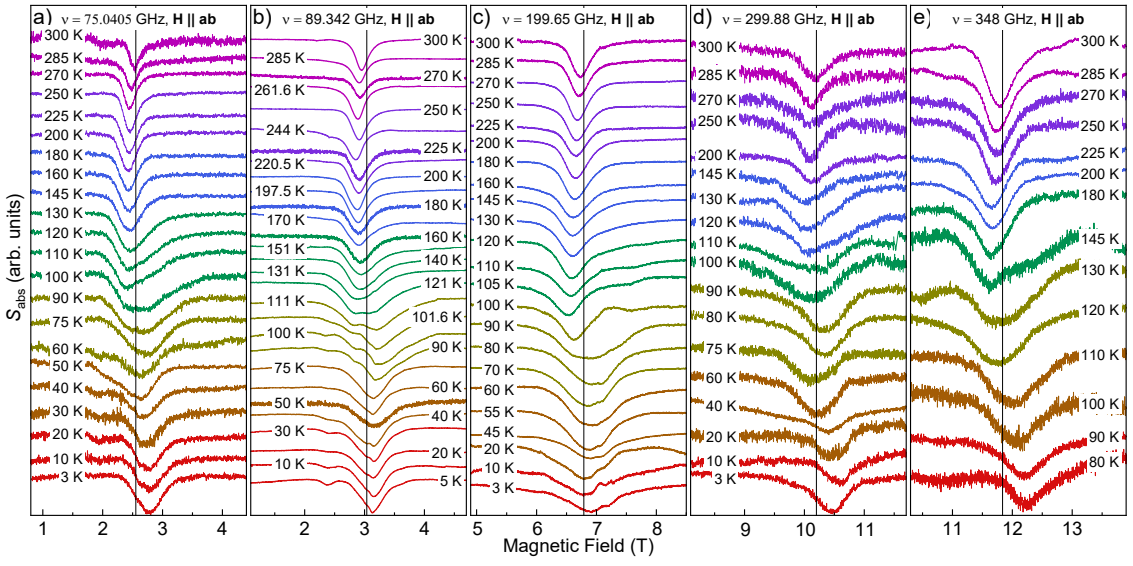

FIGURE 5.5: Temperature dependence of the HF-ESR spectra in the $\mathbf{H} \parallel ab$ configuration at fixed excitation frequencies $\nu = 75.0405\,\text{GHz}$ (a), 89.342 GHz (b), 199.65 GHz (c), 299.88 GHz (d), and 348 GHz (e). The spectra are normalized to unity and shifted vertically for clarity. Vertical solid lines represent the expected resonance position of the paramagnetic response.

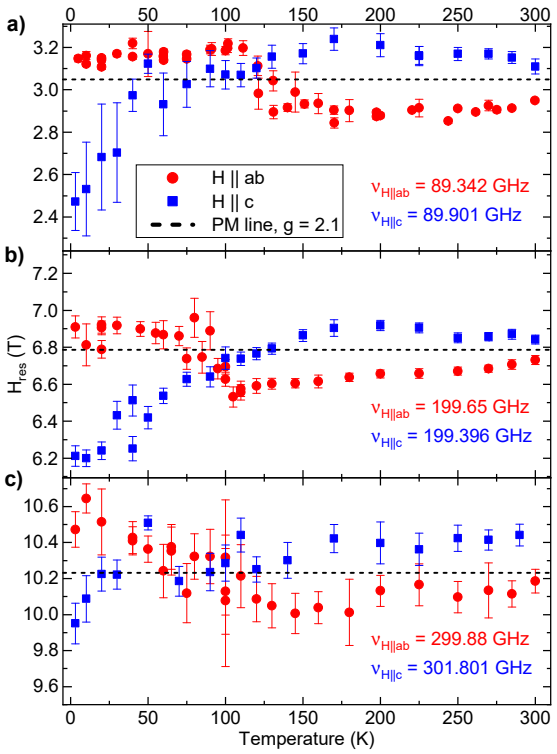

FIGURE 5.6: Resonance fields as a function of temperature measured in $\mathbf{H} \parallel ab$ and $\mathbf{H} \parallel c$ configurations at $\nu \sim 90\,\mathrm{GHz}$ (a), $\nu \sim 200\,\mathrm{GHz}$ (b), $\nu \sim 300\,\mathrm{GHz}$ (c). Horizontal dashed lines represent the expected resonance position of the paramagnetic response at H_{res}^{para} according to Equation (5.2) with g = 2.1.

from the position of the expected paramagnetic response H_{res}^{para} (dashed line) above T_{cross} is reached at $\sim 200\,\mathrm{K}$. Above this temperature H_{res} reduces; however, even at $T = 300\,\mathrm{K}$, $\sim 30\,\mathrm{K}$ above T_{C}, the shift of the lines from the expected paramagnetic position remains non-zero, as can also be seen in Figure 5.3.

5.3.2 Frequency Dependent ESR Measurements

In order to obtain detailed information on the evolution of the total MA field H_{a} and of the g-factor which both determine the resonance conditions of the ESR response in the FM ordered state, several frequency dependences of the resonance field $\nu(H_{\mathrm{res}})$ were measured in both configurations of the magnetic field $\mathbf{H} \parallel c$ and $\mathbf{H} \parallel ab$, and at a number of selected temperatures $T = 3\,\mathrm{K}$, $70\,\mathrm{K}$ (not shown), $110\,\mathrm{K}$, $200\,\mathrm{K}$, $300\,\mathrm{K}$ (Figure 5.7). To analyze these frequency dependences a linear spin-wave theory with the second quantization formalism [44, 386, 387] was used. The analytical expressions of the spin wave energies for an uniaxial ferromagnet are [386]:

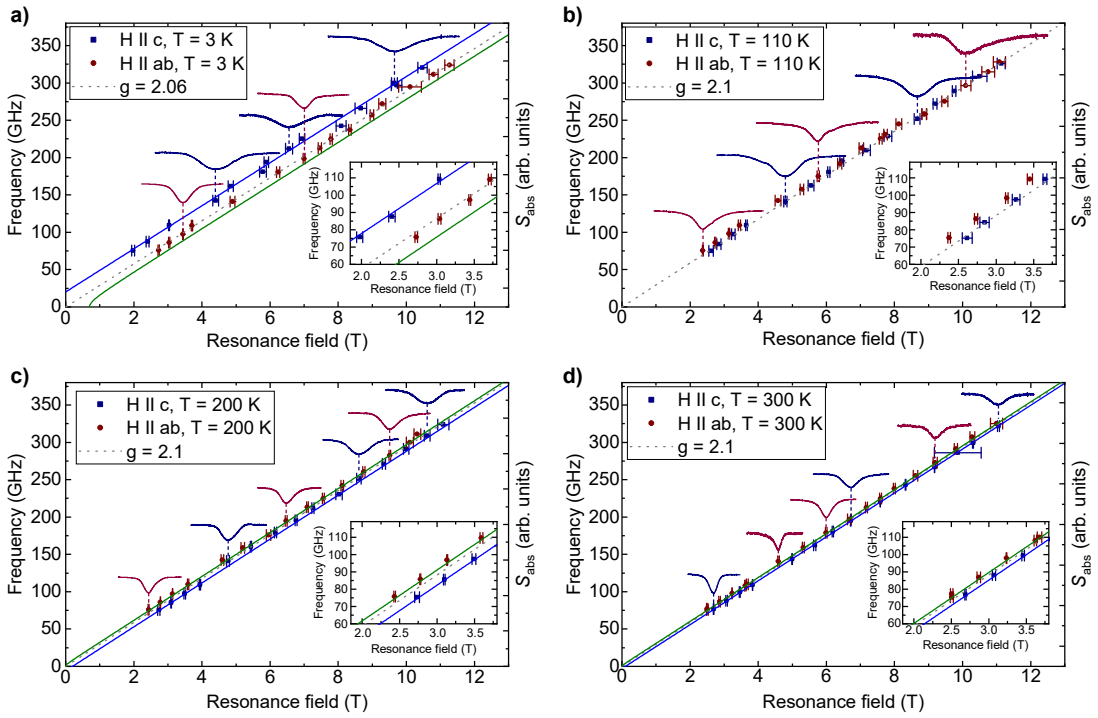

FIGURE 5.7: Frequency dependence of the resonance fields H_{res} at $T = 3\,\mathrm{K}$ (a), 110 K (b), 200 K (c), and 300 K (d), measured in $\mathbf{H} \parallel c$ (squares) and in $\mathbf{H} \parallel ab$ (circles) configurations, respectively. Dashed lines represent the paramagnetic response according to Equation (5.2) with the g-factors given in the corresponding legends. Solid lines depict the results of the best fit using Equations 5.3 and 5.4. Exemplary, normalized spectra are presented for all temperatures with colors corresponding to the respective magnetic field geometries. Insets: same $\nu - H_{\mathrm{res}}$ plots zoomed to the low-frequency and low-field regions.

(a) For easy-axis FM:

$$\mathbf{H} \parallel c\text{:} \qquad h\nu = \mathrm{g}\mu_{\mathrm{B}}\mu_0(H + |H_a|) \tag{5.3.1}$$

$$\mathbf{H} \parallel ab\text{:} \qquad h\nu = \mathrm{g}\mu_{\mathrm{B}}\mu_0\sqrt{H(H - |H_a|)} \tag{5.3.2}$$

(b) For easy-plane FM:

$$\mathbf{H} \parallel c\text{:} \qquad h\nu = \mathrm{g}\mu_{\mathrm{B}}\mu_0(H - |H_a|) \tag{5.4.1}$$

$$\mathbf{H} \parallel ab\text{:} \qquad h\nu = \mathrm{g}\mu_{\mathrm{B}}\mu_0\sqrt{H(H + |H_a|)} \tag{5.4.2}$$

Here the sign of the total MA field H_{a} defines the type of the anisotropy: It is positive for the easy-plane and is negative for the easy-axis anisotropy, respectively. All $\nu(H_{\mathrm{res}})$ dependences were fitted using these Equations 5.3 and 5.4. The best fits are presented as

solid lines in Figure 5.7. The results are summarized in Table 5.1 and the obtained values of H_a are plotted in Figure 5.9 as closed squares and closed circles.

At $T = 300\,\mathrm{K}$, i.e., $\sim 30\,\mathrm{K}$ above T_C, and at $T = 200\,\mathrm{K}$, i.e., $\sim 70\,\mathrm{K}$ below T_C, the best fits were achieved using the *easy-plane* FM model (Equation 5.4). In the former case (Figure 5.7(d)) the average value of the anisotropy field is $\mu_0 H_a \approx 0.12$ T, whereas in the latter case (Figure 5.7(c)) the average value of the anisotropy field can be estimated as $\mu_0 H_a \approx 0.2$ T. At a temperature $T = 110\,\mathrm{K}$ around T_{cross} fits using Equations 5.3 and 5.4 within the error bars yield *zero anisotropy field* (Figure 5.7(b)). Below T_{cross} at $T = 70\,\mathrm{K}$ the average value of H_a amounts to $\sim -0.06\,\mathrm{T}$. Note that at this temperature, the values of the anisotropy field are negative since the best results were obtained with the *easy-axis* FM model. Within the error bars, the g-factor at all these temperatures $T = 300\,\mathrm{K}$, $200\,\mathrm{K}$, $110\,\mathrm{K}$ and $70\,\mathrm{K}$ is found to be practically isotropic with the value of 2.1 ± 0.01.

T	$\mu_0 H_a$ for $\mathbf{H} \parallel c$	$\mu_0 H_a$ for $\mathbf{H} \parallel ab$	average $\mu_0 H_a$	g for $\mathbf{H} \parallel c$	g for $\mathbf{H} \parallel ab$	average g
3 K	-0.707 ± 0.118 T	-0.129 ± 0.109 T		2.045 ± 0.032	2.073 ± 0.015	2.06 ± 0.01
70 K	-0.128 ± 0.084 T	0 ± 0.158 T	~ -0.06 T	2.119 ± 0.025	2.085 ± 0.024	2.10 ± 0.01
270 K	0.158 ± 0.050 T	0.336 ± 0.090 T	$\sim +0.20$ T	2.117 ± 0.015	2.092 ± 0.013	2.10 ± 0.01
300 K	0.076 ± 0.023 T	0.179 ± 0.052 T	$\sim +0.12$ T	2.095 ± 0.007	2.099 ± 0.008	2.10 ± 0.01

TABLE 5.1: Total MA field H_a and g-factor values at different temperatures obtained from the fits of the $\nu(H_{res})$ dependences measured in the $\mathbf{H} \parallel c$ and $\mathbf{H} \parallel ab$ configurations. The sign of H_a defines the type of the anisotropy: It is positive for the easy-plane and is negative for the easy-axis anisotropy, respectively.

Finally, at the lowest measurement temperature of 3 K (Figure 5.7(a)) the best fit was achieved using the *easy-axis* FM model. Interestingly, the resulting values of the anisotropy field for $\mathbf{H} \parallel c$ and $\mathbf{H} \parallel ab$ (Figure 5.9 and Table 5.1) are different, even if the error bars are taken into account, which suggests that such simple uniaxial FM model cannot fully describe the observed magnetic field dependences of the spin wave energies in this low-temperature regime. Additionally, the average g-factor value at this temperature of 3 K is reduced to 2.06 ± 0.01.

Similar ESR measurements were carried out for different orientations of the applied magnetic field in the *ab*-plane of the Fe_4GeTe_2 crystal, yielding as a result no detectable in-plane anisotropy within the error bars (see 5.3.3).

5.3.3 In-plane Anisotropy

To investigate the anisotropy within the *ab*-plane, the Fe_4GeTe_2 crystal was rotated by 90 degrees with respect to the original in-plane configuration (IP1). In this second in-plane configuration (IP2), frequency dependences of the resonance fields $\nu(H_{\mathrm{res}})$ were measured both at $T = 3\,\mathrm{K}$, in the magnetically ordered state, and at $T = 300\,\mathrm{K}$, $\sim 30\,\mathrm{K}$ above T_{C}. The comparison of the results of two configurations IP1 and IP2 is shown in Figure 5.8. As can be seen, at both temperatures, two magnetic field configurations yield the same, within error bars, result, which enables a conclusion that there is no detectable in-plane anisotropy present in this Fe_4GeTe_2 crystal.

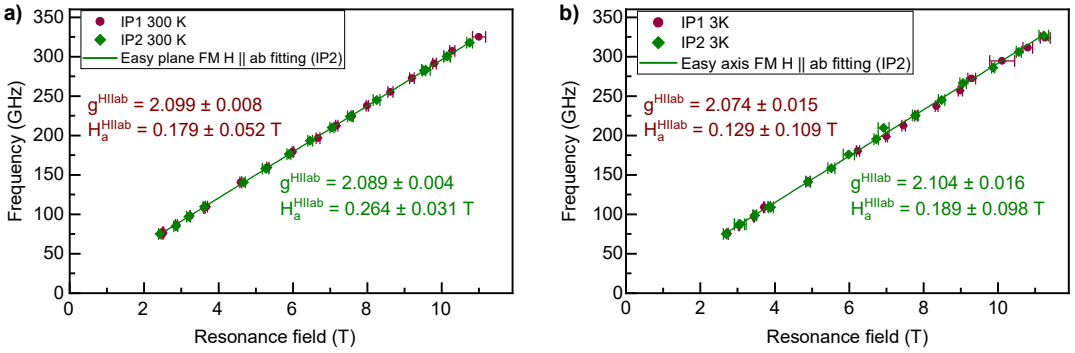

FIGURE 5.8: The frequency dependence of the resonance fields $\nu(H_{\mathrm{res}})$ at (a) 300 K and at (b) 3 K for two mutually perpendicular in-plane directions, IP1 ($\mathbf{H} \parallel ab$) and IP2 (new). The green line indicates the corresponding fitting of the IP2 data. The fitting parameters are written in the inset of the corresponding figures.

5.3.4 Estimation of Magnetic Anisotropy Field

Such a rich set of temperature dependences of H_{res} measured at four (for $\mathbf{H} \parallel c$) or five (for $\mathbf{H} \parallel ab$) frequencies, as shown in Section 5.3.1, enables us to extract the temperature evolution of the total MA field H_{a} by fitting the corresponding $\nu(H_{\mathrm{res}})$ dependences at each temperature using Equations 5.3, 5.4. In order to reduce the error bars, during the fitting procedure, the g-factor was fixed according to the result of the analysis of the detailed $\nu(H_{\mathrm{res}})$ dependences with larger amounts of points (Section 5.3.2), and therefore only H_{a} as the fit parameter was determined using this procedure. At temperatures above $\sim 70\,\mathrm{K}$ the g-factor was kept constant at a value of 2.1 for both magnetic field configurations $\mathbf{H} \parallel c$ and $\mathbf{H} \parallel ab$, and in the temperature range of 3 K - 70 K the g-factor was linearly approximated between values of 2.06 and 2.1. The result is shown as open symbols in Figure 5.9. The good matching of these results with the closed symbols, obtained from the

analysis of the detailed $\nu(H_{\mathrm{res}})$ dependences measured at selected temperatures, validates the use of such an approach.

Interestingly, below $\sim 50\,\mathrm{K}$ the absolute values of the anisotropy field $|H_{\mathrm{a}}|$ obtained in different configurations of the magnetic field, $\mathbf{H} \parallel c$ (circles) and $\mathbf{H} \parallel ab$ (squares), start to deviate from each other even if the error bars are taken into account: for $\mathbf{H} \parallel c$, $|H_{\mathrm{a}}|$ continues to increase with decreasing temperature, and for $\mathbf{H} \parallel ab$, $|H_{\mathrm{a}}|$ stays practically constant. First of all, this suggests that the model used to describe uniaxial FM spin waves is not fully applicable below $\sim 50\,\mathrm{K}$, i.e., the anisotropy becomes more complex than the uniaxial one. Second, from the point of view of the anisotropy, another characteristic temperature $T_{\mathrm{d}} \sim 50\,\mathrm{K}$ where the spin waves change qualitatively can be identified in addition to the temperature T_{cross} where H_{a} changes sign (Figure 5.9).

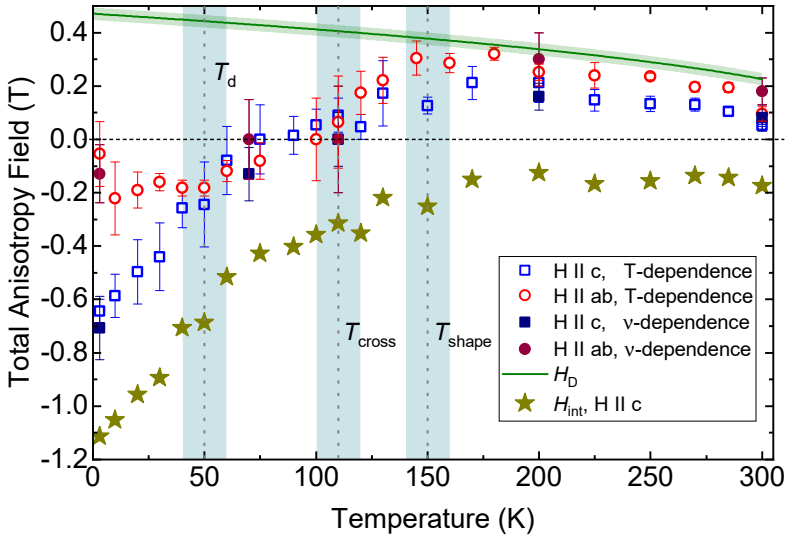

FIGURE 5.9: Total anisotropy field H_{a} as a function of temperature. Squares represent H_{a} for the $\mathbf{H} \parallel c$ configuration, and circles depict H_{a} for the $\mathbf{H} \parallel ab$ configuration obtained from the frequency (closed symbols) and temperature (open symbols) dependences of the resonance position, respectively. The solid line is the calculated anisotropy field H_{D} given by the shape anisotropy. Stars depict the extracted intrinsic anisotropy field H_{int} for the $\mathbf{H} \parallel c$ configuration. Vertical dashed lines and the shaded area around them indicate characteristic temperatures T_{shape}, T_{cross}, and T_{d} revealed in the analysis of the ESR data, as well as the estimation of the uncertainty region, respectively.

The total MA field entering in Equations (5.3.1) and (5.3.2) is the sum of two contributions: $H_{\mathrm{a}} = H_{\mathrm{int}} + H_{\mathrm{D}}$ in the entire measurement temperature range. Here, H_{int} is the intrinsic, so-called magnetocrystalline anisotropy field and $H_{\mathrm{D}} = 4\pi N M_{\mathrm{S}}$ is the shape anisotropy field determined by the demagnetization factor N of the plate-like sample and its saturation magnetization M_{S}. T_{cross} is therefore the characteristic temperature where both contributions to the total MA field cancel out, yielding zero H_{a}. In order to address

the question of the origin of the measured total anisotropy field (Figure 5.9) we have calculated the expected shape anisotropy field at different temperatures with $N \approx 0.71$ estimated from the dimensions of the studied sample [388, 389] (see Section 5.2), and with $M_S(T)$ values determined in [36] (see 5.2.2, Figure 5.2). The result is depicted as the solid line in Figure 5.9, with the shaded area around it representing the uncertainty of the estimated H_D. As can be seen, in the temperature range of 300 K – $\sim$ 150 K, the anisotropy field H_a, obtained from the analysis of the ESR data, has the same sign, temperature evolution, and the value quite close to the expected H_D. This observation suggests that, at $T > T_{shape} \sim 150$ K, the main contribution to the total MA of Fe_4GeTe_2 is given by the shape of the sample due to the demagnetization effect. Such an estimate of H_D, based on the static magnetometry measurements, enables calculation of the intrinsic, magnetocrystalline anisotropy field H_{int}. The result for the $\mathbf{H} \parallel c$ configuration is shown in Figure 5.9 as stars. As can be seen, it is negative in the whole measurement temperature range, evidencing the *easy-axis* type of the intrinsic magnetocrystalline anisotropy of Fe_4GeTe_2. The respective values of the intrinsic anisotropy constant $K_{int} = H_{int}/(2M_S)$ for two magnetic field configurations, $\mathbf{H} \parallel c$ and $\mathbf{H} \parallel ab$, are presented in Figure 5.11(a). Note, that the values obtained below $T_d \sim 50$ K should be considered as rough estimates only since, as mentioned above, the simple model used here is not fully applicable to describe the anisotropy at those low temperatures.

5.3.5 X-ray Diffraction Study

To investigate whether the spin reorientation transition stems from temperature-dependent modifications in the crystal lattice, we conducted single-crystal X-ray diffraction (XRD) measurements[3] across the temperature range of 10 K to 320 K (see Section 5.2 for details). All observed Bragg reflections are fully consistent with the reported $R\bar{3}m$ structure [210]. However, around the Bragg reflections, we discovered strong superlattice reflections with intensities approximately 10% of the adjacent Bragg reflection (see Figure 5.10(c)). The positions, intensities, and full width at half maximum (FWHM) of these superlattice peaks displayed no significant variation within the studied temperature range, indicating the stability of the detected superlattice. Notably, the width of the superlattice peaks along the h and k directions was consistently resolution-limited at all studied temperatures, indicating a truly long-range ordered superlattice within the *ab*-plane, with a modulation vector $\mathbf{q} = (1/3, 1/3, 0)$. Only along the *c*-direction, the superlattice is less well correlated, as is often the case with layered materials.

[3]This single crystal XRD study was performed by Prof. Jochen Geck's group at TU Dresden, Germany

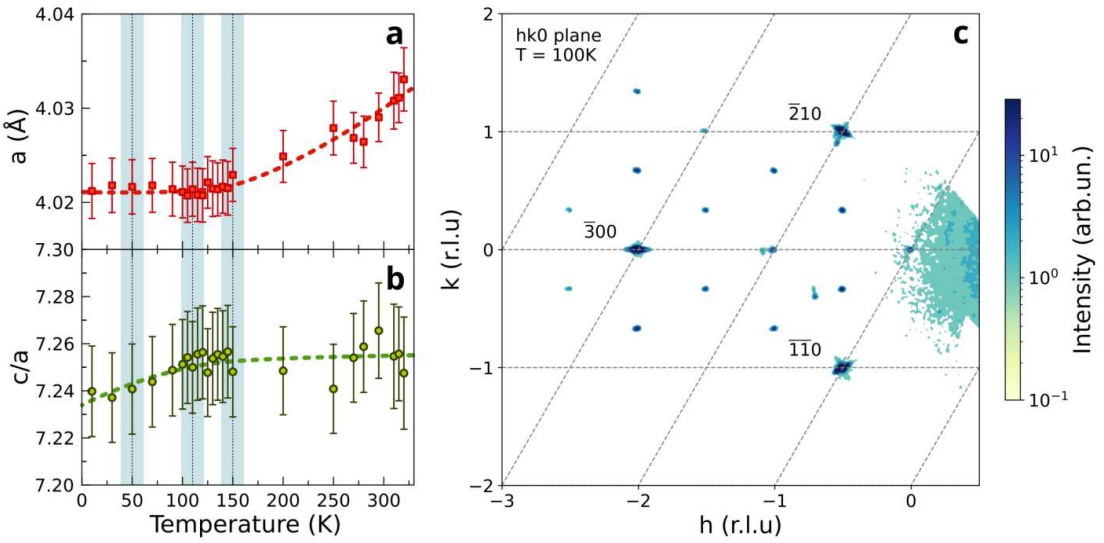

FIGURE 5.10: Lattice parameter a (a) and the c/a ratio (b) of the Fe_4GeTe_2 as a function of temperature. The dotted lines are guides to the eye. (hk0) cut of the reciprocal space, measured at 100 K (c). This single-crystal XRD study was performed by Prof. Jochen Geck's group at TU Dresden, Germany.

The lattice parameter a and the c/a ratio of the underlying $R\bar{3}m$ structure as a function of temperature are presented in Figure 5.10(a),(b). As can be observed, both quantities demonstrate a smooth and continuous temperature dependence, implying the absence of any lattice anomaly between 10 K and 320 K in our data. Given the fixed lattice symmetry and the temperature evolution of the lattice constants and the superlattice peaks, we infer that the alterations in the magnetic properties described above are unrelated to a structural transition. Nevertheless, both the parameters a and c/a exhibit minor changes in slope, suggesting the presence of a possible subtle magnetoelastic coupling. It is important to note, however, that the observed effects are minimal and fall below the resolution limit of $\Delta d/d \sim 5 \cdot 10^{-3}$ of the current XRD experiment.

5.4 Discussion

One of the central experimental observations of this work is the peculiar temperature evolution of the total anisotropy field in Fe_4GeTe_2 (Figure 5.9). As discussed in Section 5.3.4, at high temperatures the main contribution to the MA is given by the plate-like shape of the sample due to the demagnetization effect, with a small contribution of the intrinsic *easy-axis* uniaxial anisotropy. Importantly, even at a temperature $\sim 30\,\mathrm{K}$ above T_C there is a non-zero total anisotropy field, suggesting sizable short-range correlations seen on the time scale of the ESR experiment. Such correlations are typical

for the intrinsic low-dimensionality of the layered vdW materials [44, 390, 391], suggesting the 2D-like character of the magnetism in Fe_4GeTe_2. This observation is in line with the results of the analysis of the critical behavior of magnetization isotherms of Fe_4GeTe_2, reported in [14], suggesting a reduced dimensionality ($d < 3$) of this compound. Such signatures of the low-dimensional behavior pronounced in the bulk samples suggest that the peculiar magnetic properties observed in this and other works should also remain if the sample is thinned to the monolayer limit, providing an opportunity to utilize Fe_4GeTe_2 as a building block of the future nanoscale devices.

Below the characteristic temperature $T_{\text{shape}} \sim 150\,\text{K}$, our data reveals a significant growth of the easy-axis anisotropy. Interestingly, below this temperature the electrical resistivity of Fe_4GeTe_2 strongly reduces [36, 80, 210, 375] (Figure 5.11(b)). Moreover, around T_{shape} there is an anomaly in the magnetoresistance and a change of the sign of the Hall coefficient (Figure 5.11(c)). All these observations provide the first clues of a plausible relationship between the MA with the properties of the charge carriers in this system. The growing intrinsic *easy-axis* anisotropy with the temperature decrease competes with an *easy-plane* type of shape anisotropy, making the material seemingly isotropic at around T_{cross}. This temperature corresponds to the spin reorientation transition at T_{SR} observed in the static magnetometry and magnetoresistance measurements previously reported in Refs. [14, 36, 80, 81, 210, 375]. It is important to emphasize, that this spin reorientation effect turns out to be *not* an intrinsic property of Fe_4GeTe_2 but is rather due to the sample plate-like shape of the single crystals. If the sample were a sphere for which H_D is zero, then the total anisotropy would always be negative (*easy-axis*) in the measurement temperature range and never positive (*easy-plane*).

That, in turn, suggests a possible sample dependence of T_{SR}, which, however, should not be strong due to a natural tendency of the layered vdW compounds to grow as flakes. Therefore, all the studied samples likely have a similar flat shape in the first approximation. Our experimental result stands in contrast with theoretical calculations of the magnetocrystalline anisotropy for the monolayer [371, 392, 393] or for a bulk sample of Fe_4GeTe_2 [393, 394], which predict the anisotropy to be of the *easy-plane* type. However, the type of uniaxial anisotropy calculated for the bulk sample in [392] and for the monolayer sample using the GGA+U approach in [394] is in agreement with our experimental data.

Below one further characteristic temperature $T_{\text{d}} \sim 50\,\text{K}$ the anisotropy becomes more sophisticated than a simple uniaxial easy-axis type. Remarkably, this characteristic temperature is also related to the observations in the transport experiments, where around temperature $T_{\text{Q}} \sim 40\,\text{K} - 50\,\text{K}$ the change of the sign of the magnetoresistance

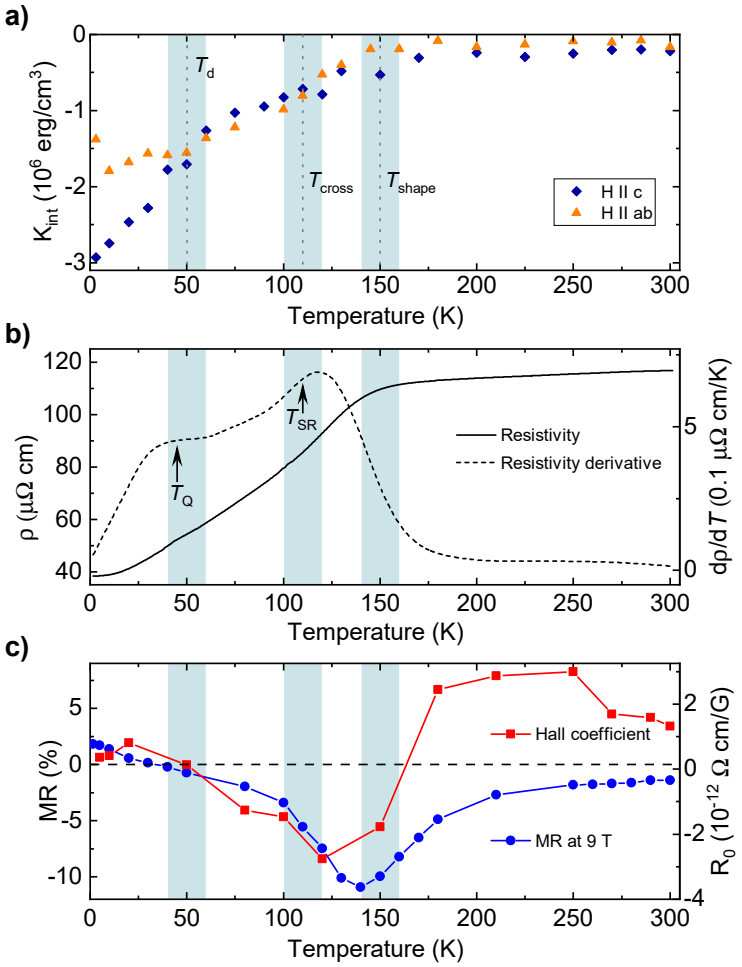

FIGURE 5.11: a) Temperature evolution of the intrinsic MA constant $K_{\mathrm{int}} = H_{\mathrm{int}}/(2M_{\mathrm{S}})$ estimated from the measurements in the $\mathbf{H} \parallel c$ (diamonds) and $\mathbf{H} \parallel ab$ (triangles) configurations, respectively. b) Resistivity and resistivity derivative as a function of temperature. c) Magnetoresistance and ordinary Hall coefficient as a function of temperature. Data in b) and c) is taken from [36]. Vertical dashed lines and the shaded area around them in a), b), and c) indicate characteristic temperatures T_{shape}, T_{cross}, and T_{d} revealed in the analysis of the ESR data, as well as the estimation of the uncertainty region, respectively.

and Hall coefficient [36] takes place together with the occurrence of an anomaly in the first derivative of the resistivity [36, 210, 375] (Figure 5.11(b),(c)). Moreover, as it is especially well seen in the temperature dependence of the ESR spectra measured in the $\mathbf{H} \parallel ab$ configuration at low frequencies (Figure 5.3(c), and Figure 5.5(a-c)), the ESR signal changes its shape in the temperature range of 3 K – $\sim$ 130 K. Starting from low temperatures, the signal develops a shoulder at the low field side, and with increasing T, the shoulder grows in intensity, whereas the main line gets smaller. At around T_{cross}, which is related to T_{SR} their intensities become almost equal, and above this temperature,

the former shoulder transforms into the dominant line of the total ESR response. One can conjecture that such behavior can indicate a gradual, *qualitative* change of the spin wave modes in Fe_4GeTe_2 contributing to the ESR response as a function of temperature. Apparently, these modes coexist in the broad temperature range. Such coexistence is likely due to the complexity of the crystal and electronic structures of Fe_4GeTe_2. The crystal structure features two crystallographically inequivalent Fe ions, which can be grouped into two pairs Fe1/Fe2 and Fe3/Fe4 considering their local environment (Figure 5.1(a),(b)). Also, a contribution of the orbital degree of freedom from the Fe ions as well as nearest ligands Te and Ge, suggested by the enhanced g-factor in comparison with the free electron value, may play an important role in the magnetic and electronic properties of Fe_4GeTe_2. Indeed, the X-ray Magnetic Circular Dichroism (XMCD) studies reported in [393] suggest that, even though the orbital moment is reduced with respect to Fe_3GeTe_2, it is found to be of $\sim 0.05\,\mu_B$/Fe in the Fe_4GeTe_2 compound.

In order to address the question of the origin of the MA in Fe_4GeTe_2 responsible for the stabilization of the ground state with the respective spin wave excitations, one has to understand the nature of the magnetism first. Without doubt, an important role is played by the conduction electrons; however, an additional contribution of the electrons localized at the Fe *d*-orbitals is suggested by the DFT calculations in [80, 395] and by the analysis of the critical magnetization isotherms in [14].

It is instructive to consider first an itinerant picture. The DFT calculations in [36] suggest that there could be two different stable states, separated by a small energy difference of $\sim 10\,\text{meV} \approx 116\,\text{K}$. An increase in the temperature may assist the population of the state with higher energy, and therefore induce a change in the spectrum of the excitations probed in the ESR experiment. However, in this case, little is known about the details of the anisotropies of these states, only that the preferred orientation of the Fe spins is close to the *c*-axis, which is qualitatively in line with observations of the ESR line shifts.

In order to address the problem of the anisotropies, it is possible to write down the crystal field (CF) or the ligand field potential, felt by the *d*-electrons of Fe^{2+}, for the arbitrary symmetry of the local environment. Such CF potential of the general form can be expressed as:

$$\begin{aligned} V_{CF} = {} & B_2^0 C_2^0 + B_2^1 (C_2^{-1} - C_2^{+1}) + B_2^2 (C_2^{-2} + C_2^{+2}) \\ & + B_4^0 C_4^0 + B_4^1 (C_4^{-1} - C_4^{+1}) + B_4^2 (C_4^{-2} + C_4^{+2}) \\ & + B_4^3 (C_4^{-3} - C_4^{+3}) + B_4^4 (C_4^{-4} + C_4^{+4}) \end{aligned} \tag{5.5}$$

Here, B_k^q are the crystal field parameters, and C_k^q are the spherical tensor operators related to spherical harmonics $C_k^q = \sqrt{\frac{4\pi}{2k+1}} Y_k^q$. With the assumption that all 6 d-electrons occupy the Fe^{2+} orbitals (localized picture), it is possible to estimate the coefficients B_k^q describing the local crystal field potential for all four Fe ions using the simple point charge model. Though this approach is applicable mostly to the ionic compounds, as it neglects effects from covalency and the itinerant charge carriers, it can still give a qualitative understanding of the symmetry of the electronic local environment [396]. This is important in this compound even if only the itinerant magnetism is considered [393]. Following the procedure described in Ref. [397], the calculated CF potential (see isosurfaces in Figure 5.1(b)) turns out to be the same within each pair Fe1/Fe2 and Fe3/Fe4; however, it is quite different between the pairs. The non-equivalence of the Fe sites from the DFT point of view is also suggested in [80, 370, 371, 374, 393–395]. Interestingly, in both cases, the sign of the estimated second-order term B_2^0 suggests an *easy-axis* anisotropy, which is in line with our experimental observation of the ESR line shift in the whole measurement temperature range. Additionally, the CF potential at the Fe3 (Fe4) position is smaller than that at the Fe1 (Fe2) position, and the contribution of the second-order terms B_2^q is smaller than the cubic ones B_4^q, which suggests that the MA might be smaller for the Fe3 (Fe4) ions. Such a difference in the CF potentials for different Fe ions is mostly due to a difference in the charge of the nearest ligands, Ge^{4-} in the case of Fe1 and Fe2, and Te^{2-} in the case of Fe3 and Fe4. Therefore, the presence of two different local Fe environments and potentially non-equivalent exchange interactions coupling the respective Fe spins suggests at least 4 magnetic sublattices with two different types of anisotropy.

Moreover, considering a complex, unusual behavior of the MA as a function of temperature revealed in the present ESR study, as well as a number of features in the static magnetization and magnetotransport measurements observed at the characteristic temperatures established in our ESR experiments (Figure 5.11), it is also possible that these peculiarities may be due to the coexistence of itinerant and localized magnetism in Fe_4GeTe_2. In both cases, the local Fe-ligand structure suggests the existence of several distinct (localized or itinerant) magnetic sublattices in Fe_4GeTe_2, with their unique anisotropies and interactions, which contribute to the formation of the FM-ordered ground state and the respective excitations. Based on our XRD study, both the average $R\bar{3}m$ lattice structure and the superlattice exhibit no discernible anomaly within the investigated temperature range, particularly between 100 K and 150 K. This suggests that the amplification of the intrinsic easy-axis anisotropy is not attributed to a structural transition; however, there could be a minor structural contribution due to a c/a parameter, exhibiting in its temperature dependence a possible change in slope.

Moreover, one might speculate that the additional potential arising from the superlattice modulation interacts with electronic states, possibly inducing variations in electronic properties as temperature decreases. In principle, this could also impact the parameters B_k^q in Equation 5.5, thereby influencing the MA. However, this scenario certainly requires further scrutiny in future studies. It is interesting, that despite such a complexity of the system, the high-temperature excitations at $T >\sim 150\,\mathrm{K}$ are well described by the simplest one-sublattice ferromagnetic model with the predominant contribution of the shape anisotropy, suggesting a temperature averaging of the differences in the local anisotropies of the individual magnetic sublattices and of the interactions coupling them.

Nevertheless, a remarkable correspondence of the characteristic temperatures observed in the ESR and transport experiments suggests a plausible strong mutual dependence of the spin waves and the charge carriers. That, in turn, opens a possibility to tune the transport properties of Fe_4GeTe_2 by controlling the magnetic excitations, and *vice versa*, which could find an application in the next generation spintronic devices. So far, this kind of coupling has been demonstrated mostly on the artificial hybrid ferromagnet/metal multilayers, as, e.g., in Ref. [398], whereas Fe_4GeTe_2 may be an example of "natural" functional material featuring an intrinsic magneto-electronic coupling.

5.5 Summary

In summary, we have performed a detailed ESR spectroscopic study of the single-crystalline quasi-2D vdW ferromagnet Fe_4GeTe_2 with the high ordering temperature $T_C = 270\,\mathrm{K}$. The measurements were carried out in a broad range of excitation frequencies and temperatures, and at different orientations of the magnetic field with respect to the sample. One of the main observations of this work is the unusual evolution of the MA field with temperature. First of all, it does not vanish at temperatures well above T_C, likely due to the sizable short-range correlations. This suggests an intrinsic low-dimensionality, which in turn should ensure the persistence of the observed magnetic properties when reaching the monolayer limit of Fe_4GeTe_2 sample. The analysis of the ESR data reveals several characteristic temperatures for the magnetic behavior of Fe_4GeTe_2 in the ferromagnetically ordered state. In between T_C and the characteristic temperature $T_{shape} \sim 150\,\mathrm{K}$ the total anisotropy is dominated by the demagnetization effect due to the plate-like shape of the sample. However, below T_{shape} the intrinsic uniaxial easy-axis MA starts to noticeably grow counteracting the easy-plane shape anisotropy, which renders the sample seemingly isotropic at the spin reorientation transition at T_{SR}. The data

reveals one further characteristic temperature $T_d \sim 50\,K$, below which the anisotropy becomes considerably more complex, likely due to a multi-sublattice nature of the ground state stabilized in this temperature regime. Importantly, our results give evidence that the main contribution to the intrinsic MA of Fe_4GeTe_2 is always of an *easy-axis* type in the entire temperature range below and above T_{SR}, and that the reorientation of the sample's magnetization from the out- to the in-plane direction observed at T_{SR} in the static magnetic measurements results from the competition between the intrinsic easy-axis anisotropy of this compound and the (extrinsic) shape anisotropy of the plate-like crystal. The ESR spectral shape exhibits a complex temperature evolution, suggesting a gradual, *qualitative* change of the spin wave modes in Fe_4GeTe_2. This is likely due to the complexity of the crystal and electronic structures of Fe_4GeTe_2, yielding several distinct magnetic sublattices that feature different temperature-dependent anisotropies and interactions. Interestingly, our XRD study suggests that the temperature evolution of the anisotropy is not driven by the structural transition. The characteristic temperatures found in the ESR experiment are in remarkable correspondence with those observed in the transport measurements, suggesting intertwined magnetic and electronic behaviors in Fe_4GeTe_2. Altogether, our findings on the peculiar intrinsic MA of Fe_4GeTe_2 provide important clues for the functionalization of this metallic near-room-temperature ferromagnet for use in magneto-electronic devices and call for the development of the microscopic theories, as well as for the experiments devoted to the detection of the spin Hall and inverse spin Hall effects, for a better understanding of a complex interplay of magnetic and electronic degrees of freedom in this material.

Chapter 6

Understanding Lattice Dynamics and Spin-Phonon Coupling in Fe_4GeTe_2 by Raman Spectroscopy

The metallic ferromagnet Fe_4GeTe_2 has drawn significant attention for its near-room-temperature ferromagnetic order ($T_C \sim 270$ K) and spin-reorientation transition ($T_{SR} \sim 110$ K), showcasing a unique interplay between spin, lattice, and electronic degrees of freedom. Here, we employ micro-Raman spectroscopy in conjunction with both first-principles and spin-dynamical calculations to investigate the intricate interdependence of lattice dynamics and spin-phonon coupling in exfoliated Fe_4GeTe_2 nanoflakes. While polarization-resolved measurements reveal the symmetry-allowed vibrational modes of the underlying lattice, the temperature dependence of the spectra highlights a pronounced spin-phonon interaction. Around T_C, hardening of the phonon modes and subsequent narrowing of their linewidths are primarily driven by anharmonic phonon-phonon scattering. Intriguingly, below T_{SR}, we observe anomalous phonon softening accompanied by linewidth broadening, indicative of strong spin-lattice coupling. The significant deviation from the anharmonic approximation below T_{SR} may be mostly attributed to enhanced spin-phonon interactions, manifesting as a peak in the phonon lifetimes at T_{SR}. These findings offer crucial insights into the magnetic and lattice dynamics of Fe_4GeTe_2 and underscore its potential for spintronic and other functional applications.

6.1 Introduction

The coupling between magnetic spins and lattice vibrations, or spin-phonon coupling, is fundamental to the emergence of diverse correlated phenomena in magnetic materials, such as superconductivity [399, 400], multiferroicity [401, 402], and spin-reorientation transitions in correlated oxides [403, 404]. This interaction becomes more complex in materials with multiple magnetic sublattices, where the interplay between distinct magnetic moments and the crystal lattice generates nonlinear responses [37]. Spin-phonon coupling mediates the interaction between magnetic and structural degrees of freedom, stabilizing coexisting orders while giving rise to new phases and instabilities [405]. In two-dimensional magnetic materials, reduced dimensionality and geometric constraints amplify the significance of spin-phonon interactions [406–408]. Magnetic anisotropy, especially uniaxial anisotropy influenced by spin-orbit coupling, determines the orientation of magnetic moments within the 2D plane and their interaction with the crystal lattice. This reduced symmetry intensifies spin-phonon coupling, observable through effects such as phonon softening and frequency shifts. For example, in CrI_3, spin-orbit coupling stabilizes a preferred magnetization direction [407, 409], while in $Cr_2Ge_2Te_6$, the interaction modifies the phonon spectrum, impacting thermal conductivity and magnetization behavior [410]. These interactions drive dynamic magneto-structural transitions [411], underpinning novel phenomena such as skyrmions and magnetically induced ferroelectricity [166].

In high-temperature metallic ferromagnets like Fe_3GeTe_2, Fe_4GeTe_2, and Fe_5GeTe_2, the situation becomes more complicated due to the presence of conduction electrons [37, 407, 412]. The coupling between the charge carriers and lattice vibrations not only modifies the electronic band structure but also mediates magnetoelastic effects that influence the magnetic ordering [413]. In particular, the near-room-temperature metallic ferromagnet Fe_4GeTe_2 ($T_C \sim 270$ K) has attracted significant attention within this 2D magnet family due to a distinctive spin-reorientation transition at $T_{SR} \sim 110$ K, where the magnetic easy axis changes with temperature [13–15, 36]. These transitions are accompanied by unconventional magneto-transport properties such as large negative magnetoresistance, anomalous Hall conductivity, and a change in sign in the ordinary Hall coefficient [36]. The electron spin resonance (ESR) studies further reveal a complex temperature-dependent evolution of spectral shapes, reflecting a gradual qualitative shift in spin-wave modes arising from the crystal's intricate electronic structure [15]. While the spin-reorientation transition is believed to arise from the competition between intrinsic easy-axis magneto-crystalline anisotropy and extrinsic shape anisotropy stemming from the plate-like shape

of the crystal, X-ray diffraction studies are unable to definitively determine whether this transition involves any structural changes [15]. Nevertheless, understanding the interactions between magnons and phonons, as well as the dynamics of phonon-phonon coupling, is crucial for comprehending how these factors evolve and compete at different temperatures, ultimately influencing the material's macroscopic properties.

Raman spectroscopy is a vital tool for probing phonon properties and their interactions with quasi-particles, offering insights into phase transitions, spin-phonon interactions, spin-wave excitations, lattice symmetry changes, and defects in condensed matter systems [410, 414–417]. In this study, we investigate the lattice dynamics of exfoliated Fe_4GeTe_2 nanoflakes using micro-Raman spectroscopy, focusing on mode symmetry and spin-phonon coupling through temperature-dependent measurements. By performing polarized Raman spectroscopy, we identify the characteristic Raman modes, further verified by the DFT-based theoretical calculations. Below T_C, significant phonon hardening and linewidth narrowing are observed and can be attributed to anharmonicity from phonon-phonon scattering, while below T_{SR}, anomalous phonon softening and linewidth broadening indicate strong spin-lattice interactions. Near T_{SR}, the interplay of spin-phonon coupling and intrinsic anharmonicity produces a distinct slope change in phonon frequency data, with maximum spin-phonon coupling strength at the lowest temperatures and peak phonon lifetime near T_{SR}. Theoretical calculations[1] reveal the presence of magnon and phonon DOS at a similar energy window, suggesting a strong coupling.

6.2 Experimental Methods

6.2.1 Fe_4GeTe_2 Single Crystal Growth and Characterization

The single crystal Fe_4GeTe_2 was grown[2] by the standard chemical vapor transport (CVT) method. Details of the sample preparation and characterization are given in our earlier report [14].

[1] Theoretical calculations were performed by Dr. Debjani Karmakar from Bhabha Atomic Research Centre, India, and Md. Nur Hasan from Uppsala University, Sweden

[2] The single crystals were grown and characterized by Suchanda Mondal from Prof. Prabhat Mandal's group at Saha Institute of Nuclear Physics, Kolkata, India

6.2.2 Fe_4GeTe_2 Exfoliation

The Fe_4GeTe_2 flakes were obtained using the Scotch tape method from the high-quality bulk materials. Initially, PDMS was applied to separate isolated flakes from bulk Fe_4GeTe_2 crystals with the assistance of scotch tape. Thickness characterization of the Fe_4GeTe_2 layers was performed optically and confirmed via atomic force microscopy. Subsequently, the exfoliated few-layer Fe_4GeTe_2 flakes on PDMS were transferred onto a Si/SiO_2 substrate using a custom transfer setup. Before the transfer process, the Si/SiO_2 substrate underwent thorough ultrasonic cleaning in acetone, 2-propanol, and deionized water, followed by oxygen plasma treatment to remove surface contaminants.

6.2.3 Raman Measurements

The Raman spectra were collected using a LABRAM HR 800 micro-Raman spectrometer with an 80 cm focal length. The system was equipped with grating of 1800 gr/mm (to get the spectral resolution of Raman signal finer than 1 cm^{-1}), a Peltier-cooled CCD detector, and a liquid-nitrogen cryostat allowing temperature control from 80 K to 370 K. A 100x objective having numerical aperture (NA) = 0.9 was employed to focus a 488 nm wavelength beam from an air-cooled argon-ion laser onto the 80 layered flake of Fe_4GeTe_2. To validate the results, the complete set of data was remeasured over a temperature range from 83 K to 370 K using a 532 nm wavelength laser on a 190 nm thick flake of Fe_4GeTe_2. This measurement utilized a 50x long-working-distance objective, also with NA of 0.9 and a laser spot diameter of 721 nm. During Raman measurements, the laser power applied to the sample was maintained below 250 μW to prevent damage to the sample and excessive heating. The time of integration for each measurement was set to 90 seconds. The temperature-dependent measurement was performed using a Linkam THMS600 with a temperature step of 3 K near the SRT temperature and in a 5 K interval for the rest of the measurements. Polarization control was realized by a set of linear polarizers and a half-wave plate. Low-temperature Raman measurements were carried out in the range of 4 K to 300 K using a Montana cryostat integrated with a Renishaw inVia Raman spectrometer in a backscattering configuration on the same 190 nm flake. A 532 nm laser was used for excitation, in combination with a 2400 g/mm grating. The Raman signal was collected from 100 cm^{-1} using a long working distance objective lens (50×, 0.8 mm working distance, NA = 0.5) across the entire temperature range (4–300 K). The spectral resolution of the system was approximately 1 cm^{-1}

6.2.4 Computational Details

Phonon-dispersion curves at various temperatures were computed using the VASP-Phonopy code with the GGA-PBE exchange-correlation functional, incorporating van der Waals corrections [418–420]. Temperature-dependent lattice parameters obtained from XRD data were integrated into the initial structure of Fe_4GeTe_2, providing computational input structures across a range of temperatures. A combination of the supercell approach and finite displacement method was employed to generate a 2×2×1 supercell, followed by a finite atomic displacement of 0.0003 Å. Applying symmetry operations yields a total of seven symmetrically distinct supercells with atomic displacements. Force constants for each symmetrically distinct supercell were calculated using first-principles VASP [418] computations. These constants, representing the interatomic potential, were subsequently processed with the Phonopy [419] code to construct the dynamical matrix. Matrix diagonalization results in phonon frequencies, enabling the calculation of phonon dispersion curves along the Brillouin zone's high-symmetry paths. The dynamical matrices were computed over a q-point grid of 5×5×3. The plane-wave cutoff energy was set to 500 eV, with a Hellmann-Feynman force minimization criterion of 0.001 eV/Å and an electronic energy convergence threshold of 10^{-8} eV.

6.3 Experimental Results and Discussion

6.3.1 Selection rules for Raman-active modes in Fe_4GeTe_2

Single crystal Fe_4GeTe_2 has a rhombohedral structure with space group $R\bar{3}m$ (No. 166) having lattice parameters $a = 9.97(2)$ Å and $\alpha = 23.3(2)°$. In hexagonal representation, the lattice parameters are $a = 4.03$ Å and $c = 29.08$ Å [13–15, 36]. Fe_4GeTe_2 possesses trigonal crystal symmetry with the D_{3d} point group [421]. From group theory analysis, symmetry assignment of Raman active modes can be represented by A_{1g} and E_g. The Raman tensors ($\boldsymbol{R}$) corresponding to these symmetries can be described as follows [421]:

$$A_{1g}: \begin{pmatrix} a & 0 & 0 \\ 0 & a & 0 \\ 0 & 0 & b \end{pmatrix}; E_g: \begin{pmatrix} c & 0 & 0 \\ 0 & -c & d \\ 0 & d & 0 \end{pmatrix}, \begin{pmatrix} 0 & -c & -d \\ -c & 0 & 0 \\ -d & 0 & 0 \end{pmatrix} \tag{6.1}$$

It's important to note that only the Raman active mode E_g exhibits double degeneracy. The Placzek approximation offers a method to calculate the non-resonant Raman intensity

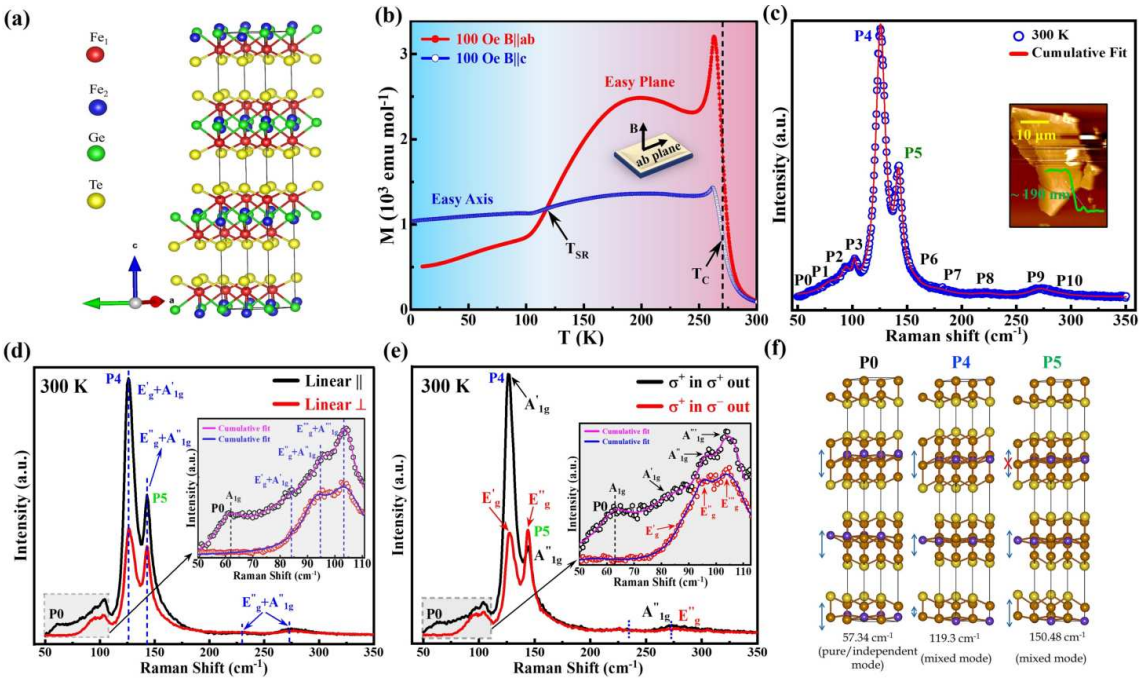

FIGURE 6.1: **(a)** Crystal structure of Fe_4GeTe_2. Seven atom-thick Fe_4GeTe_2 monolayers formed the rhombohedral structure having space group $R\bar{3}m$ (No. 166). **(b)** Temperature-dependent magnetization data (at 100 Oe) show the ferromagnetic transition temperature at $T_C \sim 270$ K and spin-reorientation transition at T_{SR}. **(c)** The room temperature (300 K) Raman spectra (blue circles) ($\lambda_{ex} \sim 532$ nm) of the Fe_4GeTe_2 flake are fitted with ten Raman modes, and the fitted curve is indicated in red color. Inset: Height profile of the Fe_4GeTe_2 flake measured by AFM with its AFM image. **(d)** Linear polarization-resolved Raman spectra at 300 K. Inset: Zoomed view of the first four peaks (P0-P3) in this configuration. **(e)** Helicity-resolved Raman spectra at 300 K. Inset: Zoomed view of the first four peaks (P0-P3) in this configuration. **(f)** Lattice dynamics of Fe_4GeTe_2 calculated using Phonopy-VASP, illustrating phonon mode frequencies (P0, P4 and P5) and the associated vibrational patterns. The calculations highlight mode-specific behavior, providing insight into the phonon dispersion and symmetry characteristics at temperature 300 K.

of a Raman-active mode, which can be represented by the Raman susceptibility tensor ($\boldsymbol{R}$) as stated in Ref. [421]. This $\boldsymbol{R}$ is distinct for each Raman band. Hence, the variation in the intensity of a phonon mode based on the polarization of incident or scattered light enables the investigation of crystal symmetry and Raman selection rules.

The non-resonant Raman scattering intensity is proportional to the square of the dot product between the polarization vectors of the incident light ($\boldsymbol{p_i}$), the Raman susceptibility tensor ($\boldsymbol{R}$), and the polarization vectors of the scattered light ($\boldsymbol{p_s}$), expressed mathematically as

$$I \propto |\boldsymbol{p_i}.\boldsymbol{R}.\boldsymbol{p_s}|^2 \tag{6.2}$$

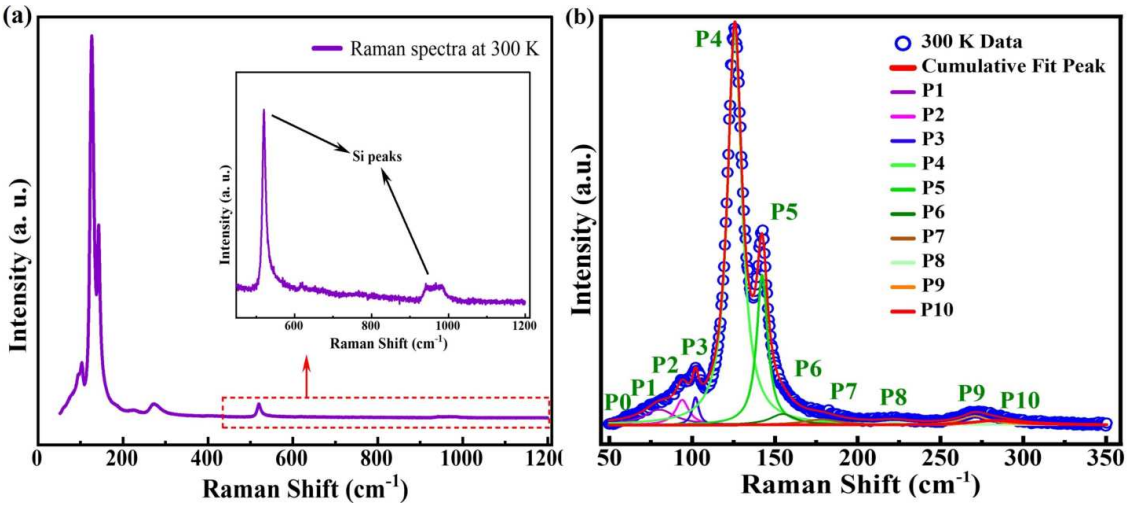

FIGURE 6.2: **(a)** Full range Raman spectra from 20 cm^{-1} to 1200 cm^{-1} at 300 K with the excitation source of 532 nm laser. Inset: Only the Si peaks are observed near 521 cm^{-1} and 935-990 cm^{-1} in the high-frequency spectral ranges. **(b)** Raman spectra of a 190 nm thick flake at 300 K consist of 11 peaks, P0-P10. The multi-Lorentzian fitting reveals that a total of 11 peaks provide the best fit for the observed spectra.

Now, in the back-scattering configuration, both incident and scattered light polarization vectors lie within the xy plane. Assuming linearly polarized light as our basis, the polarization vectors for linearly polarized light along the x and y directions can be represented as p_x: $\begin{pmatrix}1 & 0 & 0\end{pmatrix}$; p_y: $\begin{pmatrix}0 & 1 & 0\end{pmatrix}$. In this basis, the polarization vectors for left (σ^+) and right (σ^-) circularly polarized light can be expressed as σ^+: $\frac{1}{\sqrt{2}}\begin{pmatrix}1 & i & 0\end{pmatrix}$; σ^-: $\frac{1}{\sqrt{2}}\begin{pmatrix}1 & -i & 0\end{pmatrix}$. By utilizing these Raman tensors and Eq. 6.2, we can derive the Raman intensities and selection rules in different scattering configurations.

Table 6.1 provides the selection rules indicating the Raman-active phonons. This demonstrates that while both $A_{1g}(\Gamma)$ and $E_g(\Gamma)$ are Raman active, they exhibit separate selection rules.

	$\mathbf{A}_{1g}(\Gamma)$	$\mathbf{E}_g(\Gamma)$
$I_{linear\parallel}$	$\lvert a\rvert^2$	$\lvert c\rvert^2$
$I_{linear\perp}$	0	$\lvert c\rvert^2$
$I_{\sigma^+in\ \sigma^+out}$	$\lvert a\rvert^2$	0
$I_{\sigma^+in\ \sigma^-out}$	0	$2\lvert c\rvert^2$

TABLE 6.1: Selection rules for Raman-active phonons of Fe_4GeTe_2

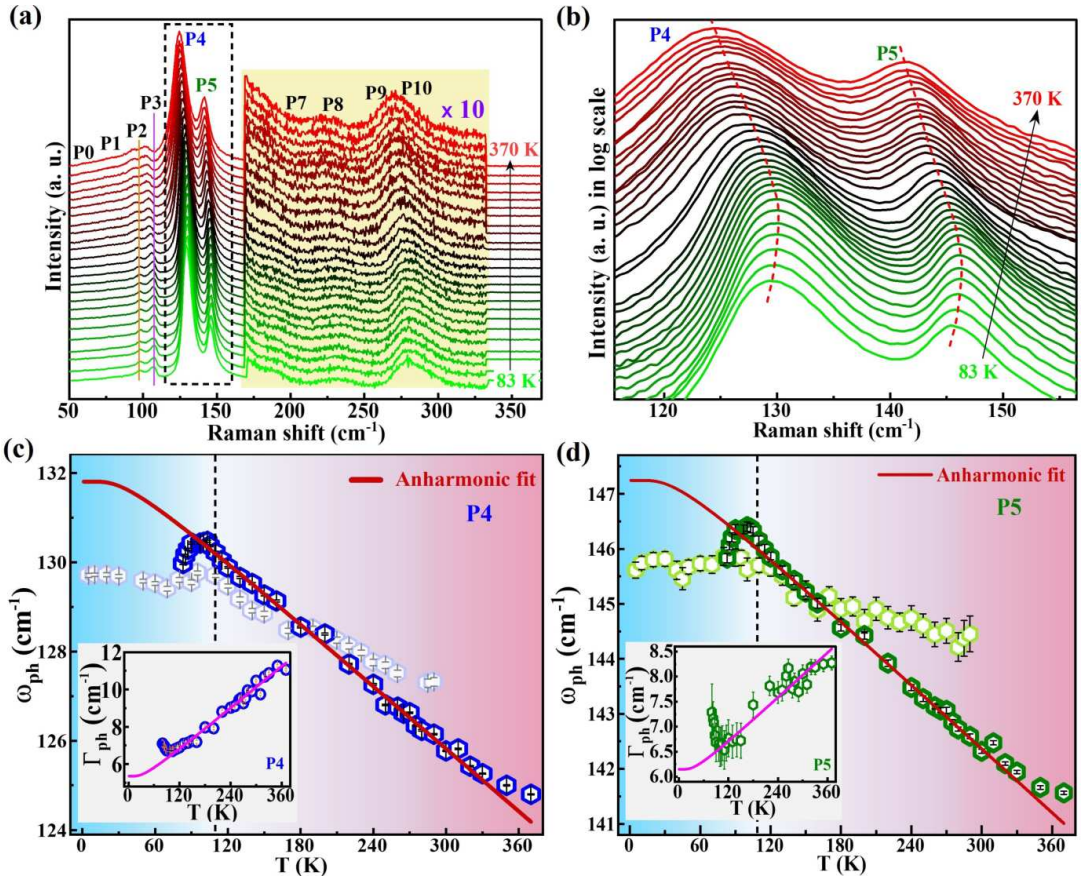

FIGURE 6.3: **(a)** Temperature-dependent Raman spectra at different temperatures down to 83 K. The peaks are named sequentially P0-P10. The black rectangular box indicates the two most intense peaks, P4 and P5. The pink and orange line indicates the shifting of the peaks P3 and P2 with temperature, respectively. **(b)** The temperature-dependent Raman spectra are plotted in a semi-logarithmic scale, for visual understanding of the shifting of the most intense peaks P4 and P5 with temperature. The red dotted line is a guide to the eye. **(c), (d)** The temperature dependence of the phonon frequencies ω_{ph}, for the Raman modes P4 and P5 deviates from the behavior predicted by the standard anharmonic model (Eq. 6.4), as shown by the red fitted lines. Inset: The temperature-dependent phonon linewidths for the corresponding modes are fitted by Eq. 6.5 in 120 K - 300 K. Light blue and green color data points indicate the measurements in another low temperature setup from 4 K to 300 K.

6.3.2 Lattice dynamics in Fe_4GeTe_2

After establishing the selection rules, we aim to examine the lattice dynamics of Fe_4GeTe_2 through Raman spectroscopy. We obtained thin-layer samples by mechanically exfoliating bulk crystals onto Si/SiO_2 substrates, as detailed in the Experimental Section. Following exfoliation, we immediately placed our sample within a high vacuum sample holder to prevent oxidation of the flakes in the ambient atmosphere. It's important to note that, similar to Fe_3GeTe_2 [413], the multi-layered flakes of Fe_4GeTe_2 remain air-stable for at

least one month. This stability was confirmed through continuous monitoring of the Raman modes over this period. However, all the measurements were conducted under high vacuum conditions, employing a liquid nitrogen flow cryostat with a temperature range of 83 - 370 K. For low-temperature measurements down to 4 K, we used a liquid Helium cryostat with the same parameters. We have conducted Raman measurements on Fe_4GeTe_2 flakes of different thicknesses using different wavelength laser excitation and validated our results. Figure 6.1(c) (inset) shows the topography of a flake with a thickness of $\sim$ 190 nm, determined by atomic force microscopy (AFM). In this main chapter, we only focused on this $\sim$ 190 nm thick Fe_4GeTe_2 sample, as it exhibits a relatively strong Raman response with distinct spectral peaks compared to the flakes with other thicknesses.

Figure 6.1(c) displays the room temperature (300 K) Raman spectra of 190 nm thick Fe_4GeTe_2 crystal, measured in the spectral range of 50 - 1000 cm^{-1} under xx eV laser excitation. In the high energy range above 350 cm^{-1}, the Raman spectra show no discernible peaks (see Fig. 6.2(a)). The Raman spectroscopy measurements were conducted in a backscattering configuration, utilizing linearly polarized incident light with the wave vector aligned parallel to the crystallographic c-axis. The scattered light was also linearly polarized. Performing a quantitative analysis of the measured spectra via the deconvolution of multiple Lorentzian curves enables us to determine the minimum number of spectral contributions required to describe the experimental spectrum accurately. By fitting the experimental data using Lorentzian functions, we distinguished eleven Raman modes (at 300 K) labeled as P0 to P10 as shown in Fig. 6.1(c) and 6.2(b). Among these modes, four modes, P2 ($\approx$ 94.2 cm^{-1}), P3 ($\approx$ 102 cm^{-1}), P4 ($\approx$ 125.8 cm^{-1}), and P5 ($\approx$ 142.3 cm^{-1}) are the most intense. In addition to these, seven extremely weak kinks (P0-P1, P6-P10) were observed at $\approx$ 61 (P0), 80.4 (P1), 154.8 (P6), 178.5 (P7), 222.4 (P8), 270.8 (P9) and 283.3 (P10) cm^{-1}, respectively in the experimental Raman spectra (see Table 6.2). While it has been confirmed that the exclusion of these seven weak peaks does not significantly affect the peak position, as well as the full width at half maximum (FWHM) of the most intense peaks (P2-P5), we chose to incorporate their contribution during spectrum analysis to strengthen the reliability of the fitting process (see Fig. 6.2(b)). To deepen our understanding of the lattice dynamics and spin-phonon coupling in this Fe_4GeTe_2 crystal, we concentrate solely on the most prominent peaks (P2-P5). These peaks exhibit substantial variations with temperature and across different polarization configurations and offer reliable data with minimal error, even at low temperatures, unlike the weaker peaks (P0-P1, P6-P10), which lack sufficient intensity for reliable temperature-dependent analysis.

Phonons: (cm^{-1})	P0	P1	P2	P3	P4	P5	P6	P7	P8	P9	P10
Experiment:	61.1 ± 2.6	80.4 ± 0.5	94.2 ± 0.2	102.02 ± 0.14	125.78 ± 0.02	142.33 ± 0.03	154.8 ± 0.7	178.5 ± 1.7	222.4 ± 2.9	270.8 ± 0.9	283.3 ± 2.4
Theory:	57.34	78.47	-	-	119.30	150.48	-	183.30	218.30	-	286.30

TABLE 6.2: Phonon energies (in cm^{-1}) of Fe_4GeTe_2 at 300 K obtained from experimental data and theoretical calculations

To gain insights into the Raman selection rules experimentally, polarization-dependent Raman measurements were conducted at room temperature (300 K). In Fig. 6.1(d), Raman spectra are shown for linear polarization, measured in both co- (black) and cross- (red) polarization geometries. Notably, the vibrational mode at approximately 61 cm^{-1} (P0) emerges solely in the co-polarized geometry, when the scattered and incident light polarizations are parallel, as shown in the Figure 6.1(d) inset. This observation leads us to conclude that the P0's symmetry is attributable to $A_{1g}(\Gamma)$ according to the selection rule provided in Table 6.1. On the other hand, features P1-P5 and P8-P10 appear in spectra obtained from both co- and cross-polarized setups. Therefore, it is expected to contain a component of $E_g(\Gamma)$. Notably, the intensity of these peaks is significantly higher in the co-polarized configuration compared to the cross-polarized setup as depicted in Fig. 6.1(d). This suggests that these peaks cannot solely originate from the $E_g(\Gamma)$ vibrational mode, followed by the selection rule in Table 6.1. Intuitively, we speculate that the observed peaks originate from a combination of the $E_g(\Gamma)$ and $A_{1g}(\Gamma)$ phonon branches.

To verify this speculation, we conducted helicity-resolved Raman spectra measurements as plotted in Fig. 6.1(e). These measurements are typically used for the assignment and differentiation of the symmetries of Raman bands. Figure 6.1(e) inset demonstrates that the phonon modes P0 and P1 are exclusively present in the co-circularly polarized configuration (σ^+ in σ^+ out, black). This observation further confirms that the symmetry at P0 can be conclusively assigned to $A_{1g}(\Gamma)$. Conversely, the modes at P1-P5, P8-P10 are detectable under both co- and cross-circular polarization conditions (σ^+ in σ^- out, red) polarized configurations. This observation provides strong evidence that both $A_{1g}(\Gamma)$ and $E_g(\Gamma)$ vibrations are indeed present at the other peaks.

To gain a more comprehensive understanding of the lattice dynamics across different phonon modes, we have systematically investigated[3] the phonon dynamical behavior of Fe_4GeTe_2 across a temperature range from 10 K to 320 K, focusing specifically on the vibrational behavior at room temperature (300 K) for comparison with experimental

[3]Theoretical calculations were performed by Dr. Debjani Karmakar from Bhabha Atomic Research Centre, India, and Md. Nur Hasan from Uppsala University, Sweden

Raman spectroscopy data. The phonon dispersion data, as shown in Fig. 6.4, is calculated along a high-symmetry path in the Brillouin zone, including points such as Γ-point, M-point, and K-point. This path captures the key vibrational characteristics of the material. We compared the phonon modes at Γ-point, with the closest value of the Raman-active modes observed experimentally at 300 K, as presented in Table 2. The computed frequencies at 57.3 cm^{-1}, 78.5 cm^{-1}, 119.3 cm^{-1}, 150.5 cm^{-1}, 183.3 cm^{-1}, 218.3 cm^{-1} and 286.3 cm^{-1} align closely with experimental peaks P0, P1, P4, P5, P7, P8 and P10 respectively. The alignment of theoretical phonon modes with experimental Raman peaks indicates that the computational model effectively captures the fundamental vibrational dynamics of Fe_4GeTe_2.

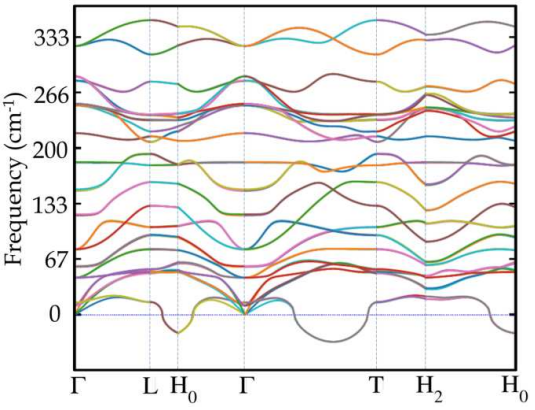

FIGURE 6.4: Phonon dispersion plot for Fe_4GeTe_2, calculated using Phonopy-VASP. It shows the frequency dispersion of phonon modes across the Brillouin zone.

To further investigate the presence of pure (independent) modes and mixed modes within the structure, we have theoretically analyzed the details of their atomic vibrational nature, as depicted in Fig. 6.1(f). The experimental Raman analysis identifies the P0 mode at 61.1 cm^{-1} as an out-of-plane vibrational mode, a characterization confirmed by our computational study. Our calculations predict a similar mode at 57.34 cm^{-1}, which closely aligns with the experimental observation for P0, highlighting the stability of an independent out-of-plane vibrational mode. The higher-frequency modes P1 to P10 exhibit more complex vibrational behavior. Observations from Fig. 6.1(f) highlights two key features: First, mode degeneracies at the Γ-symmetry point, where some phonon modes are degenerate, particularly at the Γ-symmetry point, leading to cross-dispersion patterns. These symmetry-induced degeneracies and the associated cross-dispersion patterns suggest interactions between modes with similar frequencies, indicating that these modes are not isolated but instead influenced by nearby vibrational states, characteristic of mixed phonon modes [422]. Second, layer-dependent amplitude variations, where the vibrational mode amplitudes differ across the layers, suggesting non-uniform intensity distribution typical of mixed modes. These variations imply complex interlayer couplings and vibrational interactions, which are consistent with experimental observations of mixed phonon behavior for modes P1 to P10.

6.3.3 Temperature dependent Raman spectroscopy in Fe_4GeTe_2

Temperature-dependent Raman spectroscopy offers a straightforward, convenient, and non-contact method for delving into the thermal properties of 2D materials [414, 423]. To gain deeper insight into the lattice dynamics of Fe_4GeTe_2, we conducted a temperature-dependent Raman study spanning the temperatures from 83 K to 370 K. Raman spectra obtained at various temperatures are depicted in Fig. 6.3(a). In this context, the Raman active modes P2-P5 exhibit noticeable broadening and softening as the temperature rises above approximately T_{SR}, clearly observable from the semi-logarithmic plot presented in Fig. 6.3(b). Here, as the temperature increases from 80 K, the peak positions initially exhibit a continuous blueshift till T_{SR}. However, above T_{SR}, an anomalous redshift is observed extending up to 370 K. To ensure accurate analysis of the temperature-dependent Raman data, we employed multi-Lorentzian functions to fit the spectra for all measured temperatures, following a similar approach as employed for the 300 K data, as illustrated in Fig. 6.2(b). The phonon frequencies ω_{ph} (peak positions), line widths Γ_{ph} (FWHMs), and intensity (the area under the curve) determined from the fitting procedure are plotted against temperature as depicted in Fig. 6.3(c,d) and 6.5(c,f).

6.3.3.1 Changes of peak positions and line-widths below T_{SR}

For magnetic materials, the temperature-dependent change in phonon frequency (ω) can be described by the following Eq. [424]:

$$\begin{aligned}\Delta\omega(T) \equiv \omega(T) - \omega_0 = \Delta\omega_{latt}(T) + \Delta\omega_{anh}(T) \\ +\Delta\omega_{ren}(T) + \Delta\omega_{s-ph}(T)\end{aligned} \tag{6.3}$$

So, the temperature-dependent shift of phonon frequencies stems from multiple factors: viz, the coupling between spin and phonons originates from lattice-induced variations in the exchange interaction. (phonons) ($\Delta\omega_{s-ph}$), renormalization (of the phonon frequencies) in the electronic states near the transition temperatures due to the coupling of electron and phonon ($\Delta\omega_{ren}$), lattice thermal expansion/contraction (also termed as, quasi-harmonic effect) due to anharmonicity or magnetostriction effects including lattice anomalies ($\Delta\omega_{latt}$), and intrinsic anharmonicity induced by phonon–phonon scattering (i.e. decay of phonons) ($\Delta\omega_{anh}$) [424–428].

Furthermore, the broadening of the phonon linewidth with increasing temperature in a defect-free sample is evidenced to have an intrinsic origin, such as the interactions due

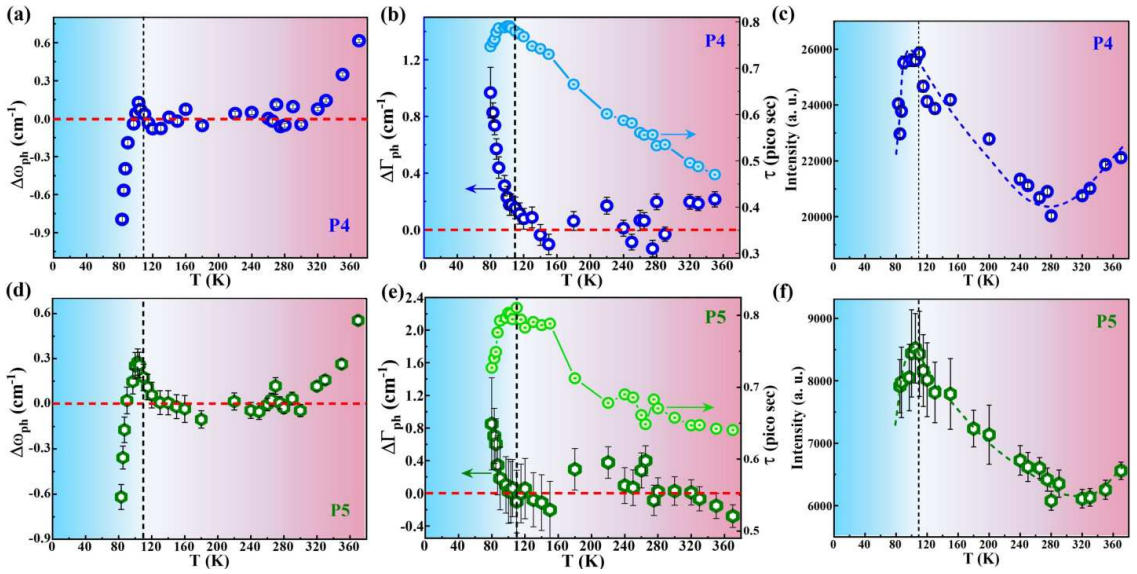

FIGURE 6.5: The temperature dependence deviation of the phonon frequencies, $\Delta\omega_{ph}(T)$ **(a,d)** and $\Delta\Gamma_{ph}(T)$ **(b,e)** from the standard anharmonic model for the Raman modes P4 and P5. Both of the modes show significant deviation below T_{SR} and a small deviation above $\sim T_C$. Right axes of **(b,e)** indicate the temperature dependence of τ for the modes P4 and P5 around T_{SR} shows significant changes. The black dotted line indicates T_{SR}. **(c,f)** The temperature dependence change of intensity of the phonon modes P4 and P5. Dashed lines are a guide to the eye for the changes observed.

to electron-phonon coupling (Γ^{e-ph}) and phonon-phonon scattering induced intrinsic anharmonicity (Γ^{ph-ph}) [426–431]. Generally Γ^{e-ph} decreases as temperature rises, whereas Γ^{ph-ph} increases with increasing temperature. So, as temperature increases, the phonon population and the linewidth of active modes increase, intensifying the phonon scattering processes.

In the ordered state of a ferromagnetic material, spin–phonon coupling emerges due to the interaction between the vibrational modes of the crystal lattice and the magnetic moments of the system [432]. This spin-phonon coupling typically results in a phonon-hardening behavior with increasing temperature, but its impact is generally weaker compared to phonon–phonon scattering. In contrast, the softening of phonon modes with increasing temperature is primarily attributed to the anharmonicity due to phonon-phonon scattering [425, 428–430, 433]. Also, the presence of magnetoelastic coupling at higher temperatures can contribute to the phonon softening behavior [427, 428, 434].

From the temperature-dependent data of Fe_4GeTe_2 (see Fig. 6.3 (c),(d)), the significant deviations of phonon frequencies from the expected behavior are observed at temperatures below $\sim T_{SR}$ for all four peaks P2-P5. A continuous blue shifting of the peak positions (phonon mode hardening) is observed while decreasing the temperature till T_{SR}. However,

below T_{SR}, we observe an anomalous redshift (phonon mode softening) extending down to $\sim$ 80 K. For phonon modes P2–P5, the FWHMs decrease gradually as temperature decreases until reaching T_{SR}. In general, when the temperature decreases, anharmonic effects result in a reduction of the phonon linewidths and an increase in phonon energies [435, 436]. However, below T_{SR}, the FWHMs exhibit a sharp and continuous increase below T_{SR}, as shown in Fig. 6.3 (c),(d) (insets). In Fe_4GeTe_2, previous XRD and transport studies show the presence of a possible subtle magneto-elastic coupling and enhancement of phonon-phonon scattering with increasing temperature above T_{SR} [15, 36]. In Fe_4GeTe_2, the pronounced hardening of phonon frequencies and narrowing of linewidths with decreasing temperature down to T_{SR} indicates the presence of significant anharmonicity and weak magneto-elastic coupling. Additionally, the anomalous phonon softening and linewidth broadening observed below T_{SR} likely result from the enhanced spin-phonon coupling in this low-temperature regime. So, the interplay between strong spin-phonon coupling and intrinsic anharmonicity near T_{SR} manifests as a change in slope behavior observed in the temperature-dependent phonon frequency data (see Fig. 6.3). This distinctive signature provides clear evidence of the spin-reorientation transition at T_{SR} in the Fe_4GeTe_2 system. Theoretically, phonon calculations were conducted over a temperature range from 10 K to 320 K, revealing minimal shifts in phonon frequencies across this range.

To investigate the unusual temperature variations in phonon frequency and linewidth, the data were analyzed at temperatures above T_{SR}, aligning our expectations with the anticipated changes due to anharmonic phonon interactions. In systems lacking spin–phonon coupling, changes in the phonon Green's function with temperature can be attributed to the three-phonon symmetric anharmonic decay process [413, 432, 435, 437, 438]. At low temperatures, intrinsic lattice dynamics make only a minor contribution to changes in the frequency and linewidth (or inverse of lifetime) of phonon modes. In the ideal harmonic approximation of phonon behavior, zone-center phonon frequencies are temperature-independent and theoretically possess infinite lifetimes. However, real-world systems are affected by anharmonicity due to phonon-phonon scattering, altering these idealized characteristics. This process describes a higher energy optical phonon with frequency ω decaying into two lower energy acoustic phonons, which have equal frequencies ($\omega/2$) but opposite momenta [432, 435, 437]. The temperature-dependent variation in phonon frequency and the presence of non-zero linewidths (indicating finite lifetime) in phonon modes observed in Raman spectra are primarily attributed to this decay pathway of optical phonons due to anharmonic coupling [438]. The real and imaginary components of the self-energy, representing the temperature-dependent phonon frequencies and

linewidths, respectively, can be effectively modeled through an anharmonic approach [435, 437] as follows:

$$\omega_{anh}(T) = \omega_0 - A\left[1 + \frac{2}{e^{\frac{\hbar\omega_0}{2k_BT}} - 1}\right] \tag{6.4}$$

$$\Gamma_{anh}(T) = \Gamma_0 + B\left[1 + \frac{2}{e^{\frac{\hbar\omega_0}{2k_BT}} - 1}\right] \tag{6.5}$$

In this model, ω_0 and Γ_0 represent the intrinsic phonon frequency and linewidth at T = 0 K, respectively, which can arise from lattice defects or electron-phonon coupling. The constants k_B and $\hbar$ denote the Boltzmann constant and reduced Planck's constant, respectively. Here, A and B are positive fitting parameters, which are related to the phonon-phonon interaction strength.

The temperature-dependent phonon frequency and linewidth data were fitted by the Eqs. 6.4, 6.5, respectively, in the temperature range from 120 K to 300 K. The fitting is in quite good agreement with the measured experimental data. The optimal fitting parameters are detailed in Table 6.3. The fitted curves highlight the anomalous behavior observed below T_{SR}. In Fig. 6.3, the temperature dependence of the phonon frequencies, $\omega_{anh}(T)$, of the four Raman modes was observed to deviate from the expected behavior predicted by the standard anharmonic model (indicated by the red fitted lines). This deviation manifests as an unusual softening at lower temperatures below T_{SR}. Figure 6.5 further illustrates this phenomenon by plotting the deviation from the anharmonic model, $\Delta\omega_{ph}(T) = \omega(T) - \omega_{anh}(T)$. This deviation clearly indicates a rapid softening of the phonon frequencies as the temperature drops just below T_{SR}. This strongly suggests that pronounced spin-phonon coupling is driving this behavior below T_{SR}. Upon careful observation (See Fig. 6.3 (c),(d) and Fig. 6.5 (a), (d)), a weak deviation of the phonon frequencies from the standard anharmonic model is noticeable above 320 K, at a temperature 50 K higher than T_{C}. This deviation may be related to the change in the phonon population just above T_{C}. Additionally, it is likely attributed to the short-range correlation of the two-dimensional magnetic material Fe_4GeTe_2 that continues to exist beyond T_{C} [15]. Below T_{C}, Fe_4GeTe_2 undergoes the magnetic ordering, where spin-spin interactions are influenced by propagating phonons. These phonons can alter superexchange angles, thereby modifying the magnetic exchange couplings [439]. Similar to $\omega_{anh}(T)$, the anharmonic model (represented by the red line in Fig. 6.3 (c), (d) insets) fails to adequately describe the temperature dependence of linewidths ($\Gamma_{anh}(T)$) below T_{SR}. Figure 6.5 (b),(e) illustrates the deviation of linewidths, $\Delta\Gamma_{ph}(T) = \Gamma(T) - \Gamma_{anh}(T)$

from the anharmonic model, showing a notable increase below T_{SR}. This strongly suggests that pronounced spin-phonon coupling significantly impacts the renormalization of both the phonon frequency and the linewidth of the phonon modes when temperatures fall below T_{SR}. Moreover, the inflection point observed near 320 K, while cooling from 370 K, can be attributed to the combined effects of anharmonicity, reduced phonon thermal populations, and diminished spin fluctuations of the magnetic ions. Collectively, these factors suppress phonon scattering mechanisms, resulting in a decrease in linewidth as the temperature decreases [440, 441].

Mode	ω_0 (cm^{-1})	A (cm^{-1})	Γ_0 (cm^{-1})	B (cm^{-1})	λ_{s-ph} (at 83 K) (cm^{-1})	τ_{max} (at T_{SR}) (pico sec)
P2	100.09 ± 0.13	0.71 ± 0.03	5.59 ± 0.27	0.504 ± 0.039	0.79	0.753
P3	109.16 ± 0.14	0.89 ± 0.02	2.26 ± 0.09	0.301 ± 0.022	1.02	1.672
P4	132.93 ± 0.11	1.13 ± 0.02	4.46 ± 0.01	0.897 ± 0.001	0.95	0.791
P5	148.29 ± 0.07	1.04 ± 0.02	5.75 ± 0.01	0.402 ± 0.001	0.74	0.811

TABLE 6.3: The fitting parameters for the phonon modes in Fe_4GeTe_2. These parameters were derived using the three-phonon fitting model.

Using a nearest-neighbor approximation, the temperature-dependent shift in phonon frequency, $\Delta\omega_{ph}(T)$, due to spin-phonon coupling can be described by the equation $\Delta\omega_{ph}(T) = \lambda_{s-ph}\langle \boldsymbol{S_i} \cdot \boldsymbol{S_j} \rangle$ [413, 424, 442–445]. Here, $\langle \boldsymbol{S_i} \cdot \boldsymbol{S_j} \rangle$ represents the spin-spin correlation function of the neighboring spins, and λ_{s-ph} indicates the spin-phonon coupling strength. Since Fe_4GeTe_2 is a non-collinear ferromagnet, directly estimating the spin correlation function is not straightforward. However, based on the Fe magnetic moment of $\sim 1.83\ \mu_B$/Fe at 83 K [14, 15, 36], we estimate $\langle \mathbf{S_i} \cdot \mathbf{S_j} \rangle \approx 0.83$ and $\lambda_{\text{s-ph}} \approx 0.95\ \mathrm{cm}^{-1}$ for the P4 and $0.74\ \mathrm{cm}^{-1}$ for P5, substantially higher than in related 2D magnets such as Fe_3GeTe_2 and $Cr_2Ge_2Te_6$ [24, 410, 446] at this high temperature. The high values of λ_{s-ph} in Fe_4GeTe_2 indicate strong spin-phonon coupling below T_{SR}, suggesting its great potential for application in magneto-caloric devices.

The spin-phonon coupling can be further confirmed by observing the lifetime of phonons (τ), which is related to the FWHM (linewidth) of the phonons ($\Gamma(T)$) by the energy uncertainty relation [447]: $\tau^{-1} = \Gamma(T)/\hbar$, where $\Gamma(T)$ is in the units of cm^{-1} and $\hbar = 5.3 \times 10^{-12}\ \mathrm{cm}^{-1}$ s. For P4 mode, the maximum phonon lifetime, $\tau = 0.791$ picoseconds,

is obtained near T_{SR} (see Table 3 for other modes). This lifetime reduces with decreasing (increasing) temperature below (above) T_{SR}. Specifically, at a temperature of 80 K, τ reduces to 0.74 picoseconds, and at 300 K, it further decreases to 0.51 picoseconds. Figure 6.5 (b) and (e) illustrate the temperature dependence of τ for the modes P4 and P5 around T_{SR}. Below T_{SR}, as the temperature decreases, the spin-phonon coupling strength rapidly increases, leading to a reduction in the lifetime of the spin-coupled phonons. Conversely, above T_{SR}, the anharmonic effects, caused by phonon-phonon scattering, become more significant, resulting in a further decrease in phonon lifetime as the temperature rises beyond T_{SR} (See Fig. 6.5).

6.3.3.2 Drastic change of intensity near T_{SR} and T_C

Figure 6.5(c,f) shows the temperature-dependent intensity of phonon modes P4 and P5. Notably, P2-P5 exhibit abrupt intensity changes near T_{SR} and T_C The intensity gradually increases with temperature up to T_{SR}, then drops sharply until T_C. Above T_C, a resurgence in intensity is observed, likely due to short-range magnetic correlations [15]. These trends reflect changes in phonon population and enhanced spin-phonon coupling near T_{SR} and T_C, respectively [448]. Below T_C, Fe_4GeTe_2 enters a magnetically ordered state where phonons modulate super-exchange angles, impacting magnetic exchange interactions [439]. Similar behavior has been reported in materials like $CdCr_2Se_4$ and $CdCr_2S_4$, where phonon intensity anomalies near T_C arise from spin-phonon interactions [432, 449, 450].

6.3.4 Thickness dependent Raman spectra in Fe_4GeTe_2

Raman spectroscopy is a powerful tool for determining the thickness of 2D materials due to its sensitivity to layer-dependent spectral changes [307–309, 451]. As the layer number increases, the primary Raman peaks shift either up or down. For example, in transition-metal dichalcogenides (TMDCs) [452–454], the out-of-plane A_{1g} mode increases in frequency (upshifts), while the in-plane E_{2g} mode decreases in frequency (downshifts) with the increase in their thicknesses, reflecting interlayer interactions. The intensity and the peak positions of Raman signals serve as a reliable indicator of the material's thickness, making it highly useful for accurately identifying layer numbers in 2D materials.

Raman spectroscopy was performed on Fe_4GeTe_2 samples with varying thicknesses, from bulk crystal to a few layers, to examine layer-dependent changes. The samples were exfoliated using mechanical exfoliation technique by a scotch tape. The thickness of

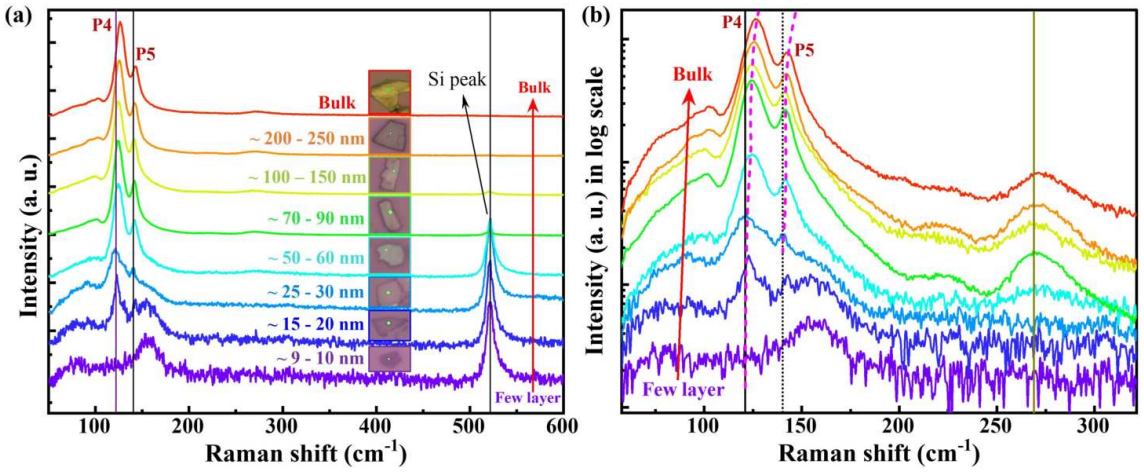

FIGURE 6.6: **(a)** Thickness dependent Raman spectra from few layers to Bulk Fe_4GeTe_2. The peaks P4 and P5 positions are shifting towards higher frequencies (blue shift) with increasing thickness. Inset: Optical microscopic image of the flakes of Fe_4GeTe_2 and their approximate thickness, estimated from the color contrast. **(b)** The thickness-dependent Raman spectra are plotted in a semi-logarithmic scale, for visual understanding of the shifting of the most intense peaks P4 and P5 with increasing thickness. The purple dotted lines are the guide to the eyes.

analyzed Fe_4GeTe_2 flakes was determined using the optical contrast method [454–458], which involves placing the 2D material on a high-contrast substrate (here Si/SiO_2) and estimating layer numbers by comparing the color/contrast with the background.

Figure 6.6 shows the Raman spectra of the exfoliated Fe_4GeTe_2 samples, highlighting the P4 and P5 peaks across different thicknesses. In bulk crystals, the P4 and P5 peaks exhibit higher intensity. As the layer count decreases, the intensity of both P4 and P5 peaks gradually reduces, and Si peaks near 520 cm^{-1} start to enhance, as expected. In flakes thinner than 50 nm, a new broad peak around 160 cm^{-1} begins to emerge. In 20-30 nm flakes, the coexistence of all three of these peaks is observed. With further reduction in thickness, this broad peak becomes more pronounced, while the intensities of the P4 and P5 peaks continue to decrease. In the thinnest measured flakes (9–10 nm), the P4 and P5 peaks completely vanished, leaving only the broad peak at the same position near 160 cm^{-1}. The gradual appearance of the broad peak is clearly observed in Fig. 6.6(b).

Additionally, as the thickness increases beyond 25 layers, both the P4 and P5 peaks exhibit a continuous frequency increase (blue shift) (see Fig. 6.6(b)). This behavior mirrors what is typically observed in transition-metal dichalcogenides (TMDCs) [452–454], where the out-of-plane vibrational modes stiffen (upshift) and the in-plane modes soften (downshift) with increasing layer numbers. In this case, the P4 and P5 modes are mixed modes,

consisting of a dominant out-of-plane vibrational mode with higher intensity and an in-plane vibrational mode with significantly lower intensity, as shown in Fig. 6.1 (d), (e), and (f). As the number of layers increases, the contribution of the out-of-plane vibrational modes becomes more significant, resulting in a continuous increase in frequency. This result is also consistent with our previous report [36]. It is important to note that the laser power used for Raman spectroscopy measurements was maintained below 250 μW for all the layers, in order to prevent the laser damage to the flakes, and all the measurements are performed in high vacuum.

Furthermore, we conducted temperature-dependent Raman measurements on thinner flakes ($\approx$ 9 nm) and observed no significant peak shifts as the temperature decreased from 300 K to 83 K.

6.3.5 Laser power degradation dependent Raman spectra

To examine the stability of unprotected Fe_4GeTe_2 flakes under laser irradiation, we performed systematic, laser power-dependent Raman measurements at 300 K. Initially, we studied a thicker Fe_4GeTe_2 flake ($\sim$ 85 nm). After progressively increasing the laser power from 49 μW to 18 mW, no observable shifts or new peaks appeared. However, we did observe a systematic increase in the intensity of all the peaks, mainly at $\sim$ 128 cm^{-1} and $\sim$ 143.5 cm^{-1}, along with an enhancement of the Si peaks, as expected (see Fig. 6.7 (a)). We repeated these measurements on other thick flakes ($>$ 60 nm), obtaining similar results. Thus, we conclude that, similar to Fe_3GeTe_2 [413], thick flakes of the 2D ferromagnet Fe_4GeTe_2 are relatively stable under atmospheric conditions and laser power.

To assess the stability of the few-layer flakes ($\sim$ 9 nm), we also conducted laser power-dependent Raman measurements. Up to 700 μW, a broad Raman spectrum was observed, likely due to surface oxidation of the thinner flakes, and this remained unchanged even after successive measurements at the same location. Furthermore, to investigate laser radiation-induced removal of the oxidation layer in the few-layer flakes, we applied a relatively high laser power ($\sim$ 1.65 mW) to a thinner flake ($\sim$ 9 nm) and monitored the Raman spectra at the same spot to track any signs of returning to the original signal. Interestingly, we found that relatively higher laser radiation could induce the removal of the oxidation layer in the unprotected thinner flakes.

Figure 6.7(b) shows a series of Raman spectra measured continuously under this higher laser power. With successive measurements, the three phonon modes of Fe_4GeTe_2 (likely arising from the oxidized top layer in ambient atmosphere) gradually disappeared

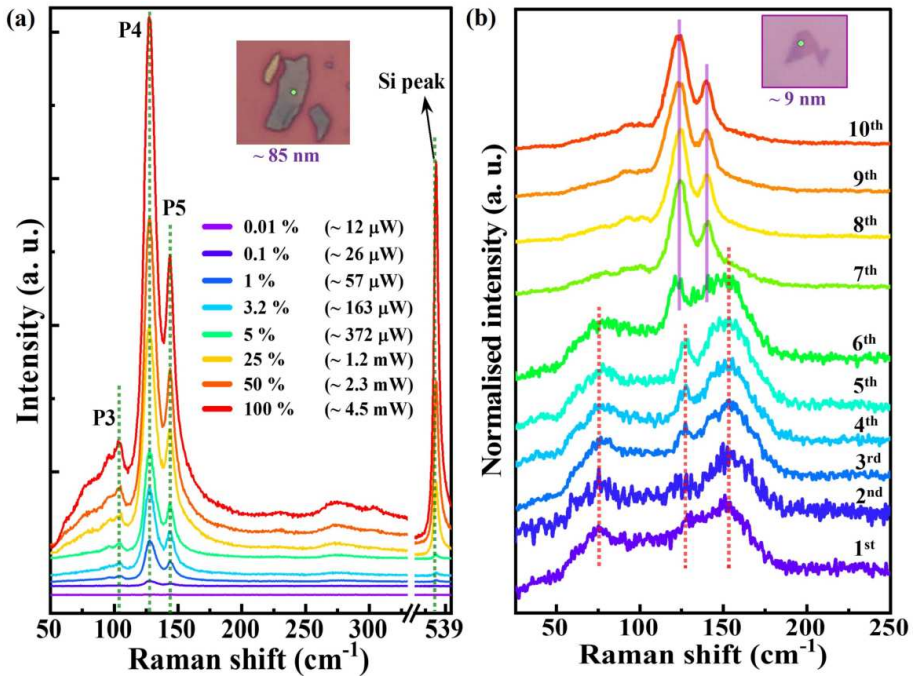

FIGURE 6.7: Laser power dependent Raman spectra **(a)** for bulk **(b)** for few layer flakes of Fe_4GeTe_2. Inset: The corresponding optical microscope image of the measured flakes.

(red dotted lines), while two expected phonon modes emerged near 123 cm^{-1} and 140 cm^{-1} (purple solid lines). The emergence of these two modes is located at different positions (around 5 and 3 cm^{-1} apart) compared to the position of P4 and P5 of the multi-layer flakes. This is expected due to the thickness-dependent shift of the Raman peak positions. While the exact origin of these three broadened peaks requires further study, the reappearance of the two Raman modes (P4 and P5) during laser exposure in Fe_4GeTe_2 offers a straightforward and efficient method for assessing the quality of thinner flakes. This characteristic provides Fe_4GeTe_2 with a unique advantage over other 2D ferromagnetic materials, like $Cr_2Ge_2Te_6$, CrI_3, etc [8, 27, 413, 459] which can hardly exist in the atmosphere, facilitating both future fundamental research and potential applications.

6.4 Summary and Conclusion

In summary, we have meticulously investigated the lattice dynamics and spin-phonon coupling in the quasi-2D vdW ferromagnet Fe_4GeTe_2 over a wide temperature range from

83 K to 370 K using micro-Raman spectroscopy. The polarization-dependent Raman measurements identified the Raman active modes A_{1g} and E_g at room temperature. In total, eleven phonon modes (P0-P10) were observed, with most of them aligning well with the theoretically predicted modes. Interestingly, the temperature dependence of the four most intense Raman modes provided clear evidence of strong spin-phonon coupling below T_{SR}, characterized by anomalous broadening of linewidths and softening of phonon energies. Additionally, the continuous hardening and narrowing of the phonon modes with decreasing temperature below T_C indicated the presence of strong anharmonicity due to phonon-phonon scattering until T_{SR}. Notably, the spin-phonon coupling strength reaches its maximum at the lowest measured temperature (5 K), while the phonon lifetime peaks near T_{SR}, consistent with our findings. The intensity of the phonon modes also exhibits significant changes near T_{SR} and the magnetic transition T_C. Furthermore, the deviation from the anharmonic model $\approx$ 50 K above T_C supports the presence of short-range correlations in Fe_4GeTe_2. Thickness-dependent Raman spectra indicate a continuous blue shift of the most intense Raman modes with increasing thickness. Thicker flakes demonstrate greater stability in air under high laser power, while thinner flakes are more susceptible to oxidation, leading to broader, temperature-independent Raman modes. However, applying higher laser power could remove the oxidized layer and restore the characteristic Raman features in the thinner layers of Fe_4GeTe_2. Together, these findings establish Fe_4GeTe_2 as a model system to probe spin-lattice coupling in 2D magnets and offer a foundation for tuning magnetic and vibrational properties in spintronic device architectures..

Chapter 7

Observation of Superconductivity and Weak Ferromagnetism in a Quasi-1D Material $(TaSe_4)_3I$

Quasi-1D materials, with electron motion confined to linear chains, form an attractive set of compounds to study the physical properties in low dimensions. In this work, we report the observation of superconductivity and weak ferromagnetism in the non-centrosymmetric phase of the quasi-1D single crystal $(TaSe_4)_3I$ (nTSI). The superconductivity is probed by both the resistive transition and the Meissner effect below 2.5 K, while the ferromagnetic transition appears at $\sim$ 9 K. The magneto-transport measurements confirm the anisotropic nature of superconductivity in nTSI, having the upper critical field $H_{c2}(0)$ with a positive curvature. A detailed investigation of the nature of superconductivity in this compound was carried out using various theoretical models, providing multiple pieces of evidence for its quasi-1D nature. The coherence length and $H_{c2}(0)$, were estimated through different approaches, while the London penetration depth (λ) extracted from I–V characteristics (IVCs) showed good agreement with BCS s-wave symmetry, yielding a superconducting energy gap close to the BCS value. Additionally, the IVCs revealed a series of voltage steps and hysteresis, strongly indicating the presence of phase-slip events— a hallmark of low-dimensional superconductors, suggesting the quasi-1D confinement of Cooper pairs. Although a definite mechanism is difficult to pinpoint, first-principles calculations based on theoretical study suggest that Se dimer vacancies may give rise to this unusual ground state, simultaneously hosting these two antagonistic quantum phases. The present results provide a platform to study complex ground states of such quasi-1D materials.

7.1 Introduction

Transition-metal-based quasi-1D chain compounds of the form $(MSe_4)_nI$, where M represents Nb or Ta and n takes values of 2, 3, or 10/3, have garnered significant research interest due to their diverse range of electronic and magnetic phases, along with notable phase coexistence phenomena [87–95]. These compounds feature MSe_4 chains that extend along the crystallographic c-axis and are spatially separated by intervening iodine atoms, giving rise to their quasi-1D structural character [87–89]. The electronic structure of these materials is highly sensitive to the parameter n, as variations in this value directly influence the degree of band filling, as indicated by tight-binding band structure calculations [89]. Historically, it was anticipated that the $n = 2$ members of this family, namely $(NbSe_4)_2I$ and $(TaSe_4)_2I$, would exhibit semiconducting transport characteristics [89, 95–97]. However, more recent investigations suggest that their electronic behavior is far more intricate than initially believed [91, 92, 94, 106, 107]. For $n = 3$, both $(NbSe_4)_3I$ and $(TaSe_4)_3I$ crystallize in the same centrosymmetric structure with space group $P4/mnc$ [88], which implies they should exhibit similar electronic properties. Experimental studies have confirmed that $(NbSe_4)_3I$ behaves as a band insulator [98]. In contrast, no detailed temperature-dependent resistivity measurements exist for $(TaSe_4)_3I$, though it has been previously suggested to exhibit weak metallicity [88]. More recently, a non-centrosymmetric structural phase of $(TaSe_4)_3I$ has been successfully stabilized, and this phase demonstrates robust metallic transport behavior [16].

Quasi-1D conductors often exhibit a tendency to undergo a Peierls instability, which triggers the formation of a charge density wave (CDW) phase transition. This phenomenon introduces additional complexity to their electronic behavior, potentially leading to intricate phase diagrams and emergent quantum states [99, 100]. Although theoretical models suggest that true long-range order is inhibited in strictly 1D systems [4], quasi-1D materials can still sustain long-range superconducting and magnetic correlations under certain conditions [101, 102, 460–466]. Nonetheless, the presence of both quantum and thermal fluctuations in these systems gives rise to distinct physical phenomena, including phase slip events [6, 7, 12], the localization of Cooper pairs [102, 103, 467], and deviations from conventional Fermi-liquid behavior [104, 105]. A particularly striking example is $(TaSe_4)_2I$, which has been identified as hosting an exotic axionic CDW phase driven by strong electronic interactions [91, 94]. Additionally, both $(TaSe_4)_2I$ [92, 106] and $(NbSe_4)_2I$ exhibit superconducting behavior when subjected to high-pressure conditions, with disorder-induced mechanisms proposed as a driving factor for superconductivity in

the latter [107]. In superconducting systems, structural defects play a crucial role by acting as pinning sites for vortices, thereby enhancing the robustness of the superconducting phase [108]. Similarly, in magnetic materials, these defects can significantly modify spin ordering by serving as pinning centers for spin density waves, ultimately altering the nature of local magnetic interactions [109]. The interplay between CDW order, superconductivity, and magnetism in the presence of disorder thus provides an exciting platform for investigating novel quantum phases and unconventional phase transitions in low-dimensional systems.

According to Cooper's theorem, electrons in the vicinity of the Fermi level within a metallic system tend to form bound states known as Cooper pairs. At sufficiently low temperatures, these pairs collectively merge into a single macroscopic quantum state, giving rise to superconductivity. Since individual electrons possess spin-$\frac{1}{2}$, their pairing can either result in an anti-parallel spin configuration (spin-singlet) or a parallel arrangement (spin-triplet). The overwhelming majority of known superconductors, including conventional s-wave superconductors as well as high-temperature superconductors such as cuprates and iron-based compounds, exhibit spin-singlet pairing. Although several materials have been postulated to exhibit spin-triplet pairing [468–470], the most well-established example remains the superfluid phase of ^{3}He, which undergoes condensation below a few millikelvin. A straightforward realization of spin-triplet pairing arises in a fully spin-polarized system. Consequently, superconducting materials exhibiting ferromagnetism [471, 472] serve as promising platforms for realizing this unconventional pairing state. A notable theoretical framework for studying triplet-paired superconductors is the Kitaev p-wave chain model [48], where a 1D superconducting system with triplet correlations has been predicted to host Majorana zero modes at its boundaries. This implies that 1D superconductors exhibiting concurrent ferromagnetic interactions could be promising candidates for the emergence of Majorana zero modes [473].

In this chapter, we discuss our observation of both superconductivity and magnetism in a quasi-1D compound, $(TaSe_4)_3I$ (nTSI). A non-centrosymmetric phase (space group: $P\bar{4}2_1c$) in nTSI was possible to stabilize over a wide temperature range[1]. Resistivity exhibits good metallic behavior starting from room temperature down to sub-Kelvin temperature, a characteristic that has never been observed or predicted in this class of materials. As the temperature is lowered, the compound undergoes a long-range magnetic transition around 9 K and eventually settles into a superconducting ground state below 2.5 K in the non-centrosymmetric phase. As a possible mechanism, based on density

[1]The crystal synthesis and characterization were performed in collaboration with Dr. Mintu Mondal's group at IACS, Kolkata.

functional theory (DFT) calculations[2] (not included in the thesis), proposed that Se_2 dimer vacancies can induce localized magnetic moments in the system along with charge doping, leading to the observed ferromagnetism, metallic behavior, and superconductivity.

7.2 Experimental Methods

(i) Crystal Structure, Sample Preparation, and Characterization:

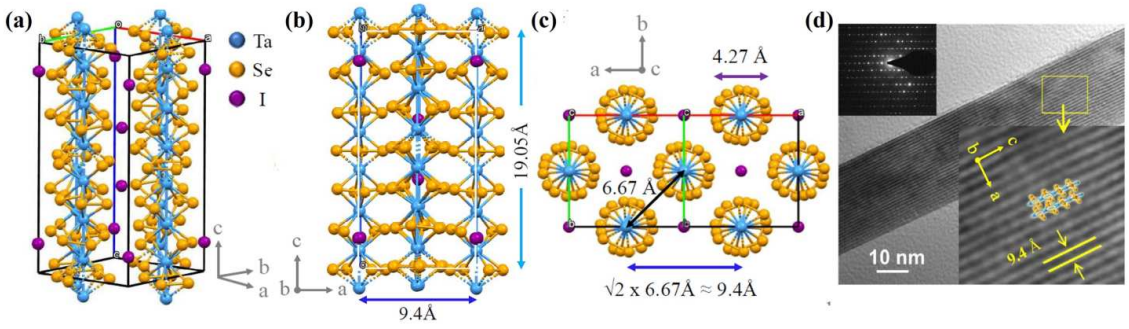

FIGURE 7.1: Crystal structure of the simple tetragonal unit cell **(a)** oblique view, **(b)** linear chains in lateral view and **(c)** projected view on the *ab*-plane **(d)** Quasi-1D structure as seen from distinct lattice chains in the HRTEM image. Upper *inset*: A selected area electron diffraction (SAED). Lower *inset* : The zoomed image showing an inter-chain separation of ≈ 9.4 Å. These structural characterizations were performed by Dr. Mintu Mondal's group at IACS, Kolkata.

The growth of *n*TSI single crystals was carried out using the chemical vapor transport (CVT) technique. High-purity tantalum (Ta) powder (Alfa Aesar, 99.97%) and selenium (Se) powder (Alfa Aesar, 99.999%) were combined with iodine (I) pieces (Alfa Aesar, 99.0%) in a weight ratio of 2.85:4.977:1 (Ta:Se:I). The mixture was thoroughly ground to ensure homogeneity before being transferred into a quartz ampoule. The ampoule was subsequently sealed under a vacuum at a pressure of 10^{-5} mbar. Crystal synthesis was conducted in a two-zone furnace, where the temperatures were maintained at 500°C in the source zone and 400°C in the growth zone for a duration of one week. The resulting single crystals exhibited a hair-like or fiber-like morphology, growing along arbitrary directions. Once the process was complete, the furnace was gradually cooled to room temperature, and the silver-grey fibrous crystals were collected by carefully breaking the quartz ampoule in ambient conditions (300 K). The obtained material remains stable when exposed to air. Single-crystal XRD analysis was conducted at 100 K using a Bruker D8 VENTURE Microfocus diffractometer equipped with a PHOTON II Detector and employing Mo Kα

[2]All first-principles DFT calculations were performed in collaboration with Prof. Tanusri Saha-Dasgupta's group at SNBNCBS, Kolkata

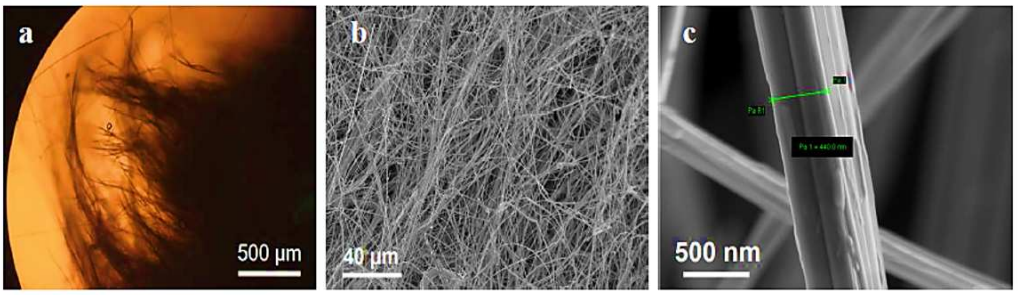

FIGURE 7.2: Optical microscopic and SEM images of nTSI samples. These structural characterizations were performed by Dr. Mintu Mondal's group at IACS, Kolkata.

radiation with $\lambda = 0.71073$ Å. Structural characterization was complemented by High-resolution transmission electron microscopy (HRTEM), which was carried out using a FEI TECNAI G2 F30 S-Twin microscope. The crystal synthesis and crystal characterization were performed by Dr. Mintu Mondal's group at IACS, Kolkata.

The crystals exhibit a ribbon-like fibrous morphology, with lengths extending to a few millimeters and widths in the micron range. A structural analysis at 100 K confirms that nTSI crystallizes in a simple tetragonal unit cell with a non-centrosymmetric space group $P\bar{4}2_1c$. The Rietveld refined lattice parameters are $a = b = 9.436(5)$ Å, $c = 19.046(11)$ Å, with $\alpha = \beta = \gamma = 90°$. The crystal structure is depicted in Fig. 7.1 (a-c). HRTEM imaging, shown in Fig. 7.1 (d), reveals a linear $TaSe_4$ chain-like arrangement along the crystallographic c axis. The interchain spacing between adjacent $TaSe_4$ chains is measured to be $d_{\text{inter}} = 6.677$ Å. The optical microscopic image and SEM images are as shown in Fig. 7.2.

Additionally, we performed mechanical exfoliation of the nTSI sample onto a Si/SiO_2 substrate and observed several sheet-like flakes (yellowish in color) and ultra-thin flakes (bluish in color) under an optical microscope. Subsequent field-emission scanning electron microscopy (FESEM) imaging of the exfoliated samples revealed a large number of narrow, thin, ribbon-like structures with varying thicknesses, lengths, and widths, as shown in Fig. 7.3. These exfoliated samples warrant deeper investigation in future studies, particularly for a comprehensive understanding of their structural, electronic, and superconducting properties, which remain beyond the scope of this thesis. Further exploration could also involve their integration into Josephson junction devices and other hybrid quantum systems.

(ii) Electronic Transport:

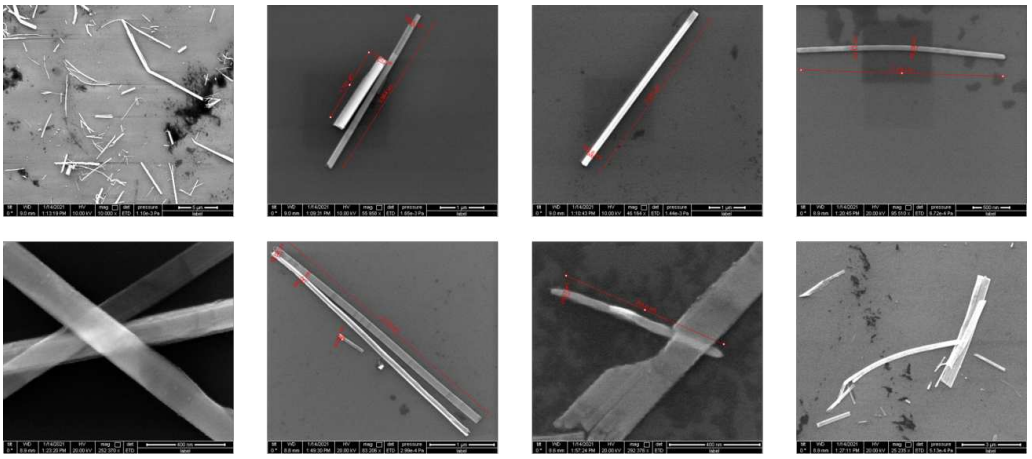

FIGURE 7.3: FESEM images of the exfoliated nTSI samples on top of Si/SiO_2 substrates

The detailed electrical transport measurements of the needle-shaped crystals were performed using conventional four-probe resistivity measurements, conducted with a Quantum Design PPMS setup (1.6 K - 300 K, ± 9 T). Electrical contacts on a bunch of ribbons, as well as on a single ribbon, were made using silver paint (RS Components) to ensure reliable connections. Additionally, sub-Kelvin transport studies were carried out in a dilution refrigerator (Oxford Instruments) in collaboration with Prof. Biswajit Karmakar's lab at SINP, Kolkata.

(iii) Magnetization Measurement:

For magnetic characterization, single-crystalline wires were carefully aligned such that the c-axis coincided with the wire's length. The crystals exhibited a flat, belt-like morphology, where the longest dimension corresponded to the c-axis, and the broad surface was within the ab-plane. To investigate anisotropic magnetic responses, measurements were conducted with the external magnetic field oriented both within the ab-plane and parallel to the c-axis. DC magnetization studies were carried out at the SINP, Kolkata, under the supervision of Prof. Prabhat Mandal, utilizing a SQUID magnetometer (SQUID-VSM Evercool, MPMS 3, Quantum Design).

7.3 Results and Discussion

7.3.1 Signature of Superconductivity

7.3.1.1 Electronic Transport Measurement

To explore the electronic characteristics of the needle-like single crystals, we conducted standard four-probe resistivity measurements down to 1.6 K on both multiple ribbons and individual ribbons. As depicted in Fig. 7.4 (a) (multi-ribbon device), the resistance (R) decreases significantly with decreasing temperature, indicating metallic behavior. Additionally, the R *vs.* T^2 curve (lower inset) displays a linear trend in the 5–25 K range, confirming that nTSI behaves as a clean Fermi liquid metal. The R *vs.* T plot exhibits a distinct slope change near 140 K, indicating a structural phase transition from centrosymmetric at higher temperatures to non-centrosymmetric as temperature decreases to low temperatures, as reported previously [16]. Below 2.5 K, a sharp decrease in resistance resembling a superconducting transition is observed. Cooling the sample further in a dilution refrigerator down to sub-Kelvin temperatures leads to a zero-resistance state below approximately 1 K, confirming the superconductivity (upper inset of Fig. 7.4 (a)). The superconducting transition temperature (T_c) is estimated to be $\sim$ 2.5 K, defined as the temperature where the electrical resistance drops to 90% of its normal-state value. Notably, a single-ribbon device displays a much sharper superconducting transition, supporting the intrinsic nature of superconductivity in these quasi-1D crystals (see Fig. 7.4 (b)). Applying a magnetic field along the crystal's length ($H \parallel I \parallel c$) systematically suppresses T_c. Fig. 7.5 shows that the transition gradually shifts beyond our measurement range, providing definitive evidence for superconductivity. This suppression follows the expected trend when the external field exceeds the upper critical field (H_{c2}), thereby breaking the superconducting state.

7.3.1.2 Magneto-transport Measurement

Magneto-transport measurements were performed under different field orientations to evaluate the H_{c2} and investigate the anisotropy in the superconducting state. Under the application of an external magnetic field parallel to the crystal's length ($H \parallel c$), T_c decreases monotonically and vanishes at approximately 2 T (see Fig. 7.5 (a). A linear extrapolation of $H_{c2}^{||c}$ *vs.* T provides an estimate of the upper critical field at 0 K, yielding $H_{c2}^{||c}(0) \approx 2.35$ T (Fig. 7.5 (a), inset). This estimation neglects minor deviations from

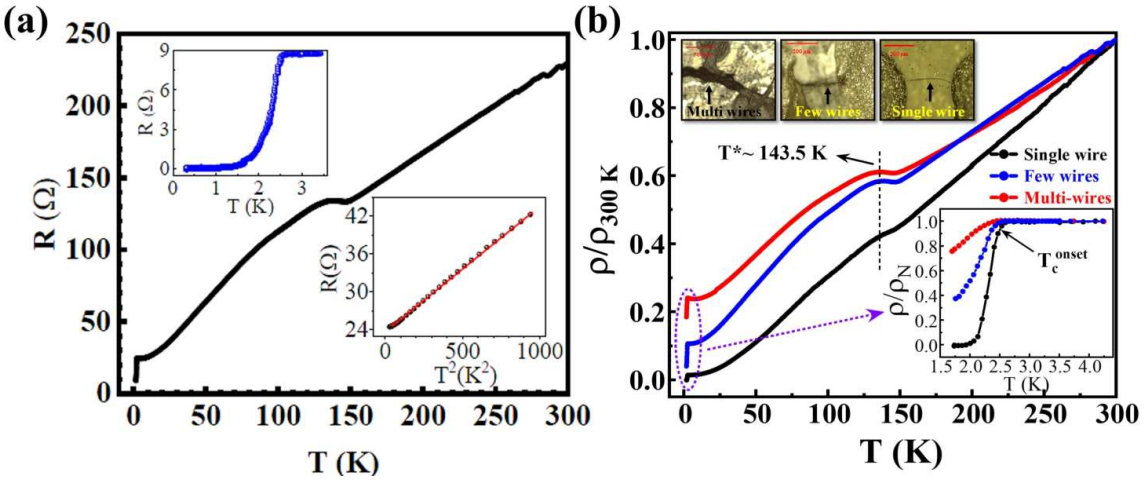

FIGURE 7.4: **(a)** Temperature dependence of resistance (R) measured in a conventional 4-probe geometry. The change in slope around 143.5 K signifies the structural transition in nTSI. Upper *inset*: The superconducting transition at zero magnetic field. Lower *inset*: Linear behaviour of R *vs.* T^2 in the temperature range of 5-25 K with zero magnetic field. **(b)** Temperature dependence of normalized resistivity for nTSI samples of different thicknesses. All samples exhibit a superconducting transition at $T_c \approx 2.5$ K and a structural transition at $T^* \approx 143.5$ K. The top inset shows the corresponding images of the measured devices. Bottom inset shows the magnified view of the temperature-dependent normalized resistivity near the superconducting transition for the three devices.

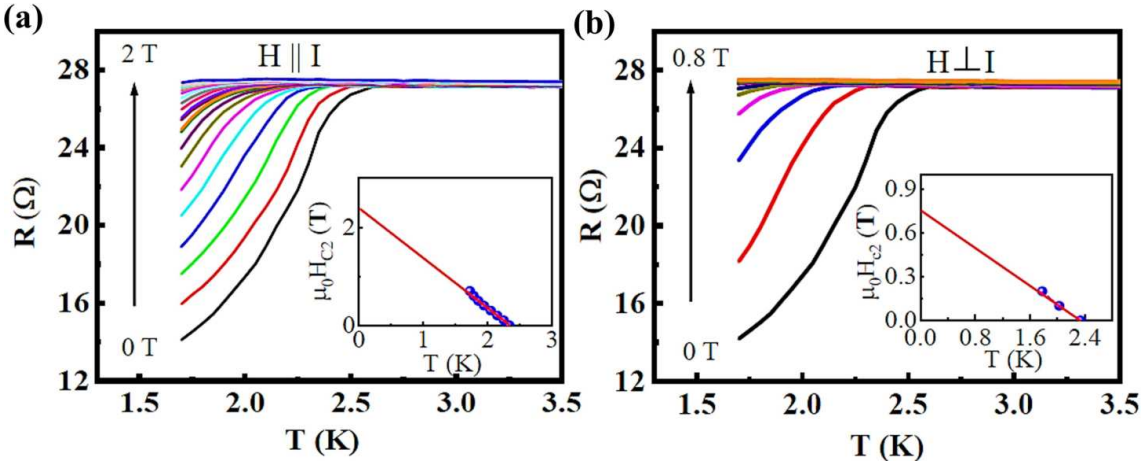

FIGURE 7.5: **(a)** Systematic suppression of the superconducting transition in the resistive measurements under an external magnetic field. (a) Magnetic field applied parallel to the sample direction and the current ($H \parallel c$). (b) Magnetic field applied perpendicular to the sample direction and the current ($H \perp c$). The insets in both panels show the corresponding H_{c2} vs. T plots for each field orientation.

linearity in the $H_{c2}^{||c}$ *vs.* T_c relation. When the field is oriented perpendicular to the c-axis ($H \perp c$), the critical field is lower, likely due to superconducting anisotropy arising from the electronic band structure of the chain-like geometry of the quasi-1D crystal. The estimated zero-temperature critical field for this configuration is $H_{c2}^{\perp c}(0) \approx 0.75$ T,

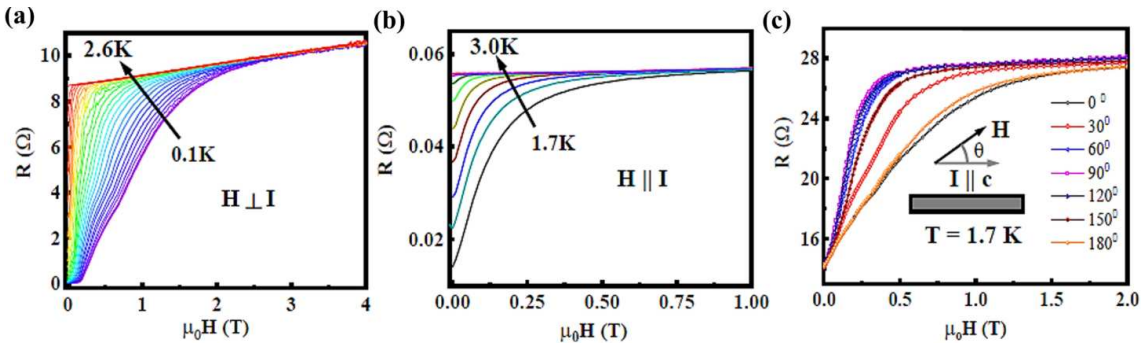

FIGURE 7.6: Temperature-dependent magnetoresistance of nTSI under different magnetic field orientations. (a) Magnetoresistance with the field applied perpendicular to the direction of current. (b) Magnetoresistance with the field aligned parallel to the current direction. (c) Magnetoresistance measured at $T = 1.7$ K for various oblique field angles, showing anisotropy of the sample in the superconducting state.

as shown in Fig. 7.5 (b) and its inset. The H_{c2} of nTSI does not exceed the Clogston-Chandrasekhar limit [474], which defines the Pauli paramagnetic field as $H_p \approx 1.84T_c \approx 4.6$ T. Alternatively, the lack of inversion symmetry in nTSI may also play a role in lowering the paramagnetic limit [475].

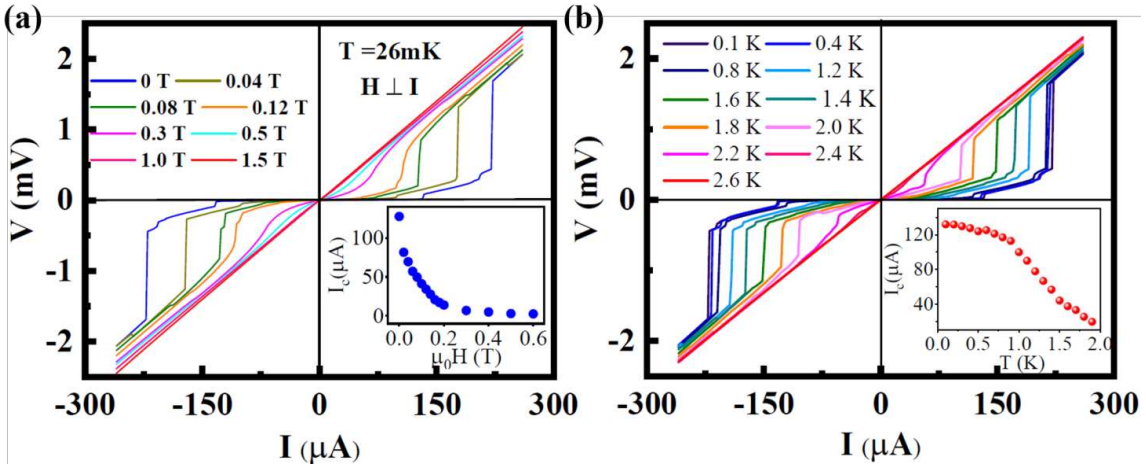

FIGURE 7.7: I–V characteristics measured at 26 mK under various magnetic fields applied perpendicular to the c-axis, showing the critical-current-dominated behavior above and below $H_{c2}^{\perp c}$. The inset displays the dependence of the magnetic field on the critical current (I_c). (d) Zero-field I–V curves at different temperatures. The inset shows the temperature dependence behavior of I_c.

7.3.1.3 I-V Characteristics

Current-voltage characteristics (IVCs) were measured down to 26 mK using a standard four-probe configuration to explore transport properties further. The obtained I-V curves

exhibit non-linearity, with a characteristic jump in voltage at a critical current (I_c), indicative of a superconducting state. Increasing the external magnetic field perpendicular to the current gradually reduces I_c (see Fig. 7.7(a) and inset). This behavior is consistent with the expected response of a type-II superconductor. Moreover, as the temperature increases, the critical current-dominated feature weakens and vanishes near T_c (see Fig. 7.7(b)). The *I-V* traces also display discrete voltage steps, a hallmark of phase slip events commonly observed in low-dimensional superconductors [11, 476]. These findings collectively provide compelling evidence that the resistive transition in *n*TSI originates from superconductivity.

7.3.1.4 Magnetization Measurements

In the framework of the microscopic theory of superconductivity, the spontaneous breaking of U(1) gauge symmetry in the superconducting phase inherently leads to strong diamagnetism. However, in systems where superconductivity coexists with ferromagnetism, a pronounced diamagnetic response is usually absent in conventional DC magnetization measurements [468, 472, 477–480]. To explore the magnetic properties of *n*TSI in detail, comprehensive magnetization measurements were conducted using a SQUID magnetometer (SQUID-VSM Evercool, MPMS 3, Quantum Design) by Prof. Prabhat Mandal's group from SINP, Kolkata, and Dr. Mintu Mondal's group at IACS, Kolkata.

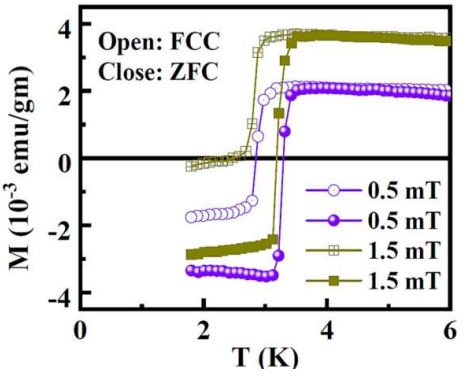

FIGURE 7.8: Temperature-dependent magnetization of the sample measured with field 0.5 mT and 1.5 mT in both ZFC and FCC modes. The onset of the Meissner state is observed below 3.0 K, confirming the superconducting transition. These measurements were performed by Prof. Prabhat Mandal and Dr. Mintu Mondal's group from SINP and IACS, Kolkata.

Figure 7.8(a) presents the low-field magnetization data recorded in both zero-field-cooled (ZFC) and field-cooled cooling (FCC) conditions at low temperatures. A distinct diamagnetic response appears below 3 K when an external magnetic field of 1.5 mT or lower is applied, providing direct evidence of superconductivity. As illustrated in Fig. 7.8(a), when the magnetic field was oriented parallel to the *c*-axis and applied with a minimal strength of 0.5 mT, the material exhibited a distinctly negative magnetic

susceptibility. This behavior indicates a diamagnetic response, which is particularly intriguing given that such signatures have not been previously identified directly in ferromagnetic superconductor systems [468, 472, 477–480]. The detection of this feature suggests the emergence of a Meissner-like state under specific magnetic and temperature conditions, pointing to an unusual interplay between superconducting and magnetic orders in this class of materials.

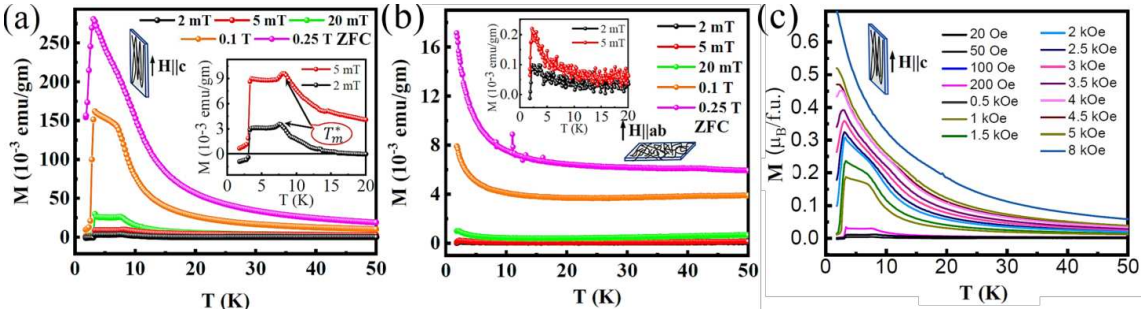

FIGURE 7.9: Temperature-dependent magnetization (M–T) curves recorded under zero-field-cooled (ZFC) conditions with the magnetic field applied (a) parallel to the c-axis ($H \parallel c$) and (b) perpendicular to the c-axis ($H \parallel ab$). Insets in each panel highlight the low-field magnetic response for the respective orientations. (c) ZFC M–T curve for $H \parallel c$ plotted to highlight the detailed evolution of magnetization with temperature. These magnetization measurements were performed by Prof. Prabhat Mandal and Dr. Mintu Mondal's group from SINP and IACS, Kolkata.

In conventional type-I superconductors, the onset of diamagnetism typically appears at the same temperature during both ZFC and FCC measurement protocols [481–484]. In contrast, nTSI samples exhibit a clear discrepancy in the transition temperatures at which the diamagnetic response emerges in the ZFC and FCC modes, as illustrated in Fig. 7.8. This deviation from type-I behavior aligns with the characteristics expected for type-II superconductors, wherein the flux-pinning and vortex dynamics lead to distinct magnetic responses in ZFC and FC cycles. Consequently, this behavior supports the classification of nTSI as a type-II superconductor. The diamagnetic response was also observed when the magnetic field was oriented perpendicular to the c-axis, as depicted in the inset of Fig. 7.9(b). It is important to highlight that the superconducting volume fraction, inferred from the Meissner effect, is approximately 9%. This value is considerably smaller than the expected theoretical estimate.

7.3.2 Signature of Ferromagnetism

7.3.2.1 M-T Measurements

To investigate the magnetic ground state of nTSI, systematic *dc* magnetization (M–T) measurements were conducted across a broad temperature span. Figure 7.9(a) illustrates the temperature evolution of magnetization under zero-field-cooled (ZFC) conditions with the magnetic field aligned along the c-axis (needle direction). As the temperature decreases, M steadily increases and reaches a local maximum near 9 K, after which it remains nearly unchanged until superconductivity sets in (see *inset* of Fig. 7.9(a) and Fig. 7.11). This behavior is consistently observed for all applied magnetic fields in the low-field regime (2–20 Oe). The observed peak and plateau-like feature in M is reminiscent of helimagnetically ordered systems [485, 486], often associated with an intrinsic ferromagnetic component. A further subtle rise in magnetization is observed below $\sim$ 6 K, suggesting the onset of a ferromagnetic-like phase (Fig. 7.11). Magnetization measurements under higher excitation fields (e.g., 0.25 T, see Fig. 7.11(b), (c)) support this inference, displaying both a ferromagnetic transition and a superconducting diamagnetic signal. The derivative plot (dM/dT vs. T) reveals two distinct features: a magnetic transition temperature $T_m^* \approx 9.6$ K and a superconducting onset at $T_c \approx 2.3$ K. Additionally, field-dependent measurements show a clear drop in M near T_c for fields up to 4 kOe (Fig. 7.9(c)), indicating a surviving superconducting response. However, beyond this field strength, the ferromagnetic contribution overwhelms the diamagnetic signal, likely approaching the upper critical field of the superconducting state, where the diamagnetic shielding becomes suppressed.

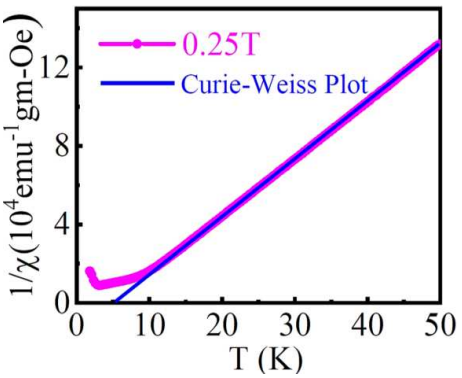

FIGURE 7.10: Temperature dependence of the inverse magnetic susceptibility ($1/\chi$) measured along the c-axis under ZFC and warming conditions at 0.25 T. The blue solid line represents the fit to the Curie–Weiss law. This analysis was performed by Dr. Mintu Mondal's group from IACS, Kolkata.

To further investigate the magnetic ground state of nTSI, the temperature-dependent paramagnetic susceptibility $\chi(T)$ was analyzed using the Curie–Weiss (CW) law, expressed as:

$$\frac{C}{\chi} = T - T_{\mathrm{CW}} \tag{7.1}$$

Where C is the Curie constant, T is the absolute temperature, and T_{CW} is the Curie–Weiss temperature. Figure 7.10 displays the inverse susceptibility, $1/\chi$, derived from M–T measurements performed under an applied magnetic field of 0.25 T. The fit yields a

positive $T_{CW} \approx 5.5\,K$, indicative of predominant ferromagnetic exchange interactions at low temperatures in nTSI.

Additionally, anisotropy in the magnetic response was examined by applying the magnetic field perpendicular to the c-axis (Fig. 7.9(b)). Under this configuration, the magnetization is significantly reduced, and no clear signature of a magnetic transition is observed, implying that the easy magnetization axis lies along the c-direction and that the ab-plane is the hard axis of magnetization. Nonetheless, a distinct drop in magnetization is visible at the superconducting transition temperature T_c in low-field ZFC measurements, as highlighted in the inset of Fig. 7.9(b).

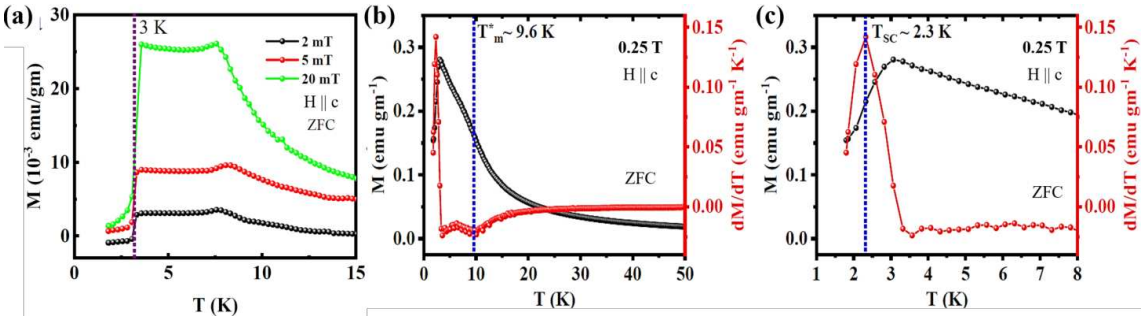

FIGURE 7.11: (a) Temperature-dependent zero-field-cooled (ZFC) magnetization curves of nTSI measured under three different small applied magnetic fields, revealing the emergence of ferromagnetic ordering. (b) ZFC M–T data measured at 0.25 T applied magnetic field parallel to the c-axis. The paramagnetic-to-ferromagnetic transition temperature, T_m^*, as evidenced by the onset of magnetic ordering in $M(T)$ and the corresponding dip in the dM/dT vs. T plot. (c) The superconducting transition temperature, T_c, is characterized by a sharp drop in magnetization due to the Meissner effect, reflected as a peak in the dM/dT curve. These magnetization measurements were performed by Prof. Prabhat Mandal and Dr. Mintu Mondal's group from SINP and IACS, Kolkata.

7.3.2.2 M-H Measurements

To investigate the magnetic ordering in nTSI, isothermal magnetization (M–H) measurements were carried out over a range of temperatures and field orientations. After applying an external magnetic field along the c-axis, the resulting M–H loop (Fig. 7.12(a)) exhibits an S-shaped profile with a clear saturation magnetization but negligible remanence, characteristic of a soft ferromagnetic material with minimal coercivity. At low temperatures and low fields, deviations from the typical ferromagnetic loop appear, indicating additional effects due to superconductivity. In the ab-plane configuration, the M–H response is influenced by an external diamagnetic background, primarily due to the GE varnish used during sample preparation (Fig. 7.12(b)). To

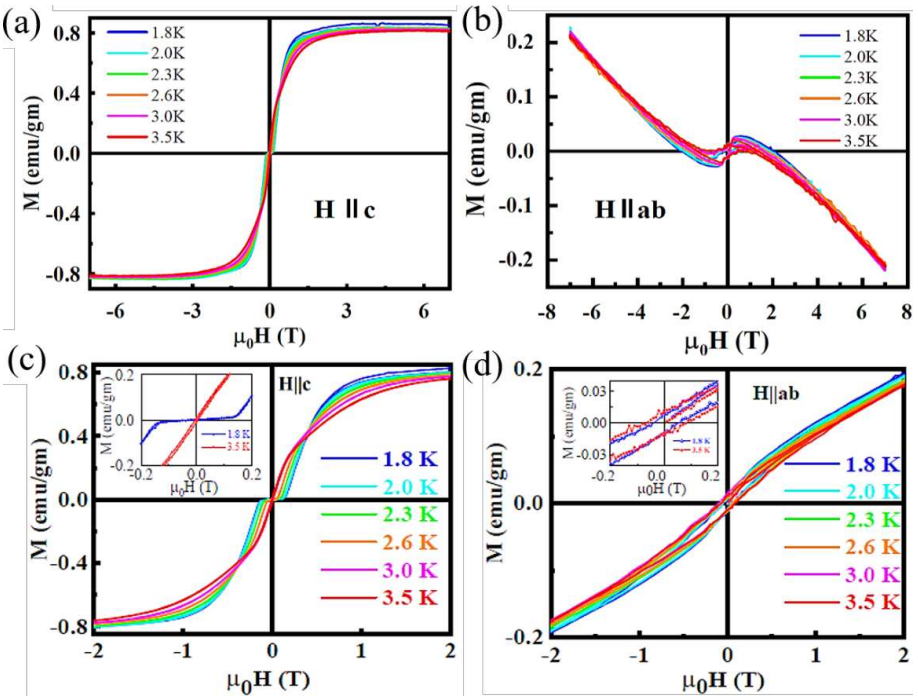

FIGURE 7.12: (a) M–H loop measured with magnetic field applied parallel to the c-axis, showing a characteristic S-shaped curve indicative of soft ferromagnetism. (b) M–H loop with field applied parallel to the ab-plane, displaying a strong diamagnetic background contribution arising from the GE varnish. (c) Hysteresis loops with $H \parallel c$ recorded at various temperatures across T_c, showing clear deviations from the S-shaped loop below T_c due to superconductivity. *Inset:* Comparison of M–H curves at 1.8 K and 3.5 K highlights the emergence of a strong diamagnetic component below T_c. (d) Hysteresis loops with $H \parallel ab$ at selected temperatures above and below T_c, after correcting for the diamagnetic background, confirming intrinsic ferromagnetic ordering. These magnetization measurements were performed by Prof. Prabhat Mandal and Dr. Mintu Mondal's group from SINP and IACS, Kolkata.

mitigate this artifact, it is assumed that the saturation magnetization is isotropic in both directions, and a paramagnetic fitting is used to correct the diamagnetic contribution. The corrected hysteresis loops with $H \parallel ab$ above and below T_c are shown in Fig. 7.12(d).

Focusing on the hysteresis loops measured across the superconducting transition, Figs. 7.12(a) and (c) show M–H data collected at various temperatures with the field applied parallel to the c-axis. Above T_c, the loops maintain a soft ferromagnetic S-shape. However, below T_c, a notable flattening near zero field emerges, deviating from the S-shape loop. This flattening indicates the coexistence of superconductivity with ferromagnetism, where at low fields, the superconducting diamagnetic response partially cancels the ferromagnetic signal, resulting in an extremely small net magnetic moment below T_c. This behavior also matches for samples having a superconducting volume fraction very small. Now, as the field increases, superconductivity is suppressed, the ferromagnetic

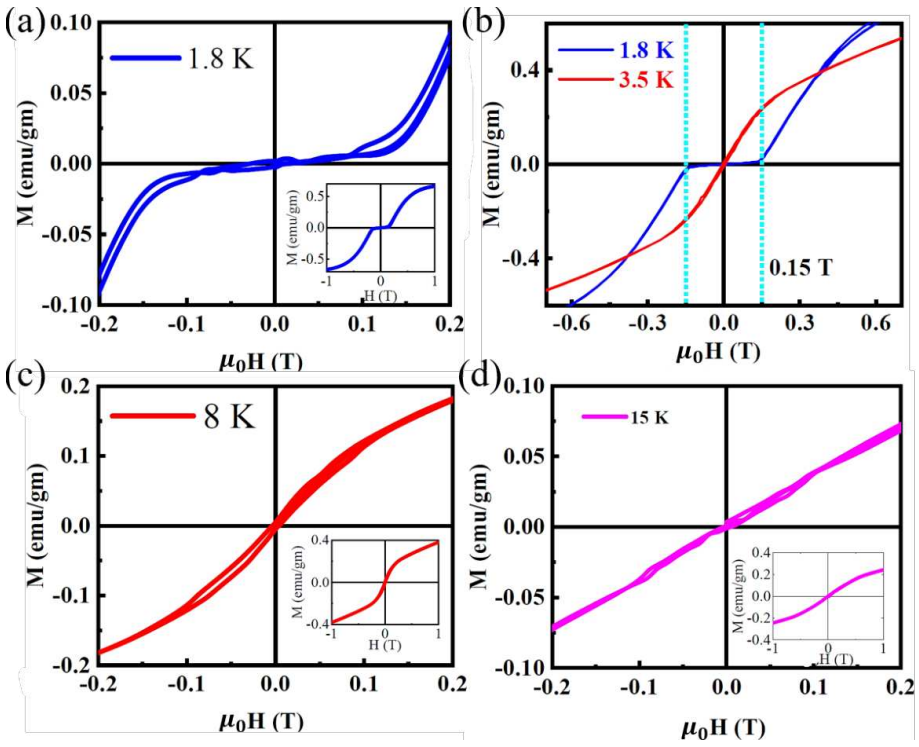

FIGURE 7.13: Temperature evolution of hysteresis loops in nTSI with $H \parallel c$ axis. (a) M–H loop measured below the superconducting transition temperature ($T < T_c$), exhibiting a characteristic flat region at low fields. (b) Comparison of the loops just above and below T_c, revealing a metamagnetic-like transition as superconductivity emerges. (c) Hysteresis behavior in the intermediate regime between the superconducting and magnetic transitions ($T_c < T < T_m^*$), showing a typical soft ferromagnetic response. (d) Loop measured above the magnetic transition temperature ($T > T_m^* > T_c$), displaying a weak paramagnetic-like behavior. These magnetization measurements were performed by Prof. Prabhat Mandal and Dr. Mintu Mondal's group from SINP and IACS, Kolkata.

behavior becomes dominant again, producing an abrupt increase in magnetization (see inset, Fig. 7.12(c)). The extent of this flat region increases with lowering the temperature below T_c, consistent with an increase in the upper critical field H_{c2} with decreasing temperature. In contrast, when the magnetic field is applied perpendicular to the c-axis (Fig. 7.12(d)), the M–H loops display prominent hysteresis across the superconducting regions (1.8–3.5 K). However, no low-field flattening is observed in this configuration below T_c, suggesting a lack of significant interplay between superconductivity and magnetism for this orientation. This strongly supports the anisotropic nature of both magnetic and superconducting properties in nTSI.

Figure 7.13 summarizes the evolution of the magnetic phase across characteristic temperature regimes. At 1.8 K (Fig. 7.13(a)), the M–H loop displays a flat segment at low fields and an S-shape at higher fields, consistent with a state where superconductivity

coexists with soft ferromagnetism. Between T_c and the magnetic ordering temperature T_m^*, the hysteresis loop (Fig. 7.13(b), (c)) resembles that of a typical soft ferromagnet, without any diamagnetic suppression. At temperatures above T_m^*, only a weak, narrow S-shaped loop with negligible hysteresis is observed (Fig. 7.13(d)), indicative of a transition to a paramagnetic state. These findings reveal a highly anisotropic and complex magnetic ground state in nTSI, marked by the coexistence of superconductivity and ferromagnetism, and sensitive to both temperature and field orientation.

7.3.3 Phase Diagram

To map out the phase behavior of nTSI, we integrated results from electrical resistivity, DC magnetization measurements, etc., over a wide span of temperatures and magnetic fields. Figure 7.14 displays the resulting temperature–field phase diagram, highlighting the regions in which superconductivity and ferromagnetism emerge and overlap.

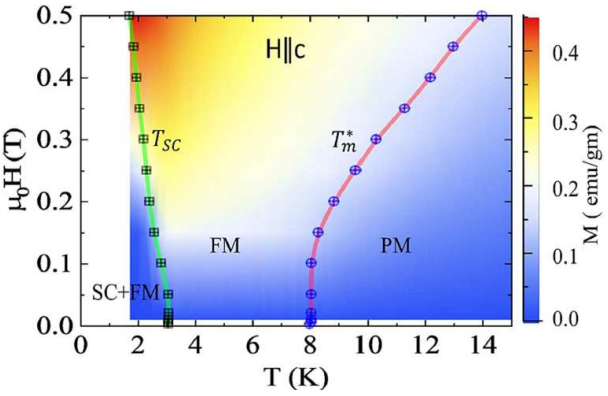

FIGURE 7.14: Temperature–magnetic field phase diagram of the ferromagnetic superconductor nTSI, constructed using ZFC M–T measurements with $H \parallel c$. The T_c (here T_{SC}) is identified by the abrupt decrease in M, indicating the onset of the Meissner state. The magnetic ordering temperature (T_m^*) is extracted from the characteristic peak in the M–T curve.

The onset of superconductivity is identified by the abrupt decrease in resistivity and the appearance of a Meissner response below $T_c \approx 2.5\,\mathrm{K}$. Meanwhile, the ferromagnetic ordering temperature $T_m^* \approx 9.6\,\mathrm{K}$ is taken from the peak in the magnetization data. Three principal regimes are evident: a high-temperature paramagnetic (PM) state above T_m^*, a ferromagnetic (FM) phase for $T_c < T < T_m^*$, and a superconducting region at $T < T_c$. Notably, for $T < T_c$, the two orders coexist over a finite field range. Anisotropy in the superconducting critical field is apparent: extrapolating $H_{c2}(T)$ to zero temperature gives $H_{c2}^{\parallel c}(0) \approx 2.35\,\mathrm{T}$ when the field is aligned with the c-axis, whereas $H_{c2}^{\perp c}(0) \approx 0.75\,\mathrm{T}$ for fields applied in the ab-plane. As the applied field exceeds these values, the superconducting state is quenched, confirming its sensitivity to external magnetic fields.

The coexistence of ferromagnetic and superconducting phases in a non-centrosymmetric crystal suggests unconventional pairing mechanisms may be at play. Moreover, mutual-inductance measurements reveal a twofold angular dependence of the superconducting response, consistent with the quasi-1D crystal structure and underscoring the anisotropic nature of the superconducting condensate in nTSI.

7.3.4 Further Analysis of Superconductivity

7.3.4.1 Determination of Coherence Length

To investigate the evolution of the upper critical field $H_{c2}(T)$ with temperature, magnetoresistance measurements were carried out across a range of temperatures, as plotted in Fig. 7.15. The upper critical field at each temperature was defined as the magnetic field at which the resistance drops to 50% of the normal-state resistance (R_N). The resulting $H_{c2}(T)$ values were then analyzed using five well-established theoretical models to extract the superconducting coherence length $\xi(0)$ at zero temperature.

The first approach to modeling the $H_{c2}(T)$ involves the Gorter-Casimir two-fluid framework [487], which assumes a quadratic temperature variation near T_c. The corresponding relation is given by:

$$\mu_0 H_{c2}^{\perp}(T) = H_{c2}(0)\left(1 - \frac{T^2}{T_c^2}\right) \tag{7.2}$$

where $H_{c2}(0)$ represents the upper critical field extrapolated to absolute zero. In cases where the superconducting layer thickness d is significantly smaller than the in-plane coherence length, $d < \xi$, dimensional confinement effects become important. Under such conditions, 2D model proposed by Tinkham is applicable [488–490], which predicts a distinct temperature dependence of H_{c2}, as follows:

$$\mu_0 H_{c2}^{\perp}(T) = H_{c2}(0)\left(1 - \frac{T}{T_c}\right) \tag{7.3}$$

Another empirical framework was introduced by Baumgartner and co-workers [491], who derived a closed-form expression that accurately mirrors the temperature dependence predicted by the WHH (Werthamer–Helfand–Hohenberg) theory. This approximation, referred to as the B-WHH model, refines the curvature of $H_{c2}(T)$ across the entire

temperature range, expressed as:

$$\mu_0 H_{c2}^{\perp}(T) = \frac{H_{c2}(0)}{0.697}\left[\left(1-\frac{T}{T_c}\right) - 0.153\left(1-\frac{T}{T_c}\right)^2\right] - \frac{H_{c2}(0)}{0.697}\left[0.152\left(1-\frac{T}{T_c}\right)^4\right] \quad (7.4)$$

An alternative formulation frequently employed to capture the full temperature evolution of the upper critical field is the Jones-Hulm-Chandrasekhar (JHC) model [492], which is a combination of Ginzburg-Landau (GL) theory and the Gorter-Casimir two-fluid model, and it is often used to fit $H_{c2}(T)$, as follows:

$$\mu_0 H_{c2}^{\perp}(T) = H_{c2}(0)\left[\frac{1-\left(\frac{T}{T_c}\right)^2}{1+\left(\frac{T}{T_c}\right)^2}\right] \quad (7.5)$$

The Gor'kov model [493], rooted in microscopic BCS theory, offers a semi-empirical formula for the temperature evolution of H_{c2}. The relation is given as:

$$\mu_0 H_{c2}^{\perp}(T) = \frac{H_{c2}(0)}{1.77}\left[1.77 - 0.43\left(\frac{T}{T_c}\right)^2 - 0.07\left(\frac{T}{T_c}\right)^4\right] \times \left(1-\frac{T^2}{T_c^2}\right) \quad (7.6)$$

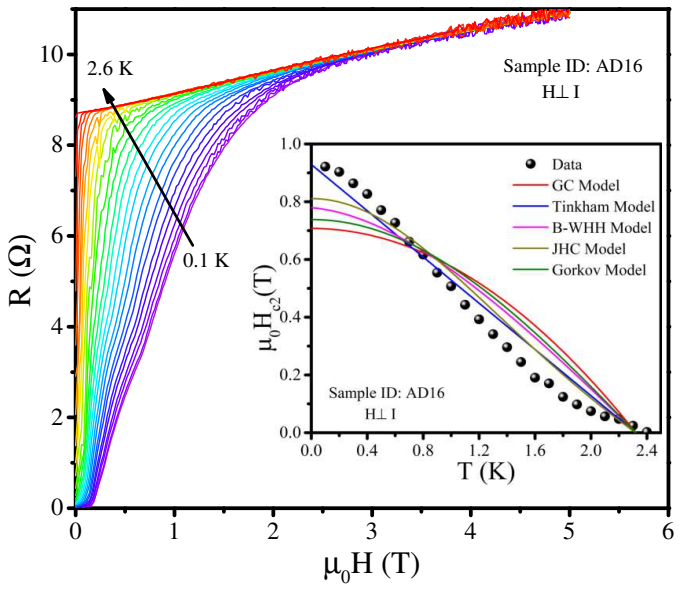

FIGURE 7.15: Resistive transition with magnetic field for different temperatures. Inset: Temperature-dependent critical field ($H_{c2}(T)$) is fitted with various models for calculating $H_{c2}(0)$.

Despite applying the above five standard fitting models, none provided a satisfactory match to the experimental $H_{c2}(T)$ data (see inset of Fig. 7.15. A notable upward curvature is

Model	**Sample ID**					
	BD		**AD16**		**AD15**	
	$H_{c2}(0)$ **(T)**	$\xi(0)$ **(nm)**	$H_{c2}(0)$ **(T)**	$\xi(0)$ **(nm)**	$H_{c2}(0)$ **(T)**	$\xi(0)$ **(nm)**
GC	0.19	41.88	0.71	21.57	0.28	33.89
Tinkham	0.34	31.04	0.93	18.78	0.51	25.28
B-WHH	0.24	36.64	0.78	20.47	0.37	29.78
JHC	0.31	32.39	0.81	20.10	0.47	26.51
Gorkov	0.21	38.69	0.74	21.07	0.33	31.44

TABLE 7.1: Values of coherence length, $\xi(0)$ and critical field, $H_{c2}(0)$ from various models

observed near low temperatures, a behavior that deviates from these conventional theories. Such positive curvature in $H_{c2}(T)$ has been widely reported in other unconventional superconducting systems and has been attributed to several mechanisms, including: (1) scattering due to magnetic impurities [494], (2) strong coupling between electrons and phonons [495], (3) dimensional confinement and structural disorder [496, 497], (4) bipolaron effects [498, 499], and (5) multiband superconductivity [500], etc. However, for the first time, we estimated the value of zero-temperature critical field $H_{c2}(0)$ and corresponding $\xi(0)$ for this material (see Table 7.1). The estimated $H_{c2}(0)$ lies between 0.5 T and 1 T, and the $\xi(0)$ at absolute zero is found to be in the range of 20–30 nm along the c-axis of this needle-like crystal. Comparing this with the known lattice parameters along the c-axis (c = 1.9046 nm) [16, 501], the ξ along the c-axis is clearly much larger than the lattice parameter 'c', suggesting that the superconducting correlations extend over several unit cells. It is also noted that the $\xi(0)$ is smaller than the nanowire thickness ($\approx$ 700-800 nm). However, the effective superconducting thickness of the nTSI nanowire should be smaller than the overall sample thickness, suggesting the quasi-1D behavior of the superconducting nTSI samples [502, 503]. Previous investigations into quasi-1D superconducting nanowires have shown that such systems typically feature cross-sectional dimensions between 10 and 1000 nm [504–508], a range that encompasses the thickness of our samples and reinforces their classification as quasi-1D superconductors.

7.3.4.2 Phase Slip Events and Estimation of Penetration Depth

To gain deeper insight into the superconducting behavior of nTSI, we performed detailed four-probe I–V measurements in the superconducting regime. Figure 7.16 displays the IVCs of a signal wire (AD15) and a few-wire (AD16) sample at different temperatures

(Fig. 7.16(b), (c), (d)) and magnetic fields ($H \perp I$) (Fig. 7.16(a)). Upon gradually increasing the applied current, both samples initially exhibited a zero-voltage state, a characteristic of superconductivity. However, beyond a specific threshold current, identified as the critical current (I_c), a finite voltage appeared, indicating the breakdown of superconducting coherence and the emergence of a resistive or dissipative state due to superconducting pair breaking. As the current was increased further, the I–V curves revealed a series of discrete voltage steps, which mark successive jumps as the system evolves from a superconducting state to a normal resistive state. The voltage steps appear reliably in both single-wire and few-wire samples and are found to be consistent, reproducible, and appear more intense and better resolved at diminished temperatures or weaker magnetic strengths. ultimately disappearing as the temperature or magnetic field gradually increases. The occurrence of such discrete voltage steps in the IVCs is widely regarded as a hallmark of quasi-1D superconductivity. Similar behavior has been reported in various low-dimensional superconducting systems, including single-crystalline Sn nanowires [505] and polycrystalline Nb nanowires [509, 510], suggesting that the nTSI nanowires may share a common underlying mechanism associated with dimensional confinement and phase-slip events.

One of the primary sources of dissipation in a quasi-1D system of current-carrying superconductors is phase slip events. In these events, across two regions of a 1D superconducting wire undergoes a 2π phase shift, leading the order parameter to momentarily vanish, and resulting in the initiation of a phase slip center (PSC) [511, 512]. At its core, the activation of phase slips is fundamentally linked to thermal origin at temperatures proximate to T_c. However, significantly below T_c, the quantum fluctuations become a dominant factor in these events [513]. In terms of technology, a phase slip junction [514], characterized by coherent phase slippage, can be regarded as the dual equivalent of the Josephson junction, where the traditional phase difference is replaced by charge [511, 515, 516]. Theoretical investigations have shown that slight inhomogeneities within a superconducting wire act as weak links exhibiting lower resistance than the wire's full normal-state value, and can serve as sites for localizing a phase slip junction [517]. Recent experiments have shown that disorder within a 1D superconducting wire can give rise to coherent quantum phase slips (CQPS) [101, 511, 512, 518, 519]. Similar to PSCs in 1D superconducting nanowires, phase slip lines (PSLs) are generated in wide 2D superconducting thin films. These PSLs can effectively function as Josephson's weak links [520]. Many theoretical and experimental results suggest that both PSCs and PSLs manifest as features resembling voltage steps in IVCs [521–523].

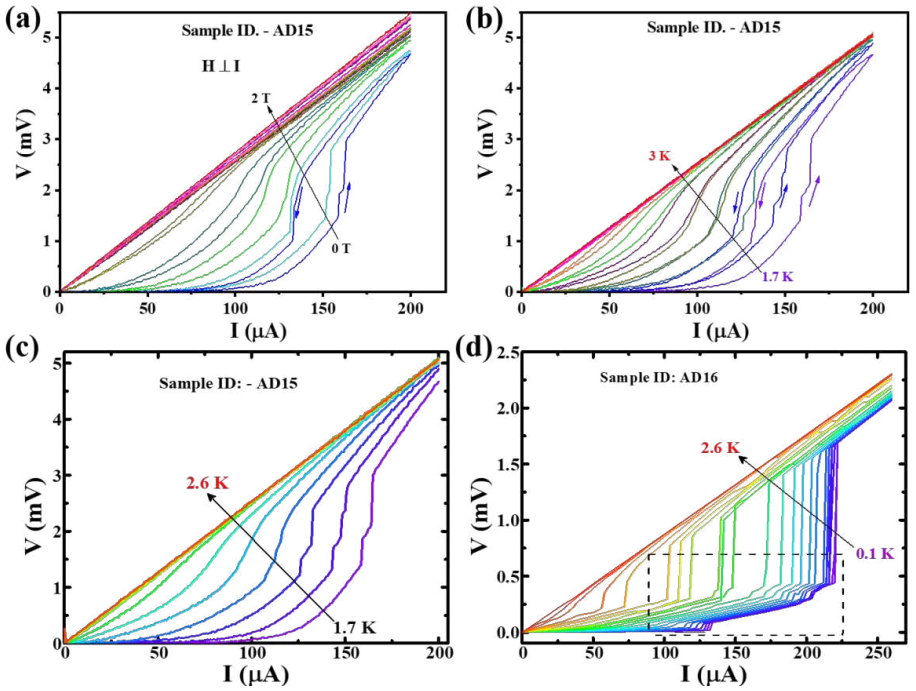

FIGURE 7.16: (a) I–V characteristics of a single nTSI wire (ID: AD15) under various magnetic fields applied perpendicular to the current direction. The arrows indicate the presence of hysteresis in the I–V response. (b) Temperature-dependent I–V curves for the same sample, with arrows marking the hysteretic behavior that persists across the transition. (c) Isothermal I–V measurements for sample AD15 at different temperatures, revealing distinct step-like features in the voltage response. (d) Similar step-like features are also observed in another multi-wire sample (AD16), persisting down to temperatures as low as 100 mK.

Hence, we anticipate that these voltage steps stem from defects or local imperfections in the nTSI nanowires, which support a smaller I_c. A voltage step occurs in the wire once the driving current exceeds the local critical threshold of a given PSC [511]. Consequently, superconducting nanowires can be interpreted as networks of Josephson junctions embedded within a continuous superconducting structure, where PSCs exhibit functional similarities to the weak links found in Josephson junctions [524].

In the superconducting regime, the IVCs display pronounced hysteresis loops during forward and reverse current sweeps, as shown in Fig. 7.16(a) and (b). This hysteretic behavior gradually diminished and eventually disappeared with increasing temperature or applied magnetic field. Such hysteresis in the IVCs is frequently observed in superconducting nanowires, due to self-heating hotspots or under-damped Josephson junction [507]. In the realm of superconducting nanostructured systems, particularly within weak links, the occurrence of hysteresis in IVCs is a common phenomenon. This hysteresis is attributed to Joule heating, that elevates the temperature locally, leading to a

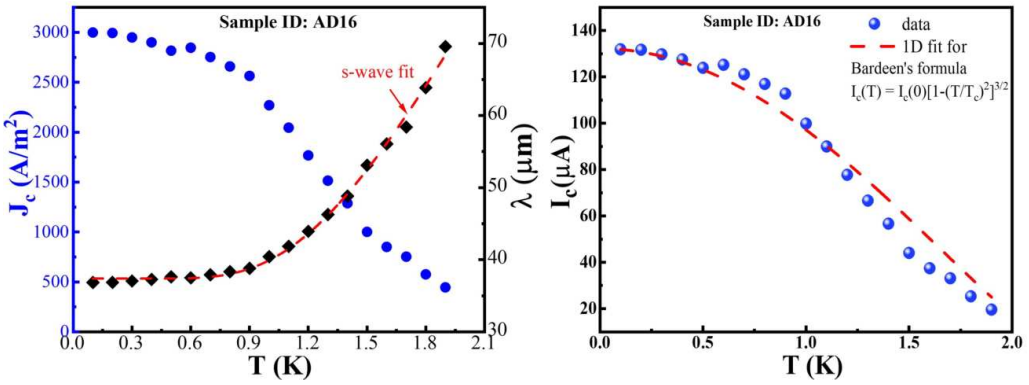

FIGURE 7.17: (a) The measured values of the critical current density (J_c) from IVCs data (left scale) and the London penetration depth $\lambda(T)$ (right scale). The red dotted line is the fit to $\lambda(T)$ using the Eq. 7.9. b) Temperature-dependent critical current (I_c) is fitted by Bardeen's formula (Eq. 7.7) for quasi-1D superconductors.

reduction in the critical current [525, 526]. The presence of hysteresis is thus explained by localized heating effects within weak links that function similarly to Josephson junction [527]. Therefore, the observed staircase-like voltage response arises from quantum phase slip activity, along with the hysteresis in IVCs indicates a hallmark of quasi-1D superconductivity in nTSI. These phenomena are also well observed in other quasi-1D superconducting nanowires like Ta_2PdS_5 [503] and Nb_2PdS_5 [528], thin superconducting Nb [509, 510] and Sn nanowires [505], which are consistent and well matching with our observations.

Hence, we observed multiple finite voltage step transitions in IVCs (Fig. 7.16(a), (b)) near T_c. These finite voltage steps indicate the appearance of phase-slip centers in the sample. We also get hysteresis IV curves as predicted by theory [529, 530]. The 'foot-like' structure for small currents suggests non-thermal or intrinsic hysteresis present in the sample. The multiple voltage steps and hysteresis IV mainly appeared due to the 1D confinement of Cooper pairs as explained by the phase slip model [507, 531, 532]. The temperature-dependent critical current (Fig. 7.17(b)) also fits well with Bardeen's formula [533, 534]:

$$I_c(T) = I_c(0)[1 - (T/T_c)^2]^{3/2} \tag{7.7}$$

where $I_c(0)$ is the critical current at $T = 0$ K and it predicts a quasi-1D- superconductor in the clean limit $\lambda(0) \gg \xi(0)$.

Upon initial inspection, there seems to be a contradiction with our calculated GL coherence length for nTSI, as it is significantly smaller than the size of the sample. Anyway, In the context of type-II superconductors, it is proposed that the characteristic length scale

defining quasi-1D superconductivity is determined by their penetration depth ($\lambda(T)$). Unlike type-II materials, in type-I superconductors, achieving quasi-1D superconductivity requires that the wire diameter be less than the GL coherence length scale ($\xi(T)$) [504, 528]. We calculated the temperature-dependent critical current density, $J_c(T)$, from I-V data of various temperatures (Fig. 7.17(a)). For type-II superconductors, the current density (J_c) is related with the London penetration depth (λ) by the following expression [535]:

$$J_c(T) = \frac{\phi_0}{4\pi\mu_0\lambda^3(T)} \left(\ln\left(\kappa(T)\right) + 0.5\right) \tag{7.8}$$

Here, $\kappa(T) = \lambda(T)/\xi(T)$ represents the Ginzburg–Landau parameter. Since $\kappa(T)$ exhibits minimal variation with temperature, it can be approximated as constant within the logarithmic expression. Employing Eqn. 7.8, we initially compute $\lambda(T = 0)$ by substituting the previously determined $\xi(0)$. Assuming the argument of the logarithm remains nearly unchanged with temperature, $\lambda(T)$ can then be estimated. The results are summarised in Fig. 7.17(a). The calculated value of $J_c(0) \approx 3 \times 10^3 \mathrm{Am}^{-2}$ and the London penetration depth, $\lambda(0) \approx 35$ μm. This $\lambda(0)$ is considerably greater than the thickness of the sample ($\approx$ 700-800 nm), thereby fulfilling the criteria for quasi-1D superconductivity in the class of type-II superconductors [528]. The energy gap has been determined by fitting the low-T behavior of $\lambda(T)$ as shown in Fig. 7.17(a). For s-wave symmetry [536, 537]:

$$\lambda^{-2}(T) = \lambda^{-2}(0)\left(1 - 2\sqrt{\frac{\pi\Delta(0)}{k_B T}}\exp^{\frac{-\Delta(0)}{k_B T}}\right) \tag{7.9}$$

The $\lambda(T)$ data is well fitted with BCS s-wave symmetry, and the fit gives the value of the superconducting energy gap $\Delta(0) = 0.5 \pm 0.015$ meV. It is in close agreement with the BCS value.

7.4 Conclusion

In summary, the comprehensive measurements of electronic transport, magneto-transport, and magnetization in newly synthesized single-crystal quasi-1D compound nTSI have revealed a rich and complex ground state. The system exhibits metallic behavior, with the emergence of weak ferromagnetic ordering below approximately 9 K, followed by the onset of superconductivity at around 2.5 K. These findings confirm the simultaneous

observation of superconductivity and ferromagnetism, two typically antagonistic quantum phases, within a narrow low-temperature window.

The magneto-transport measurements confirm the anisotropic nature of superconductivity and magnetism in nTSI, with a positive curvature in the upper critical field $H_{c2}(0)$. A detailed investigation of the nature of superconductivity in this compound was carried out using various theoretical models, providing multiple pieces of evidence for its quasi-1D nature. The coherence length (ξ) and $H_{c2}(0)$, were estimated through different approaches, while the London penetration depth (λ) extracted from IVCs showed good agreement with BCS s-wave symmetry, yielding a superconducting energy gap close to the BCS value. Additionally, the I–V measurements revealed a series of voltage steps and pronounced hysteresis, especially at low temperatures and fields. These features are strongly suggestive of quantum phase-slip phenomena, a distinctive signature of low-dimensional superconductors. The observed hysteresis is attributed to self-heating effects or underdamped Josephson-like weak links within the structure, further reinforcing the picture of a low-dimensional superconducting ground state.

Although a definite mechanism is difficult to pinpoint, first-principles calculations based on theoretical studies suggest that Se dimer vacancies may give rise to this unusual ground state, simultaneously hosting these two antagonistic quantum phases. This simultaneous presence of magnetism and superconductivity, coupled with reduced dimensionality and intrinsic disorder, makes nTSI a promising platform for exploring emergent phenomena in low-dimensional quantum systems. These findings open pathways for future studies into the interplay of dimensionality, electronic correlations, and competing quantum phases in quasi-1D superconductors.

Chapter 8

Summary and Future Perspective

8.1 Summary

As the need for faster computation and denser memory grows, conventional electronics face limitations in energy efficiency and scalability. This has driven intense research into low-dimensional quantum materials with unique physical properties for future data storage, sensing, and spintronic technologies. Among these, layered van der Waals (vdW) magnetic materials and quasi-1D superconductors offer model platforms to probe the interplay between dimensionality, electronic correlations, and emergent quantum phenomena. This thesis presented a comprehensive systematic investigation – through developing customized experimental setups and optimized device fabrication strategies – into the electronic, magnetic, and spectroscopic behavior of two such interesting materials systems: the vdW ferromagnet Fe_4GeTe_2 and the quasi-1D superconductor $(TaSe_4)_3I$ (nTSI). The major outcomes of this thesis are summarized as follows:

1. Chapter 4 presents a detailed experimental investigation of the electronic and magneto-transport properties of the near room-temperature ($T_C \sim 270$ K) vdW ferromagnet Fe_4GeTe_2, down to 16-layer thickness, focusing on the origin of its unusual spin reorientation transition (SRT, $T_{SR} \sim 120$ K) and the associated anomalous behaviors at low temperatures, supported by first-principles calculations. By developing a customized dry-transfer setup and optimizing device fabrication techniques, detailed resistivity, magnetoresistance (MR), and Hall measurements were conducted from bulk to few-layer devices to investigate the role of different inelastic scattering mechanisms at different temperature ranges, the nature of the

anomalous Hall effect and its correlation with the underlying magnetic properties. A new electronic transition is identified near 50 K, featuring positive MR and a change in the type of charge carriers. Also, the direct impact of the SRT on the charge conduction mechanism, including a change in majority carrier type, large anomalous Hall conductivity, and maximum negative MR near T_{SR}, indicates the strong coupling between magnetism and electronic transport in this system.

2. Chapter 5 focuses on the investigation of the nature of magnetic anisotropy (MA) and the origin of the SRT in Fe_4GeTe_2 using detailed high-frequency electron spin resonance (ESR) spectroscopy. This study offers a quantitative understanding of how the magnetic anisotropy of this system evolves with temperature in a non-trivial manner. The total MA is mostly dominated by demagnetization effects at high temperatures due to the plate-like shape of the crystal, accompanied by a slight contribution of the intrinsic MA (opposing in nature) of the easy axis type, which develops below a characteristic temperature $T_{\mathrm{shape}} \approx 150$ K, making the sample appear isotropic atT_{SR}. No in-plane anisotropy is observed from the measurements. Single-crystal XRD experiments confirmed no structural transition across the SRT, at least within the error bar. Interestingly, each and every characteristic temperature identified in the ESR experiment corresponds to those seen in transport measurements, confirming intrinsic coupling between magnetic and electronic degrees of freedom in Fe_4GeTe_2.

3. Chapter 6 investigates the spin-phonon interactions in exfoliated Fe_4GeTe_2 nanoflakes down to 9 layers via polarization- and temperature-dependent Raman spectroscopy, supported by first-principles calculations. Polarization-dependent Raman measurements reveal Raman active modes, while temperature-dependent studies indicate strong spin-phonon coupling below T_{SR}, manifested through temperature-dependent phonon softening and linewidth broadening, for thicker flakes. The interaction between pronounced spin-phonon coupling and intrinsic anharmonicity becomes evident near T_{SR}.

4. Chapter 7 explores the simultaneous observation of superconductivity and magnetism in a quasi-1D non-centrosymmetric single crystal $(TaSe_4)_3I$ (nTSI). Through detailed electronic, magneto-transport, and magnetization measurements under varying temperatures and magnetic fields, the nature of superconductivity, anisotropy, and the characteristics of low-dimensional superconductors are investigated. The investigations result in superconductivity below 2.5 K and weak ferromagnetism below 9 K, anisotropy in both superconductivity and magnetism,

multiple voltage steps and hysteresis in I–V characteristics – indicative of quantum phase slip events – typical of quasi-1D superconductors. The simultaneous presence of magnetism and superconductivity, coupled with reduced dimensionality and structural disorder, positions nTSI as a promising platform to investigate emergent quantum phases in low-dimensional systems.

8.2 Future Scope of Study

In this thesis, custom-designed experimental setups were developed, device fabrication strategies were established, and detailed electrical, magneto-transport, and spectroscopic studies were carried out on several Fe_4GeTe_2 devices and nTSI samples of varying thicknesses. While significant progress has been achieved, several key aspects remain unexplored and present a promising avenue to further advance our understanding of the physical properties of both Fe_4GeTe_2 and nTSI, particularly in reduced dimensions, and their potential applications in quantum devices. This section outlines possible directions to extend and deepen the current findings.

1. Fe_4GeTe_2 has shown significant promise as a 2D ferromagnetic material for spintronic applications, thanks to its unique magnetic properties and anomalous Hall behavior. However, its air sensitivity presents a challenge for device fabrication at ultra-thin scales. To overcome this, future work should focus on exfoliating and encapsulating Fe_4GeTe_2 thinner flakes entirely within a controlled inert environment (e.g., argon-filled glovebox). Glovebox-based fabrication techniques, combined with van der Waals heterostructure assembly using h-BN as capping layers, would help preserve the intrinsic properties of ultra-thin layer Fe_4GeTe_2 and provide reliable measurements of magnetic and transport properties in the ultra-lower-thickness limit.

2. The spin reorientation transition observed in thicker Fe_4GeTe_2 flakes is known to be strongly influenced by dimensionality. A systematic thickness-dependent study of SRT should be undertaken, especially in the monolayer to few-layer regime, to understand how magnetic anisotropy evolves in the 2D limit and shifts the SRT temperature. Anomalous Hall effect (AHE) measurements in ultra-thin flakes may reveal enhanced intrinsic Berry curvature effects.

3. Controlling magnetic properties via external electric fields is essential for the development of energy-efficient spintronic technologies. Future experiments should

aim at modulating the SRT in thin Fe_4GeTe_2 devices using electrostatic gating or ionic liquid gating towards room temperature. Gate-tunable transport, AHE, and magnetoresistance measurements can offer insights into the coupling between charge carriers and magnetic order, as well as into the possibility of switching magnetic anisotropy.

4. Magnetization dynamics and domain switching processes in low-dimensional ferromagnets can be probed effectively using low-frequency noise spectroscopy. Conducting magnetic field-dependent noise measurements in thin-layered Fe_4GeTe_2 devices, particularly near the SRT, may reveal valuable information about magnetic fluctuations, domain wall motion, and potential critical phenomena. Such noise studies can serve as sensitive probes of disorder and magnetic inhomogeneity, especially important in ultrathin devices where disorder can play a dominant role.

5. Spin transport studies, such as nonlocal spin valve or Hanle precession measurements, can help uncover the spin diffusion length and spin relaxation mechanisms in Fe_4GeTe_2-graphene based vdW heterostructures. Fabrication of Fe_4GeTe_2-based hybrid vdW heterostructures, integrating them with semiconducting or superconducting 2D materials (e.g., MoS_2, $NbSe_2$, graphene, etc.) may enable proximity-induced effects such as spin injection, exchange bias, or chiral edge modes, paving the way for novel device concepts.

6. One of the most promising future directions involves the exploration of spin–charge interaction dynamics in Fe_4GeTe_2 through electrically detected electron spin resonance (ED-ESR) experiments. This technique enables the direct observation of the interaction between localized spins and conduction electrons by measuring the change in electrical conductance induced by microwave-driven spin excitations. The objective of this experiment is to demonstrate the mutual dependence between spin wave behavior and charge transport, providing deeper insights into the underlying mechanisms of spin–charge coupling. Successful implementation of ED-ESR will not only enhance our understanding of spin dynamics in Fe_4GeTe_2 but may also open the pathway to studying the magnetic properties of other van der Waals ferromagnets, as a function of thickness, potentially even down to the monolayer limit, owing to the high sensitivity of the technique.

7. During preliminary attempts at mechanical exfoliation of nTSI onto Si/SiO_2 substrates, we observed the presence of sheet-like flakes with yellowish contrast and ultra-thin flakes with bluish contrast under an optical microscope. Subsequent FESEM imaging revealed numerous narrow, thin, ribbon-like structures with

varying thicknesses, lengths, and widths. These findings are promising and suggest the feasibility of isolating exfoliated quasi-1D flakes suitable for device fabrication. Future studies can focus on exploring the thickness-dependent electronic, magnetic, and superconducting properties of these exfoliated nTSI flakes. Additionally, assembling heterostructures with other two-dimensional materials, as well as fabricating Josephson junction-like devices, can provide further insights into proximity effects, interfacial coupling, and quantum phase coherence phenomena in these low-dimensional systems.

Bibliography

[1] Theis, T. N. & Wong, H.-S. P. The end of moore's law: A new beginning for information technology. *Computing in Science Engineering* **19**, 41–50 (2017).

[2] Gijs, M., Ionescu, M. A., Seabaugh, A., Fiori, G. & Luisier, M. At the end of scaling : 2D materials for computing and sensing applications (2020).

[3] Žutić, I., Fabian, J. & Das Sarma, S. Spintronics: Fundamentals and applications. *Rev. Mod. Phys.* **76**, 323–410 (2004). URL `https://link.aps.org/doi/10.1103/RevModPhys.76.323`.

[4] Mermin, N. D. & Wagner, H. Absence of ferromagnetism or antiferromagnetism in one- or two-dimensional isotropic heisenberg models. *Phys. Rev. Lett.* **17**, 1133–1136 (1966). URL `https://link.aps.org/doi/10.1103/PhysRevLett.17.1133`.

[5] Hohenberg, P. C. Existence of long-range order in one and two dimensions. *Phys. Rev.* **158**, 383–386 (1967). URL `https://link.aps.org/doi/10.1103/PhysRev.158.383`.

[6] Lau, C. N., Markovic, N., Bockrath, M., Bezryadin, A. & Tinkham, M. Quantum phase slips in superconducting nanowires. *Phys. Rev. Lett.* **87**, 217003 (2001). URL `https://link.aps.org/doi/10.1103/PhysRevLett.87.217003`.

[7] Mooij, J. E. & Nazarov, Y. V. Superconducting nanowires as quantum phase-slip junctions. *Nature Physics* **2**, 169–172 (2006). URL `https://doi.org/10.1038/nphys234`.

[8] Gong, C. *et al.* Discovery of intrinsic ferromagnetism in two-dimensional van der waals crystals. *Nature* **546**, 265–269 (2017). URL `https://doi.org/10.1038/nature22060`.

[9] Huang, B. *et al.* Electrical control of 2D magnetism in bilayer CrI3. *Nature Nanotechnology* **13**, 544–548 (2018).

[10] Zhang, W., Wong, P. K. J., Zhu, R. & Wee, A. T. Van der Waals magnets: Wonder building blocks for two-dimensional spintronics? *InfoMat* **1**, 479–495 (2019).

[11] Astafiev, O. V. *et al.* Coherent quantum phase slip. *Nature* **484**, 355–358 (2012). URL `https://doi.org/10.1038/nature10930`.

[12] Pop, I. M. *et al.* Measurement of the effect of quantum phase slips in a josephson junction chain. *Nature Physics* **6**, 589–592 (2010). URL `https://doi.org/10.1038/nphys1697`.

[13] Seo, J. *et al.* Nearly room temperature ferromagnetism in a magnetic metal-rich van der Waals metal. *Sci. Adv.* **6**, 1–10 (2020).

[14] Mondal, S., Khan, N., Mishra, S. M., Satpati, B. & Mandal, P. Critical behavior in the van der Waals itinerant ferromagnet Fe4GeTe2. *Physical Review B* **104**, 094405 (2021). URL `https://journals.aps.org/prb/abstract/10.1103/PhysRevB.104.094405`.

[15] Pal, R. *et al.* Disentangling the Unusual Magnetic Anisotropy of the Near-Room-Temperature Ferromagnet Fe_4GeTe_2. *Advanced Functional Materials* **34**, 2402551 (2024). URL `https://onlinelibrary.wiley.com/doi/abs/10.1002/adfm.202402551`.

[16] Bera, A. *et al.* Centrosymmetric-noncentrosymmetric structural phase transition in the quasi-one-dimensional compound $(TaSe_4)_3I$. *Phys. Rev. B* **108**, 035112 (2023). URL `https://link.aps.org/doi/10.1103/PhysRevB.108.035112`.

[17] Novoselov, K. S. *et al.* Electric field effect in atomically thin carbon films. *Science* **306**, 666–669 (2004). URL `https://www.science.org/doi/abs/10.1126/science.1102896`.

[18] Novoselov, K. S., Mishchenko, A., Carvalho, A. & Neto, A. H. C. 2d materials and van der waals heterostructures. *Science* **353**, aac9439 (2016). URL `https://www.science.org/doi/abs/10.1126/science.aac9439`.

[19] Song, T. *et al.* Giant tunneling magnetoresistance in spin-filter van der Waals heterostructures. *Science* **360**, 1214–1218 (2018).

[20] Jiang, S., Li, L., Wang, Z., Shan, J. & Mak, K. F. Spin tunnel field-effect transistors based on two-dimensional van der Waals heterostructures. *Nature Electronics* **2**, 159–163 (2019). URL `http://dx.doi.org/10.1038/s41928-019-0232-3`.

[21] Heisenberg, W. Zur Theorie des Ferromagnetismus. *Zeitschrift fur Physik* **49**, 619–636 (1928).

[22] Samarth, N. Magnetism in flatland. *Nature* **546**, 216–217 (2017).

[23] Wang, H. *Interfacial Engineering of the Magnetism in 2D Magnets, Topological Insulators, and Their Heterostructures.* Ph.D. thesis, Université de Lorraine; Beihang university (Pékin) (2023).

[24] Chen, B. *et al.* Magnetic properties of layered itinerant electron ferromagnet fe3gete2. *Journal of the Physical Society of Japan* **82**, 124711 (2013). URL https://doi.org/10.7566/JPSJ.82.124711. https://doi.org/10.7566/JPSJ.82.124711.

[25] Fei, Z. *et al.* Two-dimensional itinerant ferromagnetism in atomically thin fe3gete2. *Nature Materials* **17**, 778–782 (2018). URL https://doi.org/10.1038/s41563-018-0149-7.

[26] Li, B. *et al.* Van der waals epitaxial growth of air-stable crse2 nanosheets with thickness-tunable magnetic order. *Nature materials* **20**, 818–825 (2021).

[27] Huang, B. *et al.* Layer-dependent ferromagnetism in a van der Waals crystal down to the monolayer limit. *Nature* **546**, 270–273 (2017).

[28] Zhang, Z. *et al.* Direct Photoluminescence Probing of Ferromagnetism in Monolayer Two-Dimensional CrBr 3. *Nano Letters* **19**, 3138–3142 (2019). URL https://pubs.acs.org/doi/10.1021/acs.nanolett.9b00553.

[29] Cai, X. *et al.* Atomically Thin $CrCl_3$: An In-Plane Layered Antiferromagnetic Insulator. *Nano Letters* **19**, 3993–3998 (2019). URL https://doi.org/10.1021/acs.nanolett.9b01317.

[30] Lee, J.-U. *et al.* Ising-type magnetic ordering in atomically thin feps3. *Nano Letters* **16**, 7433–7438 (2016). URL https://doi.org/10.1021/acs.nanolett.6b03052. PMID: 27960508, https://doi.org/10.1021/acs.nanolett.6b03052.

[31] Gibertini, M., Koperski, M., Morpurgo, A. F. & Novoselov, K. S. Magnetic 2d materials and heterostructures. *Nature Nanotechnology* **14**, 408–419 (2019). URL https://doi.org/10.1038/s41565-019-0438-6.

[32] Lyu, B. *et al.* Probing the ferromagnetism and spin wave gap in vi3 by helicity-resolved raman spectroscopy. *Nano Letters* **20**, 6024–6031 (2020). URL https://

doi.org/10.1021/acs.nanolett.0c02029. PMID: 32628483, https://doi.org/10.1021/acs.nanolett.0c02029.

[33] Deng, Y. *et al.* Gate-tunable room-temperature ferromagnetism in two-dimensional Fe_3GeTe_2. *Nature* **563**, 94–99 (2018). URL https://doi.org/10.1038/s41586-018-0626-9.

[34] Tan, C. *et al.* Hard magnetic properties in nanoflake van der Waals Fe_3GeTe_2. *Nature Communications* **9**, 1554 (2018). URL https://doi.org/10.1038/s41467-018-04018-w.

[35] Yi, J. *et al.* Competing antiferromagnetism in a quasi-2D itinerant ferromagnet Fe3GeTe2. *2D Mater.* **4**, 011005 (2017).

[36] Pal, R. *et al.* Spin-reorientation driven emergent phases and unconventional magnetotransport in quasi-2D vdW ferromagnet Fe_4GeTe_2. *npj 2D Materials and Applications* **8**, 30 (2024). URL https://doi.org/10.1038/s41699-024-00463-y.

[37] May, A. F., Bridges, C. A. & McGuire, M. A. Physical properties and thermal stability of Fe5-xGeTe2 single crystals. *Phys. Rev. Mater.* **3**, 104401 (2019).

[38] May, A. F. *et al.* Ferromagnetism near room temperature in the cleavable van der waals crystal fe5gete2. *ACS Nano* **13**, 4436–4442 (2019). URL https://doi.org/10.1021/acsnano.8b09660.

[39] Zhang, H. *et al.* Itinerant ferromagnetism in van der waals $fe_{5-x}gete_2$ crystals above room temperature. *Phys. Rev. B* **102**, 064417 (2020). URL https://link.aps.org/doi/10.1103/PhysRevB.102.064417.

[40] Zhang, X. *et al.* Room-temperature intrinsic ferromagnetism in epitaxial crte2 ultrathin films. *Nature communications* **12**, 2492 (2021).

[41] Bonilla, M. *et al.* Strong roomerature ferromagnetism in VSe2 monolayers on van der Waals substrates. *Nature Nanotechnology* **13**, 289–293 (2018). URL http://dx.doi.org/10.1038/s41565-018-0063-9.

[42] Cui, F. *et al.* Controlled growth and thickness-dependent conduction-type transition of 2d ferrimagnetic cr2s3 semiconductors. *Advanced Materials* **32**, 1905896 (2020).

[43] Zhang, Y. *et al.* Ultrathin magnetic 2d single-crystal crse. *Advanced Materials* **31**, 1900056 (2019).

[44] Alfonsov, A. *et al.* Magnetic-field tuning of the spin dynamics in the magnetic topological insulators $(MnBi_2Te_4)(Bi_2Te_3)_n$. *Phys. Rev. B* **104**, 195139 (2021). URL `https://link.aps.org/doi/10.1103/PhysRevB.104.195139`.

[45] Kang, S. *et al.* Coherent many-body exciton in van der waals antiferromagnet nips3. *Nature* **583**, 785–789 (2020).

[46] Cao, H. B. *et al.* Low-temperature crystal and magnetic structure of $\alpha - rucl_3$. *Phys. Rev. B* **93**, 134423 (2016). URL `https://link.aps.org/doi/10.1103/PhysRevB.93.134423`.

[47] Yosida, K. Two-Dimensional XY Model — Kosterlitz-Thouless Transition 145–151 (1996).

[48] Kittel, C. & McEuen, P. *Introduction to Solid State Physics* (John Wiley & Sons Limited, 2018).

[49] Wang, Z. *et al.* Very large tunneling magnetoresistance in layered magnetic semiconductor CrI3. *Nature Communications* **9** (2018).

[50] Williams, T. J. *et al.* Magnetic correlations in the quasi-two-dimensional semiconducting ferromagnet CrSiTe3. *Physical Review B* **92**, 144404 (2015). URL `https://journals.aps.org/prb/abstract/10.1103/PhysRevB.92.144404https://link.aps.org/doi/10.1103/PhysRevB.92.144404`.

[51] Fei, Z. *et al.* Two-dimensional itinerant ferromagnetism in atomically thin Fe3GeTe2. *Nat. Mater.* **17**, 778–782 (2018).

[52] Tan, C. *et al.* Gate-Controlled Magnetic Phase Transition in a van der Waals Magnet Fe5GeTe2. *Nano Lett.* **21**, 5599–5605 (2021).

[53] Alahmed, L. *et al.* Magnetism and spin dynamics in room-temperature van der Waals magnet Fe5GeTe2. *2D Materials* **8**, 045030 (2021). URL `https://dx.doi.org/10.1088/2053-1583/ac2028`.

[54] Deng, Y. *et al.* Layer-Number-Dependent Magnetism and Anomalous Hall Effect in van der Waals Ferromagnet Fe5GeTe2. *Nano Lett.* **22**, 9839–9846 (2022).

[55] Bera, S. *et al.* Enhanced coercivity and emergence of spin cluster glass state in 2D ferromagnetic material Fe_3GeTe_2. *Journal of Magnetism and Magnetic Materials* **583**, 171052 (2022). URL `http://arxiv.org/abs/2212.14221`.

[56] Zhang, H. *et al.* Itinerant ferromagnetism in van der Waals Fe5-xGeTe2 crystals above room temperature. *Phys. Rev. B* **102**, 064417 (2020).

[57] Liu, P. *et al.* Magnetic and magneto-transport studies in van der Waals Fe5-xGeTe2 flakes. *Appl. Phys. Lett.* **121** (2022).

[58] Sau, J., Hassan, S. R., Kumar, N. & Kumar, M. Anomalous transport in itinerant van der Waals ferromagnets FenGeTe2 (n=3, 4, 5). *Preprint at http://arxiv.org/abs/2207.03547* 1–9 (2022).

[59] Ghosh, S., Ershadrad, S., Borisov, V. & Sanyal, B. Unraveling effects of electron correlation in two-dimensional Fe_nGeTe_2 (n=3, 4, 5) by dynamical mean field theory. *Preprint at http://arxiv.org/abs/2212.08552* **2** (2022).

[60] Kim, K. *et al.* Large anomalous Hall current induced by topological nodal lines in a ferromagnetic van der Waals semimetal. *Nat. Mater.* **17**, 794–799 (2018).

[61] Wang, Y. *et al.* Anisotropic anomalous Hall effect in triangular itinerant ferromagnet Fe3GeTe2. *Phys. Rev. B* **96**, 1–6 (2017).

[62] Ke, J. *et al.* Magnetic and magneto-transport studies of two-dimensional ferromagnetic compound Fe3GeTe2. *J. Phys. Condens. Matter* **32**, 405805 (2020).

[63] Jones, D. C. *et al.* Origin of spin reorientation and intrinsic anomalous Hall effect in the kagome ferrimagnet TbMn6Sn6. *arXiv* (2022).

[64] Liu, B. *et al.* Light-Tunable Ferromagnetism in Atomically Thin Fe3GeTe2 Driven by Femtosecond Laser Pulse. *Physical Review Letters* **125**, 267205 (2020). URL `https://doi.org/10.1103/PhysRevLett.125.267205`.

[65] Wang, H. *et al.* Above Room-Temperature Ferromagnetism in Wafer-Scale Two-Dimensional van der Waals Fe3GeTe2 Tailored by a Topological Insulator. *ACS Nano* **14**, 10045–10053 (2020). URL `https://pubs.acs.org/doi/full/10.1021/acsnano.0c03152https://pubs.acs.org/doi/10.1021/acsnano.0c03152`.

[66] Bander, M. & Mills, D. L. Ferromagnetism of ultrathin films. *Phys. Rev. B* **38**, 12015–12018 (1988).

[67] Hook, J. & Hall, H. *Solid State Physics* (John Wiley Sons, Ltd. Chichester, 1991).

[68] Fujita, R. *et al.* Layer-Dependent Magnetic Domains in Atomically Thin Fe5GeTe2. *ACS Nano* **16**, 10545–10553 (2022).

[69] Stahl, J., Shlaen, E. & Johrendt, D. The van der Waals Ferromagnets $Fe_{5-\delta}GeTe_2$ and $Fe_{5-\delta}Ni_xGeTe_2$ – Crystal Structure, Stacking Faults, and Magnetic Properties. *Zeitschrift fur Anorganische und Allgemeine Chemie* **644**, 1923–1929 (2018). URL `https://onlinelibrary.wiley.com/doi/10.1002/zaac.201800456`.

[70] Ershadrad, S., Ghosh, S., Wang, D., Kvashnin, Y. & Sanyal, B. Unusual Magnetic Features in Two-Dimensional Fe5GeTe2 Induced by Structural Reconstructions. *J. Phys. Chem. Lett.* **13**, 4877–4883 (2022).

[71] Wang, Q., Sun, S., Zhang, X., Pang, F. & Lei, H. Anomalous Hall effect in a ferromagnetic Fe3Sn2 single crystal with a geometrically frustrated Fe bilayer kagome lattice. *Phys. Rev. B* **94**, 1–5 (2016).

[72] Kumar, N., Soh, Y., Wang, Y. & Xiong, Y. Magnetotransport as a diagnostic of spin reorientation: Kagome ferromagnet as a case study. *Phys. Rev. B* **100**, 1–7 (2019).

[73] Biswas, A. *et al.* Spin-Reorientation-Induced Band Gap in Fe3Sn2: Optical Signatures of Weyl Nodes. *Phys. Rev. Lett.* **125**, 076403 (2020).

[74] Fenner, L. A., Dee, A. A. & Wills, A. S. Non-collinearity and spin frustration in the itinerant kagome ferromagnet Fe3Sn2. *J. Phys. Condens. Matter* **21**, 452202 (2009).

[75] Zajkov, N. K., Mushnikov, N. V., Bartashevich, M. I. & Goto, T. Magnetization processes in the TbMn6Sn6 compound. *J. Alloys Compd.* **309**, 26–30 (2000).

[76] Malaman, B. *et al.* Magnetic properties of RMn6Sn6 (R = Gd-Er) compounds from neutron diffraction and Mossbauer measurements. *J. Magn. Magn. Mater.* **202**, 519–534 (1999).

[77] Clatterbuck, D. M. & Gschneidner, K. A. Magnetic properties of RMn6Sn6 (R = Tb, Ho, Er, Tm, Lu) single crystals. *J. Magn. Magn. Mater.* **207**, 78–94 (1999).

[78] Mondal, S. & Mandal, P. Anomalous magnetic properties of quasi two-dimensional van der Waals ferromagnet Fe4GeTe2. *Preprint at http://arxiv.org/abs/2207.09885* 1–8 (2022).

[79] Wang, X. & Tan, J. Intrinsic anomalous Hall effect and Lifshitz transition in a ferromagnetic kagome-lattice metal. *Appl. Phys. Lett.* **121** (2022).

[80] Wang, H. *et al.* Interfacial engineering of ferromagnetism in wafer-scale van der Waals Fe_4GeTe_2 far above room temperature. *Nature Communications* **14**, 2483 (2023). URL `https://doi.org/10.1038/s41467-023-37917-8`.

[81] Bera, A. *et al.* Centrosymmetric-noncentrosymmetric structural phase transition in the quasi-one-dimensional compound $(tase_4)_3I$. *Phys. Rev. B* **108**, 035112 (2023). URL https://link.aps.org/doi/10.1103/PhysRevB.108.035112.

[82] Kadin, A. M. Spatial structure of the cooper pair. *Journal of Superconductivity and Novel Magnetism* **20**, 285–292 (2007).

[83] Fletcher, G. BCS Theory and Superconductivity. *Am. J. Phys* **58**, 1–5 (1972).

[84] Mooij, J. E. & Harmans, C. J. Phase-slip flux qubits. *New Journal of Physics* **7** (2005).

[85] Golubev, D. S. & Zaikin, A. D. Thermally activated phase slips in superconducting nanowires. *Physical Review B* **78**, 144502 (2008). URL https://link.aps.org/doi/10.1103/PhysRevB.78.144502.

[86] Golubev, D. S. & Zaikin, A. D. Quantum tunneling of the order parameter in superconducting nanowires. *Phys. Rev. B* **64**, 014504 (2001). URL https://link.aps.org/doi/10.1103/PhysRevB.64.014504.

[87] Gressier, P., Meerschaut, A., Guemas, L., Rouxel, J. & Monceau, P. Characterization of the new series of quasi one-dimensional compounds(mx4)ny (m =nb, ta; x =s, se; y =br, i). *Journal of Solid State Chemistry* **51**, 141–151 (1984). URL https://www.sciencedirect.com/science/article/pii/002245968490327X.

[88] Roucau, C., Ayroles, R., Gressier, P. & Meerschaut, A. Electron microscopy study of transition-metal tetrachalcogenide (mse4)ni (m=nb, ta). *Journal of Physics C: Solid State Physics* **17**, 2993 (1984). URL https://dx.doi.org/10.1088/0022-3719/17/17/007.

[89] Gressier, P., Whangbo, M. H., Meerschaut, A. & Rouxel, J. Electronic structures of transition-metal tetrachalcogenides (mse4)ni (m = nb, ta). *Inorg. Chem.* **23**, 1221–1228 (1984). URL https://doi.org/10.1021/ic00177a011.

[90] Sekine, T. & Izumi, M. Successive phase transitions in the linear-chain semiconductor $(nbse_4)_3I$ studied by raman scattering and electrical resistivity. *Phys. Rev. B* **38**, 2012–2020 (1988). URL https://link.aps.org/doi/10.1103/PhysRevB.38.2012.

[91] Shi, W. *et al.* A charge-density-wave topological semimetal. *Nature Physics* **17**, 381–387 (2021). URL https://doi.org/10.1038/s41567-020-01104-z.

[92] An, C. *et al.* Long-range ordered amorphous atomic chains as building blocks of a superconducting quasi-one-dimensional crystal. *Advanced Materials* **32**, 2002352 (2020). URL https://onlinelibrary.wiley.com/doi/abs/10.1002/adma.202002352.

[93] Zhang, Y., Lin, L.-F., Moreo, A., Dong, S. & Dagotto, E. First-principles study of the low-temperature charge density wave phase in the quasi-one-dimensional weyl chiral compound $(tase_4)_2I$. *Phys. Rev. B* **101**, 174106 (2020). URL https://link.aps.org/doi/10.1103/PhysRevB.101.174106.

[94] Gooth, J. *et al.* Axionic charge-density wave in the weyl semimetal (tase4)2i. *Nature* **575**, 315–319 (2019). URL https://doi.org/10.1038/s41586-019-1630-4.

[95] Tournier-Colletta, C. *et al.* Electronic instability in a zero-gap semiconductor: The charge-density wave in $(tase_4)_2\mathbf{I}$. *Phys. Rev. Lett.* **110**, 236401 (2013). URL https://link.aps.org/doi/10.1103/PhysRevLett.110.236401.

[96] Philipp, A. *et al.* Dynamics of the charge-density-wave mode in $(nbse_4)_2i$. *Phys. Rev. B* **39**, 7536–7544 (1989). URL https://link.aps.org/doi/10.1103/PhysRevB.39.7536.

[97] Philipp, A., Mayr, W., Kim, T. & Grüner, G. Dynamical charge density wave response in (nbse4)2i. *Solid State Communications* **62**, 521–524 (1987). URL https://www.sciencedirect.com/science/article/pii/0038109887910775.

[98] Vescoli, V. *et al.* Dynamical properties of the one-dimensional band insulator $(nbse_4)_3i$. *Phys. Rev. Lett.* **84**, 1272–1275 (2000). URL https://link.aps.org/doi/10.1103/PhysRevLett.84.1272.

[99] J.A. Wilson, F. D. S. & Mahajan, S. Charge-density waves and superlattices in the metallic layered transition metal dichalcogenides. *Advances in Physics* **24**, 117–201 (1975). https://doi.org/10.1080/00018737500101391.

[100] Majumdar, A. *et al.* Interplay of charge density wave and multiband superconductivity in layered quasi-two-dimensional materials: The case of $2H-Nbs_2$ and $2H-Nbse_2$. *Phys. Rev. Mater.* **4**, 084005 (2020). URL https://link.aps.org/doi/10.1103/PhysRevMaterials.4.084005.

[101] Giordano, N. Evidence for macroscopic quantum tunneling in one-dimensional superconductors. *Phys. Rev. Lett.* **61**, 2137–2140 (1988). URL https://link.aps.org/doi/10.1103/PhysRevLett.61.2137.

[102] Büchler, H. P., Geshkenbein, V. B. & Blatter, G. Quantum fluctuations in thin superconducting wires of finite length. *Phys. Rev. Lett.* **92**, 067007 (2004). URL https://link.aps.org/doi/10.1103/PhysRevLett.92.067007.

[103] eds Goldman, A. & Wolf, S. Percolation, localization, and superconductivity. *NATO Science Series, Plenum Press, New York* (1984).

[104] Lederer, S., Schattner, Y., Berg, E. & Kivelson, S. A. Superconductivity and non-fermi liquid behavior near a nematic quantum critical point. *Proceedings of the National Academy of Sciences* **114**, 4905–4910 (2017). URL https://www.pnas.org/doi/abs/10.1073/pnas.1620651114. https://www.pnas.org/doi/pdf/10.1073/pnas.1620651114.

[105] Mandal, I. Superconducting instability in non-fermi liquids. *Phys. Rev. B* **94**, 115138 (2016). URL https://link.aps.org/doi/10.1103/PhysRevB.94.115138.

[106] Mu, Q.-G. *et al.* Suppression of axionic charge density wave and onset of superconductivity in the chiral weyl semimetal Ta_2Se_8I. *Phys. Rev. Mater.* **5**, 084201 (2021). URL https://link.aps.org/doi/10.1103/PhysRevMaterials.5.084201.

[107] Pei, C. *et al.* Pressure-induced a partial disorder and superconductivity in quasi-one-dimensional weyl semimetal (nbse4)2i. *Materials Today Physics* **21**, 100509 (2021). URL https://www.sciencedirect.com/science/article/pii/S254252932100170X.

[108] Petrović, A. P. *et al.* A disorder-enhanced quasi-one-dimensional superconductor. *Nature Communications* **7**, 12262 (2016). URL https://doi.org/10.1038/ncomms12262.

[109] Tüttö, I. & Zawadowski, A. Theory of pinning of a spin-density wave by nonmagnetic impurities. *Phys. Rev. Lett.* **60**, 1442–1445 (1988). URL https://link.aps.org/doi/10.1103/PhysRevLett.60.1442.

[110] Mattis, D. C. *The theory of magnetism I: Statics and Dynamics*, vol. 17 (Springer, 2012).

[111] Ashcroft, N. & Mermin, N. *Solid State Physics*. HRW international editions (Holt, Rinehart and Winston, 1976). URL https://books.google.co.in/books?id=1C9HAQAAIAAJ.

[112] Jiles, D. *Introduction to Magnetism and Magnetic Materials, Second Edition* (Taylor & Francis, 1998). URL https://books.google.co.in/books?id=axyWXjsdorMC.

[113] Tombe, F. D. Lenz's law (2009).

[114] Heisenberg, W. Multibody problem and resonance in quantum mechanics. *Journal for Physics* **38**, 411–426 (1926).

[115] Heisenberg, W. Zur theorie des ferromagnetismus. *Zeitschrift für Physik* **49**, 619–636 (1928). URL `https://doi.org/10.1007/BF01328601`.

[116] Weiss, P. L'hypothèse du champ moléculaire et la propriété ferromagnétique. *J. Phys. Theor. Appl.* **6**, 661–690 (1907).

[117] Coey, J. *Magnetism and Magnetic Materials* (Cambridge University Press, 2010).

[118] Palagummi, S. & Yuan, F.-G. Magnetic levitation and its application for low frequency vibration energy harvesting. In *Structural Health Monitoring (SHM) in Aerospace Structures*, 213–251 (Elsevier, 2016).

[119] Blundell, S. *Magnetism in Condensed Matter* (Oxford University Press, 2001).

[120] Aharoni, A. *Introduction to the Theory of Ferromagnetism*, vol. 109 (Oxford University Press, 2000).

[121] Roy, S. *Experimental Techniques in Magnetism and Magnetic Materials* (Cambridge University Press, 2022). URL `https://books.google.co.in/books?id=JHoozwEACAAJ`.

[122] Kasuya, T. Electrical resistance of ferromagnetic metals. *Progress of Theoretical Physics* **16**, 58–63 (1956).

[123] Ruderman, M. A. & Kittel, C. Indirect exchange coupling of nuclear magnetic moments by conduction electrons. *Physical Review* **96**, 99 (1954).

[124] Anderson, P. W. Antiferromagnetism. theory of superexchange interaction. *Physical Review* **79**, 350 (1950).

[125] Dzyaloshinsky, I. A thermodynamic theory of "weak" ferromagnetism of antiferromagnetics. *Journal of physics and chemistry of solids* **4**, 241–255 (1958).

[126] Moriya, T. Anisotropic superexchange interaction and weak ferromagnetism. *Physical review* **120**, 91 (1960).

[127] Nembach, H. T., Shaw, J. M., Weiler, M., Jué, E. & Silva, T. J. Linear relation between heisenberg exchange and interfacial dzyaloshinskii–moriya interaction in metal films. *Nature Physics* **11**, 825–829 (2015).

[128] Stoner, E. C. & Wohlfarth, E. P. A mechanism of magnetic hysteresis in heterogeneous alloys. *Philosophical Transactions of the Royal Society of London. Series A, Mathematical and Physical Sciences* **240**, 599–642 (1948).

[129] Coey, J. & Parkin, S. *Handbook of Magnetism and Magnetic Materials*. Handbook of Magnetism and Magnetic Materials (Springer International Publishing, 2021). URL `https://books.google.de/books?id=3SLezQEACAAJ`.

[130] Fert, A. & Campbell, I. Electrical resistivity of ferromagnetic nickel and iron based alloys. *Journal of Physics F: Metal Physics* **6**, 849 (1976).

[131] Volkenshtein, N., Dyakina, V. & Startsev, V. Scattering mechanisms of conduction electrons in transition metals at low temperatures. *physica status solidi (b)* **57**, 9–42 (1973).

[132] Landau, L. On the theory of the fermi liquid. *Sov. Phys. JETP* **8**, 70 (1959).

[133] Bloch, F. Zum elektrischen widerstandsgesetz bei tiefen temperaturen. *Zeitschrift für Physik* **59**, 208–214 (1930).

[134] Grüneisen, E. Die abhängigkeit des elektrischen widerstandes reiner metalle von der temperatur. *Annalen der Physik* **408**, 530–540 (1933).

[135] Kondo, J. Resistance minimum in dilute magnetic alloys. *Progress of theoretical physics* **32**, 37–49 (1964).

[136] Hall, E. H. On a new action of the magnet on electric currents. *American Journal of Mathematics* **2**, 287–292 (1879). URL `https://doi.org/10.2307/2369245`. Full publication date: Sep., 1879.

[137] Hall, E. Xviii. on the "rotational coefficient" in nickel and cobalt. *The London, Edinburgh, and Dublin Philosophical Magazine and Journal of Science* **12**, 157–172 (1881). URL `https://doi.org/10.1080/14786448108627086`. `https://doi.org/10.1080/14786448108627086`.

[138] Nagaosa, N., Sinova, J., Onoda, S., MacDonald, A. H. & Ong, N. P. Anomalous Hall effect. *Rev. Mod. Phys.* **82**, 1539–1592 (2010).

[139] Pugh, E. M. Hall effect and the magnetic properties of some ferromagnetic materials. *Phys. Rev.* **36**, 1503–1511 (1930).

[140] Pugh, E. M. & Lippert, T. W. Hall e.m.f. and Intensity of Magnetization. *Phys. Rev.* **42**, 709–713 (1932).

[141] Lee, M., Onose, Y., Tokura, Y. & Ong, N. P. Hidden constant in the anomalous Hall effect of high-purity magnet MnSi. *Phys. Rev. B* **75**, 172403 (2007).

[142] Karplus, R. & Luttinger, J. M. Hall effect in ferromagnetics. *Phys. Rev.* **95**, 1154–1160 (1954).

[143] Jungwirth, T., Niu, Q. & MacDonald, A. H. Anomalous Hall Effect in Ferromagnetic Semiconductors. *Phys. Rev. Lett.* **88**, 207208 (2002).

[144] Onoda, M. & Nagaosa, N. Topological Nature of Anomalous Hall Effect in Ferromagnets. *J. Phys. Soc. Jpn.* **71**, 19–22 (2002).

[145] Berger, L. Side-jump mechanism for the hall effect of ferromagnets. *Phys. Rev. B* **2**, 4559–4566 (1970).

[146] Smit, J. The spontaneous hall effect in ferromagnetics I. *Physica* **XXI**, 877–887 (1955).

[147] Smit, J. The Spontenous Hall Effect in Ferromagnets II. *Physica (Amsterdam)* **24**, 39–51 (1958).

[148] Zavoisky, E. Spin-magnetic resonance in paramagnetics. *J Phys Ussr* **9**, 211–245 (1945).

[149] Dikanov, S. A. & Crofts, A. R. Electron paramagnetic resonance spectroscopy. In *Handbook of Applied Solid State Spectroscopy*, 97–149 (Springer, 2006).

[150] Turov, E. A. *Physical Properties of Magnetically Ordered Crystals* (Academic Press, New York, 1965).

[151] Abragam, A. & Bleaney, B. *Electron paramagnetic resonance of transition ions* (Oxford University Press, Oxford, 2012).

[152] Kataev, V., Büchner, B. & Alfonsov, A. Electron spin resonance spectroscopy on magnetic van der waals compounds. *Applied Magnetic Resonance* **55**, 923–960 (2024). URL `https://doi.org/10.1007/s00723-024-01671-x`.

[153] Zeeman, P. On the influence of magnetism on the nature of the light emitted by a substance. *Astrophysical Journal* **5**, 332–347 (1986). URL `https://articles.adsabs.harvard.edu/pdf/1897ApJ.....5..332Z`.

[154] Alfonsov, A. *High-field electron spin resonance study of electronic inhomogeneities in correlated transition metal compounds*. Ph.D. thesis, TU Dresden, Germany (2011).

[155] EM, L. L. L. Theory of the dispersion of magnetic permeability in ferromagnetic bodies phys. *Z. Sowjetunion* **8**, 0012–28501 (1935).

[156] Alfonsov, A. *et al.* Magnetic-field tuning of the spin dynamics in the magnetic topological insulators $(MnBi_2Te_4)(Bi_2Te_3)_n$. *Physical Review B* **104**, 195139 (2021).

[157] Farle, M. Ferromagnetic resonance of ultrathin metallic layers. *Reports on progress in physics* **61**, 755 (1998).

[158] Bardeen, J., Cooper, L. N. & Schrieffer, J. R. Theory of superconductivity. *Phys. Rev.* **108**, 1175–1204 (1957). URL https://link.aps.org/doi/10.1103/PhysRev.108.1175.

[159] Tinkham, M. *Introduction to Superconductivity.* Dover Books on Physics Series (Dover Publications, 2004). URL https://books.google.co.in/books?id=VpUk3NfwDIkC.

[160] Bussmann-Holder, A. & Keller, H. High-temperature superconductors: underlying physics and applications. *Zeitschrift für Naturforschung B* **75**, 3–14 (2020). URL https://doi.org/10.1515/znb-2019-0103.

[161] Landau, L. D. *Collected papers of LD Landau* (Pergamon, 1965).

[162] Abrikosov, A. A. On the magnetic properties of superconductors of the second group. *Soviet Physics-JETP* **5**, 1174–1182 (1957).

[163] Castro Neto, A. H., Guinea, F., Peres, N. M. R., Novoselov, K. S. & Geim, A. K. The electronic properties of graphene. *Rev. Mod. Phys.* **81**, 109–162 (2009). URL https://link.aps.org/doi/10.1103/RevModPhys.81.109.

[164] Novoselov, K. S. *et al.* A roadmap for graphene. *Nature* **490**, 192–200 (2012). URL https://doi.org/10.1038/nature11458.

[165] Geim, A. K. & Novoselov, K. S. The rise of graphene. *Nature Materials* **6**, 183–191 (2007). URL https://doi.org/10.1038/nmat1849.

[166] Huang, Y. *et al.* Universal mechanical exfoliation of large-area 2d crystals. *Nature Communications* **11**, 2453 (2020). URL https://doi.org/10.1038/s41467-020-16266-w.

[167] Lee, J. H. *et al.* van der waals force: A dominant factor for reactivity of graphene. *Nano Letters* **15**, 319–325 (2015). URL https://doi.org/10.1021/nl5036012. PMID: 25493357.

[168] Torres, J., Zhu, Y., Liu, P., Lim, S. C. & Yun, M. Adhesion energies of 2d graphene and mos2 to silicon and metal substrates. *physica status solidi (a)* **215**, 1700512 (2018). URL https://onlinelibrary.wiley.com/doi/abs/10.1002/pssa.201700512.

[169] Li, H. *et al.* Constructing van der waals heterostructures by dry-transfer assembly for novel optoelectronic device. *Nanotechnology* **33**, 465601 (2022). URL https://dx.doi.org/10.1088/1361-6528/ac5f96.

[170] Meitl, M. A. *et al.* Transfer printing by kinetic control of adhesion to an elastomeric stamp. *Nature Materials* **5**, 33–38 (2006). URL https://doi.org/10.1038/nmat1532.

[171] Castellanos-Gomez, A. *et al.* Deterministic transfer of two-dimensional materials by all-dry viscoelastic stamping. *2D Materials* **1**, 011002 (2014). URL https://dx.doi.org/10.1088/2053-1583/1/1/011002.

[172] Magda, G. Z. *et al.* Exfoliation of large-area transition metal chalcogenide single layers. *Scientific Reports* **5**, 14714 (2015). URL https://doi.org/10.1038/srep14714.

[173] Desai, S. B. *et al.* Gold-mediated exfoliation of ultralarge optoelectronically-perfect monolayers. *Advanced Materials* **28**, 4053–4058 (2016). URL https://onlinelibrary.wiley.com/doi/abs/10.1002/adma.201506171.

[174] Liu, F. *et al.* Disassembling 2D van der Waals crystals into macroscopic monolayers and reassembling into artificial lattices. *Science* **367**, 903–906 (2020). URL https://www.science.org/doi/abs/10.1126/science.aba1416.

[175] Huang, Y. *et al.* Reliable exfoliation of large-area high-quality flakes of graphene and other two-dimensional materials. *ACS Nano* **9**, 10612–10620 (2015). URL https://doi.org/10.1021/acsnano.5b04258. PMID: 26336975.

[176] Zhang, Y. *et al.* Facile exfoliation for high-quality molybdenum disulfide nanoflakes and relevant field-effect transistors developed with thermal treatment. *Frontiers in Chemistry* **9** (2021). URL https://www.frontiersin.org/journals/chemistry/articles/10.3389/fchem.2021.650901.

[177] Yi, M. & Shen, Z. A review on mechanical exfoliation for the scalable production of graphene. *J. Mater. Chem. A* **3**, 11700–11715 (2015). URL http://dx.doi.org/10.1039/C5TA00252D.

[178] Thompson, J. P., Doha, M. H., Murphy, P., Hu, J. & Churchill, H. O. Exfoliation and analysis of large-area, air-sensitive two-dimensional materials. *JoVE* e58693 (2019). URL https://app.jove.com/58693.

[179] Liu, F. Mechanical exfoliation of large area 2d materials from vdw crystals. *Progress in Surface Science* **96**, 100626 (2021). URL https://www.sciencedirect.com/science/article/pii/S0079681621000149.

[180] Jayasena, B. & Melkote, S. N. An investigation of pdms stamp assisted mechanical exfoliation of large area graphene. *Procedia Manufacturing* **1**, 840–853 (2015). URL https://www.sciencedirect.com/science/article/pii/S2351978915010732. 43rd North American Manufacturing Research Conference, NAMRC 43, 8-12 June 2015, UNC Charlotte, North Carolina, United States.

[181] Ma, X. *et al.* Capillary-force-assisted clean-stamp transfer of two-dimensional materials. *Nano Letters* **17**, 6961–6967 (2017). URL https://doi.org/10.1021/acs.nanolett.7b03449. PMID: 29058919.

[182] Jain, A. *et al.* Minimizing residues and strain in 2d materials transferred from pdms. *Nanotechnology* **29**, 265203 (2018). URL https://dx.doi.org/10.1088/1361-6528/aabd90.

[183] Kim, K. S. *et al.* Large-scale pattern growth of graphene films for stretchable transparent electrodes. *Nature* **457**, 706–710 (2009). URL https://doi.org/10.1038/nature07719.

[184] Kang, J. *et al.* Solvent exfoliation of electronic-grade, two-dimensional black phosphorus. *ACS Nano* **9**, 3596–3604 (2015). URL https://doi.org/10.1021/acsnano.5b01143. PMID: 25785299.

[185] Ramachandran, V. S. & Beaudoin, J. J. In *Handbook of Analytical Techniques in Concrete Science and Technology: Principles, Techniques and Applications* (2000). URL https://api.semanticscholar.org/CorpusID:106557839.

[186] Bragg, W. H. & Bragg, W. L. The reflection of x-rays by crystals. *Proceedings of the Royal Society of London. Series A, Containing Papers of a Mathematical and Physical Character* **88**, 428–438 (1913). URL https://royalsocietypublishing.org/doi/abs/10.1098/rspa.1913.0040.

[187] Madsen, I. C. & Hill, R. J. Effect of divergence and receiving slit dimensions on peak profile parameters in rietveld analysis of x-ray diffractometer data. *Journal of*

Applied Crystallography **21**, 398–405 (1988). URL https://onlinelibrary.wiley.com/doi/abs/10.1107/S0021889888003474.

[188] Förster, A., Brandstetter, S. & Schulze-Briese, C. Transforming x-ray detection with hybrid photon counting detectors. *Philosophical Transactions of the Royal Society A: Mathematical, Physical and Engineering Sciences* **377**, 20180241 (2019). URL https://royalsocietypublishing.org/doi/abs/10.1098/rsta.2018.0241.

[189] Talin, A., Dean, K. & Jaskie, J. Field emission displays: a critical review. *Solid State Electronics* **45**, 963–976 (2001).

[190] Ouyang, W. *et al.* Optical methods for determining thicknesses of few-layer graphene flakes. *Nanotechnology* **24**, 505701 (2013). URL https://dx.doi.org/10.1088/0957-4484/24/50/505701.

[191] Ni, Z. H. *et al.* Graphene thickness determination using reflection and contrast spectroscopy. *Nano Letters* **7**, 2758–2763 (2007). URL https://doi.org/10.1021/nl071254m. PMID: 17655269.

[192] Bayle, M. *et al.* Determining the number of layers in few-layer graphene by combining Raman spectroscopy and optical contrast. *Journal of Raman Spectroscopy* 36–45 (2018). URL https://hal.science/hal-01724311.

[193] Blake, P. *et al.* Making graphene visible. *Applied Physics Letters* **91**, 063124 (2007). URL https://doi.org/10.1063/1.2768624.

[194] Roddaro, S., Pingue, P., Piazza, V., Pellegrini, V. & Beltram, F. The optical visibility of graphene: Interference colors of ultrathin graphite on sio2. *Nano Letters* **7**, 2707–2710 (2007). URL https://doi.org/10.1021/nl0711581. PMID: 17665963.

[195] Abergel, D. S. L., Russell, A. & Fal'ko, V. I. Visibility of graphene flakes on a dielectric substrate. *Applied Physics Letters* **91**, 063125 (2007). URL https://doi.org/10.1063/1.2768625.

[196] Binnig, G., Quate, C. F. & Gerber, C. Atomic force microscope. *Phys. Rev. Lett.* **56**, 930–933 (1986). URL https://link.aps.org/doi/10.1103/PhysRevLett.56.930.

[197] Meyer, E. Atomic force microscopy. *Progress in Surface Science* **41**, 3–49 (1992). URL https://www.sciencedirect.com/science/article/pii/0079681692900097.

[198] Neuman, K. C. & Nagy, A. Single-molecule force spectroscopy: optical tweezers, magnetic tweezers and atomic force microscopy. *Nature Methods* **5**, 491–505 (2008). URL https://doi.org/10.1038/nmeth.1218.

[199] Hopster, H. & Oepen, H. P. *Magnetic microscopy of nanostructures* (Springer-Verlag, Berlin Heidelberg, 2005).

[200] Hutter, J. L. & Bechhoefer, J. Calibration of atomic-force microscope tips. *Review of Scientific Instruments* **64**, 1868–1873 (1993). URL https://doi.org/10.1063/1.1143970.

[201] Tello, M. & Garcıa, R. Nano-oxidation of silicon surfaces: Comparison of noncontact and contact atomic-force microscopy methods. *Applied Physics Letters* **79**, 424–426 (2001). URL https://doi.org/10.1063/1.1385582.

[202] Le Grimellec, C. *et al.* Imaging of the surface of living cells by low-force contact-mode atomic force microscopy. *Biophysical Journal* **75**, 695–703 (1998). URL https://www.sciencedirect.com/science/article/pii/S0006349598775599.

[203] Uchihashi, T. *et al.* Role of a covalent bonding interaction in noncontact-mode atomic-force microscopy on si(111)7×7. *Phys. Rev. B* **56**, 9834–9840 (1997). URL https://link.aps.org/doi/10.1103/PhysRevB.56.9834.

[204] Sugawara, Y., Ohta, M., Ueyama, H. & Morita, S. Defect motion on an inp(110) surface observed with noncontact atomic force microscopy. *Science* **270**, 1646–1648 (1995). URL https://www.science.org/doi/abs/10.1126/science.270.5242.1646.

[205] Cleveland, J. P., Anczykowski, B., Schmid, A. E. & Elings, V. B. Energy dissipation in tapping-mode atomic force microscopy. *Applied Physics Letters* **72**, 2613–2615 (1998). URL https://doi.org/10.1063/1.121434.

[206] Amos, N. *et al.* Magnetic force microscopy study of magnetic stripe domains in sputter deposited Permalloy thin films. *Journal of Applied Physics* **103**, 07E732 (2008). URL https://doi.org/10.1063/1.2835441.

[207] Schwarz, A. & Wiesendanger, R. Magnetic sensitive force microscopy. *Nano Today* **3**, 28–39 (2008). URL https://www.sciencedirect.com/science/article/pii/S1748013208700136.

[208] Grütter, P., Rugar, D. & Mamin, H. Magnetic force microscopy of magnetic materials. *Ultramicroscopy* **47**, 393–399 (1992). URL https://www.sciencedirect.com/science/article/pii/030439919290170O.

[209] Webb, H. K. *et al.* Roughness parameters for standard description of surface nanoarchitecture. *Scanning* **34**, 257–263 (2012). URL https://onlinelibrary.wiley.com/doi/abs/10.1002/sca.21002.

[210] Seo, J. *et al.* Nearly room temperature ferromagnetism in a magnetic metal-rich van der waals metal. *Science Advances* **6**, eaay8912 (2020). URL https://www.science.org/doi/abs/10.1126/sciadv.aay8912.

[211] Kim, D. *et al.* Antiferromagnetic coupling of van der waals ferromagnetic fe3gete2. *Nanotechnology* **30**, 245701 (2019). URL https://dx.doi.org/10.1088/1361-6528/ab0a37.

[212] Geim, A. K. & Grigorieva, I. V. Van der waals heterostructures. *Nature* **499**, 419–425 (2013). URL https://doi.org/10.1038/nature12385.

[213] Woessner, A. *et al.* Highly confined low-loss plasmons in graphene–boron nitride heterostructures. *Nature Materials* **14**, 421–425 (2015). URL https://doi.org/10.1038/nmat4169.

[214] Jaeger, R. *Introduction to Microelectronic Fabrication*. No. Bd. 5 in Introduction to Microelectronic Fabrication (Prentice Hall, 2002). URL https://books.google.de/books?id=yqi3QgAACAAJ.

[215] Ziaie, B., Baldi, A. & Atashbar, M. Z. *Introduction to Micro/Nanofabrication*, 147–184 (Springer Berlin Heidelberg, Berlin, Heidelberg, 2004). URL https://doi.org/10.1007/3-540-29838-X_5.

[216] Groves, T. R. Nanolithography. In *Nanolithography, edited by M. Feldman*, 80 (Woodhead Publishing, 2014).

[217] Martinez-Duarte, R. & Madou, M. Su-8 photolithography and its impact on microfluidics. *Microfluidics and nanofluidics handbook* 231–268 (2011).

[218] Hamlett, C., McHale, G. & Newton, M. Lithographically fabricated su8 composite structures for wettability control. *Surface and Coatings Technology* **240**, 179–183 (2014). URL https://www.sciencedirect.com/science/article/pii/S0257897213011912.

[219] Skjolding, L. H. D., Teixidor, G. T., Emnéus, J. & Montelius, L. Negative uv–nil (nuv–nil) – a mix-and-match nil and uv strategy for realisation of nano- and micrometre structures. *Microelectronic Engineering* **86**, 654–656 (2009). URL https://www.sciencedirect.com/science/article/pii/S016793170800703X. MNE '08.

[220] Grassetti, M. *Design and characterization of a microfluidic device resembling exocrine pancreas*. Ph.D. thesis, Politecnico di Torino (2023).

[221] Golden, J., Miller, H., Nawrocki, D. & Ross, J. Optimization of bi-layer lift-off resist process. *CS Mantech Technical Digest* (2009).

[222] Senftleben, O., Baumgärtner, H. & Eisele, I. Cleaning of silicon surfaces for nanotechnology. In *Materials Science Forum*, vol. 573, 77–117 (Trans Tech Publ, 2008).

[223] Yang, X., Zhong, Z., Diallo, E., Wang, Z. & Yue, W. Silicon wafer wettability and aging behaviors: Impact on gold thin-film morphology. *Materials Science in Semiconductor Processing* **26**, 25–32 (2014). URL https://www.sciencedirect.com/science/article/pii/S1369800114001851.

[224] Kaya, S. *et al.* A systematic study of plasma activation of silicon surfaces for self assembly. *ACS Applied Materials & Interfaces* **7**, 25024–25031 (2015). URL https://doi.org/10.1021/acsami.5b08358. PMID: 26509331.

[225] Roy, K. *Optoelectronic Properties of Graphene-Based Van Der Waals Hybrids* (Springer Nature, 2020).

[226] Kern, W. The evolution of silicon wafer cleaning technology. *Journal of The Electrochemical Society* **137**, 1887 (1990). URL https://dx.doi.org/10.1149/1.2086825.

[227] Itano, M., Kern, F., Miyashita, M. & Ohmi, T. Particle removal from silicon wafer surface in wet cleaning process. *IEEE Transactions on Semiconductor Manufacturing* **6**, 258–267 (1993).

[228] Kim, Y. *et al.* Study on surface modification of silicon using chf3/o2 plasma for nano-imprint lithographya). *Journal of Vacuum Science Technology A* **30**, 031601 (2012). URL https://doi.org/10.1116/1.3695995.

[229] Avram, M., Avram, A. M., Bragaru, A., Ghiu, A. & Iliescu, C. Plasma surface modification for selective hydrophobic control. *Romanian Journal of Information Science and Technology* **11**, 409–422 (2008).

[230] Williams, K. & Muller, R. Etch rates for micromachining processing. *Journal of Microelectromechanical Systems* **5**, 256–269 (1996).

[231] Paul, N., Vadnala, S., Agrawal, A., Vanjari, S. R. & Govind Singh, S. Thermal and optoelectrical analysis of la0.7sr0.3mno3 thin film thermistor in 8–12 m range for uncooled microbolometer application. In *2018 IEEE Electron Devices Kolkata Conference (EDKCON)*, 55–59 (2018).

[232] Ohnuma, H., Tsudaka, K., Kawahira, H. & Nozawa, S. Lithography computer aided design technology for embedded memory in logic. *Japanese Journal of Applied Physics* **37**, 6686 (1998). URL `https://dx.doi.org/10.1143/JJAP.37.6686`.

[233] Pan, D. Z., Yang, J.-S., Yuan, K. & Cho, M. Cad for double patterning lithography. In *2010 IEEE International Conference on Integrated Circuit Design and Technology*, 122–125 (2010).

[234] Sthuthi, A., Nithya, G. & Nagaraja, V. S. Design, modeling, fabrication, packaging and characterization of mems screech sensor. *Materials Today: Proceedings* **59**, 1132–1137 (2022). URL `https://www.sciencedirect.com/science/article/pii/S2214785322013153`. Third International Conference on Recent Advances in Materials and Manufacturing 2021.

[235] Lok, R., Karacali, H., Varol, A., Camli, U. & Yilmaz, E. Fabrication and characterization of resistance temperature detector by smart mask design. *The International Journal of Advanced Manufacturing Technology* **122**, 147–158 (2022). URL `https://doi.org/10.1007/s00170-022-09041-2`.

[236] Zhang, H. *et al.* Kaleidoscopic imaging patterns of complex structures fabricated by laser-induced deformation. *Nature Communications* **7**, 13743 (2016). URL `https://doi.org/10.1038/ncomms13743`.

[237] Pal, P. *et al.* A detailed investigation and explanation of the appearance of different undercut profiles in koh and tmah. *Journal of Micromechanics and Microengineering* **24**, 095026 (2014). URL `https://dx.doi.org/10.1088/0960-1317/24/9/095026`.

[238] Konishi, S., Nakagami, C., Kobayashi, T., Tonomura, W. & Kaizuma, Y. Lift-off process with bi-layer photoresist patterns for conformal-coated superhydrophilic

pulsed plasma chemical vapor deposition-siox on sicx for lab-on-a-chip applications. *Japanese Journal of Applied Physics* **54**, 047201 (2015). URL https://dx.doi.org/10.7567/JJAP.54.047201.

[239] Wasa, K., Kitabatake, M. & Adachi, H. *Thin film materials technology: sputtering of control compound materials* (Springer Science & Business Media, 2004).

[240] Seshan, K. *Handbook of thin film deposition* (William Andrew, 2012).

[241] Hashmi, M. S. J. *Comprehensive materials processing* (Newnes, 2014).

[242] Pyun, M. W., Kim, E. J., Yoo, D.-H. & Hahn, S. H. Oblique angle deposition of tio2 thin films prepared by electron-beam evaporation. *Applied Surface Science* **257**, 1149–1153 (2010). URL https://www.sciencedirect.com/science/article/pii/S0169433210011153.

[243] Masood, K., Iqbal, M. & Zakaullah, M. Emission characteristics of the thermionic electron beam sources developed at ebsdl. *Nuclear Instruments and Methods in Physics Research Section A: Accelerators, Spectrometers, Detectors and Associated Equipment* **584**, 9–24 (2008). URL https://www.sciencedirect.com/science/article/pii/S016890020702089X.

[244] Wang, Z. & Zhang, Z. *Electron Beam Evaporation Deposition*, chap. 2, 33–58 (John Wiley Sons, Ltd, 2016). URL https://onlinelibrary.wiley.com/doi/abs/10.1002/9783527696406.ch2.

[245] Novoselov, K. S. *et al.* Two-dimensional atomic crystals. *Proceedings of the National Academy of Sciences* **102**, 10451–10453 (2005). URL https://www.pnas.org/doi/abs/10.1073/pnas.0502848102. https://www.pnas.org/doi/pdf/10.1073/pnas.0502848102.

[246] Harman, G. G. *Wire bonding in microelectronics materials, processes, reliability and yield* (McGraw-Hill, 1997).

[247] Tian, W., Cui, H. & Yu, W. Analysis and experimental test of electrical characteristics on bonding wire. *Electronics* **8**, 365 (2019).

[248] Chao, Y., Yang, Z. & Qiao, H. Progress on technology of wire bonding. *J. Electron. Process Technol* **4**, 205–210 (2007).

[249] Fischer, A. C. *et al.* Unconventional applications of wire bonding create opportunities for microsystem integration. *Journal of Micromechanics and Microengineering* **23**, 083001 (2013).

[250] Toyozawa, K., Fujita, K., Minamide, S. & Maeda, T. Development of copper wire bonding application technology. *IEEE Transactions on Components, Hybrids, and Manufacturing Technology* **13**, 667–672 (1990).

[251] Shah, A. *et al.* Ultrasonic friction power during al wire wedge-wedge bonding. *Journal of Applied Physics* **106**, 013503 (2009). URL https://doi.org/10.1063/1.3158065. https://pubs.aip.org/aip/jap/article-pdf/doi/10.1063/1.3158065/14852853/013503_1_online.pdf.

[252] Breach, C. & Wulff, F. A brief review of selected aspects of the materials science of ball bonding. *Microelectronics Reliability* **50**, 1–20 (2010). URL https://www.sciencedirect.com/science/article/pii/S0026271409003126.

[253] Lee, J., Mayer, M., Zhou, Y., Hong, S. & Lee, S. Tail breaking force in thermosonic wire bonding with novel bonding wires. In *Materials Science Forum*, vol. 580, 201–204 (Trans Tech Publ, 2008).

[254] Vinson, J. & Liou, J. Electrostatic discharge in semiconductor devices: an overview. *Proceedings of the IEEE* **86**, 399–420 (1998).

[255] Sadiku, M. & Akujuobi, C. Electrostatic discharge (esd). *IEEE Potentials* **23**, 39–41 (2004).

[256] Kaiser, K. *Electrostatic Discharge* (Taylor & Francis, 2005). URL https://books.google.de/books?id=I_gUOcF13F4C.

[257] Liu, A. *et al.* The roadmap of 2d materials and devices toward chips. *Nano-Micro Letters* **16**, 119 (2024). URL https://doi.org/10.1007/s40820-023-01273-5.

[258] Islam, A., Lee, J. & Feng, P. X.-L. All-dry transferred single- and few-layer mos2 field effect transistor with enhanced performance by thermal annealing. *Journal of Applied Physics* **123**, 025701 (2018). URL https://doi.org/10.1063/1.5008846. https://pubs.aip.org/aip/jap/article-pdf/doi/10.1063/1.5008846/13310275/025701_1_online.pdf.

[259] Chen, J.-H. *et al.* Charged-impurity scattering in graphene. *Nature Physics* **4**, 377–381 (2008). URL https://doi.org/10.1038/nphys935.

[260] Ishigami, M., Chen, J. H., Cullen, W. G., Fuhrer, M. S. & Williams, E. D. Atomic structure of graphene on sio2. *Nano Letters* **7**, 1643–1648 (2007). URL https://doi.org/10.1021/nl070613a. PMID: 17497819, https://doi.org/10.1021/nl070613a.

[261] Seo, J. E. *et al.* Improvement of contact resistance and 3d integration of 2d material field-effect transistors using semi-metallic ptse2 contacts. *Advanced Functional Materials* **34**, 2407382 (2024). URL https://onlinelibrary.wiley.com/doi/abs/10.1002/adfm.202407382. https://onlinelibrary.wiley.com/doi/pdf/10.1002/adfm.202407382.

[262] Nath, A. *et al.* Achieving clean epitaxial graphene surfaces suitable for device applications by improved lithographic process. *Applied Physics Letters* **104** (2014).

[263] Ning, J. *et al.* Combined effects of hydrogen annealing on morphological, electrical and structural properties of graphene/r-sapphire. *Carbon* **75**, 262–270 (2014). URL https://www.sciencedirect.com/science/article/pii/S0008622314003194.

[264] Jain, A. *et al.* One-dimensional edge contacts to a monolayer semiconductor. *Nano Letters* **19**, 6914–6923 (2019). URL https://doi.org/10.1021/acs.nanolett.9b02166. PMID: 31513426, https://doi.org/10.1021/acs.nanolett.9b02166.

[265] Lin, Y.-C. *et al.* Graphene annealing: How clean can it be? *Nano Letters* **12**, 414–419 (2012). URL https://doi.org/10.1021/nl203733r. PMID: 22149394, https://doi.org/10.1021/nl203733r.

[266] Zhuang, B., Li, S., Li, S. & Yin, J. Ways to eliminate pmma residues on graphene —— superclean graphene. *Carbon* **173**, 609–636 (2021). URL https://www.sciencedirect.com/science/article/pii/S000862232031126X.

[267] Moser, J., Barreiro, A. & Bachtold, A. Current-induced cleaning of graphene. *Applied Physics Letters* **91**, 163513 (2007). URL https://doi.org/10.1063/1.2789673. https://pubs.aip.org/aip/apl/article-pdf/doi/10.1063/1.2789673/14384812/163513_1_online.pdf.

[268] Ramamoorthy, H. & Somphonsane, R. In-situ current annealing of graphene-metal contacts. *Journal of Physics: Conference Series* **1144**, 012186 (2018). URL https://dx.doi.org/10.1088/1742-6596/1144/1/012186.

[269] Valenzuela, R., Gonzalez, J. & Amano, E. Current annealing and magnetoimpedance in cofebsi amorphous ribbons. *IEEE Transactions on Magnetics* **33**, 3925–3927 (1997).

[270] Moradi, M., Dastani, M. M. & Mehrjouei, M. The step-current annealing: An easy method to improve the magnetoimpedance in co-rich ribbons. *IEEE Transactions on Magnetics* **55**, 1–6 (2019).

[271] Bae, H., Lee, K.-S., Ye, P. D. & Park, J.-Y. Current annealing to improve drain output performance of -ga2o3 field-effect transistor. *Solid-State Electronics* **185**, 108134 (2021). URL https://www.sciencedirect.com/science/article/pii/S0038110121001775.

[272] Prasad, N., Kumari, A., Bhatnagar, P. K., Mathur, P. C. & Bhatia, C. S. Current induced annealing and electrical characterization of single layer graphene grown by chemical vapor deposition for future interconnects in vlsi circuits. *Applied Physics Letters* **105**, 113513 (2014). URL https://doi.org/10.1063/1.4895802. https://pubs.aip.org/aip/apl/article-pdf/doi/10.1063/1.4895802/13307497/113513_1_online.pdf.

[273] Tanaka, S. *et al.* Effect of current annealing on electronic properties of multilayer graphene. *Journal of Physics: Conference Series* **232**, 012015 (2010). URL https://dx.doi.org/10.1088/1742-6596/232/1/012015.

[274] Wijewardena, U. K. *et al.* Effects of long-time current annealing to the hysteresis in cvd graphene on sio2. *MRS Advances* **4**, 3319–3326 (2019). URL https://doi.org/10.1557/adv.2019.366.

[275] Hertel, S. *et al.* Current annealing and electrical breakdown of epitaxial graphene. *Applied Physics Letters* **98**, 212109 (2011). URL https://doi.org/10.1063/1.3592841. https://pubs.aip.org/aip/apl/article-pdf/doi/10.1063/1.3592841/14451097/212109_1_online.pdf.

[276] *Liquid Helium Plant Operating Manual **216*** (CRYOMECH, 2010). URL https://bluefors.com/products/liquid-helium-management-products/liquid-helium-plants/.

[277] Gifford, W. E. The gifford-mcmahon cycle. In Timmerhaus, K. D. (ed.) *Advances in Cryogenic Engineering*, 152–159 (Springer US, Boston, MA, 1966).

[278] *Closed Cycle Cryo-cooler - Principles of Operation* (XXX, 2010). URL https://www.arscryo.com/cryocooler-principles-of-operation.

[279] *Cold Heads - Operating Manual* (Sumitomo Cryogenics, USA, 2007).

[280] *Physical Property Measurement System DynaCool User's Manual, Part Number* **1307-110, D1** (Quantum Design, Inc., 2017). URL https://files.wmich.edu/s3fs-public/attachments/u1045/2019/02_1307-110%2C%20Rev.%20D1%20DYNACOOL%20USERS%20MANUAL%20.pdf.

[281] *Electrical Transport Option (ETO) User's Manual, Part Number* **1084-700, B2** (Quantum Design, Inc., 2017). URL https://files.wmich.edu/s3fs-public/attachments/u1045/2019/10_1084-700%20Rev%20B2%20ELECTRICAL%20TRANSPORT%20OPTION%20USER%27S%20MANUAL.pdf.

[282] *PPMS MultiVu Application User's Manual, Part Number* **1070-110, A2** (Quantum Design, Inc., 2008). URL https://web.njit.edu/~tyson/PPMS_Documents/PPMS_Manual/1070-110%20A2%20.pdf%20PQ%20MVu.pdf.

[283] *Vibrating Sample Magnetometer (VSM) Option User's Manual., Part Number* **1096-100, B0** (Quantum Design, Inc., 2011). URL https://www.mrfn.org/sites/mrfn.org/files/instrument/VSM_manual_B0.pdf.

[284] *Oxford Instruments NanoScience TeslatronPT Cryofree System with Integrated Superconducting Magnet System Manual, Version* **CN0580** (Oxford Instruments Nanotechnology Tools Ltd., 2021). URL https://nanoscience.oxinst.com/dry-systems/products/teslatronpt.

[285] Balshaw, N. *Practical Cryogenics - An Introduction to Laboratory Cryogenics* (Oxford Instruments Superconductivity Limited, 2001).

[286] *Oxford Instruments NanoScience HelioxVT - Sorption Pumped 3He Refrigerator System Manual, Issue* **5** (Oxford Instruments Nanotechnology Tools Ltd., 2020). URL https://nanoscience.oxinst.com/assets/uploads/HelioxVT_Feb_2023.pdf.

[287] Inc., K. I. *Low Level Measurements Handbook: Precision DC Current, Voltage, and Resistance Measurements* (Keithley Instruments, 2004). URL https://books.google.de/books?id=LrviswEACAAJ.

[288] Ihn, T. *Semiconductor Nanostructures: Quantum states and electronic transport* (OUP Oxford, 2009).

[289] van der PAUW, L. J. *A Method of Measuring Specific Resistivity and Hall Effect of Discs of Arbitrary Shape*, 174–182. Semiconductor Devices: Pioneering Papers (WORLD SCIENTIFIC, 1991). URL https://doi.org/10.1142/9789814503464_0017. 0.

[290] Ramadan, A., Gould, R. & Ashour, A. On the van der pauw method of resistivity measurements. *Thin Solid Films* **239**, 272–275 (1994). URL https://www.sciencedirect.com/science/article/pii/004060909490863X.

[291] Thomson, W. Xix. on the electro-dynamic qualities of metals:—effects of magnetization on the electric conductivity of nickel and of iron. *Proceedings of the Royal Society of London* **8**, 546–550 (1857). URL https://royalsocietypublishing.org/doi/abs/10.1098/rspl.1856.0144. https://royalsocietypublishing.org/doi/pdf/10.1098/rspl.1856.0144.

[292] Raquet, B., Viret, M., Sondergard, E., Cespedes, O. & Mamy, R. Electron-magnon scattering and magnetic resistivity in 3*d* ferromagnets. *Phys. Rev. B* **66**, 24433 (2002).

[293] Huang, X. *et al.* Observation of the chiral-anomaly-induced negative magnetoresistance in 3d weyl semimetal taas. *Phys. Rev. X* **5**, 031023 (2015). URL https://link.aps.org/doi/10.1103/PhysRevX.5.031023.

[294] Li, H. *et al.* Negative magnetoresistance in dirac semimetal cd3as2. *Nature Communications* **7**, 10301 (2016). URL https://doi.org/10.1038/ncomms10301.

[295] Li, Q. *et al.* Chiral magnetic effect in zrte5. *Nature Physics* **12**, 550–554 (2016). URL https://doi.org/10.1038/nphys3648.

[296] Baibich, M. N. *et al.* Giant magnetoresistance of (001)fe/(001)cr magnetic superlattices. *Phys. Rev. Lett.* **61**, 2472–2475 (1988). URL https://link.aps.org/doi/10.1103/PhysRevLett.61.2472.

[297] Binasch, G., Grünberg, P., Saurenbach, F. & Zinn, W. Enhanced magnetoresistance in layered magnetic structures with antiferromagnetic interlayer exchange. *Phys. Rev. B* **39**, 4828–4830 (1989). URL https://link.aps.org/doi/10.1103/PhysRevB.39.4828.

[298] Jonker, G. & Van Santen, J. Ferromagnetic compounds of manganese with perovskite structure. *Physica* **16**, 337–349 (1950). URL https://www.sciencedirect.com/science/article/pii/0031891450900334.

[299] Julliere, M. Tunneling between ferromagnetic films. *Physics Letters A* **54**, 225–226 (1975). URL https://www.sciencedirect.com/science/article/pii/0375960175901747.

[300] Miyazaki, T. & Tezuka, N. Giant magnetic tunneling effect in fe/al2o3/fe junction. *Journal of Magnetism and Magnetic Materials* **139**, L231–L234 (1995). URL https://www.sciencedirect.com/science/article/pii/0304885395900012.

[301] Ritzinger, P. & Výborný, K. Anisotropic magnetoresistance: materials, models and applications. *Royal Society Open Science* **10**, 230564 (2023). URL https://royalsocietypublishing.org/doi/abs/10.1098/rsos.230564. https://royalsocietypublishing.org/doi/pdf/10.1098/rsos.230564.

[302] Campbell, I. A., Fert, A. & Jaoul, O. The spontaneous resistivity anisotropy in ni-based alloys. *Journal of Physics C: Solid State Physics* **3**, S95 (1970). URL https://dx.doi.org/10.1088/0022-3719/3/1S/310.

[303] Mott, N. F. Electrons in transition metals. *Advances in Physics* **13**, 325–422 (1964).

[304] Buschow, K. Physics of magnetism and magnetic materials (2003).

[305] Ferraro, J., Nakamoto, K. & Brown, C. *Introductory Raman Spectroscopy* (Elsevier Science, 2003). URL https://books.google.de/books?id=fuZcZSz65g0C.

[306] Ferrari, A. C. & Basko, D. M. Raman spectroscopy as a versatile tool for studying the properties of graphene. *Nature Nanotechnology* **8**, 235–246 (2013). URL https://doi.org/10.1038/nnano.2013.46.

[307] Popp, J. & Mayerhöfer, T. (eds.) *Micro-Raman Spectroscopy* (De Gruyter, Berlin, Boston, 2020). URL https://doi.org/10.1515/9783110515312.

[308] Jorio, A. & Cançado, L. G. *Disorder and Defects in Two-Dimensional Materials Probed by Raman Spectroscopy*, 99–110 (Springer Singapore, 2018). URL http://dx.doi.org/10.1007/978-981-13-1828-3_5.

[309] Tan, P. *Raman Spectroscopy of Two-Dimensional Materials* (Springer Singapore, 2019). URL http://dx.doi.org/10.1007/978-981-13-1828-3.

[310] Ferrari, A. C. *et al.* Raman spectrum of graphene and graphene layers. *Phys. Rev. Lett.* **97**, 187401 (2006). URL https://link.aps.org/doi/10.1103/PhysRevLett.97.187401.

[311] Raman, C. V. A new radiation. *Indian Journal of Physics* **2**, 387–398 (1928). URL https://repository.ias.ac.in/70648/1/36-PUb.pdf.

[312] Raman, C. V. & Krishnan, K. S. A new type of secondary radiation. *Nature* **121**, 501–502 (1928). URL https://doi.org/10.1038/121501c0.

[313] Loudon, R. The raman effect in crystals. *Advances in Physics* **13**, 423–482 (1964). URL https://doi.org/10.1080/00018736400101051. https://doi.org/10.1080/00018736400101051.

[314] Weber, R. T., Jiang, J. & Barr, D. P. Bruker emx users manual. *Bruker Instruments, Billerica* (1998). URL `https://warwick.ac.uk/fac/sci/physics/research/condensedmatt/magneticresonancecluster/diamond-epr/facilities/epr/emx.pdf`.

[315] De L. Kronig, R. On the theory of dispersion of x-rays. *Journal of the Optical Society of America* **12**, 547–557 (1926).

[316] Kramers, H. A. La diffusion de la lumiere par les atomes. In *Atti Cong. Intern. Fisica (Transactions of Volta Centenary Congress) Como*, vol. 2, 545–557 (1927).

[317] Golze, C. *Tunable high-field/high-frequency ESR and high-field magnetization on single-molecule clusters.* Ph.D. thesis, TU Dresden, Germany (2007).

[318] Abraham, J. J. *Electron Spin Resonance on Magnetic van der Waals Compounds.* Ph.D. thesis, TU Dresden, Germany (2025).

[319] Huang, B. *et al.* Layer-dependent ferromagnetism in a van der Waals crystal down to the monolayer limit. *Nature* **546**, 270–273 (2017).

[320] Gong, C. *et al.* Discovery of intrinsic ferromagnetism in two-dimensional van der Waals crystals. *Nature* **546**, 265–269 (2017).

[321] Klein, D. R. *et al.* Probing magnetism in 2D van der Waals crystalline insulators via electron tunneling. *Science* **360**, 1218–1222 (2018).

[322] Burch, K. S., Mandrus, D. & Park, J.-G. Magnetism in two-dimensional van der Waals materials. *Nature* **563**, 47–52 (2018).

[323] McGuire, M. A., Dixit, H., Cooper, V. R. & Sales, B. C. Coupling of Crystal Structure and Magnetism in the Layered, Ferromagnetic Insulator CrI3. *Chem. Mater.* **27**, 612–620 (2015).

[324] Zhong, D. *et al.* Van der Waals engineering of ferromagnetic semiconductor heterostructures for spin and valleytronics. *Sci. Adv.* **3**, 1–7 (2017).

[325] Zhang, W., Wong, P. K. J., Zhu, R. & Wee, A. T. S. Van der Waals magnets: Wonder building blocks for two-dimensional spintronics? *InfoMat* **1**, 479–495 (2019).

[326] Kim, S. J. *et al.* Interface Engineering of Magnetic Anisotropy in van der Waals Ferromagnet-based Heterostructures. *ACS Nano* **15**, 16395–16403 (2021).

[327] Xiao, Y. *et al.* Spin-reorientation transition induced magnetic skyrmion in Nd2Fe14B magnet. *Appl. Phys. Lett.* **117**, 132402 (2020).

[328] Chen, L. *et al.* Spin Reorientation Transition and Negative Magnetoresistance in Ferromagnetic NdCrSb3 Single Crystals. *Materials* **16**, 1736 (2023).

[329] Aparnadevi, M. & Mahendiran, R. Electrical detection of spin reorientation transition in ferromagnetic La0.4Sm0.3Sr0.3MnO3. *J. Appl. Phys.* **113**, 17D719 (2013).

[330] Saha, P., Singh, M., Nagpal, V., Das, P. & Patnaik, S. Scaling analysis of anomalous Hall resistivity and magnetoresistance in the quasi-two-dimensional ferromagnet Fe3GeTe2. *Phys. Rev. B* **107**, 35115 (2023).

[331] Campbell, I. & Fauchet, P. M. The effects of microcrystal size and shape on the one phonon raman spectra of crystalline semiconductors. *Solid State Communications* **58**, 739–741 (1986).

[332] Kresse, G. & Furthmüller, J. Efficient iterative schemes for ab initio total-energy calculations using a plane-wave basis set. *Phys. Rev. B* **54**, 11169–11186 (1996).

[333] Kresse, G. & Furthmüller, J. Efficiency of ab-initio total energy calculations for metals and semiconductors using a plane-wave basis set. *Comput. Mater. Sci.* **6**, 15–50 (1996).

[334] Perdew, J. P., Burke, K. & Ernzerhof, M. Generalized Gradient Approximation Made Simple. *Phys. Rev. Lett.* **77**, 3865–3868 (1996).

[335] Blöchl, P. E. Projector augmented-wave method. *Phys. Rev. B* **50**, 17953–17979 (1994).

[336] Kresse, G. & Joubert, D. From ultrasoft pseudopotentials to the projector augmented-wave method. *Phys. Rev. B* **59**, 1758–1775 (1999).

[337] Monkhorst, H. J. & Pack, J. D. Special points for Brillouin-zone integrations. *Phys. Rev. B* **13**, 5188–5192 (1976).

[338] Dudarev, S. L., Botton, G. A., Savrasov, S. Y., Humphreys, C. J. & Sutton, A. P. Electron-energy-loss spectra and the structural stability of nickel oxide: An LSDA+U study. *Phys. Rev. B* **57**, 1505–1509 (1998).

[339] Guo, Y., Zhao, Y., Zhou, S. & Zhao, J. Oxidation behavior of layered FenGeTe2 (n = 3, 4, 5) and Cr2Ge2Te6 governed by interlayer coupling. *Nanoscale* **14**, 11452–11460 (2022).

[340] Wang, V., Xu, N., Liu, J.-C., Tang, G. & Geng, W.-T. VASPKIT: A user-friendly interface facilitating high-throughput computing and analysis using VASP code. *Comput. Phys. Commun.* **267**, 108033 (2021).

[341] Momma, K. & Izumi, F. VESTA 3 for three-dimensional visualization of crystal, volumetric and morphology data. *J. Appl. Crystallogr.* **44**, 1272–1276 (2011).

[342] Jena, R. P., Kumar, D. & Lakhani, A. Scaling analysis of anomalous Hall resistivity in the Co2TiAl Heusler alloy. *J. Phys. Condens. Matter* **32**, 365703 (2020).

[343] Behnia, K. On the Origin and the Amplitude of T-Square Resistivity in Fermi Liquids. *Ann. Phys.* **534**, 2100588 (2022).

[344] Klein, L. *et al.* Anomalous spin scattering effects in the badly metallic itinerant ferromagnet SrRuO3. *Phys. Rev. Lett.* **77**, 2774–2777 (1996).

[345] Lin, X., Fauqué, B. & Behnia, K. Scalable T2 resistivity in a small single-component Fermi surface. *Science* **349**, 945–948 (2015).

[346] Pariari, A. *et al.* Interplay between charge density wave order and magnetic field in the nonmagnetic rare-earth tritelluride LaTe3. *Phys. Rev. B* **104**, 1–12 (2021).

[347] Wang, J. *et al.* T-square resistivity without Umklapp scattering in dilute metallic Bi2O2Se. *Nat. Commun.* **11**, 1–8 (2020).

[348] Roy, S., Khan, N. & Mandal, P. Unconventional transport properties of the itinerant ferromagnet $EuTi_{1-x}Nb_xO_3$ ($x = 0.10 - 0.20$). *Phys. Rev. B* **98**, 134428 (2018).

[349] Taylor, G. R., Isin, A. & Coleman, R. V. Resistivity of Iron as a Function of Temperature and Magnetization. *Phys. Rev.* **165**, 621–631 (1968).

[350] Porter, N. A., Gartside, J. C. & Marrows, C. H. Scattering mechanisms in textured FeGe thin films: Magnetoresistance and the anomalous Hall effect. *Phys. Rev. B* **90**, 024403 (2014).

[351] Pippard, A. B. *Magnetoresistance in metals* (Cambridge University Press, Cambridge, UK, 1989).

[352] Khosla, R. P. & Fischer, J. R. Magnetoresistance in degenerate CdS: Localized magnetic moments. *Phys. Rev. B* **2**, 4084–4097 (1970).

[353] Yosida, K. Magnetic Properties of Cu-Mn Alloys. *Phys. Rev.* **106**, 893–898 (1957).

[354] Liu, Y., Stavitski, E., Attenkofer, K. & Petrovic, C. Anomalous Hall effect in the van der Waals bonded ferromagnet Fe3-xGeTe2. *Phys. Rev. B* **97**, 165415 (2018).

[355] Nozieres, P. & Lewiner, C. a Simple Theory of the Anomalous Hall Effect. *J. Phys. (Paris)* **34**, 901 (1973).

[356] Tian, Y., Ye, L. & Jin, X. Proper scaling of the anomalous Hall effect. *Phys. Rev. Lett.* **103**, 1–4 (2009). 0903.5360.

[357] Miyasato, T. *et al.* Crossover Behavior of the Anomalous Hall Effect and Anomalous Nernst Effect in Itinerant Ferromagnets. *Phys. Rev. Lett.* **99**, 86602 (2007).

[358] Yang, S. A., Pan, H., Yao, Y. & Niu, Q. Scattering universality classes of side jump in the anomalous Hall effect. *Phys. Rev. B* **83**, 125122 (2011).

[359] Wang, P. *et al.* Sign change of competing contributions to the side jump by impurity, phonon, and magnon scattering. *Phys. Rev. B* **107**, 094418 (2023).

[360] Markou, A. *et al.* Thickness dependence of the anomalous hall effect in thin films of the topological semimetal co_2MnGa. *Phys. Rev. B* **100**, 054422 (2019).

[361] Bera, S. *et al.* Anomalous Hall effect induced by Berry curvature in topological nodal-line van der Waals ferromagnet Fe_4GeTe_2. *Preprint at https://arxiv.org/abs/2308.09695* (2023).

[362] Gong, C. & Zhang, X. Two-dimensional magnetic crystals and emergent heterostructure devices. *Science* **363**, eaav4450 (2019). URL https://www.science.org/doi/abs/10.1126/science.aav4450. https://www.science.org/doi/pdf/10.1126/science.aav4450.

[363] Khan, Y. *et al.* Recent breakthroughs in two-dimensional van der Waals magnetic materials and emerging applications. *Nano Today* **34**, 100902 (2020). URL https://www.sciencedirect.com/science/article/pii/S1748013220300712.

[364] Li, H., Ruan, S. & Zeng, Y.-J. Intrinsic Van Der Waals Magnetic Materials from Bulk to the 2D Limit: New Frontiers of Spintronics. *Advanced Materials* **31**, 1900065 (2019). URL https://onlinelibrary.wiley.com/doi/abs/10.1002/adma.201900065.

[365] Scheunert, G. *et al.* A review of high magnetic moment thin films for microscale and nanotechnology applications. *Applied Physics Reviews* **3**, 011301 (2016). URL https://doi.org/10.1063/1.4941311.

[366] Jimenez, V. O. *et al.* A magnetic sensor using a 2D van der Waals ferromagnetic material. *Scientific Reports* **10**, 4789 (2020). URL https://doi.org/10.1038/s41598-020-61798-2.

[367] Mermin, N. D. & Wagner, H. Absence of ferromagnetism or antiferromagnetism in one- or two-dimensional isotropic heisenberg models. *Phys. Rev. Lett.* **17**, 1133–1136 (1966). URL https://link.aps.org/doi/10.1103/PhysRevLett.17.1133.

[368] Liu, S. *et al.* Wafer-scale two-dimensional ferromagnetic fe3gete2 thin films grown by molecular beam epitaxy. *npj 2D Materials and Applications* **1**, 30 (2017). URL https://doi.org/10.1038/s41699-017-0033-3.

[369] May, A. F., Bridges, C. A. & McGuire, M. A. Physical properties and thermal stability of $fe_{5-x}gete_2$ single crystals. *Phys. Rev. Mater.* **3**, 104401 (2019). URL https://link.aps.org/doi/10.1103/PhysRevMaterials.3.104401.

[370] Li, Z. *et al.* Magnetic critical behavior of the van der waals fe5gete2 crystal with near room temperature ferromagnetism. *Scientific Reports* **10**, 15345 (2020). URL https://doi.org/10.1038/s41598-020-72203-3.

[371] Kim, D., Lee, C., Jang, B. G., Kim, K. & Shim, J. H. Drastic change of magnetic anisotropy in fe3gete2 and fe4gete2 monolayers under electric field studied by density functional theory. *Scientific Reports* **11**, 17567 (2021). URL https://doi.org/10.1038/s41598-021-96639-3.

[372] Ni, L. *et al.* Magnetic dynamics of two-dimensional itinerant ferromagnet Fe_3GeTe_2. *Chinese Physics B* **30**, 097501 (2021). URL https://dx.doi.org/10.1088/1674-1056/ac0e25.

[373] Bera, S. *et al.* Enhanced coercivity and emergent spin-cluster-glass state in 2D ferromagnetic material, Fe3GeTe2. *Journal of Magnetism and Magnetic Materials* **583**, 171052 (2023). URL https://www.sciencedirect.com/science/article/pii/S0304885323007023.

[374] Rana, D. *et al.* High transport spin polarization in the van der waals ferromagnet fe_4gete_2. *Phys. Rev. B* **107**, 224422 (2023). URL https://link.aps.org/doi/10.1103/PhysRevB.107.224422.

[375] Bera, S. *et al.* Anomalous hall effect induced by berry curvature in the topological nodal-line van der waals ferromagnet fe_4gete_2. *Phys. Rev. B* **108**, 115122 (2023). URL https://link.aps.org/doi/10.1103/PhysRevB.108.115122.

[376] Wu, B. *et al.* High-performance fe$_x$gete$_2$−based (x =4 or 5) van der waals magnetic tunnel junctions. *Phys. Rev. Appl.* **19**, 024037 (2023). URL `https://link.aps.org/doi/10.1103/PhysRevApplied.19.024037`.

[377] Shao, D.-F. *et al.* Néel spin currents in antiferromagnets. *Phys. Rev. Lett.* **130**, 216702 (2023). URL `https://link.aps.org/doi/10.1103/PhysRevLett.130.216702`.

[378] Seo, J. *et al.* Tunable high-temperature itinerant antiferromagnetism in a van der waals magnet. *Nature Communications* **12**, 2844 (2021). URL `https://doi.org/10.1038/s41467-021-23122-y`.

[379] CrysAlis PRO. Agilent Technologies Ltd, Yarnton, Oxfordshire, England. Agilent (2014).

[380] Kieffer, J., Valls, V., Blanc, N. & Hennig, C. New tools for calibrating diffraction setups. *Journal of Synchrotron Radiation* **27**, 558–566 (2020). URL `https://doi.org/10.1107/S1600577520000776`.

[381] Palatinus, L. & Chapuis, G. *SUPERFLIP* – a computer program for the solution of crystal structures by charge flipping in arbitrary dimensions. *Journal of Applied Crystallography* **40**, 786–790 (2007). URL `https://doi.org/10.1107/S0021889807029238`.

[382] Petříček, V., Palatinus, L., Plášil, J. & Dušek, M. Jana2020 – a new version of the crystallographic computing system jana. *Zeitschrift für Kristallographie - Crystalline Materials* **238**, 271–282 (2023). URL `https://doi.org/10.1515/zkri-2023-0005`.

[383] https://magicplot.com/.

[384] Jmol: an open-source Java viewer for chemical structures in 3D. http://www.jmol.org/.

[385] Abragam, A. & Bleaney, B. *Electron paramagnetic resonance of transition ions* (Oxford University Press, Oxford, 2012).

[386] Turov, E. A. *Physical Properties of Magnetically Ordered Crystals* (Academic Press, New York, 1965).

[387] Holstein, T. & Primakoff, H. Field Dependence of the Intrinsic Domain Magnetization of a Ferromagnet. *Phys. Rev.* **58**, 1098–1113 (1940). URL `https://link.aps.org/doi/10.1103/PhysRev.58.1098`.

[388] Osborn, J. A. Demagnetizing factors of the general ellipsoid. *Phys. Rev.* **67**, 351 (1945).

[389] Cronemeyer, D. C. Demagnetization factors for general ellipsoids. *J. Appl. Phys.* **70**, 2911 (1991).

[390] Benner, H. & Boucher, J. P. *Spin Dynamics in the Paramagnetic Regime: NMR and EPR in Two-Dimensional Magnets*, 323–378 (Springer Netherlands, Dordrecht, 1990). URL https://doi.org/10.1007/978-94-009-1860-3_7.

[391] Zeisner, J. *et al.* Magnetic anisotropy and spin-polarized two-dimensional electron gas in the van der Waals ferromagnet $Cr_2Ge_2Te_6$. *Phys. Rev. B* **99**, 165109 (2019). URL https://link.aps.org/doi/10.1103/PhysRevB.99.165109.

[392] Yang, X., Zhou, X., Feng, W. & Yao, Y. Strong magneto-optical effect and anomalous transport in the two-dimensional van der waals magnets fe_ngete_2 ($n = 3$, 4, 5). *Phys. Rev. B* **104**, 104427 (2021). URL https://link.aps.org/doi/10.1103/PhysRevB.104.104427.

[393] Kim, S.-R. *et al.* Role of orbital bond and local magnetism in fe3gete2 and fe4gete2: Implication for ultrathin nano devices. *ACS Applied Nano Materials* **5**, 10341–10347 (2022). URL https://doi.org/10.1021/acsanm.2c01576. https://doi.org/10.1021/acsanm.2c01576.

[394] Ghosh, S., Ershadrad, S., Borisov, V. & Sanyal, B. Unraveling effects of electron correlation in two-dimensional fengete2 (n = 3, 4, 5) by dynamical mean field theory. *npj Computational Materials* **9**, 86 (2023). URL https://doi.org/10.1038/s41524-023-01024-5.

[395] Liu, Q. *et al.* Layer-dependent magnetic phase diagram in fengete2 (3 n 7) ultrathin films. *Communications Physics* **5**, 140 (2022). URL https://doi.org/10.1038/s42005-022-00921-3.

[396] Barnes, S. Theory of electron spin resonance of magnetic ions in metals. *Advances in Physics* **30**, 801–938 (1981). URL https://doi.org/10.1080/00018738100101447. https://doi.org/10.1080/00018738100101447.

[397] Song, Z. & Liu, Q. Basic crystal field theory—a simple and useful tool to understand the structure–property relationship in luminescent materials. *Optical Materials: X* **16**, 100189 (2022). URL https://www.sciencedirect.com/science/article/pii/S2590147822000535.

[398] Saitoh, E., Ueda, M., Miyajima, H. & Tatara, G. Conversion of spin current into charge current at room temperature: Inverse spin-Hall effect. *Applied Physics Letters* **88**, 182509 (2006). URL https://doi.org/10.1063/1.2199473. https://pubs.aip.org/aip/apl/article-pdf/doi/10.1063/1.2199473/14660277/182509_1_online.pdf.

[399] Orenstein, J. & Millis, A. Advances in the physics of high-temperature superconductivity. *Science* **288**, 468–474 (2000).

[400] Lanzara, A. *et al.* Evidence for ubiquitous strong electron-phonon coupling in high-temperature superconductors. *Nature* **412**, 510–514 (2001).

[401] Eerenstein, W., Mathur, N. & Scott, J. F. Multiferroic and magnetoelectric materials. *nature* **442**, 759–765 (2006).

[402] Lee, J. H. *et al.* A strong ferroelectric ferromagnet created by means of spin–lattice coupling. *Nature* **466**, 954–958 (2010).

[403] Mochizuki, M., Furukawa, N. & Nagaosa, N. Theory of spin-phonon coupling in multiferroic manganese perovskites $RMnO_3$. *Physical Review B***84**, 144409(2011).

[404] Tokura, Y. & Nagaosa, N. Orbital physics in transition-metal oxides. *science* **288**, 462–468 (2000).

[405] Son, J. *et al.* Unconventional spin-phonon coupling via the dzyaloshinskii–moriya interaction. *npj Quantum materials* **4**, 17 (2019).

[406] Zhang, X., Tan, Q.-H., Wu, J.-B., Shi, W. & Tan, P.-H. Review on the raman spectroscopy of different types of layered materials. *Nanoscale* **8**, 6435–6450 (2016).

[407] Huang, B. *et al.* Tuning inelastic light scattering via symmetry control in the two-dimensional magnet cri3. *Nature nanotechnology* **15**, 212–216 (2020).

[408] Hu, L. *et al.* Spin-phonon coupling in two-dimensional magnetic materials. *National Science Open* **2**, 20230002 (2023).

[409] Sivadas, N., Okamoto, S., Xu, X., Fennie, C. J. & Xiao, D. Stacking-Dependent Magnetism in Bilayer CrI 3. *Nano Letters* **18**, 7658–7664 (2018).

[410] Tian, Y., Gray, M. J., Ji, H., Cava, R. J. & Burch, K. S. Magneto-elastic coupling in a potential ferromagnetic 2d atomic crystal. *2D Materials* **3**, 025035 (2016). URL https://dx.doi.org/10.1088/2053-1583/3/2/025035.

[411] Wang, X. *et al.* Raman spectroscopy of atomically thin two-dimensional magnetic iron phosphorus trisulfide (feps3) crystals. *2D Materials* **3**, 031009 (2016).

[412] Kong, X., Berlijn, T. & Liang, L. Thickness and Spin Dependence of Raman Modes in Magnetic Layered Fe3GeTe2. *Advanced Electronic Materials* **7**, 1–7 (2021).

[413] Du, L. *et al.* Lattice dynamics, phonon chirality, and spin–phonon coupling in 2d itinerant ferromagnet fe3gete2. *Advanced Functional Materials* **29**, 1904734 (2019). URL https://onlinelibrary.wiley.com/doi/abs/10.1002/adfm.201904734.

[414] Sahoo, S., Gaur, A. P. S., Ahmadi, M., Guinel, M. J.-F. & Katiyar, R. S. Temperature-dependent raman studies and thermal conductivity of few-layer mos2. *The Journal of Physical Chemistry C* **117**, 9042–9047 (2013). URL https://doi.org/10.1021/jp402509w. https://doi.org/10.1021/jp402509w.

[415] Lin, Y. *et al.* Dielectric screening of excitons and trions in single-layer mos2. *Nano Letters* **14**, 5569–5576 (2014). URL https://doi.org/10.1021/nl501988y. PMID: 25216267, https://doi.org/10.1021/nl501988y.

[416] Rice, C. *et al.* Raman-scattering measurements and first-principles calculations of strain-induced phonon shifts in monolayer mos_2. *Phys. Rev. B* **87**, 081307 (2013). URL https://link.aps.org/doi/10.1103/PhysRevB.87.081307.

[417] Castellanos-Gomez, A. *et al.* Local strain engineering in atomically thin mos2. *Nano Letters* **13**, 5361–5366 (2013). URL https://doi.org/10.1021/nl402875m. PMID: 24083520, https://doi.org/10.1021/nl402875m.

[418] Kresse, G. & Furthmüller, J. Efficiency of ab-initio total energy calculations for metals and semiconductors using a plane-wave basis set. *Computational Materials Science* **6**, 15–50 (1996). URL https://www.sciencedirect.com/science/article/pii/0927025696000080.

[419] Togo, A. & Tanaka, I. First principles phonon calculations in materials science. *Scripta Materialia* **108**, 1–5 (2015). URL https://www.sciencedirect.com/science/article/pii/S1359646215003127.

[420] Perdew, J. P., Burke, K. & Ernzerhof, M. Generalized gradient approximation made simple. *Phys. Rev. Lett.* **77**, 3865–3868 (1996). URL https://link.aps.org/doi/10.1103/PhysRevLett.77.3865.

[421] Loudon, R. The raman effect in crystals. *Advances in Physics* **50**, 813–864 (2001).

[422] Zhang, P. Symmetry and degeneracy of phonon modes for periodic structures with glide symmetry. *Journal of the Mechanics and Physics of Solids* **122**, 244–261 (2019). URL https://www.sciencedirect.com/science/article/pii/S0022509618304605.

[423] Raha, S. *et al.* Lattice dynamics of ge1xsnx alloy nanowires. *Nanoscale* **14**, 7211–7219 (2022). URL http://dx.doi.org/10.1039/D2NR00743F.

[424] Granado, E. *et al.* Magnetic ordering effects in the raman spectra of $la_{1-x}mn_{1-x}o_3$. *Phys. Rev. B* **60**, 11879–11882 (1999). URL https://link.aps.org/doi/10.1103/PhysRevB.60.11879.

[425] Saha, S. *et al.* Temperature-dependent Raman and x-ray studies of the spin-ice pyrochlore $Dy_2Ti_2O_7$ and nonmagnetic pyrochlore $Lu_2Ti_2O_7$. *Phys. Rev. B* **78**, 214102 (2008). URL https://link.aps.org/doi/10.1103/PhysRevB.78.214102.

[426] Klemens, P. G. Anharmonic decay of optical phonons. *Phys. Rev.* **148**, 845–848 (1966). URL https://link.aps.org/doi/10.1103/PhysRev.148.845.

[427] Postmus, C., Ferraro, J. R. & Mitra, S. S. Pressure dependence of infrared eigenfrequencies of kcl and kbr. *Phys. Rev.* **174**, 983–987 (1968). URL https://link.aps.org/doi/10.1103/PhysRev.174.983.

[428] Wu, P. *et al.* Evidence of spin reorientation and anharmonicity in kagome ferromagnet Fe3Sn2. *Applied Physics Letters* **119**, 082401 (2021). URL https://doi.org/10.1063/5.0063090.

[429] Maczka, M., Sanjuán, M. L., Fuentes, A. F., Hermanowicz, K. & Hanuza, J. Temperature-dependent raman study of the spin-liquid pyrochlore $tb_2ti_2o_7$. *Phys. Rev. B* **78**, 134420 (2008). URL https://link.aps.org/doi/10.1103/PhysRevB.78.134420.

[430] Jin, F. *et al.* Phonon anomalies and magnetic excitations in $bafe_2se_2O$. *Phys. Rev. B* **99**, 144419 (2019). URL https://link.aps.org/doi/10.1103/PhysRevB.99.144419.

[431] Sarkar, S. *et al.* Anharmonicity in raman-active phonon modes in atomically thin mos_2. *Phys. Rev. B* **101**, 205302 (2020). URL https://link.aps.org/doi/10.1103/PhysRevB.101.205302.

[432] Chakkar, A. G., Kumar, D. & Kumar, P. Broken weak and strong spin rotational symmetries and tunable interactions between phonons and the continuum in

$Cr_2Ge_2Te_6$. *Phys. Rev. B* **109**, 134406 (2024). URL https://link.aps.org/doi/10.1103/PhysRevB.109.134406.

[433] Menéndez, J. & Cardona, M. Temperature dependence of the first-order raman scattering by phonons in si, ge, and $\alpha - Sn$: Anharmonic effects. *Phys. Rev. B* **29**, 2051–2059 (1984). URL https://link.aps.org/doi/10.1103/PhysRevB.29.2051.

[434] Kim, K. H., Gu, J. Y., Choi, H. S., Park, G. W. & Noh, T. W. Frequency shifts of the internal phonon modes in $la_{0.7}ca_{0.3}mno_3$. *Phys. Rev. Lett.* **77**, 1877–1880 (1996). URL https://link.aps.org/doi/10.1103/PhysRevLett.77.1877.

[435] Balkanski, M., Wallis, R. F. & Haro, E. Anharmonic effects in light scattering due to optical phonons in silicon. *Phys. Rev. B* **28**, 1928–1934 (1983). URL https://link.aps.org/doi/10.1103/PhysRevB.28.1928.

[436] Kolesov, B. A. How the vibrational frequency varies with temperature. *Journal of Raman Spectroscopy* **48**, 323–326 (2017). URL https://analyticalsciencejournals.onlinelibrary.wiley.com/doi/abs/10.1002/jrs.5009.

[437] Klemens, P. G. Anharmonic decay of optical phonons. *Phys. Rev.* **148**, 845–848 (1966). URL https://link.aps.org/doi/10.1103/PhysRev.148.845.

[438] Singh, B., Kumar, S. & Kumar, P. Broken translational and rotational symmetries in limn1.5ni0.5o4 spinel. *Journal of Physics: Condensed Matter* **31**, 395701 (2019). URL https://dx.doi.org/10.1088/1361-648X/ab2bdb.

[439] Vaclavkova, D. *et al.* Magnetoelastic interaction in the two-dimensional magnetic material mnps3 studied by first principles calculations and raman experiments. *2D Materials* **7**, 035030 (2020). URL https://dx.doi.org/10.1088/2053-1583/ab93e3.

[440] López-Paz, S. A. *et al.* Dynamic magnetic crossover at the origin of the hidden-order in van der waals antiferromagnet crsbr. *Nature Communications* **13**, 4745 (2022). URL https://doi.org/10.1038/s41467-022-32290-4.

[441] Pawbake, A. *et al.* Raman scattering signatures of strong spin-phonon coupling in the bulk magnetic van der waals material crsbr. *Phys. Rev. B* **107**, 075421 (2023). URL https://link.aps.org/doi/10.1103/PhysRevB.107.075421.

[442] Sushkov, A. B., Tchernyshyov, O., II, W. R., Cheong, S. W. & Drew, H. D. Probing spin correlations with phonons in the strongly frustrated magnet $zncr_2o_4$. *Phys. Rev.*

Lett. **94**, 137202 (2005). URL https://link.aps.org/doi/10.1103/PhysRevLett.94.137202.

[443] Fennie, C. J. & Rabe, K. M. Magnetically induced phonon anisotropy in zncr$_2$o$_4$ from first principles. *Phys. Rev. Lett.* **96**, 205505 (2006). URL https://link.aps.org/doi/10.1103/PhysRevLett.96.205505.

[444] Casto, L. D. *et al.* Strong spin-lattice coupling in CrSiTe3. *APL Materials* **3**, 041515 (2015). URL https://doi.org/10.1063/1.4914134.

[445] Sun, Q.-C., Baker, S. N., Christianson, A. D. & Musfeldt, J. Magnetoelastic coupling in bulk and nanoscale mno. *Phys. Rev. B* **84**, 014301 (2011).

[446] Huang, Z. *et al.* Raman shifts in two-dimensional van der waals magnets reveal magnetic texture evolution. *Nano Letters* **24**, 1531–1538 (2024). URL https://doi.org/10.1021/acs.nanolett.3c03923. PMID: 38286029.

[447] Kuball, M., Hayes, J. M., Shi, Y. & Edgar, J. H. Phonon lifetimes in bulk AlN and their temperature dependence. *Applied Physics Letters* **77**, 1958–1960 (2000). URL https://doi.org/10.1063/1.1311948.

[448] Shepherd, I. W. Temperature dependence of phonon raman scattering in febo$_3$, inbo$_3$, and vbo$_3$: Evidence for a magnetic contribution to the intensities. *Phys. Rev. B* **5**, 4524–4529 (1972). URL https://link.aps.org/doi/10.1103/PhysRevB.5.4524.

[449] Steigmeier, E. F. & Harbeke, G. Phonons and magnetic order in ferromagnetic cdcr2se4 and cdcr2s4. *Physik der kondensierten Materie* **12**, 1–15 (1970). URL https://doi.org/10.1007/BF02422902.

[450] Baltensperger, W. Influence of Magnetic Order on Conduction Electrons and Phonons in Magnetic Semiconductors. *Journal of Applied Physics* **41**, 1052–1054 (1970). URL https://doi.org/10.1063/1.1658810.

[451] Ni, Z., Wang, Y., Yu, T. & Shen, Z. Raman spectroscopy and imaging of graphene. *Nano Research* **1**, 273–291 (2008). URL https://doi.org/10.1007/s12274-008-8036-1.

[452] Weerahennedige, H. *et al.* The effects of thickness, polarization, and strain on vibrational modes of 2d fe3gete2. *Surfaces and Interfaces* **51**, 104797 (2024). URL https://www.sciencedirect.com/science/article/pii/S2468023024009544.

[453] Lee, C. *et al.* Anomalous lattice vibrations of single- and few-layer mos2. *ACS Nano* **4**, 2695–2700 (2010). URL https://doi.org/10.1021/nn1003937. PMID: 20392077, https://doi.org/10.1021/nn1003937.

[454] Bing, D. *et al.* Optical contrast for identifying the thickness of two-dimensional materials. *Optics Communications* **406**, 128–138 (2018). URL https://www.sciencedirect.com/science/article/pii/S0030401817304789. Optoelectronics and Photonics Based on Two-dimensional Materials.

[455] Late, D. J., Liu, B., Matte, H. S. S. R., Rao, C. N. R. & Dravid, V. P. Rapid characterization of ultrathin layers of chalcogenides on sio2/si substrates. *Advanced Functional Materials* **22**, 1894–1905 (2012). URL https://onlinelibrary.wiley.com/doi/abs/10.1002/adfm.201102913.

[456] Gao, L., Ren, W., Li, F. & Cheng, H.-M. Total color difference for rapid and accurate identification of graphene. *ACS Nano* **2**, 1625–1633 (2008). URL https://doi.org/10.1021/nn800307s. PMID: 19206365, https://doi.org/10.1021/nn800307s.

[457] Ni, Z. H. *et al.* Graphene thickness determination using reflection and contrast spectroscopy. *Nano Letters* **7**, 2758–2763 (2007). URL https://doi.org/10.1021/nl071254m. PMID: 17655269, https://doi.org/10.1021/nl071254m.

[458] Yang, H., Hu, H., Wang, Y. & Yu, T. Rapid and non-destructive identification of graphene oxide thickness using white light contrast spectroscopy. *Carbon* **52**, 528–534 (2013). URL https://www.sciencedirect.com/science/article/pii/S0008622312008184.

[459] Shcherbakov, D. *et al.* Raman spectroscopy, photocatalytic degradation, and stabilization of atomically thin chromium tri-iodide. *Nano Letters* **18**, 4214–4219 (2018). URL https://doi.org/10.1021/acs.nanolett.8b01131.

[460] Ning, W. *et al.* Superconductor-insulator transition in quasi-one-dimensional single-crystal nb2pds5 nanowires. *Nano Lett.* **15**, 869–875 (2015). URL https://doi.org/10.1021/nl503538s.

[461] Jung, H. J., Bao, J.-K., Chung, D. Y., Kanatzidis, M. G. & Dravid, V. P. Unconventional defects in a quasi-one-dimensional kmn6bi5. *Nano Lett.* **19**, 7476–7486 (2019). URL https://doi.org/10.1021/acs.nanolett.9b03237.

[462] Zhang, E. *et al.* Magnetic-field-induced re-entrance of superconductivity in ta2pds5 nanostrips. *Nano letters* **21**, 288–297 (2020).

[463] Wang, J. *et al.* Observation of a v-shape superconductivity evolution on tungsten-intercalated 2h-type niobium diselenide. *ACS Nano* **18**, 27665–27671 (2024). URL https://doi.org/10.1021/acsnano.4c09443.

[464] Klein, J. *et al.* The bulk van der waals layered magnet crsbr is a quasi-1d material. *ACS Nano* **17**, 5316–5328 (2023). URL https://doi.org/10.1021/acsnano.2c07316.

[465] Zhang, G. *et al.* Superconducting ferromagnetic nanodiamond. *ACS Nano* **11**, 5358–5366 (2017). URL https://doi.org/10.1021/acsnano.7b01688.

[466] Ansermet, D. *et al.* Reentrant phase coherence in superconducting nanowire composites. *ACS Nano* **10**, 515–523 (2016). URL https://doi.org/10.1021/acsnano.5b05450.

[467] Bollinger, A. T., Dinsmore, R. C., Rogachev, A. & Bezryadin, A. Determination of the superconductor-insulator phase diagram for one-dimensional wires. *Phys. Rev. Lett.* **101**, 227003 (2008). URL https://link.aps.org/doi/10.1103/PhysRevLett.101.227003.

[468] Ran, S. *et al.* Nearly ferromagnetic spin-triplet superconductivity. *Science* **365**, 684–687 (2019). URL https://www.science.org/doi/abs/10.1126/science.aav8645. https://www.science.org/doi/pdf/10.1126/science.aav8645.

[469] Maeno, Y., Kittaka, S., Nomura, T., Yonezawa, S. & Ishida, K. Evaluation of spin-triplet superconductivity in sr2ruo4. *Journal of the Physical Society of Japan* **81**, 011009 (2012). https://doi.org/10.1143/JPSJ.81.011009.

[470] Mackenzie, A. P. & Maeno, Y. The superconductivity of sr_2ruo_4 and the physics of spin-triplet pairing. *Rev. Mod. Phys.* **75**, 657–712 (2003). URL https://link.aps.org/doi/10.1103/RevModPhys.75.657.

[471] Fay, D. & Appel, J. Coexistence of p-state superconductivity and itinerant ferromagnetism. *Phys. Rev. B* **22**, 3173–3182 (1980). URL https://link.aps.org/doi/10.1103/PhysRevB.22.3173.

[472] Huy, N. T. *et al.* Superconductivity on the border of weak itinerant ferromagnetism in ucoge. *Phys. Rev. Lett.* **99**, 067006 (2007). URL https://link.aps.org/doi/10.1103/PhysRevLett.99.067006.

[473] Sato, M. & Ando, Y. Topological superconductors: a review. *Reports on Progress in Physics* **80**, 076501 (2017). URL https://dx.doi.org/10.1088/1361-6633/aa6ac7.

[474] Clogston, A. M. Upper limit for the critical field in hard superconductors. *Phys. Rev. Lett.* **9**, 266–267 (1962). URL https://link.aps.org/doi/10.1103/PhysRevLett.9.266.

[475] Frigeri, P. A., Agterberg, D. F., Koga, A. & Sigrist, M. Superconductivity without inversion symmetry: Mnsi versus cept$_3$Si. *Phys. Rev. Lett.* **92**, 097001 (2004). URL https://link.aps.org/doi/10.1103/PhysRevLett.92.097001.

[476] Bezryadin, A., Lau, C. N. & Tinkham, M. Quantum suppression of superconductivity in ultrathin nanowires. *Nature* **404**, 971–4 (2000).

[477] Saxena, S. S. *et al.* Superconductivity on the border of itinerant-electron ferromagnetism in uge2. *Nature* **406**, 587–592 (2000). URL https://doi.org/10.1038/35020500.

[478] Aoki, D. *et al.* Coexistence of superconductivity and ferromagnetism in urhge. *Nature* **413**, 613–616 (2001). URL https://doi.org/10.1038/35098048.

[479] Pfleiderer, C. *et al.* Coexistence of superconductivity and ferromagnetism in the d-band metal zrzn2. *Nature* **412**, 58–61 (2001). URL https://doi.org/10.1038/35083531.

[480] Aoki, D., Ishida, K. & Flouquet, J. Review of u-based ferromagnetic superconductors: Comparison between uge2, urhge, and ucoge. *Journal of the Physical Society of Japan* **88**, 022001 (2019). https://doi.org/10.7566/JPSJ.88.022001.

[481] Arushi *et al.* Type-i superconductivity in single-crystal pb$_2$Pd. *Phys. Rev. B* **103**, 184506 (2021). URL https://link.aps.org/doi/10.1103/PhysRevB.103.184506.

[482] Sun, S., Liu, K. & Lei, H. Type-i superconductivity in kbi2 single crystals. *Journal of Physics: Condensed Matter* **28**, 085701 (2016). URL https://dx.doi.org/10.1088/0953-8984/28/8/085701.

[483] Tran, V. H., Bukowski, Z., Wiśniewski, P., Tran, L. M. & Zaleski, A. J. Observation of superconductivity in the intermetallic compound β-irsn4. *Journal of Physics: Condensed Matter* **25**, 155701 (2013). URL https://dx.doi.org/10.1088/0953-8984/25/15/155701.

[484] Zhao, L. L. *et al.* Type-i superconductivity in $ybsb_2$ single crystals. *Phys. Rev. B* **85**, 214526 (2012). URL `https://link.aps.org/doi/10.1103/PhysRevB.85.214526`.

[485] Sirica, N. *et al.* The nature of ferromagnetism in the chiral helimagnet cr1/3nbs2. *Communications Physics* **3**, 65 (2020). URL `https://doi.org/10.1038/s42005-020-0333-3`.

[486] Stishov, S. M. & Petrova, A. E. Itinerant helimagnet MnSi. *Physics Uspekhi* **54**, 1117–1130 (2011).

[487] Gorter, C. Kernentmagnetisierung. *Phys. Z* **35**, 923 (1934).

[488] Tinkham, M. Effect of fluxoid quantization on transitions of superconducting films. *Physical Review* **129**, 2413 (1963).

[489] White, R. & Tinkham, M. Magnetic-field dependence of microwave absorption and energy gap in superconducting films. *Physical Review* **136**, A203 (1964).

[490] Harper, F. & Tinkham, M. The mixed state in superconducting thin films. *Physical Review* **172**, 441 (1968).

[491] Baumgartner, T. *et al.* Effects of neutron irradiation on pinning force scaling in state-of-the-art nb3sn wires. *Superconductor Science and Technology* **27**, 015005 (2013).

[492] Jones, C., Hulm, J. & Chandrasekhar, B. Upper critical field of solid solution alloys of the transition elements. *Reviews of Modern Physics* **36**, 74 (1964).

[493] Gor'kov, L. The critical supercooling field in superconductivity theory. *Soviet Physics JETP* **10**, 593–599 (1960).

[494] Fischer, Ø. H. Properties of high-field superconductors containing localised magnetic moments. Tech. Rep., Univ., Geneva (1972).

[495] Marsiglio, F. & Carbotte, J. Upper critical field for a high-t c electron-phonon superconductor: Regime of t c ω 1 n 1. *Physical Review B* **36**, 3633 (1987).

[496] Maekawa, S., Ebisawa, H. & Fukuyama, H. Upper critical field in two-dimensional superconductors. *Journal of the Physical Society of Japan* **52**, 1352–1360 (1983).

[497] Klemm, R. A., Luther, A. & Beasley, M. Theory of the upper critical field in layered superconductors. *Physical Review B* **12**, 877 (1975).

[498] Alexandrov, A., Ranninger, J. & Robaszkiewicz, S. Bipolaronic superconductivity: thermodynamics, magnetic properties, and possibility of existence in real substances. *Physical Review B* **33**, 4526 (1986).

[499] Alexandrov, A. & Mott, N. Spin and charge bipolaron kinetics of high-tc superconductors. *International Journal of Modern Physics B* **8**, 2075–2109 (1994).

[500] Gurevich, A. Enhancement of the upper critical field by nonmagnetic impurities in dirty two-gap superconductors. *Physical Review B* **67**, 184515 (2003).

[501] Bera, A. *et al.* Superconductivity coexisting with ferromagnetism in a quasi-one dimensional non-centrosymmetric (tase _4) _3 i. *arXiv preprint arXiv:2111.14525* (2021).

[502] Xu, C. *et al.* Large-area high-quality 2d ultrathin mo2c superconducting crystals. *Nature Materials* **14**, 1135–1141 (2015).

[503] Zhang, E., Zhi, J., Zou, Y., Mao, Z. & Xiu, F. Signature of quantum griffiths singularity state in a layered quasi-one-dimensional superconductor. *Nat. Commun.* **9**, 1 (2018).

[504] Tidecks, R. *Current induced nonequilibrium phenomena in quasi one dimensional superconductors* (Springer, 2006).

[505] Tian, M. *et al.* Dissipation in quasi-one-dimensional superconducting single-crystal sn nanowires. *Physical Review B* **71**, 104521 (2005).

[506] Schulz, U. & Tidecks, R. Dissipative state of superconducting zinc whiskers. *J. Low Temp. Phys.* **71**, 151–171 (1988).

[507] Li, P. *et al.* Switching currents limited by single phase slips in one-dimensional superconducting al nanowires. *Physical review letters* **107**, 137004 (2011).

[508] Slama, G. & Tidecks, R. The influence of the electron mean free path on phase slip centers in indium whiskers. *Solid State Commun.* **44**, 425–429 (1982).

[509] Xu, K. & Heath, J. R. Controlled fabrication and electrical properties of long quasi-one-dimensional superconducting nanowire arrays. *Nano letters* **8**, 136–141 (2008).

[510] Rogachev, A. & Bezryadin, A. Superconducting properties of polycrystalline nb nanowires templated by carbon nanotubes. *Applied Physics Letters* **83**, 512–514 (2003).

[511] Astafiev, O. *et al.* Coherent quantum phase slip. *Nature* **484**, 355–358 (2012).

[512] Bezryadin, A., Lau, C. & Tinkham, M. Quantum suppression of superconductivity in ultrathin nanowires. *Nature* **404**, 971–974 (2000).

[513] Arutyunov, K. Y., Hongisto, T. T., Lehtinen, J. S., Leino, L. I. & Vasiliev, A. L. Quantum phase slip phenomenon in ultra-narrow superconducting nanorings. *Scientific reports* **2** (2012).

[514] Hriscu, A. M. & Nazarov, Y. V. Model of a proposed superconducting phase slip oscillator: A method for obtaining few-photon nonlinearities. *Phys. Rev. Lett.* **106**, 077004 (2011). URL `https://link.aps.org/doi/10.1103/PhysRevLett.106.077004`.

[515] Hriscu, A. M. & Nazarov, Y. V. Coulomb blockade due to quantum phase slips illustrated with devices. *Phys. Rev. B* **83**, 174511 (2011). URL `https://link.aps.org/doi/10.1103/PhysRevB.83.174511`.

[516] Guichard, W. & Hekking, F. W. J. Phase-charge duality in josephson junction circuits: Role of inertia and effect of microwave irradiation. *Phys. Rev. B* **81**, 064508 (2010). URL `https://link.aps.org/doi/10.1103/PhysRevB.81.064508`.

[517] Vanević, M. & Nazarov, Y. V. Quantum phase slips in superconducting wires with weak inhomogeneities. *Phys. Rev. Lett.* **108**, 187002 (2012). URL `https://link.aps.org/doi/10.1103/PhysRevLett.108.187002`.

[518] Bollinger, A., Dinsmore III, R., Rogachev, A. & Bezryadin, A. Determination of the superconductor-insulator phase diagram for one-dimensional wires. *Physical review letters* **101**, 227003 (2008).

[519] Tinkham, M. & Lau, C. N. Quantum limit to phase coherence in thin superconducting wires. *Applied Physics Letters* **80**, 2946–2948 (2002).

[520] Sivakov, A. G. *et al.* Josephson behavior of phase-slip lines in wide superconducting strips. *Phys. Rev. Lett.* **91**, 267001 (2003). URL `https://link.aps.org/doi/10.1103/PhysRevLett.91.267001`.

[521] Jelila, F. S. *et al.* Time of nucleation of phase-slip centers in $yba_2cu_3O_7$ superconducting bridges. *Phys. Rev. Lett.* **81**, 1933–1936 (1998). URL `https://link.aps.org/doi/10.1103/PhysRevLett.81.1933`.

[522] Delacour, C., Pannetier, B., Villegier, J.-C. & Bouchiat, V. Quantum and thermal phase slips in superconducting niobium nitride (nbn) ultrathin crystalline nanowire: Application to single photon detection. *Nano Letters* **12**, 3501–3506 (2012).

[523] Bawa, A., Jha, R. & Sahoo, S. Tailoring phase slip events through magnetic doping in superconductor-ferromagnet composite films. *Scientific reports* **5**, 1 (2015).

[524] Tinkham, M., Free, J., Lau, C. & Markovic, N. Hysteretic i- v curves of superconducting nanowires. *Physical Review B* **68**, 134515 (2003).

[525] Skocpol, W. J., Beasley, M. R. & Tinkham, M. Self-heating hotspots in superconducting thin-film microbridges. *Journal of Applied Physics* **45**, 4054–4066 (1974). URL `https://doi.org/10.1063/1.1663912`. `https://pubs.aip.org/aip/jap/article-pdf/45/9/4054/7953478/4054_1_online.pdf`.

[526] Skocpol, W. J. & Tinkham, M. Fluctuations near superconducting phase transitions. *Reports on Progress in Physics* **38**, 1049 (1975). URL `https://dx.doi.org/10.1088/0034-4885/38/9/001`.

[527] Das Gupta, K., Soman, S. S., Sambandamurthy, G. & Chandrasekhar, N. Critical currents and vortex-unbinding transitions in quench-condensed ultrathin films of bismuth and tin. *Phys. Rev. B* **66**, 144512 (2002). URL `https://link.aps.org/doi/10.1103/PhysRevB.66.144512`.

[528] Ning, W. *et al.* Superconductor–insulator transition in quasi-one-dimensional single-crystal nb2pds5 nanowires. *Nano letters* **15**, 869–875 (2015).

[529] Kramer, L. & Rangel, R. Structure and properties of the dissipative phase-slip state in narrow superconducting filaments with and without inhomogeneities. *Journal of low temperature physics* **57**, 391–414 (1984).

[530] Kadin, A., Smith, L. & Skocpol, W. Charge imbalance waves and nonequilibrium dynamics near a superconducting phase-slip center. *Journal of Low Temperature Physics* **38**, 497–534 (1980).

[531] Newbower, R., Beasley, M. & Tinkham, M. Fluctuation effects on the superconducting transition of tin whisker crystals. *Physical Review B* **5**, 864 (1972).

[532] Lukens, J., Warburton, R. & Webb, W. Onset of quantized thermal fluctuations in" one-dimensional" superconductors. *Physical Review Letters* **25**, 1180 (1970).

[533] Damaschke, B., Yang, X. & Tidecks, R. The hysteresis of the critical current in superconducting tin whiskers. *Journal of low temperature physics* **70**, 131–150 (1988).

[534] Tidecks, R. *Current-induced nonequilibrium phenomena in quasi-one-dimensional superconductors* (Springer, 2006).

[535] Talantsev, E. F. & Tallon, J. L. Universal self-field critical current for thin-film superconductors. *Nature communications* **6**, 1–8 (2015).

[536] Prozorov, R. & Kogan, V. G. London penetration depth in iron-based superconductors. *Reports on Progress in Physics* **74**, 124505 (2011).

[537] Mühlschlegel, B. Die thermodynamischen funktionen des supraleiters. *Zeitschrift für Physik* **155**, 313–327 (1959).

[538] Habermeier, H. U. Scaling problems and quantum limits in integrated circuit miniaturization. *AIP Conference Proceedings* **122**, 192–197 (1984). URL `https://doi.org/10.1063/1.34813`. `https://pubs.aip.org/aip/acp/article-pdf/122/1/192/11806948/192_1_online.pdf`.

[539] Bednorz, J. G. & Müller, K. A. Possible hightc superconductivity in the balacuo system. *Zeitschrift für Physik B Condensed Matter* **64**, 189–193 (1986). URL `https://doi.org/10.1007/BF01303701`.

[540] Cava, R. J. *et al.* Superconductivity in the quaternary intermetallic compounds lnni2b2c. *Nature* **367**, 252–253 (1994). URL `https://doi.org/10.1038/367252a0`.

[541] Nagamatsu, J., Nakagawa, N., Muranaka, T., Zenitani, Y. & Akimitsu, J. Superconductivity at 39 k in magnesium diboride. *Nature* **410**, 63–64 (2001). URL `https://doi.org/10.1038/35065039`.

[542] Kamihara, Y. *et al.* Iron-based layered superconductor: laofep. *J. Am. Chem. Soc.* **128**, 10012–10013 (2006). URL `https://doi.org/10.1021/ja063355c`.

[543] Yazyev, O. V. & Helm, L. Defect-induced magnetism in graphene. *Phys. Rev. B* **75**, 125408 (2007). URL `https://link.aps.org/doi/10.1103/PhysRevB.75.125408`.

[544] Jiao, L. *et al.* Chiral superconductivity in heavy-fermion metal ute2. *Nature* **579**, 523–527 (2020). URL `https://doi.org/10.1038/s41586-020-2122-2`.

[545] Kalimuddin, S. *et al.* Exceptionally slow, long-range, and non-gaussian critical fluctuations dominate the charge density wave transition. *Phys. Rev. Lett.* **132**, 266504 (2024). URL https://link.aps.org/doi/10.1103/PhysRevLett.132.266504.

[546] Kresse, G. & Hafner, J. Ab initio molecular dynamics for liquid metals. *Phys. Rev. B* **47**, 558–561 (1993). URL https://link.aps.org/doi/10.1103/PhysRevB.47.558.

[547] Kresse, G. & Furthmüller, J. Efficient iterative schemes for ab initio total-energy calculations using a plane-wave basis set. *Phys. Rev. B* **54**, 11169–11186 (1996). URL https://link.aps.org/doi/10.1103/PhysRevB.54.11169.

[548] Chatterjee, S., Saha-Dasgupta, T. & Sengupta, S. Visualizing frozen point defect tracks in fe-containing olivines. *Europhysics Letters* **98**, 29001 (2012). URL https://dx.doi.org/10.1209/0295-5075/98/29001.

[549] Ran, S. *et al.* Nearly ferromagnetic spin-triplet superconductivity. *Science* **365**, 684–687 (2019). URL https://www.science.org/doi/abs/10.1126/science.aav8645. https://www.science.org/doi/pdf/10.1126/science.aav8645.

[550] Allen, P. B. & Dynes, R. C. Transition temperature of strong-coupled superconductors reanalyzed. *Phys. Rev. B* **12**, 905–922 (1975). URL https://link.aps.org/doi/10.1103/PhysRevB.12.905.

[551] Bennemann, K. H. & Garland, J. W. Theory for Superconductivity in d-Band Metals. *AIP Conference Proceedings* **4**, 103–137 (1972). URL https://doi.org/10.1063/1.2946179.

[552] Margine, E. R. & Giustino, F. Anisotropic migdal-eliashberg theory using wannier functions. *Phys. Rev. B* **87**, 024505 (2013). URL https://link.aps.org/doi/10.1103/PhysRevB.87.024505.

[553] An, J. M. & Pickett, W. E. Superconductivity of mgb_2: Covalent bonds driven metallic. *Phys. Rev. Lett.* **86**, 4366–4369 (2001). URL https://link.aps.org/doi/10.1103/PhysRevLett.86.4366.

[554] Aslam, M. *et al.* Large enhancement of superconductivity in zr point contacts. *Journal of Physics: Condensed Matter* **30**, 255002 (2018). URL https://dx.doi.org/10.1088/1361-648X/aac154.

[555] Guillamón, I. *et al.* Superconducting density of states and vortex cores of 2h-nbs_2. *Phys. Rev. Lett.* **101**, 166407 (2008). URL https://link.aps.org/doi/10.1103/PhysRevLett.101.166407.

[556] Jérome, D., Mazaud, A., Ribault, M. & Bechgaard, K. Superconductivity in a synthetic organic conductor (tmtsf)2pf6. *J. Physique Lett.* **41**, 95–98 (1980).

[557] Xu, K. & Heath, J. R. Long, highly-ordered high-temperature superconductor nanowire arrays. *Nano Lett.* **8**, 3845–3849 (2008). URL https://doi.org/10.1021/nl802264x.

[558] Azuma, M., Hiroi, Z., Takano, M., Ishida, K. & Kitaoka, Y. Observation of a spin gap in $srcu_2o_3$ comprising spin-$\frac{1}{2}$ quasi-1d two-leg ladders. *Phys. Rev. Lett.* **73**, 3463–3466 (1994). URL https://link.aps.org/doi/10.1103/PhysRevLett.73.3463.

[559] Sánchez-Ramírez, I., Vergniory, M. G., Felser, C. & de Juan, F. Band structures of $(nbse_4)_3I$ and $(tase_4)_3I$: Reconciling transport, optics, and angle-resolved photoemission spectroscopy. *Phys. Rev. B* **107**, 205109 (2023). URL https://link.aps.org/doi/10.1103/PhysRevB.107.205109.

[560] Guguchia, Z. *et al.* Magnetism in semiconducting molybdenum dichalcogenides. *Science Advances* **4**, eaat3672 (2018). URL https://www.science.org/doi/abs/10.1126/sciadv.aat3672. https://www.science.org/doi/pdf/10.1126/sciadv.aat3672.

[561] Chen, B. *et al.* Environmental changes in mote2 excitonic dynamics by defects-activated molecular interaction. *ACS Nano* **9**, 5326–5332 (2015). URL https://doi.org/10.1021/acsnano.5b00985.

[562] Migdal, A. B. Interaction between electrons and lattice vibrations in a normal metal. *Soviet Physics JETP* **7**, 996 (1958).

[563] Eliashberg, G. M. Interactions between electrons and lattice vibrations in a superconductor. *Soviet Physics JETP* **11**, 696 (1960).

[564] Poncé, S., Margine, E., Verdi, C. & Giustino, F. Epw: Electron–phonon coupling, transport and superconducting properties using maximally localized wannier functions. *Computer Physics Communications* **209**, 116–133 (2016). URL https://www.sciencedirect.com/science/article/pii/S0010465516302260.

[565] Giannozzi, P. *et al.* Quantum espresso: A modular and open-source software project for quantum simulations of materials. *Journal of Physics: Condensed Matter* **21**, 395502 (2009).

[566] Baroni, S., Giannozzi, P. & Testa, A. Green's-function approach to linear response in solids. *Phys. Rev. Lett.* **58**, 1861–1864 (1987). URL `https://link.aps.org/doi/10.1103/PhysRevLett.58.1861`.

[567] Savrasov, S. Y. Linear response calculations of lattice dynamics using muffin-tin basis sets. *Phys. Rev. Lett.* **69**, 2819–2822 (1992). URL `https://link.aps.org/doi/10.1103/PhysRevLett.69.2819`.

[568] Gonze, X. First-principles responses of solids to atomic displacements and homogeneous electric fields: Implementation of a conjugate-gradient algorithm. *Phys. Rev. B* **55**, 10337–10354 (1997). URL `https://link.aps.org/doi/10.1103/PhysRevB.55.10337`.

[569] Baroni, S., de Gironcoli, S., Dal Corso, A. & Giannozzi, P. Phonons and related crystal properties from density-functional perturbation theory. *Rev. Mod. Phys.* **73**, 515–562 (2001). URL `https://link.aps.org/doi/10.1103/RevModPhys.73.515`.

[570] Pizzi, G. *et al.* Wannier90 as a community code: new features and applications. *Journal of Physics: Condensed Matter* **32**, 165902 (2020). URL `https://dx.doi.org/10.1088/1361-648X/ab51ff`.

[571] Hor, Y. S. *et al.* p-type bi_2se_3 for topological insulator and low-temperature thermoelectric applications. *Phys. Rev. B* **79**, 195208 (2009). URL `https://link.aps.org/doi/10.1103/PhysRevB.79.195208`.

[572] Xiao, D., Shi, J. & Niu, Q. Berry phase correction to electron density of states in solids. *Phys. Rev. Lett.* **95**, 137204 (2005). URL `https://link.aps.org/doi/10.1103/PhysRevLett.95.137204`.

[573] Yan, B., Zhang, D. & Felser, C. Topological surface states of bi2se3 coexisting with se vacancies. *physica status solidi (RRL) – Rapid Research Letters* **7**, 148–150 (2013). URL `https://onlinelibrary.wiley.com/doi/abs/10.1002/pssr.201206415`. `https://onlinelibrary.wiley.com/doi/pdf/10.1002/pssr.201206415`.

[574] Sung, H.-J. *et al.* Microscopic origin of polarity-dependent vth shift in amorphous chalcogenides for 3d self-selecting memory. *Advanced Science* **11**, 2408028

(2024). URL https://advanced.onlinelibrary.wiley.com/doi/abs/10.1002/advs.202408028. https://advanced.onlinelibrary.wiley.com/doi/pdf/10.1002/advs.202408028.

[575] Pracht, U. S. *et al.* Direct observation of the superconducting gap in a thin film of titanium nitride using terahertz spectroscopy. *Phys. Rev. B* **86**, 184503 (2012). URL https://link.aps.org/doi/10.1103/PhysRevB.86.184503.

[576] Wang, J., Arias, T. A. & Joannopoulos, J. D. Dimer vacancies and dimer-vacancy complexes on the si(100) surface. *Phys. Rev. B* **47**, 10497–10508 (1993). URL https://link.aps.org/doi/10.1103/PhysRevB.47.10497.

[577] Manna, K. *et al.* Noncollinear antiferromagnetism of coupled spins and pseudospins in the double perovskite $\mathbf{la_2cuiro_6}$. *Phys. Rev. B* **94**, 144437 (2016). URL https://link.aps.org/doi/10.1103/PhysRevB.94.144437.

[578] Chabanenko, V. V. *et al.* Magnetothermal instabilities in type ii superconductors: The influence of magnetic irreversibility. *Journal of Applied Physics* **88**, 5875–5883 (2000). URL https://doi.org/10.1063/1.1314611. https://pubs.aip.org/aip/jap/article-pdf/88/10/5875/19272530/5875_1_online.pdf.

[579] Hope, A., Naughton, M., Gajewski, D. & Maple, M. Flux jump avalanches in torque studies of single crystal yba2cu3o7. *Physica C: Superconductivity* **320**, 147–153 (1999). URL https://www.sciencedirect.com/science/article/pii/S0921453499003536.

[580] Ikuta, H., Kishio, K. & Kitazawa, K. Critical state models for flux-pinning-induced magnetostriction in type-ii superconductors. *Journal of Applied Physics* **76**, 4776–4786 (1994). URL https://doi.org/10.1063/1.357249. https://pubs.aip.org/aip/jap/article-pdf/76/8/4776/18670571/4776_1_online.pdf.

[581] Wang, Y. *et al.* Critical current density and vortex phase diagram in the superconductor $sn_{0.55}in_{0.45}Te$. *Phys. Rev. B* **106**, 054506 (2022). URL https://link.aps.org/doi/10.1103/PhysRevB.106.054506.

[582] Jung, S.-G. *et al.* A peak in the critical current for quantum critical superconductors. *Nature Communications* **9**, 434 (2018). URL https://doi.org/10.1038/s41467-018-02899-5.

[583] Palstra, T. T. M., Batlogg, B., van Dover, R. B., Schneemeyer, L. F. & Waszczak, J. V. Dissipative flux motion in high-temperature superconductors. *Phys. Rev. B* **41**, 6621–6632 (1990). URL https://link.aps.org/doi/10.1103/PhysRevB.41.6621.

[584] Blatter, G., Feigel'man, M. V., Geshkenbein, V. B., Larkin, A. I. & Vinokur, V. M. Vortices in high-temperature superconductors. *Rev. Mod. Phys.* **66**, 1125–1388 (1994). URL https://link.aps.org/doi/10.1103/RevModPhys.66.1125.

[585] Griessen, R. *et al.* Evidence for mean free path fluctuation induced pinning in $yba_2cu_3o_7$ and $yba_2cu_4o_8$ films. *Phys. Rev. Lett.* **72**, 1910–1913 (1994). URL https://link.aps.org/doi/10.1103/PhysRevLett.72.1910.

[586] Ghorbani, S. R., Wang, X. L., Shahbazi, M., Dou, S. X. & Lin, C. Fluctuation of mean free path and transition temperature induced vortex pinning in (ba,k)fe2as2 superconductors. *Applied Physics Letters* **100**, 212601 (2012). URL https://doi.org/10.1063/1.4714543. https://pubs.aip.org/aip/apl/article-pdf/doi/10.1063/1.4714543/14247721/212601_1_online.pdf.

[587] Xiang, F. X. *et al.* Evidence for transformation from tc to l pinning in mgb2 by graphene oxide doping with improved low and high field jc and pinning potential. *Applied Physics Letters* **102**, 152601 (2013). URL https://doi.org/10.1063/1.4799360. https://pubs.aip.org/aip/apl/article-pdf/doi/10.1063/1.4799360/14271429/152601_1_online.pdf.

[588] Valenta, J. *et al.* Antiferromagnetism and phase transitions in noncentrosymmetric $UIrSi_3$. *Phys. Rev. B* **97**, 144423 (2018). URL https://link.aps.org/doi/10.1103/PhysRevB.97.144423.

[589] Anand, V. K. *et al.* Specific heat and μsr study on the noncentrosymmetric superconductor $larhsi_3$. *Phys. Rev. B* **83**, 064522 (2011). URL https://link.aps.org/doi/10.1103/PhysRevB.83.064522.

[590] Mondal, M. *et al.* Phase fluctuations in a strongly disordered *s*-wave nbn superconductor close to the metal-insulator transition. *Phys. Rev. Lett.* **106**, 047001 (2011). URL https://link.aps.org/doi/10.1103/PhysRevLett.106.047001.

[591] Mondal, M. *et al.* Role of the vortex-core energy on the berezinskii-kosterlitz-thouless transition in thin films of nbn. *Phys. Rev. Lett.* **107**, 217003 (2011). URL https://link.aps.org/doi/10.1103/PhysRevLett.107.217003.

[592] Kamlapure, A. *et al.* Measurement of magnetic penetration depth and superconducting energy gap in very thin epitaxial nbn films. *Applied Physics Letters* **96**, 072509 (2010). URL https://doi.org/10.1063/1.3314308. https://pubs.aip.org/aip/apl/article-pdf/doi/10.1063/1.3314308/14428710/072509_1_online.pdf.

[593] Kim, Y. B., Hempstead, C. F. & Strnad, A. R. Critical persistent currents in hard superconductors. *Phys. Rev. Lett.* **9**, 306–309 (1962). URL https://link.aps.org/doi/10.1103/PhysRevLett.9.306.

[594] Kim, Y. B., Hempstead, C. F. & Strnad, A. R. Magnetization and critical supercurrents. *Phys. Rev.* **129**, 528–535 (1963). URL https://link.aps.org/doi/10.1103/PhysRev.129.528.

[595] Pospíšil, J. c. v. *et al.* Magnetic field induced phenomena in uirge in fields applied along the b axis. *Phys. Rev. B* **98**, 014430 (2018). URL https://link.aps.org/doi/10.1103/PhysRevB.98.014430.

[596] Hovančík, D. *et al.* Alloying-driven transition between ferromagnetism and antiferromagnetism in utge compounds: $\mathrm{Uco}_{1-x}\mathrm{ir}_x\mathrm{Ge}$. *Phys. Rev. B* **105**, 014436 (2022). URL https://link.aps.org/doi/10.1103/PhysRevB.105.014436.

[597] Kargar, F. *et al.* Metallic vs. semiconducting properties of quasi-one-dimensional tantalum selenide van der waals nanoribbons. *Nanoscale* **14**, 6133–6143 (2022). URL http://dx.doi.org/10.1039/D1NR07772D.

[598] Geremew, A. K., Rumyantsev, S., Bloodgood, M. A., Salguero, T. T. & Balandin, A. A. Unique features of the generation–recombination noise in quasi-one-dimensional van der waals nanoribbons. *Nanoscale* **10**, 19749–19756 (2018). URL http://dx.doi.org/10.1039/C8NR06984K.

[599] Mosqueira, J., Dancausa, J. D. & Vidal, F. Diamagnetism above the superconducting transition in underdoped $\mathrm{la}_{1.9}\mathrm{sr}_{0.1}\mathrm{cuo}_4$: Chemical disorder versus phase incoherent superconductivity. *Phys. Rev. B* **84**, 174518 (2011). URL https://link.aps.org/doi/10.1103/PhysRevB.84.174518.

[600] Carballeira, C., Mosqueira, J., Revcolevschi, A. & Vidal, F. First observation for a cuprate superconductor of fluctuation-induced diamagnetism well inside the finite-magnetic-field regime. *Phys. Rev. Lett.* **84**, 3157–3160 (2000). URL https://link.aps.org/doi/10.1103/PhysRevLett.84.3157.

[601] Cabo, L., Soto, F., Ruibal, M., Mosqueira, J. & Vidal, F. Anomalous precursor diamagnetism at low reduced magnetic fields and the role of T_C inhomogeneities in the superconductors $\mathrm{pb}_{55}\mathrm{in}_{45}$ and underdoped $\mathrm{la}_{1.9}\mathrm{sr}_{0.1}\mathrm{Cuo}_4$. *Phys. Rev. B* **73**, 184520 (2006). URL https://link.aps.org/doi/10.1103/PhysRevB.73.184520.

[602] Cabo, L., Mosqueira, J. & Vidal, F. Comment on "field-enhanced diamagnetism in the pseudogap state of the cuprate $bi_2sr_2cacu_2o_{8+\delta}$ superconductor in an intense magnetic field". *Phys. Rev. Lett.* **98**, 119701 (2007). URL https://link.aps.org/doi/10.1103/PhysRevLett.98.119701.

[603] Mosqueira, J., Cabo, L. & Vidal, F. Diamagnetism around the meissner transition in a homogeneous cuprate single crystal. *Phys. Rev. B* **76**, 064521 (2007). URL https://link.aps.org/doi/10.1103/PhysRevB.76.064521.

[604] Hardy, F. *et al.* Transverse and longitudinal magnetic-field responses in the ising ferromagnets urhge, ucoge, and uge_2. *Phys. Rev. B* **83**, 195107 (2011). URL https://link.aps.org/doi/10.1103/PhysRevB.83.195107.

[605] Gubina, A. S. & Zhitomirsky, M. E. Metamagnetism and tricriticalilty in the heavy-fermion ferromagnet urhge. *Phys. Rev. B* **110**, 155159 (2024). URL https://link.aps.org/doi/10.1103/PhysRevB.110.155159.

[606] Lévy, F., Sheikin, I., Grenier, B. & Huxley, A. D. Magnetic field-induced superconductivity in the ferromagnet urhge. *Science* **309**, 1343–1346 (2005). URL https://www.science.org/doi/abs/10.1126/science.1115498. https://www.science.org/doi/pdf/10.1126/science.1115498.

[607] Scofield, J. H. ac method for measuring low-frequency resistance fluctuation spectra. *Review of Scientific Instruments* **58**, 985–993 (1987). URL https://doi.org/10.1063/1.1139587. https://pubs.aip.org/aip/rsi/article-pdf/58/6/985/19250165/985_1_online.pdf.

[608] Ghosh, A., Kar, S., Bid, A. & Raychaudhuri, A. K. A set-up for measurement of low frequency conductance fluctuation (noise) using digital signal processing techniques. *arXiv preprint, cond-mat 0402130* (2004). URL https://arxiv.org/abs/cond-mat/0402130.

[609] *SR560 — Low-noise voltage preamplifier Operating Manual* (Stanford Research Systems, USA, 2023). URL https://www.thinksrs.com/downloads/pdfs/manuals/SR560m.pdf.

[610] Welch, P. The use of fast fourier transform for the estimation of power spectra: A method based on time averaging over short, modified periodograms. *IEEE Transactions on Audio and Electroacoustics* **15**, 70–73 (1967).

[611] Defatta, D., Lucas, J. & Hodgkiss, V. *Digital Signal Processing: A System Design Approach* (Wiley India Pvt. Limited, 2009). URL https://books.google.de/books?id=ly-NQQAACAAJ.

[612] Tongay, S. *et al.* Tuning interlayer coupling in large-area heterostructures with cvd-grown mos2 and ws2 monolayers. *Nano Letters* **14**, 3185–3190 (2014). URL https://doi.org/10.1021/nl500515q. PMID: 24845201, https://doi.org/10.1021/nl500515q.

[613] Ghosh, A. *Low-frequency conductance fluctuations near metal-insulator transition.* Ph.D. thesis, Indian Institute of Science, India (1999).

[614] Pal, A. N. *Physics of conductivity noise in graphene.* Ph.D. thesis, Indian Institute of Science, India (2012).

[615] Frisenda, R. *et al.* Recent progress in the assembly of nanodevices and van der Waals heterostructures by deterministic placement of 2D materials. *Chem. Soc. Rev.* **47**, 53–68 (2018). URL http://dx.doi.org/10.1039/C7CS00556C.

[616] Wang, H. *et al.* Interfacial engineering of ferromagnetism in wafer-scale van der Waals Fe_4GeTe_2 far above room temperature. *Nat. Commun.* **14**, 2483 (2023).

[617] Hu, L. *et al.* Spin-phonon coupling in two-dimensional magnetic materials. *National Science Open* **2**, 20230002 (2023).

[618] Jin, W. *et al.* Raman fingerprint of two terahertz spin wave branches in a two-dimensional honeycomb ising ferromagnet. *Nature Communications* **9**, 5122 (2018). URL https://doi.org/10.1038/s41467-018-07547-6.

[619] Kozlenko, D. P. *et al.* Spin-induced negative thermal expansion and spin–phonon coupling in van der waals material crbr3. *npj Quantum Materials* **6**, 19 (2021). URL https://doi.org/10.1038/s41535-021-00318-5.

[620] Du, K.-z. *et al.* Weak van der waals stacking, wide-range band gap, and raman study on ultrathin layers of metal phosphorus trichalcogenides. *ACS Nano* **10**, 1738–1743 (2016). URL https://doi.org/10.1021/acsnano.5b05927. PMID: 26607168, https://doi.org/10.1021/acsnano.5b05927.

[621] Sun, Y.-J., Pang, S.-M. & Zhang, J. Review of raman spectroscopy of two-dimensional magnetic van der waals materials*. *Chinese Physics B* **30**, 117104 (2021). URL https://dx.doi.org/10.1088/1674-1056/ac1e0f.

[622] Eiter, H.-M. *et al.* Raman study of the temperature and magnetic-field dependence of the electronic and lattice properties of mnsi. *Phys. Rev. B* **90**, 024411 (2014). URL https://link.aps.org/doi/10.1103/PhysRevB.90.024411.

[623] Kittel, C. *Introduction to Solid State Physics* (Wiley, 2004), 8 edn. URL http://www.amazon.com/Introduction-Solid-Physics-Charles-Kittel/dp/047141526X/ref=dp_ob_title_bk.

[624] He, G. *et al.* Phonon Anomalies Associated with Spin Reorientation in the Kagome Ferromagnet Fe3Sn2. *physica status solidi (b)* **259**, 2100169 (2022). URL https://onlinelibrary.wiley.com/doi/abs/10.1002/pssb.202100169.

[625] Balkanski, M., Wallis, R. F. & Haro, E. Anharmonic effects in light scattering due to optical phonons in silicon. *Phys. Rev. B* **28**, 1928–1934 (1983). URL https://link.aps.org/doi/10.1103/PhysRevB.28.1928.

[626] Sun, Q. C., Birkel, C. S., Cao, J., Tremel, W. & Musfeldt, J. L. Spectroscopic signature of the superparamagnetic transition and surface spin disorder in cofe2o4 nanoparticles. *ACS Nano* **6**, 4876–4883 (2012). URL https://doi.org/10.1021/nn301276q. PMID: 22540958, https://doi.org/10.1021/nn301276q.

[627] Fennie, C. J. & Rabe, K. M. Magnetic and electric phase control in epitaxial eutio 3 from first principles. *Physical review letters* **97**, 267602 (2006).

[628] Pal, R., Pal, B., Mondal, S., Mandal, P. & Pal, A. N. Unusual magnetotransport and anomalous Hall effect in quasi-two-dimensional van der Waals ferromagnet Fe_4GeTe_2. *Preprint at http://arxiv.org/abs/2303.07440* (2023).

[629] Sun, Y. J., Pang, S. M. & Zhang, J. Review of Raman spectroscopy of two-dimensional magnetic van der Waals materials. *Chinese Physics B* **30** (2021).

[630] Xu, C., Feng, J., Xiang, H. & Bellaiche, L. Interplay between Kitaev interaction and single ion anisotropy in ferromagnetic CrI3 and CrGeTe3 monolayers. *npj Computational Materials* **4** (2018).

[631] Awan, S. U., Zainab, S., Khan, M. D., Rizwan, S. & Iqbal, M. Z. 2-Dimensional magnetic materials for spintronics technology. In *SPR Nanoscience*, vol. 6, 91–119 (2020). URL http://ebook.rsc.org/?DOI=10.1039/9781788017053-00091.

[632] Yi, J. *et al.* Competing antiferromagnetism in a quasi-2D itinerant ferromagnet: Fe3GeTe2. *2D Materials* **4**, 0–18 (2017).

[633] Zhuang, H. L., C Kent, P. R. & Hennig, R. G. Strong Anisotropy and Magnetostriction in 2D Stoner Ferromagnet Fe3GeTe2. *Physical Review B - Condensed Matter and Materials Physics* (2016). URL `http://energy.gov/downloads/doe-public-access-plan`.

[634] Jha, R., Tiwari, B., Rani, P., Kishan, H. & Awana, V. Robust superconductivity with large upper critical field in nb2pds5. *Journal of Applied Physics* **115**, 213903 (2014).

[635] Morris, R., Coleman, R. & Bhandari, R. Superconductivity and magnetoresistance in nb se 2. *Physical Review B* **5**, 895 (1972).